NanoScience and Technology

Aleksandr I. Volokitin
Bo N.J. Persson

Electromagnetic Fluctuations at the Nanoscale

Theory and Applications

Springer

NanoScience and Technology

The series NanoScience and Technology is focused on the fascinating nano-world, mesoscopic physics, analysis with atomic resolution, nano and quantum-effect devices, nanomechanics and atomic-scale processes. All the basic aspects and technology-oriented developments in this emerging discipline are covered by comprehensive and timely books. The series constitutes a survey of the relevant special topics, which are presented by leading experts in the field. These books will appeal to researchers, engineers, and advanced students.

More information about this series at http://www.springer.com/series/3705

Aleksandr I. Volokitin · Bo N.J. Persson

Electromagnetic Fluctuations at the Nanoscale

Theory and Applications

Springer

Aleksandr I. Volokitin
Department of Physics
Samara State Technical University
Samara
Russia

Bo N.J. Persson
PGI-1, IAS-1
Forschungszentrum Jülich GmbH
Jülich
Germany

ISSN 1434-4904 ISSN 2197-7127 (electronic)
NanoScience and Technology
ISBN 978-3-662-53473-1 ISBN 978-3-662-53474-8 (eBook)
DOI 10.1007/978-3-662-53474-8

Library of Congress Control Number: 2016952901

Printed on acid-free paper

This Springer imprint is published by Springer Nature
The registered company is Springer-Verlag GmbH Germany
The registered company address is: Heidelberger Platz 3, 14197 Berlin, Germany

Preface

All media are surrounded by a fluctuating electromagnetic field due to the thermal and quantum fluctuations of the current densities inside them. Close to the surface, this fluctuating electromagnetic field is strongly enhanced due to the existence of evanescent electromagnetic waves. This enhancement is especially large when, on the surface, there are surface modes such as surface plasmons, surface polaritons, or the vibrational modes of adsorbates. In the presence of the surface modes, thermal radiation can exhibit spatial and temporal coherence.

In last few years, significant progress was achieved in the study of electromagnetic fluctuations at the nanoscale. This is connected with the development of new experimental methods, which made it possible to probe these fluctuations at the nanoscale, where fluctuations are much stronger than at larger length scales. Thus, the measurements of Casimir–van der Waals forces were recently carried out with unprecedented accuracy. These measurements agree with the theory of van der Waals forces up to very large distances, where retardation effects become essential, and where the interaction is determined by thermal fluctuations rather than quantum fluctuations.

In recent years, considerable attention has been devoted to the studies of electromagnetic fluctuations for non-equilibrium systems. It was theoretically predicted and experimentally confirmed that the radiative heat flux between two bodies with different temperature in the near-field region is many orders of magnitude larger than determined by the classical Stefan–Boltzmann law. Even more remarkable is the fact that, for two bodies in relative motion, the electromagnetic fluctuations result in a friction force, which is non-zero even in the absence of direct contact between the bodies, i.e. isolated from each other by a vacuum gap. This type of friction was measured between the electrons in quantum wells, and between ions in narrow channels filled with liquid. We expect even larger such non-contact effects as the technology for tailoring atomic and nanoscale materials improves.

In this monograph, a general theory of electromagnetic fluctuations is presented. Both equilibrium and non-equilibrium electromagnetic fluctuations are examined. The theory is applied for calculation of the thermal radiation, interaction forces, and the radiative heat transfer between bodies in relative motion.

This monograph is organized as follows. A brief survey of the Casimir forces, radiative heat transfer, and non-contact friction is given in the introduction (Chap. 1). Chapter 2 presents an introduction to the theory of surface electromagnetic waves. As shown in the subsequent sections, these surface waves play a key role in the emissive and reflective surface properties. A brief description of the theory of the fluctuating electromagnetic field is given in Chap. 3. Here, electromagnetic fluctuations in thermodynamic equilibrium, and for non-equilibrium systems, are examined. The general theory of the fluctuating electromagnetic field is applied to the thermal emission by plane sources (Chap. 4), Casimir interaction (Chap. 5), radiative heat transfer (Chap. 6) and Casimir friction for the plate–plate (Chap. 7) and particle–plate (Chap. 8) configurations. Special attention is paid to the possible mechanisms of enhancement of the radiative heat transfer and Casimir friction. The theory of the frictional drag in nanostructures, induced by the fluctuating electromagnetic field, is examined in Chap. 9. The friction drag, which appears in low-dimensional electronic systems, and in narrow channels with polar liquid, is studied. Special attention is devoted to Casimir physics for graphene (see Chap. 10), a material that has been proposed for the micro- and nanoelectromechanical systems of future generations. Quantum Vavilov–Cherenkov radiation, associated with the uniform motion of a neutral object is considered in Chap. 11. The phononic heat transfer for planar and rough interfaces is considered in Chaps. 12 and 13, respectively. The theory of electrostatic friction is presented in Chap. 14. This mechanism of friction is connected with the electromagnetic field, created outside the moving body by static electric charges, which are always present on the surface due to it heterogeneity, or due to an applied voltage. Enhancement of the electrostatic friction due to the vibrational modes of adsorbates and 2D electron structures is analyzed. The non-contact friction theory is compared with experimental measurements. The friction resulting from the emission of acoustic phonons, and due to the internal friction, is studied in the Chap. 15.

The details of some calculations, which are not of direct physical interest, are given in the appendices.

Samara, Russia — Aleksandr I. Volokitin
Jülich, Germany — Bo N.J. Persson

Contents

Abstract

The theory of the electromagnetic fluctuations at the nanoscale, which is important for many technology problems, is presented. The theory is applied to Casimir forces, near-field radiative heat transfer, and to non-contact friction between nanostructures, and many theory predictions are compared to experiments. This book is mainly based on the publications of authors on the theory of the fluctuating electromagnets field and its manifestations at the nanoscale, and will be useful to researchers, engineers, and graduate and undergraduate students, who are specialized in the field of the physics and technology of nanostructures.

Chapter 1
Introduction

Electromagnetic fluctuations are related to one of the most fundamental phenomena in nature, namely Brownian motion. In [1–4], the nature of this motion is discussed, and its statistical features are investigated. Studies of the thermal radiation from materials have played an important role in the history of physics. It is enough to mention that quantum mechanics originated from attempts to explain paradoxical experimental results related to black body radiation. In 1900, Max Planck used quantum theory to explain the puzzling nature of the spectral density of thermal far-field radiation. However, Planck realized that the situation becomes more complex in the near-field region, when the distance from the surface of the body becomes smaller than the characteristic wavelength of thermal radiation. In the early 20th century, the spectral properties of thermal electromagnetic fluctuations were reliably studied in two limiting cases. In the first case, which corresponds to the quasistationary region of the spectrum, the Nyquist formula was obtained, which describes the spectral intensity of noise in an arbitrary passive one-port with a given impedance. In the second case, the Planck and Kirchhoff formulas were obtained, which describe the energy spectral density and the equilibrium radiation intensity. In the middle of the 20th century, Rytov created the general correlation theory of electromagnetic fluctuations on the basis of Maxwell's equations [5–7]. From Rytov's theory, one can obtain the spectrum of fluctuations in the system for arbitrary relation between its significant dimensions and characteristic wavelength of thermal radiation field. In this case, the Nyquist's and Kirchhoff's laws follow as two limiting cases. A remarkable contribution to the theory of fluctuation phenomena is the fluctuation-dissipation theorem established by Callen and Welton [8], which connects the spectral density of the fluctuations of the dynamic system that are characteristic of its dissipative properties.

The study of electromagnetic fluctuations is an important part of modern fundamental and applied science, because it is precisely the fluctuations of the electromagnetic field that determine a large class of important physical phenomena, such as the van der Waals interaction; the Casimir force, which can be considered as a special

A.I. Volokitin and B.N.J. Persson, *Electromagnetic Fluctuations at the Nanoscale*,
NanoScience and Technology, DOI 10.1007/978-3-662-53474-8_1

case of the van der Waals interaction; radiative heat transfer and Casimir friction between bodies separated by a vacuum gap; the capture of atoms, molecules and coherent material states by electromagnetic traps; and a number of major physico-chemical phenomena near the surface of condensed media, such as the adsorption and desorption of atoms and molecules. Electromagnetic fluctuations lead to a change in the conditions and characteristics of the spontaneous photon emission of atoms and molecules near surfaces, the shift of their energy levels, and the complete or partial removal of degeneracy, which can substantially change the dynamics of the phenomena. We emphasize that a study of resonance states in the spectra of thermally stimulated fields allows the eigenmodes of the system to be discovered, i.e., its volume and surface polaritons, whose properties are totally determined by the electrodynamic and geometric characteristics of the system. At present, in connection with new experiments, interest in Casimir physics is being revived. Figure 1.1 illustrates the connection between the Casimir physics and Brownian motion.

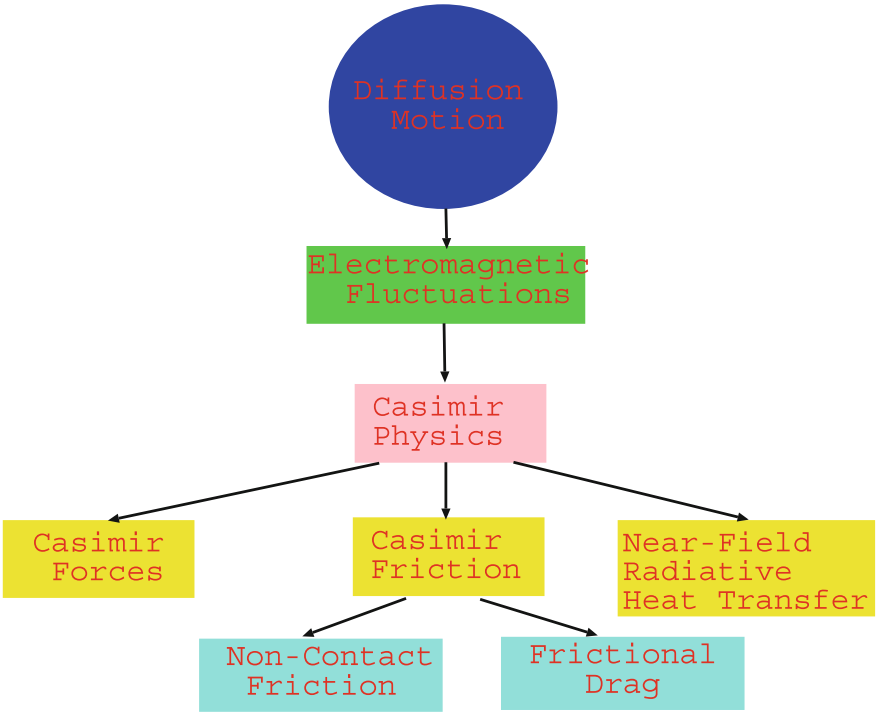

Fig. 1.1 Relationship between Casimir physics and Brownian motion. The electromagnetic fluctuations are the cornerstone of the Casimir physics, which includes Casimir forces, Casimir friction and near-field radiative heat transfer. These fluctuations are described in the fluctuational electrodynamics by introducing a 'random' field into the Maxwell equation (just as, for example, one introduces a 'random' force in the theory of Brownian motion)

In the past, the non-radiative near-field part of the electromagnetic radiation was usually ignored, because it plays no role in the far-field properties of emission from planar sources. Nevertheless, recent interest in microscale and nanoscale radiative heat transfer [9–15], together with the development of local-probe thermal microscopy [17, 18] has raised new challenges. These topics, and the recent progress in detecting the non-contact friction force on a subattonewton level [19–21, 23–27], and the observation of coherent thermal emission from materials [28–38], have the substantial role of the non-radiative (evanescent) thermal electromagnetic field in common. The physical mechanisms and phenomena occurring at the nanoscale have received significant attention over the last decade because of improvements in nanostructure fabrication, the development of advanced scanning probe microscopy and interest in basic research. The findings have implications for topics such as thermophotovoltaics, nano-electromechanical systems, heat-assisted magnetic recording, heat-assisted litography, the design of devices that rely on resonant or coherent heat emission, and nano-antennas.

1.1 Fluctuations and the Physical Origin of the van der Waals and Casimir Forces

There are four known fundamental forces: electromagnetism, gravity, and weak and strong interactions. Weak and strong interactions manifest themselves on length scales in the order of the size of a nucleus; whereas, at larger distances, electromagnetism and gravity prevail. It may therefore come as a surprise that two macroscopic non-magnetic bodies with no net electric charge (or charge moments) can experience an attractive force much stronger than gravity. This force was predicted in 1948 by Hendrik Casimir [39], and now bears his name. The existence of this force is one of the few direct macroscopic manifestations of quantum mechanics; others are superfluidity, superconductivity, kaon oscillations, and the black body radiation spectrum.

The origin of both the van der Waals and Casimir forces is connected to the existence of quantum and thermal fluctuations. Two neutral particles have fluctuating dipole moments resulting from quantum or thermal effects, which, for the particle separation d, lead to a d^{-6} interaction energy. This long-range attraction is often the dominant interactions between atoms and molecules. Physically, this attraction arises as shown in Fig. 1.2a: whenever one particle acquires a spontaneous dipole moment $\mathbf{p}_1$, the resulting dipole electric field (black lines) polarizes the adjacent particle to produce an induced dipole moment $\mathbf{p}_2 \sim d^{-3}$. Assuming positive polarizabilities, these two dipoles are oriented so as to attract each other, with an interaction energy that scales as d^{-6}. This leads to the van der Waals 'dispersion' force, and similar considerations apply to particles with permanent dipole moments that can rotate freely. The key to a more general theory of the Casimir interaction is to understand that this d^{-6} scaling of van der Waals forces is based two crucial approximations,

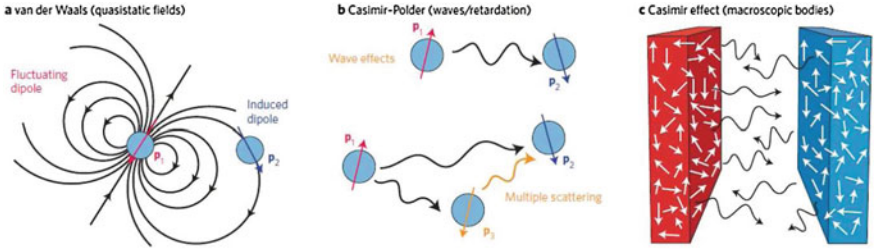

Fig. 1.2 Relationship between van der Waals, Casimir-Polder and Casimir forces, whose origins lie in the quantum fluctuations of dipoles. **a**, A fluctuating dipole $\mathbf{p}_1$ induces a fluctuating electromagnetic dipole field, which in turn induces a fluctuating dipole $\mathbf{p}_2$ on a nearby particle, leading to van der Waals forces between the particles. **b**, When the particle spacing is large, retardation/wave effects modify the interaction, leading to Casimir-Polder forces. When more than two particles interact, the non-additive field interactions lead to a breakdown of the pairwise force laws. **c**, In situations consisting of macroscopic bodies, the interaction between the many fluctuating dipoles present within the bodies leads to Casimir forces. From [64]

that are not always valid: it neglects wave effects (quasi-static approximation), and also neglects multiple scattering if there are more than two particles. The quasi-static approximation assumes that the dipole moment $\mathbf{p}_1$ polarizes the second particle instantaneously, which is valid if d is much smaller than the typical wavelength of the fluctuating fields. For such separations, retardation effects are negligible. In this separation region, the dispersion force is usually called the van der Waals force. This is a non-relativistic quantum phenomenon and its theory was pioneered by London (1930) [40]. However, the finite speed of light must be taken into account when d is much larger than the typical wavelength, as shown in Fig. 1.2b, and it turns out that the resulting Casimir-Polder interaction energy asymptotically scales as d^{-7} for large values of d. At such separations, the dispersion forces are usually called *Casimir* forces (for interaction between two macroscopic bodies) or *Casimir-Polder* forces (for atom-atom and atom-wall interactions). These are both relativistic and quantum-mechanical phenomena first described by Casimir (1948) [39] and by Casimir and Polder (1948) [41], respectively. More generally, the interaction is not a simple power law between these limits, but instead depends on an integral of fluctuations at all frequencies scaled by a frequency-dependent polarizability of the particles.

The presence of more than two particles further complicates the situation because multiple scattering must be considered (Fig. 1.2b). For example, with three particles, the initial dipole $\mathbf{p}_1$ will induce polarizations $\mathbf{p}_2$ and $\mathbf{p}_3$ in the other two particles, but $\mathbf{p}_2$ will create its own field that further modifies $\mathbf{p}_3$, and so on. Thus, the interaction between multiple particles is generally non-additive, and there is no two-body force law that can simply be summed to incorporate all interactions. Multiple scattering is negligible for a sufficiently dilute gas or for weak polarizabilities, but it becomes very important for interactions between two (or more) solid bodies, which consist of many fluctuating dipoles that all interact in a complicated way through the electromagnetic radiation (Fig. 1.2c). When these multiple scattering effects are combined with wave retardation in a complete picture, they yield the Casimir force.

Hendrik Casimir based his prediction on a simplified model involving two parallel perfectly conducting plates separated by a vacuum. Although the Casimir force arises from electromagnetic fluctuations, real photons are not involved. Quantum mechanically, these fluctuations can be described in terms of virtual photons of energy that are equal to the zero-point energies of the electromagnetic modes of the system. By considering the contribution of the electromagnetic field modes to the zero-point energy (U) of the parallel plate configuration, Casimir predicted an attractive force between the plates. Because only electromagnetic modes that have nodes on both walls can exist within the cavity, the mode frequencies (ω) depend on the separation between the plates, giving rise to a pressure of $P_0 = -\partial U_0/\partial d$:

$$U_0(d) = -\frac{\pi^2 \hbar c}{720 d^3}, \quad P_0(d) = -\frac{\pi^2 \hbar c}{240 d^4} \tag{1.1}$$

where c is the vacuum speed of light and $\hbar$ is the reduced Planck's constant. The force in this case is attractive because the mode density in free space is larger than that between the plates. Ideal metals are characterized by perfect reflectivity at all frequencies, which means that the absorption wavelength is zero. Thus, the results (1.1) are universal and valid at any separation distance. They do not transform to the non-relativistic London forces at short separations. Due to the difference in these early theoretical approaches to the description of the dispersion forces, the van der Waals and Casimir-Polder (Casimir) forces were originally thought of as two different kinds of forces rather than two limiting cases of a single physical phenomenon, which is how they are presently understood.

A unified theory of both the van der Waals and Casimir forces between plane parallel material plates in thermal equilibrium separated by a vacuum gap was developed by Lifshitz (1955) [42]. Lifshitz's theory describes dispersion forces between dissipative media as a physical phenomenon caused by the fluctuating electromagnetic field that is always present in both the interior and the exterior of any medium. To calculate the fluctuating electromagnetic field, Lifshitz used Rytov's theory [5–7]. Rytov's theory is based on the introduction into the Maxwell equation of a 'random' field (just as, for example, one introduces a 'random' force in the theory of Brownian motion). The fundamental characteristic of the random field is the correlation function, determining the average value of the product of component of this field at two different points in space. Initially, Rytov found this correlation function using a phenomenological approach. Later, Rytov's formula for the correlation function of the random field was rigorously proved on the base of the fluctuation-dissipation theorem. According to the fluctuation-dissipation theorem, there is a connection between the spectrum of fluctuations of the physical quantity in an equilibrium dissipative medium and the generalized susceptibilities of this medium, which describe its reaction to an external influence. Using the theory of the fluctuating electromagnetic field, Lifshitz derived general formulas for the free energy and force of the dispersion interaction. In the limit of dilute bodies, these formulas describe the dispersion forces acting between atoms and molecules. In the framework of the Lifshitz theory, material properties are represented by the frequency dependent dielectric

permittivities and atomic properties by the dynamic atomic polarizabilities. In the limiting cases of small and large separation distances, in comparison with the characteristic absorption wavelength, the Lifshitz theory reproduces the results obtained by London and by Casimir and Polder, respectively. It also describes the transition region between the non-relativistic and relativistic limits.

Both quantum and thermal fluctuations contribute to the Casimir force. The general theory of Casimir-van der Waals forces was developed in [43] using quantum field theory. This theory confirmed the results of Lifshitz's theory. Quantum fluctuations dominate at small separation ($d < \lambda_T = c\hbar/k_B T$) and thermal fluctuations dominate at large separation ($d > \lambda_T$). Casimir forces due to quantum fluctuations have long been studied experimentally [44–56]. However, Casimir forces due to thermal fluctuations were measured only recently, and these measurements confirmed Lifshitz's theory [57]. At present, interest in Casimir forces is increasing since it was shown that it is possible to measure these forces with high accuracy [44–57]. Casimir forces often dominate the interaction between nanostructures, and can result in adhesion and mechanical failure between moving parts in small devices such as micro- and nano-electromechanical systems [55, 56, 58, 59] (MEMS and NEMS). Due to this practical interest and the fast progress in force detection techniques, experimental [57, 60–63] and theoretical [64, 65] investigations of Casimir forces have experienced an extraordinary 'renaissance' in the past few years. Various corrections to these forces have been studied, such as finite conductivity [66], or temperature corrections [67, 68].

The Lifshitz theory was formulated for systems at thermal equilibrium. At present, there is an interest in the study of systems outside of the thermal equilibrium, in particular, in connection with the possibility of tuning the strength and sign of the interaction [69–71]. Such systems also present a way to explore the role of thermal fluctuations, which are usually masked at thermal equilibrium by the $T = 0$ K component, which dominates the interaction up to very large distances, where the interaction force is very small. In [71], the Casimir-Polder force was measured at very large distances, and it was shown that the thermal effects on the Casimir-Polder interaction agree with the theoretical prediction. This measurement was taken outside of thermal equilibrium, where thermal effects are stronger.

The fluctuating electromagnetic field in the Lifshitz theory is the classical analog of vacuum (zero-point) oscillations in the field-theoretical approach developed by Casimir. van Kampen et al. (1968) [72], Ninham et al. [73], Gerlach (1971) [74] and Schram (1973) [75] narrowed the distinction between the Casimir and Lifshitz approaches. They obtained the Lifshitz formulas for free energy and force between two non-dissipative material plates as the difference between the free energies of zero-point and thermal oscillations in the presence and in the absence of plates. The eigenfrequencies of these oscillations were found from the standard continuity boundary conditions for the electric and magnetic induction fields on the surfaces of the dielectric plates. Later, Barash and Ginzburg (1975) [76] generalized this approach for the case of plates made of dissipative materials in thermal equilibrium with a heat reservoir. This generalization was presented by Millonni (1994) [45] and by Mostepanenko and Trunov (1997) [77]. The applicability of the Lifshitz formula

to dissipative materials was also demonstrated using the scattering approach (Genet Lambrecht and Reynaud 2003) [78].

The theoretical foundations of the Casimir interaction are based on two approaches. The first approach is based on the theory of the equilibrium electromagnetic fluctuations in the media. In the second approach, the Casimir effect is a vacuum quantum effect resulting from the influence of external conditions and is described by quantum field theory. In this case, boundary conditions are imposed (in place of material boundaries) that restrict the quantization volume and affect the spectrum of zero-point and thermal oscillations. In fact, the two different approaches can be reconciled. There are derivations of the Lifshitz formulas and more general results in different media where the dispersion force is viewed as a vacuum quantum effect [79, 80]. The common roots in the theory of electromagnetic oscillations relate the Casimir effect to other fluctuation phenomena, such as the radiative heat transfer through a vacuum gap and the Casimir friction [11]. However, its origin in quantum field theory relates the Casimir effect to other quantum vacuum effects such as the Lamb shift and the anomalous magnetic moment of an electron, where virtual particles play an important role [81].

During the last few years, far-reaching generalizations of the Lifshitz formulas were obtained that express Casimir energy and the force between two separated bodies of arbitrary shape in terms of matrices of infinite dimensions. This is often referred to as the representation of Casimir energy in terms of functional determinants [82–84] or in terms of scattering matrices [85, 86]. Overviews of the Casimir effect are given, for example, in [60, 87–90].

1.2 Radiative Heat Transfer

The radiative heat flux per unit area between two black bodies separated by $d \gg \lambda_T = c\hbar/k_B T$ is given by the Stefan-Boltzmann law

$$S = \frac{\pi^2 k_B^4}{60\hbar^3 c^2}\left(T_1^4 - T_2^4\right), \tag{1.2}$$

where T_1 and T_2 are the temperatures of solid 1 and 2, respectively, and c is the velocity of light. In this limiting case, the heat transfer between two bodies is determined by the propagating electromagnetic waves (far field) radiated by the bodies and does not depend on the separation d (see Fig. 1.3). These propagating waves always exist outside any body due to thermal and quantum fluctuations of the current density inside the body. Quantum fluctuations are related to the uncertainty principle, and exist also at zero temperature. Thermal fluctuations are due to the irregular thermal motion of the particles in the medium, and vanish at zero temperature. The electromagnetic field created by this fluctuating current density exists not only in the form of propagating waves but also in the form of evanescent waves, which are damped exponentially with the distance away from the surface of the body. This fluctuating electromagnetic field exists even at zero temperature, generated by quantum fluctuations. For an isolated

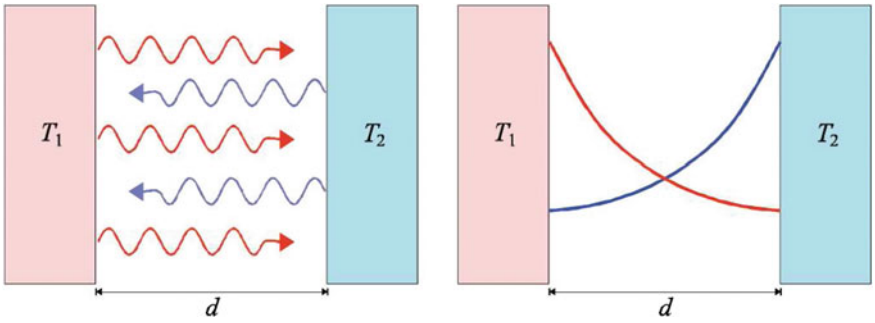

Fig. 1.3 There are two modes for exchange of heat between two surfaces separated by vacuum: **a** conventional radiative heat transfer via propagating electromagnetic waves; and **b** photon tunneling via evanescent waves

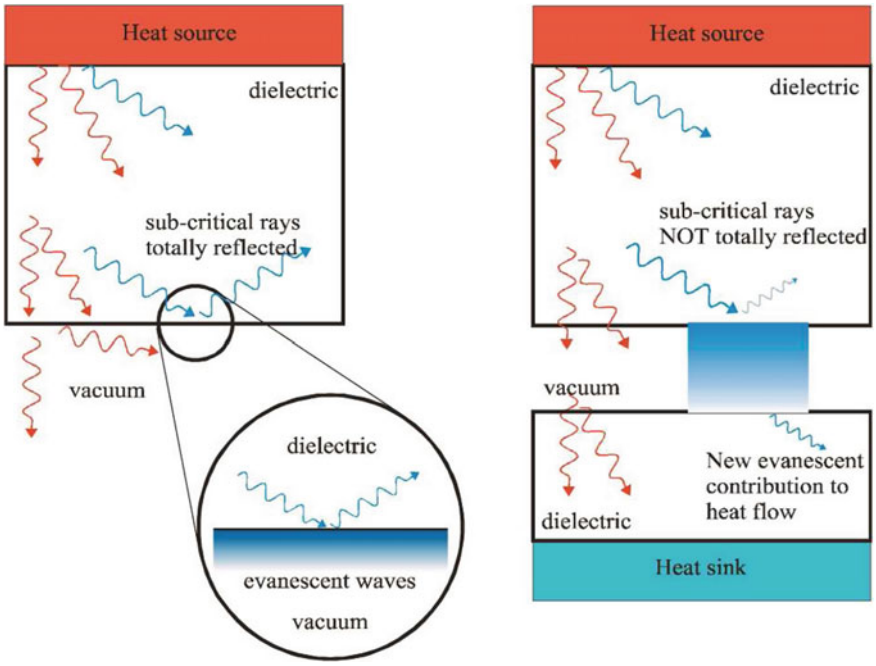

Fig. 1.4 Evanescent waves play no role in thermal radiation from a hot dielectric surface to vacuum (*left*), but evanescent waves can carry heat from a hot to a cold dielectric surface (*right*)

body the evanescent waves do not give any contribution to the energy radiation, which is determined by Stefan-Boltzmann law. However, for two solids separated by $d < \lambda_T$, the heat transfer may increase by many orders of magnitude due to the evanescent electromagnetic waves; this is often refereed to as photon tunneling. The concept of photon tunneling can be neatly illustrated by considering a transparent dielectric such as glass (see Fig. 1.4). Within the dielectric, black body radiation has

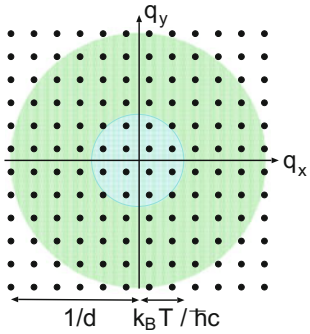

Fig. 1.5 At short distances, evanescent states dominate in phase space: propagating photon modes carry heat flux within the inner circle (with the radius $k_B T/\hbar c$), evanescent modes within the outer circle (with the radius d^{-1})

a higher density than in the vacuum, as can be seen from (1.2); if the velocity of light is reduced, the density of radiation increases. The extra radiation is contained in waves that have large wave vectors, q parallel to the surface. The normal component of the wave vector, which in the vacuum region is given by $p_z = \sqrt{(\omega/c)^2 - q^2}$, will be pure imaginary for $q > \omega/c$, where ω is the electromagnetic wave frequency. This means that the photons with $q > \omega/c$ can not escape from the body, and will be totally reflected from the surface. This phenomenon is known as total internal reflection. Thus, the surface reflects just the right amount of radiation to ensure that the intensity of the black body radiation emerging into vacuum does not exceed that allowed by (1.2).

It is well known that a second dielectric, if close enough to the first one, will modify the internal reflection condition so that some of the 'evanescent photons' tunnel across into the second medium.

Let us consider the electromagnetic field at a distance d from a surface. The region in the q-space occupied by the propagating waves is $q < k_B T/\hbar c$. The phase space region occupied by the evanescent waves is $q < d^{-1}$. Thus, as illustrated in Fig. 1.5, at short distance $d \ll \lambda_T$ the number of photon states available to conduct heat may be much larger for the evanescent waves than for the propagating waves. At low temperatures (a few Kelvin), it is possible for photon tunneling to dominate the heat transfer even at a spacing of a few mm, see Table 1.1.

A great deal of attention has been devoted to the radiative heat transfer due to evanescent waves in connection with scanning tunneling microscopy (STM), and scanning thermal microscopy (SThM), under ultrahigh vacuum conditions [9–15, 17, 18]. It is now possible to measure extremely small amounts of heat transfer into small volumes [91]. STM can be used for local heating of the surface, resulting in local desorption or decomposition of molecular species, and this offers further possibilities for the control of the local chemistry at surfaces by STM [92].

The problem of the radiative heat transfer between two flat surfaces was considered many years ago by Polder and Van Hove [93]; Levin and Rytov [94]; and, more recently, by Loomis and Maris [95]; Pendry [12]; Volokitin and Persson [13–15]; and Joulain et al. [9]. Polder and Van Hove were the first to obtain the correct formula for the heat transfer between two flat surfaces. In their investigation, they used Rytov's

Table 1.1 The critical distance λ_T as a function of temperature. For surface separation $d < \lambda_T$ the heat transfer is dominated by the contribution from the evanescent electromagnetic modes. At distances of a few nanometers, radiative heat flow is almost entirely due to the evanescent modes

T(K)	λ_T (μm)
1	2298.8
4.2	545.2
100	22.9
273	8.4
1000	2.3

theory [5–7] of the fluctuating electromagnetic field. Later, this formula was rederived in [95]. However, Polder and Van Hove presented their result within the local optic approximation, where the spatial variation of the dielectric function is neglected. Thus, material for which non-local optical properties (such as the anomalous skin effect) are important, and are excluded from their treatment. In general, non-local optic effects become very important for short separation between bodies when

$$d < v_F \hbar / k_B T,\ l,$$

where v_F is the Fermi velocity, and l is the electron mean free path [191, 197]. In typical cases, non-local optic effects become very important for $d < 1000$ Å [13]. In the subsequent treatment, they made numerical calculations not of the heat flux itself, but of its derivative with respect to temperature, i.e., their numerical result is valid only for small temperature differences. Pendry considered only the non-retarded limit. The first theory that included non-local optic and retardation effects was developed by Volokitin and Persson [13], who used the general theory described above. Levin and Rytov [94] used the generalized Kirchhoff's law [6] to obtain an expression for the radiative heat transfer between two good conductor surfaces. They studied the case of good conductors in detail, in both the normal and the anomalous skin effect region. Pendry [12] gave a more compact derivation of the formula for the heat flux between two semi-infinite bodies due to evanescent waves and calculated the heat transfer between a point-dipole and a surface. Volokitin and Persson [13] considered the problem of heat transfer between two flat surfaces as a particular application of a general theory of the fluctuating electromagnetic field for heat transfer between bodies with arbitrary shape. They numerically investigated the dependence of the heat flux on the dielectric properties of the bodies, both in the local optic approximation and using the non-local optic dielectric approach, and found that, for good conductors, even for very small distances, the heat flux is dominated by retardation effects. The efficiency of the radiative heat transfer depends strongly on the dielectric properties of the media. It was found in these works that the heat flux diverges as the distance decreases if the temperature difference is assumed to be kept at a constant value. These results were obtained using a macroscopic theory where the spatial variation of the dielectric function was neglected. This macroscopic theory

is only valid if the separation between bodies is much larger than the interatomic distances inside the bodies. However, it is possible to determine an upper limit for the heat flux, which at short separations depends only on the properties of the materials [12] (see also Chap. 6). This result is linked to quantum information theory, which dictates that the maximal heat tunneling current in one channel is determined by the temperature alone [12, 96]. The role of non-local dielectric response for the thermal electromagnetic field near a planar surface was discussed in [13, 97].

In [12, 13, 15], it was shown that the heat flux can be greatly enhanced if the conductivities of the materials are chosen to maximize the heat flow due to photon tunneling. At room temperature, the heat flow is maximal at conductivities corresponding to semi-metals. In fact, only a thin film ($\sim$10 Å) of a high-resistivity material is needed to maximize the heat flux. Another enhancement mechanism of the radiative heat transfer can be connected with resonant photon tunneling between states localized on the different surfaces. Recently it was discovered that resonant photon tunneling between surface plasmon modes gives rise to an extraordinary enhancement of the optical transmission through sub-wavelength hole arrays [98]. The same coupling will enhance the radiative heat transfer (and the Casimir friction [99, 100]) if the frequency of these modes is sufficiently low enough to be excited by thermal radiation. At room temperature, only the modes with frequencies below $\sim 10^{14}$ s^{-1} can be excited. For normal metals, surface plasmons have much too high frequencies; at thermal frequencies, the dielectric function of normal metals becomes nearly purely imaginary, which excludes surface plasmon enhancement of the heat transfer for good conductors. However, surface plasmons for semiconductors are characterized by much smaller frequencies and by damping constants, and they can contribute significantly to the heat transfer.

Enhancement of the heat transfer due to resonant photon tunneling between surface plasmon modes localized on the surfaces of semiconductors was predicted by Mulet et al. [16] and Volokitin and Persson [14, 15]. In these cases, multiple scattering of electromagnetic waves by the surfaces of the bodies becomes important. In particular, at sufficiently small separation d, the photons go back and forth several times in the vacuum gap, building up a coherent constructive interference in the forward direction, as would occur in resonant electron tunneling. In this case, the surface plasmons on the isolated surfaces combine to form a 'surface plasmon molecule', in much the same way as electronic states of isolated atoms combine to form molecular levels. This will result in a very weak distance dependence of the heat flux, because the photon transmission probability does not depend on d in this case (see below). For large d, sequential tunneling is more likely, where a surface plasmon mode decays by emitting a photon, which tunnels to the other surface where it excites a plasmon, and then couples to the other excitations in the media and exits. Other surface modes that can be excited by thermal radiation are adsorbate vibrational modes. Especially for parallel vibrations, these modes may have very low frequencies. Adsorbate vibrational mode enhancement of the radiative heat transfer was predicted by Volokitin and Persson [14, 15] using a macroscopic approach [14] for separation $d > b$, and a microscopic approach [15] for $d < b$, where b is the interatomic distance between the adsorbates. In the latter case, the heat transfer

occurs through the energy exchange between separate adsorbates. Persson et al. [92] showed that localized photon tunneling between adsorbates can be used for vibrational heating of molecules adsorbed on insulating surfaces. The heat transfer between two small particles (when the size of the particles is much smaller than separation between them) was first studied by Volokitin and Persson [13], and later by Domingues et al. [101]. It has been shown that at small separation ($d \ll \lambda_T$) the dipole-dipole interaction yields a large contribution to the heat transfer, whereas the contribution of the photon emission and absorption process is negligible. This near-field transfer between nanoparticles is analogous to the energy transfer between molecules due to the dipole-dipole coupling, known as Forster transfer [102].

The first measurements of the radiative heat transfer between two chromium bodies with flat surfaces was performed by Hargreaves [103]. However, placing two flat parallel plates at a constant separation of a few hundred nanometers was difficult to achieve. Later studies employing an indium needle in close proximity to a planar thermocouple remained inconclusive [104]. More recently, an unambiguous demonstration of near-field radiative heat transfer under ultrahigh vacuum conditions was given in [18, 105]. In the experiment, the heat transfer was measured between a gold-coated scanning tunneling microscope and a plate of gold or GaN. It was found that for tip-sample distances below 10 nm, the heat flux differs markedly from the divergent behavior predicted by macroscopic theory in which the local optic approximation is used. While the shortcomings of the local optic approximation in macroscopic theory are well known [7, 107], their manifestation in an actual experiment indicates a still unexplored potential of thermal microscopy as a new, quantitative tool for the nanometer-scale investigation of solids. Unfortunately, the geometry of the experiment in [18, 106] was too complex to allow for a quantitative comparison with theory. Even today, a constant separation of a few tens-of-nanometers between plates has not been accomplished. This problem forced most experimental groups investigating heat transfer and forces between two surfaces to switch to a plane-sphere geometry, which is much easier to align. The first measurements between two dielectric materials in the plane-sphere geometry were reported in [108, 109]. In the experiment, the heat transfer between a sphere and a plate, both made from of silica, was measured from 30 nm to 10 μm separation. It was demonstrated that surface phonon polaritons dramatically enhance energy transfer between two surfaces at small gaps. In [110], the prediction given by the theory of fluctuating electromagnetic fields was confirmed, at least for separation ranging from 30 nm to 2.5 μm. Radiative heat transfer in the extreme near field down to separation as small as two nanometers was measured in [111]. The authors observed extremely large enhancements of the radiative heat transfer in the extreme near field limit between both dielectric and metal surface. The experimental results are in excellent agreement with theoretical predictions within the framework of the fluctuational electrodynamics. Thus, the experimental data provide unambiguous evidence for the validity of the fluctuational electrodynamics and local optic approximation down to very short separation in the order of one nanometer.

1.3 Non-contact Friction

For more than 30 years physicists have been interested in how Casimir forces and radiative heat transfer are modified for bodies moving relative to each other. A number of researchers have shown that the relative motion of bodies leads to a friction force [11, 115, 117–121]. Theory predicts that the Casimir friction acts even at zero temperature, where it is determined by quantum fluctuations. However, in recent years, the existence of quantum friction was hotly debated [122–127]. A general theory of Casimir forces, Casimir friction and the radiation heat transfer between moving bodies was developed by us in [128]. This theory confirmed the correctness of the previous results obtained using quantum mechanical perturbation theory [115, 117], dynamical generalization of the Lifshitz-Rytov's theory [100, 121] and quantum field theory [129].

The problem of Casimir friction is closely related to non-contact friction between nanostructures, including, for example, the frictional drag force between electrons in 2D quantum wells [112–114], and the friction force between an atomic force microscope tip and a substrate [19–23]. A great deal of attention has been devoted to the problem of non-contact friction because of its importance for ultrasensitive force detection experiments. This is because the ability to detect small forces is inextricably linked to friction via the fluctuation-dissipation theorem. According to this theorem, the random force that makes a small particle jitter would also cause friction if the particle were dragged through the medium. For example, the detection of single spins by magnetic resonance force microscopy [130], which has been proposed 3D atomic imaging [131] and quantum computation [132], will require force fluctuations (and consequently the friction) to be reduced to unprecedented levels. In addition, the search for gravitation effects at the short length scale [133], and future measurements of the Casimir and van der Waals forces [89], may eventually be limited by non-contact friction effects.

In non-contact friction, bodies are separated by a potential barrier that is thick enough to prevent electrons or other particles with a finite rest mass from tunneling across it, but allows interaction via the long-range electromagnetic field, which is always present in the gap between bodies. Non-contact friction can be investigated using an atomic force microscope, a probe which is an extremely sharp tip attached to the elastic arm (cantilever). When scanning a surface, the tip of the cantilever slides above it at short distance. This device makes it possible to register the strength of the normal and lateral force components of the interaction between the surface and the probe-tip. Various mechanisms of non-contact friction are schematically illustrated in Fig. 1.6. If the bodies are in relative motion, the fluctuating current density inside bodies will give rise to a friction which will be denoted as the *Casimir friction*. The origin of the Casimir friction is closely connected to the van der Waals-Casimir interaction. The van der Waals interaction arises when an atom or molecule spontaneously develops an electric dipole moment due to quantum fluctuations. The short-lived atomic polarity can induce a dipole moment in a neighboring atom or molecule some distance away. The same is true for extended media, where

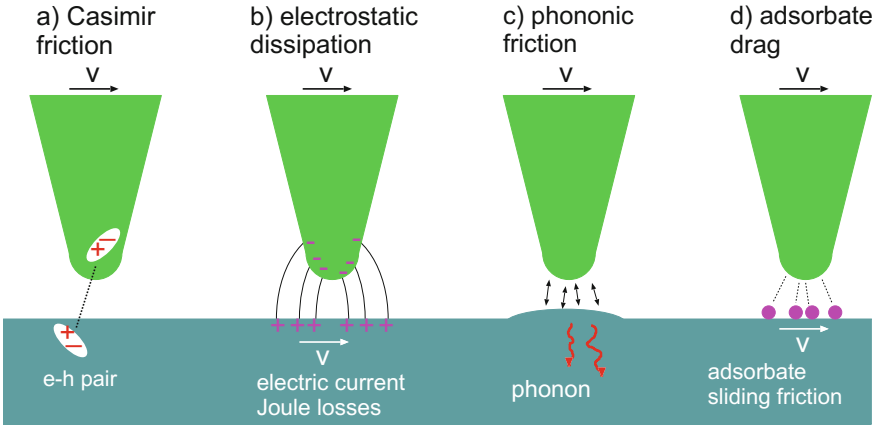

Fig. 1.6 Four different mechanisms of non-contact friction at motion of the cantilever tip parallel to the surface of a body. **a** Conservative van der Waals forces are due to the photon exchange (virtual and real) between the bodies. This process is determined by the quantum and thermal fluctuations of charge and current densities inside the bodies. In the case of a moving tip Doppler frequency shift of the emitted photons and/or time delay of the interaction leads to the Casimir friction. **b** Charged tip induces a surface image charge of opposite sign, which follows the motion of the tip and experiences the ohmic losses. That is the source of the electrostatic friction. **c** Conservative forces cause deformation of the surface. Moving deformation leads to the dissipation of energy due to emission of phonons. **d** A moving tip will induce a drag force acting on the adsorbates on surface of substrate due to the Casimir or electrostatic interaction between the tip and adsorbates. Sliding adsorbates lead to energy dissipation due to friction between adsorbates and the substrate

thermal and quantum fluctuation of the current density in one body induces a current density in the other body; the interaction between these current densities is the origin of the Casimir interaction [42, 43] (see also Chap. 5). When two bodies are in relative motion, the induced current will lag slightly behind the fluctuating current inducing it, and this is the origin of the Casimir friction (Fig. 1.6a). The van der Waals - Casimir interaction is mostly determined by exchange of virtual photons between the bodies (connected with quantum fluctuations), and does not vanish even at zero temperature. The contribution from real photons (connected with thermal fluctuations) becomes important only at large separations between bodies. On the other hand, the Casimir friction is determined by thermal or quantum fluctuations at small or large velocities, respectively. The Casimir friction at zero temperature is denoted as *quantum friction*. The Casimir friction is closely related to the Doppler effect (see Fig. 1.7). If one body emits radiation, then in the rest reference frame of the second body these waves are Doppler shifted which will result in different reflection amplitudes. Thus, photons propagating in the opposite direction will reflect differently if the reflection amplitude of the second body depends on the frequency. The same is true for radiation emitted by the second body. The exchange of 'Doppler shifted photons' is the origin of Casimir friction.

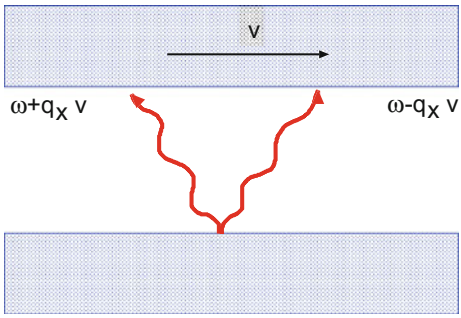

Fig. 1.7 The electromagnetic waves emitted in the opposite direction by the body at the bottom will experience opposite Doppler shift in the reference frame in which the body at the *top* is at rest. Due to the frequency dispersion of the reflection amplitude, these electromagnetic waves will reflect differently from the surface of the body at the *top*, which gives rise to momentum transfer between the bodies. This momentum transfer is the origin of Casimir friction

The presence of an inhomogeneous tip-sample electric fields is difficult to avoid, even under the best experimental conditions [21]. For example, even if both the tip and the sample were metallic single crystals, the tip would still have corners, and more than one crystallographic plane exposed. The presence of atomic steps, adsorbates, and other defects will also contribute to the spatial variation of the surface potential. This is referred to as "patch effect". The surface potential can also be easily changed by applying a voltage between the tip and the sample. An inhomogeneous electric field can also be created by charged defects embedded in a dielectric sample. The relative motion of the charged bodies will produce friction, which will be denoted as the *electrostatic friction* (Fig. 1.6b).

A moving tip will induce the dynamical deformation of surface of substrate due to the Casimir or electrostatic interaction between the tip and surface. This dynamical deformation will excite phonons in the substrate which are responsible for *phononic* mechanism of non-contact friction (Fig. 1.6c).

A moving tip will induce a drag force acting on the adsorbates on the substrate surface due to the Casimir or electrostatic interaction between the tip and adsorbates. This drag force results in a drift motion of the adsorbates relative to the substrate, and dissipation due to friction between adsorbates and substrate. This mechanism of dissipation is responsible for the adsorbate drag friction (Fig. 1.6d).

From the point of view of the quantum mechanics, the Casimir friction originates from two types of processes: (a) Excitations are created in each body with opposite momentum and the frequencies of these excitations are connected by $vq_x = \omega_1 + \omega_2$, where q_x is the momentum transfer; and (b) An excitation is annihilated in one body and created in another. The first process (a) is possible even at zero temperature, and it gives rise to a friction force, which depends cubically on sliding velocity [11, 115, 121]. The second process (b) is possible only at finite temperatures, and gives rise to a friction that depends linearly on the sliding velocity. Thus, process (b) will give the main contribution to the friction at sufficiently high temperatures, and at not too large velocities.

In contrast to the Casimir interaction, for which theory is well established, the field of Casimir friction is still controversial. As an example, different authors have studied the Casimir friction between two flat surfaces in parallel relative motion using different methods, and obtained results that are in sharp contradiction to each other. The first calculation of Casimir friction was carried out by Teodorovich [135]. Teodorovich assumed that the friction force could be calculated as the ordinary van der Waals force between bodies at rest, whose dielectric functions depend on the velocity. Such an approach is completely unjustified because it does not take into account occurrence of excitations, which are the origin of the Casimir friction. Later the same approach was used by Mahanty [136] to calculate the friction between molecules. Both theories predict wrong non-zero friction (to linear order in the sliding velocity) at absolute zero of temperature. The same nonzero linear friction at zero temperature was predicted in [137, 138]. In these works the friction force between small particle and plane surface was calculated, assuming that the friction force power is equal to the radiation power absorbed by the moving particle. From the energy conservation law it follows that in the laboratory reference frame the radiation power absorbed by moving particles is equal (with opposite sign) to the heating power inside the semi-infinite body, but it does not take into account the heating power generated inside the particle. The latter heat generation is equal to the radiation power absorbed by the particle in the rest reference frame of the particle. The right expression for the energy dissipation due to friction can be obtained as the difference between the radiation power absorbed by the particle in the rest reference frame of particle, and in laboratory reference frame [139] (see also Appendix H). A correct treatment within this approach gives a vanishing linear friction at $T = 0$ K. Schaich and Harris developed a theory [140] based on Kubo formula for the friction coefficient. This theory predicts vanishing linear friction at $T = 0$ K. However, in their calculations they made the series of unphysical approximations, and, as a result, they did not obtain the correct formula, establishing the connection of the friction coefficient with the reflection amplitude.

In [141–143], different approaches were used to calculate the friction force, and different results were obtained. The authors of these papers did not present sufficient details in order to determine exactly where there is an error. In the work by Polevoi [142], the friction force was determined from the calculation of the energy dissipation due to friction. However, as above, such an approach requires delicate considerations. All these papers predict a vanishing friction in the non-retarded limit, which formally can be obtained in the limit of infinite light velocity $c \to \infty$. However, at least for short distances, one can neglect the retardation effects when calculating Casimir friction, as well as Casimir forces. Probably, the errors of these works are related to the fact that the authors took into account the relativistic effects, but they neglected the non-relativistic effects. Pendry [115] assumed zero temperature and neglected retardation effects, in which case the friction depends cubically on the velocity. Persson and Zhang [117] obtained the formula for friction in the limit of small velocities and finite temperature, again neglecting retardation effects.

In [121, 128], we developed a theory of Casimir friction based on the dynamical modification of the well known Lifshitz theory [42] of the Casimir interaction. In the non-retarded limit and for zero temperature, this theory agrees with the results

of Pendry [115]. Similarly, in the non-retarded limit and for small sliding velocity, this theory agrees with the study of Persson and Zhang [117]. The calculation of the Casimir friction is more complicated than that of the Casimir-Lifshitz force (and of the radiative heat transfer), because it requires the determination of the electromagnetic field between moving boundaries. The solution can be found by writing the boundary conditions on the surface of each body in the rest reference frame of this body. The relation between the electromagnetic fields in the different reference frames is determined by the Lorenz transformation. In [121], the electromagnetic field in the vacuum gap between the bodies was calculated to linear order in V/c. These linear terms correspond to the mixing of electromagnetic waves with different polarizations. The waves with different polarization are statistically independent. Thus, after averaging the stress tensor over the fluctuating electromagnetic field, the mixing terms will give a contribution to the friction force in the order of $(V/c)^2$. In [121], the mixing terms were neglected, and the resulting formula for friction force is accurate to order $(V/c)^2$. The same approximation was used in [144] to calculate the frictional drag between quantum wells, and in [99, 100] to calculate the friction force between plane parallel surfaces in normal relative motion. For the case of resonant photon tunneling between surface localized states, normal motion gives drastically different result from parallel relative motion. It was shown that the friction may increase by many orders of magnitude when the surfaces are covered by adsorbates, or can support low-frequency surface plasmons. In this case, the friction is determined by resonant photon tunneling between adsorbate vibrational modes, or surface plasmon modes. When one of the bodies is sufficiently rarefied, this theory gives the friction between a flat surface and a small particle, which, in the non-retarded limit, is in agreement with the results of Tomassone and Widom [145]. A theory of the Casimir friction between a small particle and flat surface, which takes into account screening, non-local optic effects, and retardation effects, was developed in [139]. In [129], the correctness of the approach based on the dynamical modification of the Lifshitz theory was confirmed (at least to linear order in the sliding velocity v) by rigorous quantum mechanical calculations (using the Kubo formula for friction coefficient).

In [128], we presented a fully relativistic theory to the Casimir-Lifshitz forces and the radiative heat transfer at non-equilibrium conditions, when the bodies are at different temperatures, and move relative to each other with an arbitrary velocity v. In comparison with previous calculations [99, 100, 121, 144], we did not make any approximation in the Lorentz transformation of the electromagnetic field. Thus, we determined the field in one inertial reference frame from the field in another reference frame, resulting in an exact solution of the electromagnetic problem. Knowing the electromagnetic field, we calculated the stress tensor and the Poynting vector, which determined the Casimir-Lifshitz forces and the heat transfer, respectively. Upon going to the limit when one of the bodies is rarefied, we obtained the interaction force and the heat transfer for a small particle-surface configuration [150].

Philbin and Leonhardt [122, 123] (henceforth refereed to as PL) calculated the Casimir force and friction due to electromagnetic fluctuations between two perfectly flat parallel dielectric surfaces separated by a vacuum and moving parallel to each other. In [122] PL used Lifshitz theory [42, 43, 107] and considered only the case of

zero temperature. The spectral correlation function for a fluctuating electromagnetic field was expressed via the Green function of the electromagnetic field, which was assumed to have the same analytical properties as in the equilibrium case when the relative sliding velocity is zero. The cause of the discrepancy with the previous studies was identified as a failure by PL to correctly account for the modification of the analytic structure for the Green function found in the complex frequency plane when two surfaces are in relative motion [124].

The Lifshitz's theory of the van der Waals-Casimir interaction [42, 43, 107] also includes the effect of thermal radiation. The *Casimir effect* is therefore also taken to describe forces that have a contribution from thermal fluctuations as well as from the quantum fluctuations. The formalism developed by Lifshitz, however, cannot be used for plates at different temperatures. The general case of different temperatures for plates sliding relative to each other was considered in [123, 128].

In [123], PL used the same approach as in [128], which is based on a dynamic modification of the Rytov's theory. The theory presented in [123] contains, as a limiting case, the theory from [122]. For the contributions to the Casimir forces resulting from thermal fluctuations, PL obtained the same results as in [128]. However at zero temperature, PL obtained a result that contradicts a substantial body of earlier results [10, 11, 115, 121, 128]. Their conclusion was that, at zero temperature, where only quantum fluctuations occur, friction is precisely zero. In [126] (see also Appendix F), we argued for the correctness of the earlier results and pointed to the errors in the reasoning of PL.

Silveirinha proposed a theory of quantum friction [146–148], which contradicts a large number of papers devoted to the study of quantum friction, assuming that the fluctuating electromagnetic field created by moving bodies can be described by superposition of eigenmodes. All bodies have fluctuations, which are defined in the rest reference frame of the corresponding body. When bodies are moving relative to each other there is also relative motion of these fluctuations. In the simplest case, these fluctuations can be described by systems of harmonic oscillators. Thus, there may be two systems of harmonic oscillators moving relative to each other. When both systems are at rest there are eigenmodes, but when they are sliding relative to each other, the whole system has no eigenmodes because it is a time dependent problem.

At present, the Casimir friction has been studied in the configurations: plate–plate [11, 99, 100, 115, 116, 121, 128, 149], neutral particle-plate [11, 118–120, 139, 145, 150–156], and neutral particle-blackbody radiation [11, 128, 155, 157–161]. While the predictions of the theory for the Casimir forces were verified in many experiments [89], the detection of the Casimir friction is still a challenging problem for experimentalists. However, the frictional drag between quantum wells [112–114] and graphene sheets [162, 163], and the current–voltage dependence of non-suspended graphene on the surface of the polar dielectric SiO_2 [164], were accurately described using the theory of the Casimir friction [144, 149, 165]. At present frictional drag experiments [112–114, 162–164] have been performed only for weak electric fields, when the induced drift motion of the free carriers is smaller than the threshold velocity for quantum friction. Thus, in these experiments, the frictional drag is dominated by the contributions from thermal fluctuations. However, the measurements of the

current–voltage dependence [164] were performed for the high electric field, where the drift velocity is above the threshold velocity, and where the frictional drag is dominated by quantum fluctuations [149, 165]. For reviews of the Casimir friction see [10, 11].

The non-contact friction was investigated for the first time by a non-contact force microscopy setup [19–21]. Thus, Gotsmann and Fuchs [20] reported measurements of a long-range non-contact friction between an aluminum tip and a gold (111) surface. The friction force, F acting on the tip was found to be proportional to the velocity v, $F = \Gamma v$. For motion of the tip normal to the surface the friction coefficient $\Gamma(d) = C \cdot d^{-3}$, where d is the tip-sample spacing and $C = (8.0^{+5.5}_{-4.5}) \times 10^{-35}\,\mathrm{N\,s\,m^2}$. Later Stipe et al. [21] studied non-contact friction between a gold surface and a gold-coated cantilever as a function of tip-sample spacing d, temperature T, and the bias voltage V. For vibration of the tip parallel to the surface they found $\Gamma(d) = \alpha(T)(V^2 + V_0^2)/d^n$, where $n = 1.3 \pm 0.2$, and $V_0 \sim 0.2\,\mathrm{V}$. At 295 K, for the spacing $d = 100$ Å they found $\Gamma = 1.5 \times 10^{-13}\,\mathrm{kgs^{-1}}$, which is ~500 times smaller than that reported in [20] at the same distance using a parallel cantilever configuration. An applied voltage of 1 V resulted in a friction $\Gamma = 3 \times 10^{-12}$ kg/s at 300 K and $d = 20$ nm. Using the fluctuation-dissipation theorem, the force fluctuations were interpreted in terms of near-surface fluctuating electric fields interacting with static surface charge. Recently, Kuehn et al. [24] observed a large non-contact friction over polymer thin films. In [21], the non-contact friction has been also measured for fused silica samples. Near the silica surface, the friction was found to be an order of magnitude larger than for the gold sample. The silica sample had been irradiated with γ rays, which produce E' centers (Si dangling bonds) at a density of $7 \times 10^{17}\,\mathrm{cm^{-3}}$. Although the sample is electrically neutral overall, the E' centers are known to be positively charged, creating enhanced field inhomogeneity and causing the non-contact friction to rise by another order of magnitude.

Kisiel et al. [166] studied non-contact friction on a Nb film across the critical temperature, T_c using a highly sensitive cantilever oscillating in the pendulum geometry in ultrahigh vacuum. The friction coefficient Γ is reduced by a factor of three when the sample enters the superconducting state. The temperature decay of Γ is found to be in good agreement with the Bardeen-Cooper-Schrieffer theory, meaning that friction has an electronic nature in the metallic state, whereas phononic friction dominates in the superconducting state. This is supported by the dependence of friction on the probe-sample distance, d, and on the bias voltage, V Γ is found to be proportional to d^{-1} and V^2 in the metallic state, whereas $\Gamma \sim d^{-4}$ and $\Gamma \sim V^4$ in the superconducting state. Therefore, phononic friction becomes the main dissipation channel below the critical temperature.

Dorofeyev et al. [19] claim that the non-contact friction observed in [19, 20] is due to Ohmic losses mediated by the fluctuating electromagnetic field. This claim is controversial, however, since the Casimir friction for good conductors such as copper has been shown [121, 139, 144, 167] to be many orders of magnitude smaller than the friction observed by Dorofeyev et al. In [168], it was proposed that in comparison with good conductors, the Casimir friction may be strongly enhanced between the high resistivity mica substrate and silica tip. However, in the experiment et al. the

mica substrate and silica tip were coated by gold films thick enough to completely screen the electromagnetic interaction between the underlying dielectrics.

At small separation $d \sim 1$ nm, resonant photon tunneling between adsorbate vibrational modes on the tip and the sample may increase the Casimir friction by seven orders of magnitude in comparison with the good conductors with clean surfaces [99, 100]. However, the distance dependence ($\sim 1/d^6$) is stronger than that observed experimentally [21].

In [169], a theory of non-contact friction was suggested where by the friction arises from Ohmic losses associated with the electromagnetic field created by moving charges induced by the bias voltage. In the case of a spherical tip, this theory predicts the same weak distance dependence of the friction as observed in the experiment, but the magnitude of the friction is many orders of magnitude smaller than is found experimentally. In [170, 171], we have shown that the electrostatic friction can be greatly enhanced if there is an incommensurate adsorbate layer that can exhibit acoustic vibrations. This theory gives a tentative explanation for the experimental non-contact friction data [21]. The large non-contact friction observed in [24, 166] over a thin film of Nb can be also explained by the electrostatic friction [166, 172].

Chapter 2
Surface Electromagnetic Waves

As will be shown in the subsequent sections, reflection and emission of electromagnetic waves from surfaces of solids significantly depend on the presence of localized surface modes, which include surface electromagnetic waves. This particular type of wave exists at the interface between two different media. An electromagnetic surface wave propagates along the interface and decreases exponentially in the perpendicular direction. Surface waves due to a coupling between the electromagnetic field and a resonant polarization oscillation in the material are called surface polaritons. From a microscopic point of view, the surface waves at the interface of a metal is a charge density wave or plasmon. They are therefore called surface plasmon polaritons. At the interface of a dielectric, the surface wave is due to the coupling of an optical phonon with the electromagnetic field. It is thus called surface phonon polariton. Plasmon polaritons and phonon polaritons can also exist in the whole volume of the material and are called polaritons. More details on this subject can be found in textbooks such as Kittel [173, 174] and Ziman [175]. In what follows, we will focus our attention on surface polaritons propagating along a plane interface. Excellent reviews of the subject can be found in [176–179].

2.1 Surface Polaritons

Let us now study the nature of surface polaritons in the case of a plane interface separating two linear, homogeneous and isotropic media, with different dielectric constants. The system considered is depicted in Fig. 2.1.

The medium **1** (dielectric constant ε_1 and magnetic constant μ_1) fills the upper half-space $z > 0$ whereas medium **2** (dielectric constant ε_2 and magnetic constant μ_2) fills the lower half-space $z < 0$. The two media are supposed to be local and dispersive so that their complex dielectric and magnetic constants only depend on ω.

A.I. Volokitin and B.N.J. Persson, *Electromagnetic Fluctuations at the Nanoscale*,
NanoScience and Technology, DOI 10.1007/978-3-662-53474-8_2

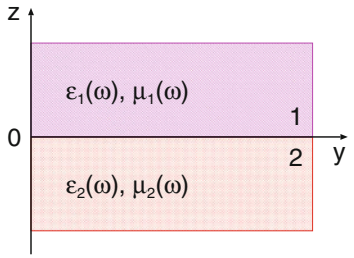

Fig. 2.1 A plane interface separating medium **1** (dielectric constant ε_1, magnetic constant μ_1) and medium **2** (dielectric constant ε_2, magnetic constant μ_2)

The three directions x, y, z shown in Fig. 2.1 are characterized by their unit vectors $\hat{\mathbf{x}}, \hat{\mathbf{y}}, \hat{\mathbf{z}}$. A point in space will be denoted $\mathbf{R} = (x, y, z) = (\mathbf{r}, z)$. Similarly, a wave vector $\mathbf{k} = (k_x, k_y, k_z) = (\mathbf{q}, k_z)$ where $\mathbf{q}$ is the component parallel to the interface and k_z is the component in the z direction.

A surface wave is a particular solution of Maxwell's equations, which propagates along the interface and decreases exponentially in the perpendicular directions. Because of the translational invariance of the system, it can be written in the form

$$\mathbf{E}_1(\mathbf{R}, z) = \begin{pmatrix} E_{x,1} \\ E_{y,1} \\ E_{z,1} \end{pmatrix} \exp\left[i(\mathbf{q} \cdot \mathbf{r} + k_{z1} z)\right], \tag{2.1}$$

$$\mathbf{E}_2(\mathbf{R}, z) = \begin{pmatrix} E_{x,2} \\ E_{y,2} \\ E_{z,2} \end{pmatrix} \exp\left[i(\mathbf{q} \cdot \mathbf{r} - k_{z2} z)\right] \tag{2.2}$$

where

$$k_{z1} = \sqrt{\varepsilon_1 \mu_1 \left(\frac{\omega}{c}\right)^2 - q^2}, \qquad \mathrm{Im} k_{z1} > 0, \tag{2.3}$$

$$k_{z2} = \sqrt{\varepsilon_2 \mu_2 \left(\frac{\omega}{c}\right)^2 - q^2}, \qquad \mathrm{Im} k_{z2} > 0, \tag{2.4}$$

where c is the speed of light in vacuum. We now look for the existence of surface waves with s (TE: transverse electric field) or p (TM: transverse magnetic field) polarization. In what follows, we shall assume that the wave propagates along the y-axis.

2.1.1 s-Polarization (TE)

In s-polarization, the electric field is perpendicular to the yz plane. The electric field, $\mathbf{E}$, is thus parallel to the x direction

$$\mathbf{E}_1(\mathbf{R}, \omega) = E_{x,1}\hat{\mathbf{x}} \exp[i(\mathbf{q} \cdot \mathbf{r} + k_{z1}z)], \tag{2.5}$$

$$\mathbf{E}_2(\mathbf{R}, \omega) = E_{x,2}\hat{\mathbf{x}} \exp[i(\mathbf{q} \cdot \mathbf{r} - k_{z2}z)]. \tag{2.6}$$

The magnetic field is then derived from the Maxwell equation $\mathbf{H} = -i\nabla \times \mathbf{E}/(\mu(\omega)\omega)$. The continuity conditions of the parallel components of the fields $\mathbf{E}$ and $\mathbf{H}$ across the interface yield the following equations:

$$E_{x,1} - E_{x,2} = 0, \tag{2.7}$$

$$\frac{k_{z1}}{\mu_1} E_{x,1} + \frac{k_{z2}}{\mu_2} E_{x,2} = 0. \tag{2.8}$$

The system of (2.7) and (2.8) has a non-trivial solution if the coefficient determinant is equal to zero. This gives

$$\mu_2 k_{z1} + \mu_1 k_{z2} = 0. \tag{2.9}$$

Taking into account (2.3) and (2.4), one obtains from (2.9) the surface wave dispersion relation for s-polarization:

$$q^2 = \frac{\omega^2}{c^2} \frac{\mu_1\mu_2[\mu_2\varepsilon_1 - \mu_1\varepsilon_2]}{\mu_2^2(\omega) - \mu_1^2(\omega)}. \tag{2.10}$$

For the particular case when $\varepsilon_1 = \varepsilon_2 = \varepsilon$, the dispersion relation takes the simple form:

$$q^2 = \frac{\omega^2}{c^2}\varepsilon \frac{\mu_1\mu_2}{\mu_2(\omega) + \mu_1(\omega)}. \tag{2.11}$$

2.1.2 *p*-Polarization (TM)

For p-polarization, the electric field lies in the yz-plane and can be written in the form:

$$\mathbf{E}_1(\mathbf{R}, z) = \begin{pmatrix} 0 \\ E_{y,1} \\ E_{z,1} \end{pmatrix} \exp\left[i(\mathbf{q} \cdot \mathbf{r} + k_{z1} z)\right], \tag{2.12}$$

$$\mathbf{E}_2(\mathbf{R}, z) = \begin{pmatrix} 0 \\ E_{y,2} \\ E_{z,2} \end{pmatrix} \exp\left[i(\mathbf{q} \cdot \mathbf{r} - k_{z2} z)\right]. \tag{2.13}$$

The continuity of the tangential electric field yields

$$E_{y,1} - E_{y,2} = 0. \tag{2.14}$$

The continuity of the z-component of displacement field yields:

$$\varepsilon_1 E_{z,1} = \varepsilon_2 E_{z,2}. \tag{2.15}$$

The condition of transversality of the electromagnetic waves gives

$$q E_{y,1} + k_{z1} E_{z,1} = 0, \quad q E_{y,2} - k_{z2} E_{z,2} = 0. \tag{2.16}$$

Using (2.14) and (2.15) in (2.16), we get

$$\varepsilon_2 k_{z1} + \varepsilon_1 k_{z2} = 0. \tag{2.17}$$

Taking into account (2.3) and (2.4), one obtains from (2.17) the surface wave dispersion relation for p-polarization:

$$q^2 = \frac{\omega^2}{c^2} \frac{\varepsilon_1 \varepsilon_2 [\mu_1 \varepsilon_2 - \mu_2 \varepsilon_1]}{\varepsilon_2^2 - \varepsilon_1^2} \tag{2.18}$$

For the particular case where $\mu_1 = \mu_2 = \mu$, the dispersion relation takes the simple form:

$$q^2 = \frac{\omega^2}{c^2} \mu \frac{\varepsilon_1 \varepsilon_2}{\varepsilon_1 + \varepsilon_2}. \tag{2.19}$$

2.1.3 Some Comments

1. When the media are non-magnetic, there are no surface waves in s-polarization. Indeed, the imaginary part of the z-components k_{zi} is always positive, so that $k_{z1} + k_{z2}$ cannot be zero.
2. At a material–vacuum interface ($\varepsilon_1 = \mu_1 = 1$), the dispersion relation for p-polarization has the form

$$q = \frac{\omega}{c}\sqrt{\frac{\varepsilon_2}{\varepsilon_2 + 1}}. \tag{2.20}$$

   It follows that the wave vector becomes very large for a frequency such that $\varepsilon_2 + 1 = 0$.
3. The conditions (2.9) and (2.17) correspond to the poles of the Fresnel reflection amplitude. Finding these poles is an alternative and simple way to find the dispersion relation. This is a particularly useful approach for the multilayers system.
4. For non-lossy media, one can find a real q corresponding to a real ω. This mode exists only if $\varepsilon_2 < -1$ in the case of an interface separating a vacuum from a material.
5. In the presence of losses, the dispersion relation yields two equations but both frequency and wavector can be complex, so that there are four parameters. Two cases are of practical interest: (i) a real frequency and a complex wavevector, (ii) a complex frequency and a real wavector. These two choices lead to different shapes of the dispersion relation as discussed in [18–21]. The imaginary part of the frequency describes the finite lifetime of the mode due to losses. Conversely, for a given real frequency, the imaginary part of the lateral component of wave vector yields a finite propagation length along the interface.
6. The dispersion relation (2.20) shows that for a real dielectric constant $\varepsilon_2 < -1$, $q > \omega/c$. This mode cannot be excited by a plane wave whose wavevector is such that $q < \omega/c$. In order to excite this mode, it is necessary to increase the wavevector. One can use a prism [14, 22, 23] or a grating [176].

2.1.4 Dispersion Relation

In this subsection, we will consider two types of surface waves: surface plasmon polaritons and surface phonon polaritons. Surface plasmon polaritons are observed at surfaces separating a dielectric from a medium with a gas of free electrons such as a metal or a doped semiconductor. The dielectric function of the latter can in the simplest case be modeled by a Drude model:

$$\varepsilon(\omega) = \varepsilon_\infty - \frac{\omega_p^2}{\omega^2 + i\Gamma\omega}, \tag{2.21}$$

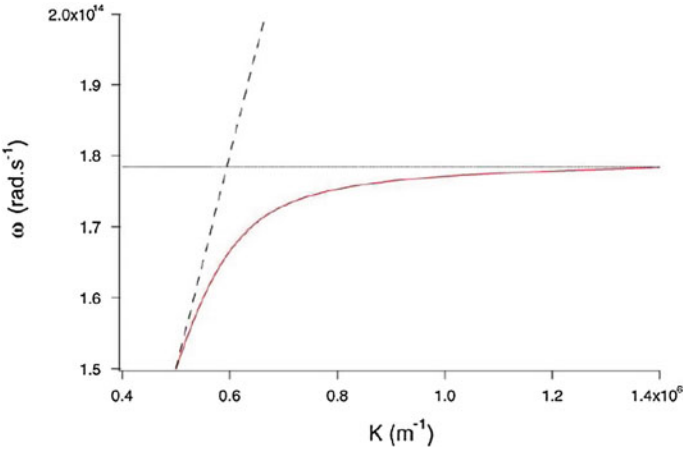

Fig. 2.2 Dispersion relation for surface phonon polariton at a SiC/Vacuum interface. The flat asymptote is situated at $\omega_{asym} = 1.784 \times 10^{14}$ s^{-1}. The *dashed line* represents the light cone, above which a wave is propagating and below which a wave is evanescent

where ω_p is the plasma frequency and Γ accounts for the losses. Using this model and neglecting the losses, we find that the resonance condition $\varepsilon(\omega) + 1 = 0$ yields $\omega = \omega_p/\sqrt{2}$. For most metals, this frequency lies in the near UV so that these surface waves are difficult to excite thermally. By contrast, surface phonon polaritons can be excited thermally because they exist in the infrared. They have been studied through measurements of emission and reflectivity spectra by Zhizhin and Vinogradov [179].

Let us study the dispersion relation of surface-phonon polaritons at a vacuum/Silicon Carbide (SiC) interface. SiC is a non-magnetic material whose dielectric constant is well described by an oscillator model in the 2–22 μm wavelength range [180]:

$$\varepsilon(\omega) = \epsilon_\infty \left(1 + \frac{\omega_L^2 - \omega_T^2}{\omega_T^2 - \omega^2 - i\Gamma\omega}\right), \tag{2.22}$$

where $\epsilon_\infty = 6.7$, $\omega_L = 1.8 \times 10^{14}$ s^{-1}, $\omega_T = 1.49 \times 10^{14}$ s^{-1}, and $\Gamma = 8.9 \times 10^{11}$ s^{-1}. The dispersion relation at a SiC/vacuum interface is shown in Fig. 2.2.

This dispersion relation has been derived by assuming that the frequency, ω is complex and the parallel wavevector, $q = K$, is real. This choice is well-suited to analyze experimental measurements of spectra for fixed angles. The width of the resonance peaks observed is related to the imaginary part of the frequency of the mode. We note that the curve is situated below the light cone $\omega = cK$ so that the surface wave is evanescent. We also observe a horizontal asymptote for $\omega_{asym} = 1.784 \times 10^{14}$ s^{-1} so that there is a peak in the density of electromagnetic states. We will see in the next sections that the existence of surface modes at a particular frequency plays a key role in many phenomena. Figure 2.3 shows the dispersion relation obtained when choosing a real frequency, ω, and a complex wavevector, $q = K$.

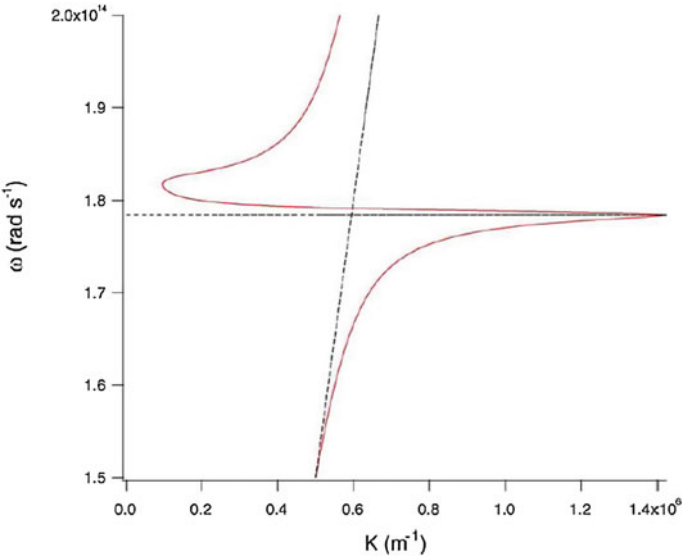

Fig. 2.3 Dispersion relation for surface phonon polariton at a SiC/vacuum interface. Real ω chosen so as to obtain a complex K. The x-axis is the real part of K. The horizontal asymptote is situated at $\omega_{asym} = 1.784 \times 10^{14}\,\mathrm{s}^{-1}$. The slanting *dashed line* represents the light line above which a wave is propagating and below which a wave is evanescent

The x-axis is the real part of the complex wavevector. It can be seen that the shape of the dispersion relation is significantly changed and a backbending of the curve is observed. This type of behavior is observed experimentally when measurements are taken at a fixed frequency and the angle is varied. Observed resonances in reflection or emission experiments have an angular width, which is related to the imaginary part of the complex wavevector.

Chapter 3
Theory of the Fluctuating Electromagnetic Field

There are two approaches for studying the fluctuating electromagnetic field. In the first approach, proposed by Rytov [5–7], it is assumed that the fluctuating electromagnetic field is created by the thermal and quantum fluctuations of current density $\mathbf{j}^f$ inside the medium. The average $\langle \mathbf{j}^f \rangle = 0$, and the correlation function $\langle \mathbf{j}^f \mathbf{j}^f \rangle \neq 0$ is expressed through the dielectric properties of medium on the basis of fluctuation-dissipative theorem. The electromagnetic field can be calculated from Maxwell's equations with the fluctuating current density as the source. Knowing the fluctuating electromagnetic field, it is possible to calculate the Poynting's vector, stress tensor, and so on, and to determine the heat transfer between the bodies [13, 93, 94, 115], the van der Waals–Casimir interaction [42, 43] and the Casimir friction [11]. Among these problems, the calculation of Casimir friction is the most complex, because it requires a complex electrodynamic problem with moving boundaries to be solved [99, 100, 121, 128]. In the second approach the electromagnetic field is described by Green's functions [43], which can be calculated using quantum electrodynamics [183]. For equilibrium problems, such as the Casimir interaction, both approaches give the same result [43], although the Green's functions method is more general. For non-equilibrium problems, Rytov's approach is simpler; therefore, correct results for the radiative heat transfer [93] and Casimir friction between two parallel planes [10, 11, 100, 121] were for the first time obtained using this approach.

3.1 Electromagnetic Fluctuations at Thermodynamical Equilibrium

3.1.1 Electromagnetic Fluctuations and Linear Response Theory

In this section, the key formulas of linear response theory are given, which then are used for the description of the fluctuations of electromagnetic fields. For a more

A.I. Volokitin and B.N.J. Persson, *Electromagnetic Fluctuations at the Nanoscale*,
NanoScience and Technology, DOI 10.1007/978-3-662-53474-8_3

detailed presentation of linear response theory and its application in the theory of the electromagnetic fluctuations, see [8, 107, 184, 185]. Consider a quantum-mechanical system characterized by a Hamiltonian H_0 and the equilibrium density matrix

$$\rho = \frac{e^{-\beta H_0}}{\mathrm{Sp}(e^{-\beta H_0})}, \quad \beta = \frac{1}{k_B T}, \tag{3.1}$$

where k_B is the Boltzmann constant and T is temperature. Let us perturb this system by an external perturbation of the form

$$H_{int} = -\int d^3 r \sum_j \hat{A}_j(\mathbf{r}, t) f_j(\mathbf{r}, t), \tag{3.2}$$

where $f_j(\mathbf{r}, t)$ are the external forces and $\hat{A}_j(\mathbf{r}, t)$ are the dynamical variables of the system under consideration. A straightforward perturbation theory shows that the linear response of the variable A_j to f_j is given by

$$A_i(\mathbf{r}, t) = \sum_j \int d^3 r' \int dt' \alpha_{ij}(\mathbf{r}, \mathbf{r}', t - t') f_j(\mathbf{r}', t'), \tag{3.3}$$

where $\alpha_{ij}(\mathbf{r}, \mathbf{r}', t - t')$ is the usual susceptibility tensor defined by

$$\alpha_{ij}(\mathbf{r}, \mathbf{r}', t - t') = \frac{i}{\hbar}\theta(t - t')\left\langle \hat{A}_i(\mathbf{r}, t)\hat{A}_j(\mathbf{r}', t') - \hat{A}_j(\mathbf{r}', t')\hat{A}_i(\mathbf{r}, t)\right\rangle, \tag{3.4}$$

where θ is the step function: $\theta(\tau) = 1$ if $\tau > 0$ and zero otherwise, and where $\langle \cdots \rangle$ denotes an average with respect to the equilibrium density matrix (3.1). It is clear from (3.3) that

$$\frac{\delta A_i(\mathbf{r}, \omega)}{\delta f_j(\mathbf{r}', \omega)} = \alpha_{ij}(\mathbf{r}, \mathbf{r}', \omega) = \frac{i}{\hbar}\int_0^\infty dt e^{i\omega t}\left\langle \hat{A}_i(\mathbf{r}, t)\hat{A}_j(\mathbf{r}', 0) - \hat{A}_j(\mathbf{r}', 0)\hat{A}_i(\mathbf{r}, t)\right\rangle, \tag{3.5}$$

where the Fourier-transformed quantities are defined by

$$\psi(t) = \frac{1}{2\pi}\int_{-\infty}^{\infty} d\omega \psi(\omega) e^{-i\omega t}. \tag{3.6}$$

According to the fluctuation-dissipative theorem, the spectral function of fluctuations is expressed through the generalized susceptibility $\alpha_{ij}(\mathbf{r}, \mathbf{r}')$

$$\varphi_{ij}(\mathbf{r}, \mathbf{r}', \omega) = \langle A_i(\mathbf{r}) A_j(\mathbf{r}')\rangle_\omega = \frac{i\hbar}{2}(\alpha^*_{ji}(\mathbf{r}', \mathbf{r}, \omega) - \alpha_{ij}(\mathbf{r}, \mathbf{r}', \omega)) \coth\left(\frac{\beta\hbar\omega}{2}\right), \tag{3.7}$$

where $\langle A_i(\mathbf{r}) A_j(\mathbf{r})'\rangle_\omega$ is the Fourier-component of the symmetrized correlation function

$$\varphi_{ij}(\mathbf{r}, \mathbf{r}', t - t') = \frac{1}{2} \langle \hat{A}_i(\mathbf{r}, t)\hat{A}_j(\mathbf{r}', t') + \hat{A}_j(\mathbf{r}', t')\hat{A}_i(\mathbf{r}, t) \rangle, \tag{3.8}$$

Equation (3.7) can be expressed through the fictitious random forces, whose action would give the result, equivalent to the spontaneous fluctuations of the values of $A_i(\mathbf{r}, t)$. We write for this

$$A_i(\mathbf{r}, \omega) = \sum_j \int d^3 r' \alpha_{ij}(\mathbf{r}, \mathbf{r}', \omega) f_j(\mathbf{r}', \omega), \tag{3.9}$$

$$f_i(\mathbf{r}, \omega) = \sum_j \int d^3 r' \alpha^{-1}_{ij}(\mathbf{r}, \mathbf{r}', \omega) A_j(\mathbf{r}', \omega), \tag{3.10}$$

so that

$$\langle f_i(\mathbf{r}) f_j(\mathbf{r}') \rangle_\omega = \sum_l \int d^3 r'' \alpha^{-1}_{il}(\mathbf{r}, \mathbf{r}'', \omega) \times$$

$$\times \sum_m \int d^3 r''' \alpha^{-1*}_{jm}(\mathbf{r}', \mathbf{r}''', \omega) \langle A_l(\mathbf{r}'') A_m(\mathbf{r}''') \rangle_\omega. \tag{3.11}$$

Using (3.7) and taking into account that

$$\int d^3 r'' \alpha^{-1}_{il}(\mathbf{r}, \mathbf{r}'', \omega) \alpha_{lj}(\mathbf{r}'', \mathbf{r}', \omega) = \delta_{ij} \delta(\mathbf{r} - \mathbf{r}'),$$

we get

$$\langle f_i(\mathbf{r}) f_j(\mathbf{r}') \rangle_\omega = \frac{i\hbar}{2} (\alpha^{-1}_{ij}(\mathbf{r}, \mathbf{r}', \omega) - \alpha^{-1*}_{ji}(\mathbf{r}', \mathbf{r}, \omega)) \coth\left(\frac{\beta\hbar\omega}{2}\right). \tag{3.12}$$

If the variables A_i and A_j have the same signature under time reversal, then $\alpha_{ij}(\mathbf{r}, \mathbf{r}', \omega) = \alpha_{ji}(\mathbf{r}', \mathbf{r}, \omega)$. In this case, (3.7) can be rewritten in the form

$$\langle A_i(\mathbf{r}) A_j(\mathbf{r})' \rangle_\omega = \hbar \mathrm{Im} \alpha_{ij}(\mathbf{r}, \mathbf{r}', \omega) \coth\left(\frac{\beta\hbar\omega}{2}\right). \tag{3.13}$$

If variables A_i and A_j have opposite parity, then $\alpha_{ij}(\mathbf{r}, \mathbf{r}', \omega) = -\alpha_{ji}(\mathbf{r}', \mathbf{r}, \omega)$. In this case, (3.7) can be rewritten in the form

$$\langle A_i(\mathbf{r}) A_j(\mathbf{r})' \rangle_\omega = -i\hbar \mathrm{Re} \alpha_{ij}(\mathbf{r}, \mathbf{r}', \omega) \coth\left(\frac{\beta\hbar\omega}{2}\right). \tag{3.14}$$

For the problem of electromagnetic fluctuations, the external probes will be taken to be external polarization $\mathbf{P}_{ext}(\mathbf{r}, t)$ and external magnetization $\mathbf{M}_{ext}(\mathbf{r}, t)$. The Hamiltonian H_{ext}, in the present case is

$$H_{int} = -\int d^3r \left[\mathbf{P}^{ext}(\mathbf{r}, t) \cdot \hat{\mathbf{E}}(\mathbf{r}, t) + \mathbf{M}^{ext}(\mathbf{r}, t) \cdot \hat{\mathbf{H}}(\mathbf{r}, t)\right], \tag{3.15}$$

where $\hat{\mathbf{E}}(\mathbf{r}, t)$ and $\hat{\mathbf{H}}(\mathbf{r}, t)$ are the second-quantized operators corresponding to the electric and magnetic field, respectively. We now introduce four types of response functions:

$$D_{ij}^{EE}(\mathbf{r}, \mathbf{r}', \omega) = \frac{\delta E_i(\mathbf{r}, \omega)}{\delta P_j^{ext}(\mathbf{r}', \omega)}, \tag{3.16}$$

$$D_{ij}^{HE}(\mathbf{r}, \mathbf{r}', \omega) = \frac{\delta H_i(\mathbf{r}, \omega)}{\delta P_j^{ext}(\mathbf{r}', \omega)}, \tag{3.17}$$

$$D_{ij}^{EH}(\mathbf{r}, \mathbf{r}', \omega) = \frac{\delta E_i(\mathbf{r}, \omega)}{\delta M_j^{ext}(\mathbf{r}', \omega)}, \tag{3.18}$$

$$D_{ij}^{HH}(\mathbf{r}, \mathbf{r}', \omega) = \frac{\delta H_i(\mathbf{r}, \omega)}{\delta M_j^{ext}(\mathbf{r}', \omega)}. \tag{3.19}$$

and we introduce the corresponding symmetrized correlation functions

$$S_{ij}^{EE}(\mathbf{r}, \mathbf{r}', t - t') = \frac{1}{2}\left\langle \hat{E}_i(\mathbf{r}, t)\hat{E}_j(\mathbf{r}', t') + \hat{E}_j(\mathbf{r}', t')\hat{E}_i(\mathbf{r}, t)\right\rangle, \tag{3.20}$$

$$S_{ij}^{HE}(\mathbf{r}, \mathbf{r}', t - t') = \frac{1}{2}\left\langle \hat{H}_i(\mathbf{r}, t)\hat{E}_j(\mathbf{r}', t') + \hat{E}_j(\mathbf{r}', t')\hat{H}_i(\mathbf{r}, t)\right\rangle, \tag{3.21}$$

$$S_{ij}^{EH}(\mathbf{r}, \mathbf{r}', t - t') = \frac{1}{2}\left\langle \hat{E}_i(\mathbf{r}, t)\hat{H}_j(\mathbf{r}', t') + \hat{H}_j(\mathbf{r}', t')\hat{E}_i(\mathbf{r}, t)\right\rangle, \tag{3.22}$$

$$S_{ij}^{HH}(\mathbf{r}, \mathbf{r}', t - t') = \frac{1}{2}\left\langle \hat{H}_i(\mathbf{r}, t)\hat{H}_j(\mathbf{r}', t') + \hat{H}_j(\mathbf{r}', t')\hat{H}_i(\mathbf{r}, t)\right\rangle. \tag{3.23}$$

Taking into account that $\mathbf{E}(\mathbf{H})$ is an even (odd) variable under time reversal, from the fluctuation-dissipation theorem we get

$$\langle E_i(\mathbf{r})E_j(\mathbf{r}')\rangle_\omega = \hbar \mathrm{Im} D_{ij}^{EE}(\mathbf{r}, \mathbf{r}', \omega) \coth\left(\frac{\beta\hbar\omega}{2}\right), \tag{3.24}$$

$$\langle H_i(\mathbf{r})H_j(\mathbf{r}')\rangle_\omega = \hbar \mathrm{Im} D_{ij}^{HH}(\mathbf{r}, \mathbf{r}', \omega) \coth\left(\frac{\beta\hbar\omega}{2}\right), \tag{3.25}$$

$$\langle H_i(\mathbf{r})E_j(\mathbf{r}')\rangle_\omega = -i\hbar \mathrm{Re} D_{ij}^{HE}(\mathbf{r},\mathbf{r}',\omega)\coth\left(\frac{\beta\hbar\omega}{2}\right), \tag{3.26}$$

$$\langle E_i(\mathbf{r})H_j(\mathbf{r}')\rangle_\omega = -i\hbar \mathrm{Re} D_{ij}^{EH}(\mathbf{r},\mathbf{r}',\omega)\coth\left(\frac{\beta\hbar\omega}{2}\right). \tag{3.27}$$

Thus, the four response functions defined by (3.16)–(3.19) completely determine the correlation functions. Note that the expressions (3.24) and (3.25) are real, and expression (3.26) and (3.27) imaginary. This means that the time correlation functions of the components of **E** (and the components of **H**) are even functions of the time $t = t_1 - t_2$ (as must be for the correlation between two functions, both of which are even or odd with respect to the time reversal). However, the time correlation function of the components **E** with the components of **H** is odd on the time (as must be for two functions, one of which is even, and another is odd relative to time reversal). Hence, it follows that the correlation functions between **E** and **H** at identical time are not correlated with each other (odd function t becomes zero at $t = 0$). Thus the average values of any bilinear product of **E** and **H** (at identical of time), for example the Poynting's vectors will vanish. The latter fact is, however, obvious: in a medium that is in the thermal equilibrium and invariant relative to time reversal, internal macroscopic energy flows cannot prevail.

Equation (3.24) can be expressed through the fictitious random components of polarization, whose action would give the result, equivalent to the spontaneous fluctuations of the values of $E_i(\mathbf{r},t)$. We write for this

$$E_i(\mathbf{r},\omega) = \sum_j \int d^3r' D_{ij}(\mathbf{r},\mathbf{r}',\omega)P_j(\mathbf{r}',\omega), \tag{3.28}$$

$$P_i(\mathbf{r},\omega) = \sum_j \int d^3r' D_{ij}^{-1}(\mathbf{r},\mathbf{r}',\omega)E_j(\mathbf{r}',\omega), \tag{3.29}$$

where $D_{ij}(\mathbf{r},\mathbf{r}',\omega) = D_{ij}^{EE}(\mathbf{r},\mathbf{r}',\omega)$. For a non-magnetic medium, $\mathbf{B} = \mathbf{H}$ (Gaussian's system of units is used) and

$$\mathbf{D}(\mathbf{r}) = \int d^3\mathbf{r}' \overleftrightarrow{\varepsilon}(\mathbf{r},\mathbf{r}',\omega)\mathbf{E}(\mathbf{r}'), \tag{3.30}$$

where $\overleftrightarrow{\varepsilon}(\mathbf{r},\mathbf{r}',\omega)$ is the dielectric diadic of surrounding media. In this case, from the Maxwell's equations:

$$\nabla\times\mathbf{E} = i\frac{\omega}{c}\left(\mathbf{B}+4\pi\mathbf{M}^{ext}\right), \tag{3.31}$$

$$\nabla\times\mathbf{H} = -i\frac{\omega}{c}\left(\mathbf{D}+4\pi\mathbf{P}^{ext}\right), \tag{3.32}$$

it follows that the generalized susceptibility $D_{ij}(\mathbf{r}, \mathbf{r}', \omega)$ obeys

$$\left(\nabla_i \nabla_k - \delta_{ik}\nabla^2\right) D_{kj}(\mathbf{r}, \mathbf{r}', \omega) - \left(\frac{\omega}{c}\right)^2 \int d^3x'' \varepsilon_{ik}(\mathbf{r}, \mathbf{r}'', \omega) D_{kj}(\mathbf{r}'', \mathbf{r}', \omega) =$$
$$= \left(\frac{4\pi\omega^2}{c^2}\right)\delta_{ij}\delta(\mathbf{r} - \mathbf{r}'), \tag{3.33}$$
$$\left(\nabla'_j \nabla'_k - \delta_{jk}\nabla'^2\right) D_{ik}(\mathbf{r}, \mathbf{r}', \omega) - \left(\frac{\omega}{c}\right)^2 \int d^3x'' \varepsilon_{kj}(\mathbf{r}'', \mathbf{r}', \omega) D_{ik}(\mathbf{r}, \mathbf{r}'', \omega) =$$
$$= \left(\frac{4\pi\omega^2}{c^2}\right)\delta_{ij}\delta(\mathbf{r} - \mathbf{r}'). \tag{3.34}$$

From (3.33) and (3.34) we get

$$D^{-1}_{ij}(\mathbf{r}, \mathbf{r}', \omega) = \left(\frac{c^2}{4\pi\omega^2}\right)\left[\left(\nabla_i \nabla_j - \delta_{ik}\nabla^2\right)\delta(\mathbf{r} - \mathbf{r}') - \left(\frac{\omega}{c}\right)^2 \varepsilon_{ij}(\mathbf{r}, \mathbf{r}', \omega)\right]. \tag{3.35}$$

Taking into account (3.12) and (3.24), we get

$$\langle P_i(\mathbf{r}) P_j(\mathbf{r}')\rangle_\omega = \frac{\hbar}{4\pi}\mathrm{Im}\varepsilon_{ij}(\mathbf{r}, \mathbf{r}', \omega)\coth\left(\frac{\beta\hbar\omega}{2}\right). \tag{3.36}$$

Since the current density $j_i(\mathbf{r}, \omega) = -i\omega P_i(\mathbf{r}, \omega)$, from (3.36) we get

$$\langle j_i(\mathbf{r}) j_j(\mathbf{r}')\rangle_\omega = \frac{\hbar\omega^2}{4\pi}\mathrm{Im}\varepsilon_{ij}(\mathbf{r}, \mathbf{r}', \omega)\coth\left(\frac{\beta\hbar\omega}{2}\right). \tag{3.37}$$

3.1.2 *Electromagnetic Fluctuations in a Homogeneous Medium*

For a spatially homogeneous medium the functions D_{ij} and ε_{ij} in (3.33) depend only on difference $\mathbf{r} - \mathbf{r}'$. Using the Fourier-transformation the differential equation (3.33) can be transformed to the system of algebraic equations

$$\left(k_i k_k - \delta_{ik}k^2\right) D_{kj}(\mathbf{k}, \omega) + \left(\frac{\omega}{c}\right)^2 \varepsilon_{ik}(\mathbf{k}, \omega) D_{kj}(\mathbf{k}, \omega) =$$
$$= -\left(\frac{4\pi\omega^2}{c^2}\right)\delta_{ij}. \tag{3.38}$$

For the long-wave fluctuations, for which the wavelength is considerably larger than interatomic distance (e.g., at room temperatures the characteristic wavelength of thermal radiation $\lambda_T = c\hbar/k_B T \approx 10^{-5}$m), it is possible to neglect the dependence of ε_{ij} on $\mathbf{k}$. In this case, for a spatially homogeneous medium, it is possible to assume $\varepsilon_{ij}(\mathbf{k}, \omega) = \delta_{ij}\varepsilon(\omega)$. In this case, the solution of equations (3.38) has the form

$$D_{ik}(\omega, \mathbf{k}) = -\frac{4\pi\omega^2/c^2}{\omega^2\varepsilon(\omega)/c^2 - k^2}\left[\delta_{ik} - \frac{c^2 k_i k_k}{\omega^2\varepsilon(\omega)}\right]. \tag{3.39}$$

In the vacuum $\varepsilon(\omega) = 1$. But since in every material medium the sign of $\mathrm{Im}\varepsilon(\omega)$ coincides with the sign of ω, then the vacuum corresponds to $\varepsilon \to 1 + i0 \cdot \mathrm{sign}\,\omega$. In this case, we get

$$D_{ik}(\omega, \mathbf{k}) = -\frac{4\pi\omega^2/c^2}{\omega^2/c^2 - k^2 + i0 \cdot \mathrm{sign}\,\omega}\left[\delta_{ik} - \frac{c^2 k_i k_k}{\omega^2}\right]. \tag{3.40}$$

For spatially homogeneous unrestricted medium, the functions of D_{ik} depend only on the difference $\mathbf{r} - \mathbf{r}'$, and they are even function of this variable ((3.33) and (3.34) contain only second order derivatives, and therefore $D_{ik}(\omega, \mathbf{r})$ and $D_{ik}(\omega, -\mathbf{r})$ satisfy identical equations). Using the Fourier-transformation on $\mathbf{r}$ on both sides of (3.24), we get

$$\left\langle E_i(\mathbf{r}) E_k(\mathbf{r}')\right\rangle_{\omega\mathbf{k}} = \hbar \mathrm{Im} D_{ij}(\mathbf{k}, \omega) \coth\left(\frac{\beta\hbar\omega}{2}\right). \tag{3.41}$$

For an isotropic nonmagnetic medium ($\mu = 1$), the function $D_{ik}(\mathbf{k}, \omega)$ is determined by (3.39). The problem of finding the spatial correlation function of fluctuations is reduced to the calculation of the integral

$$D_{ik}(\mathbf{r}, \omega) = \int \frac{d^3k}{(2\pi)^3} e^{i\mathbf{k}\cdot\mathbf{r}} D_{ik}(\mathbf{k}, \omega). \tag{3.42}$$

The integration is performed using formulas

$$\int \frac{d^3k}{(2\pi)^3} \frac{e^{i\mathbf{k}\cdot\mathbf{r}}}{k^2 + \kappa^2} = \frac{e^{-\kappa r}}{4\pi r}, \tag{3.43}$$

$$\int \frac{d^3k}{(2\pi)^3} \frac{k_i k_k e^{i\mathbf{k}\cdot\mathbf{r}}}{k^2 + \kappa^2} = -\frac{\partial^2}{\partial_i \partial_k} \frac{e^{-\kappa r}}{4\pi r}. \tag{3.44}$$

The first of which is obtained by taking the Fourier-transformation of both side of the known equality

$$(\nabla^2 - \kappa^2)\frac{e^{-\kappa r}}{r} = -4\pi\delta(\mathbf{r}), \tag{3.45}$$

and the second is obtained by the differentiation of the first. As a result, we get

$$D_{ik}(\mathbf{r}, \omega) = \left[\frac{\omega^2}{c^2}\delta_{ik} + \frac{\partial^2}{\varepsilon\partial_i\partial_k}\right]\frac{1}{r}\exp\left(-\frac{\omega}{c}\sqrt{-\varepsilon}r\right), \tag{3.46}$$

where $r = |\mathbf{r} - \mathbf{r}'|$, and square-root must be taken with such sigh that $\mathrm{Re}\sqrt{-\varepsilon} > 0$. For vacuum $\varepsilon = 1$, and $\sqrt{-\varepsilon} = -i$. Hence according to (3.24)

$$\left\langle E_i(\mathbf{r}) E_k(\mathbf{r}') \right\rangle_\omega = \hbar \coth(\beta\hbar)\, \mathrm{Im} \left\{ \frac{1}{\varepsilon} \left[\frac{\omega^2}{c^2} \delta_{ik} + \frac{\partial^2}{\partial_i \partial_k} \right] \frac{1}{r} \exp\left(-\frac{\omega}{c} \sqrt{-\varepsilon} r \right) \right\}. \tag{3.47}$$

After contraction over indexes i, k (and using (3.45)), we get

$$\left\langle \mathbf{E}(\mathbf{r}) \cdot \mathbf{E}(\mathbf{r}') \right\rangle_\omega = 2\hbar \coth\left(\frac{\beta\hbar\omega}{2} \right) \mathrm{Im} \left\{ \frac{1}{\varepsilon} \left[\frac{\varepsilon\omega^2}{c^2 r} \exp\left(-\frac{\omega}{c} \sqrt{-\varepsilon} r \right) - 2\pi\delta(\mathbf{r}) \right] \right\}. \tag{3.48}$$

Spectral correlation function for fluctuations of the magnetic field can be calculated from (3.47) taking into account the equality

$$\left\langle B_i(\mathbf{r}) B_j(\mathbf{r}') \right\rangle_\omega = \frac{c^2}{\omega^2} e_{iml} e_{jnk} \nabla_m \nabla'_n \left\langle E_l(\mathbf{r}) E_k(\mathbf{r}') \right\rangle_\omega, \tag{3.49}$$

where e_{iml} and e_{ink} are the unit fully antisymmetric tensors. Using (3.49) leads to correlation functions of the magnetic field, which differ from (3.47) and (3.48) by the absence of the coefficient $1/\varepsilon$ before the square bracket. In this case, the δ-function term under the sign Im in (3.48) becomes real and drops out. The appearance of the imaginary part of ε in (3.47) and (3.48) shows the connection between the electromagnetic fluctuations and the energy dissipation in the medium. Note that even in the limit $\mathrm{Im}\varepsilon \to 0$ (3.47) and (3.48) give non-vanishing expressions. This is connected with order of transition to two limits—to the infinite size of medium and vanishing $\mathrm{Im}\varepsilon$. Since in the infinite medium, even infinitesimally small $\mathrm{Im}\varepsilon$ leads eventually to energy absorption, then the used order of transitions to the limits concerns to physically transparent environment, in which, as in any real medium, non-vanishing absorption still exists.

Let us make, for example, the specified transition in the formula (3.48). For this purpose we notice, that at small positive $\mathrm{Im}\varepsilon$ (at $\omega > 0$)

$$\sqrt{-\varepsilon} \approx -i\sqrt{\mathrm{Re}\varepsilon} \left(1 + i \frac{\mathrm{Im}\varepsilon}{2\mathrm{Re}\varepsilon} \right)$$

(taking into account requirement $\mathrm{Re}\sqrt{-\varepsilon} > 0$). Therefore, in the limit $\mathrm{Im}\varepsilon \to 0$ we get

$$\left\langle \mathbf{E}(\mathbf{r}) \cdot \mathbf{E}(\mathbf{r}') \right\rangle_\omega = \frac{1}{n^2} \left\langle \mathbf{H}(\mathbf{r}) \cdot \mathbf{H}(\mathbf{r}') \right\rangle_\omega = \frac{2\omega^2\hbar}{c^2 r} \sin\frac{\omega n r}{c} \coth\left(\frac{\beta\hbar\omega}{2} \right), \tag{3.50}$$

where $n = \sqrt{\varepsilon}$ is a real refraction index. Due to absence of term with δ-function this expression remains finite at $\mathbf{r} = \mathbf{r}'$:

$$\left\langle \mathbf{E}^2 \right\rangle_\omega = \frac{1}{n^2} \left\langle \mathbf{H}^2 \right\rangle_\omega = \frac{2\omega^3 \hbar n}{c^3} \coth\left(\frac{\beta\hbar\omega}{2}\right). \tag{3.51}$$

Limiting transition to a case of the transparent medium can be performed at earlier stage of calculations. Taking into account that the sign of $\mathrm{Im}\varepsilon(\omega)$ coincides with the sign of ω, in the limit of transparent medium (3.39) takes the form

$$D_{ik}(\omega, \mathbf{k}) = -\frac{4\pi\omega^2/c^2}{\omega^2 n^2/c^2 - k^2 + i0 \cdot \mathrm{sign}\,\omega} \left[\delta_{ik} - \frac{c^2 k_i k_k}{\omega^2 n^2}\right]. \tag{3.52}$$

The imaginary part of this function is can be obtained using the formula

$$-\mathrm{Im}\frac{1}{\omega^2 n^2/c^2 - k^2 + i0 \cdot \mathrm{sign}\,\omega} = \pi \cdot \mathrm{sign}\,\omega\, \delta\left(\frac{\omega^2 n^2}{c^2} - k^2\right) =$$

$$= \frac{\pi}{2k}\left\{\delta\left(\frac{n\omega}{c} - k\right) - \delta\left(\frac{n\omega}{c} + k\right)\right\},$$

As a result we get

$$\langle E_i(\mathbf{r}) E_k(\mathbf{r}')\rangle_{\omega\mathbf{k}} =$$

$$= \frac{2\pi^2\hbar}{k}\left(\frac{\omega^2}{c^2}\delta_{ik} - \frac{k_i k_k}{n^2}\right)\left\{\delta\left(\frac{\omega n}{c} - k\right) - \delta\left(\frac{\omega n}{c} + k\right)\right\}\coth\left(\frac{\beta\hbar\omega}{2}\right). \tag{3.53}$$

The arguments of the δ-functions in this expression have simple physical meaning: they show that the fluctuation of field with the given value $\mathbf{k}$ are propagated in the space with the velocity c/n, i.e. with the velocity of propagation of electromagnetic waves in the medium. Using the inverse Fourier-transformation, it is possible from (3.53) to get again (3.47).

The energy density of the fluctuating electromagnetic field in the transparent medium (with $\mu = 1$), in spectral interval $d\omega$ is given by [191]

$$u(\omega)d\omega = \frac{1}{8\pi}\left[2\left\langle \mathbf{E}^2\right\rangle_\omega \frac{d(\omega\varepsilon)}{d\omega} + 2\left\langle \mathbf{H}^2\right\rangle_\omega\right]\frac{d\omega}{2\pi}. \tag{3.54}$$

The factor 2 in the square brackets is connected with fact that in the calculation of the energy density of the electromagnetic field, the integration is assumed only over positive values of ω. At the same time, in calculating energy with the use of spectral correlation function, the ω integration is assumed from $-\infty$ to ∞. The transformation of integration over infinite interval to semi-infinite interval gives an additional factor 2. Using (3.52) in (3.54), we get

$$u(\omega)d\omega = \left[\frac{\hbar\omega}{2} + \frac{\hbar\omega}{e^{\beta\hbar\omega} - 1}\right]\frac{\omega^2 n^2}{\pi^2 c^3}\frac{d(n\omega)}{d\omega}d\omega. \tag{3.55}$$

The first term in the brackets is connected with the zero-point energy of the field. The second term gives energy density of the thermodynamically equilibrium electromagnetic radiation in the transparent medium, i.e., the energy of *black-body radiation*. This part of the formula could be also obtained without consideration of fluctuations, by the corresponding generalization of the Planck formula for the black-body radiation in vacuum. According to the latter, the energy density of black-body radiation in the of the wave-vectors volume d^3k is given by the formula

$$\frac{\hbar\omega}{e^{\beta\hbar\omega}-1}\frac{2d^3k}{(2\pi)^3}$$

where the factor 2 takes into account two directions of polarization. To obtain the spectral density of energy it is necessary to replace d^3k on $4\pi k^2 dk$ and to substitute $k = n\omega/c$, i.e.:

$$k^2dk = k^2\frac{dk}{d\omega}d\omega = \frac{\omega^2 n^2}{c^3}\frac{d(n\omega)}{d\omega}d\omega,$$

what gives the required result.

3.2 Electromagnetic Fluctuations for Nonequilibrium Systems

In Sect. 3.1 the theory of electromagnetic fluctuations was presented for systems in thermodynamic equilibrium. However, it is possible to develop the theory of electromagnetic fluctuations for nonequilibrium systems. This theory is based on the fluctuation-dissipation theorem for the current density. Assuming local thermal equilibrium, it is possible to determine the statistical properties of the currents. This approach composes the content of the Rytov's theory [5–7], which is based on the introduction of "random" current density into the Maxwell's equations (similar to the "random force in the theory of Brownian motion of particle). For the monochromatic field (time factor $\exp(-\mathrm{i}\omega t)$) in a dielectric, nonmagnetic medium, these equations are:

$$\nabla \times \mathbf{E} = i\frac{\omega}{c}\mathbf{B}, \tag{3.56}$$

$$\nabla \times \mathbf{B} = -i\frac{\omega}{c}\mathbf{D} + \frac{4\pi}{c}\mathbf{j}^f, \tag{3.57}$$

where $\mathbf{E}$, $\mathbf{D}$, $\mathbf{B}$ are the electric and electric displacement field, and the magnetic induction field, respectively. In Rytov's theory the fluctuating current density has statistical properties determined by the fluctuation-dissipative theorem. According to fluctuation-dissipative theorem the average value of the product of components $\mathbf{j}^f$ is determined by the formula (3.37), which we rewrite in the form

$$\left\langle j_i^f(\mathbf{r},\omega) j_k^{f*}(\mathbf{r}',\omega')\right\rangle = \left\langle j_i^f(\mathbf{r}) j_k^{f*}(\mathbf{r}')\right\rangle_\omega \delta(\omega-\omega'), \tag{3.58}$$

$$\left\langle j_i^f(\mathbf{r}) j_k^{f*}(\mathbf{r}')\right\rangle_\omega = \frac{\hbar}{(2\pi)^2}\left(\frac{1}{2}+n(\omega)\right)\omega^2 \mathrm{Im}\varepsilon_{ik}(\mathbf{r},\mathbf{r}',\omega), \tag{3.59}$$

$$n(\omega) = \frac{1}{e^{\hbar\omega/k_BT}-1}. \tag{3.60}$$

In Rytov's theory, which will be used in the following for the nonequilibrium systems, the Fourier-transformation of the correlation functions is defined by

$$\psi(t) = \int_{-\infty}^{\infty} d\omega \psi(\omega) e^{-i\omega t}. \tag{3.61}$$

For this reason in (3.59) in comparison with (3.37) appears the additional factor $1/2\pi$. From Maxwell's equations it follows that the component of the electric field, created by the random current density $\mathbf{j}^f$, is given by

$$E_i(\mathbf{r}) = \frac{i}{\omega}\int \mathrm{d}^3\mathbf{r}' D_{ik}(\mathbf{r},\mathbf{r}',\omega) j_k^f(\mathbf{r}'), \tag{3.62}$$

where summation over repeated indexes is assumed. The Green's functions of the electromagnetic field, $D_{ij}(\mathbf{r},\mathbf{r}',\omega)$, obey (3.33) and (3.34).

Using (3.33), (3.34) and (3.59), we can calculate the spectral correlation function of the electric field, created by a body at a temperature of T by the fluctuations of current density inside the body [13] (see Appendix A):

$$\begin{aligned}\left\langle E_i(\mathbf{r}) E_j^*(\mathbf{r}')\right\rangle_\omega &= \frac{\hbar}{8\pi^2}\coth\left(\frac{\hbar\omega}{2k_BT}\right)\int \mathrm{d}\mathbf{r}''\int \mathrm{d}\mathbf{r}'''\mathrm{Im}\varepsilon_{kl}(\mathbf{r}'',\mathbf{r}''')D_{ik}(\mathbf{r},\mathbf{r}'')D_{jl}^*(\mathbf{r}',\mathbf{r}''')\\ &= \frac{\hbar c^2}{16\pi^2 i\omega^2}\coth\left(\frac{\hbar\omega}{2k_BT}\right)\int \mathrm{d}S_{ll}''\big(D_{ik}(\mathbf{r},\mathbf{r}'')\nabla_l'' D_{jk}^*(\mathbf{r}',\mathbf{r}'') -\\ &- D_{jk}^*(\mathbf{r}',\mathbf{r}'')\nabla_l'' D_{ik}(\mathbf{r},\mathbf{r}'')\big),\end{aligned} \tag{3.63}$$

where the points $\mathbf{r}$ and $\mathbf{r}'$ are outside the body. Here we have transformed an integral over the volume of the body into an integral over the surface of the body. For the evanescent waves the surface of integration can be moved to infinity. Thus, using (3.33) and (3.34), and taking into account that the surface integral vanishes in this case, we get

$$\left\langle E_i(\mathbf{r}) E_j(\mathbf{r}')\right\rangle_\omega^{evan} = \frac{\hbar}{2\pi}\coth\left(\frac{\hbar\omega}{2k_BT}\right)\mathrm{Im}D_{ij}(\mathbf{r},\mathbf{r}'). \tag{3.64}$$

In the non-retarded limit the formalism can be simplified. In this case the electric field can be written as the gradient of an electrostatic potential, $\mathbf{E}(\mathbf{r}) = -\nabla\phi(\mathbf{r})$. Thus the total Poynting's vector becomes

$$(S_{total})_\omega = \frac{c}{8\pi}\int \mathrm{d}\mathbf{S}\cdot\left\{\left\langle\left[\mathbf{E}\times\mathbf{B}^*\right]\right\rangle_\omega + c.c.\right\} =$$

$$= \frac{c}{8\pi}\int \mathrm{d}\mathbf{S}\cdot\left\{-\left\langle\left[\nabla\times(\phi\mathbf{B}^*)\right] + \phi\left[\nabla\times\mathbf{B}^*\right]\right\rangle_\omega + c.c.\right\} =$$

$$= \frac{\mathrm{i}\omega}{8\pi}\int \mathrm{d}\mathbf{S}\cdot\nabla'\left(\left\langle\phi(\mathbf{r})\phi^*(\mathbf{r}')\right\rangle_\omega - c.c.\right)_{\mathbf{r}=\mathbf{r}'} \tag{3.65}$$

In the same approximation we can write

$$D_{ik}(\mathbf{r},\mathbf{r}') = -\frac{\mathrm{i}}{\omega}\nabla_i\nabla'_k D(\mathbf{r},\mathbf{r}'),$$

where the function $D(\mathbf{r},\mathbf{r}')$ obeys the Poisson's equation

$$\Delta D(\mathbf{r},\mathbf{r}') = -4\pi\delta(\mathbf{r}-\mathbf{r}'). \tag{3.66}$$

Using the identities

$$\begin{aligned} &D_{ik}(\mathbf{r},\mathbf{r}'')\left(\nabla''_l D^*_{jk}(\mathbf{r}',\mathbf{r}'') - \nabla''_k D^*_{jl}(\mathbf{r}',\mathbf{r}'')\right) = \\ &= -\frac{\mathrm{i}}{\omega}\nabla_i\nabla''_k\left[D(\mathbf{r},\mathbf{r}'')\left(\nabla''_l D^*_{jk}(\mathbf{r}',\mathbf{r}'') - \nabla''_k D^*_{jl}(\mathbf{r}',\mathbf{r}'')\right)\right] - \\ &-\frac{1}{c^2}\nabla_i\nabla'_j D(\mathbf{r},\mathbf{r}'')\nabla''_l D^*(\mathbf{r}',\mathbf{r}''). \end{aligned} \tag{3.67}$$

Equation (A.1) from Appendix A gives

$$\left\langle E_i(\mathbf{r})E_j(\mathbf{r}')\right\rangle_\omega = \nabla_i\nabla'_j\left\langle\phi(\mathbf{r})\phi^*(\mathbf{r}')\right\rangle_\omega, \tag{3.68}$$

$$\begin{aligned} \left\langle\phi(\mathbf{r})\phi^*(\mathbf{r}')\right\rangle_\omega = \frac{\hbar}{16\pi^2 i\omega^2}\coth\left(\frac{\hbar\omega}{2k_BT}\right)\int \mathrm{d}\mathbf{S}''_1\Big\{ &D^*(\mathbf{r}',\mathbf{r}'')\nabla''D(\mathbf{r},\mathbf{r}'') - \\ &-D(\mathbf{r},\mathbf{r}'')\nabla''D^*(\mathbf{r}',\mathbf{r}'')\Big\}. \end{aligned} \tag{3.69}$$

3.3 Fluctuating Field in the Non-retarded Limit

In this section we present some applications where retardation effects can be neglected, and where the full formalism developed above is not necessary. We consider the interaction between an external charged or neutral particle (e.g., an electron, ion or an atom) and a solid with a flat surface. If the separation between the particle and the surface is small enough retardation effects can be neglected and the electric field can be described by a scalar potential.

Consider first a classical point charge moving along a prescribed path $\mathbf{x}(t)$ outside a body with a flat surface. The electric potential from the charge can be written as a sum of evanescent plane waves of the form

$$\phi_{\text{ext}} = e^{qz} e^{i(\mathbf{q}\cdot\mathbf{x}-\omega t)},$$

where $\mathbf{q} = (q_x, q_y)$ is a two-dimensional wavevector, and where the xy is in the surface, while the positive z direction point outwards from the solid. The external potential ϕ_{ext} polarizes the solid, and the induced polarization charges give rise to a potential which for $z > 0$ must take the form

$$\phi_{\text{ind}} = -g(q,\omega) e^{-qz} e^{i(\mathbf{q}\cdot\mathbf{x}-\omega t)}.$$

The linear response function $g(q,\omega)$ determines the response of the solid to any external space and time-varying potential. If the solid can be described by a local scalar dielectric function $\epsilon(\omega)$, then

$$g = \frac{\epsilon - 1}{\epsilon + 1}. \tag{3.70}$$

Since $\epsilon(\omega)$ has been measured for many materials, this expression for g is very useful. One can show that (3.70) is exact in the limit $q \to 0$ but holds only approximately for finite q. Indeed, much effort has been devoted to calculating $g(q,\omega)$ for simple metals using the jellium model and various mean-field approximations to account for the interaction between the electrons. Furthermore, the structure of $g(q,\omega)$ is constrained by exact sum rules.

So far, our discussion has assumed that ϕ_{ext} arises from an external (classical) time-varying charge distribution. In the problems which interest us here it is crusial to treat the particle and substrate quantum mechanically. The quantum degrees of freedom of the polarizable solid can be included by assuming that the induced potential ϕ_{ind} arises from a set of quantized boson excitations (e.g., surface plasmons or low-energy electron-hole pairs). The total Hamiltonin is then given by

$$H = \frac{\mathbf{p}^2}{2m} + U(\mathbf{x}) + \sum_{\mathbf{q}\alpha} \hbar\omega_{\mathbf{q}\alpha} b^+_{\mathbf{q}\alpha} b_{\mathbf{q}\alpha} + \sum_{\mathbf{q}\alpha} C_{\mathbf{q}\alpha} e^{-qz} \left(b_{\mathbf{q}\alpha} e^{i\mathbf{q}\cdot\mathbf{x}} + H.c. \right). \tag{3.71}$$

Here, $\mathbf{x}$ and $\mathbf{p}$ are the position and momentum operators of the external electron with mass m, treated as a distinguishable particle, $\omega_{\mathbf{q}\alpha}$, $b^+_{\mathbf{q}\alpha}$ and $b_{\mathbf{q}\alpha}$ are the angular frequency and the creation and anhilation operators for the boson with the quantum number $(\mathbf{q}, \alpha)$, and $C_{\mathbf{q}\alpha}$ is an energy parameter which determines its coupling to the external electron. The parameters $\omega_{\mathbf{q}\alpha}$ and $C_{\mathbf{q}\alpha}$ can be related to $g(q,\omega)$ in the following way. Assume that we constrain the electron to move (classically) along a prescribed path $\mathbf{x}(t)$. We assume that the particle starts far away at $t = 0$, then moves close to the surface of the solid, and then far away again so that $z(0) \approx z(t_0) \sim \infty$.

From (3.71), we obtain the equation of motion for the boson operator $b_{\mathbf{q}\alpha}$ (in the Heisenberg picture),

$$i\dot{b}_{\mathbf{q}\alpha} = \omega_{\mathbf{q}\alpha} b_{\mathbf{q}\alpha} + \frac{C_{\mathbf{q}\alpha}}{\hbar} e^{-qz(t)} e^{i\mathbf{q}\cdot\mathbf{x}(t)}$$

and the solution

$$b_{\mathbf{q}\alpha}(t_0) = e^{-i\omega_{\mathbf{q}\alpha}t_0} b_{\mathbf{q}\alpha}(0) - i\frac{C_{\mathbf{q}\alpha}}{\hbar}\int_0^{t_0} dt\; e^{-i\omega_{\mathbf{q}\alpha}(t_0-t)} e^{-qz(t)+i\mathbf{q}\cdot\mathbf{x}(t)} \tag{3.72}$$

Using (3.71) and (3.72), we obtain the net energy transfer from the particle to the substrate

$$\Delta E = \langle\Psi|[H(t_0) - H(0)]|\Psi\rangle = \sum_{\mathbf{q}} \int d\omega\; \omega \sum_{\alpha} |C_{\mathbf{q}\alpha}|^2 \delta(\omega - \omega_{\mathbf{q}\alpha}) |F_{\mathbf{q}}(\omega)|^2/\hbar, \tag{3.73}$$

where

$$F_{\mathbf{q}}(\omega) = \int_0^{t_0} dt\; e^{-qz(t)} e^{i[\omega t - \mathbf{q}\cdot\mathbf{x}(t)]}, \tag{3.74}$$

and where we have used the fact that the interaction energy term in H is zero at $t = 0$ and $t = t_0$ as a result of our assumptions. Note that (3.73) is independent of the state $|\Psi\rangle$ of the boson system at $t = 0$.

On the other hand, the energy transfer ΔE can also be expressed in terms of $g(q, \omega)$ as follows. By solving Poisson's equation

$$\nabla^2 \phi_{\text{ext}} = -4\pi e \delta(\mathbf{x} - \mathbf{x}(t)),$$

one obtains [for $z < z(t)$] the external potential

$$\phi_{\text{ext}} = \int d^2q d\omega\; \tilde{\phi}_{\text{ext}}(\mathbf{q}, \omega) e^{i(\mathbf{q}\cdot\mathbf{x} - \omega t) + qz},$$

where

$$\tilde{\phi}_{\text{ext}} = -\frac{e}{4\pi^2 q} F_{\text{q}}(\omega). \tag{3.75}$$

The energy transfer from the external particle is obtained by integrating the Poynting vector over the surface $z = 0$ and over time. This gives:

$$\Delta E = \frac{1}{4\pi}\int dt\; d^2x \left[\phi \frac{\partial}{\partial t}\frac{\partial}{\partial z}\phi\right], \tag{3.76}$$

where the total potential $\phi = \phi_{\text{ext}} + \phi_{\text{ind}}$ is given by [for $0 \le z < z(t)$]

$$\phi = \int d^2q d\omega \, \tilde{\phi}_{\text{ext}}(\mathbf{q}, \omega) \left[e^{qz} - g(q, \omega) e^{-qz} \right] e^{i(\mathbf{q}\cdot\mathbf{x} - \omega t)}, \tag{3.77}$$

Substituting (3.75) and (3.77) in (3.76) gives

$$\Delta E = \frac{e^2}{2\pi^2} \int d^2q \int_0^\infty d\omega \, \frac{\omega}{q} |F_{\mathbf{q}}(\omega)|^2 \text{Im} g(q, \omega). \tag{3.78}$$

Comparing (3.73) with (3.78), and replacing

$$\sum_{\text{q}} \to \frac{A}{(2\pi)^2} \int d^2q, \tag{3.79}$$

where A is the surface area, gives

$$\sum_{\alpha} |C_{\mathbf{q}\alpha}|^2 \delta(\omega - \omega_{\mathbf{q}\alpha}) = \frac{2e^2\hbar}{Aq} \text{Im} g(q, \omega) \tag{3.80}$$

which is our *fundamental result*.

As a simple example, assume that g is given by (3.70) with $\epsilon = 1 - \omega_p^2/\omega^2$ as is valid for simple metals. Then

$$g = \frac{\epsilon - 1}{\epsilon + 1} = \frac{1}{1 - \left(\frac{\omega}{\omega_{\text{s}}}\right)^2},$$

where $\omega_{\text{s}} = \omega_{\text{p}}/\sqrt{2}$ is the surface plasmon frequency. Letting $\omega \to \omega + i0$, we obtain

$$\text{Im} g = \pi \omega_{\text{s}} \delta(\omega - \omega_{\text{s}})/2,$$

and from (3.80), $\omega_{\text{q}} = \omega_{\text{s}}$ and

$$|C_{\mathbf{q}\alpha}|^2 = \pi e^2 \hbar \omega_{\text{s}}/Aq.$$

We will now give some important applications, which all involves the interaction between an external charged or neutral particle (e.g., an ion or an atom) with the fluctuating electromagnetic field of a nearby solid with a flat surface. When the separation between the external particle is small enough so that retardation effects can be neglected, but still large enough that there is negligible overlap between the wavefunction of the particle and the wavefunction of the atoms of the solid, these problems can be studied using the Hamiltonian Equation (3.71) with (3.80).

3.3.1 Interaction Energy Between a Charged Particle and a Solid: Image Potential

Consider first an external charged point particle at rest at $\mathbf{x} = (0, 0, z)$. In this case, we obtain

$$\sum_{\mathbf{q}\alpha} \hbar\omega_{\mathbf{q}\alpha} b^+_{\mathbf{q}\alpha} b_{\mathbf{q}\alpha} + \sum_{\mathbf{q}\alpha} C_{\mathbf{q}\alpha} e^{-qz} \left(b_{\mathbf{q}\alpha} + b^+_{\mathbf{q}\alpha} \right) = \sum_{\mathbf{q}\alpha} \hbar\omega_{\mathbf{q}\alpha} B^+_{\mathbf{q}\alpha} B_{\mathbf{q}\alpha} - \sum_{\mathbf{q}\alpha} |C_{\mathbf{q}\alpha}|^2 \frac{e^{-2qz}}{\hbar\omega_{\mathbf{q}\alpha}}$$

where we have introduced shifted boson operators $B_{\mathbf{q}\alpha} = b_{\mathbf{q}\alpha} + C_{\mathbf{q}\alpha} e^{-qz}/\hbar\omega_{\mathbf{q}\alpha}$. Note that $B_{\mathbf{q}\alpha}$ and $B^+_{\mathbf{q}\alpha}$ satisfy the same commutation algebra as the original operators. The last term is the relaxation energy and can be identified as the generalized static image-potential energy,

$$U_{\mathrm{im}}(z) = -\sum_{\mathbf{q}\alpha} |C_{\mathbf{q}\alpha}|^2 \frac{e^{-2qz}}{\hbar\omega_{\mathbf{q}\alpha}}$$

Using (3.80), this can also be written as

$$U_{\mathrm{im}} = -\frac{e^2}{2\pi^2} \int d^2q \int_0^\infty d\omega \, \frac{\mathrm{Im} g(q, \omega)}{q\omega} e^{-2qz}.$$

However, according to the $\omega \to 0$ limit of the appropriate Kramers–Kronig relation,

$$\int_0^\infty d\omega \, \frac{\mathrm{Im} g(q, \omega)}{\omega} = \frac{\pi}{2} g(q, 0),$$

so that

$$U_{\mathrm{im}} = -\frac{e^2}{2} \int_0^\infty dq \; g(q, 0) e^{-2qz}.$$

Using the classical expression (3.70) for g gives $g(q, 0) = 1$ and $U_{\mathrm{im}} = -e^2/4z$. A more accurate expression for g is given by

$$g(q, 0) = e^{2qd_\perp(0)}$$

where $d_\perp(0)$ is the centroid of the induced charge density at the metal surface (at zero frequency). This formula gives

$$U_{\mathrm{im}} = -\frac{e^2}{4\big[z - d_\perp(0)\big]}.$$

The quantity $d_\perp(0)$ has been tabulated by Lang and Kohn for the jellium model at different values of the electron gas density parameter r_s.

3.3.2 *Interaction Energy Between a Neutral Particle and a Solid: van der Waals Interaction*

We consider now the interaction between a neutral particle; for example, an atom, and a solid with a flat surface. The atom has many electrons with coordinates $\mathbf{x}_i$ so now (3.71) takes the form

$$H = H_0 + V$$

where

$$H_0 = \sum_i \frac{\mathbf{p}_i^2}{2m} + U\left(\mathbf{x}_1, \mathbf{x}_2, ...\right) + \sum_{\mathbf{q}\alpha} \hbar\omega_{\mathbf{q}\alpha} b^+_{\mathbf{q}\alpha} b_{\mathbf{q}\alpha}$$

where U is the interaction energy between the electrons (and the ion) of the atom, and

$$V = \sum_{\mathbf{q}\alpha} C_{\mathbf{q}\alpha} \sum_i e^{-qz_i} \left(b_{\mathbf{q}\alpha} e^{i\mathbf{q}\cdot\mathbf{x_i}} + H.c.\right). \tag{3.81}$$

We now use second order pertubation theory to calculate the interaction energy between the particle and the solid. We can write

$$\Delta E = \langle A\Psi|V|A\Psi\rangle - \left\langle A\Psi|V\frac{1}{H_0 - E_0}V|A\Psi\right\rangle$$

where $|A\rangle$ is the ground state of the atom and $|\Psi\rangle$ the ground state of the solid. Using (3.81), the first term in ΔE clearly vanishes, and the second term gives the atom-solid van der Waals interaction energy:

$$U_{\mathrm{VdW}} = -\left\langle A\Psi|V\frac{1}{H_0 - E_0}V|A\Psi\right\rangle$$

Substituting (3.81) in this expression gives

$$U_{\mathrm{VdW}} = -\sum_{\mathbf{q}\alpha} |C_{\mathbf{q}\alpha}|^2 \sum_B \frac{\left|\left\langle A\right|\sum_i e^{i\mathbf{q}\cdot\mathbf{x_i}}\left|B\right\rangle\right|^2}{\hbar\omega_{\mathbf{q}\alpha} + E_B - E_A}$$

$$= -\int_0^\infty d\omega \sum_{\mathbf{q}}\sum_{\alpha} |C_{\mathbf{q}\alpha}|^2 \delta(\omega - \omega_{\mathbf{q}\alpha}) \sum_B \frac{|\langle A|\sum_i e^{-qz_i} e^{i\mathbf{q}\cdot\mathbf{x_i}}|B\rangle|^2}{\hbar\omega + E_B - E_A}$$

where $\sum_B$ is the sum over all states of the atom excluding the ground state A. Using (3.80), this equation can be written as

$$U_{\mathrm{VdW}} = -\frac{2e^2\hbar}{A}\int_0^\infty d\omega \sum_{\mathbf{q}} \frac{1}{q}\mathrm{Im}g(q,\omega) \sum_B \frac{|\langle A|\sum_i e^{-qz_i} e^{i\mathbf{q}\cdot\mathbf{x_i}}|B\rangle|^2}{\hbar\omega + E_B - E_A} \tag{3.82}$$

Next we write

$$(\mathbf{x}_i, z_i) = \hat{z}z + \mathbf{r}_i$$

where z is the distance between the center of mass of the atom and the surface ($z = 0$) of the solid. Since the relevant q in the sum in (3.82) are of the order $1/z$ or smaller, and if we assume the size of the atom is small compare to z we can expand

$$e^{-qz_i} e^{i\mathbf{q}\cdot\mathbf{x_i}} \approx e^{-qz} \, (1 + i\mathbf{r}_i \cdot \mathbf{Q})$$

where $\mathbf{Q} = (\mathbf{q}, iq)$. Substitute this result in (3.82) gives

$$U_{\rm VdW} = -\frac{2\hbar}{A} \int_0^\infty d\omega \sum_{\mathbf{q}} \frac{1}{q} {\rm Im} g(q,\omega) e^{-2qz} \mathbf{Q}^* \cdot \sum_B \frac{\langle A| \sum_i e\mathbf{r}_i |B\rangle \langle B| \sum_i e\mathbf{r}_i |A\rangle}{\hbar\omega + E_B - E_A} \cdot \mathbf{Q}$$

For an atom the dyadic function

$$\bar{\Pi} = \sum_B \frac{\langle A| \sum_i e\mathbf{r}_i |B\rangle \langle B| \sum_i e\mathbf{r}_i |A\rangle}{\hbar\omega + E_B - E_A}$$

is proportional to the unit tensor $\bar{\Pi}_{\mu\nu}(\omega) = \Pi(\omega)\delta_{\mu\nu}$ where

$$\Pi(\omega) = \sum_B \frac{\langle A| \sum_i ex_i |B\rangle \langle B| \sum_i ex_i |A\rangle}{\hbar\omega + E_B - E_A}$$

Using this result and that $\mathbf{Q}^* \cdot \mathbf{Q} = 2q^2$ we get

$$U_{\rm VdW} = -\frac{2\hbar}{A} \int_0^\infty d\omega \sum_{\mathbf{q}} q {\rm Im} g(q,\omega) e^{-2qz} \Pi(\omega) = -\frac{\hbar}{2\pi^2} \int d^2q \, q e^{-2qz} {\rm Im} \int_0^\infty d\omega \, g(q,\omega) \Pi(\omega)$$

where we have used that $\Pi(\omega)$ is real, and where we have replaced the sum over $\mathbf{q}$ with the integral over $\mathbf{q}$ using (3.79). Since $g(q,\omega)$ is a causal response function, it has its poles in the lower complex ω-half space. Thus, we can close the integral over the upper half space and write the integral over the imaginary frequency axis. Thus, with $\omega = iu$ and using that $g(q, iu)$ is real we get:

$$U_{\rm VdW} = -\frac{\hbar}{2\pi^2} \int d^2q \, q e^{-2qz} \int_0^\infty du \, g(q,iu) {\rm Re} \, \Pi(iu)$$

Since

$${\rm Re}\Pi(iu) = \sum_B (E_B - E_A) \frac{\langle A| \sum_i ex_i |B\rangle \langle B| \sum_i ex_i |A\rangle}{(\hbar u)^2 + (E_B - E_A)^2} = \alpha(iu)$$

where $\alpha(\omega)$ is the atomic polarizability, we get

$$U_{\mathrm{VdW}} = -\frac{\hbar}{\pi}\int_0^\infty dq\, q^2 e^{-2qz}\int_0^\infty du\, g(q,iu)\alpha(iu)$$

If we assume that $g(q,\omega)$ is given by (3.70) we get

$$U_{\mathrm{VdW}} = -\frac{\hbar}{4\pi z^3}\int_0^\infty d\omega \frac{\epsilon(iu)-1}{\epsilon(iu)+1}\alpha(iu)$$

3.3.3 *Inelastic Electron Scattering from Surfaces*

As a final application of (3.71) and (3.80) consider inelastic scattering of electrons from the fluctuating electromagnetic field of a solid with a flat surface. In this case, we assume that the potential $U(\mathbf{x})$ is an infinite potential step at the surface $z = 0$, so that the stationary states for an electron, in the absence of coupling to the boson system, are given by

$$\langle \mathbf{x}|\mathbf{k}\rangle = (2\pi)^{-3/2}\left(e^{-ik_z z} - e^{ik_z z}\right)e^{i\mathbf{k}_\parallel\cdot\mathbf{x}_\parallel}.$$

If the coupling to the substrate excitations is weak, one may use first-order pertubation theory (the golden rule) to calculate the rate w of inelastic scattering $\mathbf{k}\to\mathbf{k}'$ via excitation of a single boson,

$$w = \frac{2\pi}{\hbar}\int d^3k' \sum_{\mathbf{q}\alpha}\sum_{n_{\mathbf{q}\alpha}} P(n_{\mathbf{q}\alpha})\delta(\epsilon_{\mathbf{k}}-\epsilon_{\mathbf{k}'}-\hbar\omega_{\mathbf{q}\alpha})|\langle \mathbf{k}', n_{\mathbf{q}\alpha}+1|C_{\mathbf{q}\alpha}e^{-qz-i\mathbf{q}\cdot\mathbf{x}}b^+_{\mathbf{q}\alpha}|\mathbf{k}, n_{\mathbf{q}\alpha}\rangle|^2,$$

where $P(n_{\mathbf{q}\alpha})$ is the probability that the boson mode $\mathbf{q}\alpha$ contains $n_{\mathbf{q}\alpha}$ quanta. An electron can also absorb a thermally excited boson, which is given by a similar expression to that above but with $n_{\mathbf{q}\alpha}+1$ replaced by $n_{\mathbf{q}\alpha}$ and $b^+_{\mathbf{q}\alpha}$ replaced by $b_{\mathbf{q}\alpha}$. Using (3.80) this expression for w can be rewritten as

$$w = \frac{4\pi e^2}{\hbar A}\int d^3k' \sum_{\mathbf{q}}(n_\omega+1)\frac{1}{q}\mathrm{Im}g(q,\omega)|\langle \mathbf{k}'|e^{-qz-i\mathbf{q}\cdot\mathbf{x}}|\mathbf{k}\rangle|^2,$$

where $\hbar\omega = \epsilon_{\mathbf{k}} - \epsilon_{\mathbf{k}'}$. However,

$$\langle \mathbf{k}'|e^{-qz-i\mathbf{q}\cdot\mathbf{x}}|\mathbf{k}\rangle = \frac{1}{\pi}\delta(\mathbf{k}_\parallel - \mathbf{k}'_\parallel - \mathbf{q})\left[\frac{q}{q^2+(k_z+k'_z)^2} - \frac{q}{q^2+(k_z-k'_z)^2}\right],$$

so that

$$w = \frac{e^2}{\hbar\pi^3}\frac{A}{(2\pi)^2}\int d^3k'(n_\omega+1)\frac{q_\parallel}{(q_\parallel^2+q_\perp^2)^2}\mathrm{Im}g(q,\omega),$$

where $q_\parallel = |\mathbf{k}_\parallel - \mathbf{k}'_\parallel|$ and $q_\perp = k_z - k'_z$. Finally, since the number of electrons that hit the surface area A per unit time is given by

$$\dot{N} = \frac{\hbar k A}{(2\pi)^3 m}\cos\theta,$$

we obtain, using

$$\int d^3k' = \int d\Omega_{k'} d\hbar\omega \frac{mk'}{\hbar^2},$$

$$\frac{w}{\dot{N}} = \frac{2}{(\pi e a_0)^2}\frac{1}{\cos\theta}\int d\Omega_{k'} d\hbar\omega (n_\omega + 1)\frac{k'}{k}\frac{q_\parallel}{(q_\parallel^2 + q_\perp^2)^2}\mathrm{Im}g(q,\omega),$$

where a_0 is the Bohr radius. If one defines $P(\mathbf{k}, \mathbf{k}')d\Omega_{\mathbf{k}'} d\hbar\omega$ to be the relative probability that an incident electron is scattered into the range of energy losses between $\hbar\omega$ and $\hbar(\omega + d\omega)$ and into the solid angle $d\Omega_{\mathbf{k}'}$ around the direction $\mathbf{k}'$, then

$$P(\mathbf{k}, \mathbf{k}') = \frac{2}{(\pi e a_0)^2}\frac{1}{\cos\theta}(n_\omega + 1)\frac{k'}{k}\frac{q_\parallel}{(q_\parallel^2 + q_\perp^2)^2}\mathrm{Im}g(q,\omega),$$

This equation represents the most general formulation of so-called dipole scattering theory, which has been remarkably useful in analyzing electron energy-loss measurements [186]. As an application, consider electron scattering from the (collective) C–O stretch vibrational mode of an ordered layer of CO molecules adsorbed on a Cu(100) surface. The open circles in Fig. 3.1 shows the measured inelastic electron scattering intensity, as a function of the polar collection angle θ. The solid line is the

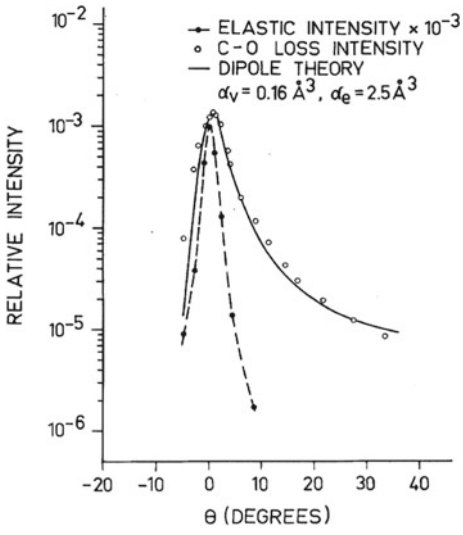

Fig. 3.1 Experimental elastic peak intensity (*solid circles*) and C–O loss peak intensity (*open circles*) versus collection angle θ. The *solid curve* is the dipole theory calculation

theory prediction using the expression for the $g(q, \omega)$ function for an ordered layer of point particles (polarizability α) on a perfect conducting substrate [187] (see (6.47)). Another important applications of the dipole scattering theory presented has been the study of non-local dielectric response of metal surfaces [188–190].

Chapter 4
Spectral Correlation Function for the Electromagnetic Field from Planar Sources

The spectral correlation function for the fluctuating electromagnetic field outside a semi-infinite solid with a planar surface can be calculated using the generalized Kirchhoff law for isotropic materials. For the more general case of anisotropic materials, the same quantity is calculated using the Green function approach. The local density of state of the electromagnetic field is calculated and analyzed in the near-field. In the near-field, the thermal electromagnetic field can be spatially and temporally coherent due to the existence of the surface plasmons or surface phonon polaritons. We show that due to the coupling of the evanescent and propagating electromagnetic waves introduced by a grating, the coherent properties of the electromagnetic field in the near-field can be used to design highly directional (as compared with Lambertian emission) thermal sources working in the far-field.

4.1 Generalized Kirchhoff Law

The theory presented in Sect. 3.2 can be used to calculate the spectral correlation functions for an electromagnetic field radiated by any body. A particularly important limiting case is the radiation from a flat surface. In Appendix A, these correlation functions are calculated using the general theory of a fluctuating electromagnetic field. However, for the planar geometry, these correlation functions can be obtained in a simpler way using the generalized Kirchhoff law. According to the classical Kirchhoff low, the intensity of emission of radiation from a flat element of a body surface in certain direction at a fixed frequency is given by

$$I(\omega, \theta, \phi) = I_0(\omega)[1 - \kappa(\omega, \theta, \phi)] \tag{4.1}$$

where θ is the angle between the normal to the surface and the direction to the radiation detector, ϕ is the azimuthal angle in plane of the sample surface, $\kappa(\omega, \theta, \phi)$ is the energy reflection coefficient of the body at a given frequency of the field in the direction specified by the polar and azimuthal angles θ and ϕ, and $I_0(\omega)$ is the

A.I. Volokitin and B.N.J. Persson, *Electromagnetic Fluctuations at the Nanoscale*,
NanoScience and Technology, DOI 10.1007/978-3-662-53474-8_4

equilibrium intensity of emission, which for a closed cavity is independent of the incidence angle and of the material. In cases of isotropic materials, $\kappa(\omega, \theta, \phi) = \kappa(\omega, \theta)$.

For planar geometry, the electromagnetic field can be decomposed on s- and p-polarized electromagnetic fields. In this representation, the electric field of the emitted radiation can be written in the form

$$\mathbf{E}(\mathbf{r}, \omega) = \int \frac{d^2q}{(2\pi)^2} \left[E_s(q, \omega)\hat{n} + E_p(q, \omega)\hat{\mathbf{K}} \right] e^{i(\mathbf{q}\cdot\mathbf{x} + k_z z)} \tag{4.2}$$

where $\mathbf{r} = (\mathbf{x}, z), k_z = \sqrt{(\omega/c)^2 - q^2}, \hat{q} = \mathbf{q}/q,\ \hat{n} = \hat{z}\times\hat{q}, \hat{\mathbf{K}} = (q\hat{z} - k_z\hat{q})/k,\ k = \omega/c$. The spectral spatial correlation function can be written in the form

$$\left\langle \mathbf{E}(\mathbf{r})\mathbf{E}^*(\mathbf{r}') \right\rangle_\omega = \int \frac{d^2q}{(2\pi)^2} \left[\hat{n} w_s \hat{n} + \hat{\mathbf{K}} w_p \hat{\mathbf{K}}^* \right] e^{i\mathbf{q}\cdot(\mathbf{x}-\mathbf{x}')} e^{i(k_z z - k_z^* z')}, \tag{4.3}$$

where $w_s = \left\langle |E_s(q, \omega)|^2 \right\rangle$ and $w_p = \left\langle |E_p(q, \omega)|^2 \right\rangle$.

The Kirchhoff law is the consequence of the energy conservation law: the intensity of the emitted radiation in thermal equilibrium should be equal to the absorbed energy. Therefore, the Kirchhoff law can be written separately for the s- and p-components of the electromagnetic field. Taking into account that the intensity of the electromagnetic wave is proportional to $\langle |E_{s(p)}|^2 \rangle$, the Kirchhoff law can be written in the form

$$\langle |E_{s(p)}(q, \omega)|^2 \rangle = \langle |E_{0,s(p)}(q, \omega)|^2 \rangle \left[1 - |R_{s(p)}(q, \omega)| \right] \tag{4.4}$$

where $E_{0,s(p)}(q, \omega)$ is the amplitude of the incident plane wave of black body radiation, and where $R_{p(s)}$ is the reflection amplitude for $p(s)$-polarized electromagnetic field. Taking into account that the energy density of the plane wave in the black body radiation can be written in the form (see (3.54) and (3.61)):

$$\begin{aligned} &\frac{1}{8\pi} \left[\langle 2|E_{s(p)}(q, \omega)|^2 \rangle + 2\langle |B_{s(p)}(q, \omega)|^2 \rangle \right] \frac{d^2q}{(2\pi)^2} d\omega \\ &\quad = \frac{1}{2\pi} \langle |E_{s(p)}(q, \omega)|^2 \rangle \frac{d^2q}{(2\pi)^2} d\omega \\ &\quad = \hbar\omega \left(\frac{1}{2} + \frac{1}{e^{(\hbar\omega/k_B T)} - 1} \right) \frac{d^2q}{(2\pi)^2} \frac{dk_z}{2\pi} = \frac{\hbar k^2}{4\pi k_z} \coth\left(\frac{\hbar\omega}{2k_B T} \right) \frac{d^2q}{(2\pi)^2} d\omega \end{aligned} \tag{4.5}$$

for the propagating electromagnetic waves we get

$$w_{p(s)}^{prop} = \coth\left(\frac{\hbar\omega}{2k_B T} \right) \frac{\hbar k^2}{2k_z} \left(1 - |R_{ps}|^2 \right) \tag{4.6}$$

To calculate the spectral correlation function for evanescent waves, we will assume that above the surface of the body at the point $\mathbf{r} = \mathbf{r}'$ there is a small particle with

fluctuating dipole moment $\mathbf{p}^f$, which is characterized by the spectral function of fluctuations

$$\left\langle p_i^f \, p_j^f \right\rangle_\omega = \frac{\hbar}{\pi}\left(\frac{1}{2} + n_i(\omega)\right) \mathrm{Im}\alpha(\omega)\delta_{ij}, \tag{4.7}$$

where $\alpha(\omega)$ is the polarizability of the particle. At each $\mathbf{q}$ it is convenient to choose coordinate axes along vectors $\hat{q}$, $\hat{n}$, $\hat{z}$. The energy absorbed by the particle due to interaction with the electromagnetic field emitted by the body is given by

$$\dot{Q}_s^{part}(q,\omega) = \mathrm{Re}(-i\omega\mathbf{p}^{ind}\cdot\mathbf{E}_s^*) = \omega\mathrm{Im}\alpha(\omega)|E_s|^2 e^{-2\mathrm{Im}k_z z'} \tag{4.8}$$

$$\dot{Q}_p^{part}(q,\omega) = \mathrm{Re}(-i\omega\mathbf{p}^{ind}\cdot\mathbf{E}_p^*) = \omega\mathrm{Im}\alpha(\omega)|E_p|^2\frac{q^2+|k_z|^2}{k^2}e^{-2\mathrm{Im}k_z z'} \tag{4.9}$$

where $\mathbf{p}^{ind} = \alpha(\omega)\mathbf{E}$ is the induced dipole moment of the particle. The electromagnetic field at the point $\mathbf{r}$ created by the particle located at the point $\mathbf{r}'$ (assuming $z < z'$) can be written in the form

$$\mathbf{E}_s^{part}(\mathbf{r},\mathbf{r}') = \frac{2\pi i k^2}{k_z}\left(e^{ik_z(z'-z)} + R_s e^{ik_z(z+z')}\right) p_n^f \hat{n} e^{i\mathbf{q}\cdot(\mathbf{x}-\mathbf{x}')}, \tag{4.10}$$

$$\begin{aligned}\mathbf{E}_p^{part} = \frac{2\pi i}{k_z}\Big[&\left(e^{ik_z(z'-z)} + R_p e^{ik_z(z+z')}\right) q\hat{z} \\ &+ \left(e^{ik_z(z'-z)} - R_p e^{ik_z(z+z')}\right) k_z\hat{q}\Big](k_z p_q^f + q f_z^f) e^{i\mathbf{q}\cdot(\mathbf{x}-\mathbf{x}')},\end{aligned} \tag{4.11}$$

$$\mathbf{B}_s^{part} = \frac{2\pi i k}{k_z}\left[\left(e^{ik_z(z'-z)} + R_s e^{ik_z(z+z')}\right) q\hat{z} + \left(e^{ik_z(z'-z)} - R_s e^{ik_z(z+z')}\right) k_z\hat{q}\right] p_n^f e^{i\mathbf{q}\cdot(\mathbf{x}-\mathbf{x}')}, \tag{4.12}$$

$$\mathbf{B}_p^{part}(\mathbf{r},\mathbf{r}') = -\frac{2\pi i k}{k_z}\left(e^{ik_z(z'-z)} + R_p e^{ik_z(z+z')}\right)(k_z p_q^f + q f_z^f)\hat{n} e^{i\mathbf{q}\cdot(\mathbf{x}-\mathbf{x}')}. \tag{4.13}$$

The energy absorbed by the body due to interaction with the evanescent waves created by the particle is determined by the z-component of the Poynting vector and can be written separately for p- and s-polarized waves:

$$\begin{aligned}\dot{Q}_s^b =& \frac{c}{8\pi}\left(\langle E_n B_q^*\rangle + c\cdot c\right) = \coth\left(\frac{\hbar\omega}{2k_B T}\right)\frac{\hbar c k^3}{4|k_z|^2} \\ &\times (k_z - k_z^*)(R_s^* - R_s)\mathrm{Im}\alpha(\omega)e^{-2\mathrm{Im}k_z z'},\end{aligned} \tag{4.14}$$

$$\dot{Q}_p^b = \frac{c}{8\pi}\left(\langle E_q B_n^*\rangle + c\cdot c\right) = \coth\left(\frac{\hbar\omega}{2k_BT}\right)\frac{\hbar ck^3}{4|k_z|^2} \times (k_z - k_z^*)(R_p^* - R_p)\mathrm{Im}\alpha(\omega)\frac{q^2+|k_z|^2}{k^2}e^{-2\mathrm{Im}k_z z'}. \tag{4.15}$$

In the thermal equilibrium, the energy absorbed by the particle should be equal to the energy absorbed by the body. From this condition, and using (4.8), (4.9), (4.14) and (4.15) we get

$$w_{s(p)}^{evan} = \coth\left(\frac{\hbar\omega}{2k_BT}\right)\frac{\hbar k^2}{4|k_z|^2}\left(k_z - k_z^*\right)\left(R_{s(p)}^* - R_{s(p)}\right) \tag{4.16}$$

Taking into account that k_z is pure real for the propagating waves ($q < k$) and pure imaginary for the evanescent waves ($q > k$), the contribution to $w_{p(s)}$ from propagating waves can be written in the form

$$w_{p(s)}^{prop} = \coth\left(\frac{\hbar\omega}{2k_BT}\right)\frac{\hbar k^2}{4|k_z|^2}\left(k_z + k_z^*\right)\left(1 - |R_{ps}|^2\right) \tag{4.17}$$

Summarizing (4.16) and (4.17) we finally get

$$w_{s(p)} = w_{s(p)}^{prop} + w_{s(p)}^{evan} = \coth\left(\frac{\hbar\omega}{2k_BT}\right)\frac{\hbar k^2}{4|k_z|^2} \times \left[(k_z + k_z^*)(1 - |R_{p(s)}|^2) + (k_z - k_z^*)(R_{s(p)}^* - R_{s(p)})\right] \tag{4.18}$$

Using Maxwell's equation

$$\nabla \times \mathbf{E}(\mathbf{r}) = \frac{i\omega}{c}\mathbf{B}(\mathbf{r}),$$

from (4.3), we get the spectral correlation function for the magnetic induction field

$$\left\langle \mathbf{B}(\mathbf{r})\mathbf{B}(\mathbf{r}')\right\rangle_\omega = \coth\left(\frac{\hbar\omega}{2k_BT}\right)\int\frac{d^2q}{(2\pi)^2}\left[\hat{n}w_p\hat{n} + \hat{\mathbf{K}}w_s\hat{\mathbf{K}}^*\right]e^{i\mathbf{q}\cdot(\mathbf{x}-\mathbf{x}')}e^{i(k_z z - k_z^* z')}, \tag{4.19}$$

and the spectral cross-correlation function

$$\left\langle \mathbf{E}(\mathbf{r})\mathbf{B}(\mathbf{r}')\right\rangle_\omega = \coth\left(\frac{\hbar\omega}{2k_BT}\right)\int\frac{d^2q}{(2\pi)^2}\left[\hat{\mathbf{K}}w_p\hat{n} + \hat{n}w_s\hat{\mathbf{K}}^*\right]e^{i\mathbf{q}\cdot(\mathbf{x}-\mathbf{x}')}e^{i(k_z z - k_z^* z')}. \tag{4.20}$$

Using (4.20), we can calculate the intensity of the radiated energy $I(\omega)$ into vacuum at $T = 0$ K:

$$I(\omega)d\omega = 2\left[\langle S_z(T,\omega)\rangle - \langle S_z(0,\omega)\rangle\right]d\omega, \tag{4.21}$$

where the factor 2 arises for the same reason as in (3.54). The z-component of the Poynting vector is given by

$$\begin{aligned}\langle S_z(T,\omega)\rangle &= \frac{c}{4\pi}\mathrm{Re}[\mathbf{E}(\mathbf{r})\times\mathbf{B}(\mathbf{r})]_z \\ &= \frac{c\hbar}{16\pi|k_z|^2}\coth\left(\frac{\hbar\omega}{2k_BT}\right)\int\int\frac{d^2q}{(2\pi)^2}\frac{(k_z+k_z^*)(w_s+w_p)}{k}\frac{d^2q}{(2\pi)^2} \\ &= \frac{c\hbar k}{4\pi^2}\coth\left(\frac{\hbar\omega}{2k_BT}\right)\int_0^{\frac{\omega}{c}}dqq\frac{1-|R_p|^2+1-|R_s|^2}{2} \end{aligned} \tag{4.22}$$

Only propagating waves ($q < \omega/c$) contribute to this expression. Using (4.22) in (4.21), we get

$$I(\omega) = \frac{c\hbar k}{2\pi^2}\frac{1}{e^{(\hbar\omega/k_BT)}-1}\int_0^{\frac{\omega}{c}}dqq\frac{1-|R_p|^2+1-|R_s|^2}{2} \tag{4.23}$$

Introducing $d\Omega$, the elementary solid angle, we have the relation $qdq/k^2 = d\Omega\cos\theta/2\pi$. The radiated intensity is then given by

$$I(\omega) = \frac{\hbar\omega^3}{2\pi^2c^2}\frac{1}{e^{(\hbar\omega/k_BT)}-1}\int_\Omega\frac{d\Omega\cos\theta}{2\pi}\frac{1-|R_p|^2+1-|R_s|^2}{2} \tag{4.24}$$

where the integration is over the upper semi-sphere for $0 < \theta < \pi/2$. In the case of a black body, i.e. a body for which the reflection factors vanish, we get

$$I(\omega) = \frac{\hbar\omega^3}{4\pi^2c^2}\frac{1}{e^{(\hbar\omega/k_BT)}-1} = \pi I_0(\omega,T) \tag{4.25}$$

where

$$I_0(\omega,T) = \frac{\hbar\omega^3}{4\pi^3c^2}\frac{1}{e^{(\hbar\omega/k_BT)}-1} \tag{4.26}$$

is the black body specific intensity. When the medium situated below the interface does not behave as a black body, the flux takes the classical form

$$I(\omega) = I_0(\omega,T)\int_\Omega\varepsilon'(\theta,\omega)\cos\theta d\Omega \tag{4.27}$$

where we have identified the emissivity $\varepsilon'(\theta,\omega) = (1-|R_p|^2+1-|R_s|^2)/2$. In the presence of a single interface, we note that the radiation emitted is not different from the usual one, i.e. near field does not play any role in this situation.

4.2 The Green's Function Approach

According to (A.4) outside of any body, the spectral correlation function for electric field is given by:

$$\left\langle E_i(\mathbf{r})E_j^*(\mathbf{r}')\right\rangle_\omega = \frac{\hbar c^2}{16\pi^2 i\omega^2}\coth\left(\frac{\hbar\omega}{2k_BT}\right) \times \int d\mathbf{S}_1''\Big\{D_{ik}(\mathbf{r},\mathbf{r}'')\nabla''D_{jk}^*(\mathbf{r}',\mathbf{r}'') - D_{jk}^*(\mathbf{r}',\mathbf{r}'')\nabla''D_{ik}(\mathbf{r},\mathbf{r}'')\Big\}. \tag{4.28}$$

For the plane surface, it is convenient to decompose the electromagnetic field into s- and p-polarized plane waves. The decomposition of the electromagnetic field on s- and p-polarized waves is determined by the vectors $\hat{n}_s = [\hat{z}\times\hat{q}] = (-q_y, q_x, 0)/q$, $\hat{n}_p^{\pm} = [\hat{k}^{\pm}\times\hat{n}_s] = (\mp q_x k_z, \mp q_y k_z, q^2)/(kq)$ where $\mathbf{k}^{\pm} = \mathbf{q} \pm \hat{z}k_z$, $k_z = ((\omega/c)^2 - q^2)^{1/2}$, $k = \omega/c$, $\mathbf{q}$ is the surface component of the wave vector. In this representation, the Green's tensor is given by

$$\hat{\mathbf{D}}(\mathbf{r},\mathbf{r}') = \int \frac{d^2q}{(2\pi)^2}\hat{\mathbf{D}}(z,z',\mathbf{q})e^{i\mathbf{q}\cdot(\mathbf{x}-\mathbf{x}')}, \tag{4.29}$$

and the spectral correlation function for the electric field is given by

$$\left\langle \mathbf{E}(\mathbf{r})\mathbf{E}^*(\mathbf{r}')\right\rangle_\omega = \frac{\hbar c^2}{16\pi^2 i\omega^2}\coth\left(\frac{\hbar\omega}{2k_BT}\right)\int\frac{d^2q}{(2\pi)^2} \times \Big(\hat{\mathbf{D}}(z,z'',\mathbf{q})\frac{\partial}{\partial z''}\hat{\mathbf{D}}^+(z',z'',\mathbf{q}) - \frac{\partial}{\partial z''}\hat{\mathbf{D}}(z,z'',\mathbf{q})\hat{\mathbf{D}}^+(z',z'',\mathbf{q})\Big)_{z''=+0} e^{i\mathbf{q}\cdot(\mathbf{x}-\mathbf{x}')}. \tag{4.30}$$

The Green's functions in (4.30) can be obtained from the Green's functions calculated in Appendix C in the vacuum gap between two semi-infinite plates, assuming the reflection amplitude for body two vanishes, $R_{2p(s)} = 0$. As a result we get the following expression for the Green's function in (4.30)

$$\hat{\mathbf{D}}(z,z') = \frac{2\pi i k^2}{k_z}\Big\{e^{\mathrm{i}k_z|z-z'|}\hat{\mathbf{I}} + \hat{\mathbf{R}}e^{\mathrm{i}k_z(z+z')}\Big\}, \tag{4.31}$$

where the 3×3 reflection matrix is given by

$$\hat{\mathbf{R}} = \hat{\mathbf{n}}^+ R\hat{\mathbf{n}}^-,$$

$\hat{\mathbf{n}}^{\pm} = (\hat{n}_s^{\pm}, \hat{n}_p^{\pm})$. The 2×2 reflection matrix $R_{\lambda\lambda'}$ determines the reflection amplitudes for the waves with different polarization $\lambda = (s, p)$. This matrix is diagonal for

isotropic materials. However, in the general case of anisotropic materials, this matrix is not diagonal

$$R = \begin{pmatrix} R_{ss} & R_{sp} \\ R_{ps} & R_{ss} \end{pmatrix}.$$

$\hat{\mathbf{I}}$ is the 3×3 unit matrix. The substitution of (4.31) in (4.30) gives

$$\left\langle \mathbf{E}(\mathbf{r})\mathbf{E}^*(\mathbf{r}') \right\rangle_\omega = \coth\left(\frac{\hbar\omega}{2k_B T}\right) \int \frac{d^2q}{(2\pi)^2} \left(\frac{\omega}{c}\right)^2 \hat{\mathbf{n}}^+ w \hat{\mathbf{n}}^{+*}, \tag{4.32}$$

where

$$w = \frac{\hbar}{4|k_z|^2}\left[(k_z + k_z^*)(I - RR^*) + (k_z^* - k_z)(R - R^+)\right],$$

where I is the 2×2 unit matrix. For the isotropic materials, the matrix w becomes diagonal: $w_{\lambda\lambda'} = w_\lambda \delta_{\lambda\lambda'}$ where

$$w_\lambda = \frac{\hbar}{4|k_z|^2}\left[(k_z + k_z^*)(1 - |R_\lambda|^2) + (k_z^* - k_z)(R_\lambda - R_\lambda^*)\right],$$

where $\lambda = (s, p)$.

For the evanescent waves we can use (3.64). In this case, the calculations are simpler. Taking into account the fact that, for the evanescent waves, k_z is pure imaginary ($k_z = i|k_z|$), we get

$$\hat{\mathbf{D}}(\mathbf{r}, \mathbf{r}', \omega) = 2\pi k^2 \int \frac{d^2q}{(2\pi)^2} \frac{e^{i\mathbf{q}\cdot(\mathbf{x}-\mathbf{x}') - |k_z|(z+z')}}{|k_z|} \hat{\mathbf{n}}^+ \mathrm{Im} R \hat{\mathbf{n}}^{+*} \tag{4.33}$$

Substituting these equation in (3.64) gives the part of (4.32) corresponding to the evanescent waves.

4.3 Density of Emitted Electromagnetic Energy

The energy density of the fluctuation electromagnetic field, radiated into the vacuum by the medium, which occupies half-space $z < 0$, is, according to (3.54), given by

$$u(\omega, T, \mathbf{r})d\omega = \frac{1}{8\pi}\left[2\langle \mathbf{E}(\mathbf{r})^2 \rangle_\omega + 2\langle \mathbf{H}^2 \rangle_\omega\right] d\omega. \tag{4.34}$$

Using (4.34) with (4.3) and (4.19), the total electromagnetic energy, radiated by the solid at a temperature of T in the vacuum at a temperature of 0 K at a distance of z from the surface of medium, is given by

$$u(\omega, T, z) = \frac{\Pi(\omega, T)\omega^2}{4\pi^2 c^3}\left\{\int_0^{\frac{\omega}{c}} \frac{dqq}{k|k_z|}\left[(1-|R_p|^2)+(1-|R_s|^2)\right]+\right.$$

$$\left.+2\int_{\frac{\omega}{c}}^{\infty} \frac{dqq^3}{k^3|k_z|}\left[\mathrm{Im}R_p+\mathrm{Im}R_s\right]e^{-2|k_z|z}\right\}, \tag{4.35}$$

where $k = \omega/c$, $\Pi(\omega, T)$ is determined by Plank's formula

$$\Pi(\omega, T) = \frac{\hbar\omega}{e^{\beta\hbar\omega}-1}. \tag{4.36}$$

In (4.36), we do not take into account the temperature-independent contribution from the zero-point oscillations of the electromagnetic field.

Let us apply the general equation (4.35) for concrete materials. Let us first consider a material that supports surface waves in the infrared, such as silicon carbide (SiC). Figure 4.1 shows the energy density $u(\omega, T, z)$ versus the frequency at different distances from a semi-infinite solid of SiC. The semi-infinite medium is at temperature $T = 300$ K whereas the vacuum is at $T = 0$ K. Note that at $T = 300$ K, Wiens law gives a peak wavelength for thermal radiation of $\lambda_W = 10$ μm. In the

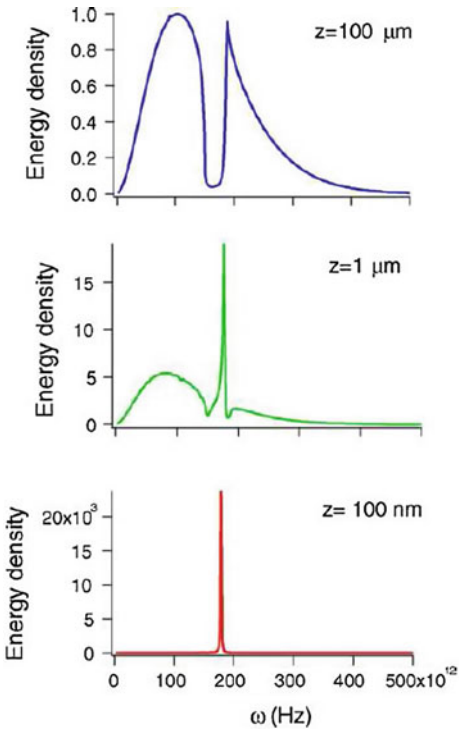

Fig. 4.1 Total electromagnetic energy density above a plane interface separating SiC at $T = 300$ K from vacuum at $T = 0$ K. From [9]

far field, i.e. for distances $z \gg \lambda_W$, the energy density spectrum resembles that of a black body. The difference from that of a Planck spectrum comes from the fact that SiC is a material with a high reflectivity of around $\lambda_W = 10\ \mu\text{m}$ or $\omega = 1.7 \times 10^{14}\ \text{s}^{-1}$. Thus, its emissivity is small at this frequency. This property follows from the expression for the electromagnetic energy due to propagating waves only (first term in (4.35))

$$u^{prop}(\omega, T, z) = u^0(\omega, T) \int \frac{d\Omega}{4\pi} \frac{\left[(1 - |R_p|^2) + (1 - |R_s|^2)\right]}{2}, \tag{4.37}$$

where we have used $2\pi q dq = k^2 \cos\theta d\Omega$, and where θ is the angle between the emission direction and the normal of the surface. The integral is performed over a half-space and $u^0(\omega, T) = (\omega^2/\pi^2 c^3)\Pi(\omega, T)$ is the electromagnetic energy density in a cavity at thermal equilibrium T. In the far field, the evanescent waves do not contribute to the energy density because of the exponential decay $e^{-2|k_z|z}$. We note that if the medium is totally absorbing ($R_{p(s)} = 0$), then the energy density due to propagating waves is half the energy calculated in a vacuum at thermal equilibrium. This is not surprising, since we are computing only the emitted part of the radiation. In the case of equilibrium radiation, there is also the contribution of the radiation coming from the upper half-space. At a distance $z = 1\ \mu\text{m}$, which is slightly larger than λ_W, the energy density spectrum changes drastically and a strong peak emerges. At $z = 100$ nm, one observes that the thermal emission is almost monochromatic around $\omega = 1.79 \times 10^{14}\ \text{s}^{-1}$. At this frequency, the energy density has increased by more than four orders of magnitude. The peak corresponds to the excitation of a surface wave. This distance is in agreement with the decay length of the surface waves as discussed in Chap. 2. At distances much smaller than the wavelength, we enter a regime that we denote as the extreme near field region. The leading contribution now comes from the very large wavevectors q in the energy density integral. At large q, it can be shown that $k_z \approx k_{z1} \approx iq$, so that R_s tends to $\approx (\varepsilon - 1)(\omega/2cq)^2$ and R_p tends to its electrostatic limit $(\varepsilon - 1)/(\varepsilon + 1)$. In this case, the contributions to the density of the electric energy from p- and s-polarized electromagnetic waves are given by

$$u_p(\mathbf{r}, \omega) = \frac{1}{8} u^0(\omega, T) \left(\frac{c}{\omega d}\right)^3 \frac{\varepsilon''}{|\varepsilon + 1|^2}, \tag{4.38}$$

$$u_s(\mathbf{r}, \omega) = \frac{1}{16} u^0(\omega, T) \left(\frac{c}{\omega d}\right) \varepsilon'', \tag{4.39}$$

where ε' and ε'' are the real and imaginary part of dielectric function $\varepsilon = \varepsilon' + i\varepsilon''$, and $u^0(\omega, T)$ is the density of the electromagnetic energy for *black body radiation*. For p-polarized electromagnetic waves and $\varepsilon'' \ll 1$, the near-field emission spectrum has a strong peak near the frequency ω_0 defined by the condition $\varepsilon'(\omega_0) = -1$. This effect results from the existence of a large number of surface modes with different wave numbers but with frequencies $\omega \approx \omega_0$ that are very close to each other. Therefore, if ε'' is not very large at $\omega = \omega_0$ the density of surface modes will necessarily

display a strong peak at $\omega = \omega_0$. From (4.38) and (4.39), it follows that $u_s/u_p \sim |\varepsilon + 1|^2(\omega d/c)^2$. For metals, $|\varepsilon| \gg 1$, and therefore the contribution in energy density from the s- polarized waves for the infrared frequencies will exceed contribution from the p- polarized waves up to the very small distances. The presence of surface waves is the origin of the peak in the near-field spectrum of SiC at $\omega = 1.78 \times 10^{14}$ s^{-1}. However, since the surface waves decay exponentially away from the surface, this peak will vanish in the far zone. The presence of a resonance in the density of modes $N(z, \omega)$ is, however, not required for observing spectral changes caused by the loss of evanescent modes. Indeed, in the short-distance regime, the spectrum is given by (4.38), whereas, in the far-field, the spectrum is given by (4.37). Thus, even in the absence of resonant surface waves, the near-field spectrum is different from the far-field spectrum, but the changes are less dramatic.

Not all materials that support surface waves exhibit strong peaks in their near-field thermal energy density spectrum. Indeed, as can be seen in (4.38), a peak is exhibited if the frequency where $\varepsilon(\omega)$ approaches -1 corresponds to a frequency range where $\Pi(\omega, T)$ is not too small. For example, metals exhibit surface plasmon polariton in the UV or visible range where $\Pi(\omega, T)$ is exponentially small at ambient temperature. Thus, metals do not exhibit any strong peak in their thermal energy density spectrum in the near field.

4.4 Local Density of States

The density of states (DOS) is a fundamental quantity from which many macroscopic quantities can be derived. In statistical physics, the DOS allows the partition function of a system, from which all the macroscopic properties follow, to be calculated. The local density of states (LDOS) is useful for studying a non-uniform system. The local density of electronic states is widely used in solid-state physics. It has been shown [192], for instance, that a scanning tunneling microscope images the electronic LDOS. The local character of the LDOS clearly describes the spatial distribution of electrons in the solid. A similar spatial dependence is also relevant for electromagnetic waves. Whereas the intensity is uniform in vacuum in equilibrium, this is not the case in a waveguide or above an interface. In addition, while the LDOS is well known and frequently used for electrons in solid-state physics [37], its electromagnetic counterpart is not well known or used in the literature. Compared with electronic systems, two differences must be taken into account: the vectorial nature of the fields and the existence of losses.

We consider a system in thermal equilibrium at temperature T. In a vacuum, one can define the electromagnetic energy $U(\omega)$ by the product of the DOS $\rho(\omega)$ and the mean energy of each state at temperature T:

$$U(\omega) = \rho(\omega)\frac{\hbar\omega}{\exp(\hbar\omega/k_B T) - 1}. \tag{4.40}$$

We now introduce an LDOS by using, as a starting point, the local density of electromagnetic energy $u(\mathbf{r}, \omega)$ at a given point $\mathbf{r}$ in space, and at a given angular frequency ω. We define the LDOS $\rho(\mathbf{r}, \omega)$ so that

$$u(\mathbf{r}, \omega) = \rho(\mathbf{r}, \omega) \frac{\hbar\omega}{\exp(\hbar\omega/k_B T) - 1}. \tag{4.41}$$

Using (4.35) for the LDOS for p- and s-propagating electromagnetic waves, we get

$$\rho_{p(s)}^{propE} = \rho_{p(s)}^{propH} = \frac{\rho_v}{4} \int_0^{\frac{\omega}{c}} \frac{dqq}{kk_z} \left(1 - |R_{p(s)}|^2\right), \tag{4.42}$$

where the superscripts E and H denote the electric and magnetic contributions, respectively; $\rho_v(\omega) = \omega^2/\pi^2 c^3$ is the vacuum density of states, and for the contributions from the evanescent waves we get

$$\rho_{p(s)}^{evanE(H)} = \frac{\rho_v}{2} \int_{\frac{\omega}{c}}^{\infty} \frac{dqq}{k|k_z|} \left(\frac{2q^2}{k^2} - 1\right) \mathrm{Im} R_{p(s)} e^{-2|k_z|z}, \tag{4.43}$$

$$\rho_{s(p)}^{evanE(H)} = \frac{\rho_v}{2} \int_{\frac{\omega}{c}}^{\infty} \frac{dqq}{k|k_z|} \mathrm{Im} R_{s(p)} e^{-2|k_z|z}. \tag{4.44}$$

From (4.42)–(4.44), it follows that, for the propagating electromagnetic waves, the energy of the magnetic field is equal to the energy of the electric field. For the evanescent waves, taking into account that $\left(2q^2/k^2 - 1\right) > 1$, we get that, for p-polarized waves, the dominate contribution to the energy comes from the electric field, and, for s-polarized waves, the dominate contribution comes from the magnetic field. This difference is explained as follows: for the plane wave, the electric field is related to the induction magnetic field by $(c/\omega)[\mathbf{k} \times \mathbf{E}] = \mathbf{B}$, where $\mathbf{k} = \mathbf{q} + \hat{z}k_z$. Thus, for the s-polarized waves, we obtain the relationship $|\mathbf{k}|(c/\omega)|E| = |B|$. For the propagating waves, $|\mathbf{k}| = \sqrt{q^2 + k_z^2} = (\omega/c)$; therefore $|E| = |B|$, which means the equality of the magnetic and electric energy. For the evanescent waves of $k_z = i\sqrt{q^2 - (\omega/c)^2}$; therefore

$$|\mathbf{k}| = \sqrt{q^2 + k_z k_z^*} = \sqrt{2q^2 - \left(\frac{\omega}{c}\right)^2}.$$

Thus, $|B| = \sqrt{2(cq/\omega)^2 - 1}|E| > |E|$, which means that the magnetic energy is larger than electric energy. Similarly, it is possible to show that for the p-polarized evanescent waves, $|E| = \sqrt{2(cq/\omega)^2 - 1}|B| > |B|$, i.e., in this case the electric energy is larger than magnetic energy.

Using (4.42)–(4.44) and the Fresnel's formulas for the reflection amplitudes, we get that in the limit $z \ll c/(\omega|\varepsilon|^{1/2})$, the contribution from the evanescent waves considerably exceeds the contribution from the propagating waves. In this limit

$$\rho_p^E = \frac{\rho_v}{8k^3z^3}\frac{\varepsilon''}{|\varepsilon+1|^2}, \tag{4.45}$$

$$\rho_s^H = \frac{\rho_v}{16kz}\varepsilon'', \tag{4.46}$$

$$\rho_p^H = \frac{\rho_v}{4kz}\frac{\varepsilon''}{|\varepsilon+1|^2}, \tag{4.47}$$

$$\rho_s^E = \frac{\rho_v}{6\sqrt{2}}\sqrt{|\varepsilon|+\varepsilon'}, \tag{4.48}$$

where, in obtaining (4.48), we have used that

$$\int_0^\infty dq e^{-2qd}\mathrm{Im}\frac{q-s}{q+s} \approx \int_0^\infty dq \mathrm{Im}\frac{q-s}{q+s} =$$
$$= \mathrm{Im}\left\{ \mid s_0 \mid e^{i\phi}\int_0^\infty dt \frac{t-\sqrt{t^2-1}}{t+\sqrt{t^2-1}}\right\} =$$
$$= \frac{1}{2}\mathrm{Im}\left\{ \mid s_0 \mid e^{\mathrm{i}\phi}\int_{-\mathrm{i}\pi/2}^\infty \mathrm{d}z\left(e^{-z}-e^{-3z}\right)\right\} = \frac{2}{3} \mid s_0 \mid \cos(\phi),$$

where $s = \sqrt{q^2-(\omega/c)^2\varepsilon}$, $s_0 = (\omega/c)\sqrt{\varepsilon} = |s_0|\exp i\phi$. From comparison of (4.45)–(4.48) it follows that, for the metals in the infrared frequency region up to very small distances, the main contribution to the energy density comes from the magnetic field of the s-polarized electromagnetic waves.

4.5 Coherence Properties of Planar Thermal Sources in the Near-Field

Equations (4.3) and (4.19) describe the temporal and spatial coherence of the thermal radiation of the near field emitted into free space from the flat surface. Thermal radiation is often presented as a typical example of an incoherent light source and is in marked contrast to a laser. Whereas a laser is a highly monochromatic and very directional light source, a thermal source has a broad spectrum and is usually quasi-isotropic. However, as is often the case, different behavior can be expected on a microscopic scale. Thus, it has been shown [28–30] that the field emitted by a thermal source made of a polar material is enhanced by more than four orders of magnitude and is partially coherent at distances in the order of 10–100 nm. This phenomenon is due to surface electromagnetic waves, and can be observed only on material supporting them. The existence conditions for surface waves was considered in Chap. 2. Surface electromagnetic waves are modes that propagate along an interface, and decrease exponentially in the perpendicular direction (evanescent waves). The

propagation length of these surface waves is typically hundred wavelengths, resulting in a long-range spatial correlation of the electromagnetic field along the interface [28–30]. The near-field properties of the thermal electromagnetic field in the presence of surface electromagnetic waves were reviewed in [9].

There are different types of optically active surface waves. Surface phonon polaritons are observed for polar material such as SiC, glass, II–IV and III–V semiconductors. They are mechanical vibrations (phonons) propagating in a partially ionic material so that each unit cell becomes an oscillating electric dipole. Surface plasmon polaritons are longitudinal electron oscillations (acoustic type wave in an electron gas) that can be observed for metals and doped semiconductors, which generate electromagnetic fields with longitudinal polarization. Surface waves due to excitons, and vibrations of alkali ions in adlayers have also been observed.

Equations (4.3) and (4.19) also suggest a new application for near-field spectroscopy. The near-field spectrum at a given distance to the interface gives access to $\mathrm{Im}R_{p(s)}$, and one can hope to obtain information about the reflection amplitude for large wave vectors, similar to the method usually used to obtain $R_{p(s)}$ for propagating electromagnetic waves from reflectivity measurements. With the rapid development of near-field optical microscopy, such near-field spectra can be measured. This could open the way to a new technique of local solid-state spectroscopy. The measurement of thermal near-field using a scanning near-field microscope has been demonstrated recently [193]. This is an important step towards the concept of local spectroscopy.

4.5.1 Spatial Coherence in the Near-Field

The spatial coherence of the electromagnetic field is characterized by its spectral correlation function $\langle \mathbf{E}(\mathbf{r})\mathbf{E}(\mathbf{r}')\rangle_\omega$ at two different points for a particular frequency. Figure 4.2 represents the spectral correlation function of the electric field for different metallic surfaces at a given distance $z = 0.05\lambda$ ($\lambda = 2\pi c/\omega$ is the wavelength) to the interface. It can be seen that the correlation oscillates and has an exponentially decaying envelope. The decay length is much larger than the wavelength, indicating that the fields are coherent over large distances. This surprising phenomenon is due to the excitation of surface waves along the interface. The physical mechanism is based on the fact that a small volume element contains random currents that excite a surface wave. This surface wave propagates along the interface over distances larger than the wavelength. It follows that different points may be illuminated by the same random source so that they are correlated. Accordingly, one does not expect any correlation between the *s*-polarized field since no surface wave exists for *s*-polarization. If one uses a material with a real part of the dielectric constant larger than -1, no surface wave can propagate and thus no correlation should be observed. Therefore, Fig. 4.2 shows the case of tungsten in the visible that does not support surface waves. It is seen that the coherence length is smaller than a wavelength so that the radiation field appears to be more incoherent than blackbody radiation.

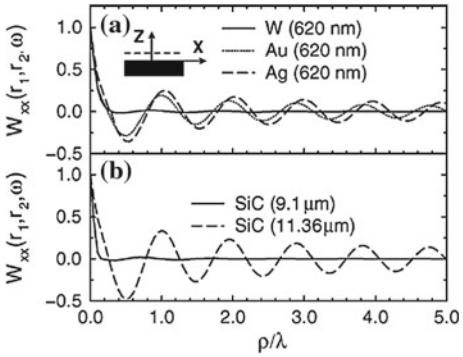

Fig. 4.2 Spectral correlation function $\langle E_x(\mathbf{r})E_x(\mathbf{r}')\rangle_\omega$(denoted as W_{xx} in the label of the figure) of the thermally emitted x-component of the electric field vs. ρ/λ, where $\rho = |\mathbf{r}_1 - \mathbf{r}_2|$ **a** for different metals and **b** for SiC at different wavelengths. The long-range correlation is due to surface-plasmon polaritons for metals, and to surface-phonon polaritons for SiC. From [29]

A similar behavior is observed for SiC, a polar material that supports surface-phonon polaritons in a frequency band. Within this band, at a wavelength of 11.36 μm, a long-range correlation is observed, whereas for a wavelength (9.1 μm) that is not in the band where surface waves exist, the correlation decays very rapidly.

Let us discuss in simple terms the physical origin of these unusual coherence properties. The long-range coherence is unexpected because the fluctuating currents are δ-correlated as shown by the fluctuation-dissipation theorem. This is the reason why the fields are typically assumed to be δ-correlated in space. However, the fluctuating currents excite weakly damped collective modes in the material. In the case of a metal, a surface plasmon can be excited. In the case of a polar crystal, a surface phonon polariton can be excited. Both surface waves are extended modes along the surface. The induced currents associated with these extended modes are therefore coherent over large distances. More precisely, the coherence length is expected to be given by the decay length of these surface modes. This has been confirmed by a detailed asymptotic analysis in [31]. The other surprising property shown in Fig. 4.2 is that the coherence length defined as the FWMH of the cross-spectral density can be smaller than the wavelength. In other words, a source can be more spatially incoherent than the black body radiation. The key idea is that, close to an interface, the field contains evanescent waves so that features smaller than the wavelength can exist. This is not the case in a vacuum and therefore the field has a minimum coherence length. Since the amplitude of evanescent waves of large wavevector q decays as $\exp(-2qz)$, it is clear that the distance z appears as a cutoff wavelength. This explains the coherence length increasing as z increases into the near-field regime.

4.5.2 Temporal Coherence in the Near-Field

The temporal coherence of the electromagnetic field is characterized by the time-correlation function (at a fixed point $\mathbf{r}$ in space) of the electromagnetic field:

$$\left\langle E_k(\mathbf{r}, t+\tau) E_l(\mathbf{r}, t) \right\rangle \tag{4.49}$$

This correlation function is a measurement of the memory of the random field. It is useful to introduce a typical decay time t_{coh} of the correlation function, called coherence time. A Michelson interferometer with aligned mirrors performs a measurement of the correlation function. Indeed, the interference term of the signal can be written as $E_k(\mathbf{r}, t+\tau)E_l(\mathbf{r}, t)$ where τ is the flight time corresponding to the optical path length difference δ_{opt} between the two paths $\delta_{opt} = c\tau$. If the path length difference is larger than the longitudinal coherence length ct_{coh}, no interferences can be observed.

The temporal coherence of the EM field is related to its power spectral density. This is clearly seen by using the Wiener–Khinchin theorem [181, 182], which shows that the power spectral density is the Fourier transform of the correlation function. Alternatively, we can start from (3.24). It follows that:

$$\left\langle E_k(\mathbf{r}, t+\tau) E_l(\mathbf{r}, t) \right\rangle = \mathrm{Re}\left[\int_0^\infty 4\hbar n(\omega, T) \mathrm{Im}[D_{kl}^{EE}(\mathbf{r}, \mathbf{r}, \omega)] e^{i\omega\tau} \frac{d\omega}{2\pi} \right] \tag{4.50}$$

Let us first consider the temporal coherence of the field in vacuum. The imaginary part of the Green's tensor (3.46) does not diverge, and yields zero for non-diagonal terms and $\omega^3/3c^3$ for diagonal terms. It follows that the time-correlation function of the blackbody radiation is given by:

$$\left\langle E_k(\mathbf{r}, t+\tau) E_l(\mathbf{r}, t) \right\rangle = \delta_{kl} \mathrm{Re}\left[\int_0^\infty 4\Pi(\omega, T) \frac{\omega^2}{3c^3} e^{i\omega\tau} \frac{d\omega}{2\pi} \right] \tag{4.51}$$

Since the integrand has a large spectral width, it appears that the coherence time is in the order of the peak radiation period.

If we now consider the case of an interface, we know that the spectrum can be very different in the near field. We have seen previously that the contribution of the surface wave dramatically modifies the density of electromagnetic energy. In particular, we have seen that the density of energy becomes quasi-monochromatic, which suggests a large coherence time. More specifically, in the extreme near field, we have seen in Sect. 4.4 that the Green's function has a resonant denominator $\varepsilon + 1$. Close to the resonance where $\mathrm{Re}[\varepsilon(\omega_0)] = -1$, we can expand the dielectric constant as

$$\varepsilon(\omega) = -1 + i\varepsilon''(\omega_0) + (\omega - \omega_0)\frac{d\varepsilon'}{d\omega} \tag{4.52}$$

where we have used the notation $\varepsilon = \varepsilon' + i\varepsilon''$. Thus, the denominator $\varepsilon + 1$ can be cast in the form

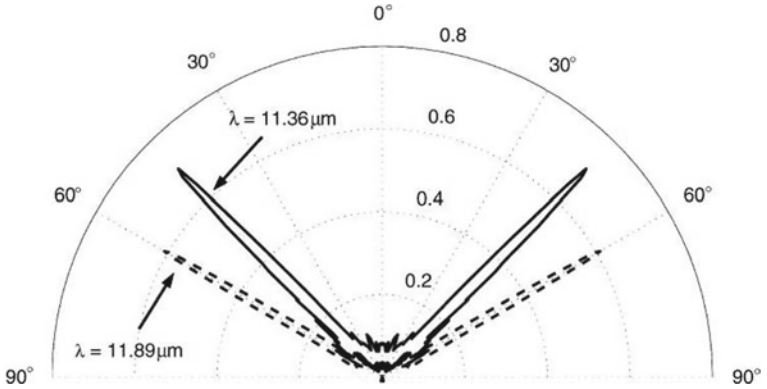

Fig. 4.3 Experimental angular emission of a SiC grating at two different wavelengths. The angular pattern has the characteristic shape of an antenna. It demonstrates the spatial coherence of the thermal source. Measurements are taken at 800 K. From [36]

$$\varepsilon(\omega) + 1 = \frac{d\varepsilon'}{d\omega}(\omega - \omega_0 + i\Gamma), \tag{4.53}$$

where $\Gamma = \varepsilon''/(d\varepsilon'/d\omega)$. It is seen that the Green's dyadic has a pole at the frequency corresponding to the asymptote of the dispersion relation of the surface wave. Its contribution to the integral (4.51) yields an exponential decay in the form $\exp(i\omega_0 t - \Gamma t)$. It follows that in the extreme near field, the thermally emitted field is temporally coherent with a coherence time given by Γ^{-1}. The origin of the temporal coherence of the electromagnetic field can thus be assigned to the very large density of states due to the surface wave. It follows that, whereas the plane interface of a hot metallic surface is a temporally incoherent source for an atom located in the far field, it is a partially temporally coherent source for an atom located within a nanometric distance from the interface.

4.5.3 Design of Coherent Thermal Sources

A spatially coherent source is a source that radiates a field that has a narrow angular aperture at a given wavelength. The typical examples of coherent sources are lasers and antennas. These sources have well-defined emission angular lobes. A narrow angular emission lobe is a signature of the spatial coherence of the field in the plane of the source. We have seen in the previous section that a source that supports a surface wave is partially spatially coherent along the surface. However, because these waves cannot propagate in vacuum, the coherence remains confined to the vicinity of the surface. However, it is possible to couple the surface waves to the propagating waves. This can be done in several ways. A practical way is to rule a grating on the surface. The grating can then diffract the surface wave. By properly choosing

the period of the grating, it is possible to control the angle of propagation of the diffracted light. This was first observed in [32–34] for a very deep grating ruled on a doped silicon surface. Such a material supports surface plasmon polaritons in the infrared. A more effective source was realized using a gold grating by Kreiter et al. [35]. In [38], a thermally stimulated midinfrared source was developed that emits radiation within a narrow range of wavelengths ($\delta\lambda/\lambda \leq 0.2$). In this experiment, the silicon wafer was covered by a metal film. A lattice of holes in the metal mediated the coupling of the surface plasmon states to the emitted light. This technology will afford tunable infrared emitters with high power in a narrow spectral band critical for sensing, spectroscopy and thermophotovoltaic applications. Figure 4.3 shows the angular emission pattern of a SiC grating. It can be clearly seen that the angular aperture is very narrow, indicating a large coherence length [36].

Chapter 5
The Casimir Forces

To obtain a simple picture of the origin of the Casimir force, we begin this section by considering a system of two plane parallel plates of ideal conductors, following the original Casimir paper [39]. These planes produce a waveguide. The number of electromagnetic modes in the waveguide is discrete and depends on the width of the waveguide. From quantum electrodynamics, it is known that each mode with frequency ω has a minimum energy $\hbar\omega/2$ referred to as vacuum fluctuations or zero point motion. If the width decreases, the mode density decreases so that the electromagnetic energy decreases. Hence, the existence of vacuum fluctuations means that there is an attractive force between the two plates. This phenomenon is clearly a macroscopic manifestation of the electromagnetic energy of the vacuum, which is a pure quantum effect. After this short introduction, we apply a general fully relativistic theory of the fluctuating electromagnetic field in the vacuum gap between the plates (see Appendix B) to calculate the normal component of the stress tensor, which determines the normal component of the force between the plates. We consider a general non-equilibrium case and are sliding with arbitrary velocity relative to each other. By considering one of the plates as sufficiently rarefied we also obtain the Casimir force between a small neutral particle moving parallel to the plate. Different limiting cases are considered.

5.1 Casimir Calculations

Casimir showed in 1948 [39] that one consequence of the zero-point field is an attraction force between two uncharged, perfectly conducting parallel plates (see Fig. 5.1 for V = 0). In this section, we present a standard calculation of the Casimir force.

Consider the electromagnetic modes appropriate to the interior of a rectangular parallelepiped of sides $L_x = L_y = L$ and L_z. For perfectly conducting walls, the tangential component of the electric field $\mathbf{E} = -\partial\mathbf{A}/\partial t$ must vanish on the walls.

A.I. Volokitin and B.N.J. Persson, *Electromagnetic Fluctuations at the Nanoscale*,
NanoScience and Technology, DOI 10.1007/978-3-662-53474-8_5

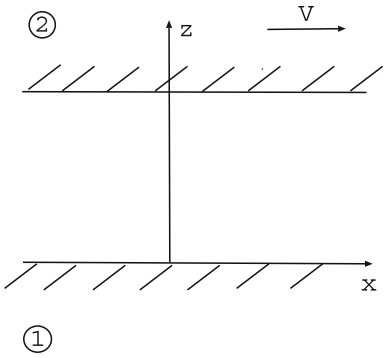

Fig. 5.1 Two semi-infinite bodies with plane-parallel surfaces separated by a distance d. The *upper solids* move parallel to other with velocity V

Thus, the components of the vector potential

$$\mathbf{A}(\mathbf{r}, t) = \mathbf{A}(\mathbf{r})e^{-i\omega t}$$

are

$$A_x(\mathbf{r}) = (8/V)^{1/2} a_x \cos(k_x x) \sin(k_y y) \sin(k_z z), \tag{5.1}$$

$$A_y(\mathbf{r}) = (8/V)^{1/2} a_y \sin(k_x x) \cos(k_y y) \sin(k_z z), \tag{5.2}$$

$$A_z(\mathbf{r}) = (8/V)^{1/2} a_y \sin(k_x x) \sin(k_y y) \cos(k_z z), \tag{5.3}$$

with $a_x^2 + a_y^2 + a_z^2 = 1$, $V = L^2 L_z$, and

$$k_x = \frac{l\pi}{L}, \quad k_y = \frac{m\pi}{L}, \quad k_z = \frac{n\pi}{L_z}, \tag{5.4}$$

with l, m, and n each taking on positive integer values and zero. In order to satisfy the transversality condition $\nabla \cdot \mathbf{A} = 0$ we also require

$$k_x A_x + k_y A_y + k_z A_z = \frac{\pi}{L}\left(l A_x + m A_y\right) + \frac{\pi n}{L_z} A_z = 0. \tag{5.5}$$

Thus there are two independent polarizations, unless one of the integers l, m, n is zero, in which case, (5.5) indicates that there is only one polarization. It is easy to verify that (5.1)–(5.3) define a function satisfying the Helmbolz equation

$$\nabla^2 \mathbf{A}(\mathbf{r}) + k^2 \mathbf{A}(\mathbf{r}), \quad \left(k = \frac{\omega}{c}\right) \tag{5.6}$$

as well as the condition that the transverse components of $\mathbf{E}$ vanish on the cavity wall. Furthermore, these mode functions for different (k_x, k_y, k_z) are orthogonal and satisfy the normalization condition

$$\int_0^L dx \int_0^L dx \int_0^{L_z} dx \left[A_x^2(\mathbf{r}) + A_y^2(\mathbf{r}) + A_z^2(\mathbf{r})\right] = 1 \tag{5.7}$$

The allowed frequencies are determined by

$$\omega_{lmn} = k_{lmn}c = \pi c \left[\frac{l^2}{L^2} + \frac{m^2}{L^2} + \frac{n^2}{L_z^2}\right]^{1/2}. \tag{5.8}$$

The zero-point energy of the field inside the cavity is therefore

$$\sum_{lmn}{}'(2)\frac{1}{2}\hbar\omega_{lmn} = \sum_{lmn}{}'\pi\hbar c \left[\frac{l^2}{L^2} + \frac{m^2}{L^2} + \frac{n^2}{L_z^2}\right]^{1/2}. \tag{5.9}$$

The factor 2 arises from the two independent polarizations of modes with $l,\ m,\ n \neq 0$. Prime on the summation symbol implies that a factor $1/2$ should be inserted if one of these integers is zero, since then we have just one independent polarization, as noted earlier.

In the physical situation of interest, L is so large compared with $L_z = d$ that we may replace the sum over l and m in (5.9) with integrals: $\sum_{lmn} \to \sum_n'(L/\pi)^2 \int\int dk_x dk_y$ and

$$E(d) = \sum_{lmn}{}'(2)\frac{1}{2}\hbar\omega_{lmn} \to \frac{L^2}{\pi^2}(\hbar c)\sum_n{}' \int_0^\infty dk_x \int_0^\infty dk_y \left[k_x^2 + k_y^2 + \frac{n^2}{L_z^2}\right]^{1/2}. \tag{5.10}$$

This integral is infinite; the zero-point energy of the vacuum is infinite in *any* finite volume. This would generate an infinite gravitational field, and effects not observed experimentally but which are we do not need to addressed here since only energy differences occur in what follows.

If d were also made arbitrarily large, the sum over n could be replaced by an integral. Then the zero-point energy (5.10) would be

$$E(d) = \frac{L^2}{\pi^2}(\hbar c)\frac{d}{\pi}\int_0^\infty dk_x \int_0^\infty dk_y \int dk_z \left[k_x^2 + k_k^2 + k_z^2\right]^{1/2}. \tag{5.11}$$

which is also infinite.

The potential energy of the system when the plates are separated by a distance d is $U(d) = E(d) - E(\infty)$. Thus, the energy required to bring the plates from a large separation to the separation d is:

$$\begin{aligned} U(d) = \frac{L^2\hbar c}{\pi^2}\Bigg[&\sum_n{}' \int_0^\infty dk_x \int_0^\infty dk_y \left[k_x^2 + k_y^2 + \frac{n^2}{L_z^2}\right]^{1/2} \\ &- \frac{d}{\pi}\int_0^\infty dk_x \int_0^\infty dk_y \int_0^\infty dk_z \left[k_x^2 + k_k^2 + k_z^2\right]^{1/2}\Bigg] \end{aligned} \tag{5.12}$$

Using polar coordinates $q,\ \phi$ in the $(k_x,\ k_y)$-plane, we have

$$U(d) = \frac{L^2\hbar c}{\pi^2}\left(\frac{\pi}{2}\right)\left[\sum_n{}' \int_0^\infty dqq\left[q^2+\frac{n^2}{L_z^2}\right]^{1/2} - \frac{d}{\pi}\int_0^\infty\int_0^\infty dqqdk_z\left[q^2+k_z^2\right]^{1/2}\right] \tag{5.13}$$

Since ϕ ranges from 0 to $\pi/2$ for $k_x,\ k_y > 0$. We now introduce a cutoff function $f(k) = f([q^2+k_z^2]^{1/2})$ such that $f(k) = 1$ for $k \ll k_m$ and $f(k) = 0$ for $k \gg k_m$. Physically, it can be argued that $f(k)$ is necessary because the assumption of perfectly conducting walls breaks down at small wavelengths, especially for wavelengths that are small compared with an atomic dimension. We might then suppose that $k_m \approx 1/a_0$, where a_0 is the Bohr radius. We thus replace (5.13) with

$$\begin{aligned} U(d) &= \frac{L^2\hbar c}{\pi^2}\left(\frac{\pi}{2}\right)\left[\sum_n{}' \int_0^\infty dqq\left[q^2+\frac{n^2}{L_z^2}\right]^{1/2} f\left(\left[q^2+\frac{n^2}{L_z^2}\right]^{1/2}\right)\right. \\ &\left. -\frac{d}{\pi}\int_0^\infty\int_0^\infty dqqdk_z\left[q^2+k_z^2\right]^{1/2} f\left(\left[q^2+k_z^2\right]^{1/2}\right)\right] \\ &= \frac{L^2\hbar c}{4\pi}\left(\frac{\pi^3}{d^3}\right)\left[\sum_n{}' \int_0^\infty dx\left[x+n^2\right]^{1/2} f\left(\frac{\pi}{d}\left[x+n^2\right]^{1/2}\right)\right. \\ &\left. -\int_0^\infty dz\int_0^\infty dx\left[x+y^2\right]^{1/2} f\left(\left[x+y^2\right]^{1/2}\right)\right], \end{aligned} \tag{5.14}$$

where we have defined the integration variables $x = q^2d^2/\pi$ and $y = k_zd/\pi$. Now

$$U(d) = \left(\frac{\pi^2\hbar c}{4d^3}\right)L^2\left[\frac{1}{2}F(0) + \sum_{n=0}^\infty F(n) - \int_0^\infty dyF(y)\right], \tag{5.15}$$

where

$$F(y) = \int_0^\infty dx\left(x+y^2\right)^{1/2} f\left(\frac{\pi}{d}\left[x+y^2\right]^{1/2}\right) \tag{5.16}$$

According to the Euler-Maclaurin summation formula

$$\sum_{n=1}^\infty F(n) - \int_0^\infty dyF(y) = -\frac{1}{2}F(0) - \frac{1}{12}F'(0) + \frac{1}{720}F'''(0)... \tag{5.17}$$

for $F(\infty) \to 0$. To evaluate the n-th derivative $F^{(n)}(y)$ we note that

$$F(y) = \int_{y^2}^{\infty} du\sqrt{u} f\left(\frac{\pi}{d}\sqrt{u}\right), \quad F'(y) = -2y^2 f\left(\frac{\pi}{d}y\right). \tag{5.18}$$

Then $F'(0) = 0$, $F'''(0) = -4$, and all higher derivatives, $F^{(n)}$ vanish if we assume that all derivatives of the cutoff function vanish at $y = 0$. Thus

$$\sum_{n=1}^{\infty} F(n) - \int_0^{\infty} dy F(y) = -\frac{1}{2}F(0) - \frac{4}{720}$$

and

$$U(d) = \left(\frac{\pi^2\hbar c}{4d^3}\right) L^2 \left(\frac{-4}{720}\right) \tag{5.19}$$

which is finite and independent of the cutoff function. The attractive force per unit area between the plates is then $F(d) = \pi^2\hbar c/240d^4$. This is the Casimir force. The principle message of this section is that *changes* in the infinite zero-point energy of the electromagnetic vacuum can be finite and observable. The role of the (infinite large) zero point energies for gravitation is still an unsolved problem (see e.g. https://en.wikipedia.org/wiki/Zero-point.energy).

5.2 Casimir Forces Between Two Plane-Parallel Surfaces

5.2.1 General Formulas

We consider two semi-infinite solids with flat parallel surfaces that are separated by a distance d, and are moving with velocity V, relative to each other, see Fig. 5.1. We introduce the two coordinate systems, K and K' with coordinate axes xyz and $x'y'z'$. In the K system, body **1** is at rest while body **2** is moving with the velocity V along the x-axis (xy and $x'y'$ planes are in the surface of body **1;** x and x'-axes have the same direction, and the z and z'-axes point toward body **2**). In the K' system, body **2** is at rest while body **1** is moving with velocity $-V$ along the x-axis. Since the system is translational invariant in the $\mathbf{x} = (x, y)$ plane, the electromagnetic field can be represented by the Fourier integrals

$$\mathbf{E}(\mathbf{x}, z, t) = \int_{-\infty}^{\infty} d\omega \int \frac{d^2q}{(2\pi)^2} e^{i\mathbf{q}\cdot\mathbf{x} - i\omega t} \mathbf{E}(\mathbf{q}, \omega, z), \tag{5.20}$$

$$\mathbf{B}(\mathbf{x}, z, t) = \int_{-\infty}^{\infty} d\omega \int \frac{d^2q}{(2\pi)^2} e^{i\mathbf{q}\cdot\mathbf{x} - i\omega t} \mathbf{B}(\mathbf{q}, \omega, z), \tag{5.21}$$

where $\mathbf{E}$ and $\mathbf{B}$ are the electric and magnetic induction field, respectively, and $\mathbf{q}$ is the 2D wave vector in the xy-plane. After Fourier transformation, it is convenient

to decompose the electromagnetic field into s- and p-polarized components. For the p- and s-polarized electromagnetic waves, the electric field $\mathbf{E}(\mathbf{q}, \omega, z)$ is in the plane of incidence, and perpendicular to that plane, respectively. In the vacuum gap between the bodies, the electric field $\mathbf{E}(\mathbf{q}, \omega, z)$, and the magnetic induction field $\mathbf{B}(\mathbf{q}, \omega, z)$ can be written in the form

$$\mathbf{E}(\mathbf{q}, \omega, z) = \left(v_s \hat{n}_s + v_p \hat{n_p}^+\right) e^{ik_z z} + \left(w_s \hat{n}_s + w_p \hat{n_p}^-\right) e^{-ik_z z}, \tag{5.22}$$

$$\mathbf{B}(\mathbf{q}, \omega, z) = \frac{c}{\omega}\Big[\left([\mathbf{k}^+ \times \hat{n}_s] v_s + [\mathbf{k}^+ \times \hat{n}_p^+] v_p\right) e^{ik_z z} + \left([\mathbf{k}^- \times \hat{n_s}] w_s + [\mathbf{k}^- \times \hat{n}_p^-] w_p\right) e^{-ik_z z}\Big], \tag{5.23}$$

$$\mathbf{k}^{\pm} = \mathbf{q} \pm \hat{z} k_z,\ k_z = \left(\left(\frac{\omega}{c}\right)^2 - q^2\right)^{1/2},\ \hat{n}_s = [\hat{z} \times \hat{q}] = (-q_y, q_x, 0)/q,$$

$$\hat{n}_p^{\pm} = [\hat{k}^{\pm} \times \hat{n}_s] = \left(\mp q_x k_z, \mp q_y k_z, q^2\right)/(kq),\ k = \frac{\omega}{c}.$$

At the surfaces of the bodies, the amplitude of the outgoing electromagnetic wave must be equal to the amplitude of the reflected wave plus the amplitude of the radiated wave. Thus, the boundary conditions for the electromagnetic field at $z = 0$ in the K-reference frame can be written in the form

$$v_{p(s)} = R_{1p(s)}(\omega, q) w_{p(s)} + E^f_{1p(s)}(\omega, q), \tag{5.24}$$

where $R_{1p(s)}(\omega)$ is the reflection amplitude for surface **1** for the $p(s)$-polarized electromagnetic field, and where $E^f_{1p(s)}(\omega)$ is the amplitude of the fluctuating electric field radiated by body **1** for a $p(s)$-polarized wave. In the K'-reference frame, the electric field can be written in the form

$$\mathbf{E}'(\mathbf{q}', \omega', z) = \left(v'_s \hat{n}'_s + v'_p \hat{n}'^+_p\right) e^{ik_z z} + \left(w'_s \hat{n}'_s + w'_p \hat{n}'^-_p\right) e^{-ik_z z}, \tag{5.25}$$

where

$$\mathbf{q}' = (q'_x, q_y, 0),\ q'_x = (q_x - \beta k)\gamma,\ \omega' = (\omega - V q_x)\gamma,\ \gamma = 1/\sqrt{1 - \beta^2},$$

$$\beta = V/c,\ \hat{n}'_s = (-q_y, q'_x, 0)/q',\ \hat{n}'^{\pm}_p = (\mp q'_x k_z, \mp q_y k_z, q'^2)/(k' q'),$$

$$q' = \gamma\sqrt{q^2 - 2\beta k q_x + \beta^2(k^2 - q_y^2)}.$$

The boundary conditions at $z = d$ in the K'-reference frame can be written in a form similar to (5.24):

$$w'_{p(s)} = e^{2ik_z d} R_{2p(s)}(\omega', q') v'_{p(s)} + e^{ik_z d} E'^{f}_{2p(s)}(\omega', q'), \tag{5.26}$$

where $R_{2p(s)}(\omega)$ is the reflection amplitude for surface **2** for $p(s)$-polarized electromagnetic field, and where $E^{f}_{2p(s)}(\omega)$ is the amplitude of the fluctuating electric field radiated by body **2** for a $p(s)$-polarized wave. A Lorentz transformation for the electric field gives

$$E'_x = E_x,\ E'_y = (E_y - \beta B_z)\gamma,\ E'_z = (E_z + \beta B_y)\gamma. \tag{5.27}$$

Using (5.22), (5.23), (5.25) and (5.27), it is possible to express the amplitudes $w'_{p(s)}$ and $v'_{p(s)}$ through $w_{p(s)}$ and $v_{p(s)}$. Using these expressions in (5.26), we get equations that, together with (5.24), form a system of equations, from which it is possible to find $w_{p(s)}$ and $v_{p(s)}$. Details of the calculations are given in Appendix B.

The Casimir force is determined by the zz-component of the Maxwell's stress tensor σ_{ij}, calculated at $z = 0$:

$$\begin{aligned}\sigma_{zz} = \frac{1}{4\pi}\int_0^\infty d\omega \int \frac{d^2q}{(2\pi)^2}\Big[&\left\langle |E_z(\mathbf{q},\omega,z)|^2\right\rangle + \left\langle |B_z(\mathbf{q},\omega,z)|^2\right\rangle - \\ &- \left\langle |E_q(\mathbf{q},\omega,z)|^2\right\rangle - \left\langle |E_n(\mathbf{q},\omega,z)|^2\right\rangle - \\ &- \left\langle |B_q(\mathbf{q},\omega,z)|^2\right\rangle - \left\langle |B_n(\mathbf{q},\omega,z)|^2\right\rangle \Big]_{z=0}.\end{aligned} \tag{5.28}$$

Using (5.22) (5.23) in (5.28), we get:

$$\begin{aligned}\sigma_{zz} = -\frac{1}{4\pi}\int_0^\infty d\omega \int \frac{d^2q}{(2\pi)^2}\frac{k_z}{k^2}\Big[&\left(k_z + k_z^*\right)\Big(\left\langle |\ w_p\ |^2\right\rangle + \left\langle |\ w_s\ |^2\right\rangle + \\ &+ \left\langle |\ v_p\ |^2\right\rangle + \left\langle |\ v_s\ |^2\right\rangle\Big) + \left(k_z - k_z^*\right)\left\langle w_p v_p^* + w_s v_s^* + c.c\right\rangle\Big].\end{aligned} \tag{5.29}$$

Substituting (B.15)–(B.18) into (5.29), and averaging over the fluctuating electromagnetic field, with the help of (B.19), we get the z-component of the force [128]:

$$\begin{aligned}F_z = \sigma_{zz} = &-\frac{\hbar}{4\pi^3}\mathrm{Re}\int_0^\infty d\omega \int d^2q k_z \Big\{ e^{2ik_z d}\Big[\left(q^2 - \beta k q_x\right)^2\Big[R_{1p}R'_{2p}D_{ss} \\ &+ R_{1s}R'_{2s}D_{pp}\Big] - \beta^2 k_z^2 q_y^2\Big[R_{1p}R'_{2s}D_{sp} + R_{1s}R'_{2p}D_{ps}\Big]\Big]\Delta^{-1} + 1\Big\}[1 + n_1(\omega) + n_2(\omega')] \\ &- \frac{\hbar}{16\pi^3}\int_0^\infty d\omega \int_{q<\frac{\omega}{c}} d^2q \frac{k_z}{|\Delta|^2}\Big[\left(q^2 - \beta k q_x\right)^2 + \beta^2 k_z^2 q_y^2\Big] \\ &\times \Big\{\left(q^2 - \beta k q_x\right)^2\Big[\left(1 - |\ R_{1p}\ |^2\right)\left(1 + |\ R'_{2p}\ |^2\right)|D_{ss}|^2 - (1 \leftrightarrow 2, \omega \leftrightarrow \omega')\Big]\end{aligned}$$

$$+\beta^2 k_z^2 q_y^2 \left[\left(1-\mid R_{1p}\mid^2\right)\left(1+\mid R'_{2s}\mid^2\right)|D_{sp}|^2-(1\leftrightarrow 2,\omega\leftrightarrow\omega')\right]$$

$$+(p\leftrightarrow s)\Big\}\left(n_1(\omega)-n_2(\omega')\right)$$

$$+\frac{\hbar}{4\pi^3}\int_0^\infty d\omega\int_{q>\frac{\omega}{c}} d^2q\,\frac{|k_z|}{|\Delta|^2}\left[\left(q^2-\beta k q_x\right)^2+\beta^2 k_z^2 q_y^2\right]e^{-2|k_z|d}$$

$$\times\Big\{\left(q^2-\beta k q_x\right)^2\left[\mathrm{Im}R_{1p}\mathrm{Re}R'_{2p}|D_{ss}|^2-(1\leftrightarrow 2,\omega\leftrightarrow\omega')\right]-\beta^2 k_z^2 q_y^2\left[\mathrm{Im}R_{1p}\mathrm{Re}R'_{2s}|D_{sp}|^2\right.$$

$$\left.-(1\leftrightarrow 2,\omega\leftrightarrow\omega')\right]+(p\leftrightarrow s)\Big\}\left(n_1(\omega)-n_2(\omega')\right). \tag{5.30}$$

where $\omega'=(\omega-q_xV)\gamma$, $R'_{2p(s)}=R_{2p(s)}(\omega')$,

$$n_i(\omega)=\frac{1}{e^{\hbar\omega/k_BT_i}-1},$$

$$D_{pp}=1-e^{2ik_zd}R_{1p}R'_{2p},\ D_{ss}=1-e^{2ik_zd}R_{1s}R'_{2s},$$

$$D_{sp}=1+e^{2ik_zd}R_{1s}R'_{2p},\ D_{ps}=1+e^{2ik_zd}R_{1p}R'_{2s},$$

$$\Delta=\left(q^2-\beta k q_x\right)^2D_{ss}D_{pp}+\beta^2k_z^2q_y^2D_{ps}D_{sp}.$$

Equation (5.30) can be written in the form

$$F_z^{neq}(T_1,T_2,V,d)=F_{z0}(V,d)+F_{z,th}^{neq}(T_1,T_2,V,d) \tag{5.31}$$

where the contribution of the zero-point ($T=0$) fluctuations, $F_{z0}(V,d)$, is separated from that produced by the thermal fluctuations, $F_{z,th}^{neq}(T_1,T_2,V,d)$. The result (5.30) diverges at $T=0$K and contains a constant (d-independent) terms in the thermal part. The divergence has the same origin as the usual divergence of the zero-point fields energy in quantum electrodynamics, while the constant terms are related to the fact that we consider infinite bodies, and hence we neglect the force of the radiation exerted on the remote, external surfaces of the two bodies. To recover the exact finite value for the zero-temperature force, $F_{z0}(V,d)$, and exclude the constant terms in $F_{z,th}^{eq}(T,V,d)$, one has to subtract the infinite vacuum contribution to the force, which does not depend on separation d [42, 194].

Taking into account that $n(-\omega)=-1-n(\omega)$, after substraction of d-independent terms, from (5.30), we get for $T_1=T_2=0$ K:

$$F_z=-\frac{\hbar}{4\pi^3}\mathrm{Re}\left\{\int_0^\infty d\omega\int d^2q-\int_{-\infty}^\infty dq_y\int_0^\infty dq_x\int_0^{q_xV}d\omega\right\}\frac{k_z}{\Delta}e^{2ik_zd}$$

$$\times\Big\{\left(q^2-\beta k q_x\right)^2\left[R_{1p}R'_{2p}D_{ss}+R_{1s}R'_{2s}D_{pp}\right]$$

$$-\beta^2 k_z^2 q_y^2 \left[R_{1p} R'_{2s} D_{sp} + R_{1s} R'_{2p} D_{ps} \right] \Big\}$$

$$+\frac{\hbar}{4\pi^3} \int_{-\infty}^{\infty} dq_y \int_0^{\infty} dq_x \int_0^{q_x V} d\omega \frac{|k_z|}{|\Delta|^2} \left[\left(q^2 - \beta k q_x \right)^2 + \beta^2 k_z^2 q_y^2 \right] e^{-2|k_z| d}$$

$$\times \Big\{ \left(q^2 - \beta k q_x \right)^2 \left[\mathrm{Im} R_{1p} \mathrm{Re} R'_{2p} |D_{ss}|^2 - \left(1 \leftrightarrow 2, \omega \leftrightarrow \omega' \right) \right] - \beta^2 k_z^2 q_y^2 \Big[\mathrm{Im} R_{1p} \mathrm{Re} R'_{2s} |D_{sp}|^2$$

$$- \left(1 \leftrightarrow 2, \omega \leftrightarrow \omega' \right) \Big] + \left(p \leftrightarrow s \right) \Big\}. \tag{5.32}$$

If, in (5.30), one neglects the terms of the order β^2, then the contributions from the waves with p- and s-polarization will be separated. In this case, after substraction of d-independent terms (5.30) reduces to

$$F_z = -\frac{\hbar}{4\pi^3} \mathrm{Re} \int_0^{\infty} d\omega \int d^2 q k_z \left(\frac{1}{R_{1p}^{-1} R_{2p}'^{-1} e^{-2ik_z d} - 1} + \frac{1}{R_{1s}^{-1} R_{2s}'^{-1} e^{-2ik_z d} - 1} \right)$$
$$\left[1 + n_1(\omega) + n_2(\omega') \right] - \frac{\hbar}{16\pi^3} \int_0^{\infty} d\omega \int_{q < \frac{\omega}{c}} d^2 q k_z$$
$$\Bigg\{ \frac{\left[(1 - \mid R_{1p} \mid^2)(1 + \mid R'_{2p} \mid^2) - (1 \leftrightarrow 2, \omega \leftrightarrow \omega') \right]}{|D_{pp}|^2}$$
$$+ (p \leftrightarrow s) \Bigg\} \left(n_1(\omega) - n_2(\omega') \right)$$
$$+ \frac{\hbar}{4\pi^3} \int_0^{\infty} d\omega \int_{q > \frac{\omega}{c}} d^2 q |k_z| e^{-2|k_z| d}$$
$$\times \left\{ \frac{\left[\mathrm{Im} R_{1p} \mathrm{Re} R'_{2p} - (1 \leftrightarrow 2, \omega \leftrightarrow \omega') \right]}{|D_{pp}|^2} + (p \leftrightarrow s) \right\} \left(n_1(\omega) - n_2(\omega') \right) \tag{5.33}$$

If we put $V = 0$, $T_1 = T_2 = T$ and use the Fresnel's formulas for the reflection amplitudes, then (5.33) reduces to the formula obtained by Lifshitz [42]. Lifshitz have shown that at $T_1 = T_2 = 0$ K, it is convenient to transform ω-integration along the real axis into the integral along the imaginary axis in the upper half of the complex ω-plane. After such transformation of the integration contour, introducing new variables $\omega = i\xi$ $q = (\xi/c)\sqrt{w^2 - 1}$, we get

$$F_z = \frac{\hbar}{2\pi^2 c^3} \int_0^{\infty} d\xi \int_1^{\infty} dw w^2 \xi^3 \left\{ \left[\frac{(s_1 + w)(s_2 + w)}{(s_1 - w)(s_2 - w)} \exp\left(\frac{2w\xi}{c} d \right) - 1 \right]^{-1} + \right.$$
$$\left. + \left[\frac{(s_1 + w\varepsilon_1)(s_2 + w\varepsilon_2)}{(s_1 - w\varepsilon_1)(s_2 - w\varepsilon_2)} \exp\left(\frac{2w\xi}{c} d \right) - 1 \right]^{-1} \right\}, \tag{5.34}$$

where $s_i = \sqrt{\varepsilon_i + w^2 - 1}$, ε_i is the dielectric function for body i at $\omega = i\xi$. In (5.34), it was taken into account that, on the imaginary axis, the dielectric function is real [184].

5.2.2 *Limiting Cases*

First, we consider the case of "small" distances, by which we mean distances that are small compared with the wavelengths λ_0, which characterize the absorption spectra of the given bodies. Because of the exponential factor $\exp(2w\xi d/c)$ in the denominators of the expression under the integral (5.34), those value of w for which $w\xi d/c \sim 1$ are dominant in the integration with respect to w. In this case, $w \gg 1$ and therefore, for d, we can put $s_i \approx w$. In this approximation, the first term in curly brackets in (5.34) is zero, while the second term, after introducing the variable of integration $x = 2w\xi d/c$, gives

$$F(d) = \frac{\hbar}{16\pi^2 d^3} \int_0^\infty d\xi \int_0^\infty dx x^2 \left[\frac{(\varepsilon_1 + 1)(\varepsilon_2 + 1)}{(\varepsilon_1 - 1)(\varepsilon_2 - 1)} e^x - 1 \right]^{-1}, \tag{5.35}$$

where, in this approximation, the lower limit of integration with respect to x is replaced by zero. The functions $\varepsilon_2(i\xi) - 1$ decreases monotonically as ξ increases and tend to zero. Therefore values of ξ that lie beyond a certain $\xi \sim \xi_0$ make a negligible contribution to the integral; the condition that d should be small is that $d \ll c/\xi_0$. The integral

$$\frac{a}{2} \int_0^\infty dx \frac{x^2}{ae^x - 1} \tag{5.36}$$

decreases monotonically as a increases, from 1.2 at $a = 1$ to 1 at $a = \infty$ to 1. Thus, with practically sufficient accuracy, (5.35) can be represented in the form

$$F(d) = \frac{\hbar\bar{\omega}}{8\pi^2 d^3}, \qquad \bar{\omega} = \int_0^\infty d\xi \frac{\big(\varepsilon_1(i\xi) - 1\big)\big(\varepsilon_2(i\xi) - 1\big)}{\big(\varepsilon_1(i\xi) + 1\big)\big(\varepsilon_2(i\xi) + 1\big)}. \tag{5.37}$$

For metals at $\xi \sim \omega_p$, where ω_p is the plasma frequency, $\varepsilon \approx 1 + (\omega_p/\xi)^2$. In this case, for two identical metals $\bar{\omega} = (\pi/2^{2.5})\omega_p$.

We now consider the opposite limiting case of "large" distances, when $\lambda_0 \ll d \ll \lambda_T = \hbar c/k_B T$. We introduce in (5.34), a new variable of integration $x = 2w\xi d/c$, and as the second variable, we take not ξ but w. Then ε_1 and ε_2 will be the function of $i\xi = ixc/2wd$. Because of the presence of factor $\exp(x)$ in the denominators of the integrand, values $x \sim 1$ are the only ones important in the integration over x. Since $w \geq 1$, the argument of the function ε for large d is nearly zero over the whole of the important range of the variables. Because of this, we can replace ε_1, ε_2 with their values for $\xi = 0$, i.e. the electrostatic dielectric constant ε_{10}, ε_{20}. Thus, finally, we get

$$F_z = \frac{\hbar c}{32\pi^2 d^4}\int_0^\infty dx \int_1^\infty dw \frac{x^3}{w^2}\left\{\left[\frac{(s_{10}+w)(s_{20}+w)}{(s_{10}-w)(s_{20}-w)}e^x - 1\right]^{-1} + \right.$$

$$\left. + \left[\frac{(s_{10}+w\varepsilon_{10})(s_{20}+w\varepsilon_{20})}{(s_{10}-w\varepsilon_{10})(s_{20}-w\varepsilon_{20})}e^x - 1\right]^{-1}\right\}, \tag{5.38}$$

$$s_{10} = \sqrt{\varepsilon_{10} - 1 + w^2}, \qquad s_{20} = \sqrt{\varepsilon_{20} - 1 + w^2}.$$

Equation (5.38) is reduced to a very simple form when both bodies are metals. For metals, the function $\varepsilon(i\xi) \to \infty$ as $\xi \to 0$; therefore, we must put $\varepsilon_0 = \infty$. If we put $\varepsilon_{01} = \varepsilon_{02} = \infty$, we get

$$F_z = \frac{\hbar c}{16\pi^2 d^4}\int_0^\infty dx \int_1^\infty dw \frac{x^2}{w^2(e^x - 1)} = \frac{\pi^2}{240}\frac{hc}{d^4}. \tag{5.39}$$

This force is independent of the nature of the metal (a property that does not hold for small distances, where the magnitude of the interaction depends on the behavior of the function $\varepsilon(i\xi)$ for all values of ξ and not just for $\xi = 0$). This formula was obtained by Casimir [39] by calculating the energy of the zero-point vibrations of an electromagnetic field in a gap between two walls that reflect ideally at all frequencies.

5.2.3 *Effect of Temperature*

Let us calculate the force F_z at thermal equilibrium ($T_1 = T_2 = T$, $V = 0$). In this case, the integrand in (5.33) contains the factor

$$1 + 2n(\omega) = \coth\left(\frac{\hbar\omega}{2k_B T}\right).$$

We can deform the ω-integration path in (5.33) so that it runs along the imaginary ω axis. Thus, the integral involves semicircles around the poles located at $\omega_n = i\xi_n = i2\pi n k_B T/\hbar$, where $n = 0, 1, \ldots$. The integration along the semicircle at ω_n contributes $i\pi$ times the residue of the integrand at the pole ω_n for $n \neq 0$, whereas, for $n = 0$, the contribution from the quarter-circle is $i\pi/2$. The integration between the poles gives purely imaginary expression. Thus, its contribution to the force will be equal to zero. Thus, the resulting expression for the force has the form [42]:

$$F_z = \frac{k_B T}{\pi c^3} {\sum_{n=0}^{\infty}}' \int_1^\infty dw w^2 \xi_n^3 \left\{ \left[\frac{(s_1 + w)(s_2 + w)}{(s_1 - w)(s_2 - w)} \exp\left(\frac{2w\xi_n}{c} d \right) - 1 \right]^{-1} + \right.$$

$$\left. + \left[\frac{(s_1 + w\varepsilon_1)(s_2 + w\varepsilon_2)}{(s_1 - w\varepsilon_1)(s_2 - w\varepsilon_2)} \exp\left(\frac{2w\xi_n}{c} d \right) - 1 \right]^{-1} \right\}, \tag{5.40}$$

where the prime on the summation sign indicates that a factor $1/2$ must be included in the $n = 0$ term. Because of the exponential factor $\exp(2w\xi_n d/c)$ in the denominators of the expression in (5.40), the dominant contribution to the sum gives the terms for which $\xi_n \sim c/d$, or $n \sim c\hbar/dk_B T$. For $dk_B T/c\hbar \ll 1$, large values of n will thus be important and we can replace the sum in (5.40) by an integration on $dn = (\hbar/2\pi k_B T)d\xi$. In this case, the temperature drop out and we are left with (5.34). Thus, (5.34) is valid for separation $d \ll c\hbar/k_B T$; at room temperatures, this gives distances of up to $\sim 1\,\mu$m.

In the case of high temperatures or large separation when

$$dk_B T/c\hbar \gg 1,$$

we need to keep only the first of the terms of the sum (5.40). However, we cannot immediately put $n = 0$ because, in this case, the integral is ill-defined (the factor ξ^3 tends to zero, but the integral over w diverges). This difficulty can be avoided by first replacing w with a new variable of integration $x = 2w\xi_n d/c$ (as a result of which the factor ξ^3 disappears). If we then put $\xi_n = 0$, we get

$$F_z = \frac{k_B T}{16\pi d^3} \int_0^\infty dx x^2 \left[\frac{(\varepsilon_{10} + 1)(\varepsilon_{20} + 1)}{(\varepsilon_{10} - 1)(\varepsilon_{20} - 1)} e^x - 1 \right]^{-1} \approx$$

$$\approx \frac{k_B T}{16\pi d^3} \frac{(\varepsilon_{10} - 1)(\varepsilon_{20} - 1)}{(\varepsilon_{10} + 1)(\varepsilon_{20} + 1)} \int_0^\infty dx x^2 e^{-x} = \frac{k_B T}{8\pi d^3} \frac{(\varepsilon_{10} - 1)(\varepsilon_{20} - 1)}{(\varepsilon_{10} + 1)(\varepsilon_{20} + 1)}. \tag{5.41}$$

Thus, at sufficiently large distances, the decrease in the interaction slows down and again goes as d^{-3}, with a coefficient that now depends both on the temperature and on the static value of the dielectric permeabilities. All other terms in the sum (5.40) decrease exponentially for large $dk_B T/\hbar c$. Thus, for two metals separated by a vacuum, the correct force is

$$F_z = \frac{k_B T}{8\pi d^3} \left[1 + 2 \left(\frac{4\pi k_B T d}{\hbar c} \right)^2 \exp\left(-\frac{4\pi k_B T d}{\hbar c} \right) \right] \tag{5.42}$$

In a more accurate calculation, the first term in (5.42) should be replaced by $\zeta(3) = 1.2021$, where $\zeta(k)$ is the Rimann zeta function. The condition $dk_B T/\hbar c \gg 1$ is,

in fact, the quasiclassical condition ($\hbar\omega \ll k_B T$, where $\omega \sim c/d$). Therefore, it is natural that (5.41) does not contains $\hbar$. The pressure (5.41) can be obtained from the thermal free energy $F = E - TS$ of the electromagnetic field (per unit area) according to the thermodynamic identity $P = -(\partial F/\partial l)_T$, where E and S are the thermal energy and entropy, respectively. It is interesting to note that, unllike the free energy, *the thermal energy E decreases exponentially with d*, which means that the pressure (5.41) has a purely entropic origin.

It is important that, at large separations, only the p-polarization contributes to the force. The reason is that, for low frequencies, the s-polarized field is nearly purely magnetic, but the magnetic field penetrates freely into a nonmagnetic material. Let us empathize that the result (5.42) was obtained for interaction between real metals. For ideal mirrors considered by Casimir, waves with both polarizations of electromagnetic field are reflected. In this case, there will be an additional factor 2 in (5.42) due to the contribution of the s-polarization. This ideal case can be realized using *superconducting* mirrors.

The formulas obtained in Sects. 5.2.2 and 5.2.3 can be generalized in such a way so as to include the case when the gap between two bodies is filled by liquid, or when on the surface of one body there is thin liquid film [43].

5.3 Interaction of a Small Particle with a Plane Surface

The Casimir force acting on a small particle moving parallel to a flat surface can be obtained from the friction between two semi-infinite bodies in the limit when one of the bodies is sufficiently rarefied. From (5.30) the contribution of the evanescent waves to the Casimir force between two moving plates is given by

$$F_z = \frac{\hbar}{4\pi^3}\mathrm{Im}\int_0^\infty d\omega \int_{q>\frac{\omega}{c}} d^2q \frac{k_z}{\Delta} e^{-2k_z d}\Big\{R_{1p}\Big[(q^2-\beta k q_x)^2 R'_{2p} D_{ss} + \beta^2 k_z^2 q_y^2 R'_{2s} D_{sp}\Big] \tag{5.43}$$

$$+ (p \leftrightarrow s)\Big\}\Big[1 + n_1(\omega) + n_2(\omega')\Big]$$

$$+ \frac{\hbar}{4\pi^3}\int_0^\infty d\omega \int_{q>\frac{\omega}{c}} d^2q \frac{k_z}{|\Delta|^2}\Big[(q^2-\beta k q_x)^2 - \beta^2 k_z^2 q_y^2\Big] e^{-2k_z d}\Big\{\mathrm{Im}R_{1p}\Big[(q^2-\beta k q_x)^2 \mathrm{Re}R'_{2p}|D_{ss}|^2$$

$$+ \beta^2 k_z^2 q_y^2 \mathrm{Re}R'_{2s}|D_{sp}|^2\Big] - \mathrm{Re}R_{1p}\Big[\mathrm{Im}R'_{2p}|D_{ss}|^2 + \beta^2 k_z^2 q_y^2 \mathrm{Im}R'_{2s}|D_{sp}|^2\Big] + (p \leftrightarrow s)\Big\}\Big(n_1(\omega) - n_2(\omega')\Big),$$

where $k_z = \sqrt{q^2 - \left(\frac{\omega}{c}\right)^2}$. In the case when one body is rarefied, it is possible to neglect the multiple scattering of the electromagnetic field in the vacuum gap between the two surfaces. In this approximation $D_{ss} \approx D_{pp} \approx D_{sp} \approx D_{ps} \approx 1$,

$$\Delta \approx (q^2 - \beta k q_x)^2 - \beta^2 k_z^2 q_y^2 = \left(\frac{qq'}{\gamma}\right)^2$$

and (5.43) can be written in the form

$$F_z = \frac{\hbar}{4\pi^3}\int_0^\infty d\omega \int_{q>\frac{\omega}{c}} d^2q k_z e^{-2k_z d} \times \Bigg\{ \Bigg[\mathrm{Im}R_{1p}\mathrm{Re}R'_{2p} + \mathrm{Im}R_{1s}\mathrm{Re}R'_{2s} + \gamma^2\beta^2\frac{k_z^2 q_y^2}{q^2 q'^2}\big(\mathrm{Im}R_{1p} + \mathrm{Im}R_{1s}\big)\big(\mathrm{Re}R'_{2p} + \mathrm{Re}R'_{2s}\big)\Bigg] \coth\left(\frac{\hbar\omega}{2k_B T_1}\right) + \Bigg[\mathrm{Re}R_{1p}\mathrm{Im}R'_{2p} + \mathrm{Re}R_{1s}\mathrm{Im}R'_{2s} + \gamma^2\beta^2\frac{k_z^2 q_y^2}{q^2 q'^2}\big(\mathrm{Re}R_{1p} + \mathrm{Re}R_{1s}\big)\big(\mathrm{Im}R'_{2p} + \mathrm{Im}R'_{2s}\big)\Bigg] \coth\left(\frac{\hbar\omega'}{2k_B T_2}\right)\Bigg\}. \tag{5.44}$$

We will assume that the rarefied plate consists of small particles, which have induced electric dipole moments. The dielectric permittivity of this plate is close to the unity, i.e. $\varepsilon - 1 \to 4\pi N\alpha \ll 1$, where N is the concentration of particles in the rarefied plate in the co-moving reference frame, and α is their electric susceptibilities. To linear order in the concentration N the reflection amplitudes are

$$R_{1p} = \frac{\varepsilon_2 k_z - \sqrt{k_z^2 - (\varepsilon_1 - 1)k}}{\varepsilon_1 k_z + \sqrt{k_z^2 - (\varepsilon - 1)k}} \approx N\pi\frac{q^2 + k_z^2}{k_z^2}\alpha,$$

$$R_{1s} = \frac{k_z - \sqrt{k_z^2 - (\varepsilon_1 - 1)k^2}}{k_z + \sqrt{k_z^2 - (\varepsilon_2 - 1)k^2}} \approx N\pi\frac{q^2 - k_z^2}{k_z^2}\alpha$$

To obtain the friction force in the K frame, where a particle is moving with velocity v parallel to a flat surface of a dielectric, the plate 2 should be assumed to be rarefied. In this case

$$F_z = N'\int_d^\infty dz f_z(z), \tag{5.45}$$

where $N' = \gamma N$ is the concentration of the particle in the plate 2 in the K frame,

$$f_z = \frac{\hbar}{2\gamma\pi^2}\int_0^\infty d\omega \int_{q>\frac{\omega}{c}} d^2q e^{-2k_z d}\Bigg\{\Big[\phi_p\mathrm{Im}R_p + \phi_s\mathrm{Im}R_s\Big]\mathrm{Re}\alpha'\coth\left(\frac{\hbar\omega}{2k_B T_1}\right) + \Big[\phi_p\mathrm{Re}R_p + \phi_s\mathrm{Re}R_s\Big]\mathrm{Im}\alpha'\coth\left(\frac{\hbar\omega'}{2k_B T_2}\right)\Bigg\}, \tag{5.46}$$

where

$$\phi_p = \left(\frac{\omega'}{c}\right)^2 + 2\gamma^2\big(q^2 - \beta^2 q_x^2\big)\frac{k_z^2}{q^2},\ \ \phi_s = \left(\frac{\omega'}{c}\right)^2 + 2\gamma^2\beta^2 q_y^2\frac{k_z^2}{q^2}$$

At $T_1 = T_2 = 0$ K

$$f_z = \frac{\hbar}{2\gamma\pi^2}\mathrm{Im}\int_0^\infty d\omega \int_{q>\omega} d^2q e^{-2k_z d}\left[\phi_p R_p + \phi_s R_s\right]\alpha' - \frac{2\hbar}{\gamma\pi^2}\int_0^\infty dq_y \int_0^\infty dq_x \int_0^{q_x v} d\omega e^{-2k_z d}\left[\phi_p \mathrm{Re}R_p + \phi_s \mathrm{Re}R_s\right]\mathrm{Im}\alpha', \quad (5.47)$$

In the non relativistic ($v \ll c$) and nonretarded ($d \ll \lambda_0 \ll \lambda_T = c\hbar/k_B T$) limit

$$f_z = \frac{\hbar}{\pi^2}\mathrm{Im}\int_0^\infty d\omega \int d^2q e^{-2qd} q^2 R_p \alpha'$$

$$-4\frac{\hbar}{\pi^2}\int_0^\infty dq_y \int_0^\infty dq_x \int_0^{q_x v} d\omega e^{-2qd} q^2 \mathrm{Re}R_p \mathrm{Im}\alpha(\omega - q_x v). \quad (5.48)$$

The force (5.48) corresponds to the (attractive) potential

$$U(d, v) = -\frac{\hbar}{2\pi^2}\int_0^\infty d\xi \int d^2q e^{-2qd} q R_p(i\xi)\mathrm{Re}\alpha(i\xi - q_x v)$$

$$+2\frac{\hbar}{\pi^2}\int_0^\infty dq_y \int_0^\infty dq_x \int_0^{q_x v} d\omega e^{-2qd} q \mathrm{Re}R_p \mathrm{Im}\alpha(\omega - q_x v) = U^{(0)}(d, v) + \Delta U(d, v). \quad (5.49)$$

where, in the first term, the integration contour is moved from the real axis to the imaginary frequency axis. Using a non-dissipative model of metallic half-space,

$$\varepsilon(\omega) = 1 - \frac{\omega_p^2}{\omega^2}, \quad R_p(i\xi) = \frac{\omega_s^2}{\omega_s^2 + \xi^2}, \quad \omega_s = \frac{\omega_p}{\sqrt{2}},$$

and the atomic polarizability determined in a single oscillator model

$$\alpha(i\xi) = \frac{\alpha(0)\omega_0^2}{\omega_0^2 + \xi^2}$$

where ω_p is the plasma frequency, $\alpha(0)$ is the static value of the atomic polarizability, and ω_0 is the atomic transition frequency, the term $U^{(0)}(d, v)$ in (5.49) simplifies to

$$U^{(0)}(d, v) = -\frac{\hbar\alpha(0)\omega_s}{16\pi d^3}\int_0^\infty \left[\frac{(1+\eta)\theta(1-\zeta x)}{(1+\eta)^2 - \zeta^2 x^2} + \frac{\theta(\zeta x - 1)}{\left[1 - (\eta + \zeta x)^2\right]}\right]\left(K_0(x) + K_2(x)\right)x^2 dx, \quad (5.50)$$

where $\eta = \omega_s/\omega_0$, $\zeta = v/2\omega_0 d$, $K_0(x)$ and $K_2(x)$ are the modified Bessel function of the second kind, and $\theta(x)$ is the step function. Taking into account that

$$\int_0^\infty \left(K_0(x) + K_2(x)\right)x^2 dx = 2\pi, \quad \int_0^\infty \left(K_0(x) + K_2(x)\right)x^4 dx = 12\pi$$

in the case $\zeta \ll 1$ from (5.50) we get

$$U^{(0)}(d,v) = -\frac{\hbar\alpha(0)\omega_s\omega_0}{8d^3(\omega_s+\omega_0)}\left[1+\frac{6v^2}{d^3(\omega_s+\omega_0)^2}\right] \tag{5.51}$$

The imaginary part of the atomic polarizability can be written in the form

$$\mathrm{Im}\alpha(\omega) = \frac{\pi\alpha(0)\omega_0}{2}\Big[\delta(\omega-\omega_0)-\delta(\omega+\omega_0)\Big] \tag{5.52}$$

Using this equation in (5.49) we get

$$\begin{aligned}\Delta U(d,v) &= 2\frac{\hbar}{\pi^2}\int_0^\infty dq_y\int_0^\infty dq_x\int_0^{q_x v} d\omega e^{-2qd}q\mathrm{Re}R_p\mathrm{Im}\alpha(\omega-q_x v)\\ &= -\frac{\hbar\alpha(0)\omega_0\eta^2}{16\pi d^3}\int_{1/\zeta}^\infty \frac{x^2\big(K_0(x)+K_2(x)\big)}{\eta^2-(1-\zeta x)^2}dx\end{aligned} \tag{5.53}$$

In (5.53), the integral is taken in the sense of the principle value. For $\zeta \ll 1$, the integral in (5.51) quickly goes to zero as $\exp(-1/\zeta)$, and therefore the van der Waals potential is given by (5.51). For $\zeta \gg 1$, taking into account that

$$K_n(x) \to_{x\to 0} \frac{1}{2}(n-1)!\left(\frac{x}{2}\right)^2,$$

we get

$$U_0(d,v) \approx \frac{\hbar\alpha(0)\omega_s}{8\pi d^3\zeta}, \tag{5.54}$$

and

$$\Delta U(d,v) \approx \frac{\hbar\alpha(0)\omega_0\eta^2}{8\pi d^3\zeta}. \tag{5.55}$$

Note that, in this limit, the sign of the potential is positive, which means that attraction is replaced by repulsion.

At $T_1 = T_2 = 0$ K and $v = 0$ for $d \ll \lambda_0$ the contribution to the interaction force from the (dynamic) electric dipole moment is

$$f_{ze} = \frac{2\hbar}{\pi}\int_0^\infty d\xi\int_0^\infty dq q^3 e^{-2qd}R_p(i\xi)\alpha_E(i\xi) = \frac{3\hbar}{4\pi d^4}\int_0^\infty d\xi\frac{\varepsilon(i\xi)-1}{\varepsilon(i\xi)+1}\alpha_E(i\xi). \tag{5.56}$$

This formula can be generalized to include the contribution from the (dynamic) magnetic moment

$$f_{zm} = \frac{2\hbar}{\pi}\int_0^\infty d\xi \int_0^\infty dq q^3 e^{-2qd} R_s(i\xi)\alpha_H(i\xi) \tag{5.57}$$
$$= \frac{2\hbar}{\pi}\int_0^\infty d\xi \int_0^\infty dq q^3 e^{-2qd} \frac{\sqrt{q^2+(\xi/c)^2} - \sqrt{q^2+(\xi/c)^2\varepsilon(i\xi)}}{\sqrt{q^2+(\xi/c)^2} + \sqrt{q^2+(\xi/c)^2\varepsilon(i\xi)}}\alpha_H(i\xi)$$
$$\approx -\frac{\hbar}{8\pi c^2 d^2}\int_0^\infty d\xi \xi^2 \big(\varepsilon(i\xi)-1\big)\alpha_H(i\xi).$$

For a spherical particle with radius R the electric and magnetic susceptibilities are given by [191]

$$\alpha_E = R^3 \frac{\varepsilon - 1}{\varepsilon + 2}, \tag{5.58}$$

$$\alpha_H = -\frac{R^3}{2}\left[1 - \frac{3}{\kappa^2 R^2} + \frac{3}{\kappa R}\cot \kappa R\right], \tag{5.59}$$

where $\kappa = k\sqrt{\varepsilon - 1}$. In Drude model ε is given by

$$\varepsilon(i\xi) = 1 + \frac{\omega_p^2}{\xi(\xi+\eta)} \approx 1 + \frac{\omega_p^2}{\xi^2}, \tag{5.60}$$

were it was taken into account that for typical metals $\eta \ll \omega_p$. Taking into account (5.60), we get $\kappa = i\omega_p/c$. When $(\omega_p/c)R \ll 1$ one can use expansion

$$\underset{x\to 0}{\cot x} \to \frac{1}{x} - \frac{x}{3} - \frac{x^3}{45} - \frac{2x^5}{945}\cdots$$

So that the magnetic susceptibility

$$\alpha_H \approx -R^3(\omega_p R/c)^2/30.$$

Using (5.58) and (5.59) in (5.56), (5.57) and taking into account that (5.59) is valid at $\omega \le \omega_l \sim c/R$, we get

$$F_{ze} \approx \frac{3}{4\pi}\frac{\hbar\omega_p R^3}{d^4}, \qquad F_{zm} \approx \frac{1}{240\pi}\frac{\hbar\omega_l R^5}{d^2 d_p^4}, \tag{5.61}$$

where $d_p = c/\omega_p$. From (5.61) we get

$$F_{zm}/F_{ze} \sim \left(\frac{dR}{180 d_p^2}\right)^2.$$

Thus, when $R \ll d \ll d_p$, the dominant contribution to the interaction force is determined by the particle dipole moment.

At large separation ($\lambda_0 \ll d \ll \lambda_T$), and assuming that the body **2** is sufficiently rarefied, from (5.38), the interaction potential

$$U(d) = -\frac{3\hbar c}{8\pi d^4}\int_1^\infty dw\,\frac{1}{w^2}\left\{\frac{(s_{10}-w)}{(s_{10}+w)2w^2}+\frac{(w\varepsilon_{10}-s_{10})}{(w\varepsilon_{10}+s_{10})}\left(1-\frac{1}{2w^2}\right)\right\}\alpha_{2E}(0), \tag{5.62}$$

A similar expression can be obtained for the contribution from the magnetic moment. For metal $\varepsilon_{10}\to\infty$, and in this case (5.62) reduces to

$$U(d) = -\frac{3\alpha_2(0)\hbar c}{8\pi d^4} \tag{5.63}$$

which coincides with the result of Casimir and Polder [7] for the interaction energy of an atom with a wall of an ideal conductor. For a metal particle $\alpha_E(0) = R^3$ and $\alpha_H(0) = -R^3/2$. Thus, in this case too, the main contribution to the interaction is determined by the electric dipole moment.

5.4 Interaction Between Small Particles

We now show how it is possible to go from the macroscopic formula (5.34) to the interaction between individual small particles in a vacuum. To do this, we assume that both bodies **1** and **2** to be sufficiently rarefied, and that they consist of the particles that have (dynamical) dipole and magnetic moments. From the point of view of macroscopic electrodynamics, this means that their dielectric and magnetic permeabilities are close to 1, i.e. differences $\varepsilon_{1(2)} - 1 = 4\pi n_{1(2)}\alpha_{E1(2)} \ll 1$ and $\mu_{1(2)} - 1 = 4\pi n_{1(2)}\alpha_{H1(2)} \ll 1$. We begin with "small" distances. From (5.35) to linear order in the particle concentration we get

$$\begin{aligned} F(d) &= \frac{\hbar}{64\pi^2 d^3}\int_0^\infty d\xi\int_0^\infty dx x^2\big[(\varepsilon_1-1)(\varepsilon_2-1)+(\mu_1-1)(\mu_2-1)\big]e^{-x} \\ &= \frac{n_1 n_2\hbar}{2d^3}\int_0^\infty d\xi\big[\alpha_{E1}(i\xi)\alpha_{E2}(i\xi)+\alpha_{H1}(i\xi)\alpha_{H2}(i\xi)\big]. \end{aligned} \tag{5.64}$$

If interaction potential of the particles is equal to $u = -a/r^n$, which corresponds to the force $f = -dU/dr = an/r^{n+1}$, then the total energy of pairwise interactions per unit surface area of all molecules in two half-spaces, separated by the gap d, will be equal to

$$U = \frac{a\pi n_1 n_2}{d^{n-4}}\frac{2}{(n-2)(n-3)(n-4)}, \tag{5.65}$$

and the force will equal to

$$F = \frac{a\pi n_1 n_2}{d^{n-3}} \frac{2}{(n-2)(n-3)}. \tag{5.66}$$

Comparing (5.64) and (5.66), we get the interaction force between particles:

$$f(r) = \frac{18\hbar}{\pi r^7} \int_0^\infty d\xi \big[\alpha_{E1}(i\xi)\alpha_{E2}(i\xi) + \alpha_{H1}(i\xi)\alpha_{H2}(i\xi)\big]. \tag{5.67}$$

For example, for hydrogen atoms, the dielectric susceptibility is determined by the expression [184]

$$\alpha_E(\omega) = \frac{e^2}{\hbar} \sum_n |x_{n0}|^2 \left[\frac{1}{\omega_{n0} - \omega - i0} + \frac{1}{\omega_{n0} + \omega + i0}\right], \tag{5.68}$$

where $x_{n0} = \langle n|x|0\rangle$ is the matrix element of the coordinates of the electron in the atom, $\omega_{n0} = (E_n - E_0)/\hbar$, E_n and E_0 are the energies of the stationary states $|n\rangle$ and $|0\rangle$. Using (5.68) in (5.67) for the interaction force between two hydrogen atoms due to the (dynamic) dipole moments we get

$$F = \frac{36e^4}{d^7} \sum_{nm} \frac{|x_{n0}|^2 |x_{m0}|^2}{E_n - E_0 + E_m - E_0}. \tag{5.69}$$

The diamagnetic susceptibility of a hydrogen atom is several orders of magnitude smaller than the dielectric susceptibility; therefore, it is possible to neglect the contribution to the interaction force of from the magnetic moments. In the case of the interaction of the metallic particles in the frequency range $\omega \sim \omega_p$ and for $R \ll d \ll d_p$, the ratio of magnetic and dielectric susceptibilities $\alpha_H/\alpha_E \sim 10^{-1}(R/d_p)^2 \ll 1$; therefore, the interaction force is determined by the dipole interaction.

For "large" distances, the formula for the attraction force between two "rarefied" bodies, consisting of particles with dipole and magnetic moments, according to (5.38) has the form

$$F = \frac{\hbar c}{2d^4}\left[\alpha^0_{E1}\alpha^0_{E2} + \alpha^0_{H1}\alpha^0_{H2}\right] \int_0^\infty dx x^3 e^{-x} \int_1^\infty dw \frac{1 - 2w^2 + 2w^4}{8w^8} =$$
$$= \frac{23}{40} \frac{\hbar c n_1 n_2}{d^4} \left[\alpha^0_{E1}\alpha^0_{E2} + \alpha^0_{H1}\alpha^0_{H2}\right]. \tag{5.70}$$

This force corresponds to the interaction of two particles with a force

$$f = \frac{161\hbar c}{4\pi r^8} \left[\alpha^0_{E1}\alpha^0_{E2} + \alpha^0_{H1}\alpha^0_{H2}\right]. \tag{5.71}$$

The static magnetic susceptibilities α_H^0 of the particles are determined by the weak diamagnetic effect. Therefore, the contribution from the magnetic moments can be neglected. Formula (5.71) coincides with the results of the quantum mechanical calculation by Casimir and Polder [41] of the attraction between two atoms when the distance between them is sufficiently large for retardation effects to be important.

5.5 Casimir Force Out of Thermal Equilibrium

We consider now the force $F_z(T_1, T_2, d)$ between two solids with temperatures T_1 seperated T_2 separated by distance d.

5.5.1 Force Between Identical Bodies

In the case of two identical materials, the force between two bodies can be found without any calculations using the following simple consideration. If body **1** is at the temperature T and body **2** be at $T = 0$, then the thermal contribution to the force will be $F_z^{neq}(T, 0, d)$. Because of the material identity, the pressure will be the same if we interchange the temperatures of the bodies: $F_{z,th}^{neq}(T, 0, d) = F_{z,th}^{neq}(0, T, d)$. In general, we know from (5.33) that the thermal part of the force is given by the sum of two terms each of which corresponding to a configuration where only one of the bodies is at non-zero temperature, i.e., $F_{z,th}^{neq}(T_1, T_2, d) = F_{z,th}^{neq}(T_1, 0, d) + F_{z,th}^{neq}(0, T_2, d)$. It is now evident that at equilibrium, where $T_1 = T_2 = T$, the latter equation $F_{z,th}^{neq}(T, 0, d) = F_{z,th}^{neq}(0, T, d) = F_{z,th}^{eq}(T, d)$ and we find for the total force

$$F_z^{neq}(T_1, T_2, d) = \frac{F_z^{eq}(T_1, d)}{2} + \frac{F_z^{eq}(T_2, d)}{2} \tag{5.72}$$

Therefore, the force between two bodies made from the same materials depends on only the equilibrium forces at T_1 and T_2. It is interesting to note that (5.72) is valid not only for the plane-parallel geometry, but also for any couple of identical bodies of any shape displaced in a symmetric configuration with respect to a plane.

5.5.2 Force Between Different Bodies

At $V = 0$, the thermal contribution to the force between two different semi-infinite bodies is according to (5.33) given by

$$\overline{F}^{neq}_{z,th}(T_1,T_2,d)=-\frac{\hbar}{4\pi^3}\mathrm{Re}\int_0^\infty d\omega\int d^2qk_z\Bigg(\frac{1}{R_{1p}^{-1}R_{2p}^{-1}e^{-2ik_zd}-1}$$

$$+\frac{1}{R_{1s}^{-1}R_{2s}^{-1}e^{-2ik_zd}-1}+1\Bigg)\big[n_1(\omega)+n_2(\omega')\big]$$

$$-\frac{\hbar}{16\pi^3}\int_0^\infty d\omega\int_{q<\frac{\omega}{c}}d^2qk_z\Bigg\{\frac{|\,R_{2p}\,|^2-|\,R_{1p}\,|^2}{|D_{pp}|^2}$$

$$+(p\leftrightarrow s)\Bigg\}\big(n_1(\omega)-n_2(\omega')\big)$$

$$+\frac{\hbar}{4\pi^3}\int_0^\infty d\omega\int_{q>\frac{\omega}{c}}d^2q|k_z|e^{-2|k_z|d}$$

$$\times\left\{\frac{\mathrm{Im}R_{1p}\mathrm{Re}R_{2p}-\mathrm{Im}R_{2p}\mathrm{Re}R_{1p}}{|D_{pp}|^2}+(p\leftrightarrow s)\right\}\big(n_1(\omega)-n_2(\omega')\big)\tag{5.73}$$

At equilibrium $T_1=T_2=T$, from (5.73) we get

$$\overline{F}^{eq}_{z,th}(T,d)=F^{eq}_{z,th}(T,d)-\frac{4\sigma T^4}{3c}\tag{5.74}$$

where $F^{eq}_{z,th}(T,d)$ is the equilibrium force determined by (5.33). The difference between $\overline{F}^{eq}_{z,th}(T,d)$ and $F^{eq}_{z,th}(T,d)$ has a clear-physical origin. In fact, the force out of equilibrium (5.73), from which (5.74) is derived, is calculated for bodies occupying two infinite half-spaces. On the contrary, the equilibrium force $F^{eq}_{z,th}(T,d)$ was obtained after proper regularization, and hence takes into account the pressure exerted on the external surfaces of bodies of finite thickness (see discussion after (5.30)). The non-equilibrium force can be written in the following useful form:

$$F^{neq,PW}_{z,th}(T_1,T_2,d)=\frac{F^{eq,PW}_{z,th}(T_1,d)}{2}+\frac{F^{eq,PW}_{z,th}(T_2,d)}{2}-B(T_1,T_2)$$
$$+\Delta F^{PW}_{th}(T_1,d)-\Delta F^{PW}_{th}(T_2,d)\tag{5.75}$$

$$F^{neq,PW}_{z,th}(T_1,T_2,d)=\frac{F^{eq,EW}_{z,th}(T_1,d)}{2}+\frac{F^{eq,EW}_{z,th}(T_2,d)}{2}$$
$$+\Delta F^{EW}_{th}(T_1,d)-\Delta F^{EW}_{th}(T_2,d)\tag{5.76}$$

where $F_{z,th}^{eq,PW}(T,d)$ and $F_{z,th}^{eq,PW}(T,d)$ are the equilibrium d-dependent contributions from propagating and evanescent waves, respectively; $B(T_1,T_2) = 2\sigma(T_1 + T_2)/3c$ is a d-independent contribution, discussed in (5.74). The expressions $\Delta F_{th}^{PW}(T,d)$ and $\Delta F_{th}^{EW}(T,d)$ are antisymmetric with respect to the interchange of the bodies $\leftrightarrow$ and are defined as

$$\Delta F_{th}^{PW}(T,d) = \frac{\hbar}{4\pi^2}\int_0^\infty d\omega \frac{1}{c^{\hbar\omega/k_BT}-1}\int_0^k dqqk_z \sum_{\mu=p,s}\frac{\left|R_{2\mu}\right|^2-\left|R_{1\mu}\right|^2}{\left|D_{\mu\mu}\right|^2}, \tag{5.77}$$

$$\Delta F_{th}^{EW}(T,d) = \frac{\hbar}{2\pi^2}\int_0^\infty d\omega \frac{1}{c^{\hbar\omega/k_BT}-1} \times \int_k^\infty dqq\mathrm{Im}k_z e^{-2Im(k_z)d}\sum_{\mu=p,s}\frac{\mathrm{Im}R_{1\mu}\mathrm{Re}R_{2\mu}-\mathrm{Im}R_{1\mu}\mathrm{Re}R_{2\mu}}{\left|D_{\mu\mu}\right|^2}, \tag{5.78}$$

Note that the EW term (5.78), corresponding to the evanescent waves, goes to 0 for $d \to \infty$ because evanescent fields decay at large distances. However, the PW term (5.77), corresponding to the propagating waves, contains an l-independent component since, in the non-equilibrium situation, there is momentum transfer between bodies. This d-independent component can be directly extracted from (5.77) using the expansion

$$\frac{1}{\left|1-Re^{2ik_zd}\right|^2} = \frac{1}{1-|R|^2}\left(1+2\mathrm{Re}\sum_{n=1}^{\infty}R^n e^{2ik_zd}\right), \tag{5.79}$$

where $R = R_{1\mu}R_{2\mu}$. This expansion shows explicitly the contributions from multiple reflections. The distance independent term corresponds to the first term in the expansion (5.79), and it is related to the radiation that passes the gap only once, i.e., without being reflected. Finally, it is possible to write $\Delta F_{th}^{PW}(T,d)$ as the sum $\Delta F_{th}^{PW}(T,d) = \Delta F_{th,a}^{PW}(T,d) + \Delta F_{th,b}^{PW}(T,d)$, where the constant and the pure d-dependent terms respectively, are

$$\Delta F_{th,a}^{PW}(T,d) = \frac{\hbar}{4\pi^2}\int_0^\infty d\omega \frac{1}{c^{\hbar\omega/k_BT}-1}\int_0^k dqqk_z \sum_{\mu=p,s}\frac{\left|R_{2\mu}\right|^2-\left|R_{1\mu}\right|^2}{1-\left|R_{1\mu}R_{2\mu}\right|^2}, \tag{5.80}$$

$$\Delta F_{th,b}^{PW}(T,d) = \frac{\hbar}{4\pi^2}\int_0^\infty d\omega \frac{1}{c^{\hbar\omega/k_BT}-1}\int_0^k dqqk_z \sum_{\mu=p,s}\frac{\left|R_{2\mu}\right|^2-\left|R_{1\mu}\right|^2}{1-\left|R_{1\mu}R_{2\mu}\right|^2}\left(R_{1\mu}R_{2\mu}\right)e^{2ink_zd}, \tag{5.81}$$

At thermal equilibrium $T_1 = T_2 = T$ the sum of (5.75) and (5.76) provides the Lifshitz formula except for the term $-4\sigma T^4/3c$, which is canceled due to the pressure exerted on the remote external surfaces of the bodies, as explicitly shown in the next section. Out of thermal equilibrium, but for identical bodies, $R_{1\mu} = R_{2\mu}$, the antisymmetric terms disappear: $\Delta F_{th}^{PW}(T,d) = \Delta F_{th}^{EW}(T,d) = 0$. In this case, (5.72) is reproduced.

Chapter 6
Radiative Heat Transfer

In this section, we consider the basic principles of radiative heat transfer. The general theory of the fluctuating electromagnetic field is applied for the calculation of the radiative heat transfer in the plate–plate and particle–plate configurations using the Green's function and scattering matrix approaches. The Green's function approach is used to calculate the radiative heat transfer between anisotropic materials, and the scattering matrix approach is used to calculate the radiative heat transfer between plates in relative motion. By considering one of the plates as sufficiently rarefied, we calculate the radiative heat transfer between a small neutral particle moving parallel to the plate and the plate in the different reference frames. Different limiting cases are considered. We consider the dependence of the heat transfer on the temperature T, the shape and the separation d, and discuss the role of non-local and retardation effects. We find that, for high-resistivity material, the heat transfer is dominated by retardation effects even for very short separations. The heat transfer at short separation between the plates may increase by many orders of magnitude when the surfaces are covered by adsorbates, or can support low-frequency surface plasmon polaritons (SPP) or surface phonon polaritons (SPhP). In this case, the heat transfer is determined by resonant photon tunneling between adsorbate vibrational modes, or SPP or SPhP modes. Using the nonlocal optic dielectric approach, we study the dependence of the heat flux between two metal surfaces on the electron concentration, and compare this with the predictions of the local optic approximation.

6.1 The Green's Function Theory

The theory of electromagnetic fluctuations presented in Chap. 4 can be used to calculate the heat transfer between any two macroscopic bodies with different temperatures, T_1 and T_2, whose surfaces are separated by a distance d, much larger than the lattice constant of the solids. In this case, the problem can be treated macroscopically.

A.I. Volokitin and B.N.J. Persson, *Electromagnetic Fluctuations at the Nanoscale*,
NanoScience and Technology, DOI 10.1007/978-3-662-53474-8_6

In order to calculate the radiative energy transfer between the bodies, we need the ensemble average of the Poynting's vector

$$\langle \mathbf{S}(\mathbf{r})\rangle_\omega = (c/8\pi)\left\langle \mathbf{E}(\mathbf{r})\times \mathbf{B}^*(\mathbf{r})\right\rangle_\omega + c.c. =$$

$$= \frac{ic^2}{8\pi\omega}\left\{\nabla'\left\langle \mathbf{E}(\mathbf{r})\cdot\mathbf{E}^*(\mathbf{r}')\right\rangle - \left\langle \left(\mathbf{E}(\mathbf{r})\cdot\nabla'\right)\mathbf{E}^*(\mathbf{r}')\right\rangle - c.c\right\}_{\mathbf{r}=\mathbf{r}'}. \tag{6.1}$$

Thus, the Poynting's vector can be expressed through the average of the product of the components of the electric field. According to the theory of the fluctuating electromagnetic field, the spectral function of fluctuations of the electric field in the vacuum gap between the bodies **1** and **2** is given by (3.63) and (3.64) [13] (see also Appendix A)

$$\left\langle \mathbf{E}(\mathbf{r})\mathbf{E}^*(\mathbf{r}')\right\rangle_\omega = \frac{\left[\Pi_1(\omega)-\Pi_2(\omega)\right]}{8\pi^2 \mathrm{i}k^2\omega}\int d\mathbf{S}_1''\Big\{\hat{\mathbf{D}}(\mathbf{r},\mathbf{r}'')\nabla''\hat{\mathbf{D}}^+(\mathbf{r}',\mathbf{r}'')-$$

$$-\nabla''\hat{\mathbf{D}}(\mathbf{r},\mathbf{r}'')\hat{\mathbf{D}}^+(\mathbf{r}',\mathbf{r}'')\Big\} + \frac{\Pi_2(\omega)}{\pi\omega}\mathrm{Im}\hat{\mathbf{D}}(\mathbf{r},\mathbf{r}'), \tag{6.2}$$

where the integration is over the surface of the body **1**,

$$\Pi_i(\omega) = \hbar\omega\left(e^{\hbar\omega/k_BT_i}-1\right)^{-1}. \tag{6.3}$$

The Green's function matrix of the electromagnetic field $\hat{\mathbf{D}}(\mathbf{r},\mathbf{r}')$ in the space between the bodies can be found by solving (3.33) and (3.34) with the appropriate boundary conditions [13, 183] (see also Appendix C). The second term in (6.1) does not give any contribution to the heat flux between two parallel surfaces because

$$\left\langle \left(\mathbf{E}(\mathbf{r})\cdot\nabla'\right)E_z^*(\mathbf{r}')\right\rangle = \left\langle \nabla\cdot\mathbf{E}(\mathbf{r})E_z^*(\mathbf{r})\right\rangle = \nabla_z\left\langle E_z(\mathbf{r})E_z^*(\mathbf{r})\right\rangle. \tag{6.4}$$

This term is purely real and does not give any contribution to the z-component of Poynting vector, which in this case is given by

$$\langle \mathbf{S}_z(\mathbf{r})\rangle_\omega = (c/8\pi)\left\langle \mathbf{E}(\mathbf{r})\times\mathbf{B}^*(\mathbf{r})\right\rangle_\omega + c.c. = \frac{ic^2}{8\pi\omega}\left\{\langle \mathbf{E}(\mathbf{r})\cdot\frac{d}{dz}\mathbf{E}^*(\mathbf{r})\rangle_\omega - c.c.\right\}. \tag{6.5}$$

Using (6.2), in (6.5) we get

$$\langle S_z\rangle_\omega = \frac{\left[\Pi_1(\omega)-\Pi_2(\omega)\right]}{64\pi^3k^4}\int\frac{d^2\mathbf{q}}{(2\pi)^2}\mathrm{Tr}\Big[\hat{\mathbf{D}}\frac{\partial^2}{\partial z\partial z'}\hat{\mathbf{D}}^+(z,z') -$$

$$-\frac{\partial}{\partial z'}\hat{\mathbf{D}}\frac{\partial}{\partial z}\hat{\mathbf{D}}^+(z,z') + c.c.\Big]_{z\to z'} \tag{6.6}$$

For the plane geometry, the solution of (3.33) and (3.34) is most conveniently obtained by representing the Green's function as Fourier integrals with respect to the transverse coordinates x, y (the z-axis being normal to the surfaces); this gives a system of linear inhomogeneous ordinary differential equations from which the Green's functions can be obtained as functions of z [13, 183]. The solution of these equations is described in details in Appendix C. The Green's function matrix for $z > z'$ can be written in the form [195, 196]:

$$\hat{\mathbf{D}} = \frac{2\pi i\omega^2}{k_z c^2}\left[\hat{\mathbf{D}}_{12}\left(\hat{\mathbf{I}}e^{ik_z(z-z')} + \hat{\mathbf{R}}_1 e^{ik_z(z+z')}\right) + \hat{\mathbf{D}}_{21}\left(\hat{\mathbf{R}}_2\hat{\mathbf{R}}_1 e^{2ik_z d}e^{ik_z(z'-z)} + \hat{\mathbf{R}}_2 e^{2ik_z d}e^{-ik_z(z+z')}\right)\right], \tag{6.7}$$

where

$$\hat{\mathbf{R}}_1 = \hat{n}^+ R_1 \hat{n}^-,\ \hat{\mathbf{R}}_2 = \hat{n}^- R_2 \hat{n}^+,\ \hat{\mathbf{I}} = \hat{n}^+ \mathrm{I}\hat{n}^+,\ \hat{\mathbf{D}}_{12} = \hat{n}^+ D_{12}\hat{n}^+,$$
$$\hat{\mathbf{D}}_{21} = \hat{n}^- D_{21}\hat{n}^-,\ D_{ij} = \left[\mathrm{I} - e^{2ik_z d}R_i R_j\right]^{-1},$$

where I is the 2×2 unit matrix, the 3×2 matrix $\hat{n}^\pm = (\hat{n}_s^\pm, \hat{n}_p^\pm)$, $k_z = ((\omega/c)^2) - q^2)^{1/2}$, $\lambda = (s, p)$, $\hat{n}_s^\pm = [\hat{z}\times\hat{q}] = (-q_y, q_x, 0)/q$, $\hat{n}_p^\pm = [\hat{k}^\pm \times \hat{n}_s^\pm] = (\mp\mathbf{q}k_z, q^2/(kq)$, $k = \omega/c$, $\hat{k}^\pm = (\mathbf{q} \pm \hat{z}k_z)/k$, $\mathbf{q} = (q_x, q_y, 0)$. The 2×2 reflection matrix R determines the reflection amplitudes for the waves with different polarization $\lambda = (s, p)$. This matrix is diagonal for isotropic materials. However, in the general cases of anisotropic materials, this matrix is not diagonal

$$R_i = \begin{pmatrix} R_{ss}^i & R_{sp}^i \\ R_{ps}^i & R_{ss}^i \end{pmatrix}.$$

For the isotropic materials $R_{\lambda\lambda'} = R_\lambda \delta_{\lambda\lambda'}$ and the Green's function matrix is simplified

$$\hat{\mathbf{D}}^{isotropic} = \frac{2\pi i\omega^2}{k_z c^2}\sum_{\lambda=(s,p)}\left[\hat{\mathbf{n}}_\lambda^+\hat{\mathbf{n}}_\lambda^+ e^{ik_z(z-z')} + \hat{\mathbf{n}}_\lambda^+\hat{\mathbf{n}}_\lambda^- R_{1\lambda}e^{ik_z(z+z')} + \hat{\mathbf{n}}_\lambda^-\hat{\mathbf{n}}_\lambda^- R_{1\lambda}R_{2\lambda}e^{2ik_z d}e^{ik_z(z'-z)}\right.$$
$$\left. + \hat{\mathbf{n}}_\lambda^-\hat{\mathbf{n}}_\lambda^+ R_{2\lambda}e^{2ik_z d}e^{-ik_z(z+z')}\right]\frac{1}{1 - e^{2ik_z d}R_{1\lambda}R_{2\lambda}}, \tag{6.8}$$

Substitution of (6.7) in (6.6) gives [195, 196]:

$$S_z = \int_0^\infty \frac{d\omega}{2\pi}\left[\Pi_1(\omega) - \Pi_2(\omega)\right]\left\{\int_{q<\frac{\omega}{c}}\frac{d^2q}{(2\pi)^2}\mathrm{Tr}\left[\left(\mathrm{I} - R_2^+R_2\right)D_{12}\left(\mathrm{I} - R_1R_1^+\right)D_{12}^+\right]\right.$$
$$\left. + \int_{q>\frac{\omega}{c}}\frac{d^2q}{(2\pi)^2}e^{-2|k_z|d}\mathrm{Tr}\left[\left(R_2^+ - R_2\right)D_{12}\left(R_1 - R_1^+\right)D_{12}^+\right]\right\}. \tag{6.9}$$

6.2 The Scattering Matrix Theory

We introduce two coordinate systems, K and K' with coordinate axes xyz and $x'y'z'$. In the K system, body **1** is at rest while body **2** is moving with the velocity V, along the x-axis (the xy and $x'y'$ planes are in the surface of body **1,** x and x'-axes have the same direction, and the z and z'-axes point toward body **2**). In the K' system, body **2** is at rest while body **1** is moving with velocity $-V$ along the x-axis. Since the system is translational invariant in the $\mathbf{x} = (x, y)$ plane, the electromagnetic field can be represented by the Fourier integrals (see (5.22) and (5.23)). In the vacuum region, the electromagnetic field is determined by (5.22). Decomposing the electromagnetic field into s- and p-electromagnetic waves and substituting (5.22) in (6.5), we obtain the heat flux, transferred through the surface **1**:

$$S_1 = \frac{1}{4\pi}\int_0^\infty d\omega \int \frac{d^2q}{(2\pi)^2}\frac{\omega}{k^2}\left[(k_z + k_z^*)\left(\langle\mid w_p \mid^2\rangle + \langle\mid w_s \mid^2\rangle - \right.\right.$$
$$\left.\left. - \langle\mid v_p \mid^2\rangle - \langle\mid v_s \mid^2\rangle\right) + (k_z - k_z^*)\left\langle(w_p v_p^* + w_s v_s^* - c.c)\right\rangle\right]. \tag{6.10}$$

In (6.10), the integration is performed only over positive values of ω, which introduce an additional factor of 2. After averaging in (6.10) over the fluctuating electromagnetic field with the use of (2.15)–(2.19) from Appendix B, we obtain the heat flux through surface **1**, separated from the surface **2** by vacuum gap (thickness d) [128]:

$$S_1 = \frac{\hbar}{8\pi^3}\int_0^\infty d\omega \int_{q<\frac{\omega}{c}} d^2q \frac{\omega}{|\Delta|^2}\Big[\left(q^2 - \beta k q_x\right)^2 + \beta^2 k_z^2 q_y^2\Big]\times$$

$$\times\Big[\left(q^2 - \beta k q_x\right)^2\left(1 - \mid R_{1p}\mid^2\right)\left(1 - \mid R'_{2p}\mid^2\right)|D_{ss}|^2 +$$

$$+\beta^2 k_z^2 q_y^2\left(1 - \mid R_{1p}\mid^2\right)\left(1 - \mid R'_{2s}\mid^2\right)|D_{sp}|^2 + \left(p \leftrightarrow s\right)\Big]\left(n_2(\omega') - n_1(\omega)\right) +$$

$$+\frac{\hbar}{2\pi^3}\int_0^\infty d\omega \int_{q>\frac{\omega}{c}} d^2q \frac{\omega}{|\Delta|^2}\Big[\left(q^2 - \beta k q_x\right)^2 + \beta^2 k_z^2 q_y^2\Big]e^{-2|k_z|d}\times$$

$$\times\Big[\left(q^2 - \beta k q_x\right)^2 \mathrm{Im}R_{1p}\mathrm{Im}R'_{2p}|D_{ss}|^2 - \beta^2 k_z^2 q_y^2 \mathrm{Im}R_{1p}\mathrm{Im}R'_{2s}|D_{sp}|^2 +$$

$$+\left(p \leftrightarrow s\right)\Big]\left(n_2(\omega') - n_1(\omega)\right). \tag{6.11}$$

The quantities entering in (6.11) have the same meaning as in (5.30). There is also a heat flux S_2 from body **2** in the K'-reference frame. Actually, S_1 and S_2 are the same quantities, looked at from different coordinate systems. These quantities are related by the equation:

$$F_x V = S_1 + S_2/\gamma, \tag{6.12}$$

where F_x is the friction force, due to the relative motion of the two bodies. Equation (6.12) has a simple meaning: the power of friction force is equal to heat flux through the surfaces of both bodies. At $V = 0$, (6.11) is reduced to the formula obtained in [13]

$$S_z = \int_0^\infty \frac{\mathrm{d}\omega}{2\pi}\big[\Pi_1(\omega) - \Pi_2(\omega)\big]\Big\{\int_{q<\frac{\omega}{c}} \frac{\mathrm{d}^2q}{(2\pi)^2} \times$$
$$\times \frac{\left(1- \mid R_{1p}(\mathbf{q},\omega)\mid^2\right)\left(1- \mid R_{2p}(\mathbf{q},\omega)\mid^2\right)}{\mid 1 - \mathrm{e}^{2ik_zd}R_{1p}(\mathbf{q},\omega)R_{2p}(\mathbf{q}\omega)\mid^2} +$$
$$+ 4\int_{q>\frac{\omega}{c}} \frac{\mathrm{d}^2q}{(2\pi)^2}\mathrm{e}^{-2|k_z|d} \times$$
$$\times \frac{\mathrm{Im}R_{1p}(\mathbf{q},\omega)\mathrm{Im}R_{2p}(\mathbf{q},\omega)}{\mid 1 - \mathrm{e}^{-2|k_z|d}R_{1p}(\mathbf{q},\omega)R_{2p}(\mathbf{q},\omega)\mid^2} +$$
$$+ [p \to s]\Big\}, \tag{6.13}$$

where the symbol $[p \to s]$ stands for the terms that are obtained from the first two terms by replacing the reflection amplitude R_p for the p-polarized electromagnetic waves with the reflection amplitude R_s for the s-polarized electromagnetic waves, and where $k_z = ((\omega/c)^2 - q^2)^{1/2}$. The contributions to the heat transfer from the propagating ($q < \omega/c$) and evanescent ($q > \omega/c$) electromagnetic waves are determined by the first and the second terms in (6.13), respectively. Because of the presence of the exponential factor in the integrals in (6.13), the q-integration is effectively limited by to $q < \lambda_T^{-1}$ for the propagating waves, and $q < d^{-1}$ for the evanescent waves. Thus from phase space arguments, it follows that the number of the available channels for the heat transfer for the evanescent waves will be by a factor of $(\lambda_T/d)^2$ larger than the number of the available channels for the propagating waves. For $d = 1$ nm and $T = 300$ K, this ratio is of the order of $\sim 10^8$.

In the local optic approximation, and in the non-retarded limit, the formula (6.13) reduces to the results first obtained in [93] and [115], respectively.

Equation (6.13) can be understood qualitatively as follows. The heat flux per unit frequency is (thermal energy) $\times$ (transmission coefficient). The transmission coefficient can be written in the form

$$\mid D \mid^2 \;=\; \mid D_1D_2e^{ik_zd}\left(1 + R_1R_2e^{2ik_zd} + \left(R_1R_2e^{2ik_zd}\right)^2 + \ldots\right)\mid^2 =$$
$$= \frac{\mid D_1 \mid^2 \mid D_2 \mid^2 e^{-2\mathrm{Im}(k_z)d}}{\mid 1 - R_1R_2e^{2ik_zd} \mid^2}, \tag{6.14}$$

where D_1 and D_2 are the transmission amplitude for the surfaces **1** and **2**, respectively. The transmission amplitude D, for two interfaces with reflection amplitude R_1 and R_2 is obtained by geometrical progression of the subsequent reflections of

the electromagnetic waves between two surfaces, while keeping proper track of the accumulated phase. Finally, one integrates over ω and the allowed q, and subtracts the opposite fluxes.

6.3 General Formulas and Limiting Cases

Let us first consider some general consequences of (6.13). In the case of heat transfer through the propagating photons ($q \leq \omega/c$), the heat transfer is maximal for black bodies with zero reflection amplitude, $R = R_r + iR_i = 0$. Now, what is the photon-tunneling equivalent of a black body? For $q > \omega/c$ there are no constraints on the reflection amplitude, $R(q, \omega)$, other than that $\mathrm{Im}R(q, \omega)$ is positive, and R_r and R_i are connected by the Kramers–Kronig relation. Therefore, assuming identical surfaces, we are free to maximize the transmission coefficient corresponding to the photon tunneling

$$T = |D|^2 = \frac{R_i^2 \mathrm{e}^{-2kd}}{\left|1 - \mathrm{e}^{-2kd} R^2\right|^2} \tag{6.15}$$

(where $k = |k_z|$) with respect to R_i (or R_r). This function is maximal when [115]:

$$R_r^2 + R_i^2 = \mathrm{e}^{2kd}, \tag{6.16}$$

so that $T = 1/4$. Substituting this result in (6.13) gives the maximal contribution from the evanescent waves:

$$(S_z)_{max}^{evan} = \frac{k_B^2 T^2 q_c^2}{24\hbar}, \tag{6.17}$$

where q_c is a cut-off in q, determined by the properties of the material. It is clear that the largest possible $q_c \sim 1/b$, where b is an inter-atomic distance. Thus, from (1.2) and (6.17) we get the ratio of the maximal heat flux connected with evanescent waves to the heat flux due to black body radiation $(S_z)_{max}/S_{BB} \approx 0.25(\lambda_T/b)^2$, where $\lambda_T = c\hbar/k_B T$. At room temperature, the contribution to the heat flux from the evanescent waves will be approximately eight orders of magnitude larger than the contribution from black body radiation, and the upper boundary for the radiative heat transfer at room temperature $(S_z)_{max} \sim 10^{11}$ Wm^{-2}. The result that there is a maximum heat flow in a given channel links with more profound ideas of entropy flow. It was shown [96] from very general arguments that the maximum of the information flow in a single channel is linked to the flow of energy. Briefly, the arguments were that the flow of information in a channel is limited by

$$\dot{E} \geq \frac{3\hbar \ln^2 2}{\pi} \dot{I}^2, \tag{6.18}$$

where $\dot{E}$ is the energy flow and $\dot{I}$ the information flow. Identifying the energy flow with heat flow, S,

$$\dot{E} = S \qquad \dot{I} = \frac{S}{k_B T \ln 2} \tag{6.19}$$

we have

$$S \leq \frac{\pi k_B^2 T^2}{3\hbar}, \tag{6.20}$$

hence,

$$S \leq S_{\max} = 2 \sum_{\mathbf{q}} \frac{\pi k_B^2 T^2}{3\hbar}, \tag{6.21}$$

where factor 2 takes into account two possible polarizations. Therefore, the maximum in the heat flux per channel is interpreted as conducting the maximum allowed amount of entropy per channel.

Let us apply the general theory to concrete materials. For the local optic case, the reflection amplitudes are determined by the Fresnel formulas (3.17). For metals, the dielectric function can be written in the form

$$\varepsilon = 1 + 4\pi i \sigma / \omega, \tag{6.22}$$

where σ is the conductivity that can be considered as constant in the mid- and far-infrared region. For good conductors, when $k_B T / 4\pi\sigma \ll 1$ and $\lambda_T |\varepsilon(\omega_T)|^{-3/2} < d < \lambda_T |\varepsilon(\omega_T)|^{1/2}$, where $\omega_T = c/\lambda_T = k_B T/\hbar$, the contribution to the heat transfer from p-polarized waves is determined by

$$S_p \approx 0.2 \frac{(k_B T)^2}{\hbar \lambda_T d} \left(\frac{k_B T}{4\pi\hbar\sigma} \right)^{1/2}, \tag{6.23}$$

while the s-wave contribution for $d < \lambda_T |\varepsilon(\omega_T)|^{-1/2}$ is distance independent:

$$S_s \approx 0.02 \frac{4\pi\sigma k_B T}{\lambda_T^2}. \tag{6.24}$$

For good conductors, the heat flux associated with p-polarized electromagnetic waves decreases with the separation as $\sim d^{-1}$, and increases with decreasing conductivity as $\sigma^{-1/2}$. When $k_B T / 4\pi\hbar\sigma \geq 1$ the heat flux decreases with separation as d^{-2}. Figure 6.1a shows the heat transfer between two semi-infinite silver bodies separated by the distance d, and at the temperatures $T_1 = 273$ K and $T_2 = 0$ K. The s- and p-wave contributions are shown separately, and the p-wave contribution has been calculated using non-local optics, i.e. spatial dispersion of the dielectric function was taken into account (the dashed line shows the result using local optics). It is remarkable how important the s-contribution is even for short distances. The nonlocal optics contribution to $(S_z)_p$, which is important only for $d < l$ (where l

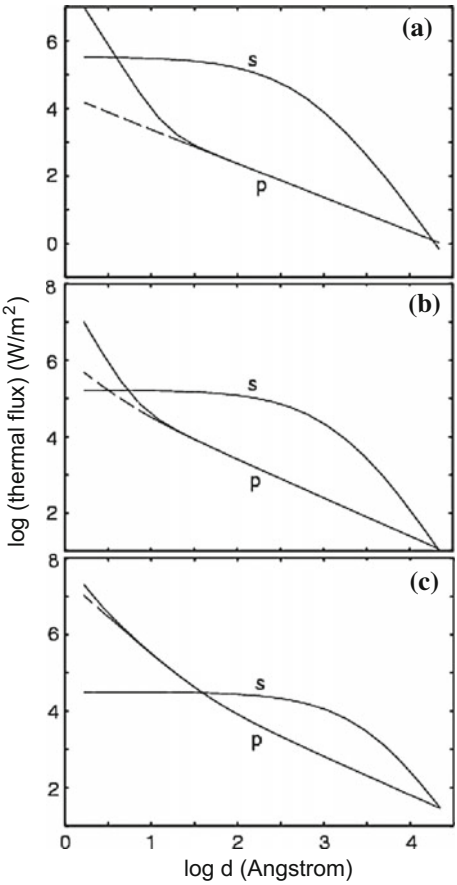

Fig. 6.1 **a** The heat transfer flux between two semi-infinite silver bodies, one at temperature $T_1 = 273$ K and another at $T_2 = 0$ K, as a function of the separation d. **b** The same as (**a**) except that we have reduced the Drude electron relaxation time τ for solid 1 from a value corresponding to a mean free path $v_F\tau = l = 560$ to 20 Å. **c** The same as (**a**) except that we have reduced l to 3.4 Å. The *dashed lines* correspond to the results obtained within local optic approximation. (The base of the logarithm is 10.)

is the electron mean free path in the bulk), is easy to calculate for free electron like metals. The non-local surface contribution to $\mathrm{Im}R_p$ is given by [117]

$$\left(\mathrm{Im}R_p\right)_{\mathrm{surf}} = 2\xi\frac{\omega}{\omega_p}\frac{q}{k_F}, \tag{6.25}$$

where $\xi(q)$ depends on the electron-density parameter r_s but typically $\xi(0) \sim 1$. Using this expression for $\mathrm{Im}R_p$ in (6.13) gives the (surface) contribution:

$$S_{\mathrm{surf}} \approx \frac{\xi^2 k_B^4}{\omega^2 k_F^2 d^4 \hbar^3}\left(T_1^4 - T_2^4\right). \tag{6.26}$$

Note from Fig. 6.1a that the local optic contribution to $(S_z)_p$ depends nearly linearly on $1/d$ in the studied distance interval, and that this contribution is much smaller than the s-wave contribution. Both of these observations are in agreement with the

analytical formulas presented above. However, for very high-resistivity materials, the p-wave contribution becomes much more important, and a crossover to a $1/d^2$-dependence of $(S_z)_p$ is observed at very short separations d. This is illustrated in Fig. 6.1b and c, which have been calculated with the same parameters as in Fig. 6.1a, except that the electron mean free path has been reduced from $l = 560$ Å (the electron mean free path for silver at room temperature) to 20 Å (approximately the electron mean free path in lead at room temperature) (Fig. 6.1b) and 3.4 Å (of the order of the lattice constant, representing the minimal possible mean free path) (Fig. 6.1c). Note that when l decreases, the p-wave contribution to the heat transfer increases while the s-wave contribution decreases. Since the mean free path cannot be much smaller than the lattice constant, the result in Fig. 6.1c represents the largest possible p-wave contribution for normal metals. However, the p-wave contribution may be even larger for other materials, such as semimetals, with lower carrier concentration than in normal metals. For high resistivity material, when $k_B T/4\pi\hbar\sigma > 1$ the heat flux is proportional to the conductivity:

$$S_p \approx 0.2\frac{k_B T\sigma}{d^2}. \tag{6.27}$$

By tuning the resistivity of the material we can optimize the photon transmission coefficient across the vacuum gap and hence the potential for heat transport by tunneling. The transmission coefficient $|T(\omega, q)|^2$ is proportional to the energy density of the electromagnetic field associated with evanescent waves:

$$T(\omega, q) \sim \mathrm{Im}R_p(\omega, q)e^{-qd}. \tag{6.28}$$

For $q \gg |\varepsilon(\omega)|^{1/2}\omega/c$

$$\mathrm{Im}R_p(\omega, q) \approx \mathrm{Im}\frac{\varepsilon - 1}{\varepsilon + 1} \approx \frac{8\pi\sigma/\omega}{4 + (4\pi\sigma/\omega)^2}. \tag{6.29}$$

Assuming that the conductivity, σ, is independent of ω and q the energy density is maximal when

$$\sigma_{\max} = \frac{\omega}{2\pi} \approx \frac{k_B T}{2\pi\hbar} = 2.3T(\Omega \cdot \mathrm{m})^{-1}, \tag{6.30}$$

where we have replaced $\hbar\omega$ with the typical thermal energy $k_B T$. At room temperature the optimum electrical conductivity is 690 $(\Omega{\cdot}\mathrm{m})^{-1}$.

To illustrate this case, Fig. 6.2 shows the thermal flux as a function of the conductivity of the solids. Again, we assume that one body is at zero temperature and the other at $T = 273$ K. The solid surfaces are separated by $d = 10$ Å. The heat flux for other separations can be obtained using scaling $\sim 1/d^2$, which holds for high-resistivity materials. The heat flux is maximal when $\sigma \approx 920$ $(\Omega\ \mathrm{m})^{-1}$.

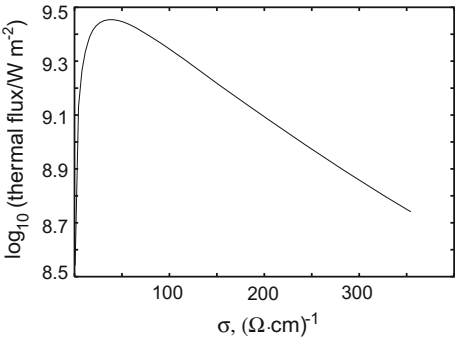

Fig. 6.2 The thermal flux as a function of the conductivity of the solids. The surfaces are separated by $d = 10$ Å. The heat flux for other separations can be obtained using scaling $\sim 1/d^2$, which holds for high-resistivity materials. (The base of the logarithm is 10.)

For good conductors, the most important contribution to the radiative heat transfer comes from the non-local optic effects in the surface region. However, it was shown above that the radiative heat transfer becomes much larger for high-resistivity material, for which the volume contribution from non-local effects is also important. Non-local optic refers to the fact that the current at point $\mathbf{r}$ depends on the electric field not only at point $\mathbf{r}$, as it is assumed in the local optic approximation, but also at points $\mathbf{r}' \neq \mathbf{r}$ in a finite region around the point $\mathbf{r}$. In the case when both points are located outside of the surface region, the dielectric response function can be expressed through the dielectric function appropriate for the semi-infinite electron gas. However, if one of the points $\mathbf{r}$ or $\mathbf{r}'$ is located in the surface region, the dielectric response function will be different from its volume value, and this gives the surface contribution from non-locality. In order to verify the accuracy of the local optic approximation, we study the dependence of the radiative heat transfer on the dielectric properties of the materials within the non-local dielectric approach, which was proposed some years ago for the investigation of the anomalous skin effects [198] (see Appendix D).

Figure 6.3 shows the thermal flux between two clean metal surfaces as a function of the electron density n. In the calculations, we have assumed that one body is at zero temperature and the other at $T = 273\,\mathrm{K}$, and the Drude relaxation time $\tau = 4 \times 10^{-14}\,\mathrm{s}$. When the electron density decreases, there is transition from a degenerate electron gas ($k_B T \ll \varepsilon_F$, where ε_F is the Fermi energy) to a non-degenerate electron gas ($k_B T \gg \varepsilon_F$) at the density $n_F \sim (K_B T m)^{3/2}/\pi^2\hbar^3$, where m is the electron mass. At $T = 273\,\mathrm{K}$, the transition density $n_F \sim 10^{25}\,\mathrm{m}^{-3}$. The full line was obtained by interpolation between the two dashed curves, calculated in the non-local dielectric function formalism for the non-degenerate electron gas (valid for $n < n_F \approx 10^{25}\,\mathrm{m}^{-3}$), and for the degenerate electron gas (for $n > n_F$) [198]. The thermal flux reaches the maximum $S_{\max} \approx 5 \times 10^8\,\mathrm{W{\cdot}m^{-2}}$ at $n_{\max} \approx 10^{25}\,\mathrm{m}^{-3}$, which corresponds to the DC conductivity $\sigma \approx 3 \times 10^3\,(\Omega{\cdot}\mathrm{m})^{-1}$. Within the local optic approximation, the radiative heat transfer is maximal at $n_{L\,\max} \approx 10^{24}\,\mathrm{m}^{-3}$ where $S_{L\,\max} \approx 10^9\,\mathrm{W{\cdot}m^{-2}}$. The thermal flux due to traveling electromagnetic waves is determined by formula (1.2) which gives $S_{BB} = 308\,\mathrm{W{\cdot}m^{-2}}$ for $T = 273\,\mathrm{K}$.

Finally, we note that a thin high-resistivity coatings can drastically increase the heat transfer between two solids. Figure 6.4 shows the heat flux when thin films

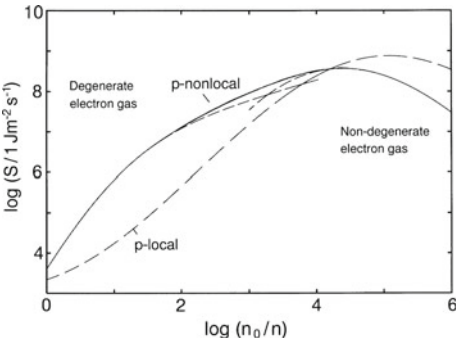

Fig. 6.3 The heat flux between two metal surfaces as a function of the free electron concentration n. One body is at zero temperature and the other at $T = 273\,\mathrm{K}$. The *full line* was obtained by interpolation between curves (*dashed lines*) calculated in the non-local dielectric formalism for a non-degenerate electron gas for $n < n_F \sim 10^{25}\,\mathrm{m}^{-3}$, and for a degenerate electron gas for $n > n_F$. Also shown are results (*dashed lines*) obtained within the local optic approximation. The calculations were performed with the damping constant $\tau^{-1} = 2.5 \times 10^{13}\,\mathrm{s}^{-1}$, separation $d = 10$ Å and $n_0 = 8.6 \times 10^{28}\,\mathrm{m}^{-3}$. (The log-function is with basis 10.)

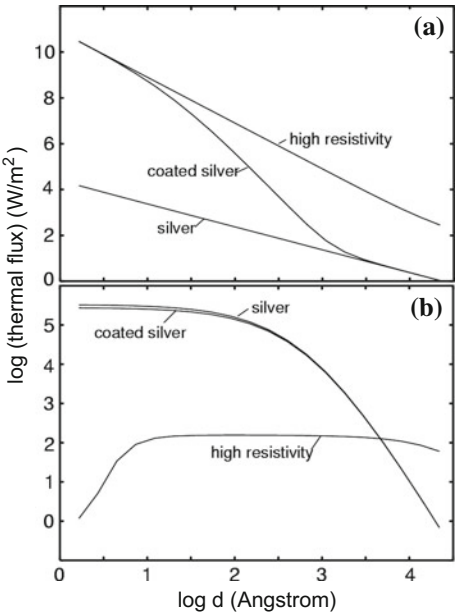

Fig. 6.4 The heat flux between two semi-infinite silver bodies coated with a 10 Å thick layer of a high resistivity ($\rho = 0.14\ \Omega$cm) material. Also shown is the heat flux between two silver bodies, and two high-resistivity bodies. One body is at zero temperature and the other at $T = 273$ K. **a**, **b** show the p- and s-wave contributions, respectively. (The base of the logarithm is 10.)

($\sim$10 Å) of a high resistivity material $\rho = 0.14\ \Omega$ cm, are deposited on silver surfaces. One body is at zero temperature and the other at $T = 273$ K. (a) and (b) show the p and s-contributions, respectively. Also shown are the heat fluxes when the two bodies are made from silver, and from a high resistivity material. It is interesting to note that while the p-wave contribution to the heat flux for the coated surfaces is strongly influenced by the coating, the s-contribution is nearly unaffected.

6.4 Resonant Photon Tunneling Enhancement of the Radiative Heat Transfer

Another case where the transmission coefficient can be close to unity is connected with resonant photon tunneling between surface states localized on the different surfaces. The resonant condition corresponds to the case when the denominators in (6.13) are small. For two identical surfaces and $R_i \ll 1 \leq R_r$, where R_i and R_r are the imaginary and real parts of the reflection amplitude, this corresponds to the resonant condition $R_r^2 \exp(-2qd) = 1$. The resonance condition can be fulfilled even for the case when $\exp(-2qd) \ll 1$, since, for the evanescent electromagnetic waves, there is no restriction on the magnitude of real part or the modulus of R. This opens up the possibility of resonant denominators for $R_r^2 \gg 1$. Close to the resonance we can use the approximation

$$R = \frac{\omega_a}{\omega - \omega_0 - i\eta}, \tag{6.31}$$

where ω_a is a constant. Then from the resonant condition ($R_r = \pm e^{qd}$) we get the positions of the resonance

$$\omega_\pm = \omega_0 \pm \omega_a e^{-qd}. \tag{6.32}$$

For the resonance condition to be valid, the separation $\Delta\omega = |\omega_+ - \omega_-|$ between two resonances in the transmission coefficient must be greater than the width η of the resonance. This condition is valid only for $q \leq q_c \approx \ln(2\omega_a/\eta)/d$. For $\omega_0 > \omega_a$ and $q_c d > 1$, we get

$$S_{p\pm} = \frac{\eta q_c^2}{8\pi}\big[\Pi_1(\omega_0) - \Pi_2(\omega_0)\big]. \tag{6.33}$$

Note, that the explicit d dependence has dropped out of (6.33). However, S may still be d-dependent, through the d-dependence of q_c. For small distances, one can expect that q_c is determined by the dielectric properties of the material, and thus does not depend on d. In this case, the heat transfer will also be distance independent.

Resonant photon tunneling enhancement of the heat transfer is possible for two semiconductor surfaces that can support low-frequency surface plasmon modes in the mid-infrared frequency region. The reflection amplitude R_p for a clean semiconductor surface at $d < \lambda_T\,|\varepsilon(\omega_T)|^{-1/2}$ is given by Fresnel's formula (see Appendix O.2). As an example, consider two clean surfaces of silicon carbide (SiC). The optical properties of this material can be described using an oscillator model [180]:

$$\varepsilon(\omega) = \epsilon_\infty \left(1 + \frac{\omega_L^2 - \omega_T^2}{\omega_T^2 - \omega^2 - i\Gamma\omega}\right), \tag{6.34}$$

with $\varepsilon_\infty = 6.7$, $\omega_L = 1.8 \times 10^{14}\ \mathrm{s}^{-1}$, $\omega_T = 1.49 \times 10^{14}\ \mathrm{s}^{-1}$, and $\Gamma = 8.9 \times 10^{11}\ \mathrm{s}^{-1}$. The frequency of surface plasmons is determined by condition $\varepsilon'(\omega_0) = -1$ and from (6.34) we get $\omega_0 = 1.78 \times 10^{14}\ \mathrm{s}^{-1}$. The resonance parameters are

$$\omega_a = \frac{\omega_L^2 - \omega_T^2}{\epsilon_\infty \omega_L} = 8.2 \times 10^{12-1},\ \eta = \Gamma/2,\ q_c = 3.6/d, \quad \omega_0 \approx \omega_p$$

Using the above parameters in (6.33), and assuming that one surface is at temperature $T = 300$ K and the other at $T = 0$ K, we get the heat flux $S(d)$ between two clean surfaces of SiC:

$$S \approx \frac{8.4 \times 10^9}{d^2} \mathrm{W} \cdot \mathrm{m}^{-2}, \tag{6.35}$$

where the distance d is in Å. Note that this heat flux is several orders of magnitude larger than between two clean good conductor surfaces (see Fig. 6.1).

6.5 Adsorbate Vibrational Mode Enhancement of the Radiative Heat Transfer

Another mechanism for resonant photon tunneling enhancement of the heat transfer is possible between adsorbate vibrational modes localized on different surfaces. If the distance between adsorbates $d \gg R$, where R stands for effective radius of the adsorbate, each adsorbate is equivalent to a point dipole. As shown in [101], the dipole approximation is valid for distances larger than a few adsorbate diameters. Let us consider two particles with dipole polarizabilities $\alpha_1(\omega)$ and $\alpha_2(\omega)$ and with the fluctuating dipole moments p_1^f and p_2^f normal to the surfaces. According to the fluctuation-dissipation theorem [8, 184], the spectral function of fluctuations for the dipole moment is given by

$$\left\langle p_i^f p_j^f \right\rangle_\omega = \frac{\hbar}{\pi} \left(\frac{1}{2} + n_i(\omega) \right) \mathrm{Im}\alpha_i(\omega) \delta_{ij}. \tag{6.36}$$

Assume that the particles are situated opposite to each other on two different surfaces, at the temperatures T_1 and T_2, respectively, and separated by the distance d. The fluctuating electric field of a particle **1** does work on a particle **2**. The rate of work is determined by

$$P_{12} = 2 \int_0^\infty d\omega\, \omega \mathrm{Im}\alpha_2(\omega) \langle E_{12} E_{12} \rangle_\omega, \tag{6.37}$$

where E_{12} is the electric field created by particle **1** at the position of particle **2**:

$$E_{12} = \frac{8 p_1^f / d^3}{1 - \alpha_1 \alpha_2 \left(8/d^3\right)^2}. \tag{6.38}$$

From (6.36)–(6.38) we get P_{12}, and the rate of cooling of a particle **2** can be obtained using the same formula by reciprocity. Thus, the total heat power exchange between the particles is given by

$$P = P_{12} - P_{21} = \frac{2\hbar}{\pi}\int_0^\infty d\omega\,\omega \frac{\mathrm{Im}\alpha_1 \mathrm{Im}\alpha_2 \left(8/d^3\right)^2}{\left|1 - \left(8/d^3\right)^2 \alpha_1\alpha_2\right|^2}\left(n_1(\omega) - n_2(\omega)\right). \tag{6.39}$$

Let us first consider some general consequences of (6.39). There are no constraints on the particle polarizability $\alpha(\omega) = \alpha' + i\alpha''$ other than that α'' is positive, and α' and α'' are connected by the Kramers–Kronig relation. Therefore, assuming identical surfaces, we are free to maximize the photon-tunneling transmission coefficient (for comparison see also (6.15))

$$t = \frac{\left(8\alpha''/d^3\right)^2}{\left|1 - \left(8\alpha/d^3\right)^2\right|^2}. \tag{6.40}$$

This function has a maximum when $\alpha'^2 + \alpha''^2 = \left(d^3/8\right)^2$ so that $t = 1/4$. Substituting this result in (6.39) gives the upper bound for the heat transfer between two particles:

$$P_{max} = \frac{\pi k_B^2}{3\hbar}\left(T_1^2 - T_2^2\right). \tag{6.41}$$

For adsorbed molecules at the concentration $n_a = 10^{19}$ m^{-2}, when one surface is at zero temperatures and the other is at the room temperature, the maximal heat flux due to the adsorbates $S_{max} = n_a P_{max} = 10^{12}$ Wm^{-2}, which is nearly 10 orders of magnitude larger than the heat flux due to the black body radiation, $S_{BB} = \sigma_B T = 4 \times 10^2$ Wm^{-2}, where σ_B is the Boltzmann constant.

The conditions for resonant photon tunneling are determined by

$$\alpha'(\omega_\pm) = \pm d^3/8. \tag{6.42}$$

Close to resonance, we can use the approximation

$$\alpha \approx \frac{C}{\omega - \omega_0 - i\eta}, \tag{6.43}$$

where $C = e^{*2}/2M\omega_0$, and where e^* and M are the dynamical charge and mass of the adsorbate, respectively.

For $\eta \ll 8C/d^3$, from (6.39) we get

$$P = \frac{\hbar\eta}{2}\left[\omega_+\left(n_1(\omega_+) - n_2(\omega_+)\right) + (+ \to -)\right], \tag{6.44}$$

where $\omega_{\pm} = \omega_0 \pm 8C/d^3$. Using (6.44), we can estimate the heat flux between identical surfaces covered by adsorbates with concentration n_a: $J \approx n_a P$. For $8C/d^3 < \eta$ we can neglect multiple scattering of the photon between the particles, so that the denominator in the integrand in (6.39) is equal to unity. For $d \gg b$, where b is the interparticle spacing, the heat flux between two surfaces covered by adsorbates with concentration n_{a1} and n_{a2} can be obtained after integration of the heat flux between two separated particles. We get

$$S = \frac{24 n_{a1} n_{a2}}{d^4} \int_0^{\infty} d\omega \, \mathrm{Im}\alpha_1 \mathrm{Im}\alpha_2 \big[\Pi_1(\omega) - \Pi_2(\omega)\big]. \tag{6.45}$$

Assuming that α can be approximated by (6.43), for $\omega_0 \ll \eta$ (6.45) gives the heat flux between two identical surfaces:

$$S = \frac{12\pi C^2 n_a^2}{d^4 \eta} \big[\Pi_1(\omega_0) - \Pi_2(\omega_0)\big]. \tag{6.46}$$

We note that (6.46) can be obtained directly from the heat flux between two semi-infinite solids (determined by (6.13)), since in the limit $d > b$ we can use a macroscopic approach, where all information about optical properties of the surface is included in reflection amplitude.

The reflection amplitude for p-polarized electromagnetic waves which takes into account the contribution from a adsorbate layer, can be obtained using the approach proposed in [99]. Using this approach we get [170, 171] (see also Appendix E):

$$R_p = \frac{1 - s/(q\varepsilon) + 4\pi n_a [s\alpha_{\parallel}/\varepsilon + q\alpha_{\perp}] - qa\left(1 - 4\pi n_a q \alpha_{\parallel}\right)}{1 + s/(q\varepsilon) + 4\pi n_a [s\alpha_{\parallel}/\varepsilon - q\alpha_{\perp}] + qa\left(1 + 4\pi n_a q \alpha_{\parallel}\right)}, \tag{6.47}$$

where $s = \sqrt{q^2 - (\omega/c)^2 \epsilon}$. The polarizability for ion vibrations (with dynamical charge e^*) normal and parallel to the surface, is given by

$$\alpha_{\perp(\parallel)} = \frac{e^{*2}}{M\left(\omega_{\perp(\parallel)}^2 - \omega^2 - i\omega\eta_{\perp(\parallel)}\right)}, \tag{6.48}$$

where $\omega_{\perp(\parallel)}$ is the frequency of the normal (parallel) adsorbate vibration, $\eta_{\perp(\parallel)}$ the corresponding damping constant, and M is the adsorbate mass. In comparison with the expression obtained in [199], (6.47) takes into account the fact that the centers of the adsorbates are located at distance a away from the image plane of the metal. Although this gives corrections of the order of $qa \ll 1$ to the reflection amplitude, for parallel adsorbate vibrations on the good conductors ($|\epsilon| \gg 1$), this correction becomes important (see Sect. 7.8.2). As an illustration, in Fig. 6.5 we compare the heat flux between two Cu(100) surfaces covered by low concentration of potassium atoms ($n_a = 10^{18}$ m^{-2}), with the heat flux between two clean Cu(100) surfaces. At separation $d = 1$ nm, the heat flux between the adsorbate-covered surfaces is enhanced by five orders of magnitude in comparison with the heat flux between the clean

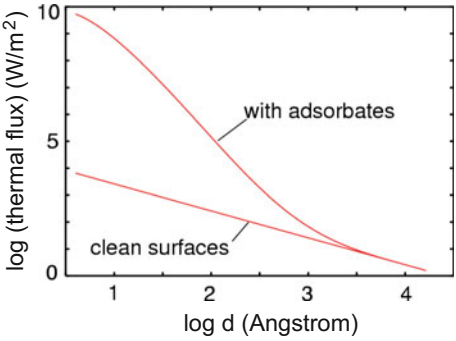

Fig. 6.5 The heat flux between two surfaces covered by adsorbates and between two clean surfaces, as a function of the separation d. One body is at zero temperature and the other at $T = 273$ K. For parameters corresponding to K/Cu(001) and Cu(001) [200] ($\omega_\perp = 1.9 \times 10^{13}$ s^{-1}, $\omega_\parallel = 4.5 \times 10^{12}$ s^{-1}, $\eta_\parallel = 2.8 \times 10^{10}$ s^{-1}, $\eta_\perp = 1.6 \times 10^{12}$ s^{-1}, $e^* = 0.88e$). (The base of the logarithm is 10.)

surfaces, and by seven orders of magnitude in comparison with the black body radiation. However, this enhancement of the heat flux disappears if only one of the surfaces is covered by adsorbates. For $d \gg b$ the numerical data can be approximated by the formula

$$S \approx 5.6 \times 10^{-24} \frac{n_a^2}{d^4} \text{ W m}^{-2}, \tag{6.49}$$

where d is in Å.

For $d < b$, the macroscopic approach is not valid and we must sum the heat flux between each pair of adatoms. For $\eta = 10^{12}$ s^{-1} and $d < 10$ Å, when one surface has $T = 300$ K and the other $T = 0$ K, from (6.44) we get a distance independent $P \approx 10^{-9}$ W. In this case, for $n_a = 10^{18}$ m^{-2} the heat flux $S \approx Pn_a \approx 10^9$ Wm^{-2}. Under the same conditions, the s-wave contribution to the heat flux between two clean surfaces is $S_{clean} \approx 10^6$ Wm^{-2}. Thus, the photon tunneling between the adsorbate vibrational states can strongly enhance the radiative heat transfer between the surfaces.

It is interesting to note that in the strong coupling case ($8c/d^3 \gg \eta$), the heat flux between two molecules does not depend on the dynamical dipole moments of the molecules (see (6.44)). However, in the opposite case of weak coupling ($8C/d^3 \ll \eta$), the heat flux is proportional to the product of the squares of the dynamical dipole moments (see (6.45)).

6.6 Vibrational Heating by Localized Photon Tunneling

The radiative heat transfer due to the evanescent electromagnetic waves (photon tunneling) may be used for surface modification. Thus, if a hot tip is brought ~1 nm from a surface with a thin layer of heat sensitive polymer, one may induce local

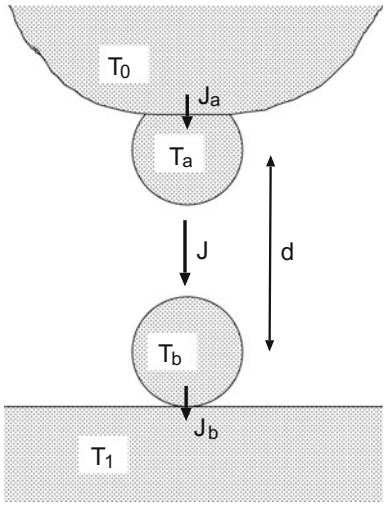

Fig. 6.6 The heat transfer (photon tunneling) between a tip atom (or molecule) and a substrate atom (or molecule)

polymerization and this may be used for nanoscale lithography. This non-contact mode of surface modification may have several advantages compared with the contact mode: for example, no wear or contamination of the tip will occur.

Let us consider the radiative heat transfer between an adsorbed molecule on a tip and another molecule adsorbed on a substrate. The temperature increase at the adsorbed molecule may be very large, which may induce local chemical reactions, such as diffusion or desorption. Heat transfer to some adsorbate vibrational mode, i.e., vibrational heating, will be particularly important when the energy relaxation time τ_b of the adsorbate mode is long compared with a relaxation time characterizing the photon tunneling from the tip to the substrate adsorbate. High-frequency adsorbate vibrations on metals typically have very short energy relaxation times (in the pico-second range) owing to the continuum of low-energy electronic excitations [201, 202]. However, low-frequency adsorbate vibrations, e.g., frustrated translations, may have rather long relaxation times (typically in the order of nanoseconds for inert adsorbates on noble metals) [203], and in these cases photon tunneling heat transfer may be important. Adsorbate vibrational modes on insulators may have very long relaxation times if the resonance frequency is above the top of the bulk phonon band. In these cases, energy relaxation is caused by multi-phonon processes, which are often very slow. One extreme example is CO adsorbed on NaCl crystals [204], where $\tau_b \approx 10^{-3}$ s. For this case, even a very weak coupling to a hot tip may result in heating of the C–O stretch vibration.

The photon tunneling energy transfer per unit time from a vibrational mode of the tip adsorbate (frequency ω_a and vibrational relaxation time $\tau_a^* = \eta_a^{-1}$) to a vibrational mode (ω_b, τ_b^*) of the substrate adsorbate (see Fig. 6.6) is given by (6.39). The molecular polarizability is given by (6.48). The energy transfer rate from the tip to the tip adsorbate is given by [205]

$$J_{\mathrm{a}} = \frac{\hbar\omega_{\mathrm{a}}}{\tau_{\mathrm{a}}}\big[n(\omega_{\mathrm{a}}/T_0) - n(\omega_{\mathrm{a}}/T_{\mathrm{a}})\big], \tag{6.50}$$

and the energy transfer rate from the substrate adsorbate to the substrate

$$J_{\mathrm{b}} = \frac{\hbar\omega_{\mathrm{b}}}{\tau_{\mathrm{b}}}\big[n(\omega_{\mathrm{b}}/T_{\mathrm{b}}) - n(\omega_{\mathrm{b}}/T_{\mathrm{l}})\big], \tag{6.51}$$

where τ_a and τ_b are the vibrational energy relaxation times. Note that, in general $1/\tau_a^* > 1/\tau_a$ and $1/\tau_b^* > 1/\tau_b$ since the vibrational relaxation rate $1/\tau^*$ which enters in the polarizability has contributions from both energy relaxation and pure dephasing. In general, the integral in (6.39) must be performed numerically, but as an illustration, let us consider the case where the relaxation time $\tau_{\mathrm{b}}^* \gg \tau_{\mathrm{a}}^*$. In this case, (6.39) reduces to

$$P = r\frac{\hbar\omega_{\mathrm{b}}}{\tau_{\mathrm{b}}}\big[n(\omega_{\mathrm{b}}/T_{\mathrm{a}}) - n(\omega_{\mathrm{b}}/T_{\mathrm{b}})\big], \tag{6.52}$$

where

$$r = \frac{(\tau_b/\tau_b^*)s}{1 + \big[2(\omega_{\mathrm{a}} - \omega_{\mathrm{b}})\tau_{\mathrm{a}}^*\big]^2 + 4s}, \tag{6.53}$$

$$s = 64\omega_{\mathrm{a}}\tau_{\mathrm{a}}^*\omega_{\mathrm{b}}\tau_{\mathrm{b}}^*\alpha_{\mathrm{va}}\alpha_{\mathrm{vb}}/d^6, \tag{6.54}$$

where $\alpha_{\mathrm{va}} = e_{\mathrm{a}}^{*2}/M_{\mathrm{a}}\omega_{\mathrm{a}}^2$ and similar for mode b.

Note that the energy transfer rate J_{a} (and similar for J_{b}) depends only on the energy relaxation rate $1/\tau_{\mathrm{a}}$ and not on the relaxation rate $1/\tau_{\mathrm{a}}^*$ which determines the width of the vibrational resonance state. The latter is the sum of $1/\tau_{\mathrm{a}}$ and a pure dephasing contribution, which reflects the fluctuation $\omega_{\mathrm{a}}(t)$ in the vibrational level position due to the irregular thermal motion of the atoms in the system, and which depends on the anharmonic coupling between the different vibrational modes. This level-fluctuation contributes to the vibrational linewidth as observed using, for example, infrared spectroscopy, but not to the energy transfer between the adsorbate and the solid on which it is adsorbed. On the other hand, the energy transfer rate P between the two adsorbates is determined by the overlap in the vibrational resonance states and it is therefore determined by τ_{a}^* (and τ_{b}^*), and does not depend on τ_{a} (or τ_{b}). (Note: the τ_{b}^{-1} factor which appears in (6.52) cancels out against the factor τ_{b} in the expression for r.)

In the high temperature limit $n(\omega/T) \approx k_{\mathrm{B}}T/\hbar\omega$, and assuming that this relation holds for all modes and temperatures relevant here, we get

$$P = r\tau_{\mathrm{b}}^{-1}k_{\mathrm{B}}(T_{\mathrm{a}} - T_{\mathrm{b}}). \tag{6.55}$$

We also get

$$J_{\mathrm{a}} = \tau_{\mathrm{a}}^{-1}k_{\mathrm{B}}(T_0 - T_{\mathrm{a}}), \tag{6.56}$$

$$J_{\mathrm{b}} = \tau_{\mathrm{b}}^{-1}k_{\mathrm{B}}(T_{\mathrm{b}} - T_{\mathrm{l}}). \tag{6.57}$$

Assuming first a steady state situation so that $P = J_a = J_b$ we get from (6.55)–(6.57) $T_a \approx T_0$ and

$$T_b \approx T_1 + \frac{r}{1+r}(T_0 - T_1), \tag{6.58}$$

where we have assumed that $\tau_b \gg \tau_a$.

The theory above can also be used to estimate the time it takes to reach the steady state where the (ensemble averaged) adsorbate temperature equals to (6.58). In general we have

$$\hbar\omega_b \frac{d}{dt} n(\omega_b / T_b(t)) = J(t) - J_b(t).$$

In the classical limit, this gives

$$\frac{dT_b}{dt} = -\frac{1}{\tau_b}(1+r)T_b + \frac{1}{\tau_b}(T_1 + rT_0).$$

If we assume $T_b(0) = T_1$, this gives

$$T_b(t) = T_1 + \frac{r}{1+r}(T_0 - T_1)\left(1 - e^{-(1+r)t/\tau_b}\right).$$

Thus for $t \gg \tau$, where $\tau = \tau_b/(1+r)$, the steady state temperature has been reached.

For adsorbates on insulating substrates τ_b will, in general, be very large if the resonance frequency ω_b is well above the highest substrate phonon frequency. We now consider this case, which is equivalent to low temperature. Assume for simplicity that the temperature of the substrate vanishes ($T_1 = 0$) and assume that $\hbar\omega_a \gg k_B T_0$ and $\hbar\omega_b \gg k_B T_0$. In this case, is easy to show from (6.50)–(6.52) that $T_a \approx T_0$ and

$$T_b \approx \frac{\omega_b T_0}{\omega_b + T_0 \ln[(1+r)/r]}, \tag{6.59}$$

where we have measured frequency in units of $k_B/\hbar$.

Let us now assume arbitrary tip and substrate temperatures but still assume $\tau_b \gg \tau_a$. Using (6.50)–(6.52) we get $T_a \approx T_0$ and

$$\frac{\omega_b}{T_b} = \ln\left[1 + \frac{1+r}{r\left(e^{\omega_b/T_0} - 1\right)^{-1} + \left(e^{\omega_b/T_1} - 1\right)^{-1}}\right]. \tag{6.60}$$

This expression reduces to (6.58) for high temperatures and to (6.59) for low temperatures. In Fig. 6.7, we show the effective temperature T_b as a function of the tip temperature T_0 when $T_1 = 0.1\hbar\omega_b/k_B$ and $r = 0.25$.

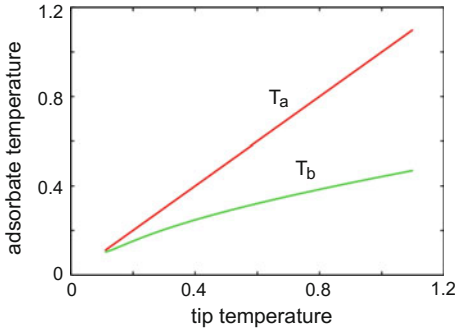

Fig. 6.7 The adsorbate temperatures T_a and T_b as a function of the tip temperature T_0 (all in units of $\hbar\omega_b/k_B$). For $r = 9.25$ and $T_1 = 0.1\hbar\omega_b/k_B$

The effective adsorbate temperature T_b, calculated above may be used to calculate (or estimate) the rate w of an activated process: $w = w_0 \exp(-E/k_\mathrm{B}T_\mathrm{b})$. When the barrier height E is large, even a very small temperature increase will result in a large increase in the reaction rate. It is also important to note that the excitation of a high frequency mode, such as the C–O stretch mode, can result in reactions involving other reaction coordinates; for example, diffusion, rotation or desorption. This is possible because of anharmonic coupling between the high frequency mode and the reaction coordinate mode. This has already been observed in STM studies of several different adsorption systems [207, 208]. Let us give an example of an adsorption system where photon tunneling may give rise to a strong temperature increase. We focus on $^{13}C^{18}O$ on NaCl(100) at $T_1 = 30$ K which has been studied in detail by Chang and Ewing [204]. In this case, $\omega_\mathrm{b} \approx 2040\ \mathrm{cm}^{-1}$, $\tau_\mathrm{b} \approx 10^{-3}$ s (due mainly to decay via multi-phonon emission [204]), and the (pure dephasing dominated) relaxation time [209] $\tau_\mathrm{b}^* \approx 10^{-10}$ s. We assume a Pt-tip at room temperature with an adsorbed $^{12}C^{18}O$ with $\omega_\mathrm{a} \approx 2064\ \mathrm{cm}^{-1}$ and $\tau_\mathrm{a}^* \approx 3 \times 10^{-12}$ s [210] mainly due to decay by excitation of electron-hole pairs. Using the experimental measured vibrational polarizability $\alpha_\mathrm{av} \approx 0.2$ Å^3 and $\alpha_\mathrm{bv} \approx 0.04$ Å^3 and assuming the tip–substrate separation of $d = 1$ nm, we get $s \approx 20$ and $2(\omega_\mathrm{a} - \omega_\mathrm{b})\tau_\mathrm{a}^* \approx 16$. Thus, from (6.53) we get $r \approx 10^6$ and from (6.60) we get $T_\mathrm{b} \approx 300$ K where we have assumed the tip temperature $T_0 = 300$ K. The CO/NaCl case is an extreme case because of the exceptional long vibrational energy relaxation time. However, the analysis presented above remains unchanged for any τ_b larger than 10^{-8} s, so the conclusions are very general. Thus, we expect strong heating effects due to photon tunneling for high-frequency modes in adsorbed layers or films on insulating substrates.

The temperature increase for the C–O stretch vibration found above is similar to the temperature increase observed (or calculated) for CO on Pd(110) during STM experiments [207]. In this the case the excitation of the C–O stretch vibration is caused by inelastic tunneling. The temperature increase in the C–O stretch mode resulted in CO diffusion as a result of energy transfer to the parallel frustrated translation because of anharmonic coupling. This has been observed for CO molecule on Pd(110) [207], and on Ag(110) [211]. We expect similar decay processes for vibrational excited CO on NaCl resulting, in, for example, diffusion or desorption of the CO molecule.

6.7 Radiative Heat Transfer Between a Small Particle and a Plane Surface

The problem of radiative heat transfer between a small particle—considered to be a point-like dipole—and a plane surface without motion of the particle relative to the surface has been studied by several authors [16, 115, 139]. The more general case of the radiative heat transfer at relativistic motion of the particle parallel to the surface was studied in [150–152, 155, 156]. This case will be considered in Sect. 9.2. The particle could be a single molecule, or a dust particle, and it is modeled by a sphere with radius $R \ll d$, where d is the separation between the particle and the plane surface. The heat flux between the particle and substrate can be obtained from for the heat flux between two semi-infinite bodies (see (6.11)), considering one of them (say the body **2**) as sufficiently "rarefied". As in Sect. 5.3, from (6.11) at $V = 0$ we get contribution to heat flux through the surface of a semi-infinite body. We assume $d \ll \lambda_T$ so that the heat flow result from the evanescent waves. In this case, in K-reference frame the heat flux is given by

$$S = \frac{4\hbar}{\pi}\int_0^\infty \mathrm{d}\omega\omega\big(n(\omega, T_1) - n(\omega, T_2)\big)\int_0^\infty \mathrm{d}qq^2\mathrm{e}^{-2qd} \times \\ \times \left\{\mathrm{Im}R_p(\omega)\mathrm{Im}\alpha_E(\omega) + \mathrm{Im}R_s(\omega)\mathrm{Im}\alpha_H(\omega)\right\}. \tag{6.61}$$

Due to presence of factor e^{-2qd} in the q-integral, the most important contribution comes from $q \approx 1/d$, and in the ω-integration due to presence of the factor $n(\omega)$ the most important contribution comes from $\omega \approx \omega_T = k_B T/\hbar$. For $d \ll \lambda_0 \ll \lambda_T$, where $\lambda_0 = \lambda_T|\varepsilon(\omega_T)|^{-1/2}$, $\lambda_T = c/\omega_T$, Fresnel's formulas for reflection amplitudes can be written in the form

$$R_p = \frac{\varepsilon k_z - k_{z1}}{\varepsilon k_z + k_{z1}} \approx \frac{\varepsilon - 1}{\varepsilon + 1}, \tag{6.62}$$

$$R_s = \frac{k_z - k_{z1}}{k_z - k_{z1}} \approx \frac{1}{4}\left(\frac{\omega}{cq}\right)^2(\varepsilon - 1), \tag{6.63}$$

where $k_z = \sqrt{(\omega/c)^2 - q^2}$, $k_{z1} = \sqrt{(\omega/c)^2\varepsilon - q^2}$. The dielectric and magnetic susceptibility of a spherical particle with radius R are determined by (5.58) and (5.59). For metals in the low frequency range $\omega \ll \nu$ the dielectric permittivity $\varepsilon = 4\pi i\sigma/\omega$, where ν^{-1} is the electron relaxation time and σ is the conductivity. Using this expression for dielectric permittivity in (5.58), (6.62) and (6.63) and assuming $\omega \ll 4\pi\sigma$, we get

$$\mathrm{Im}R_p \approx \frac{2\omega}{4\pi\sigma}, \qquad \mathrm{Im}R_s \approx \frac{1}{4}\left(\frac{\omega}{cq}\right)^2\frac{4\pi\sigma}{\omega},$$

$$\mathrm{Im}\alpha_E(\omega) = R^3 \frac{3\omega}{4\pi\sigma}. \tag{6.64}$$

From (5.59) and (5.60) at $R \ll \delta$, where $\delta = c/\sqrt{2\pi\omega\sigma}$, we get

$$\mathrm{Im}\alpha_H = \frac{1}{30}\left(\frac{R}{\delta}\right)^2 R^3 = \frac{2\pi\sigma\omega R^5}{15c^2}. \tag{6.65}$$

Using (6.64) and (6.65) in (6.61), we get $S = S_E + S_H$, where the contributions S_E and S_H due to the electric and magnetic dipole moment S are given by

$$S_E \approx \frac{2\pi^3}{5}\left(\frac{R}{d}\right)^3 \left(\frac{k_B^4}{16\pi^2\hbar^3\sigma_1\sigma_2}\right)\left(T_1^4 - T_2^4\right), \tag{6.66}$$

$$S_H \approx \frac{\pi^3}{225}\left(\frac{R}{d}\right)\left(\frac{16\pi^2 k_B^4\sigma_1\sigma_2 R^4}{\hbar^3 c^4}\right)\left(T_1^4 - T_2^4\right), \tag{6.67}$$

where $\sigma_{1(2)}$ is the conductivity of substrate (sphere). For a example, for $T_2 = 300$ K, $d = 2R = 10$ nm, $\sigma_1 = \sigma_2 = 4 \times 10^{17}$ s (which corresponds to gold), $S_E \approx$ $\approx 10^{-17}$ W and $S_H \approx 10^{-11}$ W.

As pointed out in [115], large heat transfer is expected for high-resistivity materials. The heat flux (6.66) is maximized when $k_B T/4\pi\hbar\sigma \approx 1$. In this case, for a particle at room temperature, and a distance $d = 2R = 10\,\mathrm{nm}$ above a cold ($T = 0\,\mathrm{K}$) sample, we get $P_p/d^2 \approx 10^7\ \mathrm{Wm}^{-2}$. This should be compared with the heating from black body radiation. When the sample surface at temperature T_2 is illuminated with black body radiation at temperature T_1, taking into account the surface reflectivity, the heat flux to the sample from black body radiation is approximately [15, 93, 94]:

$$S_{BB} = \frac{1}{8\pi^3}\int_0^\infty \mathrm{d}\omega\left[\Pi_1(\omega) - \Pi_2(\omega)\right]\int_{\frac{q<\omega}{c}} \mathrm{d}^2 q\left(1 - \mid R_p(\omega)\mid^2\right) + [p \to s] =$$
$$= 0.4\frac{k_B^4 T_1^4}{\hbar^3 c^2}\left(\frac{k_B T_1}{4\pi\hbar\sigma}\right)^{1/2} - [T_1 \to T_2], \tag{6.68}$$

where $[T_1 \to T_2]$ stands for the term obtained from the first term by replacing T_1 with T_2. For $T_2 \approx 300$ K and $T_1 \approx 0$ K, and for $k_B T/\hbar \approx 4\pi\sigma$, (6.68) gives $S_{BB} \approx 100\ \mathrm{Wm}^{-2}$. Thus, a particle may give rise to a large local enhancement of the heating of the surface, compared with the uniform black body radiation. When the substrate and the particle are made from the same materials, which can support surface plasmons with frequencies ω_s and ω_p, respectively, in the two poles, an approximation the rate of the heat transfer between them is given by

$$P = \left(\frac{3\Gamma R}{d}\right)\left\{\left[\Pi_1(\omega_{sp}) - \Pi_2(\omega_{sp})\right] + [\omega_{sp} \to \omega_{ss}]\right\}. \tag{6.69}$$

For SiC with $\omega_s = 1.79 \times 10^{14}\ \mathrm{s}^{-1}$ and $\omega_p = 1.76 \times 10^{14}\ \mathrm{s}^{-1}$, $d = 10$ nm, $R = 5$ nm, $T_1 = 300$ K and $T_2 = 0$ K, (6.62) gives $P \approx 1.6 \times 10^{-10}$ W. We note that a much larger heat transfer can be achieved if the surfaces are covered with adsorbates with matched frequencies [14, 15] (see Sect. 6.5).

6.8 Near-Field Radiative Heating in Ion Traps

Electric-field noise near surfaces is a common problem in diverse areas of physics and a limiting factor for many precision measurements. There are multiple mechanisms by which such noise is generated, many of which are poorly understood. Laser-cooled, trapped ions provide one of the most sensitive systems to probe electric-field noise at MHz frequencies and over a distance range 30–3000 μm from a surface [212]. This experimental setup represents one of the most promising systems for the implementation of large-scale quantum information processing. Most of the basic requirements for building a quantum computer have been demonstrated in the laboratory and the generation of entangled states of up to 14 ions has been achieved. Many experimental efforts are now focused on the development of miniaturization and microfabrication techniques for ion traps to realize more efficient and also fully scalable quantum computing architectures. However, when devices are miniaturized, physics at the short distance becomes a challenge. This is evident in measurements of the Casimir force or of noncontact friction; in the case of trapped ions, it manifests itself in the appearance of an excess ('anomalous') heating rate and electric-field noise near surfaces, as the trap-surface distance is decreased. Therefore, a detailed understanding of the origin of this noise will be essential for the future progress of trapped-ion quantum computing, as well as the development of several hybrid quantum computing approaches where, for example, ions, Rydberg atoms, polar molecules, or charged nanomechanical resonators are operated in the vicinity of solid-state systems.

The heat transfer between an electrode and an ion trap, due to the fluctuating electric field near the electrode, can for a spherically symmetric trap be written in the form

$$P = \int_{-\infty}^{\infty} \frac{d\omega}{2\pi} \omega \mathrm{Im}\alpha_t(\omega) S_E(\omega), \tag{6.70}$$

where the spectral density of the electric field fluctuations

$$S_E(\omega) = \left\langle |\mathbf{E}(\mathbf{r_0})|^2 \right\rangle_\omega = \int_{-\infty}^{\infty} dt e^{i\omega t} \left\langle \mathbf{E}(\mathbf{r}_0, t+\tau) \cdot \mathbf{E}(\mathbf{r}_0, \tau) \right\rangle,$$

where $\mathbf{r}_0$ is the position of the trap. The polarizability of the trap is given by

$$\alpha_t(\omega) = \frac{Q^2}{M} \frac{1}{\omega_t^2 - \omega^2 - i\omega\eta_t} \tag{6.71}$$

where Q and M are the charge and mass of the ion in the trap, respectively; ω_t and η_t are the frequency and damping constant of the ion vibrations in the trap, respectively. Using (6.71) in (6.70) and taking into account that for $\eta \ll \omega_t$

$$\mathrm{Im}\alpha_t(\omega) = \frac{\pi Q^2}{2M}\big[\delta(\omega-\omega_t) - \delta(\omega+\omega_t)\big],$$

we get

$$P = \frac{Q^2}{2M} S_E(\omega_t). \tag{6.72}$$

When the ion is laser cooled to the vibrational ground state, the fluctuating electric fields couple to the motion of the ion and lead to an increase of the average vibrational occupation number $\bar{n}$ with a characteristic rate

$$\dot{\bar{n}} = \frac{P}{\hbar\omega_t} = \frac{Q^2}{2M\hbar\omega_t} S_E(\omega_t) \tag{6.73}$$

Using (4.2) in (6.72) for $q \sim 1/d \gg \omega_t/c$ we get

$$S_E(\omega_t) = 4\hbar n(\omega_t, T)\int_0^\infty dq q^2 e^{-2qd}\mathrm{Im}R_p(\omega_t, q) \approx 4\frac{k_B T}{\omega_t}\int_0^\infty dq q^2 e^{-2qd}\mathrm{Im}R_p(\omega_t, q), \tag{6.74}$$

where d is a distance between trapped ion and a metal surface. R_p is the reflection amplitude for p-polarized waves. Equation (6.74) can be obtained directly from (6.61). For a clean surface and $c/\omega_t\sqrt{|\varepsilon|} \ll d \ll c/\omega_t$ the reflection amplitude can be written in the form

$$R_p = \frac{\varepsilon k_z - k_{z1}}{\varepsilon k_z + k_{z1}} \approx \frac{q - \frac{\omega}{c\sqrt{\varepsilon}}}{q + \frac{\omega}{c\sqrt{\varepsilon}}} \approx 1 - 2\frac{\omega}{cq\sqrt{\varepsilon}} \tag{6.75}$$

Using (6.75) in (6.74) with $\varepsilon = 4\pi\sigma/\omega$ we get

$$S_E(\omega_t) \approx \frac{2k_B T}{cd^2}\sqrt{\frac{\omega_t}{2\pi\sigma}} \tag{6.76}$$

For typical parameters of the ion trap ($Q = 10^{-19}$ K, $M = 10^{-26}$ kg, $\omega_t = 10^8$ s^{-1}, $d = 10^{-4}$ m, $T = 300$ K, $\sigma = 10^{18}$ s^{-1}) we get $\dot{\bar{n}} \approx 0.1$ s^{-1}, and $S_E(\omega_t) \approx 10^{-16}$ (V/m)^{2}s^{-1} which is much smaller than the experimentally observed values.

Now we consider a surface covered by adsorbates. In this case, the reflection amplitude is given by (6.47). For typical parameters of the ion trap, $\varepsilon \sim 10^{11}$ and $qa \sim 10^{-6}$. In this case, the main contribution is provided by adsorbate vibrations that are normal to the surface, and the reflection amplitude can be written in the form

$$R_p \approx 1 + 8\pi n_a q \alpha_\perp \tag{6.77}$$

where n_a is the concentration of adsorbates, and $\alpha_\perp$ is the adsorbate polarizability l. Using (6.78) in (6.74) we get

$$S_E(\omega_t) = \frac{12\pi k_B T n_a \mathrm{Im}\alpha_\perp(\omega_t)}{\omega_t d^4}, \tag{6.78}$$

where, according to (6.48)

$$\alpha_\perp(\omega_t) = \frac{e^{*2}}{M_a} \frac{\omega_t \eta_a}{\left(\omega_a^2 - \omega_t^2\right)^2 + \omega_t^2 \eta_a^2}, \tag{6.79}$$

where e^* and M_a are the adsorbate charge and mass, ω_a and η_a are the adsorbate frequency and damping constant. Using (6.79) in (6.77), we get

$$S_E(\omega_t) = \frac{12\pi k_B T n_a e^{*2}}{M_a d^4} \frac{\eta_a}{\left(\omega_a^2 - \omega_t^2\right)^2 + \omega_t^2 \eta_a^2} \tag{6.80}$$

The expression (6.80) can be very large in the case of resonance. In particular at $\omega_a = 10\eta_a$ and $\eta_a \sim \omega_t \sim 10^8$ s^{-1}, we get $S_E(\omega_t) \sim 10^{-4}$ (V/m)^{2}s and $\dot{\bar{n}} \sim 10^{10}$ s^{-1}. For the frequencies out of resonance we can neglect displacement of adsorbates relative substrate. In this case displacement of the substrate surface under the action of the stress applied to adsorbed layer is given by

$$u_z(\mathbf{x}) = M_{zz} n_a e^* E_z e^{i\mathbf{q}\cdot\mathbf{x} - i\omega t} \tag{6.81}$$

The explicit form of the stress tensor M_{ij} in the elastic continuum model is given in [213] (see also Appendix T). The displacement (6.81) will give rise to the dipole moment per unit area

$$p_z(\mathbf{x}) = n_a e^* u_z(\mathbf{x}) = M_{zz} (n_a e^*)^2 E_z e^{i\mathbf{q}\cdot\mathbf{x} - i\omega t}. \tag{6.82}$$

Thus, for this mechanism, $n_a \alpha$ in (6.78) should be replaced by $n_a e^{*2} M_{zz}$. For $d \gg c_l/\omega_t$, where c_l is the longitudinal sound velocity and ρ is the density of substrate, the stress tensor is given by

$$M_{zz} = \frac{i}{\rho \omega c_l}$$

and instead of (6.80), we get

$$S_E(\omega_t) = \frac{12\pi k_B T (n_a e^*)^2}{\rho d^4 \omega_t^2 c_l}. \tag{6.83}$$

For the same (typical) typical parameters as above, we get $S_E(\omega_t) \sim 10^{-7}$ (V/m)^{2}s and $\dot{\bar{n}} \sim 10^7$ s^{-1}. Thus, this mechanism also gives an important contribution to the heating rate.

6.9 Radiative Heat Transfer Between Two Dipole Inside a N-Dipole System

Let us consider a discrete set of N objects located at positions $\mathbf{r}_i$ and maintained at different temperatures T_i with $i = 1, \ldots, N$. Suppose that the size of these objects is small enough compared with the smallest thermal wavelength $\lambda_{T_i} = c\hbar/(k_B T)$ so that all individual objects can be modeled as simple radiating electrical dipoles. For metals, one has also to include the magnetic dipole moments due to the induction of eddy currents. Such an extension is straightforward and as such, for convenience, we will consider electric dipoles only. The Fourier component of the electric field at the frequency ω (with the convention $\hat{f}(t) = \int \frac{d\omega}{2\pi} f(\omega) e^{-i\omega t}$) generated at the position $\mathbf{r}_i$ by the fluctuating part p_j^f of electric dipole moment of the particle j which is located at $\mathbf{r}_j$ reads

$$\mathbf{E}_{ij} = k^2 \mathbf{G}^{ij} \mathbf{p}_j^f, \tag{6.84}$$

where $\mathbf{G}^{ij} = \mathbf{G}(\mathbf{r}_i, \mathbf{r}_j, \omega)$ is the dyadic Green's tensor (i.e. the propagator) between the particles i and j inside the set of N particles and $k = \omega/c$. On the other hand, by summing the contribution of fields radiated by each particle, the dipolar moment induced by the total field on the i-th particle is given by

$$\mathbf{p}_i^{ind} = \alpha_i \sum_{j \neq i} \mathbf{E}_{ij}, \tag{6.85}$$

where α_i is the particle's polarizability. Then, the power dissipated inside the particle i at a given frequency ω due to the fluctuating field $\mathbf{E}_{ij}$ generated by the particle j can be calculated from the work of the fluctuating electromagnetic field on the charge carriers as

$$P_{j \to i} = 2\mathrm{Re}\left\langle -i\omega \mathbf{p}_i^{ind} \cdot \mathbf{E}_{ij}^* \right\rangle, \tag{6.86}$$

where the brackets represent the ensemble average. Using the relations (6.84) and (6.85) between the dipole moments, and the fluctuation dissipation theorem, i.e.

$$\left\langle p_{j,\alpha}^f p_{i,\beta}^f \right\rangle = 2\hbar n_i(\omega) \delta_{\alpha\beta} \delta_{ij},$$

we find after a straightforward calculation that

$$P_{j \to i} = 3 \int_0^\infty \frac{d\omega}{2\pi} \Pi(\omega, T_j) T_{i,j}(\omega), \tag{6.87}$$

where the transmission coefficient:

$$T_{i,j}(\omega) = \frac{3}{4} k^4 \mathrm{Im}(\alpha_i) \mathrm{Im}(\alpha_j) \mathrm{Sp}\left[\mathbf{G}^{ij} \mathbf{G}^{ij+}\right]. \tag{6.88}$$

In order to present the heat flux in an obvious Landauer-like manner, we rewrite the heat flux in terms of the conductance $G_{i,j} = \partial P_{j\to i}/\partial T_j$ so that $P_{j\to i} = G_{i,j}\Delta T$. Then we find

$$P_{j\to i} = 3\left(\frac{\pi^2 k_B^2 T}{3h}\right)\overline{T}_{i,j}\Delta T, \tag{6.89}$$

where $\overline{T}_{i,j} = \int dx f(x) T_{i,j}(x)/(\pi^2/3)$ is the mean transmission coefficient with $f(x) = x^2\exp(-x)/(\exp(x)-1)^2$. In the case of two particles (N = 2), one can show (see Sect. 6.5) that $T_{i,j}(\omega, d) \in [0, 1]$ and therefore $\overline{T}_{i,j}(\omega, d) \in [0, 1]$ as well. Hence, the conductance between two dipoles is limited by three times the quantum of thermal conductance $\pi^2 k_B^2 T/(3h)$. In other words, only three channels contribute to the heat flow between two dipoles, namely the channels due to the coupling of the three components $p_{j,\alpha}$ with the same three components $p_{j,\alpha}$ (i.e. same polarization). Of course, by adding further particles, this limit cannot be exceeded, whereas the heat flux can be increased or decreased with respect to the case of two particles. Nevertheless, the number of channels increases if electric multipoles as well as the magnetic moments come into play.

Now, for calculating the Green's function for a system of N particles, we use the set of $3N$ self-consistent equations

$$\mathbf{E}_{ij} = k^2\mathbf{G}_0^{ij}\mathbf{p}_{j\neq i} + k^2\sum_{k\neq i}\mathbf{G}_0^{ik}\alpha_k/\mathbf{E}_{kj} \tag{6.90}$$

for $i = 1, \ldots, N$ with the free space Green's function

$$\mathbf{G}_0^{ij} = \frac{k^2 e^{ikr_{ij}}}{r_{ij}}\left[\left(1+\frac{ikr_{ij}-1}{k^2 r_{ij}^2}\right)\mathbf{1} + \frac{3-3ikr_{ij}-k^2r_{ij}^2}{k^2 r_{ij}^2}\hat{\mathbf{r}}_{ij}\otimes\hat{\mathbf{r}}_{ij}\right],$$

where the unit vector $\hat{\mathbf{r}}_{ij} \equiv \mathbf{r}_{ij}/r_{ij}$, $\mathbf{r}_{ij} = \mathbf{r}_i - \mathbf{r}_j$ and $\mathbf{1}$ stands for the unit dyadic tensor. Comparing (6.84) and (6.90) we get the Green's tensor

$$\begin{pmatrix}\mathbf{G}^{1k}\\ \vdots \\ \mathbf{G}^{Nk}\end{pmatrix} = [\mathbf{1}-\mathbf{A}_0]^{-1}\begin{pmatrix}\mathbf{G}_0^{1k}\\ \vdots \\ \mathbf{G}_0^{(k-1)k}\\ 0 \\ \mathbf{G}_0^{(k+1)k}\\ \vdots \\ \mathbf{G}_0^{Nk}\end{pmatrix} \tag{6.91}$$

for $k = 1, \ldots, N$ with

$$\mathbf{A}_0 = \frac{\omega^2}{c^2}\begin{pmatrix} 0 & \mathbf{G}_0^{12}\alpha_2 & \dots & \mathbf{G}_0^{1N}\alpha_N \\ \mathbf{G}_0^{21}\alpha_1 & \ddots & \ddots & \vdots \\ \vdots & \ddots & \ddots & \mathbf{G}_0^{(N-1)N}\alpha_N \\ \mathbf{G}_0^{N1}\alpha_1 & \dots & \mathbf{G}_0^{N(N-1)}\alpha_{N-1} & 0 \end{pmatrix} \tag{6.92}$$

With this relation and (6.87), it is possible to determine the interparticle heat flux in a system of N particles out of equilibrium.

Let us now apply this theoretical formalism to describe some emerging many-particle effects. We consider the simplest possible configuration where such effects occur that is a triplet of particles. We consider only the interparticle heat flux between particle **1** and **2** separated by a distance $2l$ in the presence of the third particle. Here, we assume that $T_1 = 300$ K and $T_2 = T_3 = 0$. The interparticle heat flux is then given by

$$\phi_{1\to 2} = P_{1\to 2} - P_{2\to 1}. \tag{6.93}$$

In this case, the dyadic Green's function has the form

$$\mathbf{G}^{21} = \mathbf{D}_{213}^{-1}\left[\mathbf{G}_0^{21} + \frac{\omega^2}{c^2}\mathbf{B}^{213}\mathbf{D}_{31}^{-1}\mathbf{G}_0^{31}\right] \tag{6.94}$$

where

$$\mathbf{D}_{213} = \mathbf{D}_{21} - \frac{\omega^4}{c^4}\mathbf{B}^{213}\mathbf{D}_{31}^{-1}\mathbf{B}^{312},$$

$$\mathbf{D}_{21} = \mathbf{1} - \frac{\omega^4}{c^4}\mathbf{G}_0^{12}\alpha_1\mathbf{G}_0^{12}\alpha_2,$$

and

$$\mathbf{B}^{213} = \mathbf{G}_0^{23}\alpha_3 + \frac{\omega^2}{c^2}\mathbf{G}_0^{21}\alpha_1\mathbf{G}_0^{13}\alpha_3.$$

Figure 6.8 shows the resulting interparticle flux between particle **1** and **2** in the presence of body **3** normalized to the flux for two isolated dipoles. The position of the particles, for which the interparticle flux is calculated, is fixed, but the position of the third particle is changed. It can be seen that for some geometric configurations, the heat flux mediated by the presence of the third particle can be larger than the value for two isolated dipoles. In particular, we observe an exaltation of heat flux of approximately one order of magnitude when the third particle is located between the two other particles, i.e., when all three particles are aligned. Hence, the heat flux between two dipoles can dramatically be increased when inserting a third particle in between.

The heat flux enhancement can be attributed to a three-body effect that is a resonant surface mode coupling mediated by the third particle. This effect could be used to improve, for example, the performance of near-field thermophotovoltaic devices, by placing nanoparticles on the surface of photovoltaic cells.

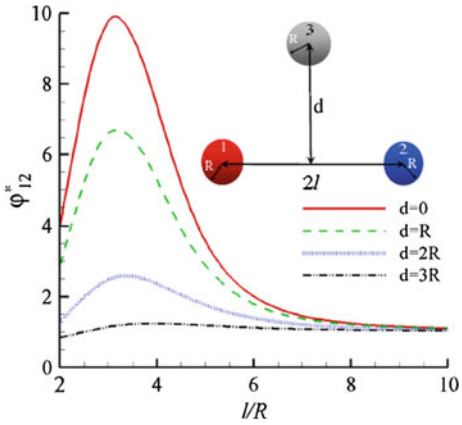

Fig. 6.8 Normalized heat flux between two spherical particles with the same radius. A third particle is located equidistant to particles 1 and 2 ($T_1 = 300$ K, $T_2 = T_3 = 0$ K). From [214]

6.10 Local Heating of the Surface by an Atomic Force Microscope Tip

An atomic force microscope tip, at a distance d above a flat sample surface with the radius of curvature $R \gg d$, can be approximated by a sphere with radius R. In this case, the heat transfer flux between the tip and the surface can be estimated using the approximate method of Derjaguin [215], later called the proximity force approximation (PFA) [216]. According to this method, the radiative flux in the gap between two smooth curved surfaces at short separations can be approximately calculated as a sum of fluxes between pairs of small parallel plates corresponding to the curved geometry of the gap. Specifically, the sphere–plane heat flux is given by

$$P = 2\pi \int_0^R d\rho\rho S(z(\rho)), \tag{6.95}$$

where R is the radius of the sphere, $z(\rho) = d + R - \sqrt{R^2 - \rho^2}$ denotes the tip–surface distance as a function of the distance ρ from the tip symmetry axis, and the heat flux per unit area $S(z(\rho))$ is determined for flat surfaces. This scheme was proposed in [215, 217] for the calculation of the conservative van der Waals interaction; in this case, the error is not larger than 5–10% in an atomic force application, and 25% in the worst case situation [218]. We assume that the same scheme is also valid for the calculation of heat transfer. We assume that the tip has a paraboloid shape given [in cylindrical coordinates (z, ρ)] by the formula: $z = d + \rho^2/2R$, where d is the distance between the tip and the flat surface. If

$$S = \frac{C}{\left(d + \rho^2/2R\right)^n}, \tag{6.96}$$

we get

$$P = \frac{2\pi R}{n-1}\frac{C}{d^{n-1}} = \frac{2\pi Rd}{n-1}S(d) \equiv A_{\text{eff}}S(d), \tag{6.97}$$

where $A_{\text{eff}} = 2\pi Rd/(n-1)$ is the effective surface area. In a more general case, one must use numerical integration to obtain the heat transfer.

As an illustration, consider the heat flux between a SiC tip and a flat SiC surface. From (6.35) and (6.97), we get that the heat transfer power between SiC tip at $T_1 =$ 300 K and a cold SiC surface ($T_2 = 0$ K) at $d \ll R$: $P(d) = 5.2 \times 10^{-10}(R/d)$ W.

The most general method available for calculating both the Casimir force and the radiative heat transfer between many bodies of arbitrary shapes, materials, temperatures and separations, expressed the Casimir force and radiative heat transfer in terms of the scattering matrices of individual bodies [89, 219–227]. Specifically, a numerically exact solution for the near-field radiative heat transfer between a sphere and an infinite plane was first obtained using the scattering matrix approach (Fig. 6.9).

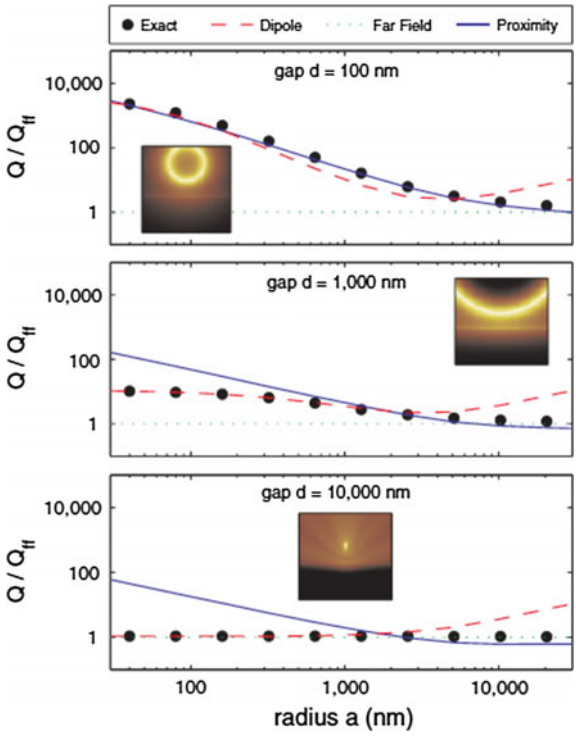

Fig. 6.9 Comparison of the numerically exact solution for NFRHT between a sphere and a plane with approximation schemes for various sphere diameters and gap sizes. From [228]

6.11 A Nanoscale ‘Heat Stamp’

It has been proposed [229] that-near field optics could be exploited to write extremely fine details for integrated circuits. The basic idea of this proposal is that the components of the electromagnetic field with short wavelengths (and therefore the potential for high resolution) are naturally evanescent, and do not contribute to the far field. Hence, fine details in any patterned mask will rapidly disappear with distance from the mask. However, if it is possible to position the wafer close to the mask, then fine details can be resolved. Roughly speaking, the separation between mask and wafer must be of the same order as the lateral details to be resolved.

An extension of this idea was suggested [115] in the form of the ‘heat stamp’. It is possible to imagine a mask consisting of a surface patterned alternatively in highly reflecting (and therefore poorly emitting) material and a second material chosen to maximize emission of heat into the evanescent modes. For adsorbate-covered structures, it is possible to have a ‘heat stamp’ with atomic resolution.

Chapter 7
Casimir Friction Between Two Plates

In this section, two approaches in the theory of Casimir friction in the plate-plate configuration are considered. The first approach is based on the fluctuation electrodynamics proposed by Rytov [5–7]. In this approach, the fluctuating electromagnetic field is considered as a classical field that can be calculated from Maxwell's equation with the fluctuating current density as the source of the field, and with appropriate boundary conditions. This approach was used by Lifshitz in the theory of the Casimir–van der Waals interaction [42] and by Volokitin and Persson for Casimir friction [99, 100, 121, 128]. The calculation of Casimir friction is more complicated than the calculation of Casimir–van der Waals forces because it requires the determination of the electromagnetic field between moving boundaries. The solution can be found by writing the boundary conditions on the surface of each body in the rest reference frame of this body. The relation between the electromagnetic fields in the different reference frames is determined by the Lorenz transformation. The advantage of this approach is that, in principle, it can be used for the calculation of friction at arbitrary relative velocities. However, the calculations become very complicated for bodies with complex geometry. At present, the solutions are known for Casimir friction between two parallel plane surfaces [11, 99, 100, 121] and between a small particle and a plane surface [11, 139, 151, 152]. The fluctuation electrodynamics approach has some features in common with the 'poor man' derivation of quantum friction given by Pendry [115].

In the second approach, the electromagnetic field is treated in the framework of the quantum field theory. This approach was used in [43] to obtain the van der Waals interaction for an arbitrary inhomogeneous medium, all parts of which are at rest. For Casimir friction, the time-dependent perturbation theory can be used to calculate the friction force [107]. In the lowest order of the perturbation theory, the friction force is determined by the Kubo formula [107, 129, 140, 184].

In a simplified version of the Casimir friction theory, the electromagnetic field of the isolated body is approximated by the system of the harmonic oscillators [115, 117–121, 124]. In the case of relative sliding of several bodies, the problem of

A.I. Volokitin and B.N.J. Persson, *Electromagnetic Fluctuations at the Nanoscale*,
NanoScience and Technology, DOI 10.1007/978-3-662-53474-8_7

Casimir friction is reduced to finding the solution for several systems of harmonic oscillators with time-dependent interaction between them. Again, the Kubo formula can be used to calculate the friction force. The calculations using oscillator model are simplified due to the simple dependence of the operators on the time for the non-interacting systems.

7.1 Kubo Formula Approach

Consider two bodies, one of which performs small vibrations relative to the other. The interaction between the bodies can be described by the Hamiltonian

$$H_{int} = -\hat{F}_i\left(u_{0i}e^{-i\omega t} + c.c.\right), \tag{7.1}$$

where $\hat{F}_i$ is the force operator for the body performing vibrations with the coordinate $\mathbf{u}(t) = \mathbf{u}_0 e^{-i\omega t}$ at the fixed separation between the bodies. According to the linear response theory, the average value of the force is determined by the formula [184]

$$\left\langle \hat{F}_i \right\rangle = \alpha_{ij}(\omega)u_{0j}e^{-i\omega t} + c.c., \tag{7.2}$$

where $\langle \ldots \rangle$ denotes averaging of the fluctuating force on the state of the thermal equlibrium. According to the Kubo formula, the generalized susceptibility $\alpha_{ij}(\omega)$ is determined by the formula [184]:

$$\alpha_{ij}(\omega) = \frac{i}{\hbar}\int_0^\infty dt e^{i\omega t}\left\langle \hat{F}_i(t)\hat{F}_j(0) - \hat{F}_j(0)\hat{F}_i(t)\right\rangle, \tag{7.3}$$

where $\hat{F}_i(t)$ is the force operator in Heisenberg representation. The imaginary part of the generalized susceptibility is determined by the formula [184]:

$$\alpha''_{ij}(\omega) = \frac{1}{\hbar}\tanh\frac{\hbar\omega}{2k_BT}\int_0^\infty dt e^{i\omega t}\left\langle \hat{F}_i(t)\hat{F}_j(0) + \hat{F}_j(0)\hat{F}_i(t)\right\rangle. \tag{7.4}$$

In the limit $\omega \to 0$, the force can be written in the form

$$F_i = \left(\alpha'_{ij}(0) + i\omega\lim_{\omega\to 0}\frac{\alpha''_{ij}(\omega)}{\omega}\right)u_{0j}e^{-i\omega t}, \tag{7.5}$$

where α'_{ij} is the real part of the generalized susceptibility. For two bodies slowly moving relative to each other with velocity $\mathbf{v}$, the force acting on the moving body can be written in the form

$$\mathbf{F} = \mathbf{F}_0 - \overleftrightarrow{\Gamma}\cdot\mathbf{v}, \tag{7.6}$$

where the adiabatic force $\mathbf{F}_0$ is independent of $\mathbf{v}$, and $\overleftrightarrow{\Gamma}$ is the so-called friction tensor. For vibrations $\mathbf{v} = -i\omega\mathbf{u}_0 e^{-i\omega t}$, after comparison of (7.5) and (7.6), and taking into account (7.4), we get the formula for the friction tensor

$$\overleftrightarrow{\Gamma} = \lim_{\omega\to 0} \frac{\alpha''_{ij}(\omega)}{\omega} = (k_B T)^{-1} \mathrm{Re} \int_0^\infty dt \left\langle \hat{\mathbf{F}}(t)\hat{\mathbf{F}}(0) \right\rangle. \tag{7.7}$$

For the interaction between a localized and an extended system, (7.7) has been derived by several authors (Schaich [230], d'Agliano et al. [231], Nourtier [232]) and is also valid for two extended systems. In the context of Casimir friction, (7.7) was used by Schaich and Harris [140], but their treatment is incomplete.

In the case of extended systems, the fluctuating force operator can be expressed through the operator of the stress tensor $\hat{\sigma}_{ik}$

$$\hat{F}_i = \int dS_k \hat{\sigma}_{ik}, \tag{7.8}$$

where the integration is over the surface of one of the bodies and

$$\hat{\sigma}_{ik} = \frac{1}{4\pi}\left[E_i E_k + B_i B_k - \frac{1}{2}\delta_{ik}\left(E^2 + B^2\right)\right], \tag{7.9}$$

where E_i and B_i are the electric and magnetic induction field operators, respectively. The calculation of the force–force correlation function can be done using the methods of the quantum field theory [183, 233]. Such calculations are described in [129] (see also Appendix J). The advantage of this approach is that it only involves finding the Green's functions of the electromagnetic field for the equilibrium system with fixed boundaries. Thus, this approach can be easily extended to bodies with complex geometry. The theory presented above is restricted to small relative velocities. However, it can be extended for large velocities.

7.2 Quantum Oscillator Model

In this section, we derive an expression for the van der Waals friction using a simple model. For simplicity, we focus on zero temperature $T = 0\,\mathrm{K}$ and assume that d is so small that retardation effects can be neglected. The calculation is based on the formalism developed in [117, 121] and already used in Sect. 3.3. Assume that a semi-infinite metal occupies the half space $z \le 0$. A charge distribution in the half space $z > d$ gives rise to an (external) potential, which must satisfy the Laplace equation for $z < d$ and which therefore can be written as a sum of evanescent plane waves in the form

$$\phi_{inc} = e^{qz} e^{i\mathbf{q}\cdot\mathbf{x} - i\omega t} \tag{7.10}$$

where $\mathbf{q} = (q_x, q_y)$ is a 2D-wavevector. This potential will induce a charge distribution in the solid (occupying $z < 0$), which in turn gives rise to an electric potential, which must satisfy the Laplace equation for $z > 0$, and which therefore can be expanded into evanescent plane waves, which decay with increasing $z > 0$. Thus, the total potential for $0 < z < d$ can be expanded in functions of the form

$$\phi_{ext} = \left(e^{qz} - R_p(\omega, q)e^{-qz}\right)e^{i\mathbf{q}\cdot\mathbf{x} - i\omega t} \tag{7.11}$$

where $R_p(\omega, q)$ is the reflection amplitude for p-polarized electromagnetic waves, which we denoted by $g(q, \omega)$ in Sect. 3.3. For the present purposes, we can treat the low-energy electron-hole pair excitations in the metals as bosons. As shown in [234], the Hamiltonian for the total system can be written as

$$\begin{aligned} H = &\sum_{\mathbf{q}\alpha_1} \hbar\omega_{\mathbf{q}\alpha_1} b^+_{\mathbf{q}\alpha_1} b_{\mathbf{q}\alpha_1} + \sum_{\mathbf{q}\alpha_2} \hbar\omega_{\mathbf{q}\alpha_2} b^+_{\mathbf{q}\alpha_2} b_{\mathbf{q}\alpha_2} + \hbar\omega b^+ b \\ &+ \sum_{\mathbf{q}\alpha_1 n} C_{q\alpha_1} e^{-qz_n} \left(b_{\mathbf{q}\alpha_1} e^{i\mathbf{q}\cdot(\mathbf{x}_n + \mathbf{V}t)} + h.c.\right). \end{aligned} \tag{7.12}$$

Here $\omega_{\mathbf{q}\alpha_1}$, $b^+_{\mathbf{q}_1}$ and $b_{\mathbf{q}\alpha_1}$ are the angular frequency and creation and annihilation operators for the bosons (of solid **1**) with the quantum numbers $(\mathbf{q}, \alpha_1)$, and $C_{\mathbf{q}\alpha_1}$ parameters determining the coupling between the boson excitations in solid **1** with the electrons in solid **2**. Similarly, $b^+_{\mathbf{q}\alpha_2}$ and $b_{\mathbf{q}\alpha_2}$ are creation and annihilation operators for bosons in solid **2**, and $(\mathbf{x}_n, z_n)$ is the position operator of electron n in solid **2**, which in principle could be expressed in terms of the operators $b^+_{\mathbf{q}\alpha_2}$ and $b_{\mathbf{q}\alpha_2}$, but for the present purpose this is not necessary. The energy dissipation per unit time induced by the electromagnetic field inside the metallic substrate is determined by integrating the Poynting vector over the surface of the metal, and is given by

$$\begin{aligned} P &= \frac{c}{4\pi} \int dS \hat{z} \cdot \left[\mathbf{E}(\mathbf{r}) \times \mathbf{B}^*(\mathbf{r})\right]_{z=+0} + c.c. \\ &= \frac{i\omega}{4\pi} \int dS \left(\varphi(\mathbf{r}) \frac{d}{dz} \varphi^*(\mathbf{r})\right)_{z=+0} + c.c. \\ &= \frac{\omega}{\pi} \int_0^\infty \frac{d^2q}{(2\pi)^2} q \, \mathrm{Im} R_p(\omega, q). \end{aligned} \tag{7.13}$$

Using the Hamiltonian (7.12) and the Golden Rule formula, the absorbed energy per unit time can also be written in the form

$$P = \frac{2\pi}{\hbar^2} \sum_{\alpha_1} \left(\frac{q}{2\pi e}\right)^2 \hbar\omega \mid C_{\mathbf{q}\alpha_1} \mid^2 \delta(\omega - \omega_{q\alpha_1}) \tag{7.14}$$

Comparing (7.13) and (7.14), we get the relation

$$\sum_{\alpha_1} \mid C_{\mathbf{q}\alpha_1} \mid^2 \delta(\omega - \omega_{q\alpha_1}) = \frac{2e^2\hbar}{Aq}\mathrm{Im}R_{1p}(\omega, q) \tag{7.15}$$

We can write the interaction Hamiltonian between solid **1** and **2** as

$$H^{'} = \sum_{\mathbf{q}}\left(\hat{V}_{\mathbf{q}}e^{i\mathbf{q}\cdot\mathbf{V}t} + h.c.\right)$$

Using time-dependent perturbation theory (with $H^{'}$ as the perturbation), we can calculate the energy transfer from the translational motion (kinetic energy) to internal excitations in the solids (boson excitations $\omega_{\mathbf{q}\alpha_1}$ and $\omega_{\mathbf{q}\alpha_2}$ in solid **1** and **2**, respectively):

$$\begin{aligned} P =& \frac{2\pi}{\hbar^2}\sum_{\mathbf{q_{12}}}\hbar\omega_{\mathbf{q}}\delta(\omega_{\mathbf{q}} - \omega_{\mathbf{q}\alpha_2} - \omega_{\mathbf{q}\alpha_1}) \mid C_{q\alpha_1} \mid^2 \\ & \times e^{-2qd} \mid \langle n_{\mathbf{q}\alpha_1} = 1, n_{\mathbf{q}\alpha_2} = 1 \mid \sum_n e^{-q(z_n-d)}e^{-i\mathbf{q}\cdot\mathbf{x_n}}b^{+}_{\mathbf{q}\alpha_1} \mid 0, 0\rangle \mid^2 \end{aligned} \tag{7.16}$$

where $\omega_{\mathbf{q}} = \mathbf{q}\cdot\mathbf{V}$. Note that that only the terms with $q_x > 0$ give contribution to the sum (7.16). To simplify (7.16), let us write

$$\delta(\omega_{\mathbf{q}} + \omega_{\mathbf{q}\alpha_2} - \omega_{\mathbf{q}\alpha_1}) = \int d\omega'\delta(\omega' - \omega_{\mathbf{q_1}})\delta(\omega_{\mathbf{q}} - \omega' - \omega_{\mathbf{q_2}}) \tag{7.17}$$

Substituting (7.17) in (7.16) and using (7.15) gives

$$P = \frac{4\pi e^2}{A}\sum_{\mathbf{q}}\frac{\omega_{\mathbf{q}}}{q}e^{-2qd}\int d\omega'\mathrm{Im}R_{1p}(\omega', q)M_q(\omega_{\mathbf{q}} - \omega') \tag{7.18}$$

where

$$M_q(\omega) = \sum_{\alpha_2}\delta(\omega - \omega_{\mathbf{q}\alpha_2}) \mid \langle n_{\mathbf{q}\alpha_2} = 1 \mid \sum_n e^{-q(z_n-d)}e^{-i\mathbf{q}\cdot\mathbf{x_n}} \mid 0\rangle \mid^2$$

The quantity $M_q(\omega)$ can be related to $\mathrm{Im}R_{2p}(\omega, q)$ using the same arguments that were used in the derivation of (7.15). The energy dissipation per unit time in solid **2** due to interaction with plane wave in the form (7.11) is given by

$$P = \frac{A\omega q\mathrm{Im}R_{2p}(\omega', q)}{\pi}. \tag{7.19}$$

The same quantity can also be written in the form

$$P = \frac{2\pi\omega}{\hbar}\sum_{\alpha_2}\delta(\omega - \omega_{\mathbf{q}\alpha_2}) \mid \langle n_{\mathbf{q}\alpha_2} = 1 \mid \sum_n e^{-q(z_n-d)}e^{-i\mathbf{q}\cdot\mathbf{x_n}} \mid 0\rangle \mid^2 \tag{7.20}$$

Comparing (7.19) and (7.20), we get

$$\frac{A\hbar q}{2\pi^2 e^2}\mathrm{Im}R_{2p}(q,\omega)=\sum_{\alpha_2}\delta(\omega-\omega_{\mathbf{q}\alpha_2})\mid\langle n_{\mathbf{q}\alpha_2}=1\mid\sum_n e^{-q(z_n-d)}e^{-i\mathbf{q}\cdot\mathbf{x_n}}\mid 0\rangle\mid^2$$

so we have that

$$M_q(\omega)=\frac{A\hbar q}{2\pi^2 e^2}\mathrm{Im}R_{2p}(q,\omega) \tag{7.21}$$

Substituting this result in (7.18) gives

$$P=\frac{2\hbar}{\pi}\sum_{\mathbf{q}}\omega_{\mathbf{q}}e^{-2qd}\int d\omega'\mathrm{Im}R_{1p}(q,\omega')\mathrm{Im}R_{2p}(q,\omega_{\mathbf{q}}-\omega') \tag{7.22}$$

Finally, replacing

$$\sum_{\mathbf{q}}\to\frac{A}{4\pi^2}\int d^2q,$$

and using the relation $P=\sigma Av$ between the power P and the shear stress σ gives

$$\sigma=\frac{\hbar}{\pi^3}\int_0^\infty dq_y\int_0^\infty dq_x q_x e^{-2qd}\int_0^{q_x v}d\omega'\mathrm{Im}R_{1p}(\omega',q)\mathrm{Im}R_{2p}(q,q_x v-\omega'), \tag{7.23}$$

where we have used that equalities (7.15) and (7.21) are valid only for $\omega>0$ (Otherwise, the expressions on the right side of these equalities should be replaced by zero). Equation (7.24) neglects multiple scattering of the electromagnetic waves between surfaces. Due to multiple scattering instead of (7.10) the wave incident on surface of solid **1** is given by

$$\begin{aligned}\phi_{inc}=\;& e^{qz}e^{i\mathbf{q}\cdot\mathbf{x}-i\omega t}\left(1+e^{-2qd}R_{1p}(\omega)R_{2p}(\omega-q_x v)\right.\\&\left.+\left(e^{-2qd}R_{1p}(\omega)R_{2p}(\omega-q_x v)\right)^2+\ldots\right)=\frac{e^{qz}e^{i\mathbf{q}\cdot\mathbf{x}-i\omega t}}{1-e^{-2qd}R_{1p}(\omega)R_{2p}(\omega-q_x v)}\end{aligned} \tag{7.24}$$

Thus, (7.23) should be replaced with

$$\begin{aligned}\sigma=\;&\frac{\hbar}{\pi^3}\int_0^\infty dq_y\int_0^\infty dq_x q_x e^{-2qd}\\&\times\int_0^{q_x v}d\omega'\frac{\mathrm{Im}R_{1p}(\omega',q)\mathrm{Im}R_{2p}(q_x V-\omega',q)}{\mid 1-e^{-2qd}R_{1p}(\omega)R_{2p}(\omega-q_x v)\mid^2}\end{aligned} \tag{7.25}$$

At finite temperature ($T>0$ K), an extra factor of $\left[1+n(\omega')+n(q_x V-\omega')\right]$ must be inserted in the frequency integral in (7.25) to take into account the enhanced probability for the excitation of bosons at finite temperature. For $T>0$ K one

must, in addition to the process considered above, also include scattering processes where a thermally excited boson is annihilated either in solid **1** or in solid **2**, namely $(n_{\mathbf{q}\alpha_1} = 0, n_{\mathbf{q}\alpha_2} = 1) \to (1, 0)$ and $(1, 0) \to (0, 1)$.

7.3 Casimir Friction Between Two Plane Surfaces in Parallel Relative Motion

Consider two semi-infinite solids with flat parallel surfaces separated by vacuum gap with thickness d and moving in parallel with relative velocity v (see Fig. 15). The frictional stress σ acting on the surface of solid **1** is determined by xz-component of Maxwell's stress tensor σ_{ij}, calculated at $z = +0$:

$$\sigma_{xz} = \frac{1}{8\pi}\int_{-\infty}^{+\infty} d\omega\Big[\big\langle E_z E_x^*\big\rangle + \big\langle E_z^* E_x\big\rangle + \big\langle B_z B_x^*\big\rangle + \big\langle B_z^* B_x\big\rangle\Big]_{z=+0}. \tag{7.26}$$

Here, symbol $\langle..\rangle$ denotes statistical averaging with respect to the random fields $\mathbf{E}_1^f$ and $\mathbf{E}_2^f$, radiated by solids **1** and **2**. Averaging is performing with the help of (4.3) and (4.19).

Calculation of the electromagnetic field in the vacuum gap between the surfaces is given in Appendix B (see also Sect. 5.2). Using (B.3) and (B.4) from Appendix B we get:

$$\begin{aligned}\sigma_{xz} = \frac{1}{4\pi}\int_0^{\infty} d\omega \int \frac{d^2q}{(2\pi)^2}\frac{q_x}{k^2}\Big[(k_z + k_z^*)\big(\big\langle |\ w_p\ |^2\big\rangle + \big\langle |\ w_s\ |^2\big\rangle\\ - \big\langle |\ v_p\ |^2\big\rangle - \big\langle |\ v_s\ |^2\big\rangle\big) + (k_z - k_z^*)\big\langle w_p v_p^* + w_s v_s^* - c.c\big\rangle\Big]\end{aligned} \tag{7.27}$$

In (7.27), the integration over ω from $-\infty$ to $-\infty$ (see (7.26)) was replaced by the integration along the positive axis, which gives an additional factor of two. Performing the averaging in (7.27) over the fluctuating electromagnetic field with the help of (B.15)–(B.19) from Appendix B, gives frictional stress acting on surface of solid **1**, separated from surface of solid **2** by vacuum gap (with thickness d) [128]:

$$\sigma_{xz} = \frac{\hbar}{8\pi^3}\int_0^{\infty} d\omega \int_{q<\frac{\omega}{c}} d^2q\,\frac{q_x}{|\Delta|^2}\big[(q^2 - \beta k q_x)^2 + \beta^2 k_z^2 q_y^2\big]\times$$

$$\times\big[(q^2 - \beta k q_x)^2(1 - |\ R_{1p}\ |^2)(1 - |\ R'_{2p}\ |^2)|D_{ss}|^2 +$$

$$+ \beta^2 k_z^2 q_y^2(1 - |\ R_{1p}\ |^2)(1 - |\ R'_{2s}\ |^2)|D_{sp}|^2 + (p \leftrightarrow s)\big]\big(n_2(\omega') - n_1(\omega)\big) +$$

$$+ \frac{\hbar}{2\pi^3}\int_0^{\infty} d\omega \int_{q>\frac{\omega}{c}} d^2q\,\frac{q_x}{|\Delta|^2}\big[(q^2 - \beta k q_x)^2 + \beta^2 k_z^2 q_y^2\big]e^{-2|k_z|d}\times$$

$$\times \left[(q^2-\beta k q_x)^2 \mathrm{Im} R_{1p} \mathrm{Im} R'_{2p} |D_{ss}|^2 - \beta^2 k_z^2 q_y^2 \mathrm{Im} R_{1p} \mathrm{Im} R'_{2s} |D_{sp}|^2 + \right.$$

$$\left. + \ (p \leftrightarrow s)\right]\big(n_2(\omega') - n_1(\omega)\big), \tag{7.28}$$

$$n_i(\omega) = \frac{1}{e^{\hbar\omega/k_B T_i} - 1},$$

$$D_{pp} = 1 - e^{2ik_z d} R_{1p} R'_{2p}, \ D_{ss} = 1 - e^{2ik_z d} R_{1s} R'_{2s},$$

$$D_{sp} = 1 + e^{2ik_z d} R_{1s} R'_{2p}, \ D_{ps} = 1 + e^{2ik_z d} R_{1p} R'_{2s},$$

$$\Delta = (q^2 - \beta k q_x)^2 D_{ss} D_{pp} + \beta^2 k_z^2 q_y^2 D_{ps} D_{sp},$$

where $R_{1p(s)}$ and $R'_{2p(s)} = R_{2p(s)}(\omega')$ are the reflection amplitudes for surfaces **1** and **2**, respectively, for $p(s)$-polarized electromagnetic waves, $\omega' = \gamma(\omega - q_x v)$, $\gamma = 1/\sqrt{1-\beta^2}$, $\beta = v/c$, T_1 and T_2 are temperatures for solids **1** and **2**, respectively. The symbol $(p \leftrightarrow s)$ denotes the terms that can be obtained from the preceding terms by permutation of the indexes p and s. The first term in (7.28) represents the contribution to the friction from propagating waves ($q < \omega/c$), and the second term from the evanescent waves ($q > \omega/c$). If, in (7.28) one neglects the terms of the order β^2 then the contributions from waves with p- and s-polarization will be separated. In this case, (7.28) is reduced to the formula obtained in [121]:

$$\sigma_{xz} = \frac{\hbar}{8\pi^3} \int_0^\infty d\omega \int_{q<\frac{\omega}{c}} d^2 q q_x \times$$

$$\times \left\{ \frac{(1 - |\ R_{1p}(\omega)\ |^2)(1 - |\ R_{2p}(\omega')\ |^2)}{|\ 1 - e^{2ik_z d} R_{1p}(\omega) R_{2p}(\omega')\ |^2} \big(n_2(\omega') - n_1(\omega)\big) + \big[R_p \to R_s\big] \right\} +$$

$$+ \frac{\hbar}{2\pi^3} \int_0^\infty d\omega \int_{q>\frac{\omega}{c}} d^2 q q_x e^{-2|k_z|d} \times$$

$$\times \left\{ \frac{\mathrm{Im} R_{1p}(\omega) \mathrm{Im} R_{2p}(\omega')}{|\ 1 - e^{-2|k_z|d} R_{1p}(\omega) R_{2p}(\omega')\ |^2} \big(n_2(\omega') - n_1(\omega)\big) + \big[R_p \to R_s\big] \right\}, \tag{7.29}$$

where $\omega' = \omega - q_x v$, $[R_p \to R_s]$ denotes the term that is obtained from the first one by replacement of the reflection amplitude $R_p(\omega)$ for p-polarized electromagnetic waves, and by the reflection amplitude $R_s(\omega)$ for s-polarized electromagnetic waves. Equation (7.29) was obtained by Volokitin and Persson [121] using the dynamical modification of Lifshitz theory [42] for the van der Waals interaction. In the non-retarded case ($c \to \infty$), and for small velocities, v, (7.29) is reduced to the formula obtained by Persson and Zhang [117]; in the non-retarded case and at zero temperature, it is reduced to formula obtained by Pendry [115]. The nonrelativistic theory from [121] is accurate to the terms of order β^2.

Comparison of (7.29) with (6.13) for radiative heat transfer shows that there is an important difference in the type of the elementary excitations that play an important role in these phenomena. For radiative heat transfer, all kinds of elementary excitations with frequencies that can be thermally excited are equally important. In the case of van der Waals friction, the large-momentum, low-frequency excitations are particularly important. Such low-energy excitations can be associated with vibrations of massive particles. In particular, many adsorbate vibrations parallel to metal surface are characterized by very low frequencies.

7.3.1 Discussion of General Formula and Limiting Cases

For $d \ll \lambda_T$ we can neglect the first term in (7.29) and the second term can be written as

$$\sigma_{xz} = \frac{\hbar}{2\pi^3}\int_{-\infty}^{\infty} dq_y \int_0^{\infty} dq_x q_x e^{-2qd}\left\{\int_0^{\infty} d\omega\big[n(\omega) - n(\omega + q_x V)\big]\right.$$

$$\times\left(\frac{\mathrm{Im}R_{1p}^{+}\mathrm{Im}R_{2p}}{|\,1 - e^{-2qd}R_{1p}^{+}R_{2p}\,|^2} + (1 \leftrightarrow 2)\right)$$

$$\left. - \int_0^{q_x v} d\omega\big[n(\omega) + 1/2\big]\left(\frac{\mathrm{Im}R_{1p}^{-}\mathrm{Im}R_{2p}}{|\,1 - e^{-2qd}R_{1p}^{-}R_{2p}\,|^2} + (1 \leftrightarrow 2)\right) + [p \to s]\right\}, \tag{7.30}$$

where $R_{1p(s)}^{\pm} = R_{1p(s)}(\omega \pm q_x v)$. At $T = 0\,\mathrm{K}$, the propagating waves do not contribute to the friction, but the contribution from evanescent waves is non-zero. Taking into account that $n(-\omega) = -1 - n(\omega)$, from (7.28) we get friction mediated by the evanescent electromagnetic waves at zero temperature (in the literature, this type of friction is denoted as quantum friction [115])

$$\sigma_{xz} = -\frac{\hbar}{\pi^3}\int_0^{\infty} dq_y \int_0^{\infty} dq_x \int_0^{q_x v} d\omega \frac{q_x}{|\Delta|^2}\big[(q^2 - \beta k q_x)^2 + \beta^2 k_z^2 q_y^2\big]e^{-2|k_z|d} \times$$
$$\times\ \big[(q^2 - \beta k q_x)^2 \mathrm{Im}R_{1p}\mathrm{Im}R'_{2p}|D_{ss}|^2 - \beta^2 k_z^2 q_y^2 \mathrm{Im}R_{1p}\mathrm{Im}R'_{2s}|D_{sp}|^2 + (p \leftrightarrow s)\big]. \tag{7.31}$$

The existence of quantum friction is still debated [122–127]. Thus, Philbin and Leonhardt [122, 123] argued that there is no quantum friction. In [126], it was shown that the theory presented in [122, 123] is incorrect (see also Appendix F). If, in (7.31), one neglects the terms of the order β^2, then (7.31) is reduced to the formula obtained by Pendry [115]:

$$\sigma_{xz} = -\frac{\hbar}{4\pi^3}\int_{-\infty}^{\infty} dq_y \int_0^{\infty} dq_x q_x e^{-2qd}\Big\{\int_0^{q_x v} d\omega \times \left(\frac{\mathrm{Im}R_{1p}(\omega')\mathrm{Im}R_{2p}}{|\,1-e^{-2qd}R_{1p}(\omega')R_{2p}\,|^2} + (1 \leftrightarrow 2)\right) + [p \to s]\Big\}. \tag{7.32}$$

In the local optic approximation for $d < \lambda_T |\varepsilon(\omega_T)|^{-1/2}$, the reflection amplitude for p-polarized electromagnetic waves is determined by Eq. (C.17) in Appendix C. Substituting (C.17) in (7.32), and using the dielectric function (6.22), in the limiting cases of small and high velocities, we get:

$$\sigma_{\parallel} = \frac{15}{2^6\pi^2}\left(\frac{\hbar v}{d^4}\right)\left(\frac{v}{4\pi\sigma d}\right)^2 \quad \text{for} \quad v << 4\pi\sigma d, \tag{7.33}$$

$$\sigma_{\parallel} = \frac{\hbar(4\pi\sigma)^2}{2\pi^2 d^2 v}\ln\left(\frac{v}{4\pi\sigma d}\right) \quad \text{for} \quad v >> 4\pi\sigma d. \tag{7.34}$$

For example, for good conductors with conductivity $\sigma = 10^{17}\,\mathrm{s}^{-1}$, for $d = 1\,\mathrm{nm}$ and $v = 1$ m/s, the friction is extremely small: $\sigma_{\parallel} \approx 10^{-18}\,\mathrm{Nm}^{-2}$ in compared with the friction observed in [21] between the gold tip and gold substrate, corresponding to $\sigma_{\parallel} \sim 1\,\mathrm{Nm}^{-2}$. The friction increases when the conductivity decreases, but there is a limit to the enhancement. Thus, according to the Drude model, the conductivity is given by

$$\sigma = \frac{ne^2\tau}{m}, \tag{7.35}$$

where the relaxation time τ can not be shorter than $\sim 10^{-16}$ s. The lowest value of the electron concentration n_{min} is restricted by the validity of the macroscopic theory, which requires that the average separation between electrons is much smaller than the length scale of variation of the electric field, which is determined by separation d. Thus $n_{min} \approx d^{-3}$ so that for $d = 1\,\mathrm{nm}$, the conductivity can not be smaller than $\sigma_{min} \approx 10^{12}\,\mathrm{s}^{-1}$ and, consequently, at $v = 1$ m/s, the frictional shear stress cannot be larger than $10^{-13}\,\mathrm{Nm}^{-2}$.

For $v < dk_BT/\hbar$ (at $d = 1\,\mathrm{nm}$ and $T = 300\,\mathrm{K}$, for $v < 10^3$ m/s), the main contribution to the friction (7.29) depends linearly on the sliding velocity v, so that the frictional stress which acts on the surfaces of the two bodies in parallel and normal relative motion, can be written in the form: $\sigma = \gamma v$. For parallel relative motion, the friction coefficient $\gamma_{\parallel} = \gamma_{\parallel}^{rad} + \gamma_{\parallel}^{evan}$ has a contribution from the propagating electromagnetic waves:

$$\gamma_{\parallel}^{rad} = \frac{\hbar}{8\pi^2}\int_0^{\infty} d\omega\left(-\frac{\partial n}{\partial\omega}\right)\int_0^{\frac{\omega}{c}} dq\, q^3 \times$$

$$\times \frac{(1-|R_{1p}|^2)(1-|R_{2p}|^2)}{\left|1-e^{2i\gamma d}R_{1p}R_{2p}\right|^2} + [p \to s], \tag{7.36}$$

and the contribution from the evanescent electromagnetic waves:

$$\gamma_{\parallel}^{evan} = \frac{\hbar}{2\pi^2}\int_0^{\infty} d\omega\left(-\frac{\partial n}{\partial \omega}\right)\int_{\frac{\omega}{c}}^{\infty} dq\, q^3 e^{-2|k_z|d}\times$$

$$\times\, \mathrm{Im}R_{1p}\mathrm{Im}R_{2p}\frac{1}{\left|1-e^{-2|k_z|d}R_{1p}R_{2p}\right|^2} + [p\to s]. \tag{7.37}$$

7.4 Casimir Friction Between Two Semi-infinite Solids in Normal Relative Motion

The case of normal relative motion of two parallel flat surfaces is more complex compared with the case of parallel relative motion. For normal motion, it cannot be assumed, as in the case of parallel relative motion, that the body moves with the constant relative velocity in the time interval from $-\infty$ to $+\infty$. As a result, in the case of arbitrary velocities for normal relative motion, the friction force will be a non-linear functional of the velocities. Here we consider the simplest case when the friction force is linear in the relative velocity, when it is possible to use linear response theory.

We consider two semi-infinite solids **1** and **2** with parallel flat surfaces. We introduce a coordinate system with the xy-plane in the surface of body **1**, and the z axis along the upward normal. The surface of body **2** is located at $z = d$, performing small amplitude vibrations along the z axes with displacement coordinate $u_z(t) = u_0 e^{-i\omega_0 t}$. Since the system is translationally invariant in the $\mathbf{x} = (x, y)$ plane, the electromagnetic field can be represented by the Fourier integrals

$$\mathbf{E}(\mathbf{x}, z) = \int \frac{d^2q}{(2\pi)^2} e^{i\mathbf{q}\cdot\mathbf{x}}\mathbf{E}(\mathbf{q}, z), \tag{7.38}$$

$$\mathbf{B}(\mathbf{x}, z) = \int \frac{d^2q}{(2\pi)^2} e^{i\mathbf{q}\cdot\mathbf{x}}\mathbf{B}(\mathbf{q}, z), \tag{7.39}$$

where $\mathbf{E}$ and $\mathbf{B}$ are the electric and magnetic induction field, and $\mathbf{q}$ is the 2D wave vector in the (x, y) plane. After the Fourier transformation, it is convenient to choose the coordinate axis in the (x, y) plane along the vectors $\mathbf{q}$ and $\mathbf{n} = [\hat{z}\times\mathbf{q}]$. The scattering of the electromagnetic wave with the frequency ω from the vibrating surface of the body **2** will give rise to the harmonics at the frequencies $\omega \pm \omega_0$. Thus in the vacuum gap between the bodies, the electric field $\mathbf{E}(\mathbf{q}, \omega, z)$ can, to linear order in the displacement coordinate, be written in the form

$$\mathbf{E}(\mathbf{q}, \omega, z) = \left(\left(\mathbf{v}_0 e^{ipz} + \mathbf{w}_0 e^{-ipz}\right) + \left(\mathbf{v}_1 e^{ip^+ z} + \mathbf{w}_1 e^{-ip^+ z}\right)e^{-i\omega_0 t}\right)e^{-i\omega t}. \tag{7.40}$$

From (7.40) and Maxwell's equation

$$-\frac{1}{c}\frac{\partial \mathbf{B}}{\partial t} = \nabla \times \mathbf{E}, \tag{7.41}$$

we get the magnetic induction field $\mathbf{B}(\mathbf{q}, \omega, z)$

$$\mathbf{B}(\mathbf{q}, \omega, z) = c\Bigg[\frac{1}{\omega}\Big(\big[\mathbf{k}^- \times \mathbf{w}_0\big]e^{-ik_z z} + \big[\mathbf{k}^+ \times \mathbf{v}_0\big]e^{ik_z z}\Big) + \\ + \frac{1}{\omega + \omega_0}\Big(\big[\mathbf{k}_+^- \times \mathbf{w}_1\big]e^{-ik_z^+ z} + \big[\mathbf{k}_+^+ \times \mathbf{v}_1 e^{ip^+ z}\big]\Big)e^{-i\omega_0 t}\Bigg]e^{-i\omega t}, \tag{7.42}$$

where $\mathbf{k}^{\pm} = \mathbf{q} \pm \hat{z}p$, $p = ((\omega/c)^2 - q^2)^{1/2}$, $p^+ = p(\omega + \omega_0)$, $\mathbf{k}_+^+ = \mathbf{k}^+(\omega + \omega_0)$, $\mathbf{k}_+^- = \mathbf{k}^-(\omega + \omega_0)$. In (7.40) and (7.42) w_0, v_0, etc. are unknown amplitudes, which can be found using appropriate boundary conditions (see below). At the surfaces of the bodies, the amplitude of the outgoing electromagnetic wave must be equal to the amplitude of the reflected wave plus the amplitude of the radiated wave. It is convenient to decompose the electromagnetic field into p- and s-polarized electromagnetic waves. For the p-polarized electromagnetic waves, the electric field is in the incident plane determined by the vectors $\mathbf{q}$ and $\mathbf{n}$, and for the s-polarized electromagnetic waves, the electric field is normal to the incident plane. Thus, the boundary conditions for the electromagnetic field at $z = 0$ can be written in the form

$$v_{0z(y)} = R_{1p(s)}(\omega) w_{0z(n)} + E^f_{1z(n)}(\omega), \tag{7.43}$$

$$v_{1z(n)} = R_{1p(s)}(\omega + \omega_0) w_{1z(n)}, \tag{7.44}$$

where $R_{1p(s)}(\omega)$ is the reflection amplitude for surface **1** for the $p(s)$-polarized electromagnetic field, and where $E^f_{1z(y)}(\omega)$ are the components of the fluctuating electric field outside the surface **1** in the absence of the body **2**. The boundary condition at the surface of the body **2** must be written in the reference frame where body **2** is at rest. The electric field in this reference frame is determined by a Lorentz transformation. To linear order in the vibrational frequency, this transformation has the form

$$\mathbf{E}' = \mathbf{E} - \frac{i\omega_0 u(t)\big[\hat{\mathbf{e}}_z \times \mathbf{B}\big]}{c}. \tag{7.45}$$

$$v'_{1z(q)} = v_{1z(q)} + ik_z u_0 v_{0z(q)}; \;\; w'_{1z(q)} = w_{1z(q)} - ik_z u_0 w_{0z(q)};$$

$$w'_{1y} = w_{1y} - \frac{\omega + \omega_0}{\omega} ik_z u_0 w_{0y}; \;\; v'_{1y} = v_{1y} + \frac{\omega + \omega_0}{\omega} ik_z u_0 v_{0y}.$$

The boundary conditions for the electromagnetic field at $z = d + u(t)$ in the rest frame of body **2** can be written in the form

$$w_{0z(n)} = e^{2ik_z d} R_{2p(s)}(\omega) v_{0z(n)} + e^{ik_z d} E^f_{2z(n)}(\omega), \tag{7.46}$$

$$w_{1z} - ik_z u_0 w_{0z} = e^{2ik_z^+ d} R^+_{2p}(w_{1z} + ik_z u_0 v_{0z}), \tag{7.47}$$

$$w_{1n} - ipu_0 \frac{(\omega+\omega_0) w_{0n}}{\omega} = e^{2ik_z d} R^+_{2s}\left(v_{1n} + ik_z u_0 \frac{(\omega+\omega_0) v_{0n}}{\omega}\right), \tag{7.48}$$

where $R_{2p(s)}(\omega)$ is the reflection amplitude for surface **2** for the $p(s)$-polarized electromagnetic field, and where $E^f_{2z(y)}(\omega)$ are the components of the fluctuating electric field radiated by body **2**. From (7.43), (7.44) and (7.46)–(7.48) we get

$$v_{0z(y)} = \frac{R_{1p(s)} E^f_{2z(n)} e^{ik_z d} + E^f_{1z(n)}}{\Delta}, \tag{7.49}$$

$$w_{0z(n)} = \frac{e^{2ik_z d} R_{2p(s)} E^f_{1z(n)} + E^f_{2z(n)} e^{ik_z d}}{\Delta}, \tag{7.50}$$

$$w_{1z} = ik_z u_0 \frac{\left(e^{2ik_z d} R^f_{2p} + e^{2ik_z^+ d} R^+_{2p}\right) E^f_{1z} + \left(1 + e^{2ik_z^+ d} R^+_{2p} R_1\right) E^f_{2z} e^{ik_z d}}{\Delta_p \Delta^+_p}, \tag{7.51}$$

$$w_{1n} = ik_z u_0 \frac{\omega+\omega_0}{\omega} \frac{\left(e^{2ik_z d} R_{2s} + e^{2ik_z^+ d} R^+_{2s}\right) E^f_{1n} + \left(1 + e^{2ik_z^+ d} R^+_{2s} R_{1s}\right) E^f_{2n} e^{ik_z d}}{\Delta_s \Delta^+_s}, \tag{7.52}$$

$$v_{1z(n)} = R^+_{1p(s)} w_{1z(n)}, \tag{7.53}$$

where $R^+_{p(s} = R_{p(s)}(\omega+\omega_0)$, $\Delta_{p(s)} = 1 - e^{2ik_z pd} R_{2p(s)} R_{1p(s)}$, and $\Delta^+_{p(s)} = \Delta_{p(s)}(\omega+ +\omega_0)$. The other components of the fluctuating electromagnetic field can be found from the transversality conditions

$$q w_x - p w_z = 0, \;\; q v_x + p v_z = 0. \tag{7.54}$$

The frictional stress σ which act on the surfaces of the two bodies can be obtained from the $zz-$ component of the Maxwell stress tensor σ_{ij}, evaluated at $z = 0$:

$$\sigma_{zz} = \frac{1}{4\pi} \int_0^\infty d\omega \int \frac{d^2 q}{(2\pi)^2} \Big[\left\langle \left| E_z(\mathbf{q}, \omega, z) \right|^2 \right\rangle + \left\langle \left| B_z(\mathbf{q}, \omega, z) \right|^2 \right\rangle -$$

$$- \left\langle \left| E_q(\mathbf{q}, \omega, z) \right|^2 \right\rangle - \left\langle \left| E_n(\mathbf{q}, \omega, z) \right|^2 \right\rangle -$$

$$- \left\langle \left| B_q(\mathbf{q}, \omega, z) \right|^2 \right\rangle - \left\langle \left| B_n(\mathbf{q}, \omega, z) \right|^2 \right\rangle \Big]_{z=0}. \tag{7.55}$$

To linear order in the vibrational coordinate $u(t)$ and the frequency ω_0, the stress acting on the surface **1** can be written in the form

$$\sigma_{zz} = \sigma_{0zz}(d) + u(t)\frac{\partial}{\partial d}\sigma_{0zz}(d) + i\omega_0\gamma_\perp u(t). \tag{7.56}$$

Here the first term determines the conservative van der Waals stress and the second term is the adiabatic change of the conservative van der Waals stress during vibration. The last term determines the frictional stress with the friction coefficient $\gamma_\perp$. After calculations, details of which are given in Appendix G, we get the friction coefficient for normal relative motion $\gamma_\perp = \gamma_\perp^{rad} + \gamma_\perp^{evan}$, where the contribution to the friction coefficient from the propagating electromagnetic waves is given by

$$\gamma_\perp^{rad} = \frac{\hbar}{4\pi^2}\int_0^\infty d\omega\left(-\frac{\partial n}{\partial\omega}\right)\int_0^{\frac{\omega}{c}} dq\, q k_z^2 \times$$

$$\times\Big[\big(1-|R_{1p}R_{2p}|^2\big)^2 + \big|\big(1-|R_{1p}|^2\big)R_{2p}e^{ik_z d} +$$

$$+\big(1-|R_{2p}|^2\big)R_{1p}^* e^{-ik_z d}\big|^2\Big]\frac{1}{\big|1-e^{2ik_z d}R_{1p}R_{2p}\big|^4} + [p\to s], \tag{7.57}$$

and where the contribution to the friction from the evanescent electromagnetic waves is given by

$$\gamma_\perp^{evan} = \frac{\hbar}{\pi^2}\int_0^\infty d\omega\left(-\frac{\partial n}{\partial\omega}\right)\int_{\frac{\omega}{c}}^\infty dq\, q|k_z|^2 e^{-2|k_z|d}\times$$

$$\times\Big[\big(\mathrm{Im}R_{1p} + e^{-2|k_z|d}\big|R_{1p}\big|^2\mathrm{Im}R_{2p}\big)\big(\mathrm{Im}R_{2p} + e^{-2|k_z|d}\big|R_{2p}\big|^2\mathrm{Im}R_{1p}\big) +$$

$$+ e^{-2|k_z|d}\big(\mathrm{Im}\big(R_{1p}R_{2p}\big)\big)^2\Big]\frac{1}{\big|1-e^{-2|k_z|d}R_{1p}R_{2p}\big|^4} + [p\to s]. \tag{7.58}$$

Equations (7.57) and (7.58) were first derived in [99, 100] using the semi-classical theory of the fluctuating electromagnetic field. In [129] an alternative derivation was given using the quantum field theory (see Appendix J).

There is a principal difference between the friction coefficients for normal and parallel relative motion, related to the denominators in the formulas for the friction coefficient. The resonant condition corresponds to the case when the denominators of the integrand in (7.37) and (7.58), which are due to multiple scattering of the electromagnetic waves from the opposite surfaces, is small. At resonance, if the imaginary part of the reflection amplitude $R_i \ll 1$ the integrand in (7.58) has a large factor $\sim 1/R_i^2$, in sharp contrast to the case of parallel relative motion, where there is no such enhancement factor.

7.5 The Case of Good Conductors

A well-conducting metal has a dielectric function $\epsilon = 1 - 4\pi i\sigma/\omega$ (σ is the conductivity) with an absolute value much larger than unity at frequencies $\omega < \omega_T = k_B T/\hbar$, and consequently $R_{pi} << 1$ and $R_{pr} \approx 1$. Thus an enhancement in the friction due to multiple scattering of the electromagnetic waves from the opposite surfaces is possible only for very small $q << 1/d$. The calculation of the friction in this section is accurate only to the leading order in the surface impedance $\zeta = \epsilon^{-1/2} = \zeta' - i\zeta''$, $|\zeta| << 1$.

It is convenient to write the friction coefficient for the two flat surfaces in the form

$$\gamma = \hbar \int_0^\infty d\omega \left(-\frac{\partial n}{\partial \omega}\right)(I_p + I_s). \tag{7.59}$$

Within the local optic approximation the reflection amplitudes for the s- and p-polarized electromagnetic waves are determined by the Fresnel formulas (C.17) from Appendix C.

7.5.1 *Parallel Relative Motion*

Taking into account that $qdq = kdk$, from (7.37) for parallel relative motion of clean surfaces within the local optic approximation, we get the following contribution to the friction from the evanescent p-and s-polarized electromagnetic waves:

$$I_{\parallel p}^{evan} = \int_0^\infty \frac{dkk^3}{2\pi^2}\left[k^2 + \left(\frac{\omega}{c}\right)^2\right] \frac{\left[\mathrm{Re}(s/\epsilon)\right]^2}{\left|\left[(s/\epsilon)^2 - k^2\right]\sinh kd + 2ik(s/\epsilon)\cosh kd\right|^2}, \tag{7.60}$$

$$I_{\parallel s}^{evan} = \int_0^\infty \frac{dkk^3}{2\pi^2}\left[k^2 + \left(\frac{\omega}{c}\right)^2\right] \frac{\left[\mathrm{Re}(s)\right]^2}{\left|\left(s^2 - k^2\right)\sinh kd + 2iks\cosh kd\right|^2}. \tag{7.61}$$

For $d \le (c/\omega)|\varepsilon(\omega)|^{-1/2}$

$$I_{p\parallel} \approx 1.8\frac{1}{d^4}\left(\frac{\omega}{4\pi^2\sigma}\right)^2, \tag{7.62}$$

$$I_{\parallel s} \approx \frac{1}{8\pi^2}\left(\frac{4\pi\sigma\omega}{c^2}\right)^2\left[0.44 - 0.5\ln\left(\frac{16\pi\sigma\omega d^2}{c^2}\right)\right]. \tag{7.63}$$

For $c/\omega \gg d \ge (c/\omega)|\varepsilon(\omega)|^{-1/2}$ we get

$$I_{\parallel p} \approx \frac{1}{4\pi^2}\left(\frac{\omega}{cd}\right)^2 \frac{\omega}{4\pi\sigma}\left\{0.3 - \ln\left[\frac{\omega d}{c}\left(\frac{\omega}{4\pi\sigma}\right)^{1/2}\right]\right\}, \tag{7.64}$$

$$I_{\parallel s} \approx 0.2 \frac{c^2}{4\pi\sigma\omega d^6}. \tag{7.65}$$

Integrating (7.65) over frequencies gives a divergent result. However, one should take into account that (7.65) is only valid if $\omega \geq \omega_{min}$, where ω_{min} is determined from condition $|\varepsilon(\omega_{min})|\omega_{min}^2 \approx c^2 d^{-2}$. From this condition we get

$$\omega_{min} \approx \frac{c^2}{4\pi\sigma d^2}. \tag{7.66}$$

After substitution of the results obtained above in (7.59), and integration over frequencies at $d \ll \lambda_c = \lambda_T |\varepsilon(\omega_T)|^{-1/2}$, where $\omega_T = c/\lambda_T = k_B T/\hbar$, and using

$$\int_0^\infty \frac{x^2}{4\sinh^2 x/2} dx = \frac{\pi^2}{3}$$

and

$$\int_0^\infty \frac{x^2 \ln x}{4\sinh^2 x/2} dx = 1.1607,$$

we get

$$\gamma_{\parallel p}^{evan} \approx 0.3 \frac{\hbar}{d^4} \left(\frac{k_B T}{4\pi\hbar\sigma} \right)^2, \tag{7.67}$$

$$\gamma_{\parallel s}^{evan} \approx 10^{-2} \frac{\hbar}{\lambda_c^4} \big(1 - 2\ln(2d/\lambda_c)\big). \tag{7.68}$$

Accordingly, for $\lambda_c \ll d \ll \lambda_T$, using

$$\int_0^\infty \frac{x^3}{4\sinh^2 x/2} dx = 7.2123,$$

$$\int_0^\infty \frac{x^3 \ln x}{4\sinh^2 x/2} dx = 7.8708$$

we get

$$\gamma_{\parallel p} \approx \frac{\hbar}{4\pi^2 \lambda_c^2 d^2} \big[9.66 - 7.2\ln(d/\lambda_c)\big], \tag{7.69}$$

$$\gamma_{\parallel s} \approx 0.1 \frac{4\pi\sigma k_B T}{c^2 d^2}. \tag{7.70}$$

In the derivation of (7.70) we have used

$$\int_{x_{min}}^{\infty} \frac{dx}{4x\sinh^2 x/2} \approx \int_{x_{min}}^{0.01} \frac{dx}{x^3} + \int_{0.01}^{\infty} \frac{dx}{4x\sinh^2 x/2} \approx \frac{1}{2x_{min}^2}.$$

Let us now consider the contribution to friction from propagating waves. As $d \to \infty$ the integration over q in (7.36) involves an integration over an infinite rapidly oscillating structure. With the aid of the averaging procedure

$$\left\langle \lim_{d\to\infty} t_p^{prop} \right\rangle = \frac{1}{2\pi}\int_0^{2\pi} d\varphi \frac{\left(1-|R_p|^2\right)^2}{|1-e^{i\varphi}|R_p|^2|^2} = \frac{1-|R_p|^2}{1+|R_p|^2}, \tag{7.71}$$

$$\left\langle \lim_{d\to\infty} t_s^{prop} \right\rangle = \frac{1-|R_s|^2}{1+|R_p|^2} \tag{7.72}$$

(where it is assumed that arguments q and ω of reflection amplitudes R_p and R_s do not change during averaging) we get

$$\gamma_{\parallel}^{rad}(d\to\infty) = \frac{\hbar}{8\pi^2}\int_0^{\infty} d\omega\left(-\frac{\partial n}{\partial\omega}\right)\int_0^{\frac{\omega}{c}} dq\, q^3 \times$$

$$\times\left(\frac{1-|R_p|^2}{1+|R_p|^2} + [p\to s]\right). \tag{7.73}$$

Using

$$\int_0^{\infty} \frac{x^{3.5}}{e^x-1}dx = 12.268,$$

from (7.73) we get

$$\gamma_{\parallel}^{rad}(d\to\infty) = 1.8\hbar\left(\frac{k_BT}{\hbar c}\right)^4\left(\frac{k_BT}{4\pi\hbar\sigma}\right)^{1/2}. \tag{7.74}$$

For good conductors at $v \ll cd/\lambda_T$, in the first term of formula (7.30) it is enough to expand to linear order in the velocity, and in the second term it is possible to put

$$n(\omega) \approx k_BT/\hbar\omega.$$

Thus, the frictional stress in this limit can be written in the form

$$\sigma_{\parallel} = \gamma_{\parallel}v + \frac{1}{2\pi^3}k_BT\int_{-\infty}^{\infty} dq_y\int_0^{\infty} dq_x q_x e^{-2qd}\times$$

$$\times\int_0^{q_xv}\frac{d\omega}{\omega}\left(\frac{\mathrm{Im}R_{1p}^{-}\mathrm{Im}R_{2p}}{|\,1-e^{-2qd}R_{1p}^{-}R_{2p}\,|^2} + (1\leftrightarrow 2)\right) + [R_p\to R_s]. \tag{7.75}$$

For $d < \lambda_c = \lambda_T |\varepsilon(\omega_T)|^{-1/2}$ for two identical surfaces of good conductors, the contribution from the p-polarized field gives:

$$\sigma_{\parallel p} = \gamma_{\parallel p}^{evan} V + \frac{\pi}{45} \frac{k_B T}{4\pi\hbar\sigma} \frac{\hbar V^2}{4\pi\sigma d^5}, \tag{7.76}$$

where the contribution to friction coefficient $\gamma_{\parallel p}^{evan}$ from the p-polarized evanescent waves is given by (7.67). Similarly, for s-polarized waves with the same condition, we get

$$\sigma_{\parallel s} = \gamma_{\parallel s}^{evan} V + \frac{1}{96\pi^3} \left(\frac{4\pi\sigma}{c}\right)^2 \left(\frac{V}{c}\right)^2 \frac{k_B T}{d}, \tag{7.77}$$

where $\gamma_{\parallel s}^{evan}$ is given by (7.69). Comparison of the linear and quadratic velocity-terms in (7.76) and (7.77) leads us to conclude that, in this case, the quadratic terms are negligibly small in comparison with linear terms, both for s- and for p-polarized electromagnetic waves.

7.5.2 Normal Relative Motion

For normal relative motion the friction coefficient can be also written in the form (7.59), where

$$I_{\perp p}^{evan} = \int_0^\infty \frac{dk}{\pi^2} k^5 \left[\mathrm{Re}(s/\epsilon)\right]^2 \Big[\left[(k^2 + |s/\epsilon|^2)\cosh kd + 2k\left[\mathrm{Im}(s/\epsilon)\right]\sinh kd\right]^2 + \\ + \left(k^2 - |s/\epsilon|^2\right)^2\Big] \frac{1}{\left|\left((s/\epsilon)^2 - k^2\right)\sinh kd + 2ik(s/\epsilon)\cosh kd\right|^4}, \tag{7.78}$$

$$I_{\perp s}^{evan} = \int_0^\infty \frac{dk}{\pi^2} k^5 \left[\mathrm{Re}s\right]^2 \Big[\left[(k^2 + |s|^2)\cosh kd + 2k\mathrm{Im}s\,\sinh kd\right]^2 + \\ + (k^2 - |s|^2)^2\Big] \frac{1}{\left|\left(s^2 - k^2\right)\sinh kd + 2iks\,\cosh kd\right|^4}. \tag{7.79}$$

For $I_{\perp p}^{evan}$, for $(c/\omega)|\epsilon|^{-3/2} < d < (c/\omega)|\epsilon|^{1/2}$ and $|\zeta| << 1$, there is a singularity (as $k \to 0$) in the integrand of the type $-1/k^3$, and the main contribution to the integral comes from this singularity. Taking into account that $\sinh kd \approx kd$ and $\cosh kd \approx 1$ as $k \to 0$, to first order in ζ we get

$$I_{\perp p}^{evan} = 2\left(\frac{\omega}{c}\right)^2 \zeta' \int_0^\infty \frac{dk}{\pi^2} \frac{k^5}{\left|k^2 d - 2i\left(\frac{\omega}{c}\right)(\zeta)\right|^4} =$$

$$= \frac{\omega\zeta'}{\pi^2 c d^3}\left(\frac{\pi}{2} + \arctan \zeta''/\zeta' - \frac{\zeta''/\zeta'}{1 + (\zeta''/\zeta')^2}\right). \tag{7.80}$$

As $k \to 0$, there is no singularity in the integrand of $I_{\perp s}^{evan}$; thus the main contribution to the integral comes from $k \sim d^{-1}$. For $d < (c/\omega)|\epsilon|^{-1/2}$, I_s becomes slowly dependent on d:

$$I_{\perp s} \approx \int_0^\infty \frac{dk}{\pi^2} k\left[\sqrt{k^4 + \left(\frac{\omega}{c}\right)^4 |\epsilon|^2} - k^2\right] e^{-2kd} \approx$$

$$\approx \frac{1}{8\pi^2}\left(\frac{\omega}{c}\right)^4 |\epsilon|^2 (1.22 - \ln\left(2d|\epsilon|^{1/2}\frac{\omega}{c}\right), \tag{7.81}$$

while for $d > (c/\omega)|\epsilon|^{-1/2}$ we get

$$I_{\perp s} \approx \left(\frac{c}{\omega}\right)^2 \zeta'^2 d^{-6}. \tag{7.82}$$

For the propagating electromagnetic waves, taking into account that $qdq = -pdp$, we get

$$I_{\perp p}^{rad} = \left(\frac{\omega}{c}\right)^2 \zeta'^2 \int_0^{\frac{\omega}{c}} \frac{dp}{\pi^2} p^5 \frac{1 + \cos^2(pd)}{\left|p \sin pd + 2i\left(\frac{\omega}{c}\right)\zeta \cos pd\right|^4}, \tag{7.83}$$

$$I_{\perp s}^{rad} = \left(\frac{\omega}{c}\right)^2 \zeta'^2 \int_0^{\frac{\omega}{c}} \frac{dp}{\pi^2} p^5 \frac{1 + \cos^2(pd)}{\left|\left(\frac{\omega}{c}\right) \sin pd + 2ip\zeta \cos pd\right|^4}. \tag{7.84}$$

For $d < (c/\omega)|\epsilon|^{-1/2}$ the contribution to the friction from propagating waves is negligibly small in the comparison with the contribution from the evanescent waves. For $d > (c/\omega)|\epsilon|^{-1/2}$ the main contribution to the integrals (7.83) and (7.84) comes from the integration near the singularities at $p = p_n = \pi n/d < \omega/c$ (where n is an integer), where $\sin pd = 0$. For the contribution to I_p^{rad} from the singularity at $n = 0$ we get

$$I_{\perp p}^{rad} \approx \frac{\omega\zeta'}{4\pi^2 c d^3}\left(\frac{\pi}{2} - \arctan \zeta''/\zeta' + \frac{\zeta''/\zeta'}{1 + (\zeta''/\zeta')^2}\right). \tag{7.85}$$

In the vicinity of other singularities $p_n \neq 0$, putting $p = p_n + p'$, we have $\sin pd \approx (-1)^n p'$ and $\cos pd \approx (-1)^n$, and the contribution to the integral from the region close to one singularity is

$$\approx 2\left(\frac{\omega}{c}\right)^2 \zeta'^2 \int \frac{dp'}{\pi^2} \frac{1}{\left|p_n p' d + 2i\left(\frac{\omega}{c}\right)\zeta\right|^4}$$

$$\approx \frac{p_n^4 c}{8\pi^2 \omega d \zeta'} \left(\frac{\pi}{2} - \arctan \zeta''/\zeta' - \frac{\zeta''/\zeta'}{1 + (\zeta''/\zeta')^2}\right) \tag{7.86}$$

The number m of such contributions is obviously equal to the integer part of the quantity $y = \omega d/\pi c$ ($m = integ[y]$), so that the total $p_n \neq 0$ contribution becomes

$$\frac{\pi^2 c}{8\omega d^5 \zeta'} \left(\frac{\pi}{2} - \arctan \zeta''/\zeta' - \frac{\zeta''/\zeta'}{1 + (\zeta''/\zeta')^2}\right) \sum_{n=1}^{m} n^4$$

$$= \frac{\pi^2 c}{8\omega d^5 \zeta'} \left(\frac{\pi}{2} - \arctan \zeta''/\zeta' - \frac{\zeta''/\zeta'}{1 + (\zeta''/\zeta')^2}\right)$$

$$\times \left(\frac{(m+1)^5}{5} - \frac{(m+1)^4}{2} + \frac{(m+1)^3}{3} - \frac{m}{30} - \frac{1}{30}\right)$$

In the integral $I_{\perp s}^{rad}$ there is no singularity at $p_n = 0$, and the contribution from the vicinity of the point $p_n \neq 0$ is

$$2\left(\frac{\omega}{c}\right)^2 \zeta'^2 \int_0^{\frac{\omega}{c}} \frac{dp'}{\pi^2} \frac{p_n^5}{\left|\left(\frac{\omega}{c}\right) p' d + 2i p_n \zeta\right|^4} =$$

$$= \frac{\omega n^2}{8cd^3 \zeta'} \left(\frac{\pi}{2} - \arctan \zeta''/\zeta' - \frac{\zeta''/\zeta'}{1 + (\zeta''/\zeta')^2}\right)$$

and consequently

$$I_{\perp s}^{rad} = \frac{\omega}{8cd^3 \zeta'} \left(\frac{\pi}{2} - \arctan \zeta''/\zeta' - \frac{\zeta''/\zeta'}{1 + (\zeta''/\zeta')^2}\right) \sum_{n=1}^{m} n^2 =$$

$$\frac{\omega}{48cd^3 \zeta'} \left(\frac{\pi}{2} - \arctan \zeta''/\zeta' - \frac{\zeta''/\zeta'}{1 + (\zeta''/\zeta')^2}\right) m(m+1)(2m+1) \tag{7.87}$$

For $m >> 1$, where we can assume $m \approx \pi\omega/cd$, the s- and p-wave contribution are approximately equal, and the total contribution from propagating electromagnetic waves in this limit is

$$I_{\perp}^{rad} = I_{\perp p}^{rad} + I_{\perp s}^{rad} \approx \frac{11\omega^4}{240\pi^3 c^4 \zeta'} \tag{7.88}$$

The above formulas were obtained from (7.57) and (7.58) by neglecting the spatial dispersion of the dielectric function. However, these formulas depend only on the

solids via the surface impedance ζ, which is equals to the ratio of the tangential components of the electric and magnetic fields on the boundary of the body. Thus, the results in this section also remain valid in the presence of spatial dispersion, provided only that the surface impedance of the medium is small enough. Thus, we would have arrived at the same formulas if we were to have assumed from the very beginning that the Leontovich boundary condition $\mathbf{E} = \zeta \mathbf{H} \times \mathbf{n}$ is satisfied on the surface of the metal.

At not too low temperatures, the impedances of metals is given by

$$\zeta' = \zeta'' = (\omega/8\pi\sigma)^{1/2}. \tag{7.89}$$

In the local optic approximation, it is assumed that there is no dependence of σ on $\mathbf{q}$. For $\omega < \omega_T = k_B T/\hbar$ it is also good approximation to neglect by the frequency dependence of σ. In this approximation, using (7.80) for $\lambda_W (k_B T/4\pi\hbar\sigma)^{3/2} < d < \lambda_W (4\pi\hbar\sigma/(k_B T)^{1/2}$, where $\lambda_W = c\hbar/(k_B T)$, we get

$$\gamma_{\perp p}^{evan} = \hbar \int_0^\infty d\omega \left(-\frac{\partial n}{\partial \omega}\right) I_{\perp p}^{evan} \approx 0.13 \frac{\hbar}{d^3 \lambda_T} \left(\frac{k_B T}{4\pi\hbar\sigma}\right)^{1/2}. \tag{7.90}$$

For comparison, the p-wave contribution for parallel relative motion for $d < \lambda_c$, ($\lambda_c = c/(4\pi\sigma k_B T)^{1/2}$) is given by (7.67). It is interesting to note that, for normal relative motion, in contrast to parallel relative motion, practically for all $d > 0$, the main contribution to friction comes from retardation effects, since (7.90), in contrast to (7.67), contains the light velocity.

From (7.81), we get the s-wave contribution to friction for $d < \lambda_c$

$$\gamma_{\perp s}^{evan} \approx 10^{-2} \frac{\hbar}{\lambda_c^4} \big(3 - 5\ln(2d/\lambda_c)\big). \tag{7.91}$$

For parallel relative motion, the s-wave contribution is a factor 1/2 smaller.

For $d > \lambda_c$, taking into account that (7.82) is valid only for $\omega > c^2/4\pi\sigma d^2$, we get

$$\gamma_{\perp s}^{evan} \approx \frac{\pi k_B T \sigma}{d^2 c^2}. \tag{7.92}$$

From (7.88) for $d > \lambda_W$, using

$$\int_0^\infty \frac{x^{2.5}}{e^x - 1} dx = 3.7445,$$

we get a distance-independent contribution to friction from propagating electromagnetic waves:

$$\gamma_\perp^{rad} \approx 0.1 \frac{\hbar}{\lambda_T^3 \lambda_c}. \tag{7.93}$$

7.6 Numerical Results

Figure 7.1 shows the dependence of the frictional stress between two semi-infinite bodies on the relative velocity v at different separations d. In the calculations the Fresnel formulas for the reflection amplitude were used with the Drude permittivity ε for copper. The frictional stress initially increases with velocity, reaches a maximum, and then decreases at large values of the velocity. The presence of a maximum is connected to the resonances, which are present in the integrand for the friction force due to the coupled plasmon-polaritons of both surfaces [9, 11]. Doppler shift leads to the displacement of the resonances relative to each other. If this displacement becomes larger than the width of the resonance, then this leads the friction force to decrease when the velocity increases. Figure 7.2 shows the contribution to the friction coefficient $\gamma_{\|}$ from the evanescent electromagnetic waves for two semi-infinite solids in parallel relative motion, with parameters chosen to correspond to copper ($\tau^{-1} = 2.5 \times 10^{13}\,\mathrm{s}^{-1}$, $\omega_p = 1.6 \times 10^{16}\,\mathrm{s}^{-1}$) at $T = 273$ K.

The same result for normal relative motion is shown in Fig. 7.3. We show the s- and p-wave contributions separately. The dashed lines show the result when the local (long-wavelength) dielectric function $\epsilon(\omega)$ is used, and full lines show the result obtained using the non-local optic dielectric formalism, which was proposed some years ago for studying the anomalous skin-effect [198] (see also Appendix D). This formalism takes into account the spatial dispersion of the dielectric function. Figure 7.2 shows that, for sufficiently small separations ($d < 1000$ Å), for parallel relative motion, the non-local optic effects become very important for the p-wave contribution. However, for the s-wave contribution, for both parallel and normal relative motion, the non-local optic effects are negligibly small for practically all separations. For normal relative motion, for the p-wave contribution, the non-local optic effects are less important than for the parallel relative motion. The presented calculations take into account the non-local effects in the bulk of the solids. In

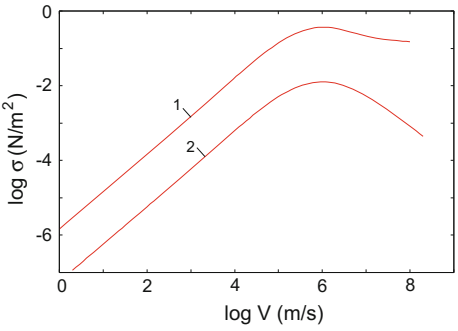

Fig. 7.1 The velocity dependence of the frictional stress acting between two semi-infinite bodies at $d = 10\,\mathrm{nm}$ (1) and $d = 100\,\mathrm{nm}$ (2), with parameters chosen to correspond to copper ($\tau^{-1} = 2.5 \times 10^{13}\,\mathrm{s}^{-1}$, $\omega_p = 1.6 \times 10^{16}\,\mathrm{s}^{-1}$). (The base of the logarithm is 10.)

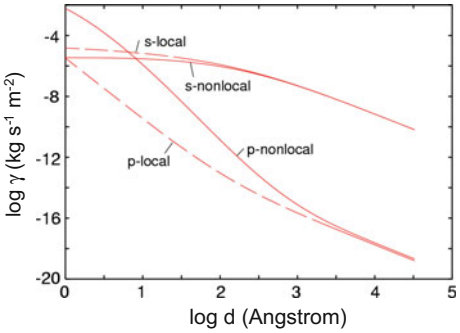

Fig. 7.2 The friction coefficient for two flat surfaces in parallel relative motion as a function of separation d at $T = 273$ K with parameter chosen to correspond to copper ($\tau^{-1} = 2.5 \times 10^{13}\,\mathrm{s}^{-1}$ $\omega_p = 1.6 \times 10^{16}\,\mathrm{s}^{-1}$). The contributions from the s- and p-polarized electromagnetic field are shown separately. The full curves represent the results obtained within the non-local optic dielectric formalism, and the dashed curves represent the result obtained within local optic approximation. (The log-function is with basis 10.)

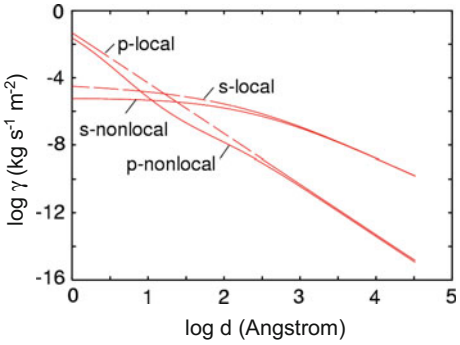

Fig. 7.3 The same as in Fig. 7.2, but for normal relative motion

addition, there is the contribution to the non-local optical response from the surface region, which was investigated in [13, 167]. For $d > 10$ Å, the non-local volume contribution is of the same importance as the surface contribution.

As pointed out in [13, 121, 139, 144], the p-wave contribution increases and the s- wave contribution decreases when the free electron density decreases. Within the local optic approximation, the friction diverges in the limit of zero conductivity. This situation is different from the radiative heat transfer, where, even in the local optics approximation, a maximum in the heat transfer occurs for conductivities corresponding to semi-metals. Figure 7.4 shows the dependence of coefficient of friction on the electron density. When the electron density decreases, there is transition from a degenerate electron gas to a non-degenerate electron gas at the density $n_F \sim (k_B T m)^{3/2}/\pi^2\hbar^3$. At $T = 273$ K, the transition density $n_F \sim 10^{25}$ m^{-3}. For $n > n_F$ we use the (non-local) dielectric function appropriate for a degenerate

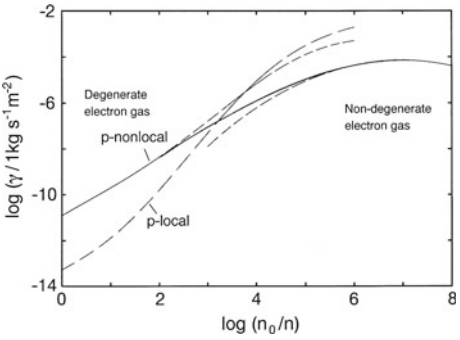

Fig. 7.4 The friction coefficient for two flat surface in parallel relative motion as a function of the free electron density n at $T = 273\,\mathrm{K}$. The full curve was obtained by interpolation between the result (*dashed lines*) obtained within the non-local optic dielectric approach, with dielectric functions corresponding to a degenerate electron gas for $n > n_F \sim 10^{25}\,\mathrm{m}^{-3}$, and to a non-degenerate electron gas for $n < n_F$. The calculation were performed with the damping constant $\tau^{-1} = 2.5 \times 10^{13}\,\mathrm{s}^{-1}$, separation $d = 100\,\text{Å}$ and $n_0 = 8.6 \times 10^{28}\,\mathrm{m}^{-3}$. (The log-function is with basis 10.)

electron gas, while for $n < n_F$ we use an expression corresponding to a non- degenerate electron gas. In the calculations, we used the electron mean free path $l \approx 600$ Å. At $d = 100$ Å, the maximum value $\gamma_{max} \sim 10^{-4}\mathrm{kg\ s}^{-1}\ \mathrm{m}^{-2}$ is obtained for $n_{max} \sim 10^{22}\mathrm{m}^{-3}$, corresponding to the DC conductivity $\sigma \sim 1(\Omega\ \mathrm{m})^{-1}$.

7.7 The Case of Bad Conductors

Casimir friction can be greatly enhanced for high resistivity materials ($k_B T/4\pi\hbar\sigma > 1$). Thus, for two surfaces in relative parallel motion, using the reflection coefficient in the electrostatic limit ($d < c(\hbar/4\pi\sigma k_B T)^{1/2}$)

$$R_p = \frac{\varepsilon - 1}{\varepsilon + 1}, \tag{7.94}$$

we get from (10.13)

$$\gamma_\perp \approx 0.48 \frac{\hbar}{d^4} \frac{k_B T}{4\pi\hbar\sigma} \tag{7.95}$$

and from (7.58) $\gamma_\perp \approx 10\gamma_\parallel$. Thus, in contrast to the heat flux, Casimir friction diverges in the limit $\sigma \to 0$. Of course, in reality, the friction must vanish in this limit because the conductivity is proportional to the concentration, n, of free electrons, and the friction must vanish when n vanishes. The origin of the discrepancy lies in the breakdown of the macroscopic theory, which is not valid at very low electron concentration (see Sect. 7.3.1). The macroscopic approach for the electromagnetic

properties of matter is valid only when the length scale of spatial variation of electromagnetic field is much larger than the average distance between the electrons. For the evanescent waves, this length scale is determined by separation, d, between the bodies. From this condition, we can estimate the maximal friction, which corresponds to high–resistivity materials. The minimal conductivity can be estimated as (see Sect. 7.3.1)

$$\sigma_{min} \sim \frac{e^2\tau}{md^3} \tag{7.96}$$

and maximum of friction

$$\gamma_{\parallel max} \sim 0.05\frac{\hbar}{d^4}\frac{k_BT}{4\pi\hbar\sigma_{min}} \sim 0.05\frac{mk_BT}{4\pi e^2\tau d}. \tag{7.97}$$

To estimate the friction coefficient Γ for an atomic force microscope tip with the radius of curvature $R >> d$, we can use the 'proximity approximation' given by (6.95), with the heat flux per unit area replaced by the friction coefficient per unit area. Using this approximation, for the friction coefficient for a spherical tip we get:

$$\Gamma_{\parallel}^{s} \approx 2\pi\int_0^\infty d\rho\rho\gamma_{\parallel}\left(d+\rho^2/2R\right) = 0.05\frac{2\pi R}{3d^3}\frac{k_BT}{4\pi\sigma}, \tag{7.98}$$

and the maximum of friction can be estimated as

$$\Gamma_{\parallel max}^{s} \sim 0.05\frac{2\pi R}{3d^3}\frac{k_BT}{4\pi\sigma_{min}} \sim 0.1\frac{mk_BTR}{4\pi e^2\tau}. \tag{7.99}$$

For $\tau \sim 10^{-16}$ s, $R \sim 1$ μm and $T = 300$ K we get $\Gamma_{max} \sim 10^{-14}$ kg s^{-1}. This friction is only one order of magnitude smaller than the friction observed in a recent experiment at $d = 10$ nm [21]. Similarly, in the case of a cylindrical tip we get:

$$\Gamma_{\parallel}^{c} \approx 2w\int_0^\infty d\rho\gamma_{\parallel}\left(d+\rho^2/2R\right) = \frac{2^{1/2}\pi}{64}\sqrt{\frac{R}{d}}\frac{k_BTw}{4\pi\sigma d^3}, \tag{7.100}$$

where w is the width of the tip, and the maximum of friction can be estimated as

$$\Gamma_{\parallel max}^{c} \sim \frac{2^{1/2}\pi}{64}\sqrt{\frac{R}{d}}\frac{k_BTw}{4\pi\sigma_{min}d^3} \sim \frac{2^{1/2}\pi}{64}\sqrt{\frac{R}{d}}\frac{mk_BTw}{4\pi e^2\tau}. \tag{7.101}$$

For $w = 7$ μm, $d = 10$ nm, and with the other parameters as above, (7.101) gives a coefficient friction of the same order of magnitude as was observed in the experiment [21]. Thus, the van der Waals friction between high resistivity materials can be measured with the present state-of-the art equipment.

Recently, a large electrostatic non-contact friction has been observed between an atomic force microscope tip and thin dielectric films [24]. Casimir friction will also be large for dielectrics with high optical absorption at low-frequencies. As an

example, we consider the van der Waals friction between thin water films adsorbed on transparent dielectric substrates such as silica or mica. Water has an extremely large static dielectric function of approximately 80. The low frequency contribution to the dielectric function, responsible for this large static value, is due to relaxation of the permanent dipoles of the water molecules. It can be accurately described by the Debye [235] theory of rotational relaxation. The theoretical fit of the experimental data is given by [236]:

$$\varepsilon(\omega) = 4.35 + \frac{C}{1 - i\omega/\omega_0}, \tag{7.102}$$

where $C = 72.24$ and $\omega_0 = 1.3 \times 10^{11}\,\mathrm{s}^{-1}$. We note that water has large absorption in the radio-frequency range at $\omega \sim \omega_0$, and shows, in this region of the spectrum, anomalous dispersion. In this frequency range, the dielectric constants ε_3 of mica or silica are nearly constant (and real) and $|\varepsilon_2| \gg \varepsilon_3$, where ε_2 denotes the dielectric function of water. For a planar film with the thickness d_f and dielectric function $\varepsilon_2(\omega)$ on-top of a substrate with the dielectric function $\varepsilon_3(\omega)$, the reflection amplitude

$$R_p = \frac{R_{p21} - R_{p23}\exp(-2qd_f)}{1 - R_{p21}R_{p23}\exp(-2qd_f)}, \tag{7.103}$$

where

$$R_{pij} = \frac{\varepsilon_i - \varepsilon_j}{\varepsilon_i + \varepsilon_j}, \tag{7.104}$$

and index 1 denotes vacuum. For $qh \ll 1$ and $q^{-1} \sim d \ll |\varepsilon_2| d_f/\varepsilon_3$ the reflection amplitude can be approximated by

$$R_p \approx 1 - \frac{2}{\varepsilon_2 q d_f}. \tag{7.105}$$

$$\Gamma_{\parallel}^{c} = \frac{\pi\hbar R^{1/2} w}{6\sqrt{2}C^2 d_f^2 d^{3/2}} \left(\frac{k_B T}{\hbar\omega_0}\right)^2. \tag{7.106}$$

Substituting (7.105) in (10.13), and using the 'proximity approximation', we obtain the friction between a cylindrical atomic force microscope tip and a sample

$$\Gamma_{\parallel}^{c} = \frac{\pi\hbar R^{1/2} w}{6\sqrt{2}C^2 d_f^2 d^{3/2}} \left(\frac{k_B T}{\hbar\omega_0}\right)^2 \tag{7.107}$$

For $d_f = 1\,\mathrm{nm}$ and with the other parameters the same as above we get $\Gamma_{\parallel}^{c} = 4.8 \times 10^{-12}\,\mathrm{kg\,s}^{-1}$. The friction observed in [21] has the same weak distance dependence predicted by (7.107), but is one order of magnitude smaller than predicted by (7.107).

7.8 Resonant Photon Tunneling Enhancement of Casimir Friction

7.8.1 *Surface Phonon–Polariton Enhancement of Casimir Friction*

As in the case of the radiative heat transfer, van der Waals friction can be greatly enhanced by resonant photon tunneling between localized surface states, for example, surface plasmon polaritons and adsorbate vibration modes. Using the same approximation as when deriving (6.4), we get [100]

$$\gamma_\perp = \frac{3}{128}\frac{\hbar^2\omega_a^2}{d^4 k_B T \eta}\frac{1}{\sinh^2(\hbar\omega_0/2k_BT)}, \tag{7.108}$$

and for parallel motion

$$\gamma_\parallel = \frac{\hbar^2\eta q_c^4}{128\pi k_B T}\frac{1}{\sinh^2(\hbar\omega_0/2k_BT)}. \tag{7.109}$$

Resonant photon tunneling enhancement of Casimir friction is possible for two semiconductor surfaces that can support low-frequency surface plasmon or surface polariton modes. As an example, we consider two clean surfaces of silicon carbide (SiC). Using the parameters describing the optical properties of this material (see Sect. 4.3) we get $\gamma_\perp = 4.2 \times 10^3/d^4\,\mathrm{kg}\cdot\mathrm{s}^{-1}\cdot\mathrm{m}^{-2}$ and $\gamma_\parallel = 2.2 \times 10^2/d^4$ $\mathrm{kg}\cdot\mathrm{s}^{-1}\cdot\mathrm{m}^{-2}$, where the distance d is in Å. Note that the friction between the two semiconductor surfaces is several orders of magnitude larger than between two clean good conductor surfaces (see Figs. 7.2 and 7.3).

7.8.2 *Adsorbate Vibrational Mode Enhancement of the van der Waals Friction*

Another enhancement mechanism of Casimir friction is connected to resonant photon tunneling between adsorbate vibrational modes localized on the different surfaces. In [99, 100], we have shown that resonant photon tunneling between two surfaces separated by $d = 1\,\mathrm{nm}$, and covered by a low concentration of potassium atoms, results in a friction that is six orders of magnitude larger than for the clean surfaces. The adsorbate induced enhancement of Casimir friction is even larger for Cs adsorption on Cu(100). In this case, even at low coverage ($\theta \sim 0.1$), the adsorbed layer exhibits an acoustic branch for vibrations parallel to the surface [200]. Thus, $\omega_\parallel = 0$ and according to (6.47), at small frequencies, the reflection amplitude is given by

$$R_p = 1 - \frac{2qa\omega_q^2}{\omega^2 - \omega_q^2 + i\omega\eta}, \tag{7.110}$$

where $\omega_q^2 = 4\pi n_a e^{*2} a q^2 / M$, e^* is the ion charge and a is the separation between an ion and the image plane. Using (7.110) in (10.13) for

$$\frac{a}{\eta d}\sqrt{\frac{4\pi n_a e^{*2} a}{Md^2}} \ll 1,$$

we get

$$\gamma_\parallel \approx 0.62 \frac{k_B T a^2}{\eta d^6}. \tag{7.111}$$

It is interesting to note that $\gamma_\parallel$ in (7.111) does not depend on n_a, e^* and M. However, (7.110) is only valid when there are acoustic vibrations in the adsorbed layer. For Cs adsorbed on the Cu(100) surface, acoustic vibrations exist only for coverages $\theta \geq 0.1$ [200]. The friction acting on an atomic force microscope tip can be estimated using a similar approximation as (6.95). Using this approximation and (7.111) for a cylindrical tip we get

$$\Gamma_\parallel^c \approx 0.68 \frac{k_B T a^2 R^{0.5} w}{\eta d^{5.5}}, \tag{7.112}$$

where R is the radius of the curvature of the tip and w its width. For Cs adsorption on Cu(100), the damping parameter η was estimated in [170] as $\eta \approx 3 \times 10^9\,\mathrm{s}^{-1}$. Using this value of η in (7.112) for $a = 2.94$ Å [200], $R = 1\,\mu\mathrm{m}$, $w = 7\,\mu\mathrm{m}$, $T = 293$ K at $d = 10\,\mathrm{nm}$ we get $\Gamma_\parallel = 0.5 \times 10^{-13}\,\mathrm{kg/s}$, which is only three times smaller than the friction observed in [21] at the same distance. However, van der Waals friction is characterized by a much stronger distance dependence ($\sim 1/d^{5.5}$) than observed in the experiment ($\sim 1/d^n$, where $n = 1.3 \pm 0.2$). Thus, at small distances, van der Waals friction will be much larger than the friction observed in [21], and can thus be measured experimentally. Figure 7.5 shows how the friction coefficient depends on the distance, d, between the copper tip and the copper substrate, when the surfaces of the tip and the substrate are covered by a low concentration of the Cs atoms, as well as for clean surfaces. In comparison, the friction between two clean surfaces at the separation $d = 1\,\mathrm{nm}$ is eleven orders of magnitude smaller. However, the friction between clean surfaces shown on Fig. 7.5 was calculated in local optic approximation. For parallel relative motion, non-local optic effects are very important (see Fig. 7.2), and, when they are taken into account, the friction at $d = 1\,\mathrm{nm}$ between adsorbate covered surfaces will be seven orders of magnitude larger than the friction between clean surfaces.

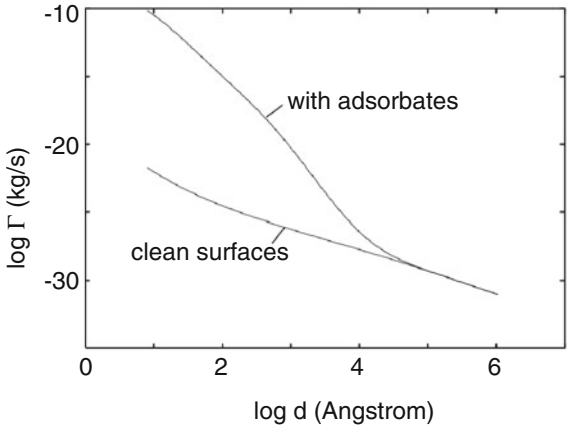

Fig. 7.5 The friction coefficient between the copper tip and copper substrate, the surfaces of which are covered by low concentration of cesium atoms, as a function of the separation d. The *cylindrical tip* is characterized by a radius of curvature $R = 1\,\mu\text{m}$ and the width $w = 7\,\mu\text{m}$. The other parameters correspond to Cs adsorbed on Cu(100) surface at coverage $\theta \approx 0.1$ [170, 200]: $e^* = 0.28e$, $\eta = 3 \times 10^9\,\text{s}^{-1}$, $a = 2.94$ Å, $T = 293\,\text{K}$. (The base of the logarithm is 10.)

Chapter 8
Casimir Friction Between a Small Particle and a Plane Surface

In this section, the friction force acting on a small neutral particle moving relative to a flat surface of a solid is considered in the framework of the fluctuation electrodynamic in non-relativistic and relativistic cases. The friction force in the particle–plate configuration is deduced from the friction force in the plate–plate configuration assuming one of the plates to be sufficiently rarefied. The effect of the multiple scattering of the electromagnetic field between a particle and substrate is also studied. These effects can be important for physisorbed molecules. For physisorbed molecules, high-order processes, which are not included in the theory of Casimir friction, can dominate the damping rate of physisorbed molecules. The results of the theoretical calculations are compared with experimental data. The special case of Casimir friction force acting on a small neutral particle moving relative to black-body radiation is also analyzed.

8.1 Friction Force on a Particle Moving Parallel to a Plane Surface: Non-relativistic Theory

The friction force acting on a small particle during motion parallel to a flat surface can be obtained from the friction between two semi-infinite bodies in the limit when one of the bodies is sufficiently rarefied. For $d \ll \lambda_T = c\hbar/k_BT$, in (7.28), it is possible to neglect the first term and, in the second term, the integration can be extended to the whole q-plane, and we can put $k_z \approx iq$. Let us assume that the rarefied body consists of particles with dipole and magnetic moments. The dielectric and magnetic susceptibilities of the rarefied body—let us say body **2** will be close to unity, i.e. $\varepsilon_2 - 1 \to 4\pi n\alpha_{E2} \ll 1$ and $\mu_2 - 1 \to 4\pi n\alpha_{H2} \ll 1$, where n is the particle concentration in body **2**, and α_{E2} and α_{H2} are their dielectric and magnetic susceptibilities, respectively. In linear order, in the particle concentration n, according to (C.17) from Appendix, C, the reflection amplitudes are given by

A.I. Volokitin and B.N.J. Persson, *Electromagnetic Fluctuations at the Nanoscale*,
NanoScience and Technology, DOI 10.1007/978-3-662-53474-8_8

$$R_{2p} = \frac{\varepsilon_2 k_z - \sqrt{\varepsilon_2\mu_2 k^2 - q^2}}{\varepsilon_2 k_z + \sqrt{\varepsilon_2\mu_2 k^2 - q^2}} \approx \frac{\varepsilon_2 - 1}{\varepsilon_2 + 1} \approx 2\pi n\alpha_E,$$

$$R_{2s} = \frac{\mu_2 k_z - \sqrt{\varepsilon_2\mu_2 k^2 - q^2}}{\mu_2 k_z + \sqrt{\varepsilon_2\mu_2 k^2 - q^2}} \approx \frac{\mu_2 - 1}{\mu_2 + 1} \approx 2\pi n\alpha_H.$$

If the particle–surface separation $d \ll \lambda_T$, then the friction force acting on a particle moving parallel to a plane surface can be obtained from (7.28) as the ratio between the change of the frictional shear stress after the displacement of body **2** by small distance, dz, and the number of the particles in a slab with thickness dz:

$$F_x^{part} = \left.\frac{d\sigma_\parallel(z)}{ndz}\right|_{z=d} = \frac{2\hbar}{\pi^2}\int_0^\infty d\omega \int d^2q q_x q e^{-2qd}\big(n_2(\omega') - n_1(\omega)\big)\times$$
$$\times\left(\mathrm{Im}R_p\mathrm{Im}\alpha'_E + \mathrm{Im}R_s\mathrm{Im}\alpha'_H\right), \tag{8.1}$$

where $\alpha'_{E(H)} = \alpha_{E(H)}(\omega')$. After the transformation, we get:

$$F_x^{part} = \frac{2\hbar}{\pi^2}\int_{-\infty}^{\infty} dq_y \int_0^\infty dq_x q_x q e^{-2qd}\left\{\int_0^\infty d\omega\big[n(\omega) - n(\omega + q_x v)\big]\times\right.$$
$$\times\Big[\big(\mathrm{Im}R_{1p}(\omega + q_x v)\mathrm{Im}\alpha_E(\omega) + [\omega + q_x v \leftrightarrow \omega]\big) +$$
$$+\big(\mathrm{Im}R_{1s}(\omega + q_x v)\mathrm{Im}\alpha_H(\omega) + [\omega + q_x v \leftrightarrow \omega]\big)\Big] -$$
$$\left. - \int_0^{q_x v} d\omega[n(\omega) + 1/2]\Big[\big(\mathrm{Im}R_{1p}(\omega - q_x v)\mathrm{Im}\alpha_E(\omega) + [\omega - q_x v \leftrightarrow \omega]\big) +\right.$$
$$\left.+\big(\mathrm{Im}R_{1p}(\omega - q_x v)\mathrm{Im}\alpha_H(\omega) + [\omega - q_x v \leftrightarrow \omega]\big)\Big]\right\}, \tag{8.2}$$

where the symbols $[\omega \pm q_x v \leftrightarrow \omega]$ stand for the terms that can be obtained from the preceding terms by interchanging $\omega \pm q_x v$ and ω. An alternative derivation of (8.2), using the law of energy conservation without taking into account the contribution from magnetic moment, is given in Appendix H. To linear order in the sliding velocity v from (8.2), we get $F_{fric} = -\Gamma_\parallel v$, where

$$\Gamma_\parallel = \frac{2\hbar}{\pi}\int_0^\infty \mathrm{d}\omega\left(-\frac{\partial n(\omega)}{\partial\omega}\right)\int_0^\infty \mathrm{d}qq^4 e^{-2qd}\times$$
$$\times\Big[\mathrm{Im}R_p(q,\omega)\mathrm{Im}\alpha_E(\omega) + \mathrm{Im}R_s(q,\omega)\mathrm{Im}\alpha_H(\omega)\Big]. \tag{8.3}$$

In the non-retarded limit, without taking into account the contribution from the magnetic moment, this equation reduces to the formula obtained by Tomassone and Widom [145].

For a spherical particle with radius R, the electrical and magnetic susceptibilities are given by (5.58) and (5.59), respectively. In this case, from (8.3) in the limit $d <\mid \varepsilon(\omega = k_B T/\hbar) \mid^{-1/2} \lambda_T$ for the contribution to the friction coefficient from p-polarized waves, we get [139]:

$$\Gamma_{p\parallel} \approx 3\frac{\hbar}{d^5}\left(\frac{k_B T}{4\pi\hbar}\right)^2 \sigma_1^{-1}\sigma_2^{-1} R^3, \tag{8.4}$$

and for the contribution from s-polarized waves, we get

$$\Gamma_{s\parallel} \approx \frac{\pi^3}{45}\frac{\hbar}{\lambda_T^2}\left(\frac{\sigma_1\sigma_2 R^2}{c^2}\right)\left(\frac{R}{d}\right)^3, \tag{8.5}$$

where σ_1 and σ_2 are the conductivities of substrate and particle, respectively. For $d = 2R = 10\,\text{nm}$, $\sigma_1 = \sigma_2 = 4 \times 10^{17}\,\text{s}^{-1}$ (which corresponds to gold at room temperature), we get the very small friction coefficients: $\Gamma_p \sim 10^{-29}\,\text{kg}\cdot\text{s}^{-1}$ and $\Gamma_s \sim 10^{-24}\,\text{kg}\cdot\text{s}^{-1}$. Note that the contribution to the friction between a small particle and a plane metal surface is mainly due to the s-polarized waves, just as in the case of the friction between two plane surfaces, and is many orders of magnitude larger than contribution from the p-polarized waves. This is related to the screening of the electromagnetic field inside the metal volume, which is stronger for the p-polarized waves. As a result, the energy dissipation and, consequently, the friction will be larger for the s-polarized waves. Figure 8.1 shows the velocity-dependence of the friction force acting on a small copper particle with $R = 10\,\text{nm}$, moving above a copper sample at $d = 20\,\text{nm}$. The contributions from the electric dipole and magnetic moments are shown separately. At small velocities, the contribution from the magnetic moment is seven orders of magnitude larger than the contribution from the electric dipole moment.

The friction can be greatly enhanced for high-resistivity materials. Using (8.3) in the non-retarded limit (which can be formally obtained in the limit $c \to \infty$), and for

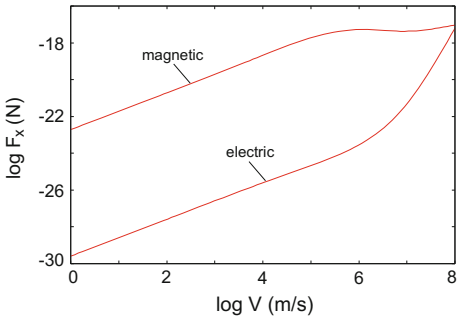

Fig. 8.1 The velocity dependence of the friction force acting on a small copper particle with radius $R = 10\,\text{nm}$ moving above a copper sample at the separation $d = 20\,\text{nm}$. The contributions from the electric dipole moment and the magnetic moment are shown separately. (The base of the logarithm is 10)

high-resistivity material ($4\pi\sigma << k_B T/\hbar$), we get:

$$\Gamma_{p\parallel} = 0.9 \frac{k_B T}{4\pi\sigma} \frac{R^3}{d^5} \tag{8.6}$$

where we have assumed that the particle and the substrate have the same dielectric function $\varepsilon = 1 + 4\pi i\sigma/\omega$. As discussed above (see Sect. 7.3.1), the macroscopic theory (which was used in obtaining (8.6)) is only valid when $\sigma \gg \sigma_{min} \sim e^2\tau/md^3$. For $\sigma \sim \sigma_{min}$, $d = 2R = 10\,\text{nm}$ and $\tau = 10^{-15}\,\text{s}$ (8.6) gives $\Gamma_{p\parallel\,\max} \sim 10^{-18}\,\text{kg}\,\text{s}^{-1}$.

If the particle and the substrate are made from the same material, able to support the surface phonon–polaritons, the friction is given by

$$\Gamma_{\parallel} = \frac{9 k_B T \eta R^3}{d^5} \left(\frac{1}{\omega_s^2} + \frac{1}{\omega_p^2} \right), \tag{8.7}$$

where ω_s and ω_p are the frequencies of the surface phonon–polaritons for the substrate and the particle, respectively. If the substrate and the particle are made from silicon carbide (SiC), $\omega_s = 1.79 \times 10^{14}\,\text{s}^{-1}$ and $\omega_p = 1.76 \times 10^{14}\,\text{s}^{-1}$. Thus, for $d = 2R = 10\,\text{nm}$, $\eta = 8.9 \times 10^{11}\,\text{s}^{-1}$, and $T = 300\,\text{K}$, we get $\Gamma \sim 10^{-21}\,\text{kg}\,\text{s}^{-1}$. This friction coefficient is three orders of magnitude larger than for the good conductors.

8.2 Friction Force on a Particle Moving Parallel to Plane Surface: Relativistic Theory

The friction force acting on a particle moving parallel to a dielectric plate can be obtained from the friction force between two plates each sliding relative to other, assuming one of the plates as sufficiently rarefied (see Fig. 8.2). According to a fully relativistic theory [128] (see also Sect. 7.3), the contributions to the friction force,

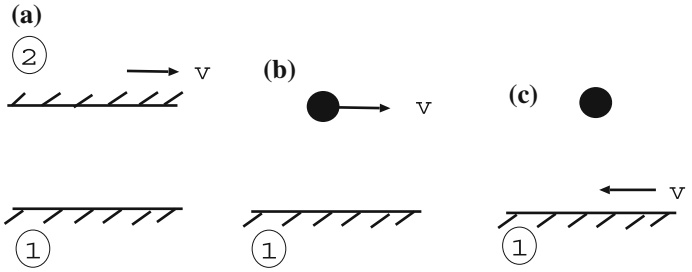

Fig. 8.2 The schemes of the configurations: **a** plate–plate; **b** particle–plate in the *lab* frame; and **c** particle–plate in the rest frame of a particle. The friction force in the particle–plate configuration in the *lab* frame can be obtained from the friction force in the plate–plate configuration, assuming that plate 2 is rarefied and in the rest frame of a particle and assuming that plate 1 is rarefied

F_{1x}, and the radiation power, P_1, absorbed by plate 1 from evanescent waves, which dominate at small separations and low temperatures, are determined by the formulas

$$\begin{pmatrix} F_{1x} \\ P_1 \end{pmatrix} = \int \frac{d^2q}{(2\pi)^2} \int_0^{cq} \frac{d\omega}{2\pi} \begin{pmatrix} \hbar q_x \\ \hbar\omega \end{pmatrix} \Gamma_{12}(\omega, \mathbf{q}) \big[n_2(\omega') - n_1(\omega) \big], \tag{8.8}$$

where the positive quantity

$$\Gamma_{12}(\omega, \mathbf{q}) = \frac{4\mathrm{sgn}(\omega')}{|\Delta|^2} \big[(q^2 - \beta k q_x)^2 - \beta^2 k_z^2 q_y^2 \big] \Big\{ \mathrm{Im} R_{1p} \big[(q^2 - \beta k q_x)^2 \mathrm{Im} R'_{2p} |D_{ss}|^2 + \beta^2 k_z^2 q_y^2 \mathrm{Im} R'_{2s} |D_{sp}|^2 \big] + (p \leftrightarrow s) \Big\} e^{-2k_z d}, \tag{8.9}$$

can be identified as a spectrally resolved photon emission rate:

$$\Delta = \big(q^2 - \beta k q_x \big)^2 D_{ss} D_{pp} - \beta^2 k_z^2 q_y^2 D_{ps} D_{sp},$$

$$D_{pp} = 1 - e^{-2k_z d} R_{1p} R'_{2p},\ D_{sp} = 1 + e^{-2k_z d} R_{1s} R'_{2p},$$

$n_i(\omega) = [\exp(\hbar\omega / k_B T_i) - 1]^{-1}$, $k_z = \sqrt{q^2 - (\omega/c)^2}$, $R_{1p(s)}$ is the reflection amplitude for surface **1** in the K frame for a $p(s)$-polarized electromagnetic wave, $R'_{2p(s)} = R_{2p(s)}(\omega', q')$ is the reflection amplitude for surface **2** in the K' frame for a $p(s)$-polarized electromagnetic wave, $\omega' = \gamma(\omega - q_x v)$, $q'_x = \gamma(q_x - \beta k)$, $D_{ps} = D_{sp}(p \leftrightarrow s)$. The symbol $(p \leftrightarrow s)$ denotes the terms that are obtained from the preceding terms by permutation of the p and s indexes.

Assuming that the dielectric permittivity of the rarefied plate is close to the unity, i.e. $\varepsilon - 1 \to 4\pi\alpha N \ll 1$, where N is the concentration of particles in a plate in the co-moving reference frame, then, to linear order in the concentration N, the reflection amplitudes for the rarefied plate in the co-moving frame are:

$$R_p = \frac{\varepsilon k_z - \sqrt{k_z^2 - (\varepsilon - 1)\left(\frac{\omega}{c}\right)^2}}{\varepsilon k_z + \sqrt{k_z^2 - (\varepsilon - 1)\left(\frac{\omega}{c}\right)^2}} \approx N\pi \frac{q^2 + k_z^2}{k_z^2} \alpha,$$

$$R_s = \frac{k_z - \sqrt{k_z^2 - (\varepsilon - 1)\left(\frac{\omega}{c}\right)^2}}{k_z + \sqrt{k_z^2 - (\varepsilon - 1)\left(\frac{\omega}{c}\right)^2}} \approx N\pi \frac{q^2 - k_z^2}{k_z^2} \alpha. \tag{8.10}$$

Because $R_{p(s)} \ll 1$ for the rarefied plate, it is possible to neglect multiple scattering of the electromagnetic waves between the surfaces. In this approximation, $\Delta_{pp} \approx \Delta_{ss} \approx \Delta_{sp} \approx \Delta_{sp} \approx 1$ and

$$\Delta \approx (q^2 - \beta k q_x)^2 - \beta^2 k_z^2 q_y^2 = \frac{(qq')^2}{\gamma^2}, \tag{8.11}$$

$$(q^2-\beta k q_x)^2 \mathrm{Im}R'_{2p}|\Delta_{ss}|^2+\beta^2 k_z^2 q_y^2 \mathrm{Im}R'_{2s}|\Delta_{sp}|^2 \approx \frac{(qq')^2}{\gamma^2}\mathrm{Im}R'_{2p}+\beta^2 k_z^2 q_y^2 \mathrm{Im}(R'_{2p}+R'_{2s}), \tag{8.12}$$

$$\Gamma_{12}=-4\left[\left(\mathrm{Im}R_{1p}\mathrm{Im}R'_{2p}+\mathrm{Im}R_{1s}\mathrm{Im}R'_{2s}\right)\left(1+\gamma^2\beta^2\frac{k_z^2 q_y^2}{q^2 q'^2}\right)+\gamma^2\beta^2\frac{k_z^2 q_y^2}{q^2 q'^2}\left(\mathrm{Im}R_{1p}\mathrm{Im}R'_{2s}+\mathrm{Im}R_{1s}\mathrm{Im}R'_{2p}\right)\right]. \tag{8.13}$$

The friction force f_x acting on a particle, and the radiation power w absorbed by it, can be obtained in the K frame from (8.13), under the assumption that plate 2 is sufficiently rarefied [150] (see Fig. 8.2b). In this case, the friction force acting on the surface 2, F_{2x}, and the radiation power absorbed by it, W_2, are

$$\begin{pmatrix} F_{2x} \\ W_2 \end{pmatrix}=\begin{pmatrix} -F_{1x} \\ -W_1 \end{pmatrix}=N'\int_d^\infty dz\begin{pmatrix} f_x(z) \\ w(z) \end{pmatrix}, \tag{8.14}$$

where $N'=\gamma N$ is the concentration of particles in plate 2 in the K frame,

$$\begin{pmatrix} f_x(z) \\ w(z) \end{pmatrix}=\frac{1}{\gamma\pi^2}\int d^2q \times\int_0^{cq} d\omega\begin{pmatrix} \hbar q_x \\ \hbar\omega \end{pmatrix}\frac{e^{-2k_z z}}{k_z}\left[\mathrm{Im}R_{1p}(\omega)\phi_p+\mathrm{Im}R_{1s}(\omega)\phi_s\right]\mathrm{Im}\alpha(\omega')\left[n_2(\omega')-n_1(\omega)\right], \tag{8.15}$$

$$\phi_p=\left(\frac{\omega'}{c}\right)^2+2\gamma^2\left(q^2-\beta^2 q_x^2\right)\frac{k_z^2}{q^2},\quad \phi_s=\left(\frac{\omega'}{c}\right)^2+2\gamma^2\beta^2 q_y^2\frac{k_z^2}{q^2}.$$

In the rest reference frame of an object, the radiation power absorbed by it is equal to the heating power for the object. Thus, $-w$ is equal to the heating power for plate 1. Equation (8.15) agrees with the results obtained in [150, 152, 155]. However, as shown in [61, 128], the acceleration and heating of the particle are determined by the friction force f'_x and by the radiation power w' absorbed by the particle in the rest reference frame of a particle (the K' frame)

$$m_0\gamma^3\frac{dv}{dt}=m_0\frac{dv'}{dt'}=f'_x, \tag{8.16}$$

$$w'=\frac{dm_0}{dt'}c^2 \tag{8.17}$$

where m_0 is the rest mass of the particle, $v' \ll v$ and t' are the velocity and time in the K' frame, respectively. These quantities can be also obtained assuming plate 2 to be sufficiently rarefied (see Fig. 8.2c). In this case, in the K' frame, the friction force acting on the surface 2, F'_{2x}, and the radiation power absorbed by it, W'_2, are

$$\begin{pmatrix} F'_{2x} \\ W'_2 \end{pmatrix} = \begin{pmatrix} -\tilde{F}_{1x} \\ \tilde{W}_1 \end{pmatrix} = N \int_d^\infty dz \begin{pmatrix} f'_x(z) \\ w'(z) \end{pmatrix}, \tag{8.18}$$

where $\tilde{F}_{1x}$ and $\tilde{W}_1$ are obtained from F_{1x} and W_1 after the replacement of the indexes $1 \leftrightarrow 2$,

$$\begin{pmatrix} f'_x \\ w' \end{pmatrix} = \frac{1}{\pi^2} \int_0^\infty dq_x \int_{-\infty}^\infty dq_y \times \int_0^{cq} d\omega \begin{pmatrix} \hbar q_x \\ -\hbar\omega \end{pmatrix} \frac{e^{-2k_z d}}{k_z} \left[\mathrm{Im} R_{1p}(\omega') \phi'_p + \mathrm{Im} R_{1s}(\omega') \phi'_s \right] \mathrm{Im}\alpha(\omega) \left[n_1(\omega') - n_2(\omega) \right], \tag{8.19}$$

$$\phi'_p = \left(\frac{\omega}{c}\right)^2 + 2\gamma^2 \left(q'^2 - \beta^2 q'^2_x\right) \frac{k_z^2}{q'^2}, \quad \phi'_s = \left(\frac{\omega}{c}\right)^2 + 2\gamma^2 \beta^2 q_y^2 \frac{k_z^2}{q'^2}.$$

The relation between the different quantities in the K and K' frames can be found using the Lorentz transformations for the energy-momentum tensor for a plate 2, according to which

$$F_{2x} = \gamma \left(F'_{2x} + v \frac{W'_2}{c^2} \right), \quad W_2 = \gamma \left(W'_2 + v F'_{2x} \right), \tag{8.20}$$

Using (8.14) and (8.18) gives

$$f_x = f'_x + v \frac{w'}{c^2}, \quad w = w' + v f'_x. \tag{8.21}$$

These relations also can be found using the Lorentz transformation for the energy-momentum for a particle, according to which

$$p_x = \gamma \left(p'_x + v m_0 \right), \quad \varepsilon = \gamma \left(m_0 c^2 + v p'_x \right), \tag{8.22}$$

where p_x and ε are the momentum and energy, respectively, of a particle in the K frame and p'_x and $m_0 c^2$ are the same quantities in the K' frame. When the derivative of the 4-momentum is taken with respect to *lab* time, then the factor γ in (8.22) disappears because $dt = \gamma dt'$ and the relations (8.21) are obtained [161]. From the inverse transformations

$$F'_{2x} = \gamma\left(F_{2x} - v\frac{W_2}{c^2}\right), \quad W'_2 = \gamma(W_2 - vF_{2x}), \tag{8.23}$$

follows

$$f'_x = \gamma^2\left(f_x - v\frac{w}{c^2}\right), \quad w' = \gamma^2(w - vf_x). \tag{8.24}$$

These relations also can be obtained as above using the Lorentz transformation for the energy-momentum for a particle. We note that, in contrast to the relations (8.21) on the right side of the relations (8.24), there is an extra factor γ^2. This is because the friction force and the radiation power are not 4-vectors. The kinetic energy of a particle in the *lab* frame is $\varepsilon_K = \varepsilon - m_0c^2$ where the total energy of a particle in the K frame is $\varepsilon = \gamma(m_0c^2 + p'_x v)$. The rate of change of the kinetic energy is

$$\frac{d\varepsilon_K}{dt} = w' + f'_x v - \frac{w'}{\gamma} = w - \frac{w'}{\gamma} = vf_x - \frac{(\gamma - 1)w'}{\gamma^2}. \tag{8.25}$$

Thus, the rate of change of the kinetic energy in the K frame is equal to the friction force power in this frame only when $w' = 0$.

8.3 Effect of Multiple Scattering of the Electromagnetic Waves

Equation (8.3) does not take into account the screening effect, which is due to multiple scattering of the electromagnetic waves between particle and substrate. This effect becomes important in the case of the resonant photon tunneling between the localized particle and substrate modes. A theory of friction that takes into account the screening effects to linear order in velocity was developed in [139] using the semi-classical theory of the fluctuating electromagnetic field. In [129] (see also Appendix K), the same results were obtained using quantum field theory. Resonances that can be excited by thermal radiation can exist only on the surfaces of semiconductors and dielectrics. For good conductors, the surface plasmoms have high frequencies, and cannot be excited by thermal radiation. Thus, for a metal particle, moving above a metal surface, multiple scattering effects can be neglected. For a dielectric particle, it is necessary to take into account only the dipole moment of the particle; the magnetic moment can be neglected.

The screening effects are especially important for physisorbed molecules, because they contribute to friction that is proportional to the absolute value of molecule susceptibility. Without taking screening effects into account, the friction for a particles is proportional to the imaginary part of the susceptibility, which is usually very small for those frequencies that can be excited by thermal radiation. However, the real part of susceptibility can be very large at the resonant frequency.

There is fundamental difference between 'vacuum' friction for two flat surfaces and for point dipole above a flat surface. In the former case, scattering of electromagnetic waves by the surfaces conserves the parallel momentum. Hence, the only possible process of momentum transfer between two flat surfaces is the emission of electromagnetic waves by one body, and the subsequent absorption by the other body. For the evanescent waves, this process gives a contribution that is proportional to the product of the imaginary part of the reflection factors for both surfaces. In the case of a particle above the flat surface, the component of the momentum parallel to the surface can change during scattering by the particle, resulting in momentum transfer. This process gives a contribution that is proportional to product of the imaginary part of the reflection factor for a metal at a different value of the momentum parallel to surface, and absolute value of the point dipole polarizability. The results obtained below are applied to the problem of the vibrational energy relaxation of a physisorbed molecule, and the friction and the heat transfer between an STM tip and a metal surface.

We consider a semi-infinite metal having with a flat surface, which coincides with the xy-coordinate plane, and with the z-axes pointed along the upward normal. A point dipole is located at $\mathbf{r}_0 = (0, 0, d)$, performing small amplitude vibrations with the displacement vector $\mathbf{u}(t) = \mathbf{u}_0 e^{-\mathrm{i}\omega_0 t}$. To linear order in the vibrational coordinate $\mathbf{u}(t)$, the polarization density corresponding to the point dipole can be written in the form:

$$\mathbf{p}(\mathbf{r}, t) = \mathbf{p}_0 \delta(\mathbf{r} - \mathbf{r}_0) e^{-\mathrm{i}\omega t} + \mathbf{p}_1(\mathbf{r}, \omega) e^{-\mathrm{i}(\omega+\omega_0)t}, \tag{8.26}$$

$$\mathbf{p}_1(\mathbf{r}, \omega) = \mathbf{p}_1 \delta(\mathbf{r} - \mathbf{r}_0) - \mathbf{p}_0 \mathbf{u}_0 \cdot \frac{\partial}{\partial \mathbf{r}} \delta(\mathbf{r} - \mathbf{r}_0), \tag{8.27}$$

where $\mathbf{p}_0 = \mathbf{p}^f + \alpha(\omega)\mathbf{E}_0$, $\mathbf{p}_1 = \alpha(\omega + \omega_0)\mathbf{E}_1$, $\mathbf{E}(t) = \mathbf{E}_0 e^{-\mathrm{i}\omega t} + \mathbf{E}_1 e^{-\mathrm{i}(\omega+\omega_0)t}$ is an external electric field at the position of the dipole, $\alpha(\omega)$ is the dipole polarizability of the particle, $\mathbf{p}^f$ is a fluctuating dipole moment, which, according to the fluctuation–dissipation theorem, is characterized by spectral function of fluctuations [8, 184, 185]:

$$\left\langle p_i^f p_j^{f*} \right\rangle_\omega = \frac{\hbar}{\pi} \left(\frac{1}{2} + n(\omega) \right) \mathrm{Im}\alpha(\omega) \delta_{ij}. \tag{8.28}$$

Outside the metal, the electric field is given by the sum of the electric field from the point dipole, $\mathbf{E}_d(\mathbf{r}, t)$, the electric field from the metal polarization charge induced by the point dipole, $\mathbf{E}_d^{ind}(\mathbf{r}, t)$, and the electric field from the metal $\mathbf{E}^s(\mathbf{r}, t)$ in absence of point dipole, and originates from thermal and quantum fluctuation of polarization inside the metal:

$$\mathbf{E}^{total}(\mathbf{r}, t) = \mathbf{E}_d(\mathbf{r}, t) + \mathbf{E}_d^{ind}(\mathbf{r}, t) + \mathbf{E}^s(\mathbf{r}, t). \tag{8.29}$$

The force acting on the dipole is only determined by the last two fields. The electric field $\mathbf{E}_d^{ind}(\mathbf{r}, t)$ can be written in the form:

$$\mathbf{E}_d^{ind}(\mathbf{r},t) = \mathbf{E}_{d0}^{ind}(\mathbf{r},\omega)e^{-\mathrm{i}\omega t} + \mathbf{E}_{d1}^{ind}(\mathbf{r},\omega+\omega_0)e^{-\mathrm{i}(\omega+\omega_0)t}, \tag{8.30}$$

$$E_{d0i}^{ind}(\mathbf{r},\omega) = D_{ij}(\mathbf{r},\mathbf{r}_0,\omega)p_{0j}, \tag{8.31}$$

$$E_{d1i}^{ind}(\mathbf{r},\omega+\omega_0) = D_{ij}(\mathbf{r},\mathbf{r}_0,\omega+\omega_0)p_{1j} + \mathbf{u}_0\cdot\frac{\partial}{\partial\mathbf{r}'}D_{ij}(\mathbf{r},\mathbf{r}',\omega+\omega_0)_{\mathbf{r}'=\mathbf{r}_0}p_{0j} \tag{8.32}$$

where $\tilde{D}_{ik}(\mathbf{r},\mathbf{r}',\omega) = D_{ik}^0(\mathbf{r},\mathbf{r}',\omega) + D_{ik}(\mathbf{r},\mathbf{r}',\omega)$ obeys (3.33) and (3.34), and the function $D_{ik}^0(\mathbf{r},\mathbf{r}',\omega)$ obeys the inhomogeneous equations (3.33) and (3.34) for free space, i.e. in absence of the medium. The function $D_{ik}(\mathbf{r},\mathbf{r}',\omega)$ determines the electric field induced by a unit dipole due to polarization of the medium. Outside the medium, this function has no singularities and obeys the homogeneous equations (3.33) and (3.34). The solution of (3.33) and (3.34) is described in detail in Appendix C. The electric field from the metal $\mathbf{E}^s(\mathbf{r},t) = \mathbf{E}^s(\mathbf{r},\omega)e^{-\mathrm{i}\omega t}$ is characterized by the following spectral function of fluctuations [10, 11, 15, 183, 185]

$$\left\langle E_i^s(\mathbf{r})E_j^{s*}(\mathbf{r}')\right\rangle_\omega = \frac{\hbar}{\pi}\left(\frac{1}{2}+n(\omega)\right)\mathrm{Im}D_{ij}(\mathbf{r},\mathbf{r}',\omega). \tag{8.33}$$

The electric fields $\mathbf{E}_0$ and $\mathbf{E}_1$ at the position of the point dipole can be found from the condition of self-consistency:

$$E_{0i} = D_{ii}(\mathbf{r}_0,\mathbf{r}_0,\omega)p_{0i} + E_i^s(\mathbf{r}_0,\omega), \tag{8.34}$$

$$E_{1i} = D_{ii}(\mathbf{r_0},\mathbf{r}_0,\omega+\omega_0)\alpha(\omega+\omega_0)E_{1i} + \mathbf{u}_0\cdot\frac{\partial}{\partial\mathbf{r}}\Big(E_i^s(\mathbf{r},\omega) + \\ + D_{ij}(\mathbf{r_0},\mathbf{r},\omega+\omega_0)p_{0j} + D_{ij}(\mathbf{r},\mathbf{r}_0,\omega)p_{0j}\Big)_{\mathbf{r}=\mathbf{r}_0}. \tag{8.35}$$

In (8.34) and (8.35), it was given that $D_{ik}(\mathbf{r},\mathbf{r}) = \delta_{ik}D_{ii}(\mathbf{r},\mathbf{r})$. From (8.34)–(8.35):

$$E_{0i} = \frac{E_i^s(\mathbf{r}_0) + D_{ii}(\mathbf{r}_0,\mathbf{r}_0,\omega)p_i^f}{1-\alpha(\omega)D_{ii}(\mathbf{r}_0,\mathbf{r}_0,\omega)}, \tag{8.36}$$

$$p_{0i} = \frac{p_i^f + \alpha(\omega)E_i^s(\mathbf{r}_0,\omega)}{1-\alpha(\omega)D_{ii}(\mathbf{r}_0,\mathbf{r}_0,\omega)}, \tag{8.37}$$

$$E_{1i} = \frac{\mathbf{u}_0\cdot\frac{\partial}{\partial\mathbf{r}}\Big(E_i^s(\mathbf{r}) + D_{ij}(\mathbf{r_0},\mathbf{r},\omega+\omega_0)p_{0j} + D_{ij}(\mathbf{r},\mathbf{r}_0,\omega)p_{0j}\Big)_{\mathbf{r}=\mathbf{r}_0}}{1-\alpha(\omega+\omega_0)D_{ii}(\mathbf{r}_0,\mathbf{r}_0,\omega+\omega_0)}. \tag{8.38}$$

The total electromagnetic force acting on a fluctuating dipole is determined by the Lorentz force:

$$\mathbf{F} = \int_{-\infty}^{\infty} \mathrm{d}\omega \int \mathrm{d}^3 r \Big(\langle \rho \mathbf{E} \rangle + \frac{1}{c} \langle \mathbf{j} \times \mathbf{B} \rangle \Big), \tag{8.39}$$

where the integration is over the volume of the dipole

$$\mathbf{E}(\mathbf{r}, t) = \mathbf{E}_0(\mathbf{r}, \omega) e^{-\mathrm{i}\omega t} + \mathbf{E}_1(\mathbf{r}, \omega + \omega_0) e^{-\mathrm{i}(\omega+\omega_0)t} \tag{8.40}$$

and the magnetic induction field, which can be obtained from the electric field using Maxwell's equations

$$\mathbf{B}(\mathbf{r}, t) = -\mathrm{i}c\nabla \times \left(\mathbf{E}_0(\mathbf{r}, \omega) \frac{e^{-\mathrm{i}\omega t}}{\omega} + \mathbf{E}_1(\mathbf{r}, \omega + \omega_0) \frac{e^{-\mathrm{i}(\omega+\omega_0)t}}{\omega + \omega_0} \right). \tag{8.41}$$

In (8.39), $\rho(\mathbf{r}, t)$ and $\mathbf{j}(\mathbf{r}, t)$ are the electron and current densities of the dipole, which can be expressed through the polarization density $\mathbf{p}(\mathbf{r}, t)$:

$$\rho(\mathbf{r}, t) = -\nabla \cdot \mathbf{p}(\mathbf{r}, t) = -\frac{\partial}{\partial x_l} \big(p_{0l}(\mathbf{r}, \omega) e^{-\mathrm{i}\omega t} + p_{1l}(\mathbf{r}, \omega) e^{-\mathrm{i}(\omega+\omega_0)t} \big), \tag{8.42}$$

$$\mathbf{j}(\mathbf{r}, t) = \frac{\partial}{\partial t} \mathbf{p}(\mathbf{r}, t) = -i \big(\omega \mathbf{p}_0(\mathbf{r}, \omega) e^{-\mathrm{i}\omega t} + (\omega + \omega_0) \mathbf{p}_1(\mathbf{r}, \omega) e^{-\mathrm{i}(\omega+\omega_0)t} \big). \tag{8.43}$$

To linear order in the vibrational coordinate $\mathbf{u}(t)$ and frequency ω_0, the total force acting on the point dipole can be written in the form

$$\mathbf{F}(t) = \mathbf{F}_{st}(\mathbf{r}_0) + \mathbf{F}_{dc}(t) + \mathbf{F}_{fric}(t). \tag{8.44}$$

Here, the first term determines the conservative van der Waals force at the position $\mathbf{r} = \mathbf{r}_0$. The second term is the change of the conservative van der Waals force during vibration, given by

$$\mathbf{F}_{dc}(t) = \mathbf{u}(t) \cdot \frac{\mathrm{d}}{\mathrm{d}\mathbf{r}_0} \mathbf{F}_{st}(\mathbf{r}_0). \tag{8.45}$$

The last term in (8.44) determines the friction force:

$$\mathbf{F}_{fric}(t) = i\omega_0 \overleftrightarrow{\Gamma} \cdot \mathbf{u}(t) = -\overleftrightarrow{\Gamma} \cdot \dot{\mathbf{u}}(t). \tag{8.46}$$

Using results from Appendix I, for a particle moving parallel to the surface we get:

$$\Gamma_{\parallel} = \frac{2\hbar}{\pi}\int_0^{\infty} \mathrm{d}\omega\left(-\frac{\partial n}{\partial \omega}\right) \times$$
$$\times\left[\sum_{l=x,y,z}\left(\frac{\partial^2}{\partial x \partial x'}\mathrm{Im}D_{ll}(\mathbf{r},\mathbf{r}')\mathrm{Im}\frac{\alpha(\omega)}{1-\alpha(\omega)D_{ll}(\mathbf{r}_0,\mathbf{r}_0,\omega)}\right) -\right.$$
$$-2 \mid \alpha(\omega)\mid^2 \mathrm{Re}\left(\frac{1}{\left(1-\alpha^*(\omega)D^*_{zz}(\mathbf{r}_0,\mathbf{r}_0,\omega)\right)\left(1-\alpha(\omega)D_{xx}(\mathbf{r}_0,\mathbf{r}_0,\omega)\right)}\right)\times$$
$$\left.\times\left(\frac{\partial}{\partial x}\mathrm{Im}D_{xz}(\mathbf{r},\mathbf{r}_0)\right)^2\right]_{\substack{\mathbf{r}=\mathbf{r}_0\\ \mathbf{r}'=\mathbf{r}_0}}, \tag{8.47}$$

and for the motion normal to the surface we get

$$\Gamma_{\perp} = \frac{2\hbar}{\pi}\int_0^{\infty}\mathrm{d}\omega\left(-\frac{\partial n}{\partial\omega}\right)\sum_{l=x,y,z}\left\{\frac{\partial^2}{\partial z\partial z'}\left[\mathrm{Im}D_{ll}(\mathbf{r},\mathbf{r}',\omega)+\right.\right.$$
$$+\mathrm{Im}\left(\frac{\alpha(\omega)D_{ll}(\mathbf{r},\mathbf{r}_0,\omega)D_{ll}(\mathbf{r}',\mathbf{r}_0,\omega)}{1-\alpha(\omega)D_{ll}(\mathbf{r}_0,\mathbf{r}_0,\omega)}\right)\Bigg]\mathrm{Im}\frac{\alpha(\omega)}{1-\alpha(\omega)D_{ll}(\mathbf{r}_0,\mathbf{r}_0,\omega)}+$$
$$\left.+\left(\frac{\partial}{\partial z}\mathrm{Im}\left(\frac{\alpha(\omega)D_{ll}(\mathbf{r},\mathbf{r}_0,\omega)}{1-\alpha(\omega)D_{ll}(\mathbf{r}_0,\mathbf{r}_0,\omega)}\right)\right)^2\right\}_{\substack{\mathbf{r}=\mathbf{r}_0\\ \mathbf{r}'=\mathbf{r}_0}}. \tag{8.48}$$

8.4 Friction Force on Physisorbed Molecules

The sliding of lubricated surfaces has been studied for many years but the microscopic origin of the friction force is still not well understood. During sliding at low velocities, the lubrication fluid will be squeezed out from the contact areas between the two solids, but usually one or a few monolayers of lubrication molecules will be trapped between the surfaces (boundary lubrication). If the lateral corrugation of the adsorbate–substrate interaction potential is weak, as is typically the case for saturated hydrocarbons, then, during sliding, the molecules will slip relative to the surfaces. One important problem in sliding friction is to understand the origin and magnitude of the friction force acting on the individual molecules during slip. If the adsorbate velocity, V, is much smaller than the sound velocity and (for a metallic substrate) the Fermi velocity of the substrate, then the friction force acting on a molecule is proportional to the velocity

$$\mathbf{F} = -M\eta\mathbf{V}, \tag{8.49}$$

where M is the molecule mass and η is the friction coefficient. For insulating surfaces (e.g., most metal oxides), this atomic scale friction η can only be due to phonon emission, but on metallic surfaces, both phonon and electronic friction occur and the latter is connected with the energy transfer to the metal conduction electrons.

Information about the friction parameter η can be deduced from infrared spectroscopy and inelastic helium scattering measurements since η determines the linewidth of adsorbate vibrations if inhomogeneous broadening and pure dephasing processes can be neglected [205, 206]. Information about η can also be deduced from quartz crystal microbalance (QCM) measurements.

In the measurements by Krim et al. [238], one side of a quartz crystal was covered by a thin silver or gold film. When a voltage is applied to the crystal, it performs in-plane oscillations. If adsorbates are adsorbed on the metal film, the resulting mass load will decrease the resonance frequency of the QC oscillator. However, Krim et al. [238] also observed an increased damping of the QC oscillator that can only result if, due to the inertia force, the adsorbates slide relative to the metal surface. If the pinning by the corrugated substrate potential can be neglected, then, from the adsorbate-induced change in the resonance frequency and damping of the QC oscillator, one can deduce both the adsorbate concentration and the damping η. Finally, for metals, the electronic contribution to the friction η can be deduced from surface resistivity measurements [203, 239, 240]. In these measurements, the adsorbate-induced change ΔR of the resistivity of a thin metallic film is measured. It is easy to prove that $\Delta R \sim \eta$ by equalizing the ohmic energy dissipation with the frictional energy dissipation calculated in a reference frame moving with the drift velocity of the conductions electrons.

In this section, we estimate the electronic friction for inert adsorbates on metal surfaces. The metal is treated in the semi-infinite jellium model and the adsorbate–substrate interaction is assumed to consist of the long-range attractive van der Waals interaction plus a short-range repulsion, resulting from the overlap of the electron clouds of the adsorbate and the substrate. We also discuss the relative importance of the phononic and electronic friction for noble gas atoms and for saturated hydrocarbons adsorbed on metal surfaces.

In Sect. 8.4.1, the friction force acting on an adsorbed molecules is studied using the theory of Casimir friction. However, this theory considers only the interaction between molecule and substrate which can be described within the framework of the dielectric formalism. At small separations between molecule and substrate, other processes, which are not described by this formalism, become important. In contrast to Casimir friction, these higher-order processes give a non-vanishing, linear in the velocity, contribution to the friction at $T = 0\,\mathrm{K}$. The friction acting on physisorbed molecules, taking into account the high-order processes, was considered in [140, 241, 243]. It is well known that accurate results for the electron response of metal surfaces requires realistic model for the surface, i.e., the Lang–Kohn model. In early calculations [140, 241], very simple models were used, and the screening by the conduction electrons was neglected, and the accuracy of the results is not clear. The theory of friction of physisorbed molecules presented in Sect. 8.4.2 takes into account high-order processes and screening effects. In this theory, the friction is related to the surface response function for which accurate calculations exist; for example, using the time-dependent local density approximation.

8.4.1 Casimir Friction

The friction force acting on the moving molecule usually is written in the form

$$\mathbf{F} = -M\eta\mathbf{V}, \tag{8.50}$$

where M is the mass and η is the coefficient of friction. For a physisorbed molecule, we can neglect retardation effects. Formally, this corresponds to the limit $c \to \infty$ in the formulae for the Green's function in (8.47) and (8.48). In Appendix C, we show that in the non-retarded limit

$$D_{xx}(\mathbf{r}, \mathbf{r}') = \int \frac{\mathrm{d}^2 q}{2\pi} \frac{q_x^2}{q} R_p(\mathbf{q}, \omega) e^{\mathrm{i}\mathbf{q}(\mathbf{x}-\mathbf{x}')-q(z+z')}, \tag{8.51}$$

$$D_{yy}(\mathbf{r}, \mathbf{r}') = \int \frac{\mathrm{d}^2 q}{2\pi} \frac{q_y^2}{q} R_p(\mathbf{q}, \omega) e^{\mathrm{i}\mathbf{q}(\mathbf{x}-\mathbf{x}')-q(z+z')}, \tag{8.52}$$

$$D_{zz}(\mathbf{r}, \mathbf{r}') = \int \frac{\mathrm{d}^2 q}{2\pi} q R_p(\mathbf{q}, \omega) e^{\mathrm{i}\mathbf{q}(\mathbf{x}-\mathbf{x}')-q(z+z')}, \tag{8.53}$$

$$D_{xz}(\mathbf{r}, \mathbf{r}') = -\mathrm{i} \int \frac{\mathrm{d}^2 q}{2\pi} q_x R_p(\mathbf{q}, \omega) e^{\mathrm{i}\mathbf{q}(\mathbf{x}-\mathbf{x}')-q(z+z')}, \tag{8.54}$$

where R_p is the reflection amplitude for p-polarized electromagnetic waves. For physical adsorption, for most molecules, the imaginary part of molecule polarizability $\alpha(\omega)$ is non-vanishing vanish only for very high frequencies. Thus, for frequencies that can be excited by thermal radiation ($\omega \leq \omega_T = k_B T/\hbar$), $\mathrm{Im}\alpha \approx 0$. Then, to linear order in $\alpha(0) z_0^{-3}$, from (8.47), (8.48) we get

$$\eta_{\parallel} = \frac{\hbar\alpha^2(0)}{2\pi M} \int_0^{\infty} \mathrm{d}\omega \left(-\frac{\partial n}{\partial \omega}\right) \left[3 \frac{\partial^2}{\partial z^2} \mathrm{Im} D_{zz}(z, z_0) \mathrm{Im} D_{zz}(z_0, z_0) - \right.$$
$$\left. -2 \left(\frac{\partial}{\partial z} \mathrm{Im} D_{zz}(z, z_0) \right)^2 \right]_{z=z_0}, \tag{8.55}$$

$$\eta_{\perp} = \frac{3\hbar\alpha^2(0)}{\pi M} \int_0^{\infty} \mathrm{d}\omega \left(-\frac{\partial n}{\partial \omega}\right) \left[\frac{\partial^2}{\partial z^2} \mathrm{Im} D_{zz}(z, z_0) \mathrm{Im} D_{zz}(z_0, z_0) + \right.$$
$$\left. + \left(\frac{\partial}{\partial z} \mathrm{Im} D_{zz}(z, z_0) \right)^2 \right]_{z=z_0}. \tag{8.56}$$

For $z_0 < \min(l, \hbar v_F/k_B T)$, where l is the electron mean free path and v_F is the Fermi velocity, the reflection amplitude $R_p(\mathbf{q}, \omega)$ must be calculated using non-local optics. The non-local surface contribution to $\mathrm{Im}R_p$ is given by (6.25). Using this expression for $\mathrm{Im}R_p$ in (8.55) and (8.56), we get the surface contribution to the friction:

$$\eta_{\parallel surf} = 1.9\frac{\xi^2\hbar\alpha^2(0)}{Mz_0^8}\left(\frac{k_BT}{\hbar\omega_p}\right)^2\frac{1}{(k_Fz_0)^2} \tag{8.57}$$

and $\eta_{\perp surf} = 8.4\eta_{\parallel surf}$. From low energy electron diffraction studies, it is known that for physical adsorption of *Xe* on $Ag(111)$, the separation between the *Xe* nucleus and the jellium edge of $Ag(111)$ is $d = 2.4$ Å. The static polarizability of *Xe* is $\alpha(0) = 4.0$ Å^3 and $k_F = 1.9$ Å^{-1}. At room temperature, $k_BT/\hbar\omega_p \sim 10^{-3}$. Using (8.57), we get $\eta_\parallel \sim 10^2\,\mathrm{s}^{-1}$ and $\eta_\perp \sim 10^3\,\mathrm{s}^{-1}$. These values are a factor $\sim 10^{-6}$ smaller than estimations obtained in [242] in the framework of a model taking into account the (Pauli) repulsion of the conduction electrons from region occupied by molecule. This means that, in the case of physisorption on normal metals, the friction is determined by higher order processes that are not considered in the present theory. The calculation of friction force taking into account these processes is given in Sect. 8.4.2.

In the case of physisorption on high-resistivity material, we can neglect non-local effects and use a local optic expression for reflection factor

$$R_p = \frac{\varepsilon(\omega) - 1}{\varepsilon(\omega) + 1}, \tag{8.58}$$

and the Green's function is given by

$$D_{zz}(z, z') = \frac{\varepsilon(\omega) - 1}{\varepsilon(\omega) + 1}\frac{2}{(z + z')^3}. \tag{8.59}$$

As an example we consider adsorption of a molecule on SiC. For this case, dielectric function $\varepsilon(\omega)$ is determined by (6.34). Using (8.55), (8.56) and (8.59) for adsorption of a molecule on SiC, in the resonance approximation (see Sect. 6.3) we get

$$\eta_\parallel = \frac{9}{128}\frac{\hbar\alpha^2(0)}{Mz_0^8}\frac{\hbar\omega_a}{k_BT}\frac{1}{\sinh^2(\hbar\omega_0/2k_BT)} \tag{8.60}$$

and $\eta_\perp = 7\eta_\parallel$. For parameters, corresponding to *Xe* (see above) on SiC (see Sect. 6.3) $\eta_\parallel \sim 4.6 \times 10^5\,\mathrm{s}^{-1}$ and $\eta_\perp \sim 3.2 \times 10^6\,\mathrm{s}^{-1}$. Thus, for physical adsorption on semiconductors and dielectrics surfaces, Casimir friction can be many orders of magnitude larger than on metal surfaces. Another possible mechanism of friction on dielectrics is related to the emission of substrate phonons (see Chap. 15). In the case of flat surfaces for the parallel motion of a particle, the effectiveness of this mechanism will be low, and the main mechanism will be determined by Casimir friction.

8.4.2 High-Order Processes

Consider a neutral molecule outside a metal surface. Let $\hat{\mu}$ be the dipole moment operator of the molecule. In the dipole approximation, the molecule–metal interaction Hamiltonian has the form

$$H' = -\hat{\mu} \cdot \nabla \int d^3x' \frac{\hat{\rho}(\mathbf{x}')}{|\mathbf{x_a} - \mathbf{x}'|}, \tag{8.61}$$

where $\rho(\mathbf{x}')$ is the charge density operator of the metal electrons and $\mathbf{x_a}$ is the ion-core position of the molecule. Instead of calculating the friction force on a uniformly moving adsorbate, it is more convenient to consider an oscillating adsorbate (both treatments give identical results). Let us write $\mathbf{x}_a = \mathbf{x}_0 + Q_0\mathbf{e}(b + b^+)$, where $Q_0 = (\hbar/2M\omega)^{1/2}$, b and b^+ are the annihilation and creation operators for the oscillator. The direction $\mathbf{e}$ of the oscillation will be taken to be $\hat{\mathbf{z}}$ or $\hat{\mathbf{x}}$, where (x, y, z) is a coordinate system with the z-axis normal to the surface, and the positive z direction pointing away from the metal. Expanding (8.61) to linear order in Q_0 gives

$$H' = -\hat{\mu} \cdot \nabla \int d^3x' \frac{\hat{\rho}(\mathbf{x}')}{|\mathbf{x_0} - \mathbf{x}'|} -$$

$$- \hat{\mu} \cdot \nabla \mathbf{e} \cdot \nabla \int d^3x' \frac{\hat{\rho}(\mathbf{x}')}{|\mathbf{x}_0 - \mathbf{x}'|} Q_0(b + b^+). \tag{8.62}$$

Using expansion in 2D integral Fourier at $(z_0 - z) > 0$

$$\frac{1}{|\mathbf{x_0} - \mathbf{x}|} = \int \frac{d^2q}{2\pi q} e^{i\mathbf{K}\cdot(\mathbf{x}-\mathbf{x_0})},$$

where $\mathbf{K} = \mathbf{q} - iq\hat{\mathbf{z}}$, and $\mathbf{q} = (q_x, q_y)$, (8.62) can be transformed to

$$H' = \mu_i \int d^3x \hat{\rho}(\mathbf{x}) V_i(\mathbf{x}) + \mu_i e_j \int d^3x \hat{\rho}(\mathbf{x}) V_{ij}(\mathbf{x}) Q_0(b + b^+), \tag{8.63}$$

where

$$V_i(\mathbf{x}) = \int \frac{d^2q}{2\pi q} K_i e^{i\mathbf{K}\cdot(\mathbf{x}-\mathbf{x}_0)}, \tag{8.64}$$

$$V_{ij}(\mathbf{x}) = \int \frac{d^2q}{2\pi q} K_i K_j e^{i\mathbf{K}\cdot(\mathbf{x}-\mathbf{x}_0)}. \tag{8.65}$$

Now, assume that the molecule is in its electronic ground state $|A\rangle$, and the oscillator is in its first vibrational excited state ($n = 1$). Consider the decay rate w from $n = 1 \to n = 0$. Since $\langle A|\hat{\mu}|A\rangle = 0$, we must go to the second order in perturbation theory when calculating w:

$$w = \frac{2\pi}{\hbar} \sum_f \left| \left\langle A, f, n = 0 \middle| H' \frac{1}{H_0 - E_0} H' \middle| A, i, n = 1 \right\rangle \right|^2 \delta(E_f - E_i - \hbar\omega), \tag{8.66}$$

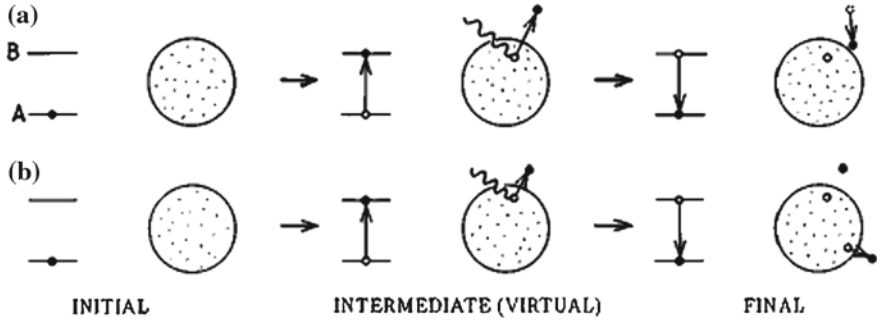

Fig. 8.3 Elementary processes involved in the damping of the adsorbate vibration: **a** A process that results in a one electron-hole pair. This process is taken into account in the theory of Casimir friction. **b** The process that results in two electron-hole pairs, this process is not taken into account in the theory of Casimir friction

where $E_0 = E_A + E_i + \hbar\omega$ is the initial energy and where $|f\rangle$ and $|i\rangle$ denote the final and initial states of the metal. Now, two final states are possible for the metal, namely with (a) one or (b) two electron-hole pair excitations, as indicated in Fig. 8.3.

Processes (a) can be described in the framework of the dielectric formalism and are taken into account with the theory of Casimir friction (see Sect. 8.4.1). As shown in Sect. 8.4.1, the contribution to the friction from this process vanishes at zero temperature. Processes (b) are not taken into account in the theory of Casimir friction. However, as will be shown below, at short separations, these processes can give a larger contribution to friction than the Casimir friction. Due to the fact that the transitions from the initial state $|i\rangle$ to the final state $|f\rangle$ in Fig. 8.3 proceed in two steps, the interaction

$$\hat{V} = H' \frac{1}{H_0 - E_0} H'$$

is non-local. However, we can formally define an effective local potential $V_{eff}(\mathbf{x})$ in such a way that the matrix element $M_{if} = e\langle|V_{eff}(\mathbf{x})|\rangle$ equals the matrix element associated with the two-step process:

$$M_{if} = \left\langle f \left| \left\langle A, n=0 \left| H' \frac{1}{H_0 - E_0} H' \right| A, n=1 \right\rangle \right| i \right\rangle. \tag{8.67}$$

If we assume that $\omega_a \gg \omega_p$, where $\hbar\omega_a = E_B - E_A$ is the energy of the virtual atomic transition and ω_p is the metal plasma frequency, we can neglect the screening during the electronic transitions $kA \to k''B \to k'A$, in Fig. 8.3. This follows from the fact that when $\omega_a \gg \omega_p$ the electrons in the metal have no time to follow the rapidly changing potential during such a virtual transition. On the other hand, the system stays a long time in the final state and screening in this state is important. Substituting (8.66) in (8.67) and neglecting screening effects during the rapid transitions, and assuming $|\epsilon_F - \epsilon_{k''}| \ll \hbar\omega_a$, gives

$$M_{fi} = \frac{1}{2}\alpha_{ij}(0)e^2 \int d^3x d^3x' \varphi_k(\mathbf{x})\varphi^*_{k'}(\mathbf{x}')\Psi(\mathbf{x},\mathbf{x}')\times$$

$$\times \left[V_i(\mathbf{x})V_{jl}(\mathbf{x}') + V_i(\mathbf{x}')V_{jl}(\mathbf{x})\right]e_l, \tag{8.68}$$

where φ_k, $\varphi_{k'}$, $\varphi_{k''}$ are the wave functions of the electron in the initial, final and intermediate states, respectively. The function

$$\Psi(\mathbf{x},\mathbf{x}') = \sum_{k''}(1-2n_{k''})\varphi_{k''}(\mathbf{x})\varphi^*_{k''}(\mathbf{x}'), \tag{8.69}$$

where $n_{k''}$ is the Fermi distribution function ($n_k = 1$, for $k < k_F$, and zero otherwise). The static polarizability for spherical molecule $\alpha_{ij}(0) = \alpha(0)\delta_{ij}$, where

$$\alpha(0) = 2\sum_B \frac{\left|\langle B|\hat{\mu}_x|A\rangle\right|^2}{E_B - E_A}. \tag{8.70}$$

Now, let us consider the function $\Psi(\mathbf{x},\mathbf{x}')$. The second part of (8.69) includes summation over occupied states and this function is only significant for $z, z' < 0$ where $z = 0$ corresponds to the jellium edge. On the other hand, the product $V_i(\mathbf{x})V_{jl}(\mathbf{x}')$ is rather small in this region of space due to the rapid decay of this function with increasing distance from the the jellium edge. In this region, we can neglect the second term in (8.69) to get

$$\Psi(\mathbf{x},\mathbf{x}') \approx \sum_{k''}\varphi_{k''}(\mathbf{x})\varphi^*_{k''}(\mathbf{x}') = \delta(\mathbf{x}-\mathbf{x}'). \tag{8.71}$$

The matrix element (8.68) can now be written as

$$M_{fi} = \alpha(0)e^2 \int d^3x \varphi_k(\mathbf{x})\varphi^*_{k'}(\mathbf{x})V_i(\mathbf{x})V_{il}(\mathbf{x})e_l. \tag{8.72}$$

so that

$$V_{eff}(\mathbf{x}) = \alpha(0)eV_i(\mathbf{x})V_{il}(\mathbf{x})e_l. \tag{8.73}$$

With this effective potential, according to the Kubo formula, the friction coefficient is given by [205, 206]

$$\eta = \frac{e^2}{M\omega}\int d^3x d^3x' V_{eff}(\mathbf{x})\mathrm{Im}\chi(\mathbf{x},\mathbf{x}',\omega)V_{eff}(\mathbf{x}'), \tag{8.74}$$

where χ is the density–density correlation function

$$\chi = \frac{i}{\hbar}\int_0^\infty dt e^{i\omega t}\langle\left[\hat{\rho}(\mathbf{x},t),\hat{\rho}(\mathbf{x}',0)\right]\rangle. \tag{8.75}$$

In order to relate η to the reflection amplitude $R_p(q,\omega)$, we must expand V_{eff} in evanescent plane waves. Such an expansion is exact only in a region of space where the function to be expanded satisfies the Laplace equation. In the present case, V_{eff} does not satisfy the Laplace equation anywhere, but in the surface region of the metal it is nevertheless possible to approximate this function accurately with a sum of evanescent plane waves (see Appendix L). We get

$$V_{eff} \approx \int \frac{d^2q}{(2\pi)^2} V_{\mathbf{q}} e^{i\mathbf{q}\cdot\mathbf{x}_\parallel + qz}, \tag{8.76}$$

where

$$V_{\mathbf{q}} = 2q\int d^3x V_{eff} e^{-i\mathbf{q}\cdot\mathbf{x}_\parallel + qz}.$$

Using (8.64), (8.65) and (8.73),we get

$$V_{\mathbf{q}} = 2i\alpha(0)e\int d^2q' \frac{qK_i'K_i''K_j''e_j}{q'q''(q+q'+q'')} e^{-i(q'+q'')z_0}, \tag{8.77}$$

where $\mathbf{q}'' = \mathbf{q} - \mathbf{q}'$, $\mathbf{K}' = \mathbf{q}' - iq'\hat{z}$ $\mathbf{K}'' = \mathbf{q}'' - iq''\hat{z}$. Using (8.76) in (8.74), we get

$$\eta = \frac{e^2}{M\omega}\int \frac{d^2q}{(2\pi)^2}\int dzdz' \left|V_{\mathbf{q}}\right|^2 e^{qz+qz'} \mathrm{Im}\chi(\mathbf{q},z,z',\omega). \tag{8.78}$$

According to the linear response theory, in the non-retarded limit, reflection amplitudes for p-polarized evanescent waves can be written in the form [244]

$$R_p(\mathbf{q},\omega) = \frac{2\pi}{q}\int dzdz' e^{qz+qz'}\chi(\mathbf{q},z,z',\omega). \tag{8.79}$$

From (8.78) and (8.79) we get

$$\eta = \frac{e^2}{2\pi M\omega}\int \frac{d^2q}{(2\pi)^2}\left|V_{\mathbf{q}}\right|^2 q\mathrm{Im}R_p(q,\omega) =$$

$$= \frac{e^2\alpha^2(0)}{\pi^2 M\omega}\int d^2q q^3 \left|\int d^2q' \frac{\mathbf{K}'\cdot\mathbf{K}''\mathbf{K}''\cdot\mathbf{e}}{q'q''(q+q'+q'')} e^{-(q'+q'')z_0}\right|^2 \mathrm{Im}R_p(q,\omega). \tag{8.80}$$

At low frequencies, we have (see [245])

$$\mathrm{Im}R_p(q,\omega) = 2\omega q\xi(q)/k_F\omega_p,$$

and (8.80) becomes

$$\eta = \frac{2e^2\alpha^2(0)}{\pi^2 M k_F\omega_p}\int d^2q q^4\xi(q)\left|\int d^2q' \frac{\mathbf{K}'\cdot\mathbf{K}''\mathbf{K}''\cdot\mathbf{e}}{q'q''(q+q'+q'')}e^{-(q'+q'')z_0}\right|^2. \tag{8.81}$$

For $\mathbf{e} = \hat{x}$

$$\eta_\parallel = \frac{e^2}{\hbar a_0}\frac{\left[k_F^3\alpha(0)\right]^2}{(k_F z_0)^{10}}\frac{m}{M}\frac{\omega_F}{\omega_p}k_F a_0 I_\parallel, \tag{8.82}$$

where

$$I_\parallel = z_0^{10}\frac{4}{\pi^2}\int d^2q q^4\xi(q)\left|\int d^2q' \frac{(\mathbf{q}'\cdot\mathbf{q}'' - q'q'')(q_x - q'_x)}{q'|\mathbf{q}-\mathbf{q}'|(q+q'+|\mathbf{q}-\mathbf{q}'|)}e^{-\{q'+|\mathbf{q}-\mathbf{q}'|\}z_0}\right|^2,$$

and for $\mathbf{e} = \hat{z}$

$$\eta_\parallel = \frac{e^2}{\hbar a_0}\frac{\left[k_F^3\alpha(0)\right]^2}{(k_F z_0)^{10}}\frac{m}{M}\frac{\omega_F}{\omega_p}k_F a_0 I_\perp, \tag{8.83}$$

where

$$I_\perp = z_0^{10}\frac{4}{\pi^2}\int d^2q q^4\xi(q)\left|\int d^2q' \frac{(\mathbf{q}'\cdot\mathbf{q}'' - q'q'')}{q'(q+q'+|\mathbf{q}-\mathbf{q}'|)}e^{-\{q'+|\mathbf{q}-\mathbf{q}'|\}z_0}\right|^2.$$

In (8.82) and (8.83), a_0 is the Bohr radius and k_F the Fermi wave vector. The function $\xi(q)$ has been calculated using the time-dependent local density approximation (TDLDA). The numerical results [246] are accurately approximated by

$$\xi \approx \xi_0/\left[1 + a(q/k_F)^3\right], \tag{8.84}$$

where $(xi_0, a) = (0.89, 6.25)$ and $(0.43, 2.49$ for $r_s = 2$ and 3, respectively. Using (8.82) and (8.83), the integrals $I_\parallel$ and $I_\perp$ have been calculated numerically [243] and the results are displayed in Fig. 8.4 as a function of $k_F z_0$ where z_0 is the distance between the nucleus.

8.4.3 Comparison of the Theory with Experiment

For inert atoms and molecules adsorbed on metal surfaces, one can (approximately) distinguish between two contributions to the electronic friction associated with (a) the long-ranged attractive van der Waals interaction and (b) the short-ranged Pauli

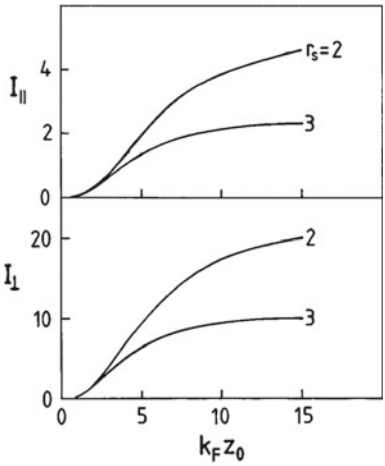

Fig. 8.4 Frictional integrals $I_{\parallel}$ and $I_{\perp}$ (defined in the text) as a function of $k_F z_0$, where z_0 is the distance of the center of the adsorbate from the jellium edge of the substrate. r_s is Wigner–Zeitz radius in atomic units

repulsion associated with the overlap of the electron clouds of the adsorbate and the substrate. The latter contribution to $\eta_{\parallel}$ has, for *Xe* on $Ag(111)$, been estimated [242] to be $\approx 6 \times 10^7\,\mathrm{s}^{-1}$, and will now be compared with the contribution from the van der Waals friction. From low-energy electron diffraction studies, it is known that the separation between the *Xe* nucleus and the jellium edge of $Ag(111)$ is $d = 2.4$ Å. The static polarizability of *Xe* is $\alpha(0) = 4.0$ Å^3. From (8.82), the contribution to $\eta_{\parallel}$ from the van der Waals interaction is estimated to be $\eta_{\parallel} \approx 4 \times 10^7\,\mathrm{s}^{-1}$, i.e., only 30 % smaller than that associated with the Pauli repulsion. The fact that the two contributions are of a similar magnitude is probably related to the fact that at the equilibrium separation, the attractive and repulsive adsorbate–substrate interactions are of identical magnitude, which should result in dissipative forces of similar magnitudes.

The electronic friction for *Xe* on $Ag(111)$ can be deduced from surface resistivity [247] data, $\eta_{\parallel} \sim 3 \times 10^8\,\mathrm{s}^{-1}$. This value is only a factor of three larger than estimated above, but it is likely that a non-negligible contribution to the electronic friction comes from 'chemical' effects, namely from the fact that the Xe-6s electronic resonance state is located around the vacuum energy [248] with a tail extending down to the Fermi energy. In [242], the chemical contribution to $\eta_{\parallel}$ was estimated to be $\sim 1.5 \times 10^8\,\mathrm{s}^{-1}$. For the lighter noble gas atoms and for saturated hydrocarbonates, chemical effects should be negligible since no electronic resonance states occur close to the Fermi energy. An example is C_2H_6, for which surface resistivity data gives [239, 240] $\eta \sim 3 \times 10^8\,\mathrm{s}^{-1}$. Since C_2H_6 has almost the same binding energy as *Xe*, and since the effective Lennard-Jones radius of C_2H_6 is practically identical to that of *Xe*, the theoretical $\eta_{\parallel}$, derived above for *Xe* should also be valid for C_2H_6 when scaled by the mass ratio $M(Xe)/M(C_2H_4) = 4.4$. This gives the electronic friction $\eta_{\parallel} \sim 4 \times 10^8\,\mathrm{s}^{-1}$, which is in good agreement with surface resistivity data.

Many lubrication fluids consist of long-chain hydrocarbons but very little experimental data relevant for sliding friction is available for such molecules adsorbed on metallic surfaces. However, Witte and Wöll [249] have performed inelastic He-atom

Table 8.1 Resonance frequencies and damping (full width at half-maximum) of the vibrational modes (frustrated translations) normal to the surface for hydrocarbons physisorbed on Cu(100). The calculated damping rates are obtained from (8.85) using the observed resonance frequencies. Experimental data are from [249]

Molecule	$\omega_\perp$(meV)	γ_{exp}(meV)	γ_{theory}(meV)
n-hexan	6.8	1.4	1.2
n-octane	7.0	1.2	1.7
n-decane	7.0	1.9	2.2
Cyclohaxane	7.3	2.2	1.5

scattering from the saturated hydrocarbons n-hexane, n-octane, n-decane, and cyclohexane adsorbed on Cu(100). The perpendicular vibrations of all these molecules was found to be $\hbar\omega_\perp \approx 7$ meV. In the most simple interaction model between a physisorbed molecule and a metal surface, the interaction strength, and the force constant, are proportional to $\alpha(0)$. Therefore the perpendicular vibrational energies should be proportional to $\sqrt{\alpha(0)/M}$. Witte and Wöll have shown that $\sqrt{\alpha(0)/M}$ is almost equal for all the saturated hydrocarbons given above, indicating that, as expected, all these molecules are physisorbed on Cu(100). In Table 8.1, we have summarized the observed linewidth γ of the perpendicular adsorbate vibrations. Assuming that the linewidth is due to energy relaxation, one can deduce the friction $\hbar\eta_\perp = \gamma$. This gives $\eta_\perp \sim 2 \times 10^{12}\,\mathrm{s}^{-1}$ for the systems quoted in Table 8.1. The large magnitudes of the frictions quoted in Table 8.1 cannot be explained as resulting from the electronic contribution which gives $(\eta_\perp)_{el} \sim 1 \times 10^9\,\mathrm{s}^{-1}$, i.e., roughly three orders of magnitude smaller than the observed friction. When $\omega_\parallel \ll \omega_D$ (where $\omega_D \approx 30$ is the Debye frequency), the phononic friction is accurately given by [250]

$$\gamma_\perp = \frac{3}{8\pi}\frac{M}{\rho}\left(\frac{\omega_\perp}{c_t}\right)^3 \omega_\perp, \tag{8.85}$$

where c_t is the transverse sound velocity and ρ the mass density. The friction values calculated from this formula are in close agreement with experiment, see Table 8.1. The reason for the importance of the phonon friction in these cases is the relative high frequency of the perpendicular vibrational modes (note that: $\eta_{ph} \sim \omega_\perp^4$) while the electronic friction η_{el} is independent of the resonance frequency $\omega_\perp$ of the adsorbate vibration). Witte and Wöll could not detect any adsorbate vibrations parallel to the surfaces, which indicates that these modes have a frequency that is too low frequency ($\hbar\omega_\parallel < 0.3$ meV), to be detected with the resolution of the He-atom equipment. Using the formula for the phononic friction,

$$\gamma_\parallel = \frac{3}{8\pi}\frac{M}{\rho}\left(\frac{\omega_\parallel}{c_t}\right)^3 \omega_\parallel, \tag{8.86}$$

gives $\eta_{\parallel} < 8 \times 10^6\,\mathrm{s}^{-1}$. This should be compared with the calculated electronic friction $(\eta_{\parallel})_{el} \sim 3 \times 10^8\,\mathrm{s}^{-1}$. Hence, the parallel friction is mainly of electronic origin.

8.5 Force on a Particle in a Thermal Field

8.5.1 The Case of Small Velocities

Casimir friction also occurs when a particle moves relative to black-body radiation; for example, relative to the walls of an oven, or relative to the cosmic microwave background. This kind of friction has no position dependence, i.e. it is spatially homogeneous. The consequence is a universal dissipative drag acting on all matter in relative motion with respect to a thermalized photon gas. To calculate this universal drag to linear order in velocity, we can use the same approach as in Sect. 8.3. Assuming that the size of the particle is smaller than λ_T, we get the friction coefficient for a particle moving relative to black-body radiation.

$$\Gamma^{BB} = \frac{2\hbar}{\pi}\int_0^\infty d\omega\left(-\frac{\partial n}{\partial\omega}\right)\sum_{k=x,y,z}\mathrm{Im}\alpha_{kk}\frac{\partial^2}{\partial x\partial x'}\mathrm{Im}D_{kk}^{BB}(\mathbf{r},\mathbf{r}',\omega)\Big|_{\mathbf{r}=\mathbf{r}'}, \tag{8.87}$$

where α_{kk} is the polarizability of the particle, and $D_{kk}^{BB}(\mathbf{r},\mathbf{r}',\omega)$ is the Green's function of the black-body radiation. For a spherical particle $\alpha_{kk} = \alpha$, and using the formula (see [107] and also Sect. 3.1.2)

$$\sum_{k=x,y,z} D_{kk}^{BB}(\mathbf{r},\mathbf{r}',\omega) = 2\left\{\frac{\omega^2}{c^2}\frac{1}{|\mathbf{r}-\mathbf{r}'|}\exp\left(\frac{i\omega}{c}|\mathbf{r}-\mathbf{r}'|\right) - 2\pi\delta(\mathbf{r}-\mathbf{r}')\right\}, \tag{8.88}$$

we get

$$\Gamma^{BB} = \frac{\beta\hbar^2}{3\pi c^5}\int_0^\infty d\omega\frac{\omega^5\mathrm{Im}\alpha(\omega)}{\sinh^2\left(\frac{1}{2}\beta\hbar\omega\right)}, \tag{8.89}$$

where $\beta^{-1} = k_B T$. Equation (8.124) was first obtained in [157] using a different approach. The photon gas exerts a drag on any polarizable particle that moves with respect to the reference frame in which the photon gas is thermalized, and this drag is proportional to the relative velocity.

Tungsten ovens can operate at temperatures as high as 3000 K. If a beam of atoms, ions or molecules passes through such an oven, it will be subject to drag due to the Casimir friction mediated by the thermal radiation. For an atom or molecule, the polarizability α can be characterized by a single absorption line at $\omega = \omega_0$. In this case, $\mathrm{Im}\alpha(\omega) = \alpha_0\delta(\omega/\omega_0 - 1)$, where α_0 is the static polarizability at $\omega = 0$.

Setting $m/\tau = \Gamma^{BB}$, where m is the mass of the molecule and τ is the relaxation time, gives

$$\tau = \frac{3\pi mc^5\hbar^4}{2^6\alpha_0(k_BT)^5}\frac{\sinh^2(x)}{x^6}, \tag{8.90}$$

where $x = \beta\hbar\omega_0/2$. The relaxation time has a minimum at a temperature-dependent frequency that coincides with the minimum of the function $f(x) = \sinh^2(x)/x^6$, at $x_m = 2.98$, where $f(x_m) = 0.137$. Ba^+ has a resonance near 2 eV, which is approximately six times the thermal energy associated with a 3000 K oven. For this resonance, the relaxation time would be near the minimum, and for the ion polarizability $\alpha_0 \approx 1.0 \times 10^{-30}$ m^3, one obtains the relaxation time $\approx 10^5$ s, i.e. 1 day. This relaxation time can be measured using ion traps.

For the cosmos, it is believed that hydrogen atoms condensed from protons and electrons when the radiation cooled to approximately 3000 K, and that the coupling of the cosmic radiation to matter due to Compton scattering becomes ineffective below this condensation temperature [251]. However atoms, ions, and molecules with absorption in the appropriate frequency range should remain coupled to the cosmic radiation as its temperature drops from 3000 K to perhaps 300 K. This coupling could influence the structure and anisotropies observed in recent experiments on the cosmic microwave background [252]. It could also influence the behavior of molecules formed from the residue of novas and supernovas, and then subject to drag from a still hot cosmic microwave (i.e. electromagnetic) background. At much lower temperatures, macroscopic bodies can coalesce, in which geometrically determined resonances may become relevant.

8.5.2 Relativistic Case

We introduce two reference frames, K and K'. K is the frame of black-body radiation, and K' moves with velocity V along the x axis. In the K' frame a particle moves with time-dependent velocity $v' \ll V$ along the x-axis. In the K' frame, we assume the velocity vanishes at $t = t_0$, $v'(t_0) = 0$. However, since $v' \ll V$, the difference between the friction forces in the K' frame and the particle rest reference frame can be neglected, and in this section the K' frame is denoted as the particle rest reference frame. The relation between the x components of the momentum in the different reference frames is given by

$$p_x = (p'_x + \beta E'/c)\gamma, \tag{8.91}$$

where $\beta = V/c$, $\gamma = 1/\sqrt{1-\beta^2}$, $E' = E_0/\sqrt{1-(v'/c)^2}$ is the total energy of a particle in the K' frame, and $E_0 = m_0c^2$ is the rest energy of a particle. The rest energy can change due to the absorption and emission of thermal radiation by a particle. The connection between forces in the K and K' frames follows from (8.91)

$$\frac{dp_x}{dt} = \frac{1}{1 + (Vv'/c^2)}\left[\frac{dp'_x}{dt'} + V\frac{dm_0}{dt'}\frac{1}{\sqrt{1-(v'/c)^2}} + m_0 V\frac{d}{dt'}\left(\frac{1}{\sqrt{1-(v'/c)^2}}\right)\right]. \tag{8.92}$$

For $v' \ll V$ from (8.92) we get

$$F_x = F'_x + V\frac{dm_0}{dt'}, \tag{8.93}$$

where F_x and F'_x are the forces in the K and K' frames, respectively. The last term in (8.93) determines the rate of change of the momentum of a particle in the K frame due to the change of its rest mass as a result of the absorption and emission of radiation by the particle. Taking into account that at $v' \ll V$

$$\frac{dp_x}{dt} = \frac{d}{dt}\left(\frac{m_0 v}{\sqrt{1-(v/c)^2}}\right) = \frac{dm_0}{dt'}V + m_0\gamma^3\frac{dv}{dt}, \tag{8.94}$$

from (8.93) we get

$$m_0\gamma^3\frac{dv}{dt} = \frac{dp'_x}{dt'} = F'_x, \tag{8.95}$$

where v is the velocity of a particle in the K frame. From (8.95) it follows that acceleration in the K frame is determined by the friction force in the K' frame.

A particle will move with a constant velocity ($v = \text{const}$) if an external force f_x is applied to it such that

$$\gamma V\frac{dm_0}{dt} = F_x + f_x. \tag{8.96}$$

If the force f_x does not change the rest mass of a particle, then its value is the same in the K and K' frames, i.e., $f_x = f'_x$. In this case

$$f_x = -F_x + \gamma V\frac{dm_0}{dt} = -F_x + \frac{dm_0}{dt'}V = -F'_x. \tag{8.97}$$

Thus, for uniform motion of a particle, an external force must be applied which is equal, but opposite in sign, to the friction force acting on the particle in the K' frame.

In the K'-reference frame, the Lorenz force on the particle is determined by the expression

$$F'_x = \int d^3\mathbf{r}'\left\langle\rho' E'^*_x\right\rangle + \frac{1}{c}\int d^3\mathbf{r}'\left\langle\left[\mathbf{j}' \times \mathbf{B}'^*\right]_x\right\rangle, \tag{8.98}$$

where $\mathbf{E}'$ and $\mathbf{B}'$ are the electric and induction field, respectively, and ρ' and $\mathbf{j}'$ are the charge and current densities of the particle, respectively, which can be written in the form

$$\rho' = -\nabla' \cdot \mathbf{P}', \tag{8.99}$$

$\mathbf{j}' = \mathbf{j}'_d + \mathbf{j}'_m$, where

$$\mathbf{j}'_d = \frac{\partial \mathbf{P}'}{\partial t'} \tag{8.100}$$

$$\mathbf{j}'_m = c[\nabla' \times \mathbf{M}'], \tag{8.101}$$

where $\mathbf{P}'$ and $\mathbf{M}'$ are the vectors of polarization and magnetization, respectively. For the point particle

$$\mathbf{P}' = \mathbf{p}'_d \delta(\mathbf{r}' - \mathbf{r}'_0), \tag{8.102}$$

$$\mathbf{M} = \mathbf{p}'_m \delta(\mathbf{r}' - \mathbf{r}'_0), \tag{8.103}$$

where $\mathbf{p}'_d$ and $\mathbf{p}'_m$ are the dipole and magnetic moments, respectively. The force that acts on the particle, can be written in the form $F'_x = F'_{xd} + F'_{xm}$, where F'_{xd} and F'_{xm} are the forces, which act on the dipole and magnetic moments, respectively. Taking into account (8.99) and (8.100) the force, acting on the dipole, can be written in the form

$$F'_{xd} = -\int d^3\mathbf{r}' \langle \nabla \cdot \mathbf{P}' E'^*_x \rangle + \frac{1}{c} \int d^3\mathbf{r}' \left\langle \left[\frac{\partial \mathbf{P}'}{\partial t} \times \mathbf{B}'^* \right]_x \right\rangle. \tag{8.104}$$

The integrand in the second term in (8.104) can be written as

$$\left\langle \left[\frac{\partial \mathbf{P}'}{\partial t} \times \mathbf{B}'^* \right]_x \right\rangle = \frac{\partial}{\partial t'} \left\langle \left[\mathbf{P}' \times \mathbf{B}'^* \right]_x \right\rangle - \left\langle \left[\mathbf{P}' \times \frac{\partial \mathbf{B}'^*}{\partial t'} \right]_x \right\rangle. \tag{8.105}$$

Due to homogeneity of time, the first term in (8.105) is equal to zero, and taking into account the Maxwell's equation

$$\nabla' \times \mathbf{E}' = -\frac{1}{c} \frac{\partial \mathbf{B}'}{\partial t'}, \tag{8.106}$$

the second term can be written in the form

$$-\left\langle \left[\mathbf{P}' \times \frac{\partial \mathbf{B}'^*}{\partial t'} \right]_x \right\rangle = \left\langle \left[\mathbf{P}' \times [\nabla \times \mathbf{E}'] \right]_x \right\rangle. \tag{8.107}$$

After substitution of (8.107) in (8.104) and integration we get

$$F'_{xd} = \langle \mathbf{p}'_\mathbf{d} \cdot \nabla' E'^*_x \rangle_{\mathbf{r}'=\mathbf{r}'_0} + \langle [\mathbf{p}'_d \times [\nabla' \times \mathbf{E}'^*]]_x \rangle_{\mathbf{r}'=\mathbf{r}'_0}. \tag{8.108}$$

Taking into account the vector equality

$$\left[\mathbf{p}'_d \times \left[\nabla' \times \mathbf{E}'^* \right] \right] = \nabla' (\mathbf{p}'_\mathbf{d} \cdot \mathbf{E}'^*) - (\mathbf{p}'_\mathbf{d} \cdot \nabla') \mathbf{E}'^* \tag{8.109}$$

we get

$$F'_{xd} = \frac{\partial}{\partial x'}\left\langle \mathbf{p}'_{\mathbf{d}} \cdot \mathbf{E}'^{*} \right\rangle_{\mathbf{r}'=\mathbf{r}'_0}. \tag{8.110}$$

To calculate F_{xm} we use vector equality

$$\left[\left[\nabla \times \mathbf{M}'\right] \times \mathbf{B}'^{*}\right]_x = -\left(\frac{\partial \mathbf{M}'}{\partial x'} \cdot \mathbf{B}'^{*}\right) + (\mathbf{B}'^{*} \cdot \nabla')M'_x. \tag{8.111}$$

Integrating (8.111) over the particle volume and taking into account that $\nabla' \cdot \mathbf{B}' = 0$, we get

$$F_{xm} = \int d^3x' \left\langle \left[\left[\nabla' \times \mathbf{M}'\right] \times \mathbf{B}'^{*}\right]_x \right\rangle = \frac{\partial}{\partial x'}\left\langle \left(\mathbf{p}'_{\mathbf{m}} \cdot \mathbf{B}'^{*}\right) \right\rangle_{\mathbf{r}'=\mathbf{r}'_0}. \tag{8.112}$$

After summation of the contributions due to interaction of the electromagnetic field with the dipole and magnetic moments of the particle, we get

$$F'_x = \frac{\partial}{\partial x'}\left\langle \mathbf{p}'_{\mathbf{e}} \cdot \mathbf{E}'^{*}(\mathbf{r}') \right\rangle_{\mathbf{r}'=\mathbf{r}'_0} + \frac{\partial}{\partial x'}\left\langle \mathbf{p}'_{\mathbf{m}} \cdot \mathbf{B}'^{*}(\mathbf{r}') \right\rangle_{\mathbf{r}'=\mathbf{r}'_0}, \tag{8.113}$$

where, according to the fluctuation electrodynamics, $\mathbf{d}'_{e(m)} = \mathbf{d}^{f'}_{e(m)} + \mathbf{d}^{in'}_{e(m)}$, $\mathbf{E}' = \mathbf{E}^{f'} + \mathbf{E}^{in'}$, $\mathbf{B}' = \mathbf{B}^{f'} + \mathbf{B}^{in'}$, where $\mathbf{d}^{f'}_{e(m)}$ and $\mathbf{E}^{f'}(\mathbf{B}^{f'})$ are the fluctuating dipole (magnetic) moment of a particle and the electric (induction) field of the black-body radiation, and $\mathbf{d}^{in'}_{e(m)}$ and $\mathbf{E}^{in'}(\mathbf{E}^{in'})$ are the dipole (magnetic) moment of a particle induced by the black-body radiation and the electric (induction) field induced by the fluctuating dipole (magnetic) moment of a particle, respectively. Because the calculations of the contributions to the friction force from the dipole and magnetic moments are very similar, below we will consider the contribution only from the dipole moment.

Taking into account the statistical independence of the fluctuating quantities, the Lorentz force can be written in the form

$$F'_x = F'_{1x} + F'_{2x}, \tag{8.114}$$

where

$$F'_{1x} = \frac{\partial}{\partial x'}\left\langle \mathbf{d}^{\mathbf{in}'}_{\mathbf{e}} \cdot \mathbf{E}^{\mathbf{f}'*}(\mathbf{r}') \right\rangle_{\mathbf{r}'=\mathbf{r}'_0}, \tag{8.115}$$

$$F'_{2x} = \frac{\partial}{\partial x'}\left\langle \mathbf{d}^{\mathbf{f}'}_{\mathbf{e}} \cdot \mathbf{E}^{\mathbf{in}'*}(\mathbf{r}') \right\rangle_{\mathbf{r}'=\mathbf{r}'_0}. \tag{8.116}$$

To calculate F'_{1x} we write the electric field in the K' frame as a Fourier integral,

$$\mathbf{E}^{f'}(\mathbf{r}', t') = \int_{-\infty}^{\infty} \frac{d\omega'}{2\pi} \int \frac{d^3k'}{(2\pi)^3} e^{i\mathbf{k}'\cdot\mathbf{r}' - i\omega' t'} \mathbf{E}^{f'}(\mathbf{k}', \omega'),$$

Using that

$$\mathbf{d}_e^{in\prime} = \int_{-\infty}^{\infty} \frac{d\omega'}{2\pi} \int \frac{d^3k'}{(2\pi)^3} \alpha(\omega') e^{i\mathbf{k}'\cdot\mathbf{r}' - i\omega' t'} \mathbf{E}^{f\prime}(\mathbf{k}', \omega').$$

where $\alpha(\omega')$ is the particle polarizability, we get

$$F'_{1x} = -i \int_{\infty}^{\infty} \frac{d\omega'}{2\pi} \int \frac{d^3k'}{(2\pi)^3} k'_x \alpha(\omega') \left\langle \mathbf{E}^{\mathbf{f}\prime} \cdot \mathbf{E}^{\mathbf{f}\prime *} \right\rangle_{\omega'\mathbf{k}'}. \tag{8.117}$$

When we change from the K' frame to the K frame, $\langle \mathbf{E}' \cdot \mathbf{E}'^* \rangle_{\omega'\mathbf{k}'}$ is transformed as the energy density of a plane electromagnetic field. From the law of transformation of the energy density of a plane electromagnetic field [253] we get

$$\left\langle \mathbf{E}^{\mathbf{f}\prime} \cdot \mathbf{E}^{\mathbf{f}\prime *} \right\rangle_{\omega'\mathbf{k}'} = \left\langle \mathbf{E}^{\mathbf{f}} \cdot \mathbf{E}^{\mathbf{f}*} \right\rangle_{\omega\mathbf{k}} \left(\frac{\omega'}{\omega} \right)^2. \tag{8.118}$$

According to the theory of the fluctuating electromagnetic field, the spectral density of the fluctuations of the electric field is determined by [107]

$$\left\langle E_i^f(\mathbf{r}) E_j^{f*}(\mathbf{r}') \right\rangle_{\omega\mathbf{k}} = \hbar \mathrm{Im} D_{ij}(\mathbf{k}, \omega) \coth\left(\frac{\hbar\omega}{2k_B T_1} \right), \tag{8.119}$$

where the Green's function of the electromagnetic field in the free space is determined by

$$D_{ik}(\omega, \mathbf{k}) = -\frac{\frac{4\pi\omega^2}{c^2}}{\frac{\omega^2}{c^2} - k^2 + i0 \cdot \mathrm{sgn}\,\omega} \left[\delta_{ik} - \frac{c^2 k_i k_k}{\omega^2} \right], \tag{8.120}$$

T_1 is the temperature of the black-body radiation. Taking into account that

$$\mathrm{Im} \frac{1}{\frac{\omega^2}{c^2} - k^2 + i0 \cdot \mathrm{sign}\,\omega} = \mathrm{Im} \frac{1}{\frac{\omega'^2}{c^2} - k'^2 + i0 \cdot \mathrm{sgn}\,\omega'},$$

we get

$$\left\langle \mathbf{E}^{\mathbf{f}\prime} \cdot \mathbf{E}^{\mathbf{f}\prime *} \right\rangle_{\omega'\mathbf{k}'} = 4\pi^2 \hbar k' \left\{ \delta\left(\frac{\omega'}{c} - k' \right) - \delta\left(\frac{\omega'}{c} + k' \right) \right\} \coth\left(\frac{\hbar\omega}{2k_B T_1} \right). \tag{8.121}$$

Substitution of (8.121) in (8.117) and integration over ω' gives

$$F'_{1x} = \frac{\hbar c}{2\pi^2} \int d^3k' k' k'_x \mathrm{Im}\alpha(ck') \coth\left(\frac{\hbar\gamma(ck' + Vk'_x)}{2k_B T_1} \right), \tag{8.122}$$

where it was taken into account, that $\omega = (\omega' + k'_x V)\gamma$. Introducing the new variable $\omega' = ck'$, (8.122) can be written in the form

$$F'_{1x} = \frac{\hbar}{\pi c^2}\int_0^\infty d\omega'\omega'^2\int_{\frac{-\omega'}{c}}^{\frac{\omega'}{c}} dk'_x k'_x \mathrm{Im}\alpha(\omega')\coth\left(\frac{\hbar\gamma(\omega'+Vk'_x)}{2k_BT_1}\right). \tag{8.123}$$

At small velocities ($V \ll c$) $F_x = -\Gamma V$, where

$$\Gamma = \frac{\hbar^2}{3\pi c^5 k_B T_1}\int_0^\infty d\omega \frac{\omega^5 \mathrm{Im}\alpha(\omega)}{\sinh^2\left(\frac{\hbar\omega}{2k_BT_1}\right)}, \tag{8.124}$$

Equation (8.124) was first derived in [157] using a different approach. The rate of change of the rest energy of a particle in the K' frame due to the absorption of black-body radiation is determined by the equation

$$P'_1 = \frac{dm_0}{dt'}c^2 = \left\langle \mathbf{j}_e^{in'}\cdot\mathbf{E}^{f'*}\right\rangle = \frac{\partial}{\partial t'}\left\langle \mathbf{d}_e^{in'}(t')\cdot\mathbf{E}^{f'*}(t'_0)\right\rangle_{t'=t'_0}. \tag{8.125}$$

After the calculations, which are similar to those used when calculating F'_{1x}, we get

$$P'_1 = \frac{\hbar}{\pi c^2}\int_0^\infty d\omega'\omega'^2\int_{\frac{-\omega'}{c}}^{\frac{\omega'}{c}} dk'_x \omega' \mathrm{Im}\alpha(\omega')\coth\left(\frac{\hbar\gamma(\omega'+Vk'_x)}{2k_BT_1}\right). \tag{8.126}$$

From (8.93), the friction force acting on a particle in the K-frame due to the interaction with the black-body radiation is given by

$$\begin{aligned} F_{1x} &= F'_{1x} + \beta\frac{P'_1}{c} \\ &= \frac{\hbar}{\pi c^2}\int_0^\infty d\omega'\omega'^2\int_{\frac{-\omega'}{c}}^{\frac{\omega'}{c}} dk'_x\left(k'_x+\beta\frac{\omega'}{c}\right)\mathrm{Im}\alpha(\omega')\coth\left(\frac{\hbar\gamma(\omega'+Vk'_x)}{2k_BT_1}\right). \end{aligned} \tag{8.127}$$

Introducing the new variables: $k'_x = \gamma(q_x - \beta\omega/c)$, $\omega' = \gamma(\omega - Vk_x)$ in the integral (8.127) we get

$$F_{1x} = \frac{\hbar\gamma}{\pi c^2}\int_0^\infty d\omega\int_{\frac{-\omega}{c}}^{\frac{\omega}{c}} dk_x k_x(\omega - Vk_x)^2 \mathrm{Im}\alpha[\gamma(\omega - Vk_x)]\coth\left(\frac{\hbar\omega}{2k_BT_1}\right), \tag{8.128}$$

where we have taken into account that $d\omega' dq'_x = d\omega dq_x$. To calculate F'_{2x} in the K' frame we use the representation of the fluctuating dipole moment of a particle as a Fourier integral

$$\mathbf{d}^f(t') = \int_{-\infty}^\infty \frac{d\omega'}{2\pi}e^{-i\omega' t'}\mathbf{d}^f(\omega'). \tag{8.129}$$

The electric field created in the K' frame by the fluctuating dipole moment of a particle is determined by the equation

$$E_i^{in\prime}(\mathbf{r}',t') = \int_{-\infty}^{\infty} \frac{d\omega'}{2\pi} \int \frac{d^3k'}{(2\pi)^3} e^{i\mathbf{k}'\cdot(\mathbf{r}'-\mathbf{r}_0')-i\omega' t'} D_{ik}(\omega',\mathbf{k}') d_k^f(\omega'). \tag{8.130}$$

According to the fluctuation–dissipation theorem, the spectral density of the fluctuations of the fluctuating dipole moment is determined by the equation [107]

$$\left\langle d_i^f d_k^{f*} \right\rangle_{\omega'} = \hbar \mathrm{Im}\alpha(\omega') \coth\left(\frac{\hbar\omega'}{2k_B T_2}\right)\delta_{ik}, \tag{8.131}$$

where T_2 is the temperature of a particle. Substituting (8.152) and (8.153) in (8.116) and taking into account (8.154), we get

$$F_{2x}' = -\frac{\hbar}{\pi c^2} \int_0^{\infty} d\omega' \omega'^2 \int_{\frac{-\omega'}{c}}^{\frac{\omega'}{c}} dk_x' k_x' \mathrm{Im}\alpha(\omega') \coth\left(\frac{\hbar\gamma\omega'}{2k_B T_2}\right) = 0. \tag{8.132}$$

Thus, in the rest reference frame of a particle, the friction force due to its own thermal radiation is zero. This result is due to the fact that, in this frame, due to the symmetry, the total radiated momentum from the dipole radiation is identically zero. Thus, the change in momentum of a particle in the rest reference frame is determined by the Lorentz force F_x' acting on a particle from the external electromagnetic field associated with the black-body radiation observed in this reference frame. The rate of change of the rest energy of a particle in the K' frame, due to its thermal radiation, can be obtained with similar calculations

$$\begin{aligned} P_2' &= \left\langle \mathbf{j}_e^{f\prime} \cdot \mathbf{E}^{in\prime *} \right\rangle = \frac{\partial}{\partial t'} \left\langle \mathbf{d}_e^{f\prime}(t') \cdot \mathbf{E}^{in\prime *}(t_0') \right\rangle_{t'=t_0'} \\ &= -\frac{\hbar}{\pi c^2} \int_0^{\infty} d\omega' \omega'^2 \int_{\frac{-\omega'}{c}}^{\frac{\omega'}{c}} dk_x' \omega' \mathrm{Im}\alpha(\omega') \coth\left(\frac{\hbar\gamma\omega'}{2k_B T_2}\right), \end{aligned} \tag{8.133}$$

and the friction force in the K frame associated with thermal radiation of a particle is given by

$$\begin{aligned} F_{2x} &= F_{2x}' + \beta \frac{P_2'}{c} \\ &= -\frac{\hbar\gamma}{\pi c^2} \int_0^{\infty} d\omega \times \int_{\frac{-\omega}{c}}^{\frac{\omega}{c}} dk_x k_x (\omega - V k_x)^2 \mathrm{Im}\alpha[\gamma(\omega - V k_x)] \coth\left(\frac{\hbar\gamma(\omega - V k_x)}{2k_B T_2}\right). \end{aligned} \tag{8.134}$$

The total friction force in the K frame is given by

$$F_x = F_{1x} + F_{2x} = \frac{2\hbar\gamma}{\pi c^2} \int_0^{\infty} d\omega \int_{\frac{-\omega}{c}}^{\frac{\omega}{c}} dk_x k_x (\omega - V k_x)^2 \mathrm{Im}\alpha(\gamma(\omega - V k_x))(n_1(\omega) - n_2(\omega')), \tag{8.135}$$

where $n_i(\omega) = [\exp(\hbar\omega/k_B T_i) - 1]^{-1}$. Equation (8.135) was first derived in [157]. Note that the friction force F_x can be either positive or negative. However, the acceleration, which is determined by the friction force F'_x, is always negative. The total heat absorbed by a particle in the K'-frame is determined by the equation

$$P' = P'_1 + P'_2 = \frac{2\hbar\gamma^2}{\pi c^2}\int_0^\infty d\omega' \int_{-\omega'/c}^{\omega'/c} dk'_x \omega'(\omega - Vq_x)^2 \mathrm{Im}\alpha[\gamma(\omega - Vq_x)](n_1(\omega) - n_2(\omega')). \tag{8.136}$$

In the K frame, the total change in energy of a particle due to the interaction with the radiation field can be calculated from the law of the transformation of energy of a particle: $E = \gamma(E' + p'_x V)$, where E and E' are the total energy of a particle in the K and K' frames, respectively. From this relation, we get the equation for the rate of change of the energy of a particle in the K frame

$$\frac{dE}{dt} = P = P' + F'_x V = \frac{2\hbar\gamma}{\pi c^2}\int_0^\infty d\omega \int_{-\omega/c}^{\omega/c} dk_x \omega(\omega - Vk_x)^2 \mathrm{Im}\alpha[\gamma(\omega - Vk_x)][n_1(\omega) - n_2(\omega')]. \tag{8.137}$$

The rate of change of the energy of the black-body radiation in the K frame is determined by the equation $dW_{BB}/dt = -P$. The steady-state temperature of a particle is determined by the condition $P'(T_1, T_2) = 0$, and for this state $F_x = F'_x$ and $P = F'_x V$.

The friction force acting on a particle moving relative to the black-body radiation is determined by the imaginary part of the particle polarizability. For an atom, the imaginary part of the polarizability is determined by the atom electronic linewidth broadening due to the radiation mechanism, which can be calculated considering the interaction of an atom with its own radiation. Taking into account this interaction, the dipole moment of an atom induced by an external electric field $E_x^{ext}(\omega, \mathbf{r}_0)$ can be written in the form [129, 139]

$$p_x^{ind} = \alpha_0(\omega)(\omega)\left[E_x^{ind}(\omega, \mathbf{r}_0) + E_x^{ext}(\omega, \mathbf{r}_0)\right], \tag{8.138}$$

where, in the single-oscillator model without the radiation linewidth broadening, the atomic polarizability is given by the equation

$$\alpha_0(\omega) = \frac{\alpha(0)\omega_0^2}{\omega_0^2 - \omega^2}, \tag{8.139}$$

where $\alpha(0)$ is the static polarizability of an atom, and $E_x^{ind}(\omega, \mathbf{r}_0)$ is the radiation electric field created by the induced dipole moment of an atom. In the Coulomb gauge, which is used in this article, the Green's function of the electromagnetic field determines the electric field created by the unit point dipole, so $E_x^{ind}(\omega, \mathbf{r}_0) = \tilde{D}_{xx}(\omega, \mathbf{r}_0, \mathbf{r}_0)p_x^{ind}$, where $\tilde{D}_{xx}(\omega, \mathbf{r}_0, \mathbf{r}_0)$ is the reduced part of the Green's function of the electromagnetic field in the vacuum, which takes into account

only the contribution from the propagating electromagnetic waves and determines the radiation in the far field. The Green's function of the electromagnetic field in the vacuum $D_{xx}(\omega, \mathbf{r}, \mathbf{r}_0)$ diverges at $\mathbf{r} = \mathbf{r}_0$. However, the contribution from the propagating waves remains finite and purely imaginary at $\mathbf{r} = \mathbf{r}_0$, and the divergent contribution from the evanescent waves is real. Therefore, $\tilde{D}_{xx}(\omega, \mathbf{r}_0, \mathbf{r}_0) = i\mathrm{Im}D_{xx}(\mathbf{r_0}, \mathbf{r_0})$. From (8.138) and (8.139) we get

$$\mathrm{Im}\alpha(\omega) = \mathrm{Im}\frac{p_x^{ind}}{E_x^{ext}(\omega, \mathbf{r}_0)} = \mathrm{Im}\frac{\alpha(0)\omega_0^2}{\omega_0^2 - \omega^2 - i\alpha(0)\omega_0^2\mathrm{Im}D_{xx}(\mathbf{r_0}, \mathbf{r_0})} = \frac{\alpha^2(0)\omega_0^4\mathrm{Im}D_{xx}(\mathbf{r_0}, \mathbf{r_0})}{(\omega_0^2 - \omega^2)^2 + \left[\alpha(0)\omega_0^2\mathrm{Im}D_{xx}\right]^2}, \tag{8.140}$$

where

$$\mathrm{Im}D_{xx}(\mathbf{r_0}, \mathbf{r_0}) = \mathrm{Im}D_{yy} = \mathrm{Im}D_{zz} = \int \frac{d^3k}{(2\pi)^3}\mathrm{Im}D_{xx}(\omega, \mathbf{k}) = \frac{2}{3}\left(\frac{\omega}{c}\right)^3 \mathrm{sgn}\,\omega. \tag{8.141}$$

At resonance ($\omega^2 \approx \omega_0^2$) usually $\alpha(0)\mathrm{Im}D_{xx} \ll 1$ (for example, for a hydrogen atom it is $\sim 10^{-6}$). Thus, the limit $\alpha(0)D_{xx} \to i0$ can be taken. In this case, the resonant contribution is given by

$$\mathrm{Im}\alpha(\omega) \approx \frac{\pi\alpha(0)\omega_0}{2}[\delta(\omega - \omega_0) - \delta(\omega + \omega_0)], \tag{8.142}$$

and the off-resonant contribution, which is far from resonance ($\omega^2 \ll \omega_0^2$), can be given by

$$\mathrm{Im}\alpha(\omega) \approx \frac{2}{3}\left(\frac{\omega}{c}\right)^3 \alpha^2(0)\mathrm{sign}\,\omega. \tag{8.143}$$

The result (8.143) was also obtained in [160] using quantum electrodynamics. However, the analysis presented above is much simpler, and it clarifies the physical meaning of the terms in the quantum electrodynamics perturbational theory. Using (8.142) and (8.143) in (8.123) we get the resonant and off-resonant contributions to the friction force

$$F_{1x}^{res} = \frac{\hbar\omega_0^5\alpha(0)}{c^4}\int_{-1}^{1} dx x\left[\exp\left(\frac{\hbar\gamma\omega_0(1+\beta x)}{k_B T_1}\right) - 1\right]^{-1}, \tag{8.144}$$

$$F_{1x}^{nonres} = -\frac{512\pi^7\hbar\alpha(0)^2\gamma^6}{945c^7}\left(\frac{k_B T_1}{\hbar}\right)^8 (7\beta + 14\beta^3 + 3\beta^5), \tag{8.145}$$

For $\beta \ll 1$ the friction force $F_{1x} = -\Gamma V$, where the resonant and off-resonant contributions to the friction coefficient are

$$\Gamma_{res} = \frac{\hbar^2 \alpha(0) \omega_0^6}{6c^5 k_B T_1} \frac{1}{\sinh^2\left(\frac{\hbar\omega_0}{2k_B T_1}\right)}, \tag{8.146}$$

$$\Gamma_{nonres} = \frac{512\pi^7 \hbar \alpha(0)^2}{135c^8} \left(\frac{k_B T_1}{\hbar}\right)^8, \tag{8.147}$$

The results (8.146) and (8.147) were obtained in [157, 160]. In the ultrarelativistic case, $(1 - \beta \ll k_B T_1/\hbar\omega_0 \ll 1)$

$$F_{1x}^{res} = \frac{\omega_0^4 \alpha(0)}{c^4} \sqrt{2} k_B T_1 \sqrt{1-\beta} \ln \frac{\hbar\omega_0 \sqrt{1-\beta}}{\sqrt{2} k_B T_1}, \tag{8.148}$$

$$F_{1x}^{nonres} = \frac{216\pi^7 \hbar \alpha(0)^2}{135c^7 (1-\beta)^3} \left(\frac{k_B T_1}{\hbar}\right)^8 \tag{8.149}$$

Thus, in this case $F_{1x}^{res} \sim \sqrt{1-\beta} \ln \sqrt{1-\beta} \to 0$ and $F_{1x}^{nonres} \sim (1-\beta)^{-3} \to \infty$ at $1 - \beta \to 0$.

For small velocities and typical temperatures, the infrared thermal peak of the black-body radiation is far below the resonance frequency ω_0, so it dominates the far-off-resonant contribution (8.146), which has already been mentioned in [159]. However, in the ultrarelativistic case, the friction is dominated by the far-off-resonant contribution for all temperatures.

According to (8.136), the total heat absorbed by an atom in the K' frame is determined by the equation

$$P' = \frac{128\pi^7 k_B^8 \alpha(0)^2}{315c^6 \hbar^7} \left[\gamma^6 (7 + 35\beta^2 + 21\beta^4 + \beta^6) T_1^8 - 7T_2^8\right]. \tag{8.150}$$

For small velocities, the steady-state temperature of a particle is $T_2 = T_1$, and, in the ultrarelativistic case, $T_2 \approx (1-\beta)^{-3/8} T_1$. The problem in calculating the imaginary part of the atom's polarizability in the far off-resonant field was considered in [159]. It was noted that in the literature that questions still remain regarding the gauge invariance of the imaginary part of the polarizability. In this Section, the imaginary part of the atomic polarizability in the field far from resonance is determined by the imaginary part of the electric field of the unit point dipole, which is a gauge-invariant quantity. In the Coulomb gauge, which is used in this article, the electric field of the unit point dipole is the same as the Green's function of the electromagnetic field. In another gauge, the expression for the Green's function will change; but, the electric field determined with this Green's function will remain unchanged. Therefore, despite the fact that the Green's function for the electromagnetic field is a gauge-dependent quantity, the imaginary part of the atomic polarizability calculated in this Section is a gauge-invariant quantity. The gauge invariance of the obtained results are also confirmed by the direct calculation using quantum electrodynamics [160]. The gauge-invariant formulation presented in this Section confirms that the polarizability of the

atom, for small frequencies, is a non-resonant effect, which is proportional to ω^3 for small driving frequency ω. This is consistent with the gauge-invariant analysis conducted in [160].

For a spherical particle with radius R, the electric and magnetic susceptibilities are given by (5.58) and (5.59), respectively. For metals with $4\pi\sigma \gg k_B T/\hbar$ and for $c\sqrt{2\pi\sigma k_B T} \gg R$, where σ is the conductivity, from (5.58) and (5.59) we get [191]

$$\mathrm{Im}\alpha_E(\omega) \approx R^3 \frac{3\omega}{4\pi\sigma}, \tag{8.151}$$

$$\mathrm{Im}\alpha_H(\omega) = \frac{4\pi\sigma\omega R^5}{30c^2}. \tag{8.152}$$

Writing the friction coefficient Γ as m_0/τ, where τ is a relaxation time, and using $m_0 = 4\pi R^3\rho/3$, from (8.127)–(8.152), we get

$$\tau_e^{-1} \approx 10^2 \frac{\hbar}{\rho\lambda_T^5}\frac{k_B T}{\hbar\sigma}, \tag{8.153}$$

$$\tau_m^{-1} \approx 10^2 \frac{\hbar R}{\rho\lambda_T^6}\frac{\sigma R}{c}. \tag{8.154}$$

where τ_e^{-1} and τ_m^{-1} are the contributions to $1/\tau$ from the electric dipole and magnetic moments, respectively. For $T = 300$ K, $\rho \approx 10^4$ kg/m^3, $\sigma \approx 10^{18}$ s^{-1} from (8.151 and 8.154) we get $\tau_e \sim 10^{16}$ s and $\tau_m \sim 10^{12}$ s. When the conductivity decreases, τ_e also decreases and reaches minimum at $2\pi\sigma \approx k_B T/\hbar$. At $T = 3000$ K, this minimum corresponds to approximately a day ($\tau_e^{min} \approx 10^5$ s). In Sect. 8.5.1 the same relaxation time was obtained for Ba^+.

8.5.3 Einstein's Formula

In this section, we give an alternative derivation of the formula for the force on a particle in thermal field. This derivation establishes a link with Einstein and Hopf derivation [254]. According to the linear response theory, the energy absorbed by a particle per unit time can be written in the form [184]

$$\frac{dE}{dt} = 2\int_0^\infty \frac{d\omega}{2\pi}\int \frac{d^3k}{(2\pi)^3}\omega\left[\mathrm{Im}\alpha_E(\omega) + \mathrm{Im}\alpha_H(\omega)\right]\left\langle \mathbf{E}\cdot\mathbf{E}^*\right\rangle_{\omega\mathbf{k}} \tag{8.155}$$

The force acting on the particle is determined by the momentum absorbed by the particle in the rest reference frame

$$F_x = \frac{dP'_x}{dt} = \frac{2}{c}\int_0^\infty \frac{d\omega'}{2\pi}\int \frac{d^3k'}{(2\pi)^3}\omega' \cos\theta'\left[\mathrm{Im}\alpha_E(\omega') + \mathrm{Im}\alpha_H(\omega')\right]\left\langle \mathbf{E}' \cdot \mathbf{E}'^*\right\rangle_{\omega'\mathbf{k}'} \tag{8.156}$$

Using (8.118), and taking into account that the elementary volume in the $(\omega, \mathbf{k})$ space is invariant under the Lorentz transformation, (8.156) can be rewritten in the form

$$F_x = \frac{dP'_x}{dt} = \frac{1}{c}\int_0^\infty \frac{d\omega}{2\pi}\int_0^\infty \frac{4\pi k^2 dk}{(2\pi)^3} \times \int_0^\pi d\theta \sin\theta\omega' \cos\theta'\left[\mathrm{Im}\alpha_E(\omega') + \mathrm{Im}\alpha_H(\omega')\right]\left\langle \mathbf{E} \cdot \mathbf{E}^*\right\rangle_{\omega\mathbf{k}}\left(\frac{\omega'}{\omega}\right)^2 \tag{8.157}$$

Using (3.54) we get

$$\int \frac{4\pi k^2 dk}{(2\pi)^3}\left\langle \mathbf{E} \cdot \mathbf{E}^*\right\rangle_{\omega\mathbf{k}} = \left\langle \mathbf{E}^2\right\rangle_\omega = 4\pi^2 u(\omega), \tag{8.158}$$

where the spectral energy density of the thermal electromagnetic field $u(\omega)$ is given by (3.55). Substituting (8.158) in (8.157) we get

$$F_x = \frac{dP'_x}{dt} = \frac{2\pi}{c}\int_0^\infty d\omega \int_0^\pi d\theta \sin\theta\omega' \cos\theta'[\mathrm{Im}\alpha_E(\omega') + \mathrm{Im}\alpha_H(\omega')]u(\omega)\left(\frac{\omega'}{\omega}\right)^2 \tag{8.159}$$

From the Lorenz transformation for a plane electromagnetic wave, we get

$$\omega = \omega'\gamma\left(1 + \frac{V}{c}\cos\theta\right). \tag{8.160}$$

$$\cos\theta = \frac{\cos\theta' + \frac{V}{c}}{1 + \frac{V}{c}\cos\theta'}. \tag{8.161}$$

Inserting (8.160) and (8.161) in (8.159) we get

$$F_x = \frac{dP'_x}{dt} = \frac{2\pi}{c}\int_0^\infty d\omega\omega \int_0^\pi \frac{d\theta \sin\theta\cos\theta}{\left(1 + \frac{V}{c}\cos\theta\right)^3}\left[\mathrm{Im}\alpha_E(\omega) + \mathrm{Im}\alpha_H(\omega)\right]u[\gamma\omega\left(1 + \frac{V}{c}\cos\theta\right)], \tag{8.162}$$

where we have omitted the index prime. For a two-level atom we can neglect $\mathrm{Im}\alpha_H(\omega)$, and $\mathrm{Im}\alpha_E(\omega)$ can be written in the form

$$\mathrm{Im}\alpha_E(\omega) = \pi M_{12}(N_1 - N_2)\delta(\omega - \omega_0), \tag{8.163}$$

where $M_{12} = e^2|\langle 0|\mathbf{r}|1\rangle|^2/3\hbar$, and where N_1 and N_2 are the probabilities of the ground and excited states, respectively; $\hbar\omega_0 = E_1 - E_2$, where E_1 and E_2 are the energies of the ground and excited states, respectively. Substituting (8.163) in (8.162) in the case of small velocities ($V/c \ll 1$) we get

$$F_x = -\left(\frac{\hbar\omega_0}{c^2}\right)B_{12}(N_1 - N_2)\left[u(\omega_0) - \frac{\omega_0}{3}\frac{du(\omega_0)}{d\omega_0}\right]V, \tag{8.164}$$

where $B_{12} = 4\pi^2 e^2|\langle 0|\mathbf{r}|1\rangle|^2/3\hbar^2$. Equation (8.164) is Einstein's equation [254] for the force on an atom moving in a thermal electromagnetic field.

Chapter 9
Casimir Frictional Drag Force in Low-Dimensional Systems

Coulomb drag is a frictional coupling between electric currents flowing in spatially separated conducting layers. It is caused by interlayer electron–electron interactions. The frictional drag between quantum wells makes it possible to directly probe the inter-particle interaction. Inter-particle interactions form the cornerstone of many-body physics. Usually it is considered using time-dependent perturbation theory. In the lowest order of this theory, the friction force is determined by the Kubo formula, which gives the friction to linear order in relative drift velocity of the electrons in the different layers. In this section, we calculate the frictional drag force in low-dimensional systems at arbitrary relative sliding velocity using the theory of Casimir friction.

We study the frictional drag force in low-dimensional systems (2D electron and 2D liquid systems) mediated by a fluctuating electromagnetic field, which originates from the Brownian motion of the ions in the liquid. The analysis is focused on the (2D system–2D system), (2D system–semi-infinite liquid), and (2D system–infinite liquid) configurations. We show that for the 2D electron systems, the friction drag depends linearly on the relative velocity of the free carries in the different media, but for 2D liquid systems, the frictional drag depends nonlinear on the relative velocity. For 2D systems, the frictional drag force induced by liquid flow may be several orders of magnitude larger than the frictional drag induced by an electronic current.

9.1 Introduction

The presence of the fluctuating electromagnetic field leads to a coupling between bodies even when they are isolated from each other by a vacuum gap or a dielectric layer. In the non-retarded limit (short separation between the bodies), this fluctuating electromagnetic field is reduced to the fluctuating Coulomb field, which determines the electron–electron (e–e) and electron–hole (e–h) interaction, which plays a leading

A.I. Volokitin and B.N.J. Persson, *Electromagnetic Fluctuations at the Nanoscale*,
NanoScience and Technology, DOI 10.1007/978-3-662-53474-8_9

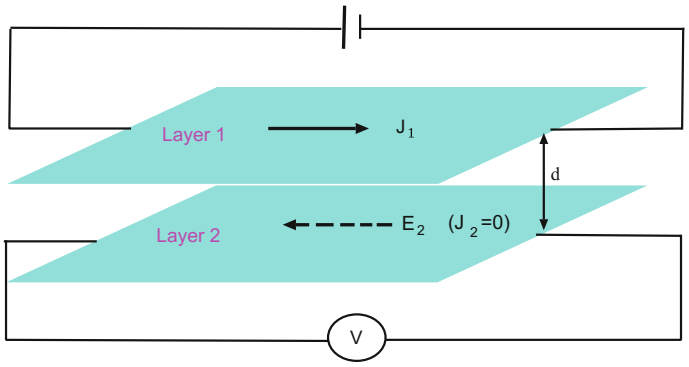

Fig. 9.1 Scheme of experiment for observation of the drag effect

role in a wide range of condensed matter phenomena such as the fractional quantum Hall effect, high-temperature superconductivity, Wigner crystallization, exciton condensates and the Mott transition. In addition, the e–e interaction is central to problems involving quantum coherence since it is a leading mechanism of electron dephasing.

Many-body effects are particularly important in low-dimensional systems. This leads to many intriguing phenomena, such as Luttinger liquid behavior in quantum wires, and the fractional quantum Hall effect and Wigner crystallization in 2D electron gases in a magnetic field. As technology improves and semiconductor devices shrink further in size, interaction effects become even more pronounced and it may become possible to probe these effects in novel experiments.

Despite its importance, the direct measurement of the e–e interaction through transport experiments is difficult. This is a consequence of the e–e interaction's momentum conserving nature. However, the e–e interaction can be tested using frictional drag. The frictional drag effect consists in driving an electric current in one metallic layer and registration of the effect of the frictional drag of the electrons in a second (parallel) metallic layer (Fig. 9.1). Such experiments were predicted by Pogrebinskii [255] and Price [256] and were performed for 2D quantum wells [112–114]. In these experiments, two quantum wells are separated by a dielectric layer thick enough to prevent electrons from tunneling across it while still allowing interlayer interaction between them. A current of density $J_2 = n_2 ev$ is driven through layer **2** (where n_2 is the carrier concentration per unit area in the second layer), see Fig. 9.1. Due to the proximity of the layers, the interlayer interactions will induce a current in layer **1** due to a friction stress $\sigma = \gamma v$ acting on the electrons in layer **1** from layer **2**. If layer **1** is an open circuit, an electric field E_1 will develop in the layer whose influence cancels the frictional stress σ between the layers. Thus the frictional stress $\sigma = \gamma v$ must equal the induced stress $n_1 eE_1$ so that

$$\gamma = n_1 eE_1/v = n_2 n_1 e^2 E_1/J_2 = n_1 n_2 e^2 \rho_{12}, \tag{9.1}$$

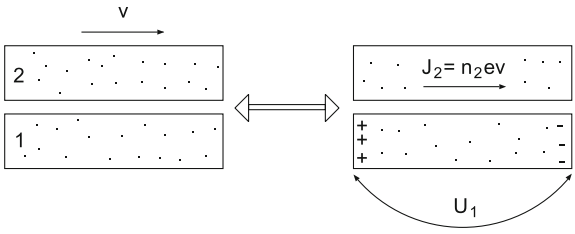

Fig. 9.2 Two ways of studying of Casimir friction. *Left* A metallic block sliding relative to the metallic substrate with the velocity v. An electronic frictional stress will act on the block (and on the substrate). *Right* The shear stress σ can be measured if instead of sliding the upper block, a voltage U_2 is applied to the block resulting in a drift motion of the conduction electrons (velocity v). The resulting frictional stress σ on the substrate electrons will generate a voltage difference U_1 (proportional to σ), as indicated in the figure. Both approaches are equivalent if in the upper block is possible to neglect scattering of the free carries by lattice defects

where the *transresistivity* $\rho_{12} = E_1/J_2$ is defined as the ratio of the induced electric field in the first layer to the driving current density in the second layer. The transresistivity is often interpreted in terms of a drag rate, which, in analogy with the Drude model, is defined by $\tau_D^{-1} = \rho_{12} n_2 e^2/m^* = \gamma/n_1 m^*$. These experiments spurred by a large body of theoretical work both on electron–hole systems and on electron–electron systems. Most of this work focused on interlayer Coulomb interaction, the most obvious coupling mechanism and the one considered in the original theoretical papers [255], though the contributions due to an exchange of phonons between the layers have also been considered [113]. The most widely used approach to study the drag effect is based on the Boltzmann equation [114, 257–259] and the Kubo formalism [260, 261]. In [114], a theory of the drag effect was developed based on the semi-classical theory of the fluctuating electromagnetic field. The retardation effects are automatically included in this approach.

The close connection of Casimir friction with frictional drag effect is illustrated in Fig. 9.2. At present, both these phenomena attract considerable attention in connection with the possibility of using them in the micro-and nano-electromechanical systems (MEMS and NEMS), and biological objects, in which local dynamic effects are intensively studied.

9.2 Fluctuating Electromagnetic Field

We consider two parallel 2D electron layers separated by a distance d. We introduce two reference systems K and K', with coordinate axes xyz and $x'y'z'$. The xy- and $x'y'$-planes coincide with layer **1**, with the x- and x'-axes pointing in the same direction, and the z- and z'-axes pointing toward layer **2**. The layers **1** and **2** are located at $z = 0$ and $z = d$, respectively. In the K system both layers are at rest. Assume now that in layer **2**, the conduction electrons move with the drift velocity v, corresponding to the

current density $j_2 = n_2 e v$, while no current flows in layer **1**. The K' reference system moves with velocity v along to the x-axis relative to frame K. In the K' frame there is no current density in layer **2**, while the surrounding dielectric moves with velocity $-v\hat{\mathrm{x}}$. Following Lifshitz [42], to calculate the fluctuating field we shall use the general theory due to Rytov, which is described in his books [5–7] (see also Sect. 3.1). This method is based on the introduction of a 'random' field in the Maxwell equations (just as, for example, one introduces a 'random' force in the theory of Brownian motion of a particle). In the K-system for $z < d$, for a monochromatic field (time factor $\exp(-\mathrm{i}\omega t)$) in a dielectric, nonmagnetic medium, these equations are:

$$\nabla \times \mathbf{E} = i\frac{\omega}{c}\mathbf{B}, \tag{9.2}$$

$$\nabla \times \mathbf{H} = -i\frac{\omega}{c}\mathbf{D} + \frac{4\pi}{c}(\mathbf{j}_1 + \mathbf{j}_{1f})\delta(z), \tag{9.3}$$

where, following Rytov, we divided the total current density $\mathbf{j}_{1tot}$ in layer **1** into two parts, $\mathbf{j}_{1tot} = \mathbf{j}_1 + \mathbf{j}_{1f}$, the fluctuating current density $\mathbf{j}_{1f}$ associated with thermal and quantum fluctuations, and the current density $\mathbf{j}_1$ induced by the electric field $\mathbf{E}$:

$$j_{1\alpha}(\mathbf{r}) = \int \mathrm{d}^2 r'\, \sigma_{1\alpha\beta}(\mathbf{r} - \mathbf{r}') E_\beta(\mathbf{r}'), \tag{9.4}$$

where $\mathbf{r}$ is the 2D vector in the xy-plane, and $\sigma_{1\alpha\beta}(\mathbf{r}-\mathbf{r}')$ is the conductivity tensor in layer **1**. $\mathbf{D}$, $\mathbf{H}$ and $\mathbf{B}$ are the electric displacement field, the magnetic and the magnetic induction fields, respectively. For nonmagnetic medium $\mathbf{B} = \mathbf{H}$ and $\mathbf{D} = \varepsilon\mathbf{E}$, where ε is the dielectric constant of the surrounded media. According to the fluctuation-dissipation theorem [184], the correlation function of the fluctuating current density $\mathbf{j}_f$, determining the average value of the product of component of $\mathbf{j}_f$ at two different point in space, is given by (3.59). In this equation the dielectric tensor $\varepsilon_{\alpha\beta}$ can be expressed through the conductivity tensor $\sigma_{\alpha\beta}$ according to the relation $\varepsilon_{\alpha\beta} = 1 + 4\pi i\sigma_{\alpha\beta}/\omega$. As a result we get

$$\left\langle j_{f\alpha}(\mathbf{r},\omega) j^*_{f\beta}(\mathbf{r}',\omega') \right\rangle = \left\langle j_{f\alpha}(\mathbf{r},\omega) j^*_{f\beta}(\mathbf{r}',\omega) \right\rangle_\omega \delta(\omega - \omega'), \tag{9.5}$$

$$\left\langle j_{f\alpha}(\mathbf{r},\omega) j^*_{f\beta}(\mathbf{r}',\omega) \right\rangle_\omega = \frac{\hbar\omega}{\pi}\left(\frac{1}{2} + n(\omega)\right) \mathrm{Re}\,\sigma_{\alpha\beta}(\mathbf{r} - \mathbf{r}', \omega), \tag{9.6}$$

where $\mathrm{Re}\,\sigma_{\alpha\beta}(\mathbf{r}-\mathbf{r}')$ is the real part of the conductivity. We write the current density in the form of a Fourier integral

$$\mathbf{j}(\mathbf{r}) = \int \mathrm{d}^2 q\, \mathbf{j}(\mathbf{q}) e^{i\mathbf{q}\cdot\mathbf{r}}, \tag{9.7}$$

where $\mathbf{q}$ is a 2D vector in the xy-plane. For the Fourier components $\mathbf{j}_f(\mathbf{q})$, the correlation function corresponding to the spatial correlation (9.6) is

$$\left\langle j_{f\alpha}(\mathbf{q},\omega) j^{*}_{f\beta}(\mathbf{q}',\omega)\right\rangle_{\omega} = \frac{\hbar\omega}{4\pi^3}\left(\frac{1}{2}+n(\omega)\right)\mathrm{Re}\,\sigma_{\alpha\beta}(\mathbf{q},\omega)\delta(\mathbf{q}-\mathbf{q}'), \tag{9.8}$$

where

$$\sigma_{\alpha\beta}(\mathbf{q},\omega) = \int \mathrm{d}^2 r\, \sigma_{\alpha\beta}(\mathbf{r},\omega) e^{-i\mathbf{q}\cdot\mathbf{r}}.$$

For the layers with assumed isotropy in the xy-plane, the conductivity tensor can be written in the form

$$\sigma_{\alpha\beta}(\mathbf{q},\omega) = \frac{q_\alpha q_\beta}{q^2}\sigma_l(\mathbf{q},\omega) + \left(\delta_{\alpha\beta} - \frac{q_\alpha q_\beta}{q^2}\right)\sigma_t(\mathbf{q},\omega), \tag{9.9}$$

where $\sigma_t(\mathbf{q},\omega)$ and $\sigma_l(\mathbf{q},\omega)$ are the transverse and longitudinal conductivity of the layer.

After decomposition of the components of the electromagnetic field into Fourier integrals, the general solution of the Maxwell equations for $z < d$ can be written in the form

$$\mathbf{E} = \begin{cases} \mathbf{v}e^{\mathrm{i}k_z z} + \mathbf{w}e^{-ik_z z},\ 0 < z < d, \\ \mathbf{u}_1 e^{-ik_z z},\ z < 0, \end{cases} \tag{9.10}$$

$$\mathbf{B} = -i\frac{c}{\omega}\begin{cases} \Big(\big[\mathbf{q}\times\mathbf{v}\big] + k_z\big[\hat{\mathrm{z}}\times\mathbf{v}\big]\Big)e^{\mathrm{i}k_z z} + \Big(\big[\mathbf{q}\times\mathbf{w}\big] - k_z\big[\hat{\mathrm{z}}\times\mathbf{w}\big]\Big)e^{-\mathrm{i}k_z z},\ 0 < z < d, \\ \Big(\big[\mathbf{q}\times\mathbf{u}_1\big] - k_z\big[\hat{\mathrm{z}}\times\mathbf{u}_1\big]\Big)e^{-\mathrm{i}k_z z},\ z < 0, \end{cases} \tag{9.11}$$

where $\mathbf{v}$, $\mathbf{w}$ and $\mathbf{u}_1$ satisfy the transversality conditions

$$\mathbf{v}\cdot\mathbf{q} + k_z v_z = 0,\quad \mathbf{w}\cdot\mathbf{q} - k_z w_z = 0,\ \mathbf{u}_1\cdot\mathbf{q} - k_z u_{1z} = 0, \tag{9.12}$$

where

$$k_z = \sqrt{\left(\frac{\omega}{c}\right)^2 \varepsilon - q^2} \tag{9.13}$$

and $\hat{\mathrm{z}}$ is a unit vector along the z-axis. We now decompose the electromagnetic field into s- and p-polarized waves. For the p-polarized waves, the electric field $\mathbf{E}$ is in the plane determined by the vectors $\hat{\mathrm{q}} = \mathbf{q}/q$ and $\hat{\mathrm{z}}$, and perpendicular to this plane, along the vector $\mathbf{n} = \hat{\mathrm{z}}\times\hat{\mathrm{q}}$, for s-polarized waves. The boundary conditions at $z = 0$ for s- and p-polarized waves are given by

$$E_{\mathbf{n}}(z = +0) = E_{\mathbf{n}}(z = -0), \tag{9.14}$$

$$\frac{dE_{\mathbf{n}}}{dz}\,|_{z=+0} - \frac{dE_{\mathbf{n}}}{dz}\,|_{z=-0} = -\frac{4\pi i\omega}{c^2}\left(\sigma_{1t}(\mathbf{q},\omega)E_{\mathbf{n}} + j_{f1\mathbf{n}}\right), \tag{9.15}$$

$$E_{\mathbf{q}}(z = +0) = E_{\mathbf{q}}(z = -0), \tag{9.16}$$

$$\frac{dE_{\mathbf{q}}}{dz}\,|_{z=+0} - \frac{dE_{\mathbf{q}}}{dz}\,|_{z=-0} = -\frac{4\pi i k_z^2}{\varepsilon\omega}\left(\sigma_{1l}(\mathbf{q},\omega)E_{\mathbf{q}} + j_{f1\mathbf{q}}\right), \tag{9.17}$$

where $E_{\mathbf{q}} = \hat{\mathrm{q}}\cdot\mathbf{E}$, $E_{\mathbf{n}} = \mathbf{n}\cdot\mathbf{E}$ and so on. From (9.15) and (9.17), we get the following equations:

$$v_{\mathbf{q}} + R_{1p}w_{\mathbf{q}} = -\frac{2\pi k_z j_{f1\mathbf{q}}}{\varepsilon\omega\varepsilon_{1p}}, \tag{9.18}$$

$$v_{\mathbf{n}} + R_{1s}w_{\mathbf{n}} = -\frac{2\pi\omega j_{f1\mathbf{n}}}{k_z c^2\varepsilon_{1s}}, \tag{9.19}$$

where $v_{\mathbf{q}} = \hat{\mathrm{q}}\cdot\mathbf{v}$ and so on, the reflection amplitudes for the layer

$$R_{1s(p)} = \frac{\varepsilon_{1s(p)} - 1}{\varepsilon_{1s(p)}},$$

and the dielectric functions of the layer

$$\varepsilon_{1s} = \frac{2\pi\omega\sigma_{1t}}{k_z c^2} + 1, \qquad \varepsilon_{1p} = \frac{2\pi k_z\sigma_{1l}}{\omega\varepsilon} + 1.$$

The Maxwell equations in the K'-system for $z > 0$ have the same form as (9.2) and (9.3) with $\mathbf{j} \to \mathbf{j}_2$ and $\mathbf{j}_f \to \mathbf{j}_{f2}$. To first order in v/c the relations between $\mathbf{D}$, $\mathbf{E}$ and $\mathbf{B}$, $\mathbf{H}$ are [191]

$$\mathbf{D} = \varepsilon\mathbf{E} - (\varepsilon - 1)\frac{v}{c}\hat{\mathrm{x}}\times\mathbf{B}, \tag{9.20}$$

$$\mathbf{H} = \mathbf{B} - (\varepsilon - 1)\frac{v}{c}\hat{\mathrm{x}}\times\mathbf{E}. \tag{9.21}$$

Under a Lorentz transformation, we have to linear order in v/c: $\omega' = \omega - q_x v$ and $\mathbf{q}' = \mathbf{q} - \hat{\mathrm{x}}\omega v/c^2$. Note also that k_z is invariant under the Lorentz transformation, i.e. $k_z = k_z'$. It can be shown that the last terms in (9.20) and (9.21) give rise only to a coupling between s- and p-polarized waves. However, as in Sect. 7.3 it can be shown that this coupling gives a correction $\sim (v/c)^2$ to the frictional drag force between the layers, so this term can be omitted. The solution of the Maxwell equations in the K' reference frame can be written as

$$\mathbf{E}' = \begin{cases} \mathbf{v}' e^{ik_z z} + \mathbf{w}' e^{-ik_z z}, & 0 < z < d \\ \mathbf{u}_2 e^{ik_z z}, & z > d \end{cases} \tag{9.22}$$

From the boundary conditions for the s- and p-polarized waves we get the equations

$$w'_{\mathbf{q}'} + R_{2p}(\mathbf{q}',\omega')\mathrm{e}^{2ik_z d}v'_{\mathbf{q}'} = -\frac{2\pi k_z j_{f\,2\mathbf{q}'}(\mathbf{q}',\omega')\mathrm{e}^{ik_z d}}{\varepsilon\omega'\varepsilon_{2p}(\mathbf{q}',\omega')}, \tag{9.23}$$

$$w'_{\mathbf{n}'} + R_{2s}(\mathbf{q}',\omega')\mathrm{e}^{2ik_z d}v'_{\mathbf{n}'} = -\frac{2\pi\omega' j_{f\,2\mathbf{n}'}(\mathbf{q}',\omega')\mathrm{e}^{ik_z d}}{pc^2\varepsilon_{2s}(\mathbf{q}',\omega')}. \tag{9.24}$$

The relations between the fields in the K and K' reference frames are determined by the Lorentz transformation. As shown in Sect. 7.3, such a Lorentz transformation gives the terms of the order v/c, which couples the s- and p-polarized waves but this results in a contribution to the frictional drag of the order $(v/c)^2$. Thus, we can take this transformation in zero order in v/c so that $v'_{\mathbf{q}'}(\omega') = v_{\mathbf{q}}(\omega)$, $v'_{\mathbf{n}'}(\omega') = \left(\omega'/\omega\right) v_{\mathbf{n}}(\omega)$ and similar equations for $\mathbf{w}$. After the transformation, the solution of the system of the equations (9.18), (9.19), (9.23) and (9.24) takes the form

$$v_{\mathbf{q}} = \frac{2\pi k_z}{\Delta_p \varepsilon}\left[\frac{j_{f2\mathbf{q}'}(\mathbf{q}',\omega')\mathrm{e}^{ik_z d}R_{1p}(q,\omega)}{\varepsilon_{2p}(\mathbf{q}',\omega')\omega'} - \frac{j_{f1\mathbf{q}}(\mathbf{q},\omega)}{\varepsilon_{1p}(\mathbf{q},\omega)\omega}\right], \tag{9.25}$$

$$w_{\mathbf{q}} = \frac{2\pi k_z}{\Delta_p \varepsilon}\left[\frac{j_{f1\mathbf{q}}(q,\omega)\,\mathrm{e}^{2ik_z d}R_{2p}(q',\omega')}{\varepsilon_{1p}(\mathbf{q},\omega)\omega} - \frac{j_{f2\mathbf{q}'}(q',\omega')\mathrm{e}^{ik_z d}}{\varepsilon_{2p}(\mathbf{q}',\omega')\omega'}\right], \tag{9.26}$$

$$v_{\mathbf{n}} = \frac{2\pi\omega}{\Delta_s k_z c^2}\left[\frac{j_{f2\mathbf{n}'}(q',\omega')\mathrm{e}^{ik_z d}R_{1s}(q,\omega)}{\varepsilon_{2s}(q',\omega')} - \frac{j_{f1\mathbf{n}}(q,\omega)}{\varepsilon_{1s}(q,\omega)}\right], \tag{9.27}$$

$$w_{\mathbf{n}} = \frac{2\pi\omega}{\Delta_s k_z c^2}\left[\frac{j_{f1\mathbf{n}}(\mathbf{q},\omega)\mathrm{e}^{2ik_z d}R_{2s}(q',\omega')}{\varepsilon_{1s}(\mathbf{q}',\omega)} - \frac{j_{f2\mathbf{n}'}(\mathbf{q}',\omega')\mathrm{e}^{ik_z d}}{\varepsilon_{2s}(\mathbf{q}',\omega')}\right], \tag{9.28}$$

$$v_z = -\frac{qv_{\mathbf{q}}}{k_z}, \qquad w_z = \frac{qw_{\mathbf{q}}}{k_z}, \tag{9.29}$$

where we have introduced the notation

$$\Delta_p = 1 - e^{2ik_z d}R_{2p}(\mathbf{q}',\omega')R_{1p}(\mathbf{q},\omega),$$
$$\Delta_s = 1 - e^{2ik_z d}R_{2s}(\mathbf{q}',\omega')R_{1s}(\mathbf{q},\omega).$$

9.3 Casimir Frictional Drag Force Between Two Quantum Wells

The frictional drag stress σ, which acts on the conduction electrons in layer **1** can be obtained from the xz-component of the Maxwell stress tensor σ_{ij}, evaluated at $z = \pm 0$

$$\sigma = \frac{1}{8\pi}\int_{-\infty}^{+\infty} \mathrm{d}\omega \left\{\left[\varepsilon\left\langle E_z E_x^*\right\rangle + \left\langle B_z B_x^*\right\rangle + c.c\right]_{z=+0} - \left[\ldots\right]_{z=-0}\right\}. \tag{9.30}$$

Here the $\langle\ldots\rangle$ denotes statistical averaging over the fluctuating current densities. The averaging is carrying out with the aid of (9.5). Note that the components of the fluctuating current density $\mathbf{j}_{f1}$ and $\mathbf{j}_{f2}$ refer to different layers, and are statistically independent, so that the average of their product is zero. Expanding the electric field and the magnetic induction in the Fourier series, we obtain

$$\sigma = \frac{1}{8\pi}\int \mathrm{d}\omega \mathrm{d}^2 q \Big\{ \Big[\varepsilon \left\langle E_z\left(\mathbf{q},\omega\right) E_x^*\left(\mathbf{q},\omega\right)\right\rangle + \left\langle B_z\left(\mathbf{q},\omega\right) B_x^*\left(\mathbf{q},\omega\right)\right\rangle + \\ + c.c\Big]_{z=+0} - \left[\ldots\right]_{z=-0} \Big\}. \tag{9.31}$$

For a given value of $\mathbf{q}$, it is convenient to express the component E_x and B_x in terms of the components along the vectors $\hat{\mathrm{q}}$ and $\mathbf{n}$

$$E_x = (q_x/q)E_{\mathbf{q}} - (q_y/q)E_{\mathbf{n}}, \tag{9.32}$$
$$B_x = (q_x/q)B_{\mathbf{q}} - (q_y/q)B_{\mathbf{n}}. \tag{9.33}$$

After substitution of expressions (9.32) and (9.33) into (9.31) and taking into account that the term that is proportional to q_y is equal to zero, we obtain

$$\sigma = \frac{1}{8\pi}\int \frac{\mathrm{d}\omega \mathrm{d}^2 q}{(2\pi)^2}\frac{q_x}{q} \Big\{ \Big[\varepsilon \left\langle E_z\left(\mathbf{q},\omega\right) E_{\mathbf{q}}^*\left(\mathbf{q},\omega\right)\right\rangle + \left\langle B_z\left(\mathbf{q},\omega\right) B_{\mathbf{q}}^*\left(\mathbf{q},\omega\right)\right\rangle + \\ + c.c\Big]_{z=+0} - \left[\ldots\right]_{z=-0} \Big\}, \tag{9.34}$$

where

$$E_z(z=+0) = (v_z + w_z) = (q/k_z)(w_{\mathbf{q}} - v_{\mathbf{q}}) = (qk_z^*/\mid k_z \mid^2)(w_{\mathbf{q}} - v_{\mathbf{q}}), \tag{9.35}$$

$$E_z(z=-0) = u_{1z} = (q/k_z)u_{\mathbf{q}} = (q/k_z)(w_{\mathbf{q}} + v_{\mathbf{q}}), \tag{9.36}$$

$$E_{\mathbf{q}}(z=+0) = E_{\mathbf{q}}(z=-0) = v_{\mathbf{q}} + w_{\mathbf{q}}, \tag{9.37}$$

$$B_z(z=+0) = (qc/\omega)(v_{\mathbf{n}} + w_{\mathbf{n}}) = B_z(z=-0) = (qc/\omega)u_{1\mathbf{n}}, \tag{9.38}$$

$$B_{\mathbf{q}}(z=+0) = (k_z c/\omega)(w_{\mathbf{n}} - v_{\mathbf{n}}), \tag{9.39}$$

$$B_{\mathbf{q}}(z=-0) = (k_z c/\omega)u_{1\mathbf{n}}, \tag{9.40}$$

After substituting these expressions into (9.34), we get

$$\sigma = \frac{1}{16\pi^3}\int_0^{+\infty} \mathrm{d}\omega \int \mathrm{d}^2 q q_x \Bigg(\frac{\varepsilon}{\mid k_z \mid^2}\Big[(k_z + k_z^*)\Big(\langle \mid w_{\mathbf{q}} \mid^2 \rangle - \langle \mid v_{\mathbf{q}} \mid^2 \rangle - \\ - \langle \mid v_{\mathbf{q}} + w_{\mathbf{q}} \mid^2 \rangle \Big) + (k_z - k_z^*)\big\langle \big(v_{\mathbf{q}} w_{\mathbf{q}}^* - v_{\mathbf{q}} w_{\mathbf{q}}^* \big) \big\rangle \Big] + \\ + \left(\frac{c}{\omega}\right)^2 \Big[(k_z + k_z^*)\Big(\langle \mid w_{\mathbf{n}} \mid^2 \rangle - \langle \mid v_{\mathbf{n}} \mid^2 \rangle - \langle \mid v_{\mathbf{n}} + w_{\mathbf{n}} \mid^2 \rangle \Big) - \\ - (k_z - k_z^*)\big\langle \big(v_{\mathbf{n}} w_{\mathbf{n}}^* - v_{\mathbf{n}} w_{\mathbf{n}}^* \big) \big\rangle \Big] \Bigg), \tag{9.41}$$

where we integrate only over positive values of ω, which gives an extra factor of two.

Substituting (9.25) and (9.29) into (9.41) and taking into account that $k_z = k_z^*$ for $q < \omega/c$ and $k_z = -k_z^*$ for $q > \omega/c$, we obtain

$$\sigma = \frac{\hbar}{8\pi^3}\int_0^\infty \mathrm{d}\omega \int_{q<(\frac{\omega}{c})\sqrt{\varepsilon}} \mathrm{d}^2 q q_x \times$$
$$\times \left[\frac{T_{1p}(\omega)T_{2p}(\omega - q_x v)\big(n(\omega - q_x v) - n(\omega)\big)}{|\,1 - \mathrm{e}^{2\mathrm{i}k_z d}R_{1p}(\omega)R_{2p}(\omega - q_x v)\,|^2} - \right.$$
$$\left. - \frac{T_{1p}(\omega)\big(\,|\,1 - R_{2p}(\omega - q_x v)\,|^2 + |\,1 - \mathrm{e}^{2\mathrm{i}k_z d}R_{2p}\big(\omega - q_x v\big)\,|^2\,\big)\big(n(\omega) + 1/2)\big)}{|\,1 - \mathrm{e}^{2\mathrm{i}k_z d}R_{1p}(\omega)R_{2p}(\omega - q_x v)\,|^2} \right] +$$
$$+ \frac{\hbar}{2\pi^3}\int_0^\infty \mathrm{d}\omega \int_{q>(\frac{\omega}{c})\sqrt{\varepsilon}} \mathrm{d}^2 q q_x \mathrm{e}^{-2|k_z|d} \times$$
$$\times \frac{\mathrm{Im}R_{1p}(\omega)\mathrm{Im}R_{2p}(\omega - q_x v)}{|\,1 - \mathrm{e}^{-2|k_z|d}R_{1p}(\omega)R_{2p}(\omega - q_x v)\,|^2}\big(n(\omega - q_x v) - n(\omega)\big) +$$
$$+ \big[p \to s\big], \tag{9.42}$$

$$T_{ip}(\omega) = 1 - |\,R_{ip}\,|^2 - |\,1 - R_{ip}\,|^2 = \frac{4\pi \mathrm{Re}\sigma_{il}(\omega)k_z}{\omega\varepsilon|\varepsilon_{il}|^2},$$
$$T_{is}(\omega) = 1 - |\,R_{is}\,|^2 - |\,1 - R_{is}\,|^2 = \frac{4\pi \mathrm{Re}\sigma_{it}(\omega)\omega}{k_z c^2|\epsilon_{it}|^2}.$$

The first integral in (9.42) is the contribution to the frictional drag force from propagating electromagnetic waves. The second term in (9.42) is derived from the evanescent field.

When the separation between quantum wells $d \ll \lambda_T$, the contribution to friction from propagating waves can be neglected. In this case, the first integral in (9.42) can be neglected, and the second integral is reduced to (7.30), where $R_i(\omega)$ is the reflection amplitude for layer i. In the random phase approximation, the equations for reflection amplitude are given in Appendix M. For $d < v_F\hbar/k_B T$, the reflection amplitude for the p-polarized electromagnetic waves is given by [13, 117]

$$R_p = 1 + \frac{i\hbar\varepsilon\omega}{2k_F e^2}, \tag{9.43}$$

where ε is the dielectric constant for surrounded dielectric, $k_F = \sqrt{2\pi n_s}$ is the Fermi wavevector and n_s is the electron concentration 2D electron layer. After substituting (9.43) in (10.13) we obtain the contribution to the drag resistivity due to the p-polarized waves

$$\rho_D = \frac{\gamma}{(ne)^2} = \frac{h}{e^2}\frac{\pi\zeta(3)}{32}\left(\frac{k_B T}{\epsilon_F}\right)^2 \frac{1}{(k_F d)^2}\frac{1}{(k_{TF} d)^2}, \tag{9.44}$$

where $q_{TF} = 2a_0^{-1}/\varepsilon$ is the single-layer Tomas-Fermi screening wavevector, $a_0 = \hbar^2/m^* e^2$, and ϵ_F is the Fermi energy. Equation (9.44) is a factor of two larger than the result obtained by Gramila et al. using an approach based on the Boltzmann equation

[113], and approximately a factor of two smaller that the result obtained by Persson and Zhang using a simple model of the van der Waals friction [117].

Figure 9.3 shows the friction coefficient γ as a function of distance d between two quantum wells at $T = 3\,\mathrm{K}$, and with $n_s = 1.5 \times 10^{15}\,\mathrm{m}^{-2}$, $m^* = 0.067\,\mathrm{m}_e$, $v_F = 1.6 \times 10^7\,\mathrm{cm\ s}^{-1}$, and, for the electron mean free path, $l = v_F\tau = 1.21 \times 10^5$ Å. We have also assumed $\varepsilon = 10$, which corresponds to the condition of the experiment [112, 113]. In this case, the s-wave contribution is negligibly small in comparison with the p-wave contribution. For $d = 175$ Å, we find $\gamma = 3.3 \times 10^{-9}$ kg·s^{-1}m^{-2}, which corresponds to a drag rate $\tau_D^{-1} = 3.3 \times 10^7\ \mathrm{s}^{-1}$, which is close to the experimental value $(\tau_D^{-1})_{exp} = 1.5 \times 10^7\,\mathrm{s}^{-1}$ [112, 113].

Figure 9.4 shows the friction coefficient for 2D-quantum wells with high electron density $n_s = 10^{19}\,\mathrm{m}^{-2}$, $T = 273\,\mathrm{K}$, $\tau = 4 \times 10^{-14}\,\mathrm{s}$, and $\varepsilon = 1$, where the result for other ε can be obtained using the scaling $\tau_{Dp} \sim \varepsilon^2$ and τ_{Ds} is independent of ε. In Figs. 9.3 and 9.4, the p- and s-wave contributions are shown separately. The

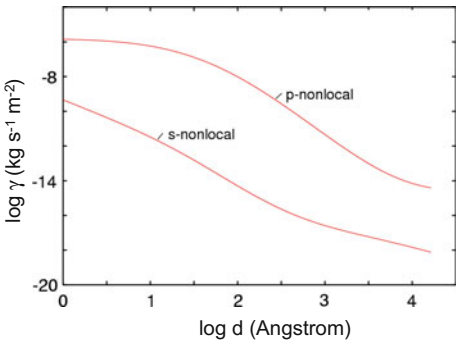

Fig. 9.3 The frictional drag coefficient for two quantum wells at $T = 3$ K as a function of separation d. The s- and p-wave contributions are shown separately. The calculations were performed with surface electron density $n_s = 1.5 \times 10^{15}\,\mathrm{m}^{-2}$, damping constant $\eta = 1.3 \times 10^{10}\,\mathrm{s}^{-1}$, effective electron mass $m^* = 0.067\,m_e$, and dielectric constant $\varepsilon = 10$, which corresponds to the condition of the experiment [112, 113]. (The base of the logarithm is 10.)

Fig. 9.4 The same as Fig. 9.3 but now for at $T = 273$ K, $n_s = 1.05 \times 10^{19}\,\mathrm{m}^{-2}$, $\eta = 2.5 \times 10^{13}\,\mathrm{s}^{-1}$, $m^* = m_e$, and $\varepsilon = 1$. (The base of the logarithm is 10)

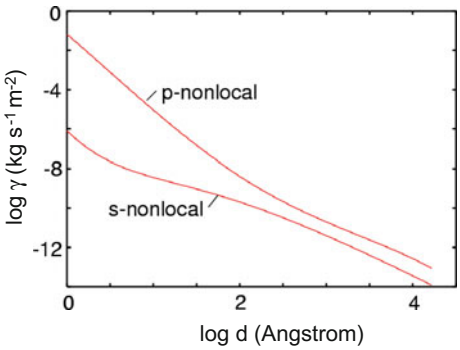

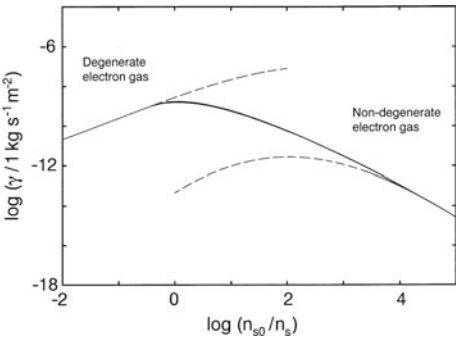

Fig. 9.5 The frictional drag coefficient for two quantum wells at $T = 3$ K as a function of electron concentration n_s. The *full curve* was obtained by interpolation between the curves (*dashed lines*) obtained within the non-local optic dielectric approach, with the dielectric functions corresponding to a degenerate electron gas ($n_s > n_F \sim 10^{14}\,\mathrm{m}^{-2}$), and to the non-degenerate electron gas ($n_s < n_F$). The electron density parameter $n_{s0} = 1.5 \times 10^{15}\,\mathrm{m}^{-2}$, damping constant $\eta = 1.3 \times 10^{10}\,\mathrm{s}^{-1}$, effective electron mass $m^* = 0.067\,m_e$, separation $d = 175\,\text{Å}$ and the dielectric constant $\varepsilon = 10$. (The base of the logarithm is 10)

calculations show that p-waves give a larger contribution for friction both for low-density and high-density 2D quantum wells.

Figure 9.5 shows the dependence of the friction coefficient on the electron density for the same parameters as in Fig. 9.3. In this case, the boundary between degenerate and non-degenerate electron density is determined by the Fermi density $n_F = 3k_B T m^*/2\pi\hbar^2 = 1.09 \times 10^{14}\,\mathrm{m}^{-2}$. From the calculations, we find the maximum of the frictional drag force for the electron density $n_{max} \approx 1 \times 10^{15}\,\mathrm{m}^{-2}$; this means that the experiment [112, 113] was performed the near optimum conditions.

The friction force per unit charge in the layer is determined by $E = \sigma_\parallel / n_s e$, where n_s is the 2D-electron concentration in the layer. For $v \ll v_F$, where v_F is the Fermi velocity, the friction force depends linearly on the velocity v. For $d = 175\,\text{Å}$ at $T = 3\,\mathrm{K}$, and with $n_s = 1.5 \times 10^{15}\,\mathrm{m}^{-2}$, the electron effective mass $m^* = 0.067\,\mathrm{m}_e$, $v_F = 1.6 \times 10^7$ cm/s, the electron mean free path $l = v_F \tau = 1.21 \times 10^5\,\text{Å}$, and $\varepsilon = 10$ (which corresponds to the condition of the experiment [113]) we get $E = 6.5 \times 10^{-6} v$ V/m, where the velocity v is in m/s. For a current 200 nA in a 2D layer with the width $w = 20\,\mu\mathrm{m}$, the drift of electrons (drift velocity $v = 60$ m/s) creates a frictional drag force per unit charge in the adjacent quantum well $E = 4 \times 10^{-4}$ V/m. Note that for the electron systems, the frictional drag force decreases when the electron concentration increases. For a example, for a 2D quantum wells with high electron density ($n_s = 10^{19}\,\mathrm{m}^{-2}$, $T = 273\,\mathrm{K}$, $\tau = 4 \times 10^{-14}\,\mathrm{s}$, $\varepsilon = 10$, $m^* = m_e$) at $d = 175\,\text{Å}$ we get $E = 1.2 \times 10^{-9} v$ V/m.

9.4 Casimir Frictional Drag Induced by Liquid Flow in Low-Dimensional Systems

In [262, 263], it was observed that the flow of a liquid over bundles of single-walled carbon nanotubes (SWNT) induces a voltage in the sample along the direction of the flow. Although several mechanisms were proposed to explain this effect [262–266, 268], only one of these mechanisms is related to a fluctuating electromagnetic field created by chaotic Brownian motion of ions in liquid flow. The free carriers in a low-dimensional system will experience frictional drag force due to this electromagnetic field in direction of liquid flow. The intriguing idea of using frictional drag as a non-contact means to detect motion in surrounding liquid was considered in [269].

9.4.1 Casimir Frictional Drag Between Two 2D Systems Induced by Liquid Flow

Consider a fluid with the ions in a narrow channel with thickness d_c. For $d \gg q_D^{-1} \gg d_c$, where $q_D = \sqrt{4\pi N_0 Q^2/\varepsilon_c k_B T}$ is the Debye screening wave number (N_0 is the concentration of ions, and ε_c is the dielectric constant of the liquid in the channel, and Q is the ion charge), the channel can be considered to be 2D. The Fourier transform of the diffusion equation for the ions (of type a) in the channel can be written in the form

$$\frac{i\omega}{D_a}\sigma_q^a = q^2\left(\sigma_q^a + \frac{N_a Q^2 d_c}{k_B T}\varphi_q\right), \tag{9.45}$$

where σ_q^a and ϕ_q are the Fourier components of the surface charge density and the electric potential, respectively, and D_a is the diffusion coefficient of the ions in the liquid in the channel. From (9.45), we get

$$\sigma_q^a = -\frac{N_a Q^2 d_c}{k_B T} q^2 \frac{\varphi_q}{q^2 - i\omega/D_a}. \tag{9.46}$$

The surface current density resulting from the diffusion and drift of the ions of type a, is determined by the formula

$$j_{iq}^a = -iqD\left(\sigma_q^a + N_a Q^2 d_c k_B T \varphi_q\right) =$$

$$= -i\omega \frac{N_a Q^2 d_c}{k_B T} \frac{1}{q^2 - i\omega/D_a} E_q, \tag{9.47}$$

where $E_q = -iq\varphi_q$ is the Fourier component of the electric field. Furthermore, there is a surface current density connected with the polarization of the liquid, which is determined by the formula

$$j_{pq} = -i\omega p_q = -i\omega d_c \frac{\varepsilon - 1}{4\pi} E_q, \tag{9.48}$$

where p_q and ε_c are the surface polarization and dielectric permeability of liquid in the channel, respectively. Thus the total current density $j_q = \sigma(\omega, q)E_q$, where the conductivity of the 2D-liquid is determined by the formula

$$\sigma(\omega, q) = -\frac{i\omega d_c}{4\pi}\left(-1 + \varepsilon_c\left(1 + \sum_a \frac{q_D^2}{q^2 - i\omega/D_a}\right)\right). \tag{9.49}$$

For the (2D electron)–(2D liquid) configuration (with the same parameters as in Sect. 9.3 for electron system (with high electron density)) at $d = 175\,\text{Å}$, and with $\varepsilon_c = 80$, $N_0 = 10^{24}\,\text{m}^{-3}$, $D = 10^{-9}\,\text{m}^2/\text{s}$, $d_c = 100\,\text{Å}$ we get $E = 4.6 \times 10^{-8} v\,\text{V/m}$, which is one order of magnitude larger than for the (2D electron)–(2D electron) configuration (with high electron density). Figure 9.6 shows the dependence of the effective electric field in the channel on the velocity of the liquid flow in the adjacent channel, with the same liquid, for the (2D liquid)–(2D liquid) configuration.

Compared on the (2D-electron)–(2D-electron) and (2D-electron)–(2D-liquid) configurations, for the (2D-liquid)–(2D-liquid) configuration the effective electric field is many orders of magnitude larger, and depends nonlinearly on the liquid flow velocity v.

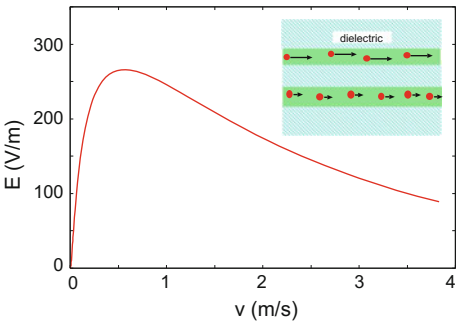

Fig. 9.6 The effective electric field in a 2D channel with liquid as a function of the flow velocity in a second 2D channel for identical liquids in both channels. The temperature $T = 300\,\text{K}$, the ion concentration in the liquid $N_0 = 10^{24}\,\text{m}^{-3}$, the thickness of the channels $d_c = 100\,\text{Å}$, the diffusion coefficients of ions $D = 10^{-9}\,\text{m}^2/\text{s}$ and the dielectric constant of the liquid $\varepsilon_c = 80$. The dielectric constant of the dielectric in the gap between channel is $\varepsilon = 10$, and the separation between the channels $d = 175\,\text{Å}$

9.4.2 Casimir Frictional Drag in a 2D System Induced by Liquid Flow in a Semi-infinite Chamber

Let us consider a 2D electron system, isolated from a semi-infinite liquid flow by a dielectric layer with the thickness d. For the 2D electron system, the reflection amplitude is given in Appendix M. To find the reflection amplitude for the interface between the dielectric and the liquid, we will assume that the liquid fills the half-space $z \geq 0$, and that the half-plane with $z < 0$ is filled by a dielectric with the dielectric constant ε. Let us study the reflection of an electromagnetic wave from the surface of the liquid in the nonretarded limit, which formally corresponds to the limit $c \to \infty$. In the region $z < 0$ the potential can be written in the form

$$\varphi_q = \left(e^{-qz} - Re^{qz}\right)e^{i\mathbf{q}\cdot\mathbf{x}-i\omega t}, \tag{9.50}$$

where q is the magnitude of the component of the wave vector parallel to surface. We will assume that the liquid consists of ions of two types a and b. The equation of continuity for the ions

$$-i\omega n_i + \nabla \cdot \mathbf{J}_i = 0, \tag{9.51}$$

where $i = a, b$, $n_i = N_i - N_0$, where N_i and N_0 are the concentration of ions in the presence and absence of the electric field, respectively. To linear order in the electric field

$$\mathbf{J}_i = -N_0\mu_i Q_i \nabla\varphi - D_i \nabla n_i, \tag{9.52}$$

where D_i is the diffusion coefficient, μ_i is the mobility and Q_i is the charge for ions of type i. The diffusion coefficient and the mobility are related to each other by the Einstein relation: $D_i = k_B T\mu_i$. We consider the case of different ion mobilities differing considerably. In this case, in the calculation of dielectric response it is possible to disregard the diffusion of the less mobile ions. Omitting the index i for the more mobile ions, after substitution of (9.52) in (9.50), we obtain

$$i\omega n + D\Delta\left(n + \frac{N_0 Q}{k_B T}\varphi\right) = 0. \tag{9.53}$$

This equation must be supplemented with the Poisson's equation

$$\nabla^2\varphi = -\frac{4\pi Q n}{\varepsilon_0}, \tag{9.54}$$

where ε_0 is the dielectric permeability of the liquid. The general solution of equations (9.53) and (9.54) can be written in the form

$$\varphi = \left(C_1 e^{-\lambda z} + C_2 e^{-qz}\right)e^{i\mathbf{q}\cdot\mathbf{x}}, \tag{9.55}$$

where $\lambda = \sqrt{q^2 + q_D^2 - i\omega/D}$ and $q_D = \sqrt{4\pi N_0 Q^2/\varepsilon_0 k_B T}$. At the interface ($z = 0$), the electric potential and the normal component of the electric displacement field must be continuous, and the normal component of the flow density must vanish. From these boundary conditions, we obtain

$$C_1 + C_2 = 1 - R, \tag{9.56}$$

$$-\varepsilon_0(\lambda C_1 + qC_2) + \varepsilon q(1 + R) = 0, \tag{9.57}$$

$$i\omega\lambda C_1 + Dq_D^2 qC_2 = 0. \tag{9.58}$$

From (9.56) to (9.58) we get

$$R_{lp} = \frac{\epsilon - 1}{\epsilon + 1}, \tag{9.59}$$

where

$$\epsilon = \frac{\varepsilon_0 \lambda\left(Dq_D^2 - i\omega\right)}{\varepsilon\left(Dq_D^2 q - i\omega\lambda\right)}. \tag{9.60}$$

For $v \ll v_F$, the frictional drag force acting on the electrons in the 2D system, due to the interaction with the ions in the liquid, increases linearly with the fluid velocity v. In particular, for $N_0 = 10^{24}\,\mathrm{m}^{-3}$, $T = 273\,\mathrm{K}$, $\varepsilon_0 = 80$, $D = 10^{-9}\,\mathrm{m}^2/\mathrm{s}$, for a high electron density ($n_s = 10^{19}\,\mathrm{m}^{-2}$) in the 2D electron system, $E = 1.4 \times 10^{-6} v\,\mathrm{V/m}$. This effective electric field is three orders of magnitude larger than that obtained for two 2D electron systems with high electron concentration, and of the same order of magnitude as friction between two 2D-electron systems with a low electron concentration.

Let us replace now the 2D electron structure with the 2D channel with polar liquid. Figure 9.7 shows the dependence of the effective electric field in the 2D-channel on the velocity of the liquid flow in the semi-infinite chamber, for identical liquid in the channel and in the chamber. We have used the same parameters as above for the liquid, with the separation between the channel and chamber $d = 1\,\mathrm{nm}$. The effective electric field in the channel initially increases with the fluid flow velocity, reaches a maximum, and then decreases. The position of the maximum decreases when the density of ions decreases. The frictional drag force induced by the liquid flow in the narrow channel is nine orders of magnitude larger than the frictional drag force induced in a 2D electron system.

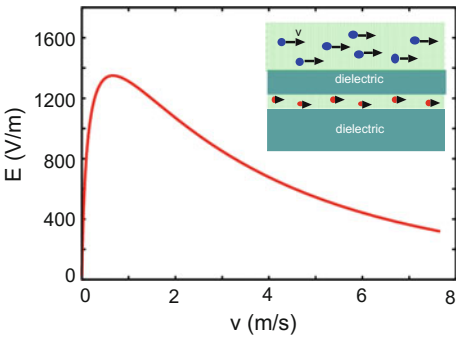

Fig. 9.7 The effective electric field in a 2D channel with liquid induced by liquid flow in a semi infinite chamber as a function of the flow velocity for identical liquids in the channel and in the chamber. The temperature $T = 300\,\mathrm{K}$, the ion concentration in liquid $N_0 = 10^{24}\,\mathrm{m}^{-3}$, the thickness of the channel $d_c = 10\,\mathrm{nm}$, the diffusion coefficients of ions $D = 10^{-9}\,\mathrm{m}^2/\mathrm{s}$ and the dielectric constant of the liquid $\varepsilon_0 = 80$. The dielectric constant of the dielectric in the gap between channel $\varepsilon = 10$, and the separation between the channel and semi-infinite chamber $d = 1\,\mathrm{nm}$

9.4.3 *Casimir Frictional Drag in Low Dimensional Structures Induced by Liquid Flow in Infinite System*

As a limiting case of the situation considered above, let us consider a 2D system immersed in a flowing liquid in an infinite chamber. We assume that the liquid flows along the x-axis, and that the plane of the 2D system coincides with the xy-plane. Let us calculate first the spectral function of the fluctuations of electric field in the quiescent infinite liquid without the 2D-system. We will examine the non-retarded limit, where only longitudinal fluctuations matters. According to the fluctuation-dissipation theorem (see Sect. 3.1), for an infinite medium the correlation function for the Fourier components of the longitudinal current density is determined by

$$\left|j_k^f\right|_\omega^2 = \frac{\hbar}{(2\pi)^2}\left[n(\omega) + 1/2\right]\omega^2 \mathrm{Im}\varepsilon(\omega, k), \tag{9.61}$$

where $\mathbf{k} = (\mathbf{q}, k_z)$ is the wave vector. Using the continuity equation, the longitudinal current density is connected to the charge density via $\rho_k = kj_k/\omega$. Thus,

$$\left|\rho_k^f\right|_\omega^2 = \frac{\hbar}{(2\pi)^2}\left[n(\omega) + 1/2\right]k^2 \mathrm{Im}\varepsilon(\omega, k). \tag{9.62}$$

Poisson's equation for the electric potential gives

$$\varphi_k^f = \frac{4\pi\rho_k}{k^2\varepsilon(\omega, k)}. \tag{9.63}$$

In the xy-plane, the $\mathbf{q}$-component of the electric potential is determined by

$$\varphi_q^f = \int \frac{dk_z e^{ik_z 0^+}}{2\pi} \varphi_k^f, \tag{9.64}$$

where $k = \sqrt{q^2 + k_z^2}$. Taking into account (9.62) and (9.63) we get

$$\left|\varphi_q^f\right|_\omega^2 = 4\hbar\big(n(\omega) + 1/2\big)\mathrm{Im}\Sigma(\omega), \tag{9.65}$$

where

$$\Sigma(\omega, q), = -\int_{-\infty}^{\infty} \frac{dk_z e^{ik_z 0^+}}{2\pi} \frac{1}{k^2 \varepsilon(\omega, k)}. \tag{9.66}$$

Taking into account that $E_q = iq\varphi_q$ we get $|E_q^f|_\omega^2 = q^2|\varphi_q^f|_\omega^2$. From the diffusion and Poisson's equations we get

$$\frac{i\omega}{D}\rho_k = k^2\left(\rho_k + \frac{N_0 Q^2}{k_B T}\varphi_k\right), \tag{9.67}$$

$$\varepsilon_0 k^2 \varphi_k = 4\pi\rho_k + 4\pi\rho_k^f. \tag{9.68}$$

From (9.65) and (9.68) we get the dielectric function of the Debye plasma

$$\varepsilon(k) = \varepsilon_0\left(1 + \frac{q_D^2}{k^2 - i\omega/D}\right). \tag{9.69}$$

Substituting (9.69) in (9.66) gives

$$\Sigma(\omega, q) = -\frac{1}{\varepsilon_0\big(q_D^2 - i\omega/D\big)}\left[-\frac{i\omega/D}{2q} + \frac{q_D^2}{2\lambda}\right]. \tag{9.70}$$

According to (9.6), the correlation function for the Fourier components of the fluctuating surface charge density in the 2D system is determined by

$$\left|\tau_q^f\right|_\omega^2 = \frac{\hbar q^2}{\pi\omega}\big(n(\omega) + 1/2\big)\mathrm{Re}\sigma(\omega, q). \tag{9.71}$$

If the 2D system is surrounded by liquid flow, the electric field created by the fluctuations of the charge density in the fluid will induce surface charge density fluctuations in the 2D system. The spectral correlation functions (9.65) and (9.71) are determined in the rest reference frame of the liquid, and of the 2D system, respectively. In order to find the connection between the electric fields in the different reference frames, we use the Galileo transformation, which leads to the Doppler frequency shift of the electrical field in the different reference frames. The electric field in the plane of the

2D system, due to the fluctuations of the charge density in the liquid, will take the form

$$E(\mathbf{x}, t) = e^{-i(\omega + q_x V)t + i\mathbf{q}\cdot\mathbf{x}} E_q^{\mathrm{I}}, \tag{9.72}$$

where E_q^I is the sum of the electric fields created by the fluctuations of the charge density in the fluid and the induced charge density in the 2D system:

$$E_q^{\mathrm{I}} = E_q^f + 4\pi i q \Sigma(\omega, q)\tau_q^I(\omega^+), \tag{9.73}$$

where $\omega^+ = \omega + q_x V$ and τ_q^I is the surface-induced charge density. According to Ohm's law

$$j_q^I = \sigma_q^+ E_q^I = \sigma_q^+ \left(E_q^f + 4\pi i q \Sigma(\omega, q)\tau_q^I(\omega^+)\right), \tag{9.74}$$

where $\sigma_q^+ = \sigma(\omega^+, q)$ is the longitudinal conductivity for the 2D system. The continuity equation for the surface charge density gives $j_q^{ind} = \omega^+ \tau_q^{ind}/q$ and from (9.74) we get

$$\tau_q^{\mathrm{I}} = \frac{q}{\omega^+} \frac{\sigma_q^+ E_q^f}{1 - 4\pi i q^2 \sigma_q^+/\omega^+ \Sigma(\omega, q)} \tag{9.75}$$

and

$$E_q^{\mathrm{I}} = \frac{E_q^f}{1 - 4\pi i q^2 \sigma_q^+/\omega^+ \Sigma(\omega, q)}. \tag{9.76}$$

In order to find the electric field created by the charge density fluctuations in the 2D system, it is necessary to solve Poisson's equation in the rest reference frame, of the liquid. In this reference frame the charge density takes the form

$$\tau(\mathbf{x}, t) = e^{-i(\omega - q_x V)t + i\mathbf{q}\cdot\mathbf{x}} \tau_q^{\mathrm{II}}, \tag{9.77}$$

where the surface charge density is composed from the fluctuating τ^f and induced τ^{ind} charge density: $\tau_q^{II} = \tau_q^f + \tau_q^{ind}$. In the presence of the liquid flow, the electric field in the plane of the 2D system, due to the fluctuating surface charge density, is determined by

$$E_q^{\mathrm{II}} = 4\pi i q \Sigma(\omega^-, q)(\tau_q^{ind} + \tau_q^f), \tag{9.78}$$

where $\omega^- = \omega - q_x V$. From Ohm's law, we get the following expression for the induced charge density

$$\tau_q^{ind} = \frac{4\pi i q^2 \sigma(\omega, q)\Sigma(\omega^-, q)}{\omega} \frac{\tau^f}{1 - 4\pi i q^2 \sigma_q \Sigma(\omega^-, q)/\omega}. \tag{9.79}$$

Substituting (9.79) in (9.78), we get

$$E_q^{\mathrm{II}} = \frac{4\pi i q \Sigma(\omega^-, q)\tau^f}{1 - 4\pi i q^2 \sigma_q \Sigma(\omega^-, q)/\omega} \tag{9.80}$$

and

$$\tau_q^{\mathrm{II}} = \frac{\tau^f}{1 - 4\pi i q^2 \sigma_q \Sigma(\omega^-, q)/\omega}. \tag{9.81}$$

The friction force per unit area of the 2D system is given by

$$\sigma_{\parallel} = \int_{-\infty}^{\infty} d\omega \int \frac{d^2\mathbf{q}}{(2\pi)^2} \frac{q_x}{q} \left\langle E_q \tau_q^* \right\rangle_{\omega}, \tag{9.82}$$

where $E_q = E_q^{\mathrm{I}} + E_q^{\mathrm{II}}$, $\tau_q = \tau_q^{\mathrm{I}} + \tau_q^{\mathrm{II}}$. Substituting (9.75), (9.76) and (9.80), (9.81) in (9.82) we get

$$\sigma_{\parallel} = \frac{2\hbar}{\pi^2} \int_{-\infty}^{\infty} dq_y \int_0^{\infty} dq_x q_x q^2 \Big\{ \int_0^{\infty} d\omega \left[n(\omega) - n(\omega + q_x v) \right] \times$$

$$\times \left(\frac{\mathrm{Re}\sigma(\omega + q_x v)\mathrm{Im}\Sigma(\omega, q)}{(\omega + q_x v) \mid 1 - 4\pi i q^2 \sigma(\omega + q_x v)\Sigma(\omega, q)/(\omega + q_x v) \mid^2} + (\omega + q_x v \leftrightarrow \omega) \right) -$$

$$- \int_0^{q_x v} d\omega \big[n(\omega) + 1/2 \big] \Big(\frac{\mathrm{Re}\sigma(\omega - q_x v)\mathrm{Im}\Sigma(\omega, q)}{(\omega - q_x v) \mid 1 - 4\pi i q^2 \sigma(\omega - q_x v)\Sigma(\omega, q)/(\omega - q_x v) \mid^2} +$$

$$+ (\omega - q_x v \leftrightarrow \omega) \Big) \Big\}. \tag{9.83}$$

where $(\omega \pm q_x v \leftrightarrow \omega)$ denotes the terms that are obtained from the preceding terms by permutations of the arguments $\omega \pm q_x v$ and ω. With the same parameters used above for the liquid, and for the high density 2D electron system, we get $E = 8.1 \times 10^{-6} v$ V/m. For a 1D-electron system, we obtained a formula that is similar to (9.83).

Figure 9.8 shows the result of the calculations of the effective electric field for a 1D-electron system with the electron density per unit length $n_l = 3 \times 10^9\,\mathrm{m}^{-1}$, the temperature $T = 300\,\mathrm{K}$, and with the same parameters for the liquid as used above. For the 1D-electron system, we obtained a slight deviation from the linear dependence of the frictional drag on the liquid flow velocity. The frictional drag for the 1D-electron system is one order of magnitude larger than for the 2D electron system.

Figure 9.9 shows the dependence of the effective electric field in the liquid in the 2D channel on the liquid flow velocity in the infinite chamber, assuming identical liquid in the channel and in the chamber. Qualitatively, we obtained the same results for a 1D channel.

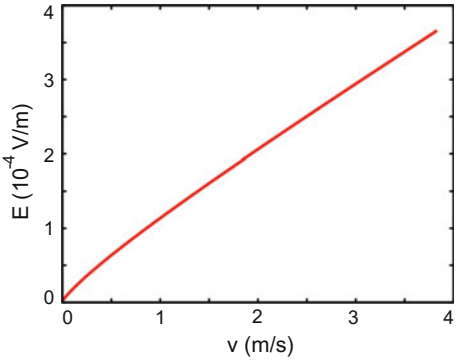

Fig. 9.8 The effective electric field in a 1D-electron system induced by liquid flow in a infinite chamber, as a function of the flow velocity. For the same parameters for the liquid as in Fig. 9.7. The electron concentration per unit length in the 1D-system $n_l = 3 \times 10^9\,\mathrm{m}^{-1}$, and the electron relaxation time $\tau = 4 \times 10^{-14}\,\mathrm{s}$

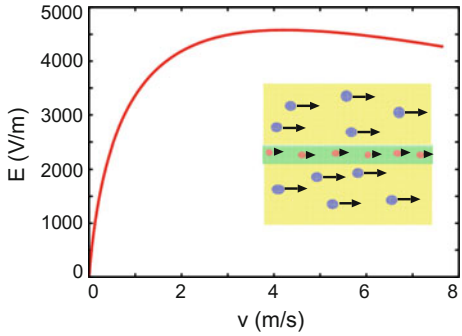

Fig. 9.9 The same as Fig. 9.7 but for infinite chamber

For a channel with open ends, the frictional drag force will induce a drift motion of the ions in the liquid with the velocity $v_d = D_c QE/k_B T$. The positive and negative ions will drift in the same direction. If ions have different mobility then the drifting ions will lead to an electric current whose direction will be determined by the current created by the ions with the largest mobility. For a channel with closed ends, the frictional drag force will lead to a change in ion concentration along the channel. In the case of ions with the different mobilities, the friction force will be different for the ions with the opposite charges. As a result, the ions of opposite charges will be characterized by different distribution functions, which, as for electronic systems, will result in an electric field and an induced voltage that can be measured. Let us write the friction force acting on the ions of different type in the form: $F_a = QE_a$ and $F_b = QE_b$. From the condition that, in the static case, the flux density in the channel must vanish, we get

$$n_a = -\frac{Q}{k_B T}\left(\varphi - E_a x\right), \tag{9.84}$$

$$n_b = \frac{Q}{k_B T}\left(\varphi + E_a x\right). \tag{9.85}$$

These equations must be supplemented with Poisson's equation

$$\frac{d^2\varphi}{d^2x} = -\frac{4\pi Q}{\varepsilon_c}(n_a - n_b). \tag{9.86}$$

Substituting (9.84) and (9.85) in (9.86), we get

$$\frac{d^2\varphi}{d^2x} = q_D^2\,(2\varphi - \Delta E x)\,, \tag{9.87}$$

where $\Delta E = E_a - E_b$. The solution of (9.87) with boundary condition

$$\left.\frac{d\varphi}{dx}\right|_{x=\pm L/2} = 0, \tag{9.88}$$

where L is the channel length, has the form

$$\varphi(x) = \frac{\Delta E}{2}\left(x - \frac{1}{\sqrt{2}q_D}\frac{\sinh\sqrt{2}q_D x}{\cosh\sqrt{2}q_D L/2}\right). \tag{9.89}$$

The voltage between the ends of the channel is determined by

$$U = \varphi(L/2) - \varphi(-L/2) = \Delta E\left(\frac{L}{2} - \frac{1}{\sqrt{2}q_D}\tanh\sqrt{2}q_D L/2\right). \tag{9.90}$$

For $q_D L \gg 1$, the voltage, which appears as a result of the frictional drag, will be approximately equal to $U \approx \Delta E L/2$. Furthermore, the frictional drag will induce a pressure difference $\Delta p = nLeE$. For example, if $N_0 = 10^{24}\,\mathrm{m}^{-3}$, $L = 100\,\mu\mathrm{m}$ and $E = 1000\,\mathrm{V/m}$, we get the pressure difference $\Delta p = 10^4$ Pa, which should be easy to measure. Assume now that one type of ions are fixed (adsorbed) on the walls of the channel and an equal number of mobile ions of opposite sign are distributed in the liquid phase. In this case, the motion of the polar liquid in the adjacent region will lead to frictional drag force acting on the mobile ions in the channel. For a channel with closed ends, this frictional drag will induce a voltage, which can be measured.

Chapter 10
Casimir Forces and Near-Field Radiative Heat Transfer in Graphene Structures

Casimir has shown that quantum fluctuations of the electromagnetic field produce an attractive force between macroscopic bodies. It has recently been shown that two non-contacting bodies moving relative to each other experience a friction due to the same quantum fluctuations of the electromagnetic field. However, until recently, there was no experimental evidence for or against this effect, because the predicted friction forces are very small, and precise measurements of quantum forces are incredibly difficult with the presently available technology. The existence of quantum friction is still debated even among theoreticians. However, the situation drastically changed with the discovery of a new material—graphene. We recently proposed that quantum friction can be detected in frictional drag experiments between graphene sheets, and in the transport properties of non-suspended graphene on an SiO_2 substrate in a high electric field.

Here, we investigate the dependence of the thermal Casimir force and the Casimir friction force between two graphene sheets on the drift velocity of the electrons in one graphene sheet. We show that the drift motion produces a measurable change of the thermal Casimir force due to the Doppler effect. The thermal Casimir force, as well as the Casimir friction, are strongly enhanced in the case of resonant photon tunneling when the energy of the emitted photon coincides with the energy of electron–hole pair excitations. In the case of resonant photon tunneling, even for temperatures above room temperature, the Casimir friction is dominated by quantum fluctuations.

We have used the theories of the Casimir friction and the near-field radiative energy transfer to study the heat generation and dissipation in graphene due to the interaction with phonon–polaritons in the (amorphous) SiO_2 substrate and acoustic phonons in graphene. For the low-field (low drift velocity) energy transfer between non-suspended graphene and the substrate, radiative energy transfer gives a significant contribution in addition to the phononic heat transfer. High-field (large drift velocity) heat transfer is determined by the phononic mechanism. For high electric field (large drift velocities) and low temperatures, quantum fluctuations give an important contribution to the energy flux and the friction force. For suspended graphene, the energy transfer coefficient at nanoscale gap is $\sim$3 orders of magnitude larger than the radiative heat transfer coefficient of the blackbody radiation limit. We

A.I. Volokitin and B.N.J. Persson, *Electromagnetic Fluctuations at the Nanoscale*,
NanoScience and Technology, DOI 10.1007/978-3-662-53474-8_10

have pointed out that graphene can be used to study near-field radiative heat transfer in the plate–plate configuration, and for shorter separations than is currently possible in the plate–sphere configuration.

10.1 Introduction

Friction is usually a very complicated process. It appears in its most elementary form when two flat surfaces, separated by a vacuum gap, are sliding relative to each other at zero Kelvin, where the friction is generated by the relative movement of quantum fluctuations. For several decades, physicists have been intrigued by the idea of quantum friction. It has recently been shown that two non-contacting bodies moving relative to each other experience a friction due to quantum fluctuations inside the bodies [11, 115, 121, 128]. However, until recently, there was no experimental evidence for or against this effect, because the predicted friction forces are very small, and precise measurements of quantum friction are incredibly difficult with presently available technology. Recently, we proposed [149, 165] that using graphene it should be possible to detect quantum friction.

Graphene, isolated monolayer of carbon, which was obtained very recently [270], consists of carbon atoms densely packed into a 2D honeycomb crystal lattice (Fig. 10.1). The unique electronic and mechanical properties of graphene are actively studied both theoretically and experimentally partly because of their importance for fundamental physics, and also because of its possible technological applications [270–273]. In particular, the valence band and conduction band in graphene touch each other, at one point named the Dirac point. Near this point, the energy spectrum for electrons and holes has a linear dispersion. Due to this linear (or 'conical') dispersion relation, electrons and holes near this point behave like relativistic particles described by the Dirac equation for massless fermions.

Graphene can also be useful for the detection of quantum friction. Consider graphene located on the surface of, for example, the polar dielectric SiO_2, or nearby on a second graphene sheet. In this case, the charge carriers in graphene experience

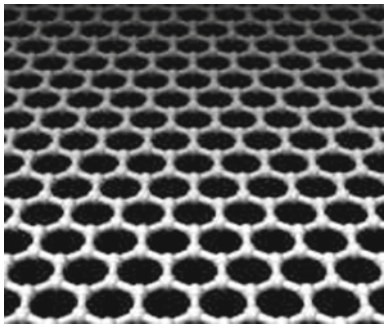

Fig. 10.1 Honeycomb lattice of graphene

additional friction due to interaction with the optical phonons in the dielectric, or the electrons in the other graphene sheet. Due to the high mobility, in a strong electric field the electrons in graphene can move with very high drift velocities ($\sim 10^6$ m/s). At such velocities, the main contribution to the friction will arise from quantum fluctuations. Thus, quantum friction can be detected by measuring the high electric field transport properties of graphene on a polar dielectric substrate, or by measuring the voltage induced by friction in a second nearby graphene sheet.

10.2 The Casimir Forces in Graphene Systems

At present, a great deal of attention is devoted to the study of the Casimir forces in graphene systems [274–282]. This is due to the unusual electronic properties of graphene, which result in Casimir forces with unusual properties. For normal materials, the contribution to the Casimir force due to thermal fluctuations dominates for $d > \lambda_T$; but, for two graphene sheets, the thermal contribution dominates of much shorter distances [282] $d > \xi_T = \hbar v_F / k_B T$, where $v_F \sim 10^6$ m/s is the Fermi velocity in graphene. At room temperature, the parameters λ_T and ξ_T are 7.6 μm and 25 nm, respectively. This property makes it possible to measure the thermal Casimir force using an atomic force microscope, or other force-measuring techniques. Tailoring the thermal Casimir force using Fermi level tuning by gate voltage was discussed in [280].

An alternative method of tailoring the thermal Casimir force consists of driving an electric current in a graphene sheet. It was shown by Pendry [115] that the reflection amplitudes from a moving metal surface are modified due to the Doppler effect. The same modification of reflection amplitudes can be obtained if, instead of the motion of a metal plate, a drift motion of charge carriers is induced in it by applied voltage [283]. The drift motion of the charge carries in graphene will result in a modification of dielectric properties (and the Casimir force) of graphene due to the Doppler effect [115] (see Fig. 1.7). If, in one of two parallel graphene sheets, an electric current is induced, then the electromagnetic waves, radiated by the graphene sheet without an electric current, will experience a frequency Doppler shift in the reference frame moving with the drift velocity v of electrons in the other graphene sheet: $\omega' = \omega - q_x v$, where q_x is the parallel to the surface component of the momentum transfer. The same is true for the waves emitted by the other graphene sheet. Due to the frequency dependence of the reflection amplitudes, the electromagnetic waves will reflect differently in comparison with the case when there is no drift motion of electrons, and this will give rise to the change of the Casimir force. The effect of the drift motion of charge carriers in one of the graphene sheet, on the thermal Casimir force between graphene sheets, was investigated in [165].

Let us consider two graphene sheets separated by a vacuum gap with thickness $d \ll \lambda_T$. Assume that the free charge carriers in one graphene sheet move with drift velocity $v \ll c$ along the x-axis (c is the light velocity) relative to the other graphene sheet. Because a drift motion of the free charge carriers produces a similar

modification of the reflection amplitudes as in the case of moving graphene sheet, the theory of the Casimir forces between moving bodies [128] can be used to calculate the Casimir forces between the sheets (both of which are at the rest) in the presence of the drift motion of the free charge carriers in one graphene sheet. The force, which acts on the surface of the sheet, can be calculated from the Maxwell stress tensor σ_{ij}, evaluated at the surface of the sheet at $z = 0$:

$$\sigma_{ij} = \frac{1}{4\pi}\int_0^\infty d\omega \int \frac{d^2q}{(2\pi)^2}\Big[\Big\langle E_i E_j^*\Big\rangle + \Big\langle E_i^* E_j\Big\rangle + \Big\langle B_i B_j^*\Big\rangle + \Big\langle B_i^* B_j\Big\rangle - \delta_{ij}\Big(\langle \mathbf{E}\cdot\mathbf{E}^*\rangle + \langle \mathbf{B}\cdot\mathbf{B}^*\rangle\Big)\Big]_{z=0} \tag{10.1}$$

where $\langle ...\rangle$ denotes statistical average over the fluctuating electromagnetic field. According to [128], the Casimir force $F_z = \sigma_{zz}$ between the moving media is determined by

$$F_z = F_{zT} + F_{z0}, \tag{10.2}$$

where the temperature-dependent term F_{zT}, and the zero-temperature contribution F_{z0} are given by

$$F_{zT} = \frac{\hbar}{\pi^3}\int_0^\infty dq_y \int_0^\infty dq_x q e^{-2qd} \Bigg\{\int_0^\infty d\omega\Bigg(\frac{\mathrm{Im}R_1(\omega)\mathrm{Re}R_2(\omega^+)n_1(\omega) + \mathrm{Re}R_1(\omega)\mathrm{Im}R_2(\omega^+)n_2(\omega^+)}{\mid 1 - e^{-2qd}R_1(\omega)R_2(\omega^+)\mid^2} + (1\leftrightarrow 2)\Bigg) + \int_0^{q_x v} d\omega\Bigg(\frac{\mathrm{Re}R_1(\omega^-)\mathrm{Im}R_2(\omega)n_2(\omega)}{\mid 1 - e^{-2qd}R_1(\omega^-)R_2(\omega)\mid^2} + (1\leftrightarrow 2)\Bigg)\Bigg\}, \tag{10.3}$$

$$F_{z0} = \frac{\hbar}{2\pi^3}\int_0^\infty dq_y \int_0^\infty dq_x \Bigg\{\mathrm{Re}\int_0^\infty d\omega s e^{-2sd}\Bigg(\frac{R_1(i\omega)R_2(i\omega + q_x v)}{1 - e^{-2sd}R_1(i\omega)R_2(i\omega + q_x v)} + (1\leftrightarrow 2)\Bigg) + \int_0^{q_x v} d\omega q e^{-2qd}\Bigg(\frac{\mathrm{Im}R_1(\omega)\mathrm{Re}R_2(\omega^-)}{\mid 1 - e^{-2qd}R_1(i\omega)R_2(\omega^-)\mid^2} + (1\leftrightarrow 2)\Bigg)\Bigg\}, \tag{10.4}$$

where $n_i(\omega) = [\exp(\hbar\omega/k_B T_i) - 1]^{-1}$ $(i = 1, 2)$, $q = \sqrt{q_x^2 + q_y^2}$, $s = \sqrt{(\omega/c)^2 + q^2}$, T_i is the temperature of i-th graphene sheet, R_i is the reflection amplitude for surface i for p-polarized electromagnetic waves, and $\omega^\pm = \omega \pm q_x v$. The symbol $(1 \leftrightarrow 2)$ denotes the terms that are obtained from the preceding terms by permutation of 1 and 2. In the first term in (10.4), the integration along the real axis was transformed into an integration along the imaginary axis.

The reflection amplitude for a 2D system is determined by [144]

$$R_i = \frac{\epsilon_i - 1}{\epsilon_i}, \quad \epsilon_i = \frac{2\pi p \sigma_i}{\omega \varepsilon} + 1, \tag{10.5}$$

where $p = \sqrt{(\omega/c)^2 - q^2}$, σ_i is the longitudinal conductivity of the sheet, which can written in the form $\sigma_i = -i\omega e^2 \Pi_i(\omega, q)/q^2$ where Π_i is the 2D polarizability. The dielectric function of the sheet is determined by $\varepsilon_i(\omega, q) = 1 + v_q \Pi_i(\omega, q)$ where $v_q = 2\pi e^2/(q\varepsilon)$ is the 2D Coulomb interaction. In terms of ε_i the reflection amplitude can be written as

$$R_i = \frac{p(\varepsilon_i - 1)}{p(\varepsilon_i - 1) + iq} \tag{10.6}$$

In the integration on the real axis $p \approx iq$ for $d < \lambda_T$. Thus, in this case

$$R_i \approx \frac{\varepsilon_i - 1}{\varepsilon_i}, \tag{10.7}$$

On the imaginary axis, $p = is$. In the finite lifetime generalization according to the Mermin approximation [354], the dielectric function is determined by

$$\varepsilon(\omega, q) \approx 1 + \frac{(\omega + i\gamma)\big(\varepsilon_0(\omega + i\gamma, q) - 1\big)}{\omega + i\gamma\big(\varepsilon_0(\omega + i\gamma, q) - 1\big)/\big(\varepsilon_0(0, q) - 1\big)}, \tag{10.8}$$

where $\varepsilon_0(\omega, q)$ is the RPA dielectric function and γ is the damping parameter. In the study below, we used the dielectric function of graphene, which was calculated recently within the random-phase approximation (RPA). The small (and constant) value of the graphene Wigner-Seitz radius r_s indicates that it is a weakly interacting system for all carries densities, making the RPA an excellent approximation for graphene (RPA is asymptotically exact in the $r_s \ll 1$ limit). The dielectric function is an analytical function in the upper half-space of the complex ω-plane:

$$\varepsilon_0(\omega, q) = 1 + \frac{4k_F e^2}{\hbar v_F q} - \frac{e^2 q}{2\hbar\sqrt{\omega^2 - v_F^2 q^2}}\left\{G\left(\frac{\omega + 2v_F k_F}{v_F q}\right) - G\left(\frac{\omega - 2v_F k_F}{v_F q}\right) - i\pi\right\}, \tag{10.9}$$

where

$$G(x) = x\sqrt{x^2 - 1} - \ln\left(x + \sqrt{x^2 - 1}\right), \tag{10.10}$$

where the Fermi wave vector $k_F = (\pi n)^{1/2}$, n is the concentration of charge carriers, the Fermi energy $\epsilon_F = \hbar v_F k_F$, $v_F \approx 10^6$ m/s is the Fermi velocity. The damping parameter γ is due to electron scattering against impurities and acoustic phonons in graphene sheet, and can be expressed through the low-field mobility μ: $\gamma = ev_F/(\hbar k_F \mu)$. Scattering of the graphene carries by the acoustic phonons of graphene places an intrinsic limits on the low-field room temperature ($T_0 = 300$

K) mobility, given by $\mu_0 = 20$ m^2/Vs at the graphene carriers density 10^{16} m^{-2} (see [357]), which gives $\gamma = 8 \times 10^{11}$ s^{-1}. At other temperatures the mobility can be obtained using the relation $\mu = \mu_0 T_0/T$.

In addition to the intrinsic friction due to scattering against impurities and phonons, during drift motion of the electrons in the graphene sheet, the extrinsic friction occurs due to the interaction with the electrons in the nearby graphene sheet. According to the theory of the Casimir friction [128], the friction force $F_x = \sigma_{xz} = F_{xT} + F_{x0}$, where at $d \ll \lambda_T$ and $v \ll c$ the contributions from thermal (F_{xT}) and quantum (F_{x0}) fluctuations are given by [11, 115, 121, 149]

$$F_{xT} = \frac{\hbar}{\pi^3}\int_0^\infty dq_y \int_0^\infty dq_x q_x e^{-2qd} \left\{ \int_0^\infty d\omega \left(\frac{\mathrm{Im}R_1(\omega)\mathrm{Im}R_2(\omega^+)}{|\,1 - e^{-2qd}R_1(\omega)R_2(\omega^+)\,|^2} \times \left[n_1(\omega) - n_2(\omega^+) \right] + (1 \leftrightarrow 2) \right) - \int_0^{q_x v} d\omega \left(\frac{\mathrm{Im}R_1(\omega)\mathrm{Im}R_2(\omega^-)}{|\,1 - e^{-2qd}R_1(\omega)R_2(\omega^-)\,|^2} n_1(\omega) + (1 \leftrightarrow 2) \right) \right\}, \tag{10.11}$$

$$F_{x0} = -\frac{\hbar}{2\pi^3}\int_0^\infty dq_y \int_0^\infty dq_x q_x e^{-2qd} \int_0^{q_x v} d\omega \left(\frac{\mathrm{Im}R_1(\omega)\mathrm{Im}R_2(\omega^-)}{|\,1 - e^{-2qd}R_1(\omega)R_2(\omega^-)\,|^2} + (1 \leftrightarrow 2) \right). \tag{10.12}$$

Equations (10.11) and (10.12) were initially obtained for 3D systems in [115] at $T = 0$ and in [121] for finite temperatures. However, in [144] it was shown that the same formulas are valid for 2D systems. For $v < dk_B T/\hbar$ (at $d = 1$ nm and $T = 300$ K for $v < 4 \times 10^4$ m/s) the main contribution to the friction (10.11) depends linearly on the sliding velocity v so that the friction force $F_{xT} = \Gamma v$, where at $T_1 = T_2 = T$ the friction coefficient Γ is given by

$$\Gamma = \frac{\hbar^2}{8\pi^2 k_B T}\int_0^\infty \frac{d\omega}{\sinh^2\left(\frac{\hbar\omega}{2k_B T}\right)} \int_0^\infty dq\, q^3 e^{-2qd} \frac{\mathrm{Im}R_1(\omega)\mathrm{Im}R_2(\omega)}{|\,1 - e^{-2qd}R_1(\omega)R_2(\omega)\,|^2}. \tag{10.13}$$

Due to the presence of an exponential factor in the expression (10.3) for the thermal contribution to the Casimir force, the integration over frequency is effectively limited to $\omega < \omega_T = k_B T/\hbar$. Thus, for $q_x v \sim v/d > \omega_T$ (at room temperature and for $d = 1$ nm, this condition corresponds to the velocities $v > 10^5$ m/s), the integrand will be modified in the whole range of integration, which will give rise to the significant change of the thermal Casimir force. This change will be especially large in the case of resonant photon tunneling when the integrand has sharp resonances. The integrand in the expression for the zero-temperature contribution to the Casimir force does not contain any sharp cut-off in the frequency integration. Thus, the range of integration will be wider and the change of the zero-temperature contribution will be significant only for much higher velocities than for the thermal contribution.

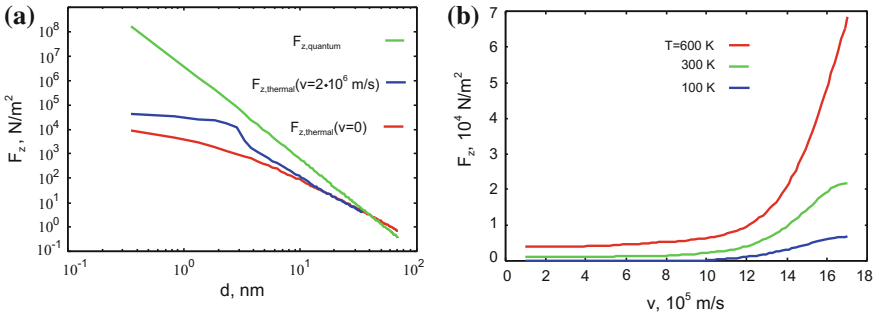

Fig. 10.2 The Casimir forces between two graphene sheets with carrier concentration $n = 10^{16}\text{m}^{-2}$. **a** The dependence of the Casimir force on the separation d between the sheets. The thermal and quantum contributions to the total Casimir force are shown separately. The thermal contribution is shown for $T = 600$ K and for the drift velocities $v = 0$ and $v = 2 \times 10^6$ m/s; **b** The dependence of the thermal Casimir force on the drift velocity of electrons v in one of the graphene sheet at $d = 1$ nm

Figure 10.2a shows the dependence of the Casimir force between two graphene sheets on the separation, d, between the sheets. The thermal and quantum contributions are shown separately. The thermal contribution was calculated for $T = 600$ K and for the electron drift velocities $v = 0$ and $v = 2 \times 10^6$ m/s. The thermal contribution becomes larger than the quantum contribution for $d > 50$ nm. For $d < 5$ nm, the thermal contribution calculated for $v = 2 \cdot 10^6$ m/s is significantly larger then the thermal contribution calculated at $v = 0$. For example, at $d \approx 3$ nm the drift motion of the electrons gives rise to an increase of the thermal Casimir force by one order of magnitude, and in this case the thermal contribution is only one order of magnitude smaller than the quantum contribution, and can be measured experimentally. Figure 10.2b shows the dependence of the thermal Casimir force F_{zT} on the drift velocity of the electrons in the graphene sheet at $d = 1$ nm. Note the significant change of the thermal Casimir force for $v/d > \omega_T$ (at room temperature and for $d = 1$ nm, this condition corresponds to the velocities $v > 10^5$ m/s).

Let us assume that in the rest reference frame, in which there is no drift motion of electrons, an electron hole pair excitation has the energy $\omega_{eh}(q)$ and momentum $\mathbf{q}$, then in the laboratory reference frame, in which the electron system is moving with drift velocity v, due to the Doppler effect, the energy of this excitation will be equal to $\omega_{eh}(q) - q_x v$. For $v > \omega_{eh}(q)/q_x$ the excitation energy will be negative. Thus, for velocities larger than critical velocity ($v_{cr} = \omega_{eh}(q)/q_x$), as a result of such excitation, the photon can be created with energy $\omega_{ph}(q) = q_x v - \omega_{eh}(q) > 0$, i.e. radiation arises. This radiation is reminiscent of the Cherenkov radiation, which arises when an electron moves in a medium with a velocity exceeding the light velocity in the medium. The difference between the two phenomena is that Cherenkov radiation is connected to the radiation of electromagnetic waves, but the radiation which arises from drift motion of the electron in the graphene sheet results from the excitations of electron–hole pairs in graphene. Resonance arises

when the photon emitted by the moving electron system in one graphene sheet with energy $\omega_{ph}(q) = q_x v - \omega_{eh}(q) > 0$ will create excitation with energy $\omega_{eh}(q)$ in the other graphene sheet. In the case of graphene, the energy of the electron hole pair excitation $\omega_{eh}(q) \approx v_F q$, where v_F is the Fermi velocity. Thus, resonance arises when $q_x v \approx 2v_F q$, which requires that $v > 2v_F \approx 2 \times 10^6$ m/s, in accordance with the numerical calculations.

10.3 Using Graphene to Detect Quantum Friction

Quantum friction determines the ultimate limit to which the friction can be reduced. In order to detect quantum friction, it is necessary to reduce the contribution to friction from other mechanisms up to unprecedented levels. However, even in non-contact friction experiments [166, 359], when two bodies are not in direct contact, there are several contributions to the friction [11]. Moreover, quantum friction dominates over thermal friction at velocities $v > dk_B T/\hbar$ (at $d = 1$ nm and room temperature: $v > 10^5$m/s). However, at present, even for a hard cantilever, the velocity of the tip cannot exceed 1 m/s [359].

We recently proposed [149] that it should be possible to detect quantum friction in graphene adsorbed on an amorphous SiO_2 substrate (Fig. 10.3). The electrons, moving in graphene under the action of an electric field, will experience an intrinsic friction due to interaction with the acoustic and optical phonons in graphene, and an extrinsic friction due to interaction with the optical phonons in the SiO_2-substrate. In high electric fields, the electrons move with high velocities, and in this case the main contribution to the friction arises from the interaction with the optical phonons in graphene and in SiO_2. However, the frequency of the optical phonons in graphene is approximately four times larger than in SiO_2. Therefore, the main contribution to the friction will result from the interaction with the optical phonons in SiO_2. Thus, this frictional interaction determines the electrical conductivity of graphene at high electric field.

The dissipated energy due to the friction results in heating of the graphene, and is transferred to the SiO_2 substrate via the near-field radiative heat transfer process and direct phononic coupling. Using the theories of Casimir friction and the near-field radiative heat transfer, we have formulated a theory that describes these phenomena and allows us to predict experimentally measurable effects. In comparison with the existing microscopic theories of transport in graphene [360, 361], our theory is macroscopic. The electromagnetic interaction between graphene and a substrate is described by the dielectric functions of the materials, which can be accurately determined from theory and experiment.

Let us consider graphene and a substrate with flat parallel surfaces at separation $d \ll \lambda_T = c\hbar/k_B T$. Assume that the free charge carriers in graphene move with the velocity $v \ll c$ (c is the light velocity) relative to the substrate. According to [11, 121, 128], the frictional stress F_x acting on the charge carriers in graphene, and the radiative heat flux S_z across the surface of substrate, both mediated by a fluctuating

electromagnetic field, are determined by

$$F_x = \frac{\hbar}{\pi^3}\int_0^\infty dq_y \int_0^\infty dq_x q_x e^{-2qd}\left\{\int_0^\infty d\omega\left(\frac{\mathrm{Im}R_d(\omega)\mathrm{Im}R_g(\omega^+)}{|\,1-e^{-2qd}R_d(\omega)R_g(\omega^+)\,|^2}\right.\right.$$
$$\times\left[n_d(\omega)-n_g(\omega^+)\right]+\left.\frac{\mathrm{Im}R_d(\omega^+)\mathrm{Im}R_g(\omega)}{|\,1-e^{-2qd}R_d(\omega^+)R_g(\omega)\,|^2}\left[n_g(\omega)-n_d(\omega^+)\right]\right)$$
$$\left.+\int_0^{q_x v} d\omega\frac{\mathrm{Im}R_d(\omega)\mathrm{Im}R_g(\omega^-)}{|\,1-e^{-2qd}R_d(\omega)R_g(\omega^-)\,|^2}\left[n_g(\omega^-)-n_d(\omega)\right]\right\}, \tag{10.14}$$

$$S_z = \frac{\hbar}{\pi^3}\int_0^\infty dq_y \int_0^\infty dq_x e^{-2qd}\left\{\int_0^\infty d\omega\left(\frac{\omega\mathrm{Im}R_d(\omega)\mathrm{Im}R_g(\omega^+)}{|\,1-e^{-2qd}R_d(\omega)R_g(\omega^+)\,|^2}\right.\right.$$
$$\times\left[n_d(\omega)-n_g(\omega^+)\right]+\left.\frac{\omega^+\mathrm{Im}R_d(\omega^+)\mathrm{Im}R_g(\omega)}{|\,1-e^{-2qd}R_d(\omega^+)R_g(\omega)\,|^2}\left[n_g(\omega)-n_d(\omega^+)\right]\right)$$
$$\left.+\int_0^{q_x v} d\omega\frac{\omega\mathrm{Im}R_d(\omega)\mathrm{Im}R_g(\omega^-)}{|\,1-e^{-2qd}R_d(\omega)R_g(\omega^-)\,|^2}\left[n_g(\omega^-)-n_d(\omega)\right]\right\}, \tag{10.15}$$

where $n_i(\omega)=[\exp(\hbar\omega/k_BT_i-1]^{-1}\,(i=g,d)$, $T_{g(d)}$ is the temperature of graphene (substrate), R_i is the reflection amplitude for surface i for p-polarized electromagnetic waves, and $\omega^\pm=\omega\pm q_x v$. The reflection amplitude for graphene is determined by (10.7) and for the substrate

$$R_d=\frac{\epsilon_d-1}{\epsilon_d+1}, \tag{10.16}$$

where ϵ_d is the dielectric function for substrate. The dielectric function of amorphous SiO_2 can be described using an oscillator model [358]

$$\epsilon(\omega)=\epsilon_\infty+\sum_{j=1}^{2}\frac{\sigma_j}{\omega_{0,j}^2-\omega^2-i\omega\gamma_j}, \tag{10.17}$$

where parameters $\omega_{0,j}$, γ_j and σ_j were obtained by fitting the measured ϵ for SiO_2 to the above equation, and are given by $\epsilon_\infty=2.0014$, $\sigma_1=4.4767\times10^{27}\mathrm{s}^{-2}$, $\omega_{0,1}=8.6732\times10^{13}\mathrm{s}^{-1}$, $\gamma_1=3.3026\times10^{12}\mathrm{s}^{-1}$, $\sigma_2=2.3584\times10^{28}\mathrm{s}^{-2}$, $\omega_{0,2}=2.0219\times10^{14}\mathrm{s}^{-1}$, and $\gamma_2=8.3983\times10^{12}\mathrm{s}^{-1}$.

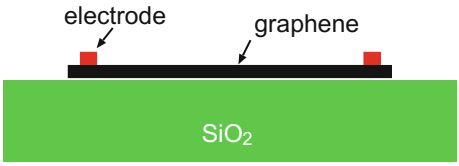

Fig. 10.3 Scheme of the graphene field effect transistor

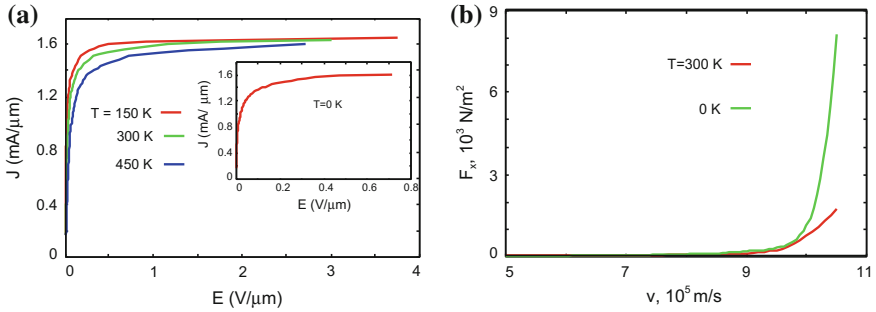

Fig. 10.4 The role of the interaction between phonon polaritons in SiO_2 and free carriers in graphene for graphene field-effect transistor transport. The separation between graphene and the SiO_2 is $d = 3.5$ Å, and the charge density $n = 10^{12}$ cm^{-12} **a** Current density-electric field dependence for different temperatures. *Inset* shows the same dependence at $T = 0$ K; **b** Dependence of the quantum and thermal contributions to the friction force (per unit area) between SiO_2 and the free carriers in graphene per unit area on the drift velocity of electrons in graphene. The finite temperature curve shows only the thermal contribution

The steady-state temperature can be obtained from the condition that the power generated by friction must be equal to the energy transfer across the substrate surface

$$F_x(T_d, T_g)v = S_z(T_d, T_g) + \alpha_{ph}(T_g - T_d), \tag{10.18}$$

where the second term in (10.18) takes into account the heat transfer through direct phononic coupling; α_{ph} is the thermal contact conductance due to phononic coupling.

Figure 10.4a shows the dependence of the current density on the electric field at the carrier concentration $n = 10^{12}$ cm^{-2}, and for different temperatures. We have found that, in agreement with the experiment [164], the current density saturates at $E \sim 0.5$–2.0 V/μm. According to the experiment, the saturation current density $J_{sat} = nev_{sat} \approx 1.6$ mA/μm, and using the charge density concentration $n = 10^{12}$ cm^{-2}: $v_{sat} \approx 10^6$ m/s. The saturation current density depends weakly on the temperature. In Fig. 10.4b, the contributions to the friction force from quantum and thermal fluctuations are shown separately. In the saturation region, the contribution to the friction force from quantum fluctuations dominates.

According to the theory of the Casimir friction [11] (see also above discussion), the quantum friction, which exists even at zero temperature, is determined by the creation of excitations (electron hole pairs or optical phonons) in each of the interacting media. The frequency of the photon associated with the excitations in moving body is determined by $\omega_{ph} = vq_x - \omega_1$, where ω_1 is the excitation frequency in the rest reference frame. This photon will create excitation in the other body with the frequency $\omega_2 = \omega_{ph} = vq_x - \omega_1$. The relevant excitations in graphene are the electron–hole pairs with energy $\omega_{eh}(q) \approx v_F q$, while for SiO_2 the frequency of surface phonon polaritons $\omega_0 \approx 60$ meV (9×10^{13} s^{-1}). Resonant photon tunneling occurs at $v > v_F + \omega_0/q_x$. The maximal value of wave vector is $\sim 1/d$. Thus, at $d = 0.35$ nm, resonance occurs for $v > v_{sat} = v_F + \omega_0 d \sim 10^6$ m/s, in accordance

with the numerical calculations. Thus, measurements of the current density–electric field relation of graphene adsorbed on SiO_2 provide the possibility of detecting quantum friction.

10.4 Casimir Frictional Drag Force Between Graphene Sheets

An alternative method of studying Casimir friction consists of driving an electric current in one metallic layer and studying the effect of the frictional drag on the electrons in a second (parallel) metallic layer (Fig. 9.1). Such experiments were proposed by Pogrebinskii [255] and Price [256], and were performed for 2D quantum wells [112–114]. In these experiments, a current is driven through layer **1**. Due to the proximity of the layers, the interlayer interactions will induce a current in layer **2** due to a frictional stress acting on the electrons in the layer **2** from layer **1**. If the layer **2** is an open circuit, an electric field E_1 will develop in the layer whose influence cancels the frictional stress σ between the layers. In the experiment [112], the drift velocity $v \sim 10^2$ m/s. According to the theory of the Casimir friction [121, 144], at such velocities, the thermal fluctuation gives the dominant contribution to the friction, and the theoretical predictions are in agreement with experiment.

Frictional drag between graphene sheets was measured recently in [162, 163]. This study has fueled the recent theoretical investigations of frictional drag between graphene sheets [362–368] mediated by a fluctuating Coulomb field. In all of these investigations, the current density (or drift velocity v of the charge carries) is linearly related to the driving electric field. Thus, only the thermal contribution to the frictional drag was included. In the linear approximation, the electric field induced by the frictional drag depends linearly on the current density $J = nev$ (or drift velocity v of the charge carries), $E = \rho_D J = F_{xT}/ne = \Gamma J/(ne)^2$, where Γ is the friction coefficient and $\rho_D = \Gamma/(ne)^2$ is the drag resistivity. For $\omega < v_F q$ and $q < 2k_F$ the dielectric function of graphene has the following form [356]

$$\varepsilon_0(\omega, q) \approx 1 + \frac{4e^2 k_F}{\hbar v_F q}\left(1 + i\frac{\omega}{v_F q}\right), \tag{10.19}$$

and the reflection amplitude

$$R_0(\omega, q) = \frac{\varepsilon_0(\omega, q) - 1}{\varepsilon_0(\omega, q)} \approx 1 + i\frac{\hbar\omega}{4e^2 k_F}, \tag{10.20}$$

and (10.20) and (10.13) give the known result [362]

$$\rho_D = \frac{\Gamma}{(ne)^2} = \frac{h}{e^2}\frac{\pi\zeta(3)}{32}\left(\frac{k_B T}{\epsilon_F}\right)^2 \frac{1}{(k_F d)^2}\frac{1}{(k_{TF} d)^2}, \tag{10.21}$$

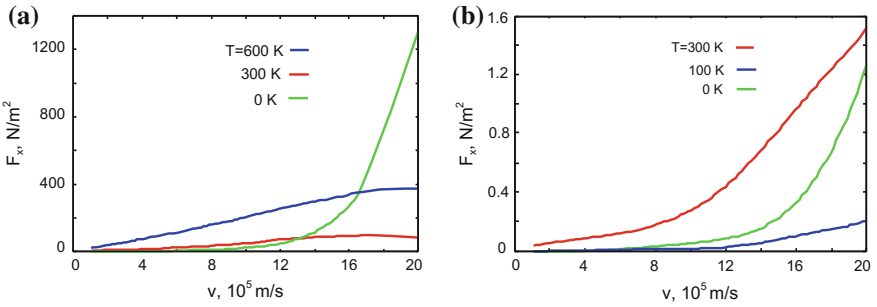

Fig. 10.5 Frictional drag between two graphene sheets at the carrier concentration $n = 10^{12}$ cm^{-2}. The finite temperature curves show only the thermal contributions to the friction. **a** Dependence of friction force between graphene sheets on the drift velocity of charge carriers in one graphene sheet at the layer separation $d = 1$ nm. **b** The same as in (**a**) but at $d = 10$ nm

where $k_{TF} = 4e^2 k_F/\hbar v_F$ is the Thomas-Fermi screening wave vector. The frictional drag force is much higher for high drift velocities ($\sim 10^6$ m/s), where it depends non-linearly on the drift velocity, and is dominated by the quantum friction [149]. For $v < v_F$ (10.20) and (10.12) give the following result for quantum friction

$$F_{x0} = \frac{\hbar v}{d^4}\frac{15\zeta(5)}{128\pi^2}\left(\frac{v}{v_F}\right)^2 \frac{1}{(k_{TF}d)^2}. \tag{10.22}$$

In the linear approximation $E = 5 \times 10^{-4} v$ (SI-units) for $T = 300$ K and $d = 10$ nm. For a graphene sheet of length 1 μm, and with $v = 100$ m/s, this electric field will induce the voltage $V = 10$ nV. From (10.21) and (10.22), the ratio between the quantum and thermal friction $F_{x0}/F_{xT} = F_{x0}/(ne)^2\rho_D v \approx (15/8\pi^2)(v/v_T)^2$, where $v_T = \omega_T d$. Thus, for $v > v_T$ the friction is dominated by quantum friction (at $d = 1$ nm and room temperature: $v_T \approx 4 \times 10^4$m/s).

Figure 10.5a, b show that much larger electric fields can be induced at $d = 1$ nm (a) and $d = 10$ nm (b) at large velocities. In these figures, the contributions to friction from thermal and quantum fluctuations are shown separately. For $v < 10^5$ m/s, the frictional drag effect for the graphene sheets strongly depends on temperature, i.e. it is determined mainly by the thermal fluctuations. However, for $v > 10^6$m/s it will be dominated by quantum fluctuations. Strong enhancement of friction occurs in the case of resonant photon tunneling. As discussed above, resonant photon tunneling occurs for $v > 2v_F \approx 2 \times 10^6$ m/s. For such velocities and $d = 1$ nm, quantum friction dominates over the thermal contribution even at room temperature (see Fig. 10.5a). For $d = 10$ nm, quantum friction dominates at low temperatures (see Fig. 10.5b).

The use of graphene in frictional drag experiments has considerable advantages in comparison with quantum wells. Such experiments can be performed in a vacuum where the contribution from the phonon exchange can be excluded. In a vacuum, one can easily measure the dependence of the frictional drag force on the separation between graphene sheets. Due to the high mobility of the charge carriers in graphene, the charge carriers can move with much higher drift velocity than in quantum wells.

10.5 Near-Field Radiative Heat Transfer Between Closely Spaced Graphene and Amorphous SiO_2

In this Section, we investigate heat generation and dissipation due to friction produced by the interaction between moving (drift velocity v) charge carriers in graphene and the optical phonons in a nearby amorphous SiO_2, and the acoustic phonons in graphene. Friction produces thermal heating of the graphene, which results in near-field radiative energy transfer and phononic heat transfer between the graphene and SiO_2. A self-consistent theory that describes these phenomena was formulated by us in [149] (see also Sect. 10.3) and it allows us to predict experimentally measurable effects. In comparison with the existing microscopic theories of energy transfer and transport in graphene [360, 361], our theory is macroscopic.

According to (10.14) and (10.15) in the case when free carriers are moving relative to the substrate both thermal and quantum fluctuations give contributions to the frictional stress and the radiative energy transfer. This situation is different from that considered in [370, 371] where it was assumed that the free carries in graphene had vanishing drift velocity. The contribution of the quantum fluctuations to the frictional stress was investigated by us in [149] (see also Sect. 10.3). According to (10.15) the contribution to the near-field energy transfer from quantum fluctuations is determined by

$$S_z^{quant} = S_z(T_d = T_g = 0) = -\frac{\hbar}{\pi^3}\int_0^\infty dq_y \int_0^\infty dq_x \int_0^{q_x v} d\omega \omega e^{-2qd} \frac{\mathrm{Im} R_d(\omega)\mathrm{Im} R_g(\omega^-)}{|\,1 - e^{-2qd} R_d(\omega) R_g(\omega^-)\,|^2} \tag{10.23}$$

As discussed in Sect. 10.3, for graphene on SiO_2 the excess heat generated by the current is transferred to the substrate through the near-field radiative heat transfer, and via the direct phononic coupling (for which the heat transfer coefficient $\alpha \approx 10^8 \mathrm{Wm}^{-2}\mathrm{K}^{-1}$). At small temperature difference ($\Delta T = T_g - T_d \ll T_d$), from (10.18) we get

$$\Delta T = \frac{F_{x0} v - S_{z0}}{\alpha_{ph} + S'_{z0} - F'_{x0} v} \tag{10.24}$$

where $F_{x0} = F_x(T_d, T_g = T_d)$, $S_{z0} = S_z(T_d, T_g = T_d)$,

$$F'_{x0} = \frac{dF_x(T_d, T_g)}{dT_g}\Big|_{T_g = T_d}, \quad S'_{z0} = \frac{dS_z(T_d, T_g)}{dT_g}\Big|_{T_g = T_d}$$

We note that, in contrast to the heat transfer between bodies at rest, for moving bodies the energy flux $S_z(T_d, T_g)$ is not equal to zero even for the case when there is no temperature difference between the bodies. The energy transfer coefficient is given by

$$\alpha = \frac{S_z(T_d, T_g) + \alpha_{ph}\Delta T}{\Delta T} \approx \frac{(\alpha_{ph} + S'_{z0})F_{x0}v - S_{z0}F'_{x0}v}{F_{x0}v - S_{z0}} \tag{10.25}$$

For small velocities $F_{x0} \sim v$ and $S_{z0} \sim v^2$. Thus, from (10.25) it follows that in the limit $v \to 0$ the energy transfer coefficient between moving bodies is not reduced to the heat transfer coefficient between bodies at rest, which is determined by $\alpha_{th} = \alpha_{ph} + S'_{z0}$. This effect is due to the term S_{z0} in the total energy flux which exists only between moving bodies. The energy transfer coefficient can be strongly enhanced in comparison with the heat transfer coefficient when $F_{t0}v \approx S_{z0}$. Figure 10.6a shows the ratio of the energy transfer coefficient to the phononic heat transfer coefficient for $d = 0.35\,\text{nm}$ and $n = 10^{16}\ \text{m}^{-2}$. For low and intermediate fields, this ratio is larger than unity, which means that, in this region, the near-fields radiative energy transfer gives an additional significant contribution to the heat transfer. For nonsuspended graphene on SiO_2, the energy and heat transfer are very effective and the temperature difference does not rise high, even for such high electric fields that saturation in $I - E$ characteristic starts [164] (see Fig. 10.6b). The

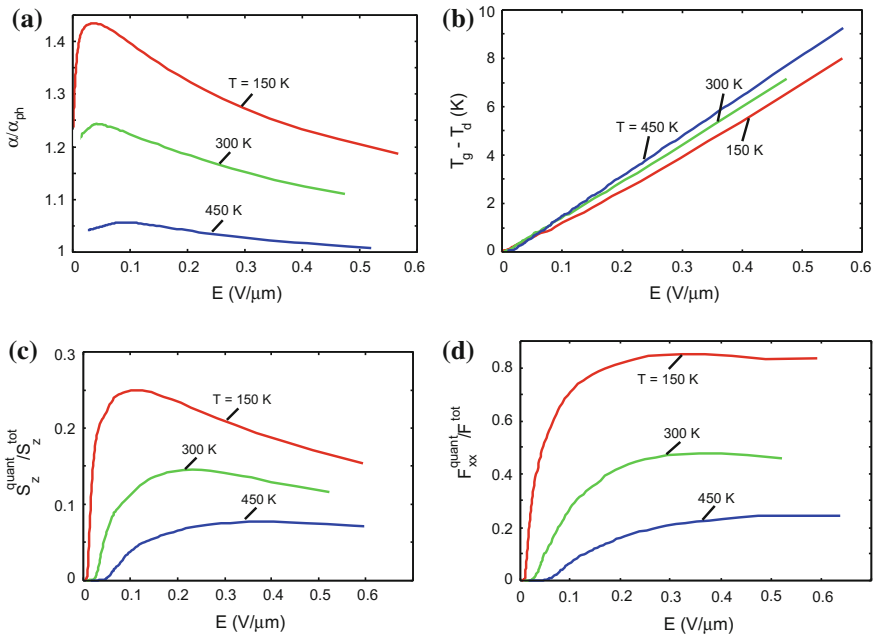

Fig. 10.6 Radiative energy transfer between graphene and SiO_2 for $n = 10^{16}\text{m}^{-2}$, $d = 0.35\,\text{nm}$ and $\alpha_{ph} = 1.0 \times 10^8 \text{Wm}^{-2}\text{K}^{-1}$. **a** The dependence of the ratio between the total energy transfer coefficient and the phononic heat transfer coefficient, on the electric field. **b** Dependence of the temperature difference between graphene and substrate on the electric field. **c** Dependence of the ratio between the heat flux only due to quantum fluctuations S_z^{quant} and the total energy flux, on the electric field. **d** Dependence of the ratio between the friction force due to quantum fluctuations F_x^{quant} and the total friction force, on the electric field

radiative heat transfer between bodies at rest is determined only by thermal fluctuations, in contrast to the radiative energy transfer between moving bodies, which is determined by both thermal and quantum fluctuations. Figure 10.6c shows that quantum fluctuations can give significant contribution to the total energy transfer for low temperatures and large electric field (high drift velocity). Similarly, in the (electric current) saturation region, quantum fluctuations give significant contribution to the total friction force which is determined, as discussed above, by the sum of the extrinsic and intrinsic friction forces (see Fig. 10.6d). The extrinsic friction force has contributions from both thermal and quantum fluctuations. The friction force due to quantum fluctuations is denoted as quantum friction, which was discussed in Sect. 10.3 (see also [149]).

Figure 10.7a shows the dependence of the energy transfer coefficient on the separation d for low electric field ($v \to 0$). At $d \sim 5$ nm and $T = 300$ K the energy transfer coefficient, due to the near-field radiative energy transfer, is $\sim 10^4\,\mathrm{Wm^{-2}K^{-1}}$, which is ∼three orders of magnitude larger than the radiative heat transfer coefficient due to

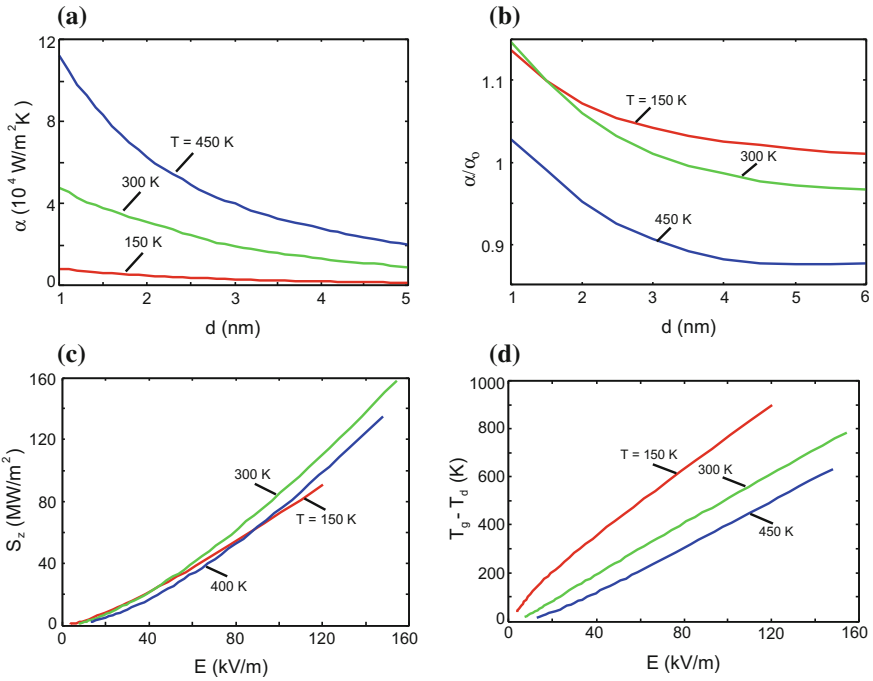

Fig. 10.7 Radiative energy transfer between graphene and SiO_2 for $n = 10^{12}\mathrm{cm^{-2}}$ and $\alpha_{ph} = 0$. **a** Dependence of the energy transfer coefficient on the separation d for low electric field ($v \to 0$); **b** Dependence of the ratio between the energy transfer coefficient and the heat transfer coefficient on the separation d for low electric field ($v \to 0$); **c** Dependence of the radiative energy flux on electric field for $d = 1.0$ nm; **d** Dependence of the temperature difference between graphene and substrate on electric field for $d = 1.0$ nm

the black-body radiation. In comparison, the near-field radiative heat transfer coefficient in the SiO_2–SiO_2 system for the plate–plate configuration, when extracted from experimental data [109] for the plate–sphere configuration, is $\sim 2230\,\mathrm{Wm^{-2}K^{-1}}$ at a ~ 30 nm gap. For this system, the radiative heat transfer coefficient depends on the separation as $1/d^2$. Thus $\alpha \sim 10^5\,\mathrm{Wm^{-2}K^{-1}}$ at $d \sim 5$ nm, which is one order of magnitude larger than for the graphene-SiO_2 system in the same configuration. However, the sphere has a characteristic roughness of ~ 40 nm, and the experiments [109, 110] were restricted to separation wider than 30 nm (at smaller separation the surface roughness affects the measured heat transfer). Thus, the extreme near-field-separation, with d less than approximately 10 nm, may not be accessible using a plate–sphere geometry. A suspended graphene sheet has a roughness ~ 1 nm [372], and measurements of the thermal contact conductance can be performed from separation larger than ~ 1 nm. At such separation one, would expect the emergence of non-local and non-linear effects. This range is of great interest for the design of nanoscale devices, as modern nanostructures are considerably smaller than 10 nm and are separated in some cases by only a few Angstroms.

Figure 10.7b shows that, at small separations, there is significant difference between the radiative energy transfer coefficient and the radiative heat transfer coefficient determined (in the absence of direct phononic coupling) by $\alpha_0 = S'_{z0}$. This difference vanishes for large separations because S_{z0} and F_{x0} rapidly decrease when the separation increases. At large separation, the friction force is dominated by the intrinsic friction and in this case $\alpha \approx \alpha_0$. Figure 10.7c shows the dependence of the radiative energy flux on electric field for $d = 1$ nm. For this separation, the energy transfer is considerably less effective than for $d = 0.35$ nm, which leads to a rapid increase of the temperature difference (see Fig. 10.7d). High temperatures are achieved at low electric field (small drift velocities), where contribution to the radiative energy transfer from quantum fluctuations is very small, and the energy transfer is mainly determined by thermal fluctuations.

Chapter 11
Radiation by Uniformly Moving Sources

When a charged particle uniformly moves through a medium with the velocity higher than the velocity of light in that medium, the Vavilov–Cherenkov radiation is produced by the medium. However, a uniformly moving neutral object can also excite radiation in a medium of quantum origin. This phenomenon (denoted as the quantum Vavilov– Cherenkov (QVC) radiation) is due to quantum fluctuations of the electromagnetic field, is closely related with quantum friction, and exists only when the velocity of an object relative to a medium exceeds a threshold velocity. In this chapter, we consider the QVC radiation occurring during relative sliding of the two transparent dielectric plates with the index of refraction n. We study this problem using a non-relativistic and a fully relativistic theory.

Two transparent dielectric plates during relative sliding emit QVC radiation when the sliding velocity exceeds a threshold velocity $v_c = 2nc/(n^2 + 1)$. Close to the threshold velocity, the friction force $\sim(v - v_c)^{5/2}$ and is dominated by the contribution from the s-polarized electromagnetic waves. However, close to the light velocity, the contributions from both polarizations are strongly enhanced, and a new contribution occurs that is connected to the mixing of the waves with the different polarizations.

A small neutral particle moving parallel to a transparent dielectric plate emits QVC radiation when the velocity exceeds a threshold velocity $c_c = c/n$. This radiation is responsible for quantum friction, which we will study in the particle rest reference frame and in the *lab* frame, using a fully relativistic theory. The friction forces in the particle-plate configuration in the different reference frames will be calculated from the corresponding results in the plate-plate configuration, considering one of the plates as sufficiently rarefied. We will show that in the realistic situation, the friction force acting on a neutral nanoparticle due to QVC radiation can be comparable in magnitude to the friction force acting on a charged particle due to the classical Vavilov–Cherenkov (CVC) radiation. Thus, in principle QVC radiation can be detected using the same experimental setup as for CVC radiation. The challenges for future experiments are to accelerate a particle, having sufficiently large fluctuating dipole moment, and to a velocities close to the light velocity, at small separation

A.I. Volokitin and B.N.J. Persson, *Electromagnetic Fluctuations at the Nanoscale*,
NanoScience and Technology, DOI 10.1007/978-3-662-53474-8_11

from a transparent dielectric surface. Non-relativistic QVC radiation can be observed using a transparent dielectric with refractive index ∼10 in the near UV region.

11.1 Vavilov-Cherenkov Effect

A remarkable manifestation of the interaction between the electromagnetic field and matter is the emission of light by charged particle moving at a constant superluminally velocity in a medium: Vavilov–Cherenkov (VC) radiation [284–289], which has broad applications in the detection of high-energy charged particles in astrophysics and particle physics. Radiation with a frequency ω occurs only if the charge velocity v exceeds the phase velocity of light in a given transparent medium $v_0 = c/n(\omega)$, i.e.

$$v > \frac{c}{n(\omega)}, \tag{11.1}$$

where $n(\omega)$ is the refractive index (at the frequency ω) in the medium (c is the velocity of light in vacuum). The specificity of radiation angular distribution is reflected in the angle θ_0 between the wave vector of emitted waves $\mathbf{k}$ and the velocity $\mathbf{v}$, with

$$\cos\theta_0 = \frac{c}{n(\omega)v}. \tag{11.2}$$

The results (11.1) and (11.2) can be obtained using the Huygens principle according to which, each point on the path of a charge moving with a constant velocity v is a source of a spherical wave emitted as the charge passes the point (Fig. 11.1). If the condition (11.1) is fulfilled, these spheres have a common envelope, a cone whose apex coincides with the instantaneous charge position, the angle θ_0 being defined by expression (11.2). For a dispersionless medium (i.e. n is a constant), the angle θ is the

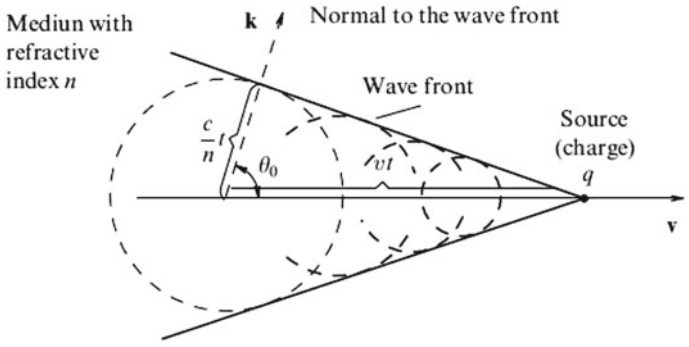

Fig. 11.1 Generation of the Vavilov–Cherenkov (VC) radiation ($(c/n)t$ is the light path during time t, $vt = [c/(n\cos\theta_0)]t$ is the distance covered by a charge (source)) for the same period

same for all frequencies ω and radiation has a clear-cut front, which forms a cone with the angle of opening $\pi - 2\theta_0$ with the charge (source) in its apex (Fig. 11.1). This cone is totally analogous to the Mach cone, which characterizes a shock wave generated by the motion of a supersonic source (bullet, shell, aircraft, missile) in the air or other media, the velocity of the shock wave or sound v playing the role of the phase velocity of light $v_0 = c/n$ in expressions (11.1) and (11.2). The hydrodynamic (acoustic) front at the Mach cone is very sharp and easy to observe (e.g., as a supersonic plane flies by) because the dispersion of sound, i.e. the dependence of its velocity v on frequency, is normally very small.

The VC effect also occurs when a charge (source) propagates not in a continuous medium but inside a narrow empty channel made in such matter. This is because VC radiation is formed not only on the charge path but also near it, at a distance of the order of the wavelength of emitted light $\lambda = 2\pi c/(n\omega)$. The corresponding radiation intensity naturally decreases with increasing radius r of the empty channel in which a charge propagates axially. At $\sqrt{1-(v/c)^2} \sim 1$ radiation is almost as high as it is in the absence of the channel provided $r/\lambda \leq 0.01$ (in optics, this means that $r < 5\,\text{nm}$). A qualitatively similar picture is obtained if a channel is replaced by a slit, or when a charge moves near the medium (dielectric). This is essential because the loss of energy for VC radiation when a charge moves in a medium is relatively small and ionization losses in the immediate proximity to the trajectory dominate. However, ionization losses are excluded when a charge propagates in channels, slits or near the medium, while VC radiation persists. This is important, but not crucial, for charges. However, in the case of the motion of a neutral particle, the phenomenon is possible only if channels or gaps are available; otherwise, the particle is destroyed.

The radiation intensity can be calculated from the solution of the equations of electrodynamics in a medium. From such a solution, the radiation intensity can be obtained as a flux of the Poynting vector through the cylindrical surface surrounding the charge trajectory. Another approach consists of in determining the force, which slows down the moving charge (using, of course, the same equations). The work of this force in a transparent medium is equivalent to the radiation energy. Such calculations for a continuous medium are included in a textbook by Landau and Lifshitz [191].

The VC radiation from a point charge e moving parallel to a transparent dielectric surface at the separation d was studied by many authors (see [292] for review). Here, we present a new, very simple consideration of this problem. We introduce a Cartesian coordinate system with the x-axis along the line of motion of the charge. The z-axis is normal to the dielectric surface so that the equation of the surface is $z = 0$, and the charge is located at $z = d$. The rest reference for a dielectric is denoted as the K frame, and the rest reference frame for the point charge is the K' frame. In the K frame, the electromagnetic field can be represented as the sum of the waves incident on the surface of a dielectric as well as those it reflects. The electric field for $z < d$ can be written in the form

$$\mathbf{E}(\mathbf{q}, \omega, z) = \left(R_s(\omega, q) w_s \hat{n}_s + R_p(\omega, q) w_p \hat{n}_p^+\right) e^{-k_z z} + \left(w_s \hat{n}_s + w_p \hat{n}_p^-\right) e^{k_z z} \quad (11.3)$$

where the second term represents the electric field created by a point charge in free space in the K frame, $R_{p(s)}$ is the reflection amplitude for $p(s)$-polarized electromagnetic waves $k_z = ((q^2 - (\omega + i0^+/c)^2)^{1/2}$, $\hat{n}_s = [\hat{z} \times \hat{q}] = (-q_y, q_x, 0)/q$, $\hat{n}_p^{\pm} = [\hat{k}^{\pm} \times \hat{n}_s] = (\mp q_x i k_z, \mp q_y i k_z, q^2)/(kq)$, $k = \omega/c$, $\hat{k}^{\pm} = (\mathbf{q} \pm i\hat{z}k_z)/k$. In the K' reference frame, co-moving with a charge, the electric field created by a point charge in the free space for $z < d$ is determined by the Coulomb law ($\omega' = 0$), and can be written in the form

$$\mathbf{E}^{0\prime}(\mathbf{q}', 0, z) = -\frac{2\pi e}{q'}(i\mathbf{q}' + \hat{z}q')e^{-q'(d-z)}. \tag{11.4}$$

From the Lorenz transformation, for the electric field (see Appendix B), taking into account that $\omega' = 0$, it follows

$$w_p = -\frac{2\pi e k\gamma}{q}e^{-k_z d}, \;\; w_s = i\frac{2\pi e k\gamma q_y}{qq'}e^{-k_z d}, \tag{11.5}$$

where $k_z = q'$, $\omega = q_x v$. The Fourier component of the force acting on the point charge e is given by

$$\begin{aligned} F_x(q_x, q_y) &= e\mathrm{Re}\left[R_p w_p(\hat{n}^+ \cdot \hat{x}) + R_s w_s(\hat{n}_s \cdot \hat{x})\right]e^{-k_z d} \\ &= -\frac{2\pi e^2\gamma}{q_x}\left\{k_z \mathrm{Im}R_p + \frac{q_y^2}{q^2 k_z}\mathrm{Im}\left[\beta^2 q_x^2 R_s - k_z^2 R_p\right]\right\}e^{-2k_z d} \end{aligned} \tag{11.6}$$

The Fresnel's formulas for the reflection amplitudes can be written in the form

$$R_p = \frac{i\varepsilon k_z - k_{zn}}{i\varepsilon k_z + k_{zn}}, \;\; R_s = \frac{ik_z - k_{zn}}{ik_z + k_{zn}}, \tag{11.7}$$

where ε is the dielectric permeability, $k_{zn} = \sqrt{q_x^2(\varepsilon\beta^2 - 1) - q_y^2}$ and $k_z = \sqrt{q_y^2 + q_x^2(1 - \beta^2)}$. The imaginary part of the reflection amplitude is non-vanishing only if $\varepsilon\beta^2 > 1$ and $q_y^2 < q_x^2(\varepsilon\beta^2 - 1)$. Taking into account that

$$\beta^2 q_x^2 R_s - k_z^2 R_p = -q^2\left(1 + \frac{2ik_z}{i\varepsilon k_z + k_{zn}}\right),$$

(11.6) can be written in the form

$$F_x(q_x, q_y) = -\frac{4\pi e^2\gamma k_{zn}}{q_x}\frac{\varepsilon k_z^2 + q_y^2}{\varepsilon^2 k_z^2 + k_{zn}^2}e^{-2k_z d}. \tag{11.8}$$

Integration over $q'_x = q_x/\gamma$ and q_y, after introducing the new variable $\omega = q_x/v$, yields

$$F = 2\int_0^\infty \frac{d\omega}{2\pi\gamma v}\int_{-\infty}^{\infty}\frac{dq_y}{2\pi}F(q_x,q_y) = -\frac{2e^2}{\pi}\int_0^\infty \frac{d\omega}{\omega}\int_{-q_{ymax}}^{q_{ymax}} dq_y \frac{k_{zn}\left(\varepsilon k_z^2 + q_y^2\right)}{\varepsilon^2 k_z^2 + k_{zn}^2} e^{-2k_z d}, \quad (11.9)$$

where $q_{ymax} = (\omega/v)\sqrt{\varepsilon\beta^2 - 1}$. It is convenient to replace variable q_y by another variable $q_y = q_{ymax}\sin\theta$, where θ is the angle between the negative z-axis and the projection of the radiation wave vector on the yz-plane. Thus, (11.9) can be rewritten in the form

$$F = \frac{2e^2}{\pi v^2}\int_0^\infty \frac{d\omega}{\omega}\frac{\varepsilon\beta^2 - 1}{\varepsilon - 1}\int_{-\frac{\pi}{2}}^{\frac{\pi}{2}} d\theta\cos^2\theta \frac{(\varepsilon+1)(\varepsilon\beta^2-1)\sin^2\theta + \varepsilon(1-\beta^2)}{(\varepsilon+1)(\varepsilon\beta^2-1)\cos^2\theta - \varepsilon^2\beta^2} e^{-2d\frac{\omega}{v}\sqrt{(\varepsilon\beta^2-1)\sin^2\theta + 1 - \beta^2}}. \quad (11.10)$$

For the dispersionless medium ($\varepsilon = n^2$ independent on ω, n is the refractive index), carrying out the integration first over frequency, and then angle, from (11.10) we obtain

$$f_x^{clas} = -\frac{e^2}{2\beta d^2}\frac{1}{n^2-1}\left[\frac{n^2\gamma}{\sqrt{\gamma^2+n^2}} - \frac{\sqrt{n^2-1}}{\gamma} - \beta\right]. \quad (11.11)$$

In the ultrarelativistic case ($\beta = 1$) (11.11) is simplified to

$$f_x^{clas}(\beta = 1) = -\frac{e^2}{2d^2}. \quad (11.12)$$

11.2 Photon Emission and Anomalous Doppler Effect

The sources of VC radiation examined above (i.e. charges) have no internal degrees of freedom. Another important case is a neutral particle without charge or any static moment, but with a fluctuating dipole moment. For this case, a kinematic explanation for the radiation and friction, above the Cherenkov threshold, can be given with the following arguments [293]. The conservation of energy and momentum laws for the case of photon emission by a particle are:

$$\begin{cases} E_1 = E_2 + \hbar\omega, \;\; E_{1,2} = \sqrt{m_{1,2}^2c^4 + c^2p_{1,2}^2} \\ \mathbf{p}_1 = \mathbf{p}_2 + \hbar\mathbf{q}, \;\; \mathbf{p}_{1,2} = m_{1,2}\mathbf{v}_{1,2}\gamma_{1,2} \end{cases}, \quad (11.13)$$

where $E_{1,2}$ and $\mathbf{p}_{1,2}$ are the energy and momentum of a particle with the rest mass $m_{1,2} = M + \epsilon_{1,2}/c^2$ before (subscript 1) and after (subscript 2) the emission of a photon with the energy $\hbar\omega$ and momentum $\hbar\mathbf{q}$, $q = n\omega/c$, $\gamma_{1,2} = 1/\sqrt{1 - v_{1,2}^2}$, and $\epsilon_{1,2}$ is the internal energy of a particle. From (11.13) follows

$$\left(\frac{E_1-\hbar\omega}{c}\right)^2-(\mathbf{p}_1-\hbar\mathbf{k})^2$$

$$=m_1^2c^2-\left(\frac{\hbar\omega}{c}\right)^2(n^2-1)-\frac{2E_1\hbar\omega}{c^2}\left(1-\frac{v_1n\cos\theta}{c}\right)=m_2^2c^2, \tag{11.14}$$

or

$$(\epsilon_1-\epsilon_2)\left(2M+\frac{\epsilon_1+\epsilon_2}{c^2}\right)=\frac{2E_1\hbar\omega}{c^2}\left(1-\frac{v_1n\cos\theta}{c}\right)+\left(\frac{\hbar\omega}{c}\right)^2(n^2-1). \tag{11.15}$$

Assuming $\epsilon_{1,2}\ll Mc^2$ and that the recoil is negligible ($\hbar\omega/Mc^2\ll 1$), (11.15) implies that

$$\hbar\omega=-\frac{\epsilon_2-\epsilon_1}{\gamma\left(1-vn\cos\theta/c\right)}. \tag{11.16}$$

Assuming $\omega>0$ from (11.16) follows that in the region of the normal Doppler effect, when $vn/c\cos\theta<1$ one has $\epsilon_2<\epsilon_1$. Thus, the emission of a photon is possible only when the state of the particle change from an upper energy level 1 to the lower level 2. On the other hand in the anomalous Doppler effect region, when $vn/c\cos\theta>1$ (i.e. $\theta<\theta_0$, where $\cos\theta_0=c/nv$, θ_0 is the Vavilov-Cherenkov radiation angle) then $\epsilon_2>\epsilon_1$ and, therefore, the emission of a photon is accompanied by excitation of the particle. The energy necessary for this process is gained from the kinetic energy of motion of the particle. It is important to note that the superlight motion ($v>c/n$), and therefore the anomaloas Doppler effect, which is absent for the sublight ($v<c/n$) motion, are only possible in presence of a medium. Taking into account that for a transparent dielectric $\omega=\omega(q)=cq/n$, and introducing the projection of the wave vector on the direction of the velocity $q_x=q\cos\theta$, (11.16) can be written in the form

$$\omega'=-\omega_0=\gamma\left[\omega(q)-q_xv\right], \tag{11.17}$$

where $\omega_0=(\epsilon_2-\epsilon_1)/\hbar$ is the excitation frequency for the particle and $\omega'=-\omega_0<0$ is the photon frequency, as seen from the moving particle. This is an illustration of the so-called anomalous Doppler effect where the photon frequency, as seen from the moving particle, is negative.

The above arguments can also be applied for an extended media. For the relative sliding of two identical transparent dielectric plates, $\omega'=-cq'/n$ where

$$q'=\sqrt{\gamma^2(q_x-vq/cn)^2+q_y^2}>\gamma\left(q_x-vq/cn\right)$$

and (11.17) can be written in the form

$$q_xv=\omega(q)+\frac{\omega(q')}{\gamma}>(cq_x/n)\left(2-\frac{v}{cn}\right). \tag{11.18}$$

Thus, radiation exists only if the sliding velocity v exceeds the threshold velocity v_c:

$$v > v_c = \frac{2nc}{n^2+1}. \tag{11.19}$$

11.3 Quantum Friction Between Two Transparent Plates

We consider two semi-infinite solids with flat parallel surfaces separated by a distance d and moving with the velocity v relative to each other, see Fig. 5.1. We introduce the two reference frames, K and K', with coordinate axes xyz and $x'y'z'$. In the K frame body **1** is at rest while body **2** is moving with the velocity v along the x-axis relative to body **1** (the xy and $x'y'$ planes are in the surface of body **1,** the x and x'-axes have the same direction, and the z and z'-axes point toward body **2**). In the K' frame, body **2** is at rest while body **1** is moving with velocity $-v$ along the x-axis. According to a fully relativistic theory [128] (see also Sect. 7.3) the quantum friction force F_{1x}, and the radiation power P_1 absorbed by plate 1 at $T_1 = T_2 = 0$, are determined by the formulas

$$\begin{pmatrix} F_{1x} \\ P_1 \end{pmatrix} = \int_{-\infty}^{\infty} \frac{dq_y}{2\pi} \int_0^{\infty} \frac{dq_x}{2\pi} \int_0^{q_x v} \frac{d\omega}{2\pi} \begin{pmatrix} \hbar q_x \\ \hbar\omega \end{pmatrix} \Gamma_{12}(\omega, \mathbf{q}). \tag{11.20}$$

where the positive quantity

$$\Gamma_{12}(\omega, \mathbf{q}) = \frac{4\mathrm{sgn}(\omega')}{|\Delta|^2}\big[(q^2 - \beta k q_x)^2 - \beta^2 k_z^2 q_y^2\big]\Big\{\mathrm{Im}R_{1p}\big[(q^2 - \beta k q_x)^2 \mathrm{Im}R'_{2p}|\Delta_{ss}|^2$$

$$+ \beta^2 k_z^2 q_y^2 \mathrm{Im}R'_{2s}|\Delta_{sp}|^2\big] + (p \leftrightarrow s)\Big\} e^{-2k_z d} \tag{11.21}$$

can be identified as a spectrally resolved photon emission rate,

$$\Delta = (q^2 - \beta k q_x)^2 \Delta_{ss}\Delta_{pp} - \beta^2 k_z^2 q_y^2 \Delta_{ps}\Delta_{sp},$$

$$\Delta_{pp} = 1 - e^{-2k_z d} R_{1p} R'_{2p},\ \Delta_{sp} = 1 + e^{-2k_z d} R_{1s} R'_{2p},$$

$k_z = \sqrt{q^2 - (\omega/c)^2}$, $R_{1p(s)}$ is the reflection amplitude for surface **1** in the K frame for a $p(s)$-polarized electromagnetic wave, and $R'_{2p(s)} = R_{2p(s)}(\omega', q')$ is the reflection amplitude for surface **2** in the K' frame for a $p(s)$-polarized electromagnetic wave, $\omega' = \gamma(\omega - q_x v)$, $q'_x = \gamma(q_x - \beta k)$, $\Delta_{ps} = \Delta_{sp}(p \leftrightarrow s)$. The symbol $(p \leftrightarrow s)$ denotes the terms that are obtained from the preceding terms by permutation of indexes p and s. If, in (11.20), one neglects terms of order β^2, the contributions from the p- and s- polarized waves will be separated. In this case, (11.20) is reduced to the approximate (relativistic) formula

$$\begin{pmatrix} F_x \\ P_1 \end{pmatrix} = -\frac{\hbar}{\pi^3}\int_0^\infty dq_y \int_0^\infty dq_x \int_0^{q_x v} d\omega \begin{pmatrix} \hbar q_x \\ \hbar\omega \end{pmatrix} \left(\frac{\mathrm{Im}R_{1p}\mathrm{Im}R'_{2p}}{|D_{pp}|^2} + \frac{\mathrm{Im}R_{1s}\mathrm{Im}R'_{2s}}{|D_{ss}|^2} \right) e^{-2k_z d}, \tag{11.22}$$

For transparent dielectrics the reflection amplitudes are given by the Fresnel's formulas

$$R_p = \frac{in^2 k_z - \sqrt{n^2\left(\frac{\omega}{c}\right)^2 - q^2}}{in^2 k_z + \sqrt{n^2\left(\frac{\omega}{c}\right)^2 - q^2}},\ R_s = \frac{ik_z - \sqrt{n^2\left(\frac{\omega}{c}\right)^2 - q^2}}{ik_z + \sqrt{n^2\left(\frac{\omega}{c}\right)^2 - q^2}}. \tag{11.23}$$

In this case, the friction force can be written in the form

$$F_{1x} = \frac{\hbar v_0}{d^4}\tilde{g}\left(\frac{v}{v_0}, \frac{v}{c}, n\right), \tag{11.24}$$

where $\tilde{g}$ is a function of two dimensionless velocity ratios, and the refractive index n. In the non-relativistic limit ($\beta^2 \ll 1$), the dependence on the vacuum light velocity c drops out and

$$F_{1x}^{nrel} = \frac{\hbar v_0}{d^4}\left[g_s\left(\frac{v}{v_0}\right) + g_p\left(\frac{v}{v_0}, n\right)\right], \tag{11.25}$$

where the s-wave contribution g_s depends only on the ratio of the velocity v to the light speed in the medium v_0. However, the p-wave contribution depends also on the refractive index n.

The imaginary part of the reflection amplitude $R_{1p(s)}$, given by (11.23), is only nonzero when $\omega > v_0 q > v_0 q_x$. Similarly, $\mathrm{Im}R_{2p(s)}$ is non-zero only when $q_x v - \omega > v_0 q'/\gamma > v_0(q_x - \beta\omega/c)$. Both of these conditions limit the range of integration to

$$v_0 q_x < \omega < \frac{(v - v_0)q_x}{1 - vv_0/c^2}. \tag{11.26}$$

From this condition, it follows that the minimal velocity v_c, at which friction occurs, is determined by (11.19).

For transparent dielectrics, where there are no resonances in the reflection amplitudes in the frequency range where the quantum friction is non-vanishing, $|R_{s(p)}| \leq 1$. Thus, a good estimation of the friction force and the radiative heat transfer can be obtained by neglecting the multiple-scattering of the electromagnetic waves by the dielectric surfaces. In this approximation, $D_{pp} \approx D_{ss} \approx D_{sp} \approx D_{sp} \approx 1$,

$$\Delta \approx (q^2 - \beta k q_x)^2 - \beta^2 k_z^2 q_y^2 = \frac{(qq')^2}{\gamma^2},$$

$$(q^2 - \beta k q_x)^2 \mathrm{Im}R'_{2p}|\Delta_{ss}|^2 + \beta^2 k_z^2 q_y^2 \mathrm{Im}R'_{2s}|\Delta_{sp}|^2 \approx \frac{(qq')^2}{\gamma^2}\mathrm{Im}R'_{2p} + \beta^2 k_z^2 q_y^2 \mathrm{Im}(R'_{2p} + R'_{2s}),$$

$$\Gamma_{12} = 4\mathrm{sgn}(\omega') \left[\left(\mathrm{Im}R_{1p}\mathrm{Im}R'_{2p} + \mathrm{Im}R_{1s}\mathrm{Im}R'_{2s} \right) \left(1 + \gamma^2\beta^2 \frac{k_z^2 q_y^2}{q^2 q'^2} \right) \right.$$
$$\left. + \gamma^2\beta^2 \frac{k_z^2 q_y^2}{q^2 q'^2} \left(\mathrm{Im}R_{1p}\mathrm{Im}R'_{2s} + \mathrm{Im}R_{1s}\mathrm{Im}R'_{2p} \right) \right]. \qquad (11.27)$$

Thus, the relativistic effects produce not only a mixing of the waves with the different polarizations, but also modify the contributions from the different polarizations.

Close to the threshold velocity $v \approx v_c$, when $\xi_{min} \approx \xi_{max}$ and

$$y_{max} = \frac{n^2+1}{n\sqrt{n^2-1}} \sqrt{\frac{v - v_c}{v_0}} \ll 1,$$

the integration over q_y in (11.20) is restricted by the range $0 < |q_y| < y_{max} q_x \ll q_x$. In this case, to lowest order in y_{max}, the mixing of the waves with different polarizations can be neglected and the friction force is determined by the formula (see Appendix O.1)

$$F_{1x} \approx \frac{\hbar v_0}{d^4} \left[\tilde{g}_s \left(\frac{v}{v_0}, n \right) + \tilde{g}_p \left(\frac{v}{v_0}, n \right) \right], \qquad (11.28)$$

and the radiative heat transfer $P_1 = v_0 F_{1x}$, where

$$\tilde{g}_s \left(\frac{v}{v_0}, n \right) = \frac{\zeta(3)}{5\pi^2} \frac{n(n^2+1)^5}{(n^2-1)^5\sqrt{n^2-1}} \left(\frac{v - v_c}{v_0} \right)^{5/2},$$

and $\tilde{g}_p = \tilde{g}_s / n^4$. In the non-relativistic limit ($n \gg 1$)

$$g_s \left(\frac{v}{v_0} \right) = \frac{\zeta(3)}{5\pi^2} \left(\frac{v - v_c}{v_0} \right)^{5/2},$$

and $g_p(v/v_0, n) = g_s(v/v_0)/n^4$.

Close to the light velocity ($v \to c$) (see Appendix N.2), the s-wave contributions to the friction force, given by the approximate formula (11.22), is finite:

$$F_{xs}^{approx} \approx \frac{3\hbar v}{4\pi^2 d^4} \frac{\sqrt{2}}{n^2-1} \ln\left(n + \sqrt{n^2-1} \right), \qquad (11.29)$$

and diverges as $\sim\gamma$ in a fully relativistic theory given by (N.7),

$$F_{xs} \approx \frac{3\hbar v}{4\pi^2 d^4} \frac{\sqrt{n-1}}{2(n+1)^{3/2}} \gamma \qquad (11.30)$$

Other contributions can be estimated in a similar way.

Figures 11.2 and 11.3 show the dependence of the friction force between two transparent dielectric plates on the relative sliding velocity in a non-relativistic theory (Fig. 11.2a, b), and a fully relativistic theory for $n = 2$ (Fig. 11.3a) and $n = 10$ (Fig. 11.3b). In the non-relativistic theory, the contributions to the friction force from s-and p-polarized waves are separated. The threshold velocity v_c for appearance of the VC radiation in the non-relativistic theory is equal to $2v_0$. The friction in this theory is dominated by the s-wave contribution, which depends only on the velocity ratio v/v_0. In a fully relativistic theory, friction and radiation only exist for $v > v_c = 2nc/(n^2 + 1)$, which is equal to $0.8c$ for $n = 2$ (Fig. 11.3a) and $0.2c$ for

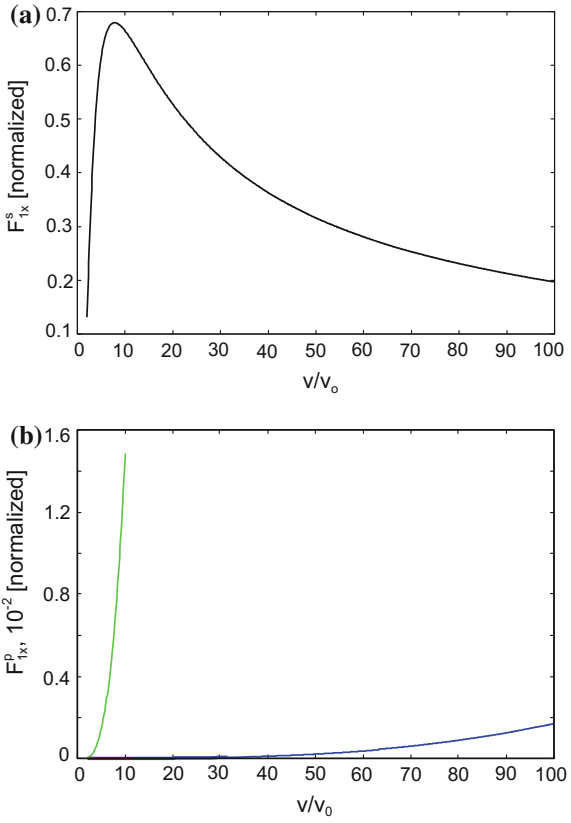

Fig. 11.2 The dependence of friction force between two transparent dielectric plates on the relative sliding velocity. The normalization factor for the forces $\hbar v_0/\pi^3 d^4$, $v_0 = c/n$. **a** and **b** Results of a non-relativistic theory for the contributions from s- and p-polarized electromagnetic waves, respectively. The s-wave contribution in a non-relativistic theory depends only on the ratio v/v_0. The p-wave contributions are shown for $n = 10$ (*green line*) and $n = 100$ (*blue line*)

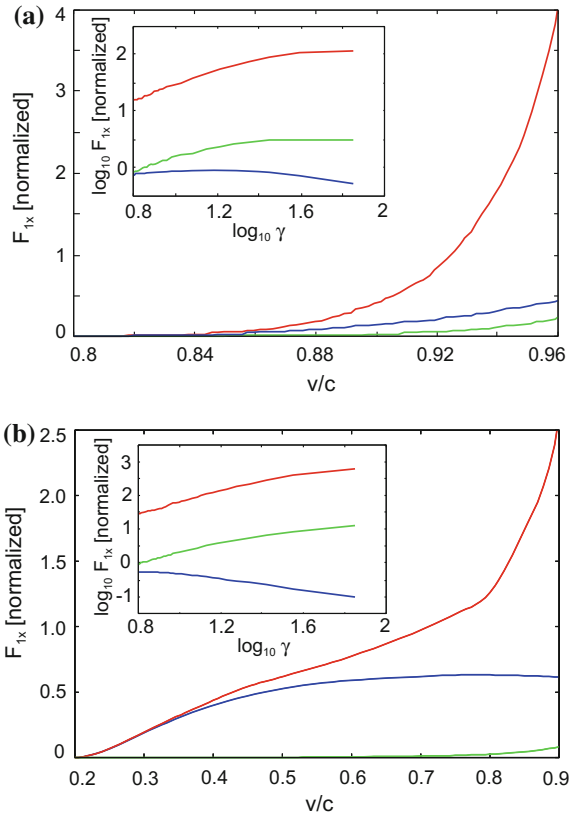

Fig. 11.3 The same as Fig. 11.2 but for a fully relativistic theory. Figures **a** and **b** Results of a fully relativistic theory (*red line*) for $n = 2$ and $n = 10$, respectively. The *blue* and *green lines* show the separate contributions from the *s*- and *p*-polarized electromagnetic waves, respectively, obtained using the approximate (11.22). *Insets* show the friction forces in the ultrarelativistic case $(1 - \beta \ll 1)$

$n = 10$ (Fig. 11.3b). Figure 11.3a, b also show results of an approximate relativistic theory for the contributions to the friction force from *s*-polarized waves (blue line) and *p*-polarized waves (green line) given by (11.22). In the approximate theory, the reflection amplitude from the moving surface is approximated by the reflection amplitude in the co-moving reference frame at the frequencies and wavevectors determined by the Lorenz transformation. The polarization mixing is not taken into account in this theory, where the coupling between waves with different polarizations are neglected. Close to the threshold velocity, the mixing of the waves with different polarizations is unimportant and the friction is dominated by the contribution from the *s*polarized electromagnetic waves, which can be accurately described using the approximate theory. However, in the ultrarelativistic case ($\gamma \gg 1$), both contributions from the different polarizations are strongly enhanced in the comparison with the approximate theory, and a new contribution occurs that is connected with the polarization mixing.

11.4 Quantum Friction Between a Particle and Transparent Plate

According to Sect. 8.2 the friction force acting on a particle f_x, and the radiation power absorbed by it p, in the K frame are

$$\begin{pmatrix} f_x(z) \\ p(z) \end{pmatrix} = \frac{1}{\gamma\pi^2}\int d^2q \int_0^{vq_x} d\omega \begin{pmatrix} \hbar q_x \\ \hbar\omega \end{pmatrix} \frac{e^{-2k_z z}}{k_z}\left[\mathrm{Im}R_p(\omega)\phi_p + \mathrm{Im}R_s(\omega)\phi_s\right]\mathrm{Im}\alpha(\omega'), \tag{11.31}$$

$$\phi_p = \left(\frac{\omega'}{c}\right)^2 + 2\gamma^2(q^2 - \beta^2 q_x^2)\frac{k_z^2}{q^2},\ \ \phi_s = \left(\frac{\omega'}{c}\right)^2 + 2\gamma^2\beta^2 q_y^2\frac{k_z^2}{q^2}.$$

Similarly, the friction force f_x' and the radiation power p' absorbed by the particle in the rest reference frame of a particle (the K' frame) are

$$\begin{pmatrix} f_x' \\ p' \end{pmatrix} = \frac{1}{\pi^2}\int_0^\infty dq_x \int_{-\infty}^\infty dq_y \int_0^{q_x v} d\omega \begin{pmatrix} \hbar q_x \\ -\hbar\omega \end{pmatrix} \frac{e^{-2k_z d}}{k_z}\left[\mathrm{Im}R_p(\omega')\phi_p' + \mathrm{Im}R_s(\omega')\phi_s'\right]\mathrm{Im}\alpha(\omega), \tag{11.32}$$

$$\phi_p' = \left(\frac{\omega}{c}\right)^2 + 2\gamma^2(q'^2 - \beta^2 q_x'^2)\frac{k_z^2}{q'^2},\ \ \phi_s' = \left(\frac{\omega}{c}\right)^2 + 2\gamma^2\beta^2 q_y^2\frac{k_z^2}{q'^2}.$$

For transparent dielectrics the reflection amplitudes are given by the Fresnel's formulas

$$R_p = \frac{in^2 k_z - \sqrt{n^2\left(\frac{\omega}{c}\right)^2 - q^2}}{in^2 k_z + \sqrt{n^2\left(\frac{\omega}{c}\right)^2 - q^2}},\ R_s = \frac{ik_z - \sqrt{n^2\left(\frac{\omega}{c}\right)^2 - q^2}}{ik_z + \sqrt{n^2\left(\frac{\omega}{c}\right)^2 - q^2}}. \tag{11.33}$$

There is no restriction on the imaginary part of the particle polarizability in the integration range $0 < \omega < v_x v$. The integrand in (11.31) is nonzero only in the range $v_0 q_x < \omega < q_x v$, where the imaginary part of the reflection amplitude is nonzero, and thus the critical velocity $v_c = v_0 = c/n$.

We assume that the imaginary part of the particle polarizability is determined by the formula

$$\mathrm{Im}\alpha = R^3\omega_0^2\frac{\omega/\tau}{\left(\omega^2 - \omega_0^2\right)^2 + (\omega/\tau)^2},$$

where R is the radius of the particle, ω_0 is the plasmon frequency for the particle and τ is the damping constant, then close to the resonance at $\omega \approx \omega_0$

$$\mathrm{Im}\alpha = R^3\omega_0\frac{\pi}{2}\delta(\omega - \omega_0),$$

and from (11.32), the resonant contributions to the friction force and the heating power close to the threshold velocity in the K' frame are dominated by the contribu-

tions from p-polarized waves, and are given by (see Appendix O.1)

$$f_{xp}^{res\prime} = -\frac{\hbar R^3 \omega_0}{4d^4(n^2-1)} \frac{v-v_0}{v_0} \left[3 + 4q_0 d + 2(q_0 d)^2\right] e^{-2q_0 d}, \tag{11.34}$$

$$w_p^{res\prime} = \frac{\hbar R^3 \omega_0^2}{2d^3(n^2-1)} \frac{v-v_0}{v_0} \left[(1+q_0 d) e^{-2q_0 d}\right] \tag{11.35}$$

where $q_0 = (n^2-1)\omega_0/((v-v_0)n^2)$. In the off-resonant region $\omega \ll \omega_0$

$$\mathrm{Im}\alpha = R^3 \frac{\omega}{\omega_0 \tau},$$

and again the dominant contributions are given by the p-polarized waves (see Appendix Q.1):

$$f_{xp}^{offres\prime} \approx -\frac{5}{4\pi} \frac{\hbar R^3 v_0^2}{d^6 \omega_0^2 \tau} \frac{n^4}{(n^2-1)^3} \left(\frac{v-v_0}{v_0}\right)^3, \tag{11.36}$$

$$w_p^{offres\prime} \approx \frac{35}{64\pi} \frac{\hbar R^3 v_0^3}{d^6 \omega_0^2 \tau} \frac{n^6}{(n^2-1)^4} \left(\frac{v-v_0}{v_0}\right)^4. \tag{11.37}$$

From (11.34)–(11.37), it follows that close to the threshold velocity $w' \ll f_x' c$. Thus, from (8.21), it follows that $f_x \approx f_x'$, which agrees with the results obtained in [156], and $w \approx f_x v$. The change of the kinetic energy in this limit is determined by the radiation power from a particle in the K frame; however, the change of the internal energy and, consequently, the change of the rest mass of the particle, is small. The off-resonant contribution to friction force from the frequency range $\omega \ll \omega_0$ is only important close to the threshold velocity ($(v-v_0)/v_0 \ll 1$), while, far from the threshold velocity, the friction force is dominated by the resonant contribution from $\omega \approx \omega_0$, as was already noted in [156] (Fig. 11.4a).

The friction force acting on the elementary charge e, due to the CVC radiation, is determined by the well-known formula in [292] (see also Sect. 11.1)

$$f_x^{clas} = -\frac{e^2}{2\beta d^2} \frac{1}{n^2-1} \left[\frac{n^2\gamma}{\sqrt{\gamma^2+n^2}} - \frac{\sqrt{n^2-1}}{\gamma} - \beta\right]. \tag{11.38}$$

In the ultra relativistic limit ($\gamma \gg 1$) (11.38) is significantly simplified to $f_x^{clas} = -e^2/2d^2$. In Fig. 11.3 it is compared with the friction force due to the QVC radiation on a neutral silver nano particle with the radius $R = 4\,\mathrm{nm}$, and the particle-surface separation $d = 10\,\mathrm{nm}$. The surface plasmon frequency for a particle $\omega_0 = \omega_p/\sqrt{3}$, where ω_p=9.01 eV is the bulk plasmon frequency for silver, and with losses (red curve, $\tau^{-1} = 2.4 \times 10^{14}\mathrm{s}^{-1}$) and no losses (green curve, $\tau^{-1} = +0$). Far from the threshold velocity, these friction forces are of the same order of the magnitude (see Fig. 11.4a).

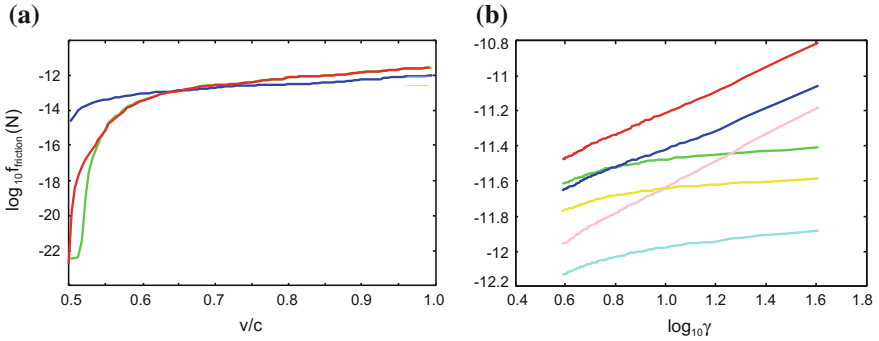

Fig. 11.4 The dependence of the friction force acting on a silver nanoparticle, and on the elementary charge e at motion parallel to the transparent dielectric on the ,relative sliding velocity. The radius of particle $R = 4\,\text{nm}$, the separation $d = 10\,\text{nm}$, the refractive index $n = 2$. **a** The *red* and *green* curves show the friction forces for a particle with losses ($\tau^{-1} = 2.4 \times 10^{14}\text{s}^{-1}$) and no losses ($\tau^{-1} = +0$). The *blue* curve shows the friction force on a elementary charge; e. **b** The *red, blue* and *pink* curves show the total friction force, and the contributions from the p- and s-polarized waves, respectively, in the particle rest reference (the K' frame) in the ultra relativistic case ($\gamma \gg 1$). The *green, yellow* and *light-blue* curves—the same but in the *lab* frame (the K frame)

In the ultra relativistic limit ($\gamma \gg 1$)

$$\text{Im}\alpha(\omega') = -\frac{\pi}{2}\omega_0 R^3 \delta(\omega' + \omega_0) = -\frac{\pi}{2\gamma}\frac{\omega_0 R^3}{v}\delta\left(q_x - \frac{\omega}{v} - \frac{\omega_0}{\gamma v}\right) \tag{11.39}$$

The negative sign of the imaginary part of the particle polarizability means that a particle behaves like an object with negative absorption, amplifying certain incident waves. This phenomenon is closely connected to superradiance first introduced by Zel′dovich [294]. He argued that a rotating object amplifies certain incident waves and speculated that this would lead to spontaneous emission when quantum mechanics is considered. The contributions to the friction force, and the radiation power, from the s- and p-polarized waves in the K frame are given by (see Appendix O.1)

$$f_{sx} = -\frac{3\hbar\omega_0 R^3}{2d^4(n+1)}\left[1 + \left(\frac{\omega_0 d}{c\gamma}\right)C\right], \quad p_s = -\frac{3\hbar v\omega_0 R^3}{2d^4(n+1)} \tag{11.40}$$

$$f_{px} = -\frac{3\hbar\omega_0 R^3}{2d^4}\frac{n}{n+1}\left[1 + \left(\frac{\omega_0 d}{c\gamma}\right)C'\right], \quad p_p = -\frac{3\hbar v\omega_0 R^3}{2d^4}\frac{n}{n+1}, \tag{11.41}$$

where

$$C = \frac{2}{3\pi}\sqrt{\frac{n+1}{n-1}}\left[\frac{n}{\sqrt{n^2-1}}\tanh^{-1}\frac{\sqrt{n^2-1}}{n} - 1\right],$$

$$C' = \frac{2}{3\pi}n\sqrt{\frac{n+1}{n-1}}\left[\frac{n^2}{\sqrt{n^4-1}}\tanh^{-1}\frac{\sqrt{n^4-1}}{n^2} - \frac{n}{\sqrt{n^2-1}}\tanh^{-1}\frac{\sqrt{n^2-1}}{n}\right],$$

In the K' frame, the friction force and the heat absorbed by a particle can be obtained from the corresponding quantities in the K frame using the Lorenz transformations (8.24). For example, for the contributions from the s-polarized waves

$$f'_s = \gamma^2(f_s - \beta w_s) \approx -\frac{3\hbar\omega_0 R^3}{2d^4(n+1)}\left[1 + C\gamma\frac{\omega_0 d}{c}\right], \tag{11.42}$$

and

$$w'_s = \gamma^2(w_s - v f_s) \approx \frac{3\hbar v\omega_0 R^3}{2d^4(n+1)}C\gamma\frac{\omega_0 d}{c}. \tag{11.43}$$

Thus, contrary to the K frame, where the friction force and the power of photon emission are finite, in the K' frame the friction force and the radiation power both diverge as $\sim\gamma$ (see Fig. 11.4b). These results also can be obtained by direct calculations in the K' frame. The radiation power w is determined mostly by the friction force power $f_x v$ in the K frame (see (8.24)). From (8.25), it follows that the particle heating power also contributes significantly in this limit to the change of the kinetic energy.

11.5 Discussion

A silver particle with $R = 4\,\text{nm}$ has the mass $m_0 \approx 2.68\times10^{-21}\,\text{kg}$. Close to the threshold velocity ($v \approx v_0 = c/n$) at $n = 2$, it has the kinetic energy $E_K = m_0c^2(\gamma-1) \approx 200\,\text{TeV}$, which is larger than the energy of two proton in Large Hadron Collider 7 TeV. However the energy of a particle can be decreased by decreasing its radius. According to (11.38) and (11.34), the intensity of the QVC radiation exceeds the intensity of the CVC radiation when

$$\hbar\omega_0\left(\frac{R}{d}\right)^3 > \frac{e^2}{2d} \tag{11.44}$$

The point dipole approximation is valid for $d \gg R$. Assuming $d = 2R$, the condition (11.44) gives $d > 4\alpha d_0$ where the fine structure constant $\alpha \approx 1/137$ and $d_0 = c/\omega_0$. Using the typical value of ω_0 in the UV range, $d_0 \sim 10\,\text{nm}$ and thus $d > 0.3\,\text{nm}$. For a particle with $R = 0.4\,\text{nm}$ and $d = 1\,\text{nm}$, the reduction factor for the particle mass

$\sim 10^{-3}$ and the energy $\sim$0.1 TeV. The characteristic frequency of radiation $\omega \sim v/d$. The threshold velocity v_0 depends on the refractive index n. Recently transparent metamaterials were developed with a very high reflective index in the UV range [295]. At $n = 20$, the threshold velocity $v_0 \sim 10^7$m/s and at $d = 1$ nm, the frequency of the radiation $\sim 10^{16}$s^{-1} i.e. in the near-UV range. The energy of a particle in this case is $\sim$1 GeV. Thus, in principle, QVC radiation can be detected with the present experimental setups but only in the region where relativistic effects are small.

Chapter 12
Phononic Heat Transfer at Planar Interfaces

12.1 Introduction

Almost all surfaces in nature and technology have roughness on many different length scales [385]. When two macroscopic solids are brought into contact, even if the applied force is very small for example, just the weight of the upper solid block, the pressure in the asperity contact regions can be very high, usually close to the yield stress of the (plastically) softer solid. As a result, good thermal contact may occur within each microscopic contact region, but owing to the small area of real contact, the (macroscopic) heat transfer coefficient may still be small. In fact, recent studies have shown that in the case of surfaces with roughness on many different length scales, the heat transfer is nearly *independent* of the area of real contact [296]. We emphasize that this remarkable and counter-intuitive result is only valid when roughness occur over several decades in length scale.

For micro or nanoscale systems, the situation may be very different. Often, the surfaces are very smooth with typically nanometer (or less) roughness on micrometer-sized surface areas, and, because of adhesion, the solids often make contact over a large fraction of the nominal contact area. The heat transfer between solids in perfect contact is usually calculated using the so called acoustic and diffusive mismatch models [297, 298], where it is assumed that all phonons scatter elastically at the interface between two materials. In these models, there is no direct reference to the nature of the solid–solid interaction across the interface, and the models cannot describe the heat flow between weakly interacting solids. An acoustic mismatch model for the thermal contact resistance of van der Waals contacts has been developed by Prasher [299]

Here, we will discuss the heat transfer across interfaces. We focus mainly on perfectly flat interfaces, but we also give some comments on the role of surface roughness, a topic which will be discussed in detail in Chap. 13. The theory we present is general, valid for both solid–solid, solid–liquid or solid–membrane systems with arbitrary strength of the interaction across the contacting interface. We present simple analytical results that can be used to estimate the heat transfer coefficient. We present

A.I. Volokitin and B.N.J. Persson, *Electromagnetic Fluctuations at the Nanoscale*,
NanoScience and Technology, DOI 10.1007/978-3-662-53474-8_12

numerical results for the heat transfer for solid–solid, solid–liquid He and solid–membrane contacts. We consider in detail the heat transfer between graphene and amorphous SiO_2. For this system, the calculated value of the heat transfer coefficient is in good agreement with the value deduced from experimental data.

12.2 Theory

Consider the interface between two solids, and assume that local thermal equilibrium occurs everywhere except close to the interface. For weakly coupled systems, this should be an excellent approximation up to atomic distances from the interface; however, for strongly coupled systems, one cannot expect full local thermal equilibrium within one phonon mean free path from the interface. The energy flow (per unit area) through the interface is given by [266]

$$J = \alpha(T_0 - T_1),$$

where T_0 and T_1 are the local temperatures at the interface in solid **0** and **1**, respectively. The stress or pressure acting on the surface of solid **1** from solid **0** can be written as

$$\sigma(\mathbf{x}, t) = K\big[u_0(\mathbf{x}, t) - u_1(\mathbf{x}, t)\big],$$

where u_0 and u_1 are the (perpendicular) surface displacement of solid **0** and **1** (see Fig. 12.1) ($\mathbf{x} = (x, y)$ is a coordinate system in the interfacial plane), respectively, and where K is a spring constant per unit area characterizing the interaction between the two solids. For weakly interacting solids, the parallel interfacial spring constant $K_\parallel$ is usually much smaller than the perpendicular spring constant $K_\perp = K$, and we will neglect the heat transfer resulting from the tangential interfacial stress associated with thermal vibrations (phonons).

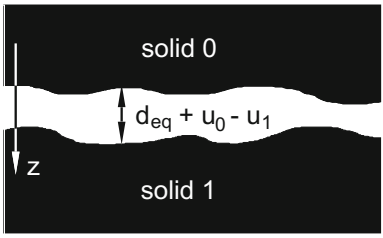

Fig. 12.1 Two solids **0** and **1** in contact. The interfacial surface separation is the sum of the equilibrium separation $d_{\rm eq}$ and the difference in the surface displacements $u_0 - u_1$, due to thermal movements, where both u_0 and u_1 are positive when the displacement points along the z-axis towards the interior of solid **1**. Due to interaction between the solids, a perpendicular stress (or pressure) $\pm K(u_0(\mathbf{x}, t) - u_1(\mathbf{x}, t))$ will act on the (interfacial) surfaces of the solid

If we define

$$u(\mathbf{q},\omega)=\frac{1}{(2\pi)^3}\int d^2x dt\; u(\mathbf{x},t)e^{-i(\mathbf{q}\cdot\mathbf{x}-\omega t)},$$

we get

$$\sigma(\mathbf{q},\omega)=K\left[u_0(\mathbf{q},\omega)-u_1(\mathbf{q},\omega)\right]. \tag{12.1}$$

Within linear elasticity theory [301]

$$u_1(\mathbf{q},\omega)=M_1(\mathbf{q},\omega)\sigma(\mathbf{q},\omega), \tag{12.2}$$

where $M_1(\mathbf{q},\omega)$ is determined by the elastic properties of solid **1**. We consider the heat transfer from solid **0** to solid **1**. The displacement of an atom in solid **0** is the sum of a contribution derived from the applied stress $-\sigma$, and a stochastic fluctuating contribution $u_{0\mathrm{f}}$ due to the thermal movement of the atoms in the solid in the absence of interaction between the solids:

$$u_0(\mathbf{q},\omega)=u_{0\mathrm{f}}(\mathbf{q},\omega)-M_0(\mathbf{q},\omega)\sigma(\mathbf{q},\omega), \tag{12.3}$$

Combining (12.1)–(12.3) gives

$$u_1(\mathbf{q},\omega)=\frac{KM_1(\mathbf{q},\omega)}{1+K\left[M_0(\mathbf{q},\omega)+M_1(\mathbf{q},\omega)\right]}u_{0\mathrm{f}}(\mathbf{q},\omega), \tag{12.4}$$

$$u_0(\mathbf{q},\omega)=\frac{1+KM_1(\mathbf{q},\omega)}{1+K\left[M_0(\mathbf{q},\omega)+M_1(\mathbf{q},\omega)\right]}u_{0\mathrm{f}}(\mathbf{q},\omega). \tag{12.5}$$

The energy transferred to solid **1** from solid **0** during the time period t_0 can be written as

$$\Delta E=\int d^2x dt\; \dot{u}_1(\mathbf{x},t)\sigma(\mathbf{x},t),$$

where $\dot{u}=\partial u/\partial t$, and where the time-integral is over $-t_0/2<t<t_0/2$ and the spatial integral over the interfacial surface area $A_0=L_0^2$ ($-L_0/2<x<L_0/2$, $-L_0/2<y<L_0/2$). One can also write

$$\Delta E=(2\pi)^3\int d^2q d\omega\;(-i\omega)u_1(\mathbf{q},\omega)\sigma(-\mathbf{q},-\omega)$$

Using (12.1), (12.4) and (12.5), we obtain

$$\Delta E=(2\pi)^3\int d^2q d\omega$$

$$\times\frac{\omega K^2\mathrm{Im}M_1(\mathbf{q},\omega)}{\left|1+K\left[M_0(\mathbf{q},\omega)+M_1(\mathbf{q},\omega)\right]\right|^2}\left\langle|u_{0\mathrm{f}}(\mathbf{q},\omega)|^2\right\rangle, \tag{12.6}$$

where we have performed an ensemble (or thermal) average denoted by $\langle..\rangle$. Next, note that (see Appendix P1)

$$\left\langle |u_{0\mathrm{f}}(\mathbf{q},\omega)|^2 \right\rangle = \frac{A_0 t_0}{(2\pi)^3} C_{uu}(\mathbf{q},\omega), \tag{12.7}$$

where A_0 is the surface area, and

$$C_{uu}(\mathbf{q},\omega) = \frac{1}{(2\pi)^3}\int d^2x dt \left\langle u_{0\mathrm{f}}(\mathbf{x},t) u_{0\mathrm{f}}(0,0)\right\rangle e^{i(\mathbf{q}\cdot\mathbf{x}-\omega t)},$$

is the displacement correlation function. Using the fluctuation–dissipation theorem [300] we have (see also Appendix P2 and P3)

$$C_{uu}(\mathbf{q},\omega) = \frac{2}{(2\pi)^3}\frac{\Pi(\omega)}{\omega}\mathrm{Im}M_0(\mathbf{q},\omega) \tag{12.8}$$

where $\Pi(\omega) = \hbar\omega\left[\exp(\hbar\omega/k_{\mathrm{B}}T_0) - 1\right]^{-1}$. Substituting (12.7) in (12.6) and using (12.8) gives the heat current $J_{0\to 1} = \Delta E/A_0 t_0$ from solid **0** to solid **1**:

$$J_{0\to 1} = \frac{4}{(2\pi)^3}\int d^2q \int_0^\infty d\omega\, \Pi(\omega)$$

$$\times \frac{K\mathrm{Im}M_0(\mathbf{q},\omega) K\mathrm{Im}M_1(\mathbf{q},\omega)}{\left|1 + K\left[M_0(\mathbf{q},\omega) + M_1(\mathbf{q},\omega)\right]\right|^2},$$

A similar equation with T_0 replaced by T_1 gives the energy transfer from solid **1** to solid **0**, and the net energy flow $J = J_{0\to 1} - J_{1\to 0}$. The heat transfer coefficient $\alpha = (J_{0\to 1} - J_{1\to 0})/(T_0 - T_1)$ gives in the limit $(T_0 - T_1) \to 0$:

$$\alpha = \frac{4}{(2\pi)^3}\int d^2q \int_0^\infty d\omega\, \frac{\partial\Pi(\omega)}{\partial T}$$

$$\times \frac{K\mathrm{Im}M_0(\mathbf{q},\omega) K\mathrm{Im}M_1(\mathbf{q},\omega)}{\left|1 + K\left[M_0(\mathbf{q},\omega) + M_1(\mathbf{q},\omega)\right]\right|^2}, \tag{12.9}$$

To proceed we need expressions for $M_0(\mathbf{q},\omega)$ and $M_1(\mathbf{q},\omega)$. Here, we give the M-function for (a) solids, (b) liquids and (c) membranes. In what follows, we do not account for the atomistic nature of matter but use a continuum description so that all vibrational modes of 3D -solids have linear dispersion relation, and the bending mode of the (2D) membrane quadratic dispersion.

12.2.1 Solids

Within the elastic continuum model, for an elastic solid with isotropic elastic properties we have [301, 302]

$$M = \frac{i}{\rho c_{\mathrm{T}}^2} \frac{p_{\mathrm{L}}(q,\omega)}{S(q,\omega)} \left(\frac{\omega}{c_{\mathrm{T}}}\right)^2 \tag{12.10}$$

where

$$S = \left[\left(\frac{\omega}{c_{\mathrm{T}}}\right)^2 - 2q^2\right]^2 + 4q^2 p_{\mathrm{T}} p_{\mathrm{L}}$$

$$p_{\mathrm{L}} = \left[\left(\frac{\omega}{c_{\mathrm{L}}}\right)^2 - q^2 + i0\right]^{1/2}$$

$$p_{\mathrm{T}} = \left[\left(\frac{\omega}{c_{\mathrm{T}}}\right)^2 - q^2 + i0\right]^{1/2}$$

where c_{L}, c_{T} and ρ are the longitudinal and transverse sound velocities, and the mass density, respectively.

12.2.2 Liquids

Since the shear modulus vanish for liquids, only longitudinal sound waves can propagate in liquids. The M-function of liquids can be obtained directly from the solid case by letting $c_{\mathrm{T}} \to 0$:

$$M = \frac{i p_{\mathrm{L}}}{\rho\omega^2} = \frac{i}{\rho\omega^2}\left[\left(\frac{\omega}{c_{\mathrm{L}}}\right)^2 - q^2 + i0\right]^{1/2} \tag{12.11}$$

12.2.3 Membranes

We assume that the out-of-plane displacement $u(\mathbf{x}, t)$ satisfies

$$\rho_0 \frac{\partial^2 u}{\partial t^2} = -\kappa \nabla^2 \nabla^2 u + \sigma, \tag{12.12}$$

where $\rho_0 = n_0 m_0$ is the mass density per unit *area* of the 2D-system (m_0 is the atom mass and n_0 the number of atoms per unit area), κ is the bending elasticity (for graphene, $\kappa \approx 1$ eV [303]), and $\sigma(\mathbf{x}, t)$ an external stress acting perpendicular to the membrane (or xy-plane). Using the definition $M(\mathbf{q}, \omega) = u(\mathbf{q}, \omega)/\sigma(\mathbf{q}, \omega)$ from (12.12) we get

$$M = \frac{1}{\kappa q^4 - \rho_0 \omega^2 - i0^+}. \tag{12.13}$$

12.3 Some Limiting Cases

Assuming weak coupling between the solids (i.e., K is so mall that $K[M_0(\mathbf{q}, \omega) + M_1(\mathbf{q}, \omega)] \ll 1$), (12.9) reduces to

$$\alpha = \frac{4K^2}{(2\pi)^3} \int d^2q \int_0^\infty d\omega \, \frac{\partial \Pi(\omega)}{\partial T} \mathrm{Im} M_1(\mathbf{q}, \omega) \mathrm{Im} M_0(\mathbf{q}, \omega). \tag{12.14}$$

In the opposite limit of strong coupling ($K[M_0(\mathbf{q}, \omega) + M_1(\mathbf{q}, \omega)] \gg 1$), we get

$$\alpha = \frac{4}{(2\pi)^3} \int d^2q \int_0^\infty d\omega \, \frac{\partial \Pi(\omega)}{\partial T} \frac{\mathrm{Im} M_0(\mathbf{q}, \omega) \mathrm{Im} M_1(\mathbf{q}, \omega)}{|M_0(\mathbf{q}, \omega) + M_1(\mathbf{q}, \omega)|^2}, \tag{12.15}$$

which does not depend on K. Note also that for very low temperatures only very low frequency phonons will be thermally excited. Assuming a semi-infinite solid, as $\omega \sim q \to 0$, from (12.10) we have $|M| \approx 1/(\rho c \omega) \to \infty$ (where c is the sound velocity and ρ the mass density). Thus, at low enough temperatures (12.9) reduces to (12.15) i.e., for very low temperatures the heat transfer is *independent* of the strength of the interaction across the interface. The physical reason for this is that at very low temperature the wavelength of the phonons becomes very long and the interfacial interaction becomes irrelevant. The transition between the two regions of behavior occurs when $K|M| \approx 1$. Since $|M| \approx 1/(\rho c \omega)$ we get $K \approx \rho c \omega$. But $\hbar\omega \approx k_B T$ and defining the thermal length $\lambda_T = c/\omega = c\hbar/k_B T$ we get the condition $K \approx \rho c^2/\lambda_T$. Since the elastic modulus $E \approx \rho c^2$ we get $K \approx E/\lambda_T$. We can define a spring constant between the atoms in the solid via $k' = Ea$, where a is the lattice constant. Since $K = k/a^2$ we get $k \approx (a/\lambda_T)k'$ as the condition for the transition between the two different regimes in the heat transfer behavior. For most solids at room temperature $\lambda_T \approx a$, but at very low temperatures $\lambda_T \gg a$ which means that even a very weak (soft) interface (for which k is small), will appear as very strong (stiff) with respect to the heat transfer at low temperatures (this result has also been obtained by Prasher [299]).

Let us consider the case where the two solids are identical, and assume strong coupling where (12.15) holds. For this case, we do not expect that the interface will restrict the energy flow. If we consider high temperature, the kinetic energy per

atom in solid **0** will be $\sim k_B T_0$ so the energy density $Q \approx k_B T_0/a_0^3$ (where a_0 is the lattice constant). Thus, if solid **1** is at zero temperature, we expect the energy flow current across the interface to be of order $J \approx Qc/4$ (the factor of $1/4$ results from the fact that only half of the phonons propagate in the positive z-direction and the average velocity of these phonons in the z-direction is $c/2$). Thus, we expect $\alpha \approx k_B c/(4a_0^3)$. This result follows also from (12.15) if we notice that for $M_0 = M_1$ and high temperatures

$$\alpha = \frac{k_B}{(2\pi)^3} \int d^2q \int_0^\infty d\omega \left[\frac{\mathrm{Im} M_0(\mathbf{q}, \omega)}{|M_0(\mathbf{q}, \omega)|} \right]^2 \tag{12.16}$$

If we assume for simplicity that M_0 is given by (12.11) (but the same qualitative result is obtained for solids), then the factor involving M_0 is equal to unity for $\omega > c_L q$ and zero otherwise. Thus, (12.16) reduces to

$$\alpha = \frac{k_B}{(2\pi)^2} \int_0^{c_L q_c} d\omega \int_0^{\frac{\omega}{c_L}} dq\, q = \frac{\pi c_L k_B}{24 a_0^3} \tag{12.17}$$

where we have used that $q_c \approx \pi/a_0$. Thus, for identical materials and strong coupling (12.9) reduces to the expected result.

Let us now briefly discuss the temperature-dependence of the heat transfer coefficient for high and low temperatures. For very low temperatures, α is given by (12.15). Consider first a solid in contact with a solid or liquid. For these cases it follows that $M \sim 1/\omega$ (where we have used that $\omega \sim q$) so the temperature-dependence of the heat transfer coefficient is determined by the term

$$\alpha \sim \int_0^\infty d\omega \, \frac{\partial \Pi(\omega)}{\partial T} \omega^2$$

where we also have used that $d^2q \sim \omega^2$. Thus, we get

$$\alpha \sim \int_0^\infty d\omega \frac{\exp(\hbar\omega/k_B T)}{\left[\exp(\hbar\omega/k_B T) - 1\right]^2} \left(\frac{\hbar\omega}{k_B T} \right)^2 \omega^2 \sim T^3$$

which agrees with the low-temperature dependence predicted by the acoustic mismatch model [297]. For high temperatures, and assuming weak coupling, it can be obtained from (12.14) in the same way that α is temperature independent. However, the spring constant (per unit area) K may depend on the temperature; for example, as a result of a thermally induced rearrangement of the atoms at the contacting interface, or a thermally induced increase in the separation of the two surfaces at the interface, which may be particularly important for weakly interacting systems. The temperature dependence of α for the case of solid–solid and solid–membrane contacts will be discussed in Sect. 12.5.

12.4 Phonon Heat Transfer at Disordered Interfaces: Friction Model

At high temperature and for atomically disordered interfaces, the interfacial atoms will perform very irregular, stochastic motion. In this case, the heat transfer coefficient α can be obtained (approximately) from a classical 'friction' model. This treatment does not take into account, in a detailed way, the restrictions on the energy transfer process by the conservation of parallel momentum, which arise for periodic (or homogeneous) solids. See also Appendix D.

Let us assume that solid **0** has a lower maximal phonon frequency than solid **1**. In this case, most elastic waves (phonons) in solid **0** can in principle propagate into solid **1**, while the opposite is not true, since a phonon in solid **1** with higher energy than the maximum phonon-energy in solid **0** will, because of energy conservation, be totally reflected at the interface between the solids.

Consider an atom in solid **0** (with mass m_0) vibrating with the velocity $(\mathbf{v}_\parallel, v_\perp)$. The atom will exert a fluctuating force on solid **1**, which will result in elastic waves (phonons) being excited in solid **1**. The emitted waves give rise to a friction force acting on the atom in solid **0** (from solid **1**), which we can write as [302]

$$\mathbf{F}_f = -m_0\eta_\parallel \mathbf{v}_\parallel - m_0\eta_\perp \mathbf{v}_\perp,$$

and the power transfer to solid **1** will be

$$P = -\langle \mathbf{F}_f \cdot \mathbf{v} \rangle = m_0\eta_\parallel \langle v_\parallel^2 \rangle + m_0\eta_\perp \langle v_\perp^2 \rangle .$$

At high temperatures

$$m_0 \langle v_\parallel^2 \rangle = 2k_B T_0, \qquad m_0 \langle v_\perp^2 \rangle = k_B T_0.$$

Hence

$$P = (2\eta_\parallel + \eta_\perp) k_B T_0.$$

A similar formula (with T_0 replaced by T_1) gives the power transfer from solid **1** to solid **0**. Hence

$$J = n_0(2\eta_\parallel + \eta_\perp) k_B (T_0 - T_1),$$

where $n_0 = 1/a_0^2$ is the number of interfacial atoms per unit area in solid **0**. Thus we get

$$\alpha = n_0(2\eta_\parallel + \eta_\perp) k_B. \tag{12.18}$$

For weak interfacial coupling we expect $\eta_\perp \gg \eta_\parallel$, and we can neglect the $\eta_\parallel$-term in (12.18).

The damping or friction coefficient $\eta_\perp$ due to phonon emission was calculated within elastic continuum mechanics in [302]. We have

$$\eta_\perp \approx \frac{k^2\xi'}{\rho_1 m_0 c_{\rm T}^3} = \frac{K^2 a_0^4 \xi'}{\rho_1 m_0 c_{\rm T}^3}, \tag{12.19}$$

where $\xi' \approx 0.13$ (see [304]). Using that $n_0 = 1/a_0^2$ and substituting (12.19) in (12.18) gives

$$\alpha = \frac{k_{\rm B} K^2 \xi'}{\rho_0 \rho_1 c_{\rm T}^3}, \tag{12.20}$$

where

$$\xi' = \frac{1}{8\pi} {\rm Re} \int_0^\infty dx \frac{2\,(\gamma - x)^{1/2}}{(1-2x)^2 + 4\,(1-x)^{1/2}\,(\gamma - x)^{1/2}}$$

where $\gamma = (c_{\rm T}/c_{\rm L})^2$, and where $\rho_0 = n_0 m_0$ is the (one atomic layer) mass per unit surface area of solid $\mathbf{0}$. There are two contributions to the integral ξ'. One is derived from the region $x < 1$ where the integral clearly has a non-vanishing real part. This contribution corresponds to the excitation of transverse and longitudinal acoustic phonons. The second contribution arises from the vicinity of the point (for $x > 1$) where the denominator vanishes. This pole contribution corresponds to excitation of surface (Rayleigh) waves. As shown in [302], approximately 65% of the radiated energy is due to the surface (Rayleigh) phonons, and the rest by bulk acoustic phonons.

We emphasize that (12.20) is only valid for high temperatures and weak coupling. A more general equation for the heat transfer between solids when the phonon emission occurs incoherently is derived in Appendix P4:

$$\alpha \approx \frac{4A^*}{(2\pi)^3} \int_0^\infty d\omega\, \frac{\partial \Pi(\omega)}{\partial T} \frac{K{\rm Im}M_0(\omega) K{\rm Im}M_1(\omega)}{\left|1 + K\left[M_0(\omega) + M_1(\omega)\right]\right|^2}, \tag{12.21}$$

where

$$M(\omega) = \frac{1}{A^*} \int_{q<q_{\rm c}} d^2q\, M(\mathbf{q}, \omega),$$

where the integral is over $|\mathbf{q}| < q_{\rm c}$, where $\pi q_{\rm c}^2 = A^*$. The cut-off wavevector $q_{\rm c}$ is the smallest of q_1 and q_2, where $\pi q_1^2 = (2\pi)^2/a_0^2$ (where a_0 is the lattice constant) and where $q_2 = k_{\rm B}T/\hbar c_0$ (where c_0 is the smallest sound velocity of solid $\mathbf{0}$) is the thermal wavevector. For high temperatures and weak coupling, for an Einstein model of solid $\mathbf{0}$, (12.21) reduces to (12.20) (see Appendix P5).

12.5 Numerical Results

We now present some numerical results to illustrate the theory presented above. We consider (a) solid–solid, (b) solid–liquid and (c) solid–membrane systems.

12.5.1 Solid-Solid

We consider the heat transfer between two solids with perfectly flat contacting surfaces. We take the sound velocities and the mass density and the (average) lattice constant to be that of SiO_2. We consider two cases: weakly interacting solids (soft interface) with $K = 2.52 \times 10^{19}$ N/m^3 (see Fig. 12.4), and solids with stronger interaction (stiff interface), with 10 times larger K. In Fig. 12.2, we show the heat transfer coefficient as a function of temperature. Note that, for high temperatures, α is nearly 100 times larger for the stiff case as compared with the soft case. This result is expected based on (12.9), which shows that $\alpha \sim K^2$ as long as K is not too large and the temperature is not too low. For low temperatures, both cases gives very similar results, and for $T < 3$ K the heat transfer coefficient $\alpha \sim T^3$. The reason for why, at low temperatures, the heat transfer is independent of the strength of the interfacial interaction was explained in Sect. 12.3, and is due to the long wavelength of the thermally excited phonons at low temperature.

For incoherent phonon transmission, using (12.21), we obtained the result shown by dashed curves in Fig. 12.2. For both the soft and stiff interface, the results obtained assumed that coherent and incoherent phonon transmission are similar.

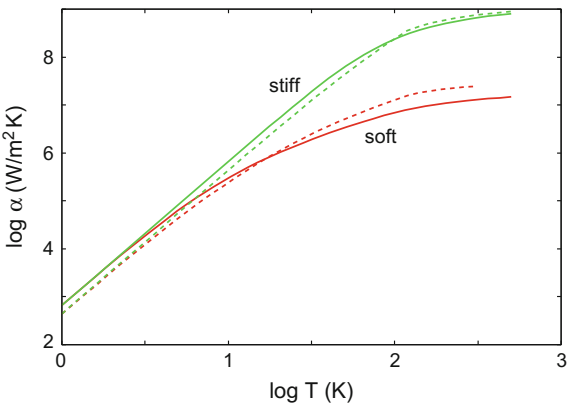

Fig. 12.2 The logarithm (with 10 as basis) of the heat transfer coefficient as a function of the logarithm of the temperature for weakly interacting solids (soft) with $K = 2.52 \times 10^{19}$ N/m^3, and for solids with that interact stronger (stiff) with 10 times larger K. The *solid lines* are for coherent phonon transmission, and the *dashed lines* are for incoherent phonon transmission. The initial slope (for low temperature) of the curves is 3, corresponding to a $\sim T^3$ temperature dependence

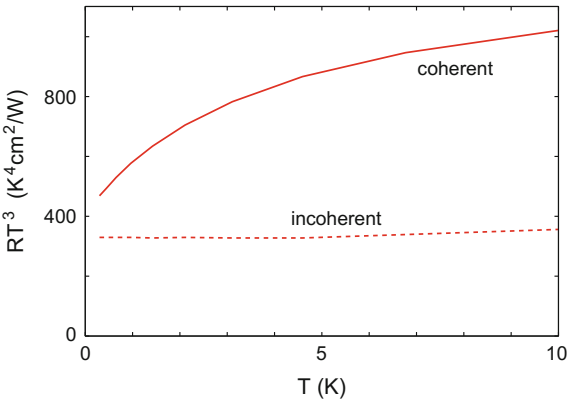

Fig. 12.3 The calculated contact resistance (multiplied by T^3) between liquid ^{4}He and a-SiO_2 as a function of the temperature, with $K = 1.18 \times 10^{19}$ N/m^3

12.5.2 Solid-Liquid

Heat transfer between liquid ^{4}He and solids was studied by Kapitza [305] ~60 years ago, and $R = 1/\alpha$ is usually denoted as the Kapitza resistance [297, 306]. Let us apply the theory above to the heat transfer between liquid ^{4}He and a-SiO_2. In the calculation we use a He-substrate potential with well depth 10.2 meV and ^{4}He-substrate equilibrium bond distance $d_{eq} = 2.2$ Å, which agrees with the model parameters used in [311]. With these parameters, we get the perpendicular He-substrate vibration frequency $\omega_\perp \approx 91$ cm^{-1} and the spring constant $K = 1.18 \times 10^{19}$ N/m^3. In Fig. 12.3 we show the calculated contact resistance R (multiplied by T^3), as a function of the temperature T. In this calculation, we have assumed that all the parameters (e.g., ^{4}He sound velocity c_0 and mass density ρ_0) characterizing the system are temperature independent [309]. The Kapitza resistance has been measured (for $T > 1$ K) for liquid ^{4}He in contact with Quartz [308] and Sapphire [307] and this scales roughly with temperature as T^{-3}; the magnitude for $T = 1$ K is approximately 10 times smaller than our calculated result, assuming incoherent phonon transfer. Experimental data show that, for $T < 0.5$ K, the Kapitza resistance increases much faster with decreasing temperature than expected from the $R \sim T^{-3}$-dependence predicted by our theory and most other theories. It is not clear what the origin of this discrepancy may be, but it has been suggested to be associated with surface roughness. Unfortunately, most measurements of the Kapitza resistance were performed before recent advances in surface science, and many of the studied systems are likely to have oxide and unknown contamination layers, which may explain the large fluctuations in the measured contact resistance for nominally identical systems.

12.5.3 Solid-Membrane

Recently, it has been found that the heat generation in graphene field-effect transistors can result in high temperatures and device failure [164].Thus, it is important to

understand the mechanisms that influence the heat flow. Graphene can be considered to be a 2D system (membrane). In this case, from (12.13), we get:

$$\mathrm{Im}M_0(\mathbf{q},\omega) = \pi\delta(\kappa q^4 - \rho_0\omega^2) = \frac{\pi}{2\rho_0\omega_1}\delta(\omega-\omega_1) \tag{12.22}$$

where $\omega_1 = (\kappa/\rho_0)^{1/2}q^2 = c(q)q$, where we have defined the velocity $c(q) = (\kappa/\rho_0)^{1/2}q$. Substituting (12.22) in (12.9) and assuming high temperatures ($k_\mathrm{B}T_0 \gg \hbar\omega_1$) so that $\Pi(\omega) \approx k_\mathrm{B}T_0$ gives:

$$J_{0\to1} = \frac{k_\mathrm{B}T_0}{2\pi\rho_0}\int_0^\infty dq\ \frac{q}{\omega_1}K^2\mathrm{Im}M_1(\mathbf{q},\omega_1).$$

The heat transfer coefficient $\alpha = (J_{0\to1} - J_{1\to0})/(T_0 - T_1)$ is given by

$$\alpha = \frac{k_\mathrm{B}}{2\pi\rho_0}\int_0^\infty dq\ \frac{q}{\omega_1}K^2\mathrm{Im}M_1(\mathbf{q},\omega_1). \tag{12.23}$$

Using the expression for $M_1(\mathbf{q},\omega)$ derived in [301, 302] and $\omega_1 = c(q)q$ gives

$$\alpha = \frac{k_\mathrm{B}K^2\xi}{\rho_0\rho_1 c_\mathrm{T}^3}, \tag{12.24}$$

where

$$\xi = \frac{1}{2\pi}\int_0^{q_\mathrm{c}} dq\ \frac{1}{q}\frac{c(q)}{c_\mathrm{T}}$$

$$\times\ \mathrm{Re}\left(\frac{\left[\frac{c^2(q)}{c_\mathrm{L}^2}-1\right]^{1/2}}{\left[\frac{c^2(q)}{c_\mathrm{T}^2}-2\right]^2 + 4\left[\frac{c^2(q)}{c_\mathrm{T}^2}-1\right]^{1/2}\left[\frac{c^2(q)}{c_\mathrm{L}^2}-1\right]^{1/2}}\right),$$

where c_L, c_T and ρ_1 are the longitudinal and transverse sound velocities, and the mass density, respectively, of solid **1**. The cut off wavevector $q_\mathrm{c} \approx \pi/a_1$ (a_1 is the lattice constant, or the average distance between two nearby atoms) of solid **1**.

There are two contributions to the integral ξ. One is derived from $c(q) > c_\mathrm{L}$, but for graphene on a-SiO_2, this gives only ~10% of the contribution to the integral. For $c(q) < c_\mathrm{L}$, the term after the Re operator is purely imaginary (and will therefore not contribute to the integral), *except* for the case where the denominator vanishes. It is found that this pole-contribution gives the main contribution (~90%) to the integral, and corresponds to the excitation of a Rayleigh surface (acoustic) phonon of solid **1**. This process involves energy exchange between a bending vibrational mode of the graphene and a Rayleigh surface phonon mode of solid **1**. The denominator vanishes when $c(q) = c_\mathrm{R}$ where

$$\left[\frac{c_\mathrm{R}^2}{c_\mathrm{T}^2}-2\right]^2 - 4\left[1-\frac{c_\mathrm{R}^2}{c_\mathrm{T}^2}\right]^{1/2}\left[1-\frac{c_\mathrm{R}^2}{c_\mathrm{L}^2}\right]^{1/2} = 0.$$

Note that the Rayleigh velocity $c_R < c_T$ but close to c_T. For example, when $c_L/c_T = 2$, $c_R \approx 0.93c_T$, and the pole contribution to the integral in ξ is 0.083. Note that (12.23) is of the same form as (12.19), and since $\xi' \approx 0.13 \approx \xi$ they give very similar results.

In the model above, the heat transfer between the solids involves a single bending mode of the membrane or 2D system. Because of the weak interaction (and large separation) between the graphene and the substrate, it is likely that the coupling between the in-plane vibrational modes of graphene and the substrate is negligible. However, in reality there will always be some roughness at the interface, which will blur the wavevector conservation rule. We therefore expect a narrow band of bending modes to be involved in the energy transfer, rather than a single mode. The model study above assumes implicitly that, due to lattice non-linearity (and defects), there exist phonon scattering processes that rapidly transfer energy to the bending mode involved in the heat exchange with the substrate. This requires very weak coupling to the substrate, so that the energy transfer to the substrate is so slow that the bending mode can be repopulated by phonon scattering processes in the 2D system—from the in-plane phonon modes— in such a way that its population is always close to what would be the case if complete thermal equilibrium occurs in the 2D system. This may require high temperatures in order for multi-phonon scattering processes to occur with enough rates.

We now consider graphene on amorphous SiO_2. Graphene, the recently isolated 2D carbon material with unique properties due to its linear electronic dispersion, is being actively explored for electronic applications [310]. Important properties include the high mobilities reported especially, in suspended graphene; the fact that graphene is the ultimately thin material; the stability of the carbon–carbon bond in graphene; the ability to induce a band gap by electron confinement in graphene nanoribbons; and its planar nature, which allows established pattering and etching techniques to be applied. Recently, it has been found that the heat generation in graphene field-effect transistors can result in high temperatures and device failure [164]. Thus, it is important to understand the mechanisms that influence the heat flow.

The graphene–a-SiO_2 interaction is probably of the van der Waals type. In [312], the interaction between the graphene C-atoms and the substrate Si and O atoms was assumed to be described by Lennard-Jones (LJ) pair-potentials. Here, we use a simplified picture where the substrate atoms form a simple cubic lattice with the lattice constant determined by $a_1 = (\bar{m}/\rho_1)^{1/3} \approx 0.25$ nm, where $\bar{m} = (m_{Si} + 2m_O)/3 \approx 3.32 \times 10^{-26}$ kg is the average substrate atomic mass, and $\rho_1 \approx 2200$ kg/m^3 the mass density of a-SiO_2. We also use the effective LJ energy parameter, $\epsilon = (\epsilon_{Si} + 2\epsilon_O)/3 \approx 5.3$ meV, and the bond-length parameter $\sigma = (\sigma_{Si} + 2\sigma_O)/3 \approx 0.31$ nm. With these parameters, we can calculate the graphene–a-SiO_2 interaction energy, $U(d)$, per graphene carbon atom, as a function of the separation, d, between the center of a graphene carbon atom and the center of the first layer of substrate atoms. We find (see Fig. 12.4) the graphene–a-SiO_2 binding energy $E_b = -U(d_{eq}) \approx 35$ meV per carbon atom, and the force constant $k = U''(d_{eq})$ (where $d_{eq} \approx 0.32$ nm is the equilibrium separation)

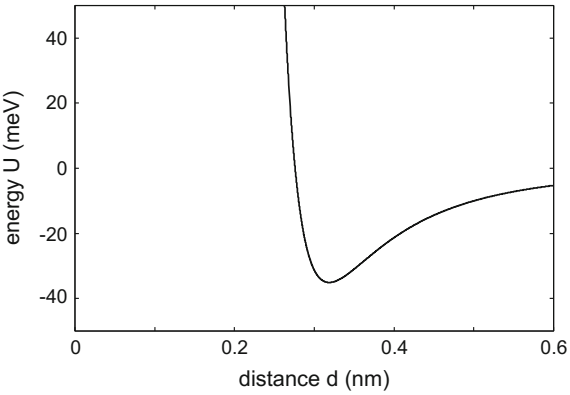

Fig. 12.4 The calculated graphene–a-SiO_2 interaction energy $U(d)$ per graphene carbon atom, as a function of the separation d (in nm) between the center of a graphene carbon atom and the center of the first layer of substrate atoms. See text for details

$k = Ka_0^2 = 2.4$ N/m per carbon atom. This gives the perpendicular graphene—a-SiO_2 (uniform) vibration frequency $\omega_\perp \approx (k/m_0)^{1/2} \approx 55\ \text{cm}^{-1}$, which is similar to what is observed for the perpendicular vibrations of linear alkane molecules on many surfaces (e.g., approximately $50 - 60\ \text{cm}^{-1}$ for alkanes on metals and on hydrogen terminated diamond C(111) [313]). Using $K = k/a_0^2 = 1.82 \times 10^{20}\ \text{N/m}^3$, and the transverse and longitudinal sound velocities of solid **1** ($c_\text{T} = 3743$ m/s and $c_\text{L} = 5953$ m/s), from (12.20) we obtain $\alpha \approx 3 \times 10^8\ \text{W/Km}^2$.

The heat transfer coefficient between graphene and a *perfectly flat* a-SiO_2 substrate has not been measured directly, but measurements of the heat transfer between carbon nanotubes and sapphire by Maune et al. [314] indicate that it may be of order $\alpha \approx 8 \times 10^8\ \text{W/m}^2\text{K}$. This value was deduced indirectly by measuring the breakdown voltage of carbon nanotubes, which could be related to the temperature increase in the nanotubes. Molecular dynamics calculations [312] for nanotubes on a-SiO_2 gives $\alpha \approx 3 \times 10^8\ \text{W/m}^2\text{K}$ (here it has been assumed that the contact width between the nanotube and the substrate is 1/5 of the diameter of the nanotube). Finally, using a so called 3 ω method, Chen et al. [315] have measured the heat transfer coefficient $\alpha \approx 2 \times 10^8\ \text{W/m}^2\text{K}$.

We now discuss the temperature dependence of the heat transfer coefficient. If we assume that most of the heat transfer is via a substrate phonon mode at the frequency ω_0, then the temperature dependence of α should be given by

$$\frac{d\Pi(\omega_0)}{dT} = \frac{x^2 e^x}{(e^x - 1)^2}, \tag{12.25}$$

where $x = \hbar\omega_0/k_\text{B}T$. In Fig. 12.5, we show the temperature dependence of the heat transfer coefficient measured by Chen et al. [315] for $42\ \text{K} < T < 310\ \text{K}$. The solid lines were calculated using (24) with $\hbar\omega_0 = 11$ meV (upper curve) and 7 meV (lower curve). In our model, all the substrate vibrational modes have linear dispersion relation, for example, $\hbar\omega = c_\text{R} q$ for the Rayleigh mode—and, since the measured phonon frequency $\omega(q)$ falls below the line obtained by extending the initial linear

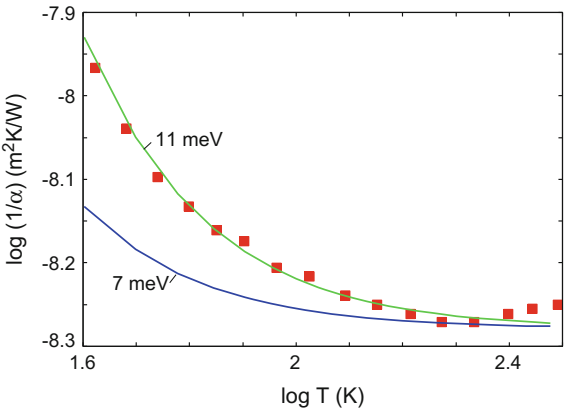

Fig. 12.5 The logarithm of the contact resistance for graphene on a-SiO_2 as a function of the logarithm of the temperature. *Square symbols* measured data from [315]. *Solid lines* show the calculated contact resistance using (12.24) with $\hbar\omega_0 = 11$ meV (*upper curve*) and $\hbar\omega_0 = 7$ meV (*lower curve*)

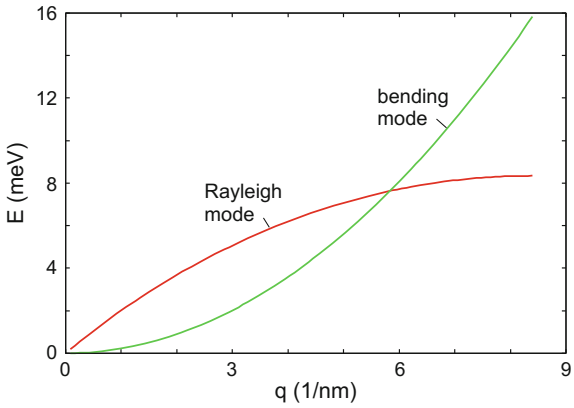

Fig. 12.6 The frequency of the graphene bending mode becomes equal to the frequency of the Rayleigh mode when $\omega_{\rm bend}(q) = \omega_{\rm R}(q)$. The Rayleigh mode dispersion was measured for α-quartz (0001) [316] and the bending mode dispersion was calculated using $\omega_{\rm bend} = (\kappa/\rho_0)^{1/2} q^2$ with the bending stiffness $\kappa = 1.1$ eV as obtained in [303]

dispersion to higher frequencies, it follows that the frequency where the graphene-bending mode becomes equal to the frequency of the Rayleigh mode will occur at a higher frequency than expected using the measured Rayleigh mode dispersion relation. This is illustrated in Fig. 12.6 where we show the measured Rayleigh mode dispersion for α-quartz (0001) [316]. Note that the frequencies of the bending mode and the Rayleigh mode become equal when $\hbar\omega \approx 7$ meV. However, using this excitation energy in (12.25) gives too weak temperature dependence. There are two possible explanations for this:

(a) In an improved calculation using the measured dispersion relations for the substrate phonon modes, emission of bulk phonons may become more important than in the present study where we assumed the linear phonon-dispersion is valid for all wavevectors q. This would make higher excitation energies more important and could lead to the effective (or average) excitation energy 11 meV necessary to fit the observed temperature dependence.

(b) As pointed out above, the model developed above for the heat transfer involves a single, or a narrow band, of bending modes of the membrane or 2D system. In order for this model to be valid, the coupling to the substrate must be so weak that the energy transfer to the substrate from the bending mode occurs so slowly that the mode can be repopulated by phonon scattering processes, in such a way that its population is always close to what is expected if full thermal equilibrium would occur within the 2D system. This may require high temperatures in order for multi-phonon scattering processes to occur by sufficiently high enough rates. This may contribute to the decrease in the heat transfer coefficient observed for the graphene–a-SiO_2 system below room temperature [315].

12.6 Role of Surface Roughness

Surfaces of engineering interest are never perfectly smooth and this must always be taken into account when analyzing interfacial heat transfer between contacting solids. As discussed above, surface roughness and interfacial disorder on the same length scale as the phonon wavelength may result in strong diffusive-like phonon scattering, which may drastically affect the interfacial heat transfer. In addition, for elastically hard solids, the area of real (atomic) contact A is usually a very small fraction of the apparent contact area A_0, which has a strong influence on the heat transfer [296], and in many cases most of the heat may flow in the air film separating the non-contact region. The heat transfer via the area of real contact is determined not just by the heat transfer resistance across the contacting interface (of atomic scale thickness) as studied above, but often most of the heat flow resistance is caused by the so-called spreading resistance, related to the interaction between the heat flow filaments, which emerge from the areas of real contact. This latter contribution depends on the wide (fractal-like) distribution of surface roughness length scales exhibited by most of the surfaces of macroscopic solids (see Fig. 12.7). We will discuss this topic in detail in Chap. 13, but here we give some additional comments.

For the contact between rough surfaces, the total heat transfer resistance is (approximately) the sum of the two contributions:

$$\frac{1}{\alpha} \approx \frac{1}{\alpha_{\rm spred}} + \frac{1}{\alpha_{\rm c}}$$

where $1/\alpha_{\rm spred}$ is the spreading resistance studied in Chap. 13, and $1/\alpha_{\rm c}$ the resistance that determines the temperature jump (on atomistic length scale) across the area of real contact. One can show that (see Appendix P6):

$$\frac{1}{\alpha_{\rm c}} \approx \frac{1}{\alpha_{\rm b}} \frac{1}{A_0 J_0^2} \int d^2x \, J_z^2(\mathbf{x})$$

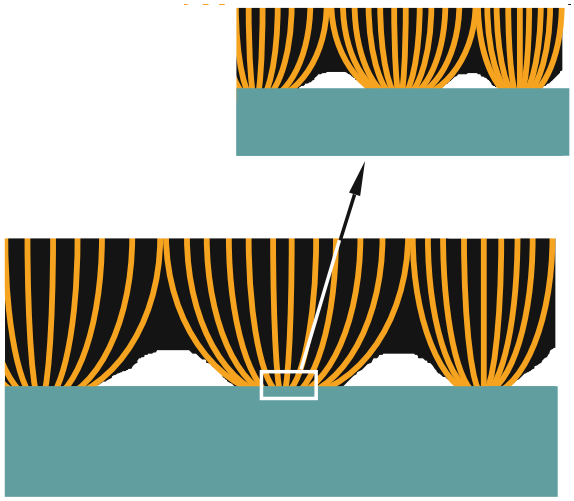

Fig. 12.7 Heat flow in the contact region between a rigid block with a flat surface (*bottom*) and en elastic solid with a randomly rough surface (*top*). The orange lines denote the heat current flux lines in the upper solid. The heat current filaments expand laterally until the filaments from the different contact regions touch each other. The "interaction" between the filaments gives rise to the spreading resistance. Because of the fractal nature of most surfaces the interaction between the heat flow filaments occur, on many different length scales

where $J_z(\mathbf{x})$ is the heat current at the interface, J_0 the average heat current, and α_b the (boundary) heat transfer coefficient studied above. If the heat current would be constant through the area of real contact, then $J_z = (A_0/A)J_0$, where A is the area of real contact. In this case, we get $\alpha_c \approx (A/A_0)\alpha_b$ and

$$\frac{1}{\alpha} \approx \frac{1}{\alpha_{\text{spred}}} + \frac{1}{\alpha_b}\frac{A_0}{A} \tag{12.26}$$

For most hard macroscopic solids, the local pressure in the contact regions is very high, which may result in 'cold welded' contact regions with good thermal contact, in which case the contribution from the spreading resistance dominates the contact resistance. However, for weakly coupled microscopic solids, the contribution from the second term in (12.26) may be very important.

In [164], the temperature profile in graphene under current was studied experimentally. The heat transfer coefficient between graphene and the a-SiO_2 substrate was determined by modeling the heat flow using the standard heat flow equation with the heat transfer coefficient as the only unknown quantity. The authors found that using a constant (temperature-independent) heat transfer coefficient $\alpha \approx 2.5 \times 10^7$ W/m^{2}K the calculated temperature profiles in graphene are in good agreement with experimental data. This α is approximately 10 times smaller than expected for perfectly flat surfaces. In [369–371], we studied the heat transfer between graphene and a-SiO_2.

We assumed that because of surface roughness the graphene only makes partial contact with the SiO_2 substrate, which will reduce the heat transfer coefficient as compared to the perfect contact case. The analysis indicated that the spreading resistance contribution in (12.26) may be very important, and could explain the magnitude of the observed heat contact resistance. However, assuming that (due to the roughness) $A/A_0 \approx 0.1$, the second term in (12.26) becomes of the same order of magnitude as the measured heat contact resistance. Thus, in this particular application it is not clear which term in (12.26) dominates the contact resistance, and probably both terms are important.

12.7 Summary

To summarize, we have studied the heat transfer between coupled systems with a flat interface. We have presented simple analytical results, which can be used to estimate the heat transfer coefficient. The interaction between the solids is characterized by a spring constant (per unit area) K. The formalism developed is general and valid both for strongly interacting ($K \to \infty$) and weakly interacting ($K \to 0$) solids. We have shown that, at low enough temperatures, even a very weak interfacial interaction will appear strong, and the heat transfer is then given by the limiting formula obtained as $K \to \infty$. Earlier analytical theories of heat transfer [297] do not account for the strength of the interaction between the solids, but correspond to the limiting case $K \to \infty$. However, we have shown that, at room temperature (or higher temperatures), the heat transfer between weakly interacting solids may be 100 times (or more) slower than between strongly interacting solids.

Detailed results were presented for the heat transfer between a membrane (graphene) and a semi-infinite solid (a-SiO_2). For this case, the energy transfer was dominated by energy exchange between a bending vibrational mode of the graphene, and a Rayleigh surface phonon mode of the substrate. This model assumes implicitly that, due to lattice non-linearity (and defects), phonon scattering processes exist, which rapidly transfer energy to the bending mode involved in the heat exchange with the substrate. This may require high temperatures in order for multi-phonon scattering processes to occur at a sufficiently high rate. The calculated value of the heat transfer coefficient was found to be in good agreement with the value deduced from the experimental data.

Chapter 13
Heat Transfer: Role of Surface Roughness

In this section, we study the heat transfer between elastic solids with randomly rough surfaces. We include both the heat transfer from the area of real contact, and the heat transfer between the surfaces in the non-contact regions. We apply a recently developed contact mechanics theory, which accounts for the hierarchical nature of the contact between solids with roughness on many different length scales. For elastic contact, at the highest (atomic) resolution, the area of real contact typically consists of atomic (nanometer) sized regions, and we discuss the implications of this for the heat transfer. For solids with very smooth surfaces, as is typical in many modern engineering applications, the interfacial separation in the non-contact regions will be very small, and for this case we show the importance of the radiative heat transfer associated with the evanescent electromagnetic waves, which exists outside of all bodies.

13.1 Introduction

The heat transfer between solids is a topic of great importance. Classical applications include topics such as cooling of microelectronic devices, spacecraft structures, satellite bolted joints, nuclear engineering, ball bearings, tires and heat exchangers. Other potential applications involve microelectromechanical systems (MEMS). Heat transfer is also of crucial importance in friction and wear processes; for example, rubber friction on hard and rough substrates depends crucially on the temperature increase in the rubber–counter surface asperity contact regions [373]. Another important application is friction on ice where a thin meltwater film may form due to frictional heating of the ice surface [426].

A large number of papers have been published on the heat transfer between randomly rough surfaces [375]. However, most of these studies are based on asperity contact models such as the model of Greenwood and Williamson (GW) [376]. Recent studies have shown that the GW-model (and other asperity contact models [377]) are very inaccurate [378, 379], mainly because of the neglect of the long-range elastic

A.I. Volokitin and B.N.J. Persson, *Electromagnetic Fluctuations at the Nanoscale*,
NanoScience and Technology, DOI 10.1007/978-3-662-53474-8_13

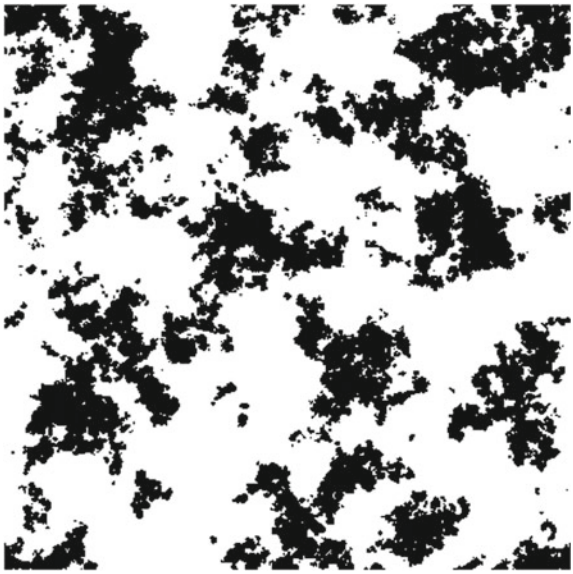

Fig. 13.1 The *black area* is the contact between two elastic solids with randomly rough surfaces. For surfaces that have fractal-like roughness, the whole way down to the atomic length scale, the contact at the highest magnification (atomic resolution) typically consists of nanometer-sized atomic clusters. The result is obtained using Molecular Dynamics (MD), but since there is no natural length scale in elastic continuum mechanics, the picture could also be the contact observed between two macroscopic elastic *solids*. Adapted from [386]

coupling [380]. That is, if an asperity is pushed downwards somewhere, the elastic deformation field extends a long distance away from the asperity, which will influence the contact involving other asperities further away [381]. This effect is neglected in the GW theory, but it is included in the contact mechanics model of Persson [382–386], which we use in the present study. In addition, in the GW model, the asperity contact regions are assumed to be circular (or elliptical) while the actual contact regions (at high enough resolution) have fractal-like boundary lines [386–388], see Fig. 13.1. Thus, because of their complex nature, one should try to avoid directly involving the nature of the contact regions when studying contact mechanics problems, such as the heat or electric contact resistance. The approach we use in this section does not directly involve the nature of the contact regions. Finally, we note that, for elastically hard solids, the area of real (atomic) contact A may be a very small fraction of the nominal or apparent contact area A_0, even at high nominal squeezing pressures [389, 390].

Another important discovery in recent contact mechanics studies is that for elastic contacts, the contact regions observed at atomic resolution may be just a few atoms wide, i.e., the diameter of the contact regions may be of the order of $\sim$1 nm [391–393]. The heat transfer via such small junctions may be very different from the heat transfer through macroscopic-sized contact regions, where the heat transfer is

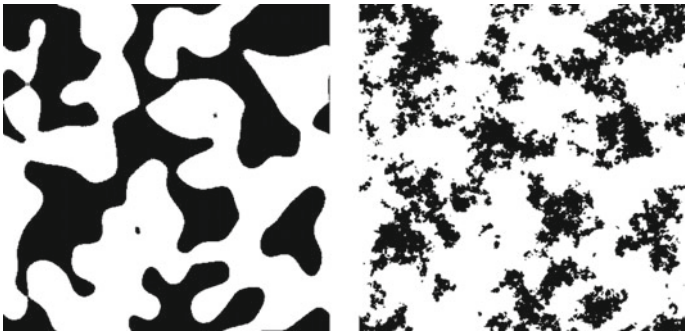

Fig. 13.2 The contact region (*black area*) between two elastic solids observed at low (*left*) and high (*right*) magnification. The contact resistance depends mainly on the long-wavelength roughness, and can usually be calculated accurately from the nature of the contact observed at low magnification (*left*)

usually assumed to be proportional to the linear size of the contact regions (this is also the prediction of the macroscopic heat diffusion equation), rather than the contact area. In particular, if the typical phonon wavelength involved in the heat transfer becomes larger than the linear size of the contact regions (which will always happen at a low enough temperature), the effective heat transfer may be strongly reduced. Similarly, if the phonons mean free path is longer than the linear size of the contact regions, ballistic (phonon) energy transfer may occur that cannot be described by the macroscopic heat diffusion equation. These effects are likely to be of crucial importance in many modern applications involving micro- (or nano-) sized objects, such as MEMS, where just a few atomic-sized contact regions may occur. However, for macroscopic solids, the thermal (and electrical) contact resistance is usually very insensitive to the nature of the contact regions observed at the highest magnification, corresponding to atomistic (or nanoscale) length scales. In fact, the heat transfer is determined mainly by the nature of the contact regions observed at lower magnifications where the contact regions appear larger (see Sect. 13.5 and [394, 395]), see Fig. 13.2. For example, in Sect. 13.2.3, we show that for self-affine fractal surfaces, the contact resistance depends on the range of surface roughness included in the analysis as $\sim r(H) - (q_0/q_1)^H$, where q_0 and q_1 are the smallest and the largest wavevector of the surface roughness included in the analysis, respectively, and H is the Hurst exponent related to the fractal dimension via $D_f = 3 - H$. The number $r(H)$ depends on H but is of the order of unity. In a typical case, $H \approx 0.8$, and including surface roughness over one wavevector decade $q_0 < q < q_1 = 10q_0$ results in a heat resistance which typically is only $\sim$10% smaller than obtained when including infinitely many decades of length scales (i.e., with $q_1 = \infty \times q_0$). At the same time, the area of real contact approaches zero as $q_0/q_1 \to 0$. Thus, there is, in general, no relation between the area of real contact (which is observed at the highest magnification, and which determines the friction force in most cases, among other things), and the heat (or electrical) contact resistance between the solids. One aspect

of this in the context of electric conduction was pointed out a long time ago [396]: if an insulating film covers the solids in the area of real contact, and if electrical contact occurs by a large number of small breaks in the film, the resistance may be almost as low as with no film. Similarly, the thermal contact resistance of macroscopic solids usually does not depend on whether the heat transfer occurred by diffusive or ballistic phonon propagation, but rather the contact resistance is usually determined mainly by the nature of the contact regions observed at relative low magnification.

Note that as H decreases towards zero (or the fractal dimension $D_f \to 3$), it is necessary to include more and more decades in the length scales in order to obtain the correct (or converged) contact resistance, and for $H = 0$ (or $D_f = 3$) it is necessary to include the roughness on the whole way down to the atomic length scale (assuming that the surfaces remain fractal-like with $H = 0$ the whole way down to the atomic length scale). Most natural surfaces and surfaces of engineering interest have (if self-affine fractal) $H > 0.5$ (or $D_f < 2.5$); for example, surfaces prepared by crack propagation or sand blasting typically have $H \approx 0.8$ (see [397]), and in these cases the contact resistance can be calculated accurately from the (apparent) contact observed at relatively low magnification. However, some surfaces may have smaller Hurst exponents. One interesting case is surfaces (of glassy solids) with frozen capillary waves [385, 398] (which are of great engineering importance [398]), which have $H = 0$. The heat transfer between such surfaces may be understood only by studying the system at the highest magnification corresponding to atomic resolution.

In this section, we will consider the heat transfer between (macroscopic-sized) solids in the light of recent advances in contact mechanics. We will study the contribution to the heat transfer, not just from the area of real contact (observed at atomic resolution), but also the heat transfer across the area of non-contact, in particular the contribution from the fluctuating electromagnetic field, which surrounds all solid objects [9, 11]. For high-resistivity materials and for hard and very flat surfaces, such as those involved in many modern applications, (e.g., MEMS applications), this non-contact radiative heat transfer may in fact dominate in the total heat transfer (at least under vacuum condition). We note that for flat surfaces (in a vacuum) separated by a distance d larger than the thermal length $d_T = c\hbar/k_B T$, the non-contact heat transfer is given by the classical Stefan–Boltzman law, and is independent of d. However, for very short distances, the contribution from the evanescent electromagnetic waves to the heat transfer will be many orders of magnitude larger than the contribution from propagating electromagnetic waves (as given by the Stefan–Boltzman law) [11].

In most applications (but not in spacecraft applications), one is interested in the heat transfer between solid objects located in the normal atmosphere and sometimes in a fluid. Most solid objects in the normal atmosphere have organic and water contamination layers, which may influence the heat transfer for at least two reasons: (a) thin (nanometer) contamination layers may occur at the interface in the asperity contact regions, which will affect the acoustic impedance of the contact junctions, and hence the propagation of phonons between the solids (which usually is the origin of the heat transfer, at least for most non-metallic systems); (b) in addition, capillary bridges may form in the asperity contact regions and effectively increase the size of the contact regions and increase the heat transfer. In the normal atmosphere, heat

can also be transferred between the non-contact regions via heat diffusion or (at short separation) ballistic processes in the surrounding gas. For larger separations convective processes may also be important.

In the discussion above, we have assumed that the solids deform elastically and we have neglected the adhesional interaction between the solids. The contact mechanics theory of Persson can also be applied to cases where adhesion and plastic flow are important, and we will briefly study how this may affect the heat transfer. Most solids have modified surface properties, e.g., metals are usually covered by thin oxide layers with very different conductivities than the underlying bulk materials. However, as mentioned above, this may not have any major influence on the contact resistance.

Recently, intense research has focused on heat transfer through atomic or molecular-sized junctions [399, 400]. In light of the discussion presented above, this topic may also be important for the heat transfer between solids, because of the nanometer-sized nature of the contact regions between solids with random roughness.

13.2 Theory

13.2.1 Heat Transfer Coefficient

Consider two elastic solids (rectangular blocks) with randomly rough surfaces squeezed in contact as illustrated in Fig. 13.3. Assume that the temperature at the outer surfaces $z = -d_0$ and $z = d_1$ is kept fixed at T_0 and T_1, respectively, with $T_0 > T_1$. Close to the interface, the heat current will vary rapidly in space, $\mathbf{J} = \mathbf{J}(\mathbf{x}, z)$, where $\mathbf{x} = (x, y)$ denotes the lateral coordinate in the xy-plane. Far from the interface, we will assume that the heat current is constant and in the z-direction, i.e., $\mathbf{J} = J_0\hat{z}$. We denote the average distance between the macro asperity contact regions by λ (see [385]). We assume that $\lambda << L$, where L is the linear size of the apparent contact between the elastic blocks. The temperature a distance $\sim\lambda$ from the contacting inter-

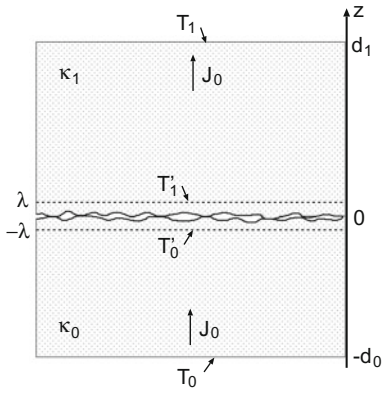

Fig. 13.3 Two elastic solids with nominally flat surfaces squeezed together with the nominal pressure p_0. The heat current $J_z(\mathbf{x})$ at the contacting interface varies strongly with the coordinate $\mathbf{x} = (x, y)$ in the xy-plane. The average heat current is denoted by $J_0 = \langle J_z(\mathbf{x})\rangle$

face will be approximately independent of the lateral coordinate $\mathbf{x} = (x, y)$ and we denote this temperature by T_0' and T_1' for $z = -\lambda$ and $z = \lambda$, respectively. The heat current for $|z| >> \lambda$ is independent of $\mathbf{x}$ and can be written as (to zero order in λ/d_0 and λ/d_1):

$$J_0 = -\kappa_0 \frac{T_0' - T_0}{d_0} = -\kappa_1 \frac{T_1 - T_1'}{d_1}, \tag{13.1}$$

where κ_0 and κ_1 are the heat conductivities of the two solid blocks. We assume that the heat transfer across the interface is proportional to $T_0' - T_1'$ and we define the heat transfer coefficient α so that

$$J_0 = \alpha(T_0' - T_1') \tag{13.2}$$

Combining (13.1) and (13.2) gives

$$J_0 = \frac{T_0 - T_1}{d_0\kappa_0^{-1} + d_1\kappa_1^{-1} + \alpha^{-1}} \tag{13.3}$$

This equation is valid as long as $\lambda << L$ and $\lambda << d_0,\ d_1$. Note that α depends on the macroscopic (or nominal) pressure, which acts at the interface. Thus, if the macroscopic pressure is non-uniform, as is the case in many practical applications, e.g., when a ball is squeezed against a flat, it is necessary to include the dependence of α on $\mathbf{x}$. Thus, in general

$$J(\mathbf{x}) = \alpha(\mathbf{x}) \left[T_0'(\mathbf{x}) - T_1'(\mathbf{x})\right] \tag{13.4}$$

It is expected that the contribution to α from the area of real contact would be proportional to the heat conductivity κ (for simplicity, we assume here two solids of the same material). Assuming only elastic deformation, contact mechanics theories show that for low enough squeezing pressure p_0, the area of real contact is proportional to p_0, and the size distribution of contact regions (and the interfacial stress probability distribution) are independent of p_0. Thus, it is expected that α is proportional to p_0. For randomly rough surfaces, the contact mechanics depends only on the (effective) elastic modulus E^* and on the surface roughness power spectrum $C(q)$. Thus, the only way to construct a quantity which is proportional to $p_0\kappa$ and with the same dimension as $J_0/\Delta T$, using the quantities that characterize the problem, is

$$\alpha \approx \frac{p_0\kappa}{E^* u_0}$$

where u_0 is a length parameter that is determined from the surface roughness power spectrum $C(q)$. For self-affine fractal surfaces, $C(q)$ depends only on the root-mean-square roughness $h_{\rm rms}$, the fractal dimension $D_{\rm f}$, which is dimensionless, and on the low and high cut-off wavevectors q_0 and q_1. Thus in this case $u_0 = h_{\rm rms} f(D_{\rm f}, q_0/q_1, q_0 h_{\rm rms})$. This result is consistent with the analysis presented in Sect. 13.2.3. Using the GW-theory results in an expression for α of the form given

above, but with a different function f, which now (even for low squeezing pressures) also depends on p_0/E^* (see, e.g., [401]).

13.2.2 Calculation of α

The heat current $\mathbf{J}$ and the heat energy density Q are assumed to be given by

$$\mathbf{J} = -\kappa \nabla T, \qquad Q = \rho C_V T$$

where κ is the heat conductivity, ρ the mass density and C_V the heat capacitivity. We consider a steady state condition where Q is time independent. Thus, the heat energy continuity equation

$$\nabla \cdot \mathbf{J} + \frac{\partial Q}{\partial t} = 0$$

reduces to

$$\nabla^2 T = 0$$

We assume that the surface roughness at the interface is so small that, when solving the heat flow equation, we can consider the surfaces as flat. However, the heat flow across the interface will be highly non-uniform and given by the heat current $J_z(\mathbf{x})$ (we assume $|\nabla h| << 1$, where $h(\mathbf{x})$ is the surface height profile). Let us first study the heat flow in the upper solid. We can take into account the heat flow from the lower solid by introducing a heat source at the interface $z = 0$ i.e.

$$\nabla^2 T = -2J_z(\mathbf{x})\delta(z)/\kappa_1 \tag{13.5}$$

Similarly, when studying the temperature in the lower solid, we introduce a heat sink on the surface $z = 0$ so that

$$\nabla^2 T = 2J_z(\mathbf{x})\delta(z)/\kappa_0 \tag{13.6}$$

Let us first study the temperature for $z > 0$. We write

$$J_z(\mathbf{x}) = \int d^2q \; J_z(\mathbf{q}) e^{i\mathbf{q}\cdot\mathbf{x}}, \tag{13.7}$$

$$J_z(\mathbf{q}) = \frac{1}{(2\pi)^2} \int d^2x \; J_z(\mathbf{x}) e^{-i\mathbf{q}\cdot\mathbf{x}}, \tag{13.8}$$

where $\mathbf{q} = (q_x, q_y)$ is a 2D wavevector. From (13.5), we get

$$T(\mathbf{x}, z) = T_1 - \frac{1}{\kappa_1} J_0(z - d_1) - \frac{1}{\pi\kappa_1} \int d^2q dk \frac{\Delta J_z(\mathbf{q})}{-q^2 - k^2} e^{i(\mathbf{q}\cdot\mathbf{x} + kz)}, \tag{13.9}$$

where k is the z-component of the wavevector. In (13.9), $J_0 = \langle J_z(\mathbf{x}) \rangle$ is the average heat current and

$$\Delta J_z(\mathbf{x}) = J_z(\mathbf{x}) - J_0 \tag{13.10}$$

Performing the k-integral in (13.9) gives

$$T(\mathbf{x}, z) = T_1 - \frac{1}{\kappa_1} J_0 (z - d_1) + \frac{1}{\kappa_1} \int d^2q \, \frac{1}{q} \Delta J_z(\mathbf{q}) e^{i\mathbf{q}\cdot\mathbf{x} - qz} \tag{13.11}$$

Similarly, temperature field for $z < 0$ can be obtained with:

$$T(\mathbf{x}, z) = T_0 - \frac{1}{\kappa_0} J_0 (z + d_0) - \frac{1}{\kappa_0} \int d^2q \, \frac{1}{q} \Delta J_z(\mathbf{q}) e^{i\mathbf{q}\cdot\mathbf{x} + qz} \tag{13.12}$$

Let us define

$$\phi(\mathbf{x}) = T(\mathbf{x}, -0) - T(\mathbf{x}, +0)$$

Using (13.11) and (13.12) we get

$$\phi(\mathbf{x}) = T_0 - T_1 - \left(\frac{d_0}{\kappa_0} + \frac{d_1}{\kappa_1} \right) J_0 - \frac{1}{\kappa} \int d^2q \, \frac{1}{q} \Delta J_z(\mathbf{q}) e^{i\mathbf{q}\cdot\mathbf{x}} \tag{13.13}$$

where

$$\frac{1}{\kappa} = \frac{1}{\kappa_0} + \frac{1}{\kappa_1} \tag{13.14}$$

From (13.13) we get

$$\phi(\mathbf{q}) = M \delta(\mathbf{q}) - \frac{1}{\kappa q} \Delta J_z(\mathbf{q}) \tag{13.15}$$

where

$$M = T_0 - T_1 - \left(\frac{d_0}{\kappa_0} + \frac{d_1}{\kappa_1} \right) J_0 \tag{13.16}$$

We will now consider two different cases:

13.2.3 Heat Flow Through the Area of Real Contact

Let us consider the heat flow through the area of real contact between two blocks squeezed together with the nominal pressure p_0. Since the average separation $\bar{u}$ between the surfaces at the interface decreases monotonically with increasing squeezing pressure p_0 we can consider p_0 as a function of $\bar{u}$. An exact and remarkable simple relationship exists between the heat flow coefficient α and the interfacial normal stiffness $dp_0/d\bar{u}$ of the contact.

In the contact region, $J_z(\mathbf{x})$ will be non-zero but $T(\mathbf{x}, +0) - T(\mathbf{x}, -0)$ will vanish. On the other surface area, $J_z(\mathbf{x})$ will vanish. Using these boundary conditions, and (13.15) in Appendix Q1 we show that

$$\alpha \approx -\frac{2\kappa}{E^*}\frac{dp_0}{d\bar{u}}. \tag{13.17}$$

where E^* is the effective elastic modulus

$$\frac{1}{E^*} = \frac{1-\nu_0^2}{E_0} + \frac{1-\nu_1^2}{E_1},$$

where E_0 and ν_0 are the Young's elastic modulus and the Poisson ratio, respectively, for solid **0** and similar for solid **1**. Equation (13.17) is, in fact, exact (see Appendix Q1 and [395]), which shows that the heat transfer is mainly determined by the geometrical distribution of the contact area (given by the region where $\sigma_z(\mathbf{x})$ is non-vanishing), and by the thermal interaction between the heat flow through the various contact spots (see Appendix Q1). Note that, for a small load the squeezing pressure p_0 depends on the (average) interfacial separation $\bar{u}$ via the exponential law [383] $p_0 \sim \exp(-\bar{u}/u_0)$. Thus, the vertical stiffness $dp_0/d\bar{u} = -p_0/u_0$ so we can also write

$$\alpha \approx \frac{p_0 2\kappa}{E^* u_0}. \tag{13.18}$$

The length parameter u_0 in (13.18) can be calculated (approximately) from the surface roughness power spectrum $C(q)$ using [384]

$$u_0 = \sqrt{\pi}\int_{q_0}^{q_1} dq\; q^2 C(q) w(q)$$

where

$$w(q) = \left(\pi\int_{q_0}^{q} dq' q'^3 C(q')\right)^{-1/2}$$

where q_0 is the long-distance cut-off (or roll-off) wavevector and q_1 the wavevector of the shortest wavelength roughness included in the analysis. Assume that the combined surface roughness is selfaffine fractal for $q_0 < q < q_1$. In this case,

$$C(q) = \frac{H}{\pi}\left(\frac{h_{\rm rms}}{q_0}\right)^2 \left(\frac{q_0}{q}\right)^{2(H+1)}$$

where H is the Hurst exponent related to the fractal dimension via $D_{\rm f} = 3 - H$. Substituting this $C(q)$ into the equations above gives

$$u_0 \approx \left(\frac{2(1-H)}{\pi H}\right)^{1/2} h_{\rm rms}\left[r(H) - \left(\frac{q_0}{q_1}\right)^H\right].$$

where

$$r(H) = \frac{H}{2(1-H)} \int_1^\infty dx \ (x-1)^{-1/2} x^{-1/[2(1-H)]}$$

Note that $r(H)$ is of order unity (see [383]). As discussed in the introduction, this implies that the contact resistance in general is determined accurately by one or two decades of the longest-wavelength roughness components, and that in general there is no relationship between the area of real contact (which is observed at the highest magnification, and which determines, the friction force in most cases, among other things), and the contact resistance between the solids.

Note that from (13.3) it follows that one can neglect the heat contact resistance if

$$\kappa/d << \alpha$$

where κ/d is the smallest of κ_0/d_0 and κ_1/d_1. Using (13.18), this gives

$$d >> u_0(E^*/p_0)$$

We note that in modern high-tech applications the linear size (or thickness) d of the physical system may be very small, and in these cases the heat contact resistance may be particular important.

If roughness occurs only on one length scale, say with wavelength λ and height h, then the pressure necessary for complete contact will be of order

$$p_0 \approx E^* h/\lambda$$

Substituting this in (13.18) gives

$$\alpha \approx \kappa/\lambda \tag{13.19}$$

where we have used that $u_0 \approx h$. Thus, $\alpha^{-1} \approx \lambda\kappa^{-1}$ which is the expected result because the denominator in (13.3) is only accurate to zero order in $\lambda\kappa^{-1}$. (Alternatively, substituting (13.19) in (13.3) gives a term of the type $(d+\lambda)\kappa^{-1}$ which is the correct result since d in (13.3) should really be $d-\lambda$.)

As an example [402], consider two nominal flat steel plates (in vacuum) with the thickness $d_0 = d_1 = 0.5\,\text{cm}$ and with the root-mean-square roughness $\sim 1\,\mu\text{m}$. The plates are squeezed together with the nominal pressure $p_0 = 0.1\,\text{MPa}$. The ratio between the measured surface and bulk thermal contact resistance is approximatey 150. Using (13.3) we get

$$\Delta T/J_0 = 2d_0\kappa_0^{-1} + \alpha^{-1}.$$

Thus, the (theoretical) ratio between the surface and the bulk contributions to the thermal resistance is:

$$\frac{\kappa_0}{2\alpha d_0},$$

where κ_0 is the heat conductivity of the bulk steel. Using (13.18) with $\kappa = \kappa_0/2$ this gives

$$\frac{\kappa_0}{2\alpha d_0} = \frac{u_0}{d_0}\frac{E^*}{p_0} \tag{13.20}$$

With (from theory) $u_0 \approx 1\,\mu$m, and $E^* \approx 110\,$GPa, $p_0 = 0.1\,$MPa and $2d_0 = 1\,$cm, from (13.20) the ratio between the thermal surface and bulk resistance is ≈200, in good agreement with the experimental data.

The discussion above assumes purely elastic deformations. However, plastic flow is likely to occur in the present application at sufficiently short length-scales, observed at high magnification. Since the heat flow is determined mainly by the long-wavelength roughness components, i.e., by the roughness observed at relative low magnification, when calculating the heat transfer, one may often assume that the surfaces deform purely elastically, even if plastic deformation is observed at high magnification, see Sect. 13.5.

13.2.4 Heat Flow Through the Non-contact Area

Let us now assume that

$$J_z(\mathbf{x}) = \beta(\mathbf{x})\big[T(\mathbf{x}, -0) - T(\mathbf{x}, +0)\big] = \beta(\mathbf{x})\phi(\mathbf{x})$$

From (13.15) we get

$$\phi(\mathbf{q}) = M\delta(\mathbf{q}) - \frac{1}{\kappa q}\int d^2q'\,\beta(\mathbf{q}-\mathbf{q}')\left[1 - \frac{(2\pi)^2}{A_0}\delta(\mathbf{q})\right]\phi(\mathbf{q}') \tag{13.21}$$

Next, note that

$$J_0 = \frac{1}{A_0}\int d^2x\; J_z(\mathbf{x}) = \frac{1}{A_0}\int d^2x\;\beta(\mathbf{x})\phi(\mathbf{x}) = \frac{(2\pi)^2}{A_0}\int d^2q\;\beta(-\mathbf{q})\phi(\mathbf{q}) \tag{13.22}$$

Equation (13.21) can be solved by iteration. The zero-order solution

$$\phi(\mathbf{q}) = M\delta(\mathbf{q})$$

Substituting this in (13.22) gives

$$J_0 = M\frac{(2\pi)^2}{A_0}\beta(\mathbf{q}=\mathbf{0}) = M\bar{\beta} \tag{13.23}$$

where

$$\bar{\beta} = \langle\beta(\mathbf{x})\rangle = \frac{1}{A_0}\int d^2x\;\beta(\mathbf{x})$$

is the average of $\beta(\mathbf{x})$ over the whole interfacial area A_0. Substituting (13.16) in (13.23) and solving for J_0 gives an equation of the form (13.3) with $\alpha = \bar{\beta}$.

The first-order solution to (13.21) is

$$\phi(\mathbf{q}) = M\delta(\mathbf{q}) - \frac{M}{\kappa q}\beta(\mathbf{q})\left[1 - \frac{(2\pi)^2}{A_0}\delta(\mathbf{q})\right] \tag{13.24}$$

Substituting (13.24) in (13.22) gives again an equation of the form (13.3) with

$$\alpha = \bar{\beta} - \frac{(2\pi)^2}{\kappa A_0}\int d^2q \frac{1}{q}\left\langle|\beta(\mathbf{q})|^2\right\rangle\left[1 - \frac{(2\pi)^2}{A_0}\delta(\mathbf{q})\right], \tag{13.25}$$

where we have added $\langle..\rangle$ which denotes ensemble average, and where we used that

$$\left\langle\beta(\mathbf{q})\beta(-\mathbf{q})\right\rangle = \left\langle|\beta(\mathbf{q})|^2\right\rangle$$

We can rewrite (13.25) as follows. Let us define the correlation function

$$C_\beta(\mathbf{q}) = \frac{1}{(2\pi)^2}\int d^2x \left\langle\beta(\mathbf{x})\beta(\mathbf{0})\right\rangle e^{i\mathbf{q}\cdot\mathbf{x}} \tag{13.26}$$

Note that

$$C_\beta(\mathbf{q}) = \frac{(2\pi)^2}{A_0}\left\langle|\beta(\mathbf{q})|^2\right\rangle \tag{13.27}$$

This equation follows from the fact that the statistical properties are assumed to be translational invariant in the $\mathbf{x}$-plane, and is proved as follows:

$$\begin{aligned} C_\beta(\mathbf{q}) &= \frac{1}{(2\pi)^2}\int d^2x\left\langle\beta(\mathbf{x})\beta(\mathbf{0})\right\rangle e^{i\mathbf{q}\cdot\mathbf{x}} \\ &= \frac{1}{(2\pi)^2}\int d^2x\left\langle\beta(\mathbf{x}+\mathbf{x}')\beta(\mathbf{x}')\right\rangle e^{i\mathbf{q}\cdot\mathbf{x}} \\ &= \frac{1}{(2\pi)^2}\int d^2x''\left\langle\beta(\mathbf{x}'')\beta(\mathbf{x}')\right\rangle e^{i\mathbf{q}\cdot(\mathbf{x}''-\mathbf{x}')} \end{aligned}$$

This equation must be independent of $\mathbf{x}'$ and we can therefore integrate over the $\mathbf{x}'$-plane and divide by the area A_0 giving

$$\begin{aligned} C_\beta(\mathbf{q}) &= \frac{1}{(2\pi)^2 A_0}\int d^2x' d^2x''\left\langle\beta(\mathbf{x}'')\beta(\mathbf{x}')\right\rangle e^{i\mathbf{q}\cdot(\mathbf{x}''-\mathbf{x}')} \\ &= \frac{(2\pi)^2}{A_0}\left\langle|\beta(\mathbf{q})|^2\right\rangle \end{aligned}$$

Let us define

$$\Delta\beta(\mathbf{x}) = \beta(\mathbf{x}) - \bar{\beta} \tag{13.28}$$

We get

$$\Delta\beta(\mathbf{q}) = \beta(\mathbf{q}) - \bar{\beta}\delta(\mathbf{q})$$

and thus

$$\left\langle |\Delta\beta(\mathbf{q})|^2 \right\rangle = \left\langle |\beta(\mathbf{q})|^2 \right\rangle \left[1 - \frac{(2\pi)^2}{A_0}\delta(\mathbf{q}) \right] \tag{13.29}$$

where we have used that

$$\bar{\beta}\delta(\mathbf{q}) = \frac{(2\pi)^2}{A_0}\beta(\mathbf{q})\delta(\mathbf{q})$$

and that

$$\delta(\mathbf{q})\delta(-\mathbf{q}) = \delta(\mathbf{q})\frac{1}{(2\pi)^2}\int d^2x\ e^{-i\mathbf{q}\cdot\mathbf{x}} = \delta(\mathbf{q})\frac{A_0}{(2\pi)^2}$$

Using (13.25) and (13.29) gives

$$\alpha = \bar{\beta} - \frac{1}{\kappa}\int d^2q q^{-1} C_{\Delta\beta}(\mathbf{q}) \tag{13.30}$$

Let us write

$$\left\langle \Delta\beta(\mathbf{x})\Delta\beta(\mathbf{0}) \right\rangle = \left\langle (\Delta\beta)^2 \right\rangle f(\mathbf{x}) \tag{13.31}$$

where $f(\mathbf{0}) = 1$. We write

$$f(\mathbf{x}) = \int d^2q\ f(\mathbf{q}) e^{i\mathbf{q}\cdot\mathbf{x}}$$

so that $f(\mathbf{x} = \mathbf{0}) = 1$ gives

$$\int d^2q\ f(\mathbf{q}) = 1 \tag{13.32}$$

Using (13.31) and (13.32), (13.30) takes the form

$$\alpha = \bar{\beta} - \left\langle (\Delta\beta)^2 \right\rangle \kappa^{-1} l \tag{13.33}$$

where the *correlation length*

$$l = \frac{\int d^2q\ q^{-1} f(\mathbf{q})}{\int d^2q\ f(\mathbf{q})}$$

For randomly rough surfaces with isotropic statistical properties, $f(\mathbf{q})$ depends only on $q = |\mathbf{q}|$ so that

$$l = \frac{\int_0^\infty dq\ f(q)}{\int_0^\infty dq\ qf(q)}$$

Most surfaces of engineering interest are fractal-like, with the surface roughness power spectrum having a (long-distance) roll-off wavevector q_0. In this case, it can be shown from that $l \approx q_0^{-1}$. For the surface used in the numerical study presented below in Sect. 13.4 one have $q_0 \approx 10^7\ \mathrm{m}^{-1}$ (see Fig. 13.8). Furthermore, in this case (for amorphous silicon dioxide solids) $\kappa \approx 1\ \mathrm{W/mK}$ and if we assume that $\langle(\Delta\beta)^2\rangle$ is of order $\bar{\beta}^2$ we get the ratio between the second and the first term in (13.33) to be of order $\bar{\beta}/(q_0\kappa) \approx 0.01$, where we have used the fact that, typically (see Fig. 13.9), $\bar{\beta} \approx 0.1\ \mathrm{MW/m^2K}$. Thus, in the application presented in Sect. 13.4 the second term in the expansion (13.33) is negligible.

Equation (13.33) represents the first two terms in an infinite series which would result if (13.21) is iterated to infinite order. The result, (13.33), is only useful if the first term $\bar{\beta}$ is much larger that the second term. If this is not the case one would need to also include higher order terms (in principle, to infinite order), which becomes very hard to calculate using the iterative procedure. By comparing the magnitude between the two terms in (13.33), one can determine if it is legitimate to include only the lowest order term $\bar{\beta}$.

We now consider two applications of (13.33), namely the contribution to the heat transfer from (a) the electromagnetic field (in vacuum) and (b) from heat transfer via a gas (e.g., the normal atmosphere), which we assume is surrounding the two solids.

13.2.5 (a) Radiative Contribution to α (in Vacuum)

The heat flux per unit area between two black bodies separated by $d >> d_T = c\hbar/k_B T$ is given by the Stefan–Boltzmann law

$$J_0 = \frac{\pi^2 k_{\mathrm{B}}^4}{60\hbar^3 c^2}\left(T_0^4 - T_1^4\right)$$

where T_0 and T_1 are the temperatures of solids **1** and **2**, respectively, and c is the light velocity. In this limiting case, the heat transfer between the bodies is determined by the propagating electromagnetic waves radiated by the bodies and does not depend on the separation d between the bodies. Electromagnetic waves (or photons) always exist outside any body due to thermal or quantum fluctuations of the current density inside the body. The electromagnetic field created by the fluctuating current density also exists in the form of evanescent waves, which are damped exponentially with the distance away from the surface of the body. For an isolated body, the evanescent waves do not give a contribution to the energy radiation. However, for two solids separated by $d < d_T$, the heat transfer may increase by many orders of magnitude due to the evanescent electromagnetic waves—this is often referred to as photon tunneling.

For short separation between two solids with flat surfaces ($d << d_T$), the heat current due to the evanescent electromagnetic waves is given by (6.13) [11]

$$J_0 = \frac{4}{(2\pi)^3}\int_0^\infty d\omega \left(\Pi_0(\omega) - \Pi_1(\omega)\right)\int d^2q\, e^{-2qd}\frac{\mathrm{Im}R_0(\omega)\mathrm{Im}R_1(\omega)}{|1 - e^{-2qd}R_0(\omega)R_1(\omega)|^2} \tag{13.34}$$

where

$$\Pi(\omega) = \hbar\omega\left(e^{\hbar\omega/k_\mathrm{B}T} - 1\right)^{-1}$$

and

$$R(\omega) = \frac{\epsilon(\omega) - 1}{\epsilon(\omega) + 1}$$

where $\epsilon(\omega)$ is the dielectric function. From (13.34), it follows that the heat current scale as $1/d^2$ with the separation between the solid surfaces. The heat current is especially large in the case of resonant photon tunneling between surface modes localized on the two different surfaces. The resonant condition corresponds to the case when the denominator in the integrand of (13.34) is small. Close to the resonance we can use the approximation

$$R \approx \frac{\omega_1}{\omega - \omega_0 - i\gamma},$$

where ω_1 is a constant and ω_0 is determined by the equation $\mathrm{Re}[\epsilon(\omega_0) + 1] = 0$. In this case, the heat current is determined by [11]

$$J_0 \approx \mu\frac{\gamma}{d^2}\big[\Pi_0(\omega_0) - \Pi_1(\omega_0)\big],$$

where $\mu \approx [\log(2\omega_a/\gamma)]^2/(8\pi)$. If we write $T_1 = T_0 - \Delta T$ and assume $\Delta T/T_0 << 1$ we get $J_0 = \alpha\Delta T$ with

$$\alpha \approx \mu\frac{k_\mathrm{B}\gamma}{d^2}\frac{\eta^2\exp(\eta)}{\big[\exp(\eta) - 1\big]^2} \tag{13.35}$$

where $\eta = \hbar\omega_0/k_\mathrm{B}T_0$.

Resonant photon tunneling enhancement of the heat transfer is possible for two semiconductor or insulator surfaces, which can support low-frequency surface phonon–polariton modes in the mid-infrared frequency region. As an example, consider two clean surfaces of (amorphous) silicon dioxide (SiO_2). The optical properties of this material can be described using an oscillator model [358]

$$\epsilon(\omega) = \epsilon_\infty + \frac{a}{\omega_a^2 - \omega^2 - i\omega\gamma_a} + \frac{b}{\omega_b^2 - \omega^2 - i\omega\gamma_b}$$

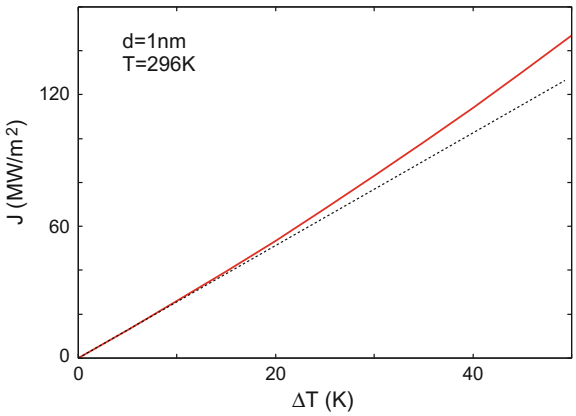

Fig. 13.4 *Solid line* calculated (using (13.34)) heat current per unit area, J_0, between two (amorphous) silicon dioxide bodies, as a function of the temperature difference ΔT. The solids have flat surfaces separated by $d = 1$ nm. One solid is at the temperature $T = 296$ K and the other at $T + \Delta T$. *Dashed line* linear function with the slope given by the initial slope (at $\Delta T = 0$) of the *solid line*

The frequency-dependent term in this expression is due to optical phonons. The values for the parameters ϵ_∞, (a, ω_a, γ_a) and (b, ω_b, γ_b) are given in [358], In Fig. 13.4, we show the calculated heat current per unit area, J_0, as a function of the temperature difference ΔT. The solids have flat surfaces separated by $d = 1$ nm. One solid is at the temperature $T = 296$ K and the other at $T + \Delta T$. When $\Delta T << T$, the heat transfer depends (nearly) linearly on the temperature difference ΔT (see Fig. 13.4), and we can define the heat transfer coefficient $\alpha = J_0/\Delta T$. In the present case (for $d = d_0 = 1$ nm), $\alpha = \alpha_0 \approx 2 \times 10^6$ W/m^{2}K. If the surfaces are not smooth but if roughness occurs so that the separation d varies with the coordinate $\mathbf{x} = (x, y)$, we have to first order in the expansion (13.33):

$$\alpha = \bar{\beta} = \alpha_0 \langle (d_0/d)^2 \rangle \tag{13.36}$$

where $\langle .. \rangle$ stands for ensemble average, or average over the whole surface area, and where α_0 is the heat transfer between flat surfaces separated by $d = d_0$.

In the present case, the heat transfer is associated with thermally excited optical (surface) phonons. That is, the electric field of a thermally excited optical phonon in one solid excites an optical phonon in the other solid, leading to energy transfer. The excitation transfer occurs in both directions, but if one solid is hotter than the other, there will be a net transfer of energy from the hotter to the colder solid. For metals, low-energy excited electron–hole pairs will also contribute to the energy transfer; however, for good metals, the screening of the fluctuating electric field by the conduction electrons leads to very ineffective heat transfer. However, if the metals are covered with metal oxide layers, and if the separation between the solids is smaller than the oxide layer thickness, the energy transfer may again be due mainly to the optical phonons of the oxide, and the magnitude of the heat current will be similar to what we calculated above for (amorphous) silicon dioxide.

Let us consider a high-tech application. Consider a MEMS device involving very smooth (amorphous) silicon dioxide slabs. Consider, for example, a very thin silicon

dioxide slab rotating on a silicon dioxide substrate. During operation, a large amount of frictional energy may be generated at the interface. Assume that the disk is pressed against the substrate with the nominal stress or pressure p_0. This does not need to be an external applied force but may be due to the long-ranged van der Waals attraction between the solids, or due to capillary bridges formed in the vicinity of the (asperity) contact regions between the solids. The heat transfer due to the area of real contact (assuming purely elastic deformation) can be calculated from (13.18). Let us make a very rough estimate: surfaces used in MEMS application typically have a roughness of the order of a few nanometers. Thus, $u_0 \sim 1\,\text{nm}$ and for (amorphous) silicon dioxide the heat conductivity $\kappa \approx 1\,\text{W/Km}$. Thus, from (13.18):

$$\alpha \approx (p_0/E) \times 10^9\,\text{W/m}^2\text{K} \tag{13.37}$$

In a typical case, the nominal pressure p_0 may be (due to the van der Waals interaction and capillary bridges) between 10^6–10^7 Pa and with $E \approx 10^{11}$ Pa we get from (13.37) $\alpha \approx 10^4$–$10^5\,\text{W/Km}^2$. If the root-mean-square roughness is of the order $\sim$1 nm we expect the average separation between the surfaces to be of the order a few nanometer so that $\langle (d_0/d)^2 \rangle \approx 0.1$ giving the non-contact contribution to α from the electromagnetic field of order (from (13.36)) $10^5\,\text{W/Km}^2$, i.e., larger than or of similar magnitude to the contribution from the area of real contact.

13.2.6 (b) Contribution to α from Heat Transfer via the Surrounding Gas or Liquid

Consider two solids with flat surfaces separated by a distance d. Assume that the solids are surrounded by a gas. Let Λ be the gas mean free path. If $d >> \Lambda$, the heat transfer between the solids occurs via heat diffusion in the gas. If $d << \Lambda$, the heat transfer occurs by ballistic propagation of gas molecules from one surface to the other. In this case, gas molecules reflected from the hotter surface will have (on the average) higher kinetic energy than the gas molecules reflected from the colder surface. This will result in heat transfer from the hotter to the colder surface. The heat current is approximately given by [403]:

$$J_0 \approx \frac{\kappa_{\text{gas}} \Delta T}{d + a\Lambda}$$

where a is a number of order unity and depends on the interaction between the gas molecules and the solid walls [375]. For air (and most other gases) at the normal atmospheric pressure and at room temperature, $\Lambda \approx 65\,\text{nm}$ and $\kappa_{\text{gas}} \approx 0.02\,\text{W/mK}$. For contacting surfaces with surface roughness, we get to first order in the expansion in (13.33):

$$\alpha \approx \kappa_{\text{gas}} \left\langle (d + \Lambda)^{-1} \right\rangle = \kappa_{\text{gas}} \int_0^\infty du P(u)(u + \Lambda)^{-1} \tag{13.38}$$

where $\langle..\rangle$ stands for ensemble average or averaging over the surface area, and where $P(u)$ is the probability distribution of interfacial separations. Equation (13.38) also holds if the surfaces are surrounded by a liquid rather than a gas. In this case, $\kappa_{\rm gas}$ must be replaced with the liquid heat conductivity $\kappa_{\rm liq}$ and in most cases one can put Λ equal to zero.

If we again consider a MEMS application where the average surface separation is of the order of nanometers, we can neglect the d-dependence in (13.38) and get $\alpha \approx \kappa_{\rm gas}/\Lambda \approx 3 \times 10^5\,{\rm W/m^2K}$, which is similar to the contribution from the electromagnetic coupling.

13.2.7 (c) Contribution to α from Heat Transfer via Capillary Bridges

If the solid walls are wetted by water, in a humid atmosphere, capillary bridges will form spontaneously at the interface in the vicinity of the asperity contact regions. For very smooth surfaces, such as in MEMS applications, the fluid (in this case water) may occupy a large region between the surfaces and will then dominate the heat transfer between the solids. Similarly, contamination layers (mainly organic molecules), which cover most natural surfaces may form capillary bridges between the contacting solids, and contribute in an important way to the heat transfer coefficient. The fraction of the interfacial surface area occupied by fluid bridges, and the separation between the solids in the fluid-covered region, can be calculated using the theory developed in [404]. From this, it is possible to calculate the contribution to the heat transfer using (13.38):

$$\alpha \approx \kappa_{\rm liq}\langle d^{-1}\rangle \approx \kappa_{\rm liq}\int_a^{d_{\rm K}} du\, P(u)u^{-1} \tag{13.39}$$

where $P(u)$ is the distribution of interfacial separation u. The lower cut-off a in the integral is a distance in the order of a molecular length and $d_{\rm K}$ is the maximum height of the liquid bridge, which, for a system in thermal equilibrium and for a wetting liquid, is in the order of the Kelvin length. Note that $P(u)$ is normalized and that

$$\int_a^{d_{\rm K}} du\, A_0 P(u) = \Delta A \tag{13.40}$$

is the surface area (projected on the xy-plane) where the surface separation is between $a < u < d_{\rm K}$. In (13.40), A_0 is the nominal contact area.

13.3 Contact Mechanics: Short Review and Basic Equations

The theory of heat transfer presented above depends on quantities that can be calculated using contact mechanics theories. Thus, the heat flux through the non-contact area (Sect. 13.2.4) depends on the average of some function $f[d(\mathbf{x})]$ of the interfacial separation $d(\mathbf{x})$. If $P(u)$ denotes the probability distribution of interfacial separation u then

$$\langle f(d)\rangle = \int_a^\infty du\ f(u)P(u) \tag{13.41}$$

where a is a short-distance cut-off (typically of molecular dimension). The contribution from the area of real contact depends on the elastic energy $U_{\rm el}$ stored in the asperity contact regions. In the limit of small contact pressure $U_{\rm el} = p_0 u_0$, where u_0 is a length that is of order the root-mean-square roughness of the combined roughness profile. All the quantities $P(u)$, $U_{\rm el}$ and u_0 can be calculated with good accuracy using the contact mechanics model of Persson. Here, we will briefly review this theory and give the basic equations relevant for heat transfer.

Consider the frictionless contact between two elastic solids with the Young's elastic modulus E_0 and E_1 and the Poisson ratios ν_0 and ν_1. Assume that the solid surfaces have the height profiles $h_0(\mathbf{x})$ and $h_1(\mathbf{x})$, respectively. The elastic contact mechanics for the solids is equivalent to those of a rigid substrate with the height profile $h(\mathbf{x}) = h_0(\mathbf{x}) + h_1(\mathbf{x})$ and a second elastic solid with a flat surface and with the Young's modulus E and the Poisson ratio ν chosen so that [405]

$$\frac{1-\nu^2}{E} = \frac{1-\nu_0^2}{E_0} + \frac{1-\nu_1^2}{E_1}. \tag{13.42}$$

The contact mechanics formalism developed elsewhere [382–385] is based on studying the interface between two contacting solids at different magnification ζ, see Fig. 13.5. When the system is studied at the magnification ζ it appears as if the contact area (projected on the xy-plane) equals $A(\zeta)$, but, when the magnification increases, it is observed that the contact is incomplete and the surfaces in the apparent contact area $A(\zeta)$ are in fact separated by the average distance $\bar{u}(\zeta)$, see Fig. 13.6. The (apparent) relative contact area $A(\zeta)/A_0$ at the magnification ζ is given by [382, 384]

$$\frac{A(\zeta)}{A_0} = \frac{1}{(\pi G)^{1/2}} \int_0^{p_0} d\sigma\ {\rm e}^{-\sigma^2/4G} = {\rm erf}\left(\frac{p_0}{2G^{1/2}}\right) \tag{13.43}$$

where

$$G(\zeta) = \frac{\pi}{4}\left(\frac{E}{1-\nu^2}\right)^2 \int_{q_0}^{\zeta q_0} dq q^3 C(q) \tag{13.44}$$

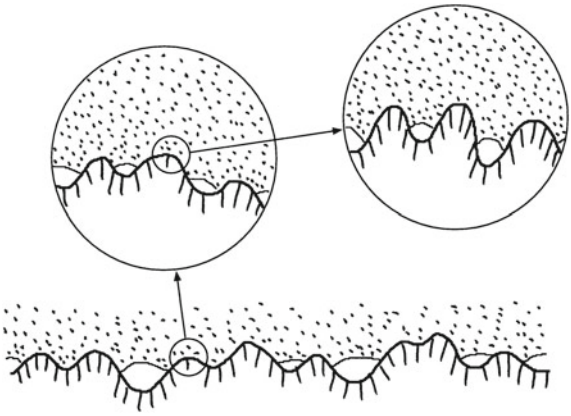

Fig. 13.5 An rubber block (*dotted area*) in adhesive contact with a hard rough substrate (*dashed area*). The substrate has roughness on many different length scales and the rubber makes partial contact with the substrate on all length scales. When a contact area is studied at low magnification it appears as if complete contact occur, but when the magnification is increased it is observed that, in reality, only partial contact occurs

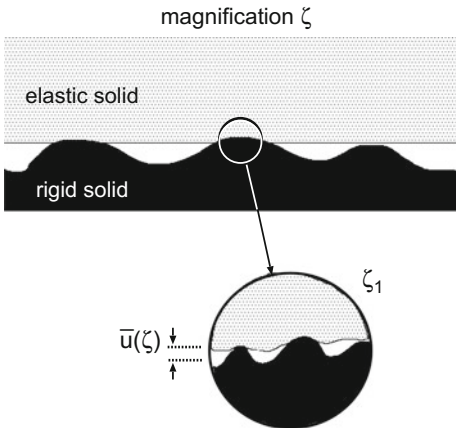

Fig. 13.6 An asperity contact region observed at the magnification ζ. It appears that complete contact occurs in the asperity contact region, but when the magnification increase to the highest (atomic scale) magnification ζ_1, it is observed that the solids are actually separated by the average distance $\bar{u}(\zeta)$

where the surface roughness power spectrum

$$C(q) = \frac{1}{(2\pi)^2} \int d^2x \langle h(\mathbf{x}) h(\mathbf{0}) \rangle e^{-i\mathbf{q}\cdot\mathbf{x}} \tag{13.45}$$

where $\langle ... \rangle$ stands for ensemble average. The height profile $h(\mathbf{x})$ of the rough surface can be measured routinely today on all relevant length scales using optical and stylus experiments.

We define $u_1(\zeta)$ to be the (average) height separating the surfaces that appear to come into contact when the magnification decreases from ζ to $\zeta - \Delta\zeta$, where $\Delta\zeta$ is a small (infinitesimal) change in the magnification. $u_1(\zeta)$ is a monotonically decreasing function of ζ, and can be calculated from the average interfacial separation $\bar{u}(\zeta)$ and $A(\zeta)$ using (see [384])

$$u_1(\zeta) = \bar{u}(\zeta) + \bar{u}'(\zeta) A(\zeta)/A'(\zeta), \tag{13.46}$$

where [384]

$$\bar{u}(\zeta) = \sqrt{\pi} \int_{\zeta q_0}^{q_1} dq\, q^2 C(q) w(q) \int_{p(\zeta)}^{\infty} dp'\, \frac{1}{p'} e^{-[w(q,\zeta)p'/E^*]^2}, \tag{13.47}$$

where $E^* = E/(1-\nu^2)$, and where $p(\zeta) = p_0 A_0/A(\zeta)$ and

$$w(q,\zeta) = \left(\pi \int_{\zeta q_0}^{q} dq'\, q'^3 C(q')\right)^{-1/2}.$$

The distribution of interfacial separations

$$P(u) = \left\langle \delta[u - u(\mathbf{x})] \right\rangle$$

where $u(\mathbf{x})$ is the separation between the surfaces at point $\mathbf{x}$. As shown in [384] we have (approximately)

$$P(u) = \int_1^{\infty} d\zeta \big[-A'(\zeta) \big] \delta\big[u - u_1(\zeta)\big] \tag{13.48}$$

Thus we can write (13.41) as

$$\left\langle f(d) \right\rangle = \int_1^{\zeta_1} d\zeta \big[-A'(\zeta) \big] f\big[u_1(\zeta)\big] \tag{13.49}$$

where ζ_1 is defined by $u_1(\zeta_1) = a$.

Finally, the elastic energy $U_{\rm el}$ (see Fig. 13.7) and the length parameter u_0 can be calculated as follows. The elastic energy $U_{\rm el}$ has been studied in [380]:

$$U_{\rm el} = A_0 E^* \frac{\pi}{2} \int_{q_0}^{q_1} dq\, q^2 W(q,p) C(q). \tag{13.50}$$

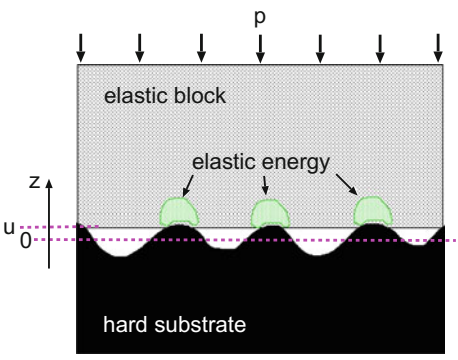

Fig. 13.7 An elastic block squeezed against a rigid rough substrate. The separation between the average plane of the substrate and the average plane of the lower surface of the block is denoted by u. Elastic energy is stored in the block in the vicinity of the asperity contact regions

In the simplest case, one take $W(q, p) = P(q, p) = A(\zeta)/A_0$ can be taken as the relative contact area when the interface is studied at the magnification $\zeta = q/q_0$, which depends on the applied pressure $p = p_0$. A more accurate expression is

$$W(q, p) = P(q, p)\left[\gamma + (1-\gamma)P^2(q, p)\right]. \tag{13.51}$$

However, in this case (13.47) must be modified appropriately (see [384]). For the parameter γ in (13.51) we have found that $\gamma \approx 0.5$ gives good agreement between the theory and numerical studies [386].

For small pressures, one can show that [384]:

$$p = \beta E^* e^{-\bar{u}/u_0}, \tag{13.52}$$

where

$$u_0 = \sqrt{\pi\gamma}\int_{q_0}^{q_1} dq\; q^2 C(q) w(q), \tag{13.53}$$

where $w(q) = w(q, 1)$, and where

$$\beta = \epsilon \exp\left[\frac{\int_{q_0}^{q_1} dq\; q^2 C(q) w(q) \log w(q)}{\int_{q_0}^{q_1} dq\; q^2 C(q) w(q)}\right], \tag{13.54}$$

where (for $\gamma = 1$) $\epsilon = 0.7493$.

13.4 Numerical Results

In this section, we present numerical results to illustrate the theory. We focus on an MEMS-like application. In Fig. 13.8, we show the surface roughness power spectrum $C(q)$ as a function of the wavevector q on a log-log scale (with 10 as a basis) for a typical surface used in MEMS applications, with the root mean square roughness 2.5 nm when measured over an area $10\,\mu\text{m} \times 10\,\mu\text{m}$. In Fig. 13.9, we show for this case the contribution to the heat transfer coefficient α from the direct contact area, and the non-contact contribution due to the fluctuating electromagnetic (EM) field and due to heat transfer via the surrounding gas. In the calculation of the EM-contribution, we have used (13.36) with $\alpha_0 = 2.0\,\text{MW/m}^2\text{K}$ (and $d_0 = 1\,\text{nm}$). For the contribution from the surrounding gas, we have used (13.38) with $\kappa_{\text{gas}} = 0.024\,\text{W/mK}$ and $\Lambda = 65\,\text{nm}$ (and $a = 1$). For the contact contribution, we used (13.18) with $\kappa = 1\,\text{W/mK}$. In all calculations, we have assumed $E^* = 86\,\text{GPa}$ and that the contact is elastic (no plastic yielding). The relative weak (squeezing) pressure-dependence of the contribution from the non-contact area is due to the fact that the (average) surface separation is smaller than the mean-free-path Λ of the gas

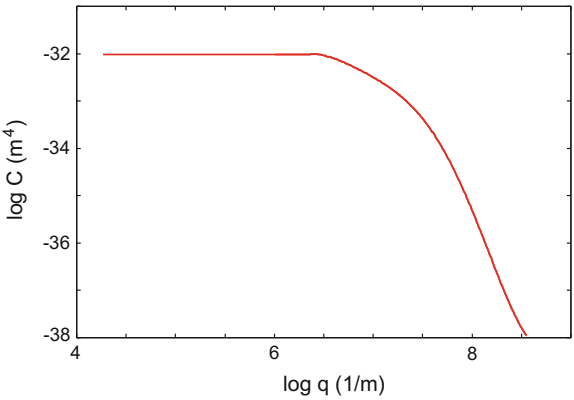

Fig. 13.8 Surface roughness power spectrum $C(q)$ as a function of the wavevector q on a log-log scale (with 10 as basis). (for a typical surface used in MEMS applications with the root mean square roughness 2.5 nm when measured over an area $10\,\mu\text{m} \times 10\,\mu\text{m}$)

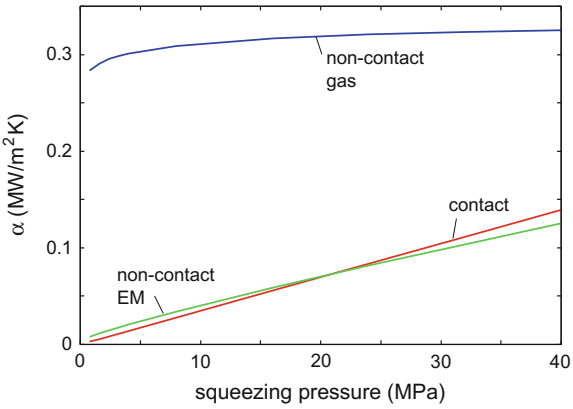

Fig. 13.9 The contribution to the heat transfer coefficient α from the direct contact area, and the non-contact contribution due to the fluctuating electromagnetic (EM) field and due to heat transfer via the surrounding gas. (for a randomly rough surface with the (combined) surface roughness power spectrum shown in Fig. 13.8)

molecules in the non-contact area. Thus, for squeezing pressures above $\sim$100 MPa the contact contribution will dominate the heat transfer.

We have also studied the contribution to the heat transfer from capillary bridges, which, on hydrophilic surfaces, form spontaneously in a humid atmosphere. The capillary bridges gives an attractive force (to be added to the external squeezing force), which pulls the solids closer together. We have used the theory presented in [404] to include the influence of capillary bridges on the contact mechanics, and to determine the fraction of the interface area filled with fluid at any given relative humidity. In Fig. 13.10, we show the logarithm (with 10 as the basis) of the contribution to the heat transfer coefficient α from the real contact areas, and from the water in the capillary bridges, as a function of the relative (water) humidity. For relative humidity below $\sim$0.4, the contribution to the heat transfer from capillary bridges decreases roughly linearly with decreasing humidity (and vanishes at zero humidity), and for relative humidity below $\sim$0.015, the heat transfer via the area of real contact will be more important than the contribution from the capillary bridges. However, the contribution from heat transfer via the air or vapor phase (not shown)

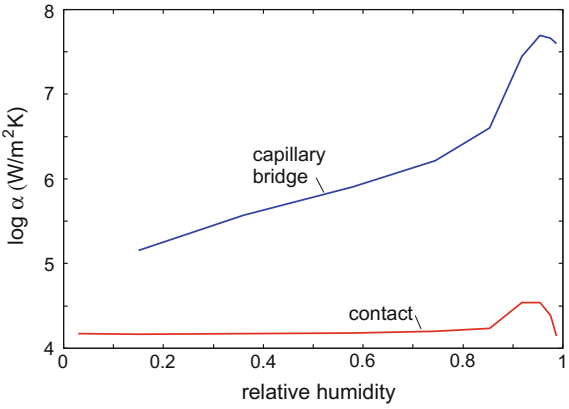

Fig. 13.10 The logarithm (with 10 as the basis) of the contribution to the heat transfer coefficient α from the real contact areas, and from the water in the capillary bridges, as a function of the relative (water) humidity. (for a randomly rough surface with the (combined) surface roughness power spectrum shown in Fig. 13.8. The squeezing pressure $p_0 = 4\,\text{MPa}$ and the effective solid elastic modulus $E^* = 86\,\text{GPa}$. The heat conductivity of water $\kappa_{\text{fluid}} = 0.58\,\text{W/mK}$)

is approximately $\sim 0.3\,\text{MW/m}^2\text{K}$ (see Fig. 13.9), and will hence give the dominant contribution to the heat transfer for relative humidity below 0.3. The small increase in the contribution from the area of real contact for relative humidity around ~ 0.94 is due to the increase in the contact area due to the force from the capillary bridges. For soft elastic solids (such as rubber), this effect is much more important: see [404] for a detailed discussion of this effect, which will also affect (increase) the heat transfer in a drastic way.

We note that heat transfer via capillary bridges has recently been observed in nanoscale point contact experiments [406] in which the authors investigated the heat transfer mechanisms at a $\sim 100\,\text{nm}$ diameter point contact between a sample and a probe tip of a scanning thermal microscope. They observed heat transfer both due to the surrounding (atmospheric) air as well as via capillary bridges.

13.5 Role of Adhesion and Plastic Deformation

In the theory above, we have assumed that the solids deform purely elastically. However, in many practical situations, the solids will deform plastically at sufficiently short length scales. Similarly, in many practical situations, in particular for elastically soft solids, the area of real contact may depend strongly on the adhesive interaction across the contacting interface. Here, we will briefly discuss under which circumstances this will affect the heat transfer between the solids.

The contribution to the heat transfer from the area of real contact between two solids depends on the elastic energy U_{el} stored in the asperity contact regions,

or, at applied loads that are sufficiently small, on the length parameter u_0. For most randomly rough surfaces, these quantities are determined mainly by the long-wavelength, large amplitude surface roughness components. Similarly, the interfacial separation, which determines the non-contact contribution to the heat transfer, depends mainly on the long-wavelength, large amplitude surface roughness components. On the other hand, plastic deformation and adhesion often manifests only at short length scales, corresponding to high magnification. For this reason, in many cases, one may assume purely elastic deformation when calculating the heat transfer, even if, at sufficiently short length scales, all asperities have yielded plastically, or the adhesion has strongly increased the (apparent) contact area. Let us illustrate this with the amorphous silicon dioxide system studied in Sect. 13.4.

In Fig. 13.11, we show the elastic and plastic contact area as a function of magnification on a log-log scale (with 10 as the basis). Also shown is the asperity-induced elastic energy $U_{\rm el}(\zeta)$ in units of the full elastic energy $U_{\rm el}(\zeta_1)$ obtained when all the roughness (with wavevectors below $q_1 = \zeta_1 q_0$) is included. Note that approximately 90% of the full elastic energy is already obtained at the magnification where the elastic and plastic contact areas are equal, and approximately 60% of the full elastic energy is obtained when $A_{\rm pl}/A_{\rm el} \approx 0.01$. Thus, in the present case, to a good approximation, we can neglect the plastic deformation when studying the heat transfer. In the calculation, we have assumed the penetration hardness $\sigma_{\rm Y} = 4\,{\rm GPa}$ and the squeezing pressure $p_0 = 4\,{\rm MPa}$. Thus, at high magnification, where all the contact regions are plastically deformed, the relative contact area $A/A_0 = p_0/\sigma_{\rm Y} = 0.001$ is in good agreement with the numerical data in Fig. 13.11.

If necessary, it is easy to include adhesion and plastic deformation when calculating the heat transfer coefficient α. Thus, (13.17) is also valid when adhesion is

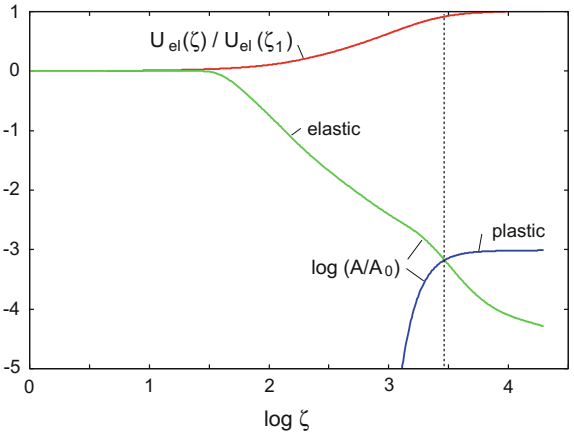

Fig. 13.11 The elastic $A_{\rm el}$ and plastic $A_{\rm pl}$ contact area as a function of magnification on a log-log scale (with 10 as basis). The penetration hardness $\sigma_{\rm Y} = 4\,{\rm GPa}$ and the applied pressure $p_0 = 4\,{\rm MPa}$. Also shown is the asperity-induced elastic energy $U_{\rm el}(\zeta)$ in units of the full elastic energy $U_{\rm el}(\zeta_1)$ obtained when all the roughness (with wavevectors below $q_1 = \zeta_1 q_0$) is included. The *vertical dashed line* indicates the magnification where $A_{\rm el} = A_{\rm pl}$

included, at least as long as adhesion is treated as a contact interaction. However, in this case, the interfacial stiffness $dp_0/d\bar{u}$ must be calculated including the adhesion (see [407]). Plastic deformation can be included in an approximate way as follows. If two solids are squeezed together at the pressure p_0, they will deform elastically and, at short length scales, plastically. If the contact is then removed, the surfaces will be sufficiently locally plastically deformed. Assume now that the surfaces are moved into contact again at exactly the same position as the original contact, and with the same squeezing pressure p_0 applied. In this case, the solids will deform purely elastically and the theory outlined in this section can be (approximately) applied, assuming that the surface roughness power spectrum $\bar{C}(q)$ of the (plastically) deformed surface is known. In [385], we have described an approximate way of how to obtain $\bar{C}(q)$ from $C(q)$ by defining (with $q = \zeta q_0$) [408]

$$\bar{C}(q) = \left[1 - \left(\frac{A_{\rm pl}(\zeta)}{A_{\rm pl}^0}\right)^6\right] C(q)$$

where $A_{\rm pl}^0 = F_{\rm N}/\sigma_{\rm Y}$. The basic picture behind this definition is that surface roughness at short length scales get smoothed out by plastic deformation, resulting in an effective cut-off of the power spectrum for large wavevectors (corresponding to short distances).

13.6 Application to Tires

Here, we will briefly discuss heat transfer in the context of tires. The rolling resistance $\mu_{\rm R}$ of a tire determines the heat production in a tire during driving on a strait planar road at a constant velocity v. In a stationary state the energy produced per unit time, $W = \mu_{\rm R} F_{\rm N} v$, must equal to the transfer of energy per unit time, from the tire to the surrounding atmosphere and to the road surface. Here, we will briefly discuss the relative importance of these two different contributions to the heat transfer.

Assume, for simplicity, that the frictional heat is produced uniformly in the tread rubber, and assume a tire without tread pattern. Let z be a coordinate axis perpendicular to the rubber surface. In this case, at stationary conditions, the temperature in the tread rubber satisfies $T''(z) = -\dot{q}/\kappa$ where $\dot{q}$ is the frictional heat produced per unit volume and unit time. We assume that the heat current vanishes at the inner rubber surface ($z = 0$, see Fig. 13.12), so that $T'(0) = 0$. Thus, we get $T(z) = T_0 - \dot{q} z^2/2\kappa$. The heat current at the outer rubber surface

$$J_0 = -\kappa T'(d) = \dot{q} d. \tag{13.55}$$

The temperature of the outer surface of the tread rubber

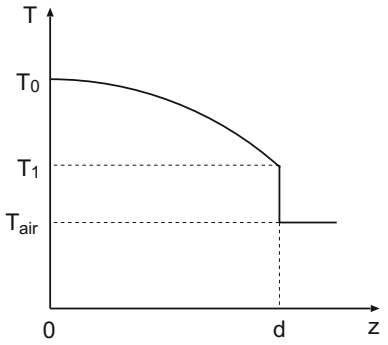

Fig. 13.12 Temperature distribution of rubber tread (thickness d) in contact with the air. The air temperature (for $z > d$) and the temperature at the outer ($z = d$) and inner ($z = 0$) rubber surfaces are denoted by T_{air}, T_1 and T_0, respectively

$$T_1 = T(d) = T_0 - \dot{q}d^2/2\kappa \tag{13.56}$$

Let us now assume that the heat transfer to the surrounding

$$J_0 = \alpha(T_1 - T_{\text{air}}) \tag{13.57}$$

Combining (13.55)–(13.57) gives

$$T_1 = T_0 - \frac{T_0 - T_{\text{air}}}{1 + 2\kappa/d\alpha} \tag{13.58}$$

For rubber $\kappa \approx 0.2\,\text{W/mK}$ and with $d = 1\,\text{cm}$ and $\alpha \approx 100\,\text{W/m}^2\text{K}$, as is typical for (forced) convective heat transfer between a tire and (dry) air (see Appendix Q2 and [409]), we get

$$T_1 \approx 0.3T_0 + 0.7T_{\text{air}}.$$

The temperature profile is shown (schematically) in Fig. 13.12. In reality, the heat production, even during pure rolling, will be somewhat larger close to the outer surface of the tread and the resulting temperature profile in the tread rubber will therefore be more uniform than indicated by the analysis above.

Let us now discuss the relative importance of the contributions to the heat transfer to the air and to the road. We assume that the heat transfer to the atmosphere and to the road are proportional to the temperature difference $T_1 - T_{\text{air}}$ and $T_1 - T_{\text{road}}$, respectively. We get

$$\mu_{\text{R}} F_{\text{N}} v = \alpha_{\text{air}} A_{\text{surf}}(T_1 - T_{\text{air}}) + \alpha_{\text{road}} A_0(T_1 - T_{\text{road}}) \tag{13.59}$$

where A_{surf} is the outer surface area of the tread, and A_0 the nominal tire-road footprint area. For rubber in contact with a road surface, κ in (13.18) is $\approx$0.2 W/mK and with $p_0/E^* \approx 0.04$ and $u_0 \approx 10^{-3}$ m (as calculated for a typical case) we get $\alpha_{\text{road}} \approx 10\,\text{W/m}^2\text{K}$, which is smaller than the contribution from the forced

convection. Since the nominal contact area between the tire and the road is much smaller than the total rubber tread area, we conclude that the contribution from the area of real contact between the road and the tire is rather unimportant. During fast acceleration, wear processes may occur, involving the transfer of hot rubber particles to the road surface, but such processes will not considered here. In addition, at the inlet of the tire-road footprint area, air may be compressed and then rapidly squeezed out from the tire-road contact area resulting in strong forced convective cooling of the rubber surface in the contact area. A similar process involving the inflow of air occurs at the exit of the tire-road footprint area. A detailed study of this complex process is necessary in order to accurately determine the heat transfer from a tire to the surrounding atmosphere and the road surface.

For a passenger car tire during driving on a strait planar road at a constant velocity v, the tire temperature that follows from (13.59) is in reasonably agreement with experiment. Thus, using (13.59) we get

$$\Delta T = T_1 - T_{\rm air} \approx \frac{\mu_{\rm R} F_{\rm N} v}{\alpha_{\rm air} A_{\rm surf}} \tag{13.60}$$

and with $\alpha_{\rm air} = 100\,{\rm W/m^2K}$, $A_{\rm surf} \approx 0.5\,{\rm m}^2$ and $\mu_{\rm R} \approx 0.02$, $F_{\rm N} = 3500\,{\rm N}$ and $v = 30\,{\rm m/s}$ we get $\Delta T \approx 40\,^\circ{\rm C}$.

The discussion above has focused on the stationary state where the heat energy produced in the tire per unit time is equal to the energy given off to the surrounding per unit time. However, for a rolling tire it may take a very long time to arrive at this stationary state. In the simplest picture, assuming a uniform temperature in the tire rubber, we get from energy conservation

$$\rho C_{\rm v} \frac{dT}{dt} = \dot{q} - \frac{\alpha}{d}(T - T_{\rm air})$$

or, if $T(0) = T_{\rm air}$,

$$T(t) = T_{\rm air} + \frac{\dot{q} d}{\alpha}\left(1 - e^{-t/\tau}\right),$$

where the relaxation time $\tau = \rho C_{\rm V} d/\alpha \approx 200\,{\rm s}$. In reality, the temperature in the tire is not uniform, and this will introduce another relaxation time τ', defined as the time it takes for heat to diffuse a distance d, which is of order $\tau' = \rho C_{\rm V} d^2/\kappa$. The ratio $\tau'/\tau = \alpha d/\kappa$. For rubber $\kappa \approx 0.2\,{\rm W/mK}$ and assuming $d = 1\,{\rm cm}$ and $\alpha = 100\,{\rm W/m^2K}$ gives $\tau'/\tau \approx 5$ or $\tau' \approx 10^3\,{\rm s}$. Experimental data have shown that it typically takes ~30 min to fully build up the tire temperature during rolling [409].

Rubber friction depends sensitively on the temperature of the rubber; in particular, the temperature close to the rubber surface in contact with the road. The temperature in the surface region of a tire varies rapidly in space and time, which must be considered when calculating the rubber friction [373]. The shortest time and length scales are related to the contact between the road asperities and the rubber surface in the tire-road footprint contact area. During a slip, this generates intense heating, which

varies over length scales from a few micrometers to several milometers, and over time scales shorter than the time a rubber patch stays in the footprint, which typically may be of the order a few milliseconds. During this short time, very little heat is transferred to the surrounding, and very little heat conduction has occured inside the rubber, i.e., the heat energy mainly stays where it is produced by the internal friction in the rubber. This results in a *flash temperature* effect, which has a crucial influence on rubber friction [373]. However, rubber friction also depends on the *background temperature* (usually denoted by T_0), which varies relatively slowly in space and time, e.g., on time scales from the time ($\sim$0.1 s) it takes for the tire to perform a few rotations, up to the time ($\sim$30 min) necessary to build up the full tire temperature after any change in the driving condition (e.g., from the start of driving). Note that the time variation of the background temperature T_0 depends on the surrounding (e.g., the air and road temperatures, humidity and rain) and on the driving history, while the flash temperature effect mainly depends on the slip history of a tread block (or rubber surface patch) in the footprint contact area, but not on the outside air or road temperature, or atmospheric condition.

13.7 Experimental Test of the Theory

We have performed a very simple experiment to test the theoretical predictions for the heat transfer. The setup consists of two containers (see Fig. 13.13), both filled with distilled water, standing on top of each other with a thin silicon rubber film in between. The upper container is made from copper (inner diameter 5 cm), and the water is heated to the boiling temperature (i.e., $T_0 = 100\,^{\circ}\mathrm{C}$). The lower container is made from PMMA with a cylindrical copper block at the top. To study the effect of surface roughness on the heat transfer, the copper block can be replaced by another copper block with different surface roughness. In the experiments presented below we used three copper blocks with different surface roughness.

The temperature $T_1(t)$ of the water in the lower container will increase with time t due to the heat current J_0 flowing from the upper container to the lower container:

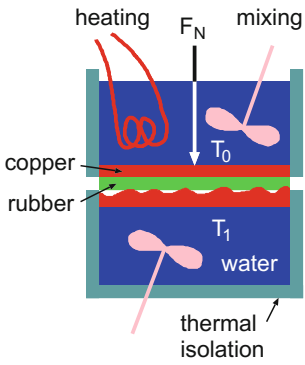

Fig. 13.13 Experiment to test the theoretical predictions for the heat transfer across interfaces. The increase in the temperature $T_1(t)$ of the water in the *lower* container, with increasing time t, determines the heat transfer between the *upper* and *lower* water container

$$J_0 = \rho C_V \dot{T}_1 d \tag{13.61}$$

where d is the height of the water column in the lower container (in our experiment $d = 3.5\,\text{cm}$), and where ρ and C_V are the water mass density and heat capacity, respectively. We measure the temperature of the water in the lower container as a function of time, starting at 25 °C. To obtain a uniform temperature of the water in the lower container we mix it using a (magnetic-driven) rotating metal bar.

We have investigated the heat transfer using copper blocks with different surface roughness. To prepare the rough surfaces, we have pressed annealed (plastically soft) copper blocks with smooth surface against sandpaper, using a hydraulic press. We repeated this procedure several times to obtain randomly rough surfaces. The roughness of the copper surfaces can be changed by differing the grade of the sandpaper used (consisting of particles with different average diameter). Due to the surface roughness, the contact between the top surface of the lower container and the thin silicon rubber sheet (thickness $d_0 = 2.5\,\text{mm}$) attached to the upper container, is only partial. The bottom surface of the upper container has been highly polished and we can neglect the heat resistance at this rubber–copper interface. Thus, most of the resistance to the heat flow arises from the heat diffusion through the rubber sheet, and from the resistance to the heat flow at the interface between the rubber and the rough copper block.

The rubber sheet (elastic modulus $E = 2.5\,\text{MPa}$, Poisson ratio $\nu = 0.5$) was made from a silicone elastomer (polydimethylsiloxane; PDMS). We have used PDMS because of its almost purely elastic behavior on the time scales involved in our experiments. The PDMS sample was prepared using a two-component kit (Sylgard 184) purchased from Dow Corning (Midland, MI). This kit consists of a base (vinyl-terminated PDMS) and a curing agent (methylhydrosiloxane-dimethylsiloxane copolymer) with a suitable catalyst. From these two components, we prepared a mixture of 10:1 (base/cross linker) in weight. The mixture was degassed to remove the trapped air induced by stirring from the mixing process and then poured into cylindrical casts (diameter 5 cm and height $d_0 = 2.5\,\text{mm}$). The bottom of these casts were made from glass in order to obtain smooth surfaces (negligible roughness). The samples were cured in an oven at 80 °C for over 12 h.

Using (13.3), we can write

$$J_0 \approx \frac{T_0 - T_1(t)}{d_0 \kappa_0^{-1} + \alpha^{-1}} \tag{13.62}$$

where κ_0 the heat conductivity of the rubber. Here, we have neglected the influence of the copper blocks on the heat transfer resistance, which is a good approximation because of the high thermal conductivity of copper. Combining (13.61) and (13.62) gives

$$\tau_0 \dot{T}_1 = T_0 - T_1(t)$$

where the relaxation time

$$\tau_0 = \rho C_V d \left(\frac{d_0}{\kappa_0} + \frac{1}{\alpha} \right).$$

If we assume that τ_0 is time independent, we get

$$T_1(t) = T_0 + \big[T_1(0) - T_0\big] e^{-t/\tau_0}. \tag{13.63}$$

In the study above, we have assumed that there is no heat transfer from the lower container to the surrounding. However, if necessary, one can easily take into account such a heat transfer: If we assume that the heat transfer depends linearly on the temperature difference between the water and the surrounding, we can write

$$J_1 = \alpha_1 \left(T_1 - T_{\text{surr}} \right)$$

In this case, it is easy to show that (13.63) is replaced with

$$T_1(t) = T_a + \big[T_1(0) - T_a\big] e^{-t/\tau}. \tag{13.64}$$

where T_a is the temperature in the water after a long time (stationary state where $J_0 = J_1$), and where the relaxation time τ now is given by

$$\tau = \rho C_V d \frac{T_a - T_{\text{surr}}}{T_0 - T_{\text{surr}}} \left(\frac{d_0}{\kappa_0} + \frac{1}{\alpha} \right).$$

The heat transfer across the rubber–copper interface can occur via the area of real contact, or via the non-contact area via heat diffusion in the thin air film or via radiative heat transfer. Since all these heat transfer processes act in parallel, we have

$$\alpha \approx \alpha_{\text{gas}} + \alpha_{\text{con}} + \alpha_{\text{rad}}.$$

Let us estimate the relative importance of these different contributions to α. Using the (diffusive) heat conductivity of air $\kappa_{\text{gas}} \approx 0.02\,\text{W/mK}$ and assuming $\langle d^{-1} \rangle = (20\,\mu\text{m})^{-1}$ gives

$$\alpha_{\text{gas}} = \kappa_{\text{gas}} \big\langle (d + \Lambda)^{-1} \big\rangle \approx \kappa_{\text{gas}} \big\langle d^{-1} \big\rangle \approx 1000\,\text{W/m}^2\text{K}.$$

Let us assume that $p_0 \approx 0.01\,\text{MPa}$, $E^* \approx 2\,\text{MPa}$, $u_0 \approx 10\,\mu\text{m}$ and (for rubber) $\kappa_0 = 0.2\,\text{W/mK}$. Thus

$$\alpha_{\text{con}} = \frac{p_0 \kappa_0}{E^* u_0} \approx 100\,\text{W/m}^2\text{K}.$$

Here we have used that $\kappa \approx \kappa_0$ (since the heat conductivity κ_1 of copper is much higher than that for the rubber). Finally, assuming that the radiative heat transfer is well approximated by the Stefan–Boltzmann law and assuming that $(T_0 - T_1)/T_1 << 1$, we get with $T_0 = 373\,\text{K}$

$$\alpha_{\rm rad} \approx \frac{\pi^2 k_{\rm B}^4}{60\hbar^3 c^2} 4T_0^3 \approx 10\,{\rm W/m^2K}$$

Note that $\alpha_{\rm rad}$ is independent of the squeezing pressure p_0, while $\alpha_{\rm con} \sim p_0$. The pressure dependence of $\alpha_{\rm gas}$ will be discussed below.

In the experiment reported on below, the silicon rubber film has the thickness $d_0 = 2.5\,{\rm mm}$ so that $d_0^{-1}\kappa_0 \approx 100\,{\rm W/m^2K}$. Thus

$$\frac{1}{d_0^{-1}\kappa_0} + \frac{1}{\alpha} \approx \left(\frac{1}{100} + \frac{1}{1000+100+10}\right)({\rm W/m^2K})^{-1}$$

and it is clear from this equation that, in the present case, the thin rubber film will give the dominant contribution to the heat resistance. This is in accordance with our experimental data presented below.

13.8 Experimental Results and Discussion

To test the theory, we have performed the experiment described in Sect. 13.7. We have performed experiments on four different (copper) substrate surfaces; namely, one highly polished surface (surface **0**) with the root-mean-square (rms) roughness of 64 nm, and three rough surfaces with rms roughness of 42, 88 and 114 μm. In Fig. 13.14, we show the surface roughness power spectrum of the three latter surfaces. Including only the roughness with wavelength above ∼30 μm, the rms slope of all three surfaces are of order unity, and the normalized surface area $A/A_0 \approx 1.5$ in all cases.

In Fig. 13.15, we show for the surfaces **1**, **2** and **3**, the pressure dependence of heat transfer coefficient from the contact area ($\alpha_{\rm con}$) and from the air-gap ($\alpha_{\rm gas}$). In calculating the results in Fig. 13.15, we have used (13.18) (with u_0 from (13.53))

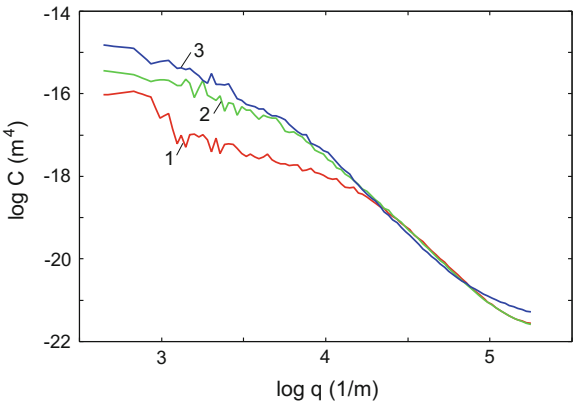

Fig. 13.14 The surface roughness power spectrum of the three copper surfaces used in the experiment. The surfaces **1**, **2** and **3** have a root-mean-square roughness of 42, 88 and 114 μm, respectively

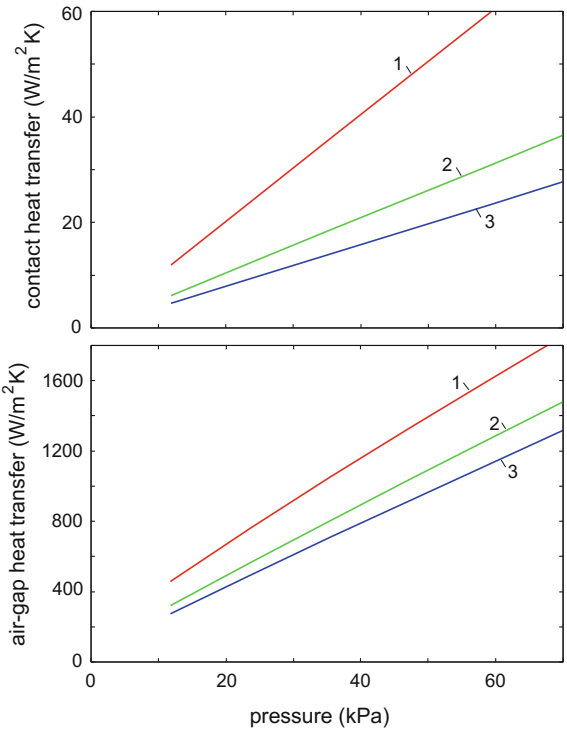

Fig. 13.15 The variation of the heat transfer coefficient from the contact area (α_{con}) and from the air-gap (α_{gas}) with the squeezing pressure. The surfaces **1**, **2** and **3** have the power spectra shown in Fig. 13.14

(top figure) and (13.38) (with $P(u)$ from (13.48)) (bottom figure). Note that both α_{con} and α_{gas} vary (nearly) linearly with p_0. The latter may at first appear remarkable because we know that at the low (nominal) squeezing pressures used in the present calculation (where the area of real contact varies linearly with p_0), the average surface separation $\bar{u} = \langle u \rangle$ depends logarithmically on p_0. However, the heat transfer via heat diffusion in the air gap depends on $\langle (u + \Lambda)^{-1} \rangle$, which depends on p_0 almost linearly as long as $\bar{u} >> \Lambda$, which is obeyed in our case. This can be understood as follows: $\langle u \rangle$ is determined mainly by the surface regions where the surface separation is close to its largest value. On the other hand $\langle (u + \Lambda)^{-1} \rangle$ is determined mainly by the surface regions where u is very small, i.e., narrow strips (which we will refer to as boundary strips) of surface area close to the area of real contact. Now, for small p_0, the area of real contact increases linearly with p_0 while the distribution of sizes of the contact regions is independent of p_0. It follows that the total area of the boundary strips will also increase linearly with p_0. Thus, since $\langle (u + \Lambda)^{-1} \rangle$ is determined mainly by this surface area, it follows that $\langle (u + \Lambda)^{-1} \rangle$ will be nearly proportional to p_0. We note that in Fig. 13.9, α_{gas} is nearly pressure independent, but this is due to the fact that the (combined) surface in this case is extremely smooth (rms roughness 2.5 nm) so that the u-term in $\langle (u + \Lambda)^{-1} \rangle$ can be neglected compared with the gas mean free path Λ, giving a nearly pressure-independent gas heat transfer coefficient.

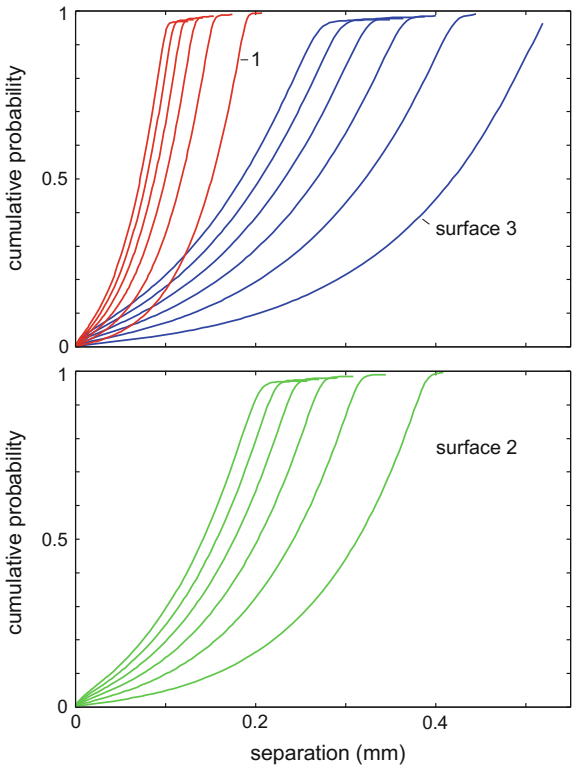

Fig. 13.16 The variation of the cumulative probability with the height (or gap-separation) u. The surfaces **1** and **3** (*top*) and **2** (*bottom*) have the power spectras shown in Fig. 13.14. For each surface, the curves are for the nominal squeezing pressures (from *right* to *left*): 11.8, 23.7, 35.5, 47.3, 59.2 and 71.0 kPa

However, in the system studied above, $\bar{u}$ is much larger than Λ and the result is nearly independent of Λ.

Note that in the present case (see Fig. 13.15), $\alpha_{\text{gas}} >> \alpha_{\text{con}}$ so that the present experiment mainly tests the theory for the heat flow in the air gap.

In Fig. 13.16, we show the variation of the cumulative probability with the height (or gap-separation) u for the surfaces **1** and **3** (top) and **2** (bottom).

In Fig. 13.17, we show the measured (dots) and calculated (using (70b)) (solid lines) temperatures in the lower container as a function of time. Results are for all four surfaces and for the nominal squeezing pressure $p_0 = 0.012$ MPa. The experiments were repeated 16 times and all the experimental data points are shown in the figure. In Fig. 13.18, we show the measured (dots) and calculated (solid lines) temperatures in the lower container as a function of time. Results are for surface **2** for the nominal squeezing pressure $p_0 = 0.012$ (lower curve) and 0.071 MPa (upper curve). Note that there is no fitting parameter in the theory calculations, and the agreement between theory and experiment is relatively good.

It would be interesting to repeat the experiment presented above under vacuum conditions. In this case, approximately half of the heat transfer resistance will arise from heat diffusion in the thin rubber film and half arises from the area of real

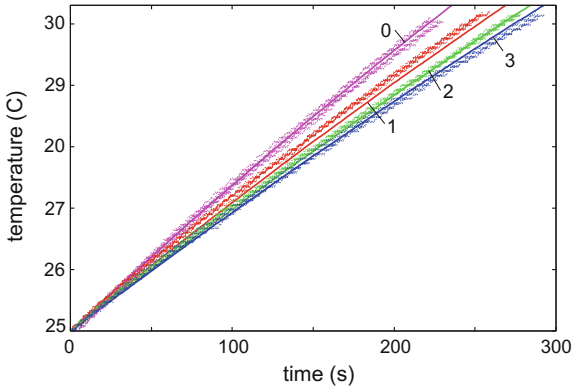

Fig. 13.17 The measured (*dots*) and calculated (*solid lines*) temperatures in the *lower* container as a function of time. Results are for all four surfaces and for the nominal squeezing pressure $p_0 = 0.012\,\text{MPa}$

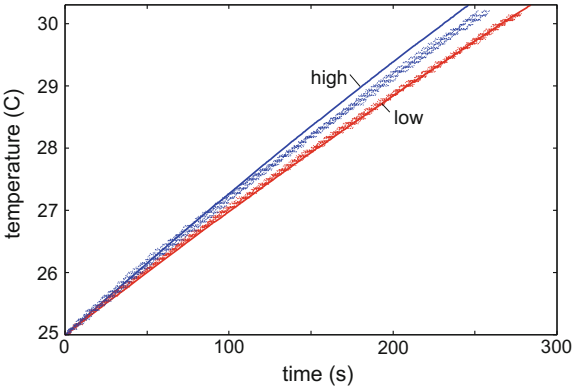

Fig. 13.18 The measured (*dots*) and calculated (*solid lines*) temperature in the *lower* container as a function of time. Results are for surface **2** for the nominal squeezing pressure $p_0 = 0.012$ (*lower curve*) and 0.071 MPa (*upper curve*)

contact, and it would be easy to accurately test the theory for the latter contribution. It would also be interesting to repeat the experiment using elastic materials with thermal conductivities much higher than that of silicon rubber.

The heat resistance of the system studied above is dominated by the thin rubber film. The reason for this is the low heat conductivity of rubber (approximately 100 times lower than for metals). For direct metal–metal contact the contact resistance will be much more important. However, for very rough surfaces it is likely that plastic flow is already observed at such low magnifications (corresponding to large length scales) such that it will affect the contact resistance. Nevertheless, it is interesting to compare the theory predictions for elastic contact with experimental data for metal–metal contacts.

In Fig. 13.19, we show the measured heat transfer coefficient for metal–metal contacts with steel, copper and aluminum [410]. The surfaces have the effective (or combined) rms surface roughness $h_{\text{rms}} = 7.2\,\mu\text{m}$ (steel), $2.2\,\mu\text{m}$ (Cu) and $5.0\,\mu\text{m}$ (Al). Assume that the variation of α with p_0 is mainly due to the area of real contact, i.e., we neglect the heat transfer via the thin air film between the surfaces. For the experiments involving rubber discussed above, the contribution to the heat transfer

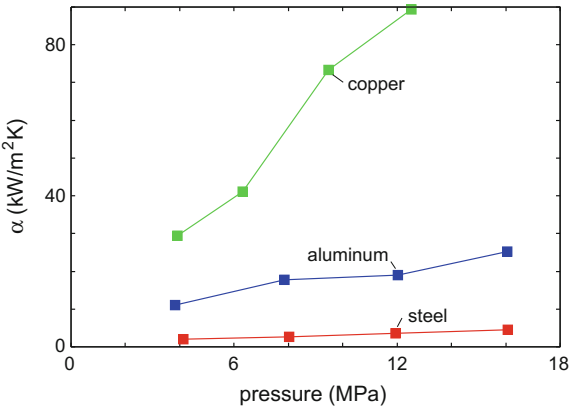

Fig. 13.19 Variation of the heat transfer coefficient α with the squeezing pressure p_0 for metal–metal contact with steel, copper and aluminum. The surfaces have the effective (or combined) root-mean-square surface roughness values $h_{\rm rms} = 7.2\,\mu$m (steel), $2.2\,\mu$m (copper) and $5.0\,\mu$m (aluminum). The heat conductivity of the metals are $\kappa = 54\,$W/mK (steel), 381 W/mK (copper) and 174 W/mK (aluminum). Based on experimental data from [410]

coefficient α from the area of real contact was smaller by a factor of $\sim$20 than the contribution from heat diffusion in the air gap, but because of the much higher thermal conductivity of metals (typically $\sim$100–1000 times higher) the contribution to α from the area of real contact (which is proportional to κ) will be much more important. Fitting the data points in Fig. 13.19 with straight lines gives the slope $d\alpha/dp_0$(exp) (in units of m/sK):

$$2 \times 10^{-4}\ \text{(steel)}, \quad 7 \times 10^{-3}\ \text{(Cu)}, \quad 1.2 \times 10^{-3}\ \text{(Al)}$$

Using (13.18) with $u_0 \approx 0.4 h_{\rm rms}$ (here we have assumed $\gamma = 0.4$) gives $d\alpha/dp_0$ (theory) $= \kappa/E^* u_0$:

$$1 \times 10^{-4}\ \text{(steel)}, \quad 4 \times 10^{-3}\ \text{(Cu)}, \quad 1.3 \times 10^{-3}\ \text{(Al)}$$

The agreement between theory and experiment is very good, taking into account that plastic deformation may have some influence on the result, and that an accurate analysis requires the full surface roughness power spectrum $C(q)$ (in order to calculate u_0 accurately, and in order to include plastic deformation if necessary, which was not reported on in [410]). We note that experimental results such as those presented in Fig. 13.19 are usually analyzed with a phenomenological model, which assumes plastic flow and neglects elastic deformation. In this theory, the heat transfer coefficient [411]

$$\alpha \approx \frac{\kappa s p_0}{h_{\rm rms}\sigma_{\rm Y}} \tag{13.65}$$

is proportional to the rms *surface slope*, s, but it is well known that this quantity is dominated by the very shortest wavelength roughness, which in fact makes the theory ill-defined. In [410], the data presented in Fig. 13.19 were analyzed using (13.65) with $s = 0.035$, 0.006 and 0.03 for the steel, Cu and Au surfaces, respectively. However, analysis of polished surfaces with a similar rms roughness to those used in the experiments usually gives slopes of order unity when all roughness, down to the nanometer, is included in the analysis [412]. Using $s \approx 1$ in (13.65) gives heat transfer coefficients approximately ∼100 times larger than observed in the experiments. (In our theory (13.18) s/σ_Y in (13.65) is replaced by $1/E^*$, and since, typically, $E^*/\sigma_Y \approx 100$, our theory is consistent with experimental observations.) [413]. We conclude that the theory behind (13.65) is incorrect or incomplete. A theory that includes both elastic and plastic deformation was described in Sect. 13.5.

13.9 Electric Contact Resistance

It is easy to show that the problem of the electrical contact resistance is mathematically equivalent to the problem of the thermal contact resistance. Thus, the electric current (per unit nominal contact area) J_0 through an interface between solids with randomly rough surfaces can be related to the electric potential drop $\Delta\phi$ at the interface via $J_0 = \alpha' \Delta\phi$ where, in analogy with (13.17),

$$\alpha' = \frac{2p_0\kappa'}{E^* u_0} \tag{13.66}$$

where κ' is the electrical conductivity. However, from a practical point of view the problem of the electrical contact resistance is more complex than for the heat contact resistance because of the great sensitivity of the electric conductivity on the type of material (see Appendix Q3). Thus, in a metal–metal contact, the contact resistance will depend sensitively on whether the thin insulating oxide layers, which cover most metals, are fractured, so that direct metal–metal contact can occur. On the other hand, in most cases there will be a negligible contribution to the electric conductivity from the non-contact regions.

13.10 Summary

We have studied the heat transfer between elastic solids with randomly rough but nominally flat surfaces squeezed in contact with the pressure p_0. Our approach is based on studying the heat flow and contact mechanics in wavevector space rather than real space, which has the advantage that we do not need to consider the very complex fractal-like shape of the contact regions in real space. We have included both the heat flow in the area of real contact as well as the heat flow across the

non-contact surface region. For the latter contribution, we have included the heat transfer both from the fluctuating electromagnetic field (which surrounds all material objects), and the heat flow via the surrounding gas or liquid. We have also studied the contribution to the heat transfer from capillary bridges, which form spontaneously in a humid atmosphere (e.g., as a result of organic and water contamination films which occur on most solid surfaces in the normal atmosphere). We have presented an illustrative application relevant for MEMS applications involving very smooth amorphous silicon dioxide surfaces. In this case, we find that all the mentioned heat transfer processes may be of approximately equal importance.

We have briefly discussed the role of plastic deformation and adhesion on the contact heat resistance. We have pointed out that even if plastic deformation and adhesion are important at short length scales (or high magnifications), they may have a negligible influence on the heat transfer since the elastic energy stored in the asperity contact regions, which mainly determines both the interfacial separation and the contact heat transfer coefficient, is usually mainly determined by the long–wavelength surface roughness components, at least for fractal-like surfaces with fractal dimension $D_f < 2.5$ (which is typically obeyed for natural surfaces and surfaces of engineering interest).

Chapter 14
Electrostatic Friction

We consider the effect of an external bias voltage and the spatial variation of the surface potential on the damping of cantilever vibrations. The electrostatic friction is due to energy losses in the sample created by the electromagnetic field from the oscillating charges induced on the surface of the tip by the bias voltage and spatial variation of the surface potential. A similar effect arises when the tip is oscillating in the electrostatic field created by charged defects in a dielectric substrate. The electrostatic friction can be compared with Casimir friction originating from the fluctuating electromagnetic field due to quantum and thermal fluctuation of the current density inside the bodies. We show that electrostatic and Casimir friction can be greatly enhanced if, on the surfaces of the sample and the tip, there are 2D systems; for example, a 2D electron system or on incommensurate layers of adsorbed ions exhibiting acoustic vibrations. We show that the damping of the cantilever vibrations due to the electrostatic friction may be of similar magnitude as the damping observed in experiments. We also show that, at short separation, the Casimir friction may be large enough to be measured experimentally. We consider the contribution from contact electrification to the work necessary to separate two solid bodies. The variations of the surface potential resulting from contact electrification give the contribution to the work necessary to separate two solid bodies. For silicon rubber (polydimethylsiloxane, PDMS), we discuss in detail the relative importance of the different contributions to the observed work of adhesion.

14.1 Effect of a Bias Voltage and the Spatial Variation of the Surface Potential

The electrostatic potential at the surface of a metal relative to its interior depends on the magnitude of the surface dipole moment per unit area, which, in turn, depends on the separation of the lattice planes that are parallel to the surface [317]. Variations of the crystallographic directions at the surface of a clean polycrystalline metal results

A.I. Volokitin and B.N.J. Persson, *Electromagnetic Fluctuations at the Nanoscale*,
NanoScience and Technology, DOI 10.1007/978-3-662-53474-8_14

in a variation of the surface potential. This is referred to as the 'patch effect'. Patch potentials are also generated and influenced by surface contamination and, in the case of alloys, by variation in the chemical composition. The surface potential can be easily changed by applying a voltage between an atomic force microscope tip and the sample. The electrostatic forces between conducting surfaces due to spatial variation of the surface potential were studied in [318].

Patch potential variation is specific to the particular sample and depends on environmental factors. Spatial variation of surface potential is expected to be related to the physical size of the surface crystallites, which, in the case of metal, is typically of the order of 1 μm. Thin films deposited on substrates at temperatures much lower than the melting point of the film are often amorphous, with non-uniform thickness and crystallite size of the same order as the thickness of the film [319]. Annealing of the film can produce grain structures that are substantially larger than the film thickness. The patch-potential variations have been measured under various conditions using vibrating or rotating plate electrometers [320]. Notably, it was shown that large-scale variations in surface potential were caused by adsorption of contaminants, which was transient and found to *reduce* the variation of surface potential of the clean surfaces [50, 52].

a. General theory We begin by considering a model in which the tip of a metallic cantilever of length L is a section of a cylindrical surface with the radius of curvature R (Fig. 14.1). The cantilever is perpendicular to a flat sample surface, which occupies the xy plane, with the z-axis pointing away from the sample. The tip displacement $\mathbf{u}(t) = \hat{x}u_0 e^{-i\omega t}$ is assumed to be parallel to the surface (along the x axis), which will be a good approximation when the oscillation amplitude u_0 is sufficiently small. The cantilever width w, i.e. the size in the direction perpendicular to the xz plane, is taken to be much larger than its thickness c ($w \gg c$), and d is the separation between the tip and the sample surface. It is straightforward to obtain the static electric field distribution when $d \ll R$. In this case, the electrostatic field of the entire cylinder is effectively the same as that due to its bottom part. The problem is then reduced to solving the 2D Laplace equation with the boundary conditions that the potential has the constant values V and 0 at the metallic surfaces of the tip and the sample, respectively. In this case, the electric field distribution outside the conductors is equal to the field due to two charged wires passing through points at $z = \pm d_1 = \pm\sqrt{(d+R)^2 - R^2}$ [191]. The wires have charges $\pm Q$ per unit length, $Q = CV$, where $C^{-1} = 2\ln[(d + R + d_1)/R]$. The electric potential at a point $\mathbf{r}$ exterior to the tip and the sample is given by

$$\begin{aligned}\varphi_0(\mathbf{r}) &= -2Q\left[\ln|\mathbf{r}-\mathbf{r}_+| - \ln|\mathbf{r}-\mathbf{r}_-|\right] = \\ &= Q\int_{-\infty}^{\infty}\frac{dq}{|q|}e^{iqx}\left[e^{-|q||z-z_+|} - e^{-|q||z-z_-|}\right], \end{aligned} \tag{14.1}$$

where $\mathbf{r}_\pm = \pm\hat{z}d_1$. The attractive cantilever-surface force can be calculated in a straightforward manner using (14.1) [169].

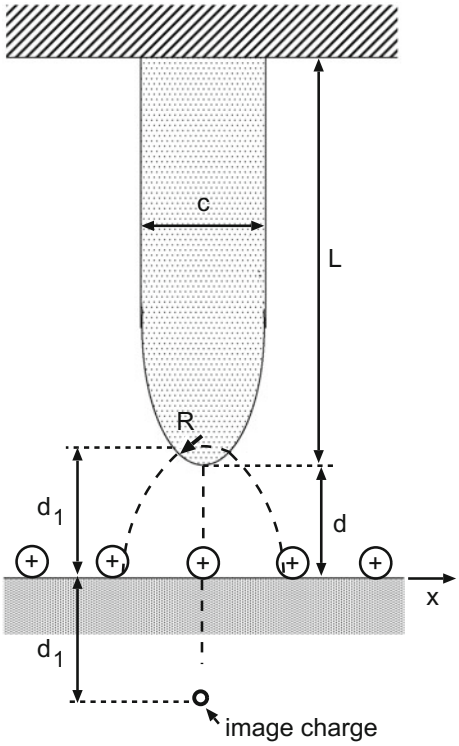

Fig. 14.1 Scheme of the tip–sample system. The tip shape is characterized by its length L and the cylindrical tip radius of curvature, R

A somewhat different picture applies in the case of an oscillating charged tip. The cantilever charge does not change when its tip moves parallel to the surface, while the sample charge varies in time at any fixed point. Thus, the electric field from the oscillating tip will be the same as from an oscillating wire located at $z = d_1$. The oscillating electric potential due to the tip, at a point $\mathbf{r}$ exterior to the tip and the sample is given by

$$\varphi_1(\mathbf{r}, t) = \varphi_1(\mathbf{r})\mathbf{e}^{-i\omega t} + c.c., \tag{14.2}$$

where

$$\varphi_1(\mathbf{r}) = i\,Qu_0 \int_{-\infty}^{\infty} \frac{dqq}{|q|} e^{iqx} \left[e^{-|q||z-z_+|} - e^{-|q||z-z_-|} R_p(q,\omega)\right], \tag{14.3}$$

and $R_p(q, \omega)$ is the reflection amplitude for the p polarized electromagnetic waves. The electric field is given by $\mathbf{E}(\mathbf{r}) = -\nabla\varphi(\mathbf{r})$. The energy dissipation per unit time induced by the electromagnetic field inside of the metallic substrate is determined by integrating the Poynting vector over the surface of the metal, and is given by

$$P = \frac{c}{4\pi}\int dS\hat{z}\cdot\left[\mathbf{E}(\mathbf{r})\times\mathbf{B}^*(\mathbf{r})\right]_{z=+0} + c.c. =$$
$$= -\frac{i\omega}{4\pi}\int dS\left(\varphi_1(\mathbf{r})\frac{d}{dz}\varphi_1^*(\mathbf{r})\right)_{z=+0} + c.c. =$$
$$= 4\omega Q^2|u_0|^2 w\int_0^\infty dqqe^{-2qd_1}\mathrm{Im}R_p(\omega,q). \tag{14.4}$$

Taking into account that the energy dissipation per unit time must be equal to $2\omega^2\Gamma\,|u_0|^2$, using (14.4) gives the friction coefficient:

$$\Gamma = \lim_{\omega\to 0} 2C^2V^2 w\int_0^\infty dqqe^{-2qd_1}\frac{\mathrm{Im}R_p(\omega,bq)}{\omega}. \tag{14.5}$$

An alternative derivation of (14.5) is given in Appendix R. Now, assume that the electric potential at the surface of the tip is inhomogeneous and consists of the domains or 'patches'. The cylinder with linear size w is 'divided' into cylinder segments with the linear size w_i: $w = \sum_i w_i \gg w_i \gg \sqrt{dR}$, and with the surface potential $V_{is} = V + V_i$, where V is the bias voltage and V_i is the randomly fluctuating surface potential for the domain i. In the case of a cylindrical tip geometry, all domains give independent contributions to the friction, which can be obtained from (14.5) after replacement $V \to V + V_i$ and $w \to w_i$. The contribution to friction from all domains is given by

$$\Gamma = \sum_i \Gamma_i = \sum_i \lim_{\omega\to 0} 2C^2(V+V_i)^2 w_i\int_0^\infty dqqe^{-2qd_1}\frac{\mathrm{Im}R_p(\omega,q)}{\omega} =$$
$$= \lim_{\omega\to 0} 2C^2\left(V^2+V_0^2\right)w\int_0^\infty dqqe^{-2qd_1}\frac{\mathrm{Im}R_p(\omega,vq)}{\omega}, \tag{14.6}$$

where we have used that the average value of the fluctuating surface potential $\langle V_i\rangle = \sum_i w_i V_i = 0$ and $V_0^2 = \sum_i w_i V_i^2/w$, so that V_0 is the root mean square variation of the surface potential. According to (14.6), bias voltage and patch contributions to the friction have the same dependence on d.

Many experiments use thermally evaporated thin films of gold [21]. The work function of gold is 5.47, 5.37, and 5.31 eV for the $\langle 100\rangle$, $\langle 110\rangle$, and $\langle 111\rangle$ direction, respectively [321]. If the surfaces are clean and amorphous then we can assume that they consist of equal areas of these three crystallographic planes, and the root-mean-square $\langle\sigma_v^2\rangle^{1/2}$ of the potential distribution becomes:

$$\left\langle\sigma_v^2\right\rangle^{1/2} = \sqrt{\left\langle(V_i-V_j)^2\right\rangle} = \sqrt{2\left(\left\langle V_i^2\right\rangle - \left\langle V_i\right\rangle^2\right)} \approx 90\mathrm{mV}. \tag{14.7}$$

When annealed, thin gold films form mesa structures with the $\langle 111\rangle$ crystallographic planes exposed. In this case, variations of the surface potential are presumably

generated by the material lying between the mesas. The size of the mesas depends on the temperature of the substrate during the formation of the film.

Sukenik et al. measured the root mean square variation of the surface potential due to thermally evaporated gold using the Stark effect in sodium atoms [322]. The films were partially optically transparent with a thickness of 42 nm and heated at 120 °C for several hours in vacuum. They deduced that the magnitude of the fluctuating surface potential is $V_0 = 150\,\text{mV}$, and showed that the scale of the lateral variation of the surface potential is of the order of the film thickness. The measurement of the non-contact friction between a gold tip and the gold sample gave $V_0 \sim 200\,\text{mV}$ [21], thus confirming the prediction of the theory that this parameter is determined by the root mean square variation of the surface potential.

Now, let us consider a spherical tip (radius R) with (constant voltage) surface domains with the linear size R_i. If $R \gg R_i \gg \sqrt{dR}$, the domain on the apex of the tip will give the main contribution to the friction. In this case, we can neglect the spatial variation of the surface potential and the electric field induced by the bias voltage is approximately the same as that which would be produced in the vacuum region between two point charges $\pm Q_i = \pm C(V + V_i)$ located at [170, 171]

$$z = \pm d_1 = \pm\sqrt{3Rd/2 + \sqrt{(3Rd/2)^2 + Rd^3 + d^4}}, \tag{14.8}$$

where

$$C = \frac{d_1^2 - d^2}{2d}. \tag{14.9}$$

It can be shown that the electrostatic force between the tip and the metal surface within this approximation agrees very well with the exact expression for a sphere above a metal surface [323]. The vibrations of the tip will produce an oscillating electromagnetic field, which, in the vacuum region, coincides with the electromagnetic field of an oscillating point charge. The friction coefficient for a point charge moving parallel to the surface due to the electromagnetic energy losses inside the sample is determined by [242] (see also Appendix R)

$$\Gamma_\parallel = \lim_{\omega\to 0} \frac{Q_i^2}{2} \int_0^\infty dq q^2 e^{-2qd_1} \frac{\text{Im} R_p(\omega, q)}{\omega}. \tag{14.10}$$

For motion normal to the surface, $\Gamma_\perp = 2\Gamma_\parallel$. Thus, just as for the cylindrical tip geometry, for a spherical tip, the friction depends quadratically on the bias voltage. However, for a spherical tip, the parabola begins from zero in contrast to the cylindrical tip where the parabola begins from a finite positive value.

b. Clean surfaces For clean flat surfaces, the reflection amplitude is determined by the Fresnel formula (O.2). In this case, for a cylindrical tip with radius $R \gg d$ and for a metal substrate, (14.6) gives:

$$\Gamma_{cl}^c = \frac{w\left(V^2 + V_0^2\right)}{2^6 \pi \sigma d^2}. \tag{14.11}$$

With $w = 7 \times 10^{-6}$ m and $\sigma = 4 \times 10^{17}\,\mathrm{s}^{-1}$ (which corresponds to gold at 300 K), and with $d = 20$ nm and $V = 1$ V, (14.11) gives $\Gamma = 2.4 \times 10^{-20}$ kg/s, which is eight orders of magnitude smaller than the experimental value 3×10^{-12} kg/s [21].

Assuming $R >> d$, using (14.10) and (O.2) gives the friction between a spherical tip and a clean sample surface

$$\Gamma_{cl}^{s} = \frac{3^{1/2} R^{1/2} V^2}{2^7 d^{3/2} \pi \sigma}. \tag{14.12}$$

This expression is only a factor of 1.6 smaller than the result obtained independently in [169]. For the same parameters as above and at $d = 20$ nm, the friction for a spherical tip is two orders of magnitude smaller than for the cylindrical tip. The friction determined by (14.12) has the same distance dependence as in the experiment [21]. However, the magnitude of the friction is too small to explain the experimental data.

To get insight into the possible mechanisms of the enhancement of non-contact friction, it is instructive to note that (14.11) can be obtained qualitatively from the following simple geometrical arguments [324]. The vibrating tip will induce a current in the sample in a volume with the spatial dimensions L_x, L_y and L_z. The instantaneous dissipated power in the sample is given by $P \sim I^2 r$, where I is the current and r is the effective resistance. The current I is proportional to the tip velocity v_x, and can be written as $I \sim v_x Q_t / L_x$, where Q_t is the charge of the tip. The effective resistance r can be approximated by the macroscopic relation $r = \rho L_x / L_y L_z$, where ρ is the resistivity. Using these simple expressions for the current I and the resistance, and using the relation $Q_t = C_t V_s$ (where C_t is the tip–sample capacitance) for the induced charge, the instantaneous power dissipation is

$$P \sim \rho \frac{v_x^2 C_t^2 V_s^2}{L_x L_y L_z}. \tag{14.13}$$

Comparing this expression with $P = \Gamma v_x^2$ we get

$$\Gamma \sim \rho \frac{C_t^2 V_s^2}{L_x L_y L_z}. \tag{14.14}$$

For cylindrical tip vibrating above the clean surface $L_y \sim w$ and $L_x \sim L_z \sim d_1$. For $d \ll R$ the tip–sample capacitance $C_t \sim w\sqrt{R/8d}$ and $d_1 \sim \sqrt{2dR}$. Substituting these expressions in (14.14) gives (14.11) to within a numerical factor of order of unity. From (14.14), it follows that the friction will increase when the thickness L_z of the 'dissipation volume' decreases. This is the reason that 2D systems may exhibit higher friction than 3D systems.

c. Film on top of a higher resistivity substrate From the qualitative arguments given above, it follows that, for a thin metal film on top of a higher resistivity substrate—for example. a dielectric or a high resistivity metal—the friction will be

larger, than for a semi-infinite sample with the same bulk resistivity as for the film. In this case, the main part of the dissipation occurs within the film, and according to (14.14) this will give rise to a strong enhancement of the friction.

For a planar film with thickness d_f and dielectric constant ϵ_2 on top of a substrate with dielectric constant ϵ_3, the reflection amplitude is determined by (7.103). For a metallic film on a dielectric substrate, or a metallic film on a metallic substrate with $\sigma_2 \gg \sigma_3$, for $d_1 \gg d_f$ and $R \gg d$, (14.6) and (7.103) give

$$\Gamma_f^c = \frac{w\left(V^2 + V_0^2\right) R^{1/2}}{2^{9/2}\pi\sigma_2 d_f d^{3/2}}. \tag{14.15}$$

This is greater, by a factor of $2\sqrt{2dR}/d_f$, than the corresponding friction for a semi-infinite sample with the clean surface with the same bulk conductivity as for the film. For a thin film, the effective resistivity of the substrate is increased, giving rise to additional ohmic dissipation. In [169], (14.15) was obtained using a different approach, and neglecting the spatial variation of the surface potential.

d. 2D system on top of a dielectric or metal substrate Let us now consider a 2D system such as an electronic surface states or a quantum well, or an incommensurate layer of ions adsorbed on a metal surface. For example, for the Cs/Cu(100) system, experimental data suggest the existence of an acoustic film mode even for the dilute phase (coverage $\theta \approx 0.1$). This implies that the Cs/Cu(100) adsorbate layer experiences a negligible surface pinning potential. The reflection amplitude for a 2D system is given by (7.110) and

$$\mathrm{Im}\, R_p \approx \frac{2\omega\eta q a \omega_q^2}{\left(\omega^2 - \omega_q^2\right)^2 + \omega^2\eta^2}, \tag{14.16}$$

where $\omega_q^2 = 4\pi n_a e^{*2} a q^2/M$. In the case of a 2D structure on top of a dielectric, the factor qa in (14.16) and in the expression for ω_q^2 must be replaced by $1/\epsilon$, where ϵ is the dielectric function of the substrate. Using (14.16) in (14.6) for $R \gg d$ we get

$$\Gamma_{ad}^c = \frac{w\eta M R^{1/2}\left(V^2 + V_0^2\right)}{2^{9/2} d^{3/2}\pi n_a e^{*2}}. \tag{14.17}$$

This friction exhibits the same distance dependence as observed experimentally [21]. The same expression for the friction is valid for a 2D structure on top of a dielectric. Comparing (14.11) and (14.17), we find that a 2D structure on top of a substrate gives the same magnitude of friction as for a semi-infinite solid (with a clean surface) with the effective conductivity $\sigma_{eff} = n_a e^{*2}/M\eta 2d_1$. Agreement with experiment [21] for $d = 20\,\mathrm{nm}$ is obtained if $\sigma_{eff} \approx 4 \times 10^9\ \mathrm{s}^{-1}$. In the case of a 2D electron system, for $R = 1\,\mu\mathrm{m}$, such an effective conductivity is obtained if $\eta_\parallel = 10^{14}\ \mathrm{s}^{-1}$ and $n_a = 10^{15}\ \mathrm{m}^{-2}$. For Cs/Cu(100) and for $n_a = 10^{18}\ \mathrm{m}^{-2}$ ($\theta \approx 0.1$), the electric charge of the Cs ions $e^* = 0.28e$ (see [200]). Due to the similarities of Cu and Au surfaces, a similar effective charge can be expected for the Cs/Au surface. For such a 2D system,

agreement with experimental data is obtained for $n_a = 10^{18}\,\mathrm{m}^{-2}$ and $\eta_\parallel = 10^{11}\,\mathrm{s}^{-1}$. In [170] we estimated the damping parameter associated with the covalent bond for Cs atom on Cu(100): $\eta_{\parallel cov} = 3 \times 10^9\,\mathrm{s}^{-1}$. However, the collisions between the ions, and between the ions and other surface defects, will also contribute to η. In this case, $\eta_{col} \sim v_T/l$ where $v_T \sim \sqrt{k_B T/M}$, and l is the ion mean free path. For $T = 293$ K and $l \sim 1$ nm, we get $\eta_{col} = 10^{11}\,\mathrm{s}^{-1}$.

For a spherical tip and a 2D system on top of the substrate, from (14.16) and (14.10) for $R \gg d$, we get the contribution to the friction from the 2D system

$$\Gamma^s_{ad} = \frac{3RM\eta V^2}{2^6 d\pi n_a e^{*2}}. \tag{14.18}$$

At $d = 20$ nm, this friction is $\sim$ two orders of magnitude smaller than for the cylindrical tip.

14.2 Friction Due to Spatial Fluctuations of Static Charge in the Bulk of the Sample

In this section, we consider a dielectric substrate with a stationary, inhomogeneous distribution of charged defects. Such a situation was investigated experimentally [21] by employing a fused silica sample irradiated with γ rays. In the course of irradiation, positively charged centers (Si dangling bonds) are generated. Randomly distributed positive charges are compensated for by randomly distributed negative charges; thus, on average, the sample is electrically neutral. We model the sample as though it consists of microscopically small volume elements ΔV_i. Each volume element chosen is sufficiently small that, within it, not more than one charge center is present. Thus, the electric charge q_i of each element is equal to $\pm e$ or 0, in such a way that the average $\langle q_i \rangle = 0$. We will consider the fluctuations of charges in different volume elements i, j to be statistically independent, so that $\langle q_i q_j \rangle = 0$ for $i \neq j$. The mean square of charge fluctuations within a given element $\langle q_i q_i \rangle \approx 2Ne^2$, N is the average number of positive charges in one volume element. In the absence of the cross terms the average tip-sample friction coefficient is determined by adding the friction coefficient from all the charges q_i. According to (14.10), the contribution to the friction coefficient from the charge q_i in the element ΔV_i is given by

$$\Delta\Gamma_{i\parallel} = \lim_{\omega\to 0} Ne^2 \int_0^\infty dq q^2 e^{-2qd_i} \frac{\mathrm{Im}\, R_p(\omega, q)}{\omega}, \tag{14.19}$$

where $d_i = D(x_i, y_i) - z_i$. Here the coordinates x_i, y_i, z_i give the position of the ith volume element in the substrate, and $D(x_i, y_i)$ is the distance between the sample and points x_i, y_i located on the surface of the tip. The total friction coefficient is obtained by summing all of the volume elements. Replacing the sum by an integral ($N \sum \to n \int d^3 r$, where n is the number of the positive charge centers per unit

volume), and integration over z gives

$$\Gamma_{\parallel} = \lim_{\omega \to 0} \frac{ne^2}{2} \int_0^{\infty} dqq \int dx \int dy e^{-2qD(x,y)} \frac{\mathrm{Im} R_p(\omega, q)}{\omega}. \tag{14.20}$$

For a cylindrical tip, $D(x, y) = d + x^2/2R$, and we get

$$\Gamma_{\parallel}^{c} = \lim_{\omega \to 0} \frac{\sqrt{\pi R} n e^2 w}{2} \int_0^{\infty} dq q^{1/2} e^{-2qd} \frac{\mathrm{Im} R_p(\omega, q)}{\omega}. \tag{14.21}$$

Using the same parameters as in Sect. 14.1, for a cylindrical gold tip separated by $d = 10\,\mathrm{nm}$ from a dielectric sample with $n = 7 \times 10^{17}\,\mathrm{cm}^{-3}$ we get $\Gamma_{\parallel} = 4.4 \times 10^{-20}\,\mathrm{kg\,s}^{-1}$.

For the tip surface with a 2D structure on it, using (14.16) we get

$$\Gamma_{2D\parallel}^{c} = \frac{1}{2^{5/2}} \left(\frac{e}{e^*}\right)^2 \sqrt{\frac{R}{d}} \frac{nw}{n_a} M\eta = \frac{e^2 n w}{16 \sigma_{eff} d}. \tag{14.22}$$

With $\sigma_{eff} = n_a e^{*2}/2M\eta d_1 = 4 \times 10^9\,\mathrm{s}^{-1}$, $n = 7 \times 10^{17}\,\mathrm{cm}^{-3}$, and with the other parameters the same as before, we get, for $d = 10\,\mathrm{nm}$, $\Gamma_{2D\parallel}^{c} = 3.5 \times 10^{-12}\,\mathrm{kg\,s}^{-1}$, which is nearly the same as the experimental observations [21]. Thus, the theory of the friction between a gold tip and silica substrate with an inhomogeneous distribution of the charged defects is consistent with the theory of friction between a gold tip and gold substrate (see Sect. 14.1). In both theories, we have assumed that the gold surfaces are covered by a 2D structure.

The analysis above has ignored the screening of the electric field in the dielectric substrate. This can be justified in the case of very small tip–sample separations (substantially smaller than the screening length), since only defects in the surface layer of thickness d contribute to the integral in (14.20). When the screening is included, the effective electric field outside the sample will be reduced by the factor $(\varepsilon+1)/2$ [191], and the friction coefficient will be reduced by the factor $((\varepsilon+1)/2)^2$, which is equal to 6.25 in the case of silica. However, the heterogeneity of the tip surface can be larger than for the sample surface, so that the damping parameter η can be larger for the 2D structure on the surface of the tip. This increase in η and screening effect will compensate for each other.

14.3 Contact Electrification and the Work of Adhesion

When two solid objects are removed after adhesional or frictional contact, they will in general remain charged [325–329]. At the macroscopic level, charging usually manifests itself as spark discharging upon contact with a third (conducting) body, or as an adhesive force. The long-range electrostatic force resulting from charging

is important in many technological processes such as photocopying, laser printing, electrostatic separation methods, and sliding-triboelectric nanogenerators based on in-plane charge separation [330]. Contact charging is also the origin of unwanted effects such as electric shocks, explosions or damage of electronic equipment.

Contact electrification is one of the oldest areas of scientific study, originating more than 2500 years ago when Thales of Miletus carried out experiments showing that rubbing amber against wool leads to electrostatic charging [331]. In spite of its historical nature and practical importance, there are many problems related to contact electrification that are not well understood, such as the role of surface roughness [332–334], surface migration [335] and contact de-electrification [336].

The influence of contact electrification on adhesion has been studied in pioneering work by Derjaguin et al. [337, 338] and by Roberts [339]. These studies, and most later studies, have assumed that removing the contact between two bodies results in the bodies having uniform surface charge distributions of opposite signs. However, a very recent work [340–342] has shown that the bodies in general have surface charge distributions that vary rapidly in space (on the sub-micrometer scale) between positive and negative values, and that the net charge on each object is much smaller (sometimes by a factor of $\sim$1000) than would result by integrating the absolute value of the fluctuating charge distribution over the surface area of a body.

Contact electrification occurs even between solids made from the same material [340]. This has been demonstrated for silicon rubber (PDMS). If two rubber sheets in adhesive contact (contact area A) are separated, they obtain net charges $\pm Q$ of opposite sign. However, as discussed above, each surface has surface charge distributions that fluctuate rapidly between positive and negative values, with magnitudes much higher than the average surface charge densities $\pm Q/A$. The net charge scales with the contact surface area $Q \sim A^{1/2}$, as expected based on a picture where the net charge results from randomly adding positively and negatively charged domains (with individual area ΔA) on the surface area A: when $N = A/\Delta A >> 1$, we expect from statistical mechanics that the net charge on the surface A is proportional to $N^{1/2}$ as observed [340]. Note that in the thermodynamic limit, $A \to \infty$, the net surface charge density $Q/A = 0$.

In this Section, we will present an accurate calculation of the contribution from contact electrification to the work of adhesion to separate two solids. The same problem has been addressed in a less accurate approach by Brörmann et al. [343]. They assumed that the charged domains formed a mosaic pattern of squares, where each nearby square has a charge of the opposite sign but of equal magnitude. The authors applied an approximate procedure [325] (see also [344, 345]) to this problem, in order to obtain the contribution to the work of adhesion from charging. In this Section, we will present a general theory in which, the surface charge distribution $\sigma(\mathbf{x})$ is characterized by the density–density correlation function $\langle \sigma(\mathbf{x})\sigma(\mathbf{0})\rangle$, the power spectrum of which can be deduced directly from Kelvin Force Microscopy (KFM) potential maps. We find that, for polymers, the contact electrification may only contribute a small amount to the observed work of adhesion. However, more KFM measurements at smaller tip–substrate separations are necessary to confirm the conclusion presented below.

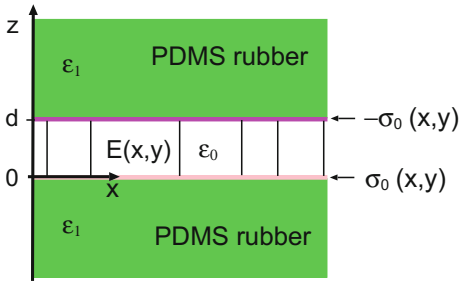

Fig. 14.2 After separation the bottom solid has the surface charge distribution $\sigma_0(\mathbf{x})$ and the top solid has the surface charge distribution $-\sigma_0(\mathbf{x})$, i.e., the charge distribution on one surface is the negative of that of the other surface

We will calculate the force between the two charged solids when the surfaces are separated by the distance d, see Fig. 14.2. The lower surface has the surface charge density $\sigma_0(\mathbf{x})$, where $\mathbf{x} = (x, y)$ is the in-plane coordinate, and the upper surface has the surface charge density $-\sigma_0(\mathbf{x})$, i.e., the charge distribution on one surface is the negative of that of the other surface. We write the electric field as $\mathbf{E} = -\nabla\phi$ so that the electric potential ϕ satisfies $\nabla^2\phi = 0$ everywhere except for $z = 0$ and $z = d$. We write

$$\sigma_0(\mathbf{x}) = \int d^2q\ \sigma_0(\mathbf{q}) e^{i\mathbf{q}\cdot\mathbf{x}}.$$

The electrostatic stress tensor

$$\sigma_{ij} = \frac{1}{4\pi}\left(E_i E_j - \frac{1}{2}\mathbf{E}^2\delta_{ij}\right).$$

Here we are interested in the zz-component:

$$\sigma_{zz} = \frac{1}{8\pi}\left(E_z^2 - \mathbf{E}_\parallel^2\right). \tag{14.23}$$

In the space between the surfaces, the electric potential:

$$\phi = \int d^2q \left[\phi_0(\mathbf{q}) e^{-qz} + \phi_1(\mathbf{q}) e^{qz}\right] e^{i\mathbf{q}\cdot\mathbf{x}}$$

where $\mathbf{q} = (q_x, q_y)$ and $\mathbf{x} = (x, y)$ are 2D vectors. Thus for $z = 0$:

$$E_z = \int d^2q\ q \left[\phi_0(\mathbf{q}) - \phi_1(\mathbf{q})\right] e^{i\mathbf{q}\cdot\mathbf{x}}, \tag{14.24}$$

and

$$\mathbf{E}_\parallel = \int d^2q (-i\mathbf{q}) \left[\phi_0(\mathbf{q}) + \phi_1(\mathbf{q})\right] e^{i\mathbf{q}\cdot\mathbf{x}}. \tag{14.25}$$

Using (14.23), (14.24) and (14.25) gives

$$\int d^2x\ \sigma_{zz} = 2\pi \mathrm{Re} \int d^2q\ q^2 \phi_0(\mathbf{q}) \phi_1^*(\mathbf{q}). \tag{14.26}$$

We now calculate $\phi_0(\mathbf{q})$ and $\phi_1(\mathbf{q})$. We write the electric potential $\phi(\mathbf{q}, z)$ as:

$$\phi = \phi_0 e^{-qz} + \phi_1 e^{qz} \quad \text{for } 0 < z < d,$$

$$\phi = \phi_2 e^{qz} \quad \text{for } z < 0,$$

$$\phi = \phi_3 e^{-q(z-d)} \quad \text{for } z > d.$$

Since ϕ must be continuous for $z = 0$ and $z = d$, we get:

$$\phi_0 + \phi_1 = \phi_2, \tag{14.27}$$

$$\phi_0 e^{-qd} + \phi_1 e^{qd} = \phi_3. \tag{14.28}$$

Let ϵ_0 and ϵ_1 be the dielectric function of the region between the bodies ($0 < z < d$) and in the bodies ($z < 0$ and $z > d$), respectively. In our application, the space between the bodies is filled with non-polar gas and $\epsilon_0 \approx 1$. From the boundary conditions $\epsilon_0 E_z(0^+) - \epsilon_1 E_z(-0^+) = 4\pi\sigma_0$ and $\epsilon_1 E_z(d + 0^+) - \epsilon_0 E_z(d - 0^+) = -4\pi\sigma_0$, and using (14.27) and (14.28), we get:

$$\phi_0 + g\phi_1 = \frac{2\pi}{q}\sigma$$

$$g\phi_0 e^{-qd} + \phi_1 e^{qd} = -\frac{2\pi}{q}\sigma$$

where $\sigma = \sigma_0 2/(\epsilon_1 + \epsilon_0)$ and $g = (\epsilon_1 - \epsilon_0)/(\epsilon_1 + \epsilon_0)$. Solving these equations gives:

$$\phi_0 = \frac{2\pi}{q} \frac{\sigma}{1 + ge^{-qd}}, \qquad \phi_1 = e^{-qd}\phi_0.$$

Using these equations in (14.26) gives

$$\langle F_z \rangle = \int d^2x\ \langle \sigma_{zz} \rangle = (2\pi)^3 \int d^2q\ \left\langle |\sigma(\mathbf{q})|^2 \right\rangle \frac{e^{-qd}}{(1 + ge^{-qd})^2}, \tag{14.29}$$

where we have performed an ensemble average denoted by $\langle .. \rangle$.

Consider the correlation function:

$$\left\langle |\sigma(\mathbf{q})|^2 \right\rangle = \frac{1}{(2\pi)^4} \int d^2x d^2x' \left\langle \sigma(\mathbf{x})\sigma(\mathbf{x}') \right\rangle e^{i\mathbf{q}\cdot(\mathbf{x}-\mathbf{x}')}.$$

Assuming that the statistical properties of the surface charge distribution are translational invariant, we get:

$$\langle \sigma(\mathbf{x})\sigma(\mathbf{x}')\rangle = \langle \sigma(\mathbf{x}-\mathbf{x}')\sigma(\mathbf{0})\rangle$$

and

$$\langle |\sigma(\mathbf{q})|^2\rangle = \frac{A_0}{(2\pi)^4}\int d^2x \langle \sigma(\mathbf{x})\sigma(\mathbf{0})\rangle e^{i\mathbf{q}\cdot\mathbf{x}}$$

where A_0 is the surface area. If $\bar{\sigma} = \langle \sigma(\mathbf{x})\rangle$ denotes the average surface charge density, then we define the charge density power spectrum:

$$C_{\sigma\sigma}(\mathbf{q}) = \frac{1}{(2\pi)^2}\int d^2x \langle [\sigma(\mathbf{x})-\bar{\sigma}][\sigma(\mathbf{0})-\bar{\sigma}]\rangle e^{i\mathbf{q}\cdot\mathbf{x}}. \tag{14.30}$$

Using this definition, we get:

$$\langle |\sigma(\mathbf{q})|^2\rangle = \frac{A_0}{(2\pi)^2}\left[C_{\sigma\sigma}(\mathbf{q}) + \bar{\sigma}^2\delta(\mathbf{q})\right]. \tag{14.31}$$

Substituting (14.31) in (14.29) gives

$$\langle F_z\rangle = 2\pi A_0\bar{\sigma}^2 + 2\pi A_0\int d^2q\ C_{\sigma\sigma}(\mathbf{q})\frac{e^{-qd}}{(1+ge^{-qd})^2}.$$

We expect the statistical properties of the surface charge distribution to be isotropic, which implies that $C_{\sigma\sigma}(\mathbf{q})$ only depends on the magnitude $q = |\mathbf{q}|$. This gives:

$$\langle F_z(d)\rangle = 2\pi A_0\bar{\sigma}^2 + (2\pi)^2 A_0\int dq\ qC_{\sigma\sigma}(q)\frac{e^{-qd}}{(1+ge^{-qd})^2}.$$

The first term in this expression is the attraction between the surfaces due to the (average) uniform component of the charge distribution, which, as expected, is independent of the separation between the surfaces (similar to a parallel condenser). The second term is the contribution from the fluctuating components of the surface charge distribution. The contribution to the work of adhesion from the surface charge is given by:

$$U = \int_0^d dz\ \langle F_z(z)\rangle = 2\pi A_0\bar{\sigma}^2 d$$

$$+ (2\pi)^2 A_0\int_0^\infty dq\ qC_{\sigma\sigma}(q)\int_0^d dz\frac{e^{-qz}}{(1+ge^{-qz})^2}. \tag{14.32}$$

For an infinite system, the first term in U increases without limit as the surfaces are separated. For bodies of finite size, the expression given above for the contribution

from the net charging is of course only valid for separations smaller than the linear size of the bodies (i.e. $d < L$, where $A_0 = L^2$), and the interaction energy will decay like $\sim 1/d$ for large separation. Thus, for a finite-sized system, the contribution to the normalized work U/A_0 to separate the solids, from the first term in U, will be of order $\sim\bar{\sigma}^2 L$, with a prefactor which depends on the actual shape of the bodies. Note that, in the thermodynamic limit $L \to \infty$, since $\bar{\sigma} \sim 1/L$ this contribution to U/A_0 will actually vanish. Roberts (see [339]) has argued that the first term in (14.32) gives a negligible contribution to the work of adhesion also for finite-sized objects. Here, we take a more pragmatic approach and we will not include this term in the work of adhesion, in particular since it depends on the shape of the bodies, and also because, experimentally, it is easy to measure the work to separate the solids such small distance that the first term in (14.32) is completely negligible, see [346]. The contribution to the work of adhesion from the second term in (14.32) (for $d \to \infty$) is:

$$w_{\rm ch} = \frac{U}{A_0} = \frac{(2\pi)^2}{1+g}\int_0^\infty dq\; C_{\sigma\sigma}(q). \tag{14.33}$$

Note that the integral

$$\int d^2q\; C_{\sigma\sigma}(\mathbf{q}) = \left\langle [\sigma(\mathbf{x}) - \bar{\sigma}]^2 \right\rangle = \left\langle \Delta\sigma^2 \right\rangle \tag{14.34}$$

is the mean of the square of the fluctuating surface charge distribution. Using this equation we can write:

$$w_{\rm ch} = \frac{2\pi}{1+g}\frac{\left\langle \Delta\sigma^2 \right\rangle}{\langle q \rangle} \tag{14.35}$$

where

$$\langle q \rangle = \frac{\int_0^\infty dq\; qC_{\sigma\sigma}(q)}{\int_0^\infty dq\; C_{\sigma\sigma}(q)}. \tag{14.36}$$

The study above is for the limiting case where the surfaces separate so fast that no decay in the surface charge distribution takes place before the separation is so large as to give a negligible interaction force. Experiments [341] have shown that the charge distribution decays with increasing time as $\exp(-t/\tau)$, where the relaxation time $\tau \approx 10^3$ s depends on the atmospheric condition (e.g., the humidity and concentration of ions in the surrounding gas). Taking into account the decay in the surface charge distribution, and assuming $z = vt$ (where v is the normal separation velocity), we need to replace the integral over z in (14.32) with:

$$f(q, v) = \int_0^\infty dz \frac{e^{-qz}e^{-2t/\tau}}{(1+ge^{-qz})^2} = \int_0^\infty dz \frac{e^{-(qz+2z/v\tau)}}{(1+ge^{-qz})^2}$$

and (14.32) becomes

$$w_{\rm ch} = (2\pi)^2 \int_0^\infty dq\; qC_{\sigma\sigma}(q) f(q, v). \tag{14.37}$$

In the limit $v \to \infty$, we have $f \to 1/[q(1+g)]$ and, in this limit, (14.37) reduces to (14.35). In the opposite limit of very small surface separation velocity, $f \to v\tau/[2(1+g)^2]$ and in this limit

$$w_{\rm ch} = \frac{(2\pi)^2 v\tau}{2(1+g)^2}\int_0^\infty dq\, qC_{\sigma\sigma}(q) = \frac{\pi v\tau\left\langle\Delta\sigma^2\right\rangle}{(1+g)^2}. \tag{14.38}$$

Note that this expression is of the form (14.35) with $1/\langle q\rangle$ replaced by $v\tau/[2(1+g)]$. Since, typically, $\tau \approx 10^3$ s and $(1+g) \approx 1$ and $\langle q\rangle \approx q_1 \approx 10^9$ m^{-1} (where q_1 is defined below), we get $v_{\rm c} = 2(1+g)/(\langle q\rangle\tau) \approx 10^{-12}$ m/s. In most applications, we expect the separation velocity to be in the vicinity of the crack tip $v >> v_{\rm c}$, and in this case the limiting equation (14.35) holds accurately. Note, however, that the separation velocity v may be much smaller than the crack tip velocity.

In the KFM measurement, the local potential at some fixed distance d above the surface is measured, rather than the surface charge density. From the measured data, the potential power spectrum

$$C_{\phi\phi}(\mathbf{q}) = \frac{1}{(2\pi)^2}\int d^2x\left\langle[\phi(\mathbf{x})-\bar\phi][\phi(\mathbf{0})-\bar\phi]\right\rangle e^{i\mathbf{q}\cdot\mathbf{x}}$$

can be directly obtained. However, we can relate the potential to the charge density:

$$\phi(\mathbf{q}) = \frac{2\pi}{q}\sigma(\mathbf{q})e^{-qd}.$$

Thus

$$C_{\sigma\sigma}(\mathbf{q}) = \frac{q^2}{(2\pi)^2}C_{\phi\phi}(\mathbf{q})e^{2qd}. \tag{14.39}$$

The results presented above are in Gaussian units. To obtain (14.39) in SI units we must multiply the right-hand side with $(4\pi\epsilon_0)^2$, where $\epsilon_0 = 8.8542\times10^{-12}\,{\rm CV^{-1}m^{-1}}$. Thus:

$$C_{\sigma\sigma}(\mathbf{q}) = 4\epsilon_0^2 q^2 C_{\phi\phi}(\mathbf{q})e^{2qd}. \tag{14.40}$$

To get (14.33) in SI units we must multiply the right-hand side by $(4\pi\epsilon_0)^{-1}$:

$$w_{\rm ch} = \frac{\pi}{2\epsilon_0(1+g)}\int_0^\infty dq\; C_{\sigma\sigma}(q). \tag{14.41}$$

We now analyze experimental data involving elastically soft solids with smooth surfaces, where the initial contact between the solids is complete due to the adhesion between the solids. In [341], several such systems were studied and here we focus on PDMS rubber against PDMS. After breaking the adhesive contact between two sheets of PDMS (which involves interfacial crack propagation), the electrostatic potential a distance d above one of the surfaces was probed using KFM measurements. From the

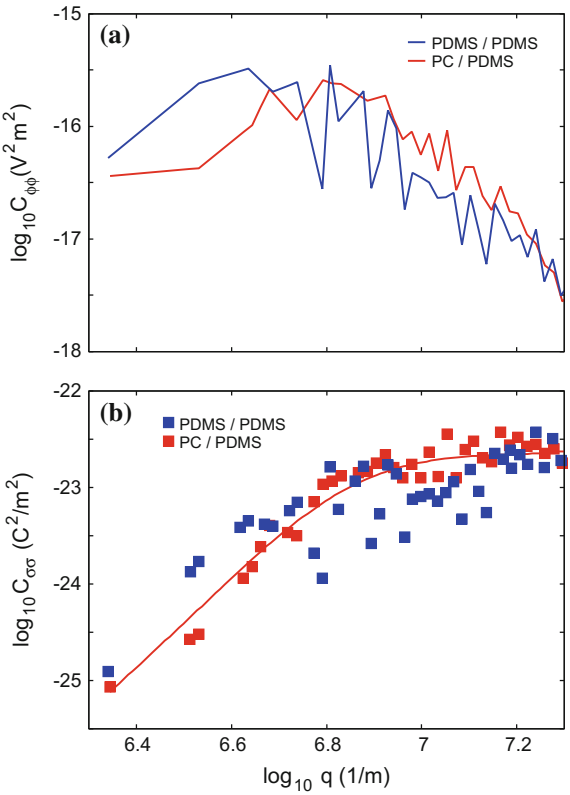

Fig. 14.3 **a** The voltage power spectrum $C_{\phi\phi}$ and **b** the surface charge density power spectrum $C_{\sigma\sigma}$ as a function of the wavevector. The results have been calculated from the measured (KFM) voltage maps for PDMS/PDMS (*blue*) and PDMS/polycarbonate (PC) (*red*) [341]

measured potential map, we have calculated the potential power spectrum $C_{\phi\phi}(q)$ and then, from (14.40), the charge density power spectrum $C_{\sigma\sigma}(q)$. The measurements were done at the tip–substrate separation $d \approx 10^{-7}$ m, and since the electric potential from a surface charge density distribution with the wavevector q decay as $\exp(-qd)$ with the distance d from the surface, the KFM is effectively limited to probing the surface charge distribution with wavevector $q < 1/d$. In Fig. 14.3 we show both power spectra for $q < 2 \times 10^7$ m^{-1}. Note that the charge density power spectrum appears to saturate for a large wavevector, say $q > q_0$, with $q_0 \approx 10^7$ m^{-1}. This result follows if, as expected, the process of creating surface charges is uncorrelated in space at short length scales. In that case, $\langle \sigma(\mathbf{x})\sigma(\mathbf{0})\rangle \sim \delta(\mathbf{x})$ and using (14.30), this gives $C_{\sigma\sigma}(\mathbf{q}) = \text{const}$. The fact that $C_{\sigma\sigma}(\mathbf{q})$ decays for decreasing q for $q < q_0 \approx 10^7$ m^{-1} implies that at some length scales $\lambda_0 = 2\pi/q_0 \approx 0.6\,\mu$m the charge distribution becomes correlated. The physical reason for this may relate to inhomogeneities on the PDMS surface; for example. due to filler particles (see below).

We assume that the charge density power spectrum saturate for $q > q_0$ at $C^0_{\sigma\sigma} \approx 2.2 \times 10^{-23}$ C^2/m^2 (see Fig. 14.3b). The assumption that the process of creating surface charges is uncorrelated in space at short length scales gives $C^0_{\sigma\sigma} = (2\pi)^{-2}e^2 n$,

where $n = 1/\lambda_1^2$ is the number of elementary charges ($\pm e$) per unit surface area. Thus, we obtain $n = 3.4 \times 10^{16}\ \mathrm{m}^{-2}$ and $\lambda_1 \approx 6\,\mathrm{nm}$ and $q_1 = 2\pi/\lambda_1 \approx 10^9\ \mathrm{m}^{-1}$. The charge density $\langle|\sigma|\rangle = ne \approx 0.5\,\mu\mathrm{C/cm}^2$ is similar to what was estimated by Baytekin et al. [341]. Using (14.34) we get the mean square charge fluctuation $\langle\Delta\sigma^2\rangle \approx \pi q_1^2 C_{\sigma\sigma}^0 \approx 7 \times 10^{-5}\,\mathrm{C}^2/\mathrm{m}^4$ or the rms charge fluctuation $\approx 1\mu\mathrm{C/cm}^2$, which, as expected, is similar to ne.

From (14.41) we get $w_{\mathrm{ch}} \approx (q_1 - q_0)C_{\sigma\sigma}^0/\epsilon_0$, where we have used that $\pi/[2(1+g)] \approx 1$. The large wavevector cut-off q_1 is of order $2\pi/\lambda_1$, where λ_1 is of the order of the average separation between the surface charges (which we assume to be point charges of magnitude $\pm e$, where e is the electron charge). Since $q_0 << q_1 \approx 10^9\ \mathrm{m}^{-1}$ we get $w_{\mathrm{ch}} \approx q_1 C_{\sigma\sigma}^0/\epsilon_0 \approx 0.002\,\mathrm{J/m}^2$. This value is smaller than the measured work of adhesion during adiabatic (very slow) separation of the surfaces where [346] $w \approx 0.05\,\mathrm{J/m}^2$.

The calculation above does not include the interaction between the charges when the surface separation is smaller than $\sim$1 nm. However, this contribution cannot be accurately estimated without an accurate knowledge of the exact location and spatial extent of the localized charges, and probably also require knowledge about how the charge separation processes occur; for example, whether it involves electron tunneling at some finite surface separation.

The analysis above is based on the assumption that the surface charge density power spectrum saturates at a value $C_{\sigma\sigma}^0 \approx 2.2 \times 10^{-23}\,\mathrm{C}^2/\mathrm{m}^2$ for large wavevectors. This hypothesis should be tested by performing KFM measurements to smaller tip–substrate separations. The number of surface charges per unit area, n, which determines the cut-off q_1 in the study above, may also be probed by surface reaction experiments, such as the bleaching experiments reported on in [342].

Sylgard 184, which was used in [341], is intrinsically a heterogeneous polymer with siliceous fillers [347]. Even though the filler is partially modified by organic groups, it imparts non-negligible polarity of the polymer as evidenced from the high contact angle hysteresis ($\sim$20°–40°) of water on this polymer as compared with that ($\sim$5°) on a pure PDMS matrix. X-ray photoelectron spectroscopy [348] also shows that the Silicon (Si2p) peak of the silica is 1 eV higher than that of the surrounding matrix, thus suggesting that the electron affinity of the silica rich region is probably different from that of the surrounding matrix. So, when two surfaces of sylgard 184 are brought close to each other, electrons may be transferred from one type of domain to another, which may show up as heterogeneous patches when the surfaces are separated. If the binding energy of the Si2p peak is an indicator, the PDMS matrix is more electron-rich than the silica-rich region. The breaking of the siloxane bond requires a very large force and is unlikely to contribute to charging [348–350]. Silica almost always has silanol (SiOH) groups. The silanol groups may form very weak hydrogen bond with the oxygen of polydimethylsiloxane. If that happens, some charge transfer may occur during the separation of the surfaces, which will show up as heterogeneous charge after the two surfaces are separated. This idea may be tested experimentally by performing KFM experiments using a clean PDMS network that does not have silica fillers.

At low crack-tip velocities, where the viscoelastic energy dissipation at the crack tip, and other non-equilibrium effects, are negligible (see [346]), the work of adhesion is usually assumed to result from the van der Waals interaction between the surfaces at the interface. The study above indeed indicated that the contributions from contact electrification gives only a small fraction (∼4%) of the observed work of adhesion.

To summarize, we have derived a general expression for the contribution to the work of adhesion from contact electrification, and we have shown that, for PDMS (and probably for polymers in general), the contact electrification gives only a small fraction of the observed work of adhesion. More KFM measurements at smaller tip–substrate separations are necessary to confirm this conclusion.

14.4 Influence of Attractive Force on Cantilever Eigenfrequencies

Besides the damping of vibrations, interaction of the tip with a sample leads to a change in the cantilever eigenfrequency. When the cantilever geometry satisfies the conditions $L \gg w \gg c$, where the L, w and c are the length, the width, and the thickness of the cantilever, respectively, we can employ the equation of elasticity [351] to describe the dynamics. In the case of an isotropic material, the transverse displacement $X(z, t)$, of the beam centerline (along the x axis) (see Fig. 14.4), sat-

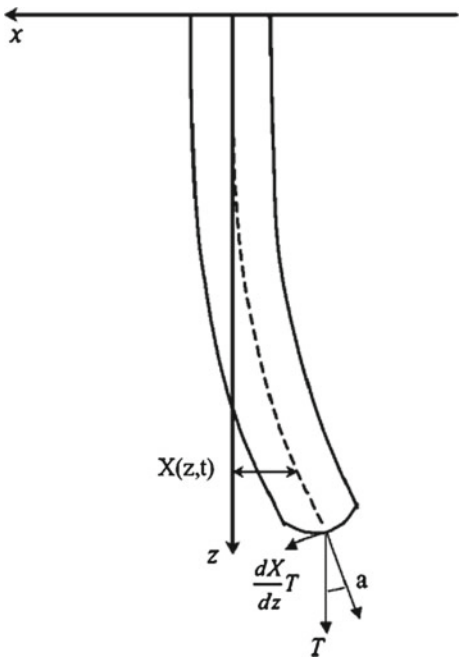

Fig. 14.4 Transverse displacement $X(z, t)$ of the cantilever centerline. The attractive force T acts along the z axis. A restoring force $X'T$ acts on the tip when $\alpha \neq 0$. From [169]

isfies the differential equation:

$$\rho_c S \frac{\partial^2}{\partial t^2} X(z,t) = -EI_i \frac{\partial^4}{\partial z^4} X(z,t) + T \frac{\partial^2}{\partial z^2} X(z,t), \tag{14.42}$$

where ρ_c is the density of the cantilever material, $S = wc$ is the cross-section area, E is Young's modulus, $I_i = c^3 w/12$ is the bending moment of inertia, and T is a stretching force. The clamped end, at $z = 0$, imposes the boundary conditions $X(z = 0) = X'(z = 0) = 0$. The free end at $z = L$ imposes the boundary conditions $M_y \equiv EI_i X'' = 0$ and $F_x \equiv -EI_i X''' + TX' = 0$, where M_y and F_x are the moment of the elastic force and the elastic force in the y and x directions, respectively. The term TX' describes the effect of the restoring force when there is a non-vanishing angle between T and the centerline direction at $z = L$ (see Fig. 14.4). This expression for the restoring force is valid in the case of small angles α between vertical axis and the beam baseline, i.e. when $\sin\alpha \approx \tan\alpha = -X'(z = L)$. The fundamental vibration eigenfunction is given by $X(z,t) = X_0(z)\cos(\omega t)$, where

$$\begin{aligned} X_0(z) = A\big[&(\Lambda^2 \cos\lambda L + \lambda^2 \cosh\Lambda L)(\cos\lambda z - \cosh\Lambda z) + \\ &+(\Lambda \sin\lambda L - \lambda \sinh\Lambda L)(\Lambda \sin\lambda z - \lambda \sinh\Lambda z)\big]. \end{aligned} \tag{14.43}$$

Here A is a constant,

$$\begin{aligned} \Lambda = \big[\tau/2 + (\kappa^4 + \tau^2/4)^{1/2}\big]^{1/2}, \quad \lambda = \big[&-\tau/2 + (\kappa^4 + \\ &+\tau^2/4)^{1/2}\big]^{1/2}, \quad \tau = T/EI_i, \quad \kappa^4 = \omega^2 \rho_c S/EI_i. \end{aligned} \tag{14.44}$$

The value of κ in (14.44) obeys the following eigenvalue equation:

$$2\kappa^4 + (\tau^2 + 2\kappa^4)\cos\lambda L \cosh\Lambda L + \kappa^2 \tau \sin\lambda L \sinh\Lambda L = 0. \tag{14.45}$$

The minimum value of κ (κ_{min}) that obeys (14.45) determines the fundamental eigenfrequency and the explicit form of the fundamental eigenfunction $X(z,t)$. In the absence of the stretching force, ($T = 0$), we get $\kappa^2 = 3.516/L^2$ and

$$\omega = (3.516/L^2)(EI_i/\rho_i S)^{1/2}. \tag{14.46}$$

To estimate ω we set $c = 250$ nm, $w = 7\,\mu$m, $L = 250\,\mu$m, and use the material constants of *Si*: $\rho_c = 2.33 \times 10^3\,\mathrm{kg{\cdot}m^{-3}}$, $E = 9 \times 10^{10}\,\mathrm{kg \cdot m^{-1} \cdot s^{-2}}$. Then, we have $\omega/2\pi \approx 4 \times 10^3\ \mathrm{s^{-1}}$, which is approximately the same as the value quoted in [21].

In the general case, the fundamental frequency is a function of the tip–sample separation, d, bias voltage V, tip geometry, and concentration of charge centers via the attraction force, $T(V)$. In the case of attraction due only to an external bias voltage, there is a quadratic dependence of T on V. The proportionality coefficient depends on the geometry of the tip–sample system. The results of numerical calculations of

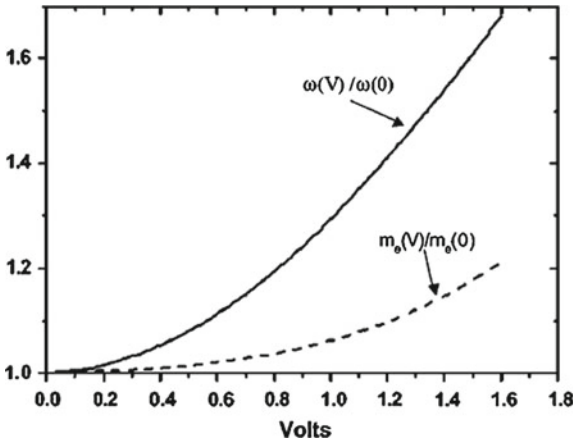

Fig. 14.5 Numerical results for the cantilever frequency ω and effective mass m_{ef} as a function of the bias voltage V in the case of a cylindrical tip and $d = 20$ nm (see text). From [169]

the $\omega(V)$ dependence are shown in Fig. 14.5 for a cylindrical geometry showing that the bias voltage can have a considerable effect on the frequency shift.

In the limit of very large V (when $TL^2/(EI_i) \gg 1$), the first term on the right-hand-side of (14.42) can be omitted, and (14.42) is transformed into the equation for the vibration of a string. In this case, a linear dependence of ω on V ($\omega \propto V/L$) should occur.

Along with the resonant frequency, the cantilever effective mass also depends on V. The effective mass m_{eff} is the coefficient entering the oscillator equation,

$$m_{eff}\frac{\partial^2 X(t)}{\partial t^2} + \Gamma\frac{\partial X(t)}{\partial t} + kX(t) = 0, \tag{14.47}$$

as a parameter that determines the inertial force (Γ is a friction coefficient, k a spring constant, and $X(t)$, as stated previously, is the coordinate of the tip). The mass m_{eff} depends on the coefficients in (14.42). This dependence can be obtained from the requirement that the kinetic energy of the flexible beam equals that of the oscillator, the two being of one and the same physical quantity. This condition defines m_{eff} as

$$m_{eff} = \rho_c S\int_0^L dz X_0^2(z)/X_0^2(L), \tag{14.48}$$

where $X_0(z)$ is given by (14.43).

Thus, m_{eff} depends on the variation of X_0 with z, which in turn depends on the stretching force T and the other parameters in (14.42). In the simplest case, $T = 0$, we have $m_{eff} = \rho_c LS/4$, i.e., a quarter of the beam's actual mass. In general, the possible variation of m_{eff} should be taken into account when the friction coefficient Γ is obtained experimentally from the relation $\Gamma = m_{eff}\omega/Q$, where Q is the quality factor. In other words, not only the quality factor and the eigenfrequency, but also the value of m_{eff} is required to obtain Γ. The dependence $m_{eff}(V)$ is shown in Fig. 14.5. It is seen to be similar to that of $\omega(V)$ at small values of V.

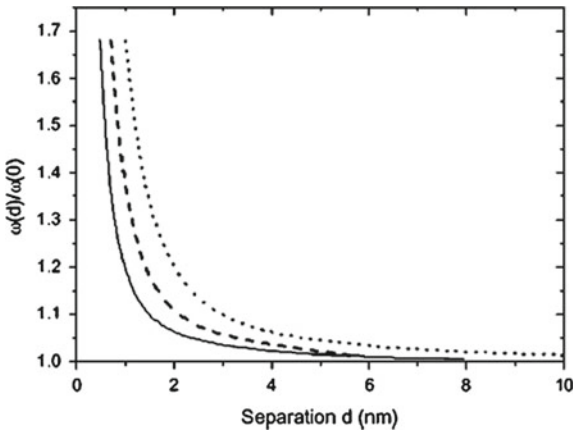

Fig. 14.6 Effect of Casimir–Lifshitz force on the frequency ω. *Solid line*, $R = 0.5\,\mu$m; *dashed line*, $R = 1.0\,\mu$m; *dotted line*, $R = 2\,\mu$m. From [169]

Figure 14.6 shows the effect of the Casimir–Lifshitz force on the fundamental frequency in the case of a spherical tip. The three curves illustrate the tendency of $\omega(d, R)$ to increase with the attractive force, which varies with d and R as $T \sim R/d^2$ (see (S.4) in Appendix S1). The frequency shift observed in [21] at $d = 2$ nm for a gold sample corresponds to the curve $R = 0.5\,\mu$m in Fig. 14.6. When we use the experimental value $1\,\mu$m for the radius of curvature in the y direction, and set the radius of curvature in the x direction equal to the cantilever thickness $c = 0.25\,\mu$m, then, according to Appendix S2, we obtain radius of equivalent spherical tip $R_{exp} = \sqrt{R_x R_y} = 0.5\,\mu$m, i.e., $R_{exp} = R$. Hence the frequency shift observed by Stipe et al. [21] might be attributable to the Casimir–Lifshitz effect.

There are other physical mechanisms that may contribute to the frequency shift. Spatial variation of the surface potential, whose role in damping of vibrations was discussed in Sect. 14.1, will also contribute to the attraction force between the tip and the sample. In the presence of a bias voltage V, the attraction force of the tip to the sample is given by (see (S.8) from Appendix S2)

$$T^s(d) = \frac{RV^2}{4d}. \tag{14.49}$$

In the case of variation of the surface potential bias voltage, V in (14.49), should be replaced on V_0, where V_0 is the root-mean-square variation of the surface potential. As discussed in Sect. 14.1, in the experiment in [21] $V_0 \approx 0.2$V. Thus, the ratio of the Casimir–Lifshitz force (see (S.4) in Appendix S1) to the force induced by the work function anisotropy is of the order

$$\frac{R\hbar\omega_p}{32\sqrt{2}d^2} \Big/ \frac{RV_0^2}{4d} \approx (12\text{ nm}/d). \tag{14.50}$$

For $d = 2$ nm, this ratio is equal to 6. Hence, the anisotropy of the work function has a negligible effect on the frequency shift obtained in [21].

Chapter 15
Phonon and Internal Non-contact Friction

A moving tip will induce the dynamic deformation of the surface of the substrate due to the Casimir or electrostatic interaction between the tip and the surface. This dynamic deformation will excite phonons in the substrate, which are responsible for phononic mechanism of non-contact friction. In this section, phononic friction is studied using the elastic continuum model. The obtained results are used to explain non-contact friction measurement over the metal superconductor transition, which allows phononic and electronic contribution to friction to be distinguished from one another. In the upcoming discussion of phononic friction in Sect. 15.1, it is assumed that the deformations of the solids are purely elastic. However, deformation will be purely elastic (or adiabatic) only for infinitely small velocities, so that, at every moment, the system stays in the equilibrium state. Real motion in fact always occurs with finite velocity, and the body does not stay in equilibrium. Thus, non-adiabatic 'flow-processes' occur, resulting in dissipation of the mechanical energy. At least two kinds of processes result in energy dissipation: (a) heat flow resulting from the temperature gradient, and (b) some kind of internal motion, such as point defect flipping. These processes of energy dissipation can be denoted (as in liquids) as internal friction or viscosity.

15.1 Non-contact Friction Due to Excitation of Substrate Phonons

Consider a tip that performs harmonic oscillation, $u = u_0 \exp(-\mathrm{i}\omega t) + c.c.$, above an elastic body with a flat surface. This will result in an oscillating stress acting on the surface of the solid that excites acoustic waves with parallel wave number $q < \omega/c_s$, where c_s is the sound velocity. The stress σ_{iz} acting on the surface of the elastic solid can be represented through the Fourier integral

$$\sigma_{iz}(\mathbf{x}, t) = \int \frac{d^2q}{(2\pi)^2} \sigma_i(\mathbf{q}) u_0 e^{i\mathbf{q}\cdot\mathbf{x} - i\omega t} + c.c. \tag{15.1}$$

A.I. Volokitin and B.N.J. Persson, *Electromagnetic Fluctuations at the Nanoscale*,
NanoScience and Technology, DOI 10.1007/978-3-662-53474-8_15

Using the theory of elasticity (assuming an isotropic elastic medium for simplicity), it is possible to calculate the displacement field u_i at the surface $z = 0$ in response to the surface stress distribution σ_{iz},

$$u_i(\mathbf{x}, t) = \int \frac{d^2q}{(2\pi)^2} M_{ij}(\mathbf{q}, \omega)\sigma_j(\mathbf{q})u_0 e^{i\mathbf{q}\cdot\mathbf{x}-i\omega t} + c.c. \tag{15.2}$$

Using the elastic continuum model, the explicit form of the tensor M_{ij} was derived in [213] (see also Appendix T). The energy dissipation per unit time is equal to

$$P = \int d^2x \langle \dot{u}_i\ (\mathbf{x}, t)\sigma_{iz}(\mathbf{x}, t)\rangle = z$$

$$= 2\omega \int \frac{d^2q}{(2\pi)^2} \mathrm{Im} M_{ij}(\mathbf{q}, \omega)\sigma_i(\mathbf{q})\sigma_j^*(\mathbf{q})|u_0|^2, \tag{15.3}$$

where $\langle ... \rangle$ stands for time averaging. The energy dissipation per unit time must be equal to $\Gamma <\dot{u}\ (t)^2 >= \Gamma 2\omega^2\ |u_0|^2$. Comparing this expression with (15.3) gives

$$\Gamma = \int \frac{d^2q}{(2\pi)^2} \frac{\mathrm{Im} M_{ij}(\mathbf{q}, \omega)}{\omega} \sigma_i(\mathbf{q})\sigma_j^*(\mathbf{q}). \tag{15.4}$$

At typical experimental conditions, we have $\omega \sim 10^3$–$10^6\ \mathrm{s}^{-1}$ and $qr^* < \omega r^*/c_s < 10^{-3} \ll 1$, where the effective radius of the interaction $r^* \approx \sqrt{dR}$, d is the separation between the tip and the sample, and R is the radius of curvature of the tip. In this case, the contribution to the friction from excitation of acoustic waves can be determined by calculating the energy dissipation due to an oscillating point force applied to the surface of the semi-infinite elastic continuum (see Appendix T). These calculations were carried out in connection with the vibrational energy relaxation of adsorbates [250]. According to this theory (see also Appendix T) the friction coefficient for vibration of the tip normal to the surface is given by

$$\Gamma_\perp = \frac{\xi_\perp}{4\pi} \frac{K^2}{\rho c_t^3}, \tag{15.5}$$

where $\xi_\perp \approx 1.65$, c_t is the transverse sound velocity of the solid, ρ is the mass density of the sample, $K = \partial F/\partial d$, where $F(d)$ is the static force acting on the tip due to interaction with the sample. For vibration of the tip parallel to the sample surface, the friction coefficient due to excitation of the acoustic waves is given by (see Appendix T):

$$\Gamma_\parallel = \frac{\xi_\parallel}{4\pi} \frac{\omega^2}{\rho c_t^5} F_z^2(d), \tag{15.6}$$

where $\xi_{\parallel} \approx 1.50$. Using (15.5) and (15.6), we get that $\Gamma_{\parallel}/\Gamma_{\perp} \sim (\omega d/c_t)^2 \ll 1$. Thus, the phononic friction coefficient for parallel vibrations of the tip will be by many orders of magnitude smaller than for normal vibrations. We consider now two different contributions to the tip sample interaction.

For spherical tip with the radius of curvature R, the attraction force of the tip to the surface due to Casimir Lifshitz interaction is determined by (see Appendix S1):

$$F_z(d) = \frac{R\hbar\omega_p}{32\sqrt{2}d^2} \tag{15.7}$$

and

$$K^s = \frac{R\hbar\omega_p}{16\sqrt{2}d^3}. \tag{15.8}$$

Similarly, in the case of a cylindrical tip, we have

$$F_z^c(d) = \frac{3wR^{1/2}\hbar\omega_p}{2^8 d^{5/2}} \tag{15.9}$$

and

$$K^c = \frac{15wR^{1/2}\hbar\omega_p}{2^9 d^{7/2}}. \tag{15.10}$$

For a copper tip separated from a copper substrate by $d = 10\,\text{nm}$, and with $R = 1\,\mu\text{m}$, $w = 7\,\mu\text{m}$, we get for a spherical tip $\Gamma_{\perp}^s = 6.3 \times 10^{-18}\ \text{kgs}^{-1}$ and for a cylindrical tip $\Gamma_{\perp}^c = 1.3 \times 10^{-14}\ \text{kgs}^{-1}$. The phononic friction decreases as d^{-6} and d^{-7} for spherical and cylindrical tip, respectively.

In the presence of the bias voltage, V, the attractive force between the tip and the sample at $d \ll R$ is given by (see Appendix S2)

$$F^c(d) = \frac{wV^2R^{1/2}}{2^{7/2}d^{3/2}} \tag{15.11}$$

for a cylindrical tip, and

$$F^s(d) = \frac{RV^2}{4d} \tag{15.12}$$

for a spherical tip. For bias voltage $V = 1$ Volt, and with the other parameters the same as above, we get $\Gamma_{\perp}^s = 8.8 \times 10^{-17}\ \text{kgs}^{-1}$ and $\Gamma_{\perp}^c = 1.2 \times 10^{-13}\ \text{kgs}^{-1}$ for the spherical and cylindrical tip, respectively. Note that, in this case, the friction depends on the bias voltage as V^4.

15.2 Suppression of Electronic Friction in the Superconducting State

The ratio between the electron and phonon mechanisms of friction plays an important role in understanding the nature of friction. The non-contact friction was reported on both metal [21] and dielectric materials [24]. This means that the pendulum can induce both phononic and electronic excitations while oscillating in close proximity to a substrate. The atomic force microscopy (AFM) experiments in contact mode have shown how the friction forces acting on a sharp tip crossing a silicon surface are influenced by the isotopic composition [417] and the doping conditions [418] of the sample. This can be attributed to different degrees of phononic and electronic excitations.

For metals, the van der Waals and electrostatic friction, associated with the drift motion of charges in the medium, the relative importance of the electronic and phononic mechanisms of energy dissipation can be probed by changing the resistance of a material. In the most elegant way, this can be done by turning on and off the resistance of the material by changing the temperature near the critical point of transition to the superconducting state T_c. This was first done by means of a quartz crystal microbalance technique [419]. The results showed that the slip times of N_2 molecules on Pb films rise significantly below the critical temperature T_c, corresponding to a reduction of the friction, and indicating the importance of the electronic friction compared with phononic friction. However, the transition in the friction coefficient observed in this experiment was quite abrupt. This is in contrast with the predictions of the Bardeen–Cooper–Schrieffer (BCS) theory, which is commonly accepted to describe superconductivity at low temperatures [420].

Another experiment of this type was carried out in [166] in which the friction force acting on a sharp silicon tip oscillating in the pendulum geometry was measured at distances up to 3 nm from a Nb film. The cantilever tip performed small oscillations parallel to silicon surface covered with a film of niobium with thickness of 150 nm (see Fig. 15.1). Friction was measured in a range of 7 K across the critical temperature $T_c = 9.2$ K of Nb. Furthermore, the variations of the friction coefficient with the tip surface distance and the bias voltage in both normal and superconducting states were studied.

A comparison with the BCS theory [420, 421] and a model developed in [171, 422] allowed the authors to conclude that the electronic friction is the main dissipative channel in the metallic state, and it smoothly decays below the critical temperature, until phononic friction becomes dominant.

The temperature variation of the friction coefficient when the Nb sample was warmed up crossing the critical point $T_c = 9.2$ K is shown in Fig. 15.2. The tip was oscillated at a distance $d = 0.5$ nm from the Nb layer. Friction increases significantly when the critical temperature T_c is approached and it levels off when $T > T_c$. In Fig. 15.2, the friction transition appears smooth, which is in contrast to the quartz crystal microbalance measurements on Pb films by Dayo and colleagues [419]. Figure 15.2 also shows the friction coefficient Γ_0 of the free cantilever in the

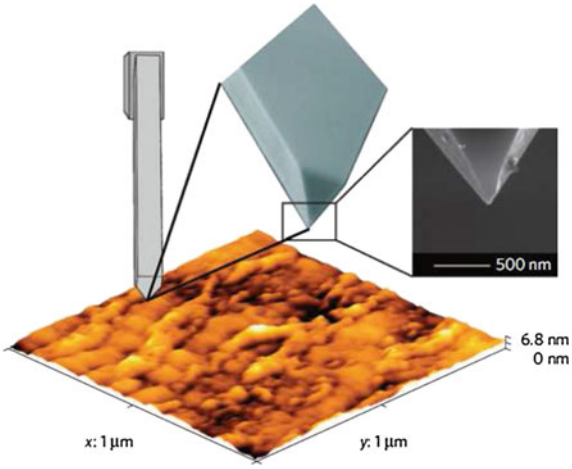

Fig. 15.1 AFM topography image of the Nb film studied in the experiment. The cantilever is oriented perpendicular to the surface (pendulum geometry), while its tip can oscillate parallel to the film surface. The inset shows the tip at different scales. From [166]

same range of temperatures. This coefficient is determined by thermoelastic damping as well as by bulk and surface losses. It is equal to $\Gamma_0 = 2.9 \times 10^{-12}$ kg s^{-1} when $T = 13$ K and decreases in a rather continuous way down to 2.0×10^{-12} kg s^{-1} at $T = 6$ K. This is in qualitative agreement with studies of internal friction of silicon cantilevers [25].

The distance dependencies of the friction coefficient Γ in the metal ($T = 13$ K) and in the superconducting phase ($T = 5.8$ K) are compared in Fig. 15.3.

At a separation $d = 0.5$ nm from the Nb surface, the coefficient Γ in the metal phase is approximately three times larger when compared with the superconducting phase. At closer distances, the friction coefficient levels off in the metal phase (but not in the superconducting phase), which is also shown in Fig. 15.3. The experimental data can be fitted by a power law $\Gamma \sim 1/d^n$, with the exponent $n = 1.0 \pm 0.1$ in the metallic state and $n = 3.8 \pm 0.3$ in the superconducting state.

The data in Figs. 15.2 and 15.3 were recorded after compensating for the contact potential with a bias voltage V applied between the tip and the sample. In this way, the contribution to the friction force due to long-range electrostatic-induced losses is suppressed. Figure 15.4 shows the energy dissipation as a function of the bias voltage V. The curves in Fig. 15.4 correspond again to the temperatures $T = 13$ K and $T = 5.8$ K, where the sample is in the metal and in the superconducting phases. The tip sample distance was again set to $d = 0.5$ nm, as in Fig. 15.2. The voltage dependence of the friction coefficient $\Gamma(V)$ is now well fitted by a power law $\Gamma \sim (V - V_0)^\alpha$ with exponents $\alpha = 2.2 \pm 0.3$ and $\alpha = 4.2 \pm 0.4$ in the metal and in the superconducting phases, respectively. The quantity V_0 is the contact potential. In the experiment, V_0 is approximately 0.14 V in the superconducting phase and 0.17 V in the metal phase.

Interpretation of the experimental data in [166] was based on the theoretical analysis proposed by Persson [420]. When the cantilever tip oscillates in close proximity to the Nb film, the time-dependent mechanical stresses induced in the sample produce

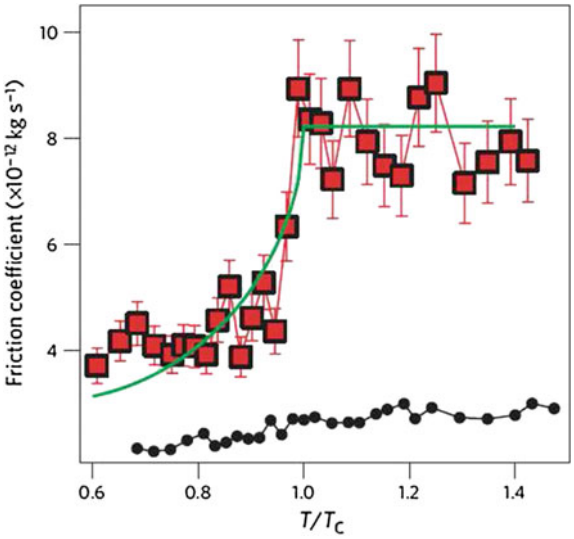

Fig. 15.2 Temperature variation of the friction coefficient Γ across the critical point $T_c = 9.2$ K of Nb. The *red squares* correspond to a separation $d = 0.5$ nm between the tip and the sample. The data are well fitted by the analytic curve expected from the BCS theory (*green line*). The *black dots* correspond to the temperature dependence of the friction coefficient Γ_0 measured at a separation d of several micrometres (free cantilever). From [166]

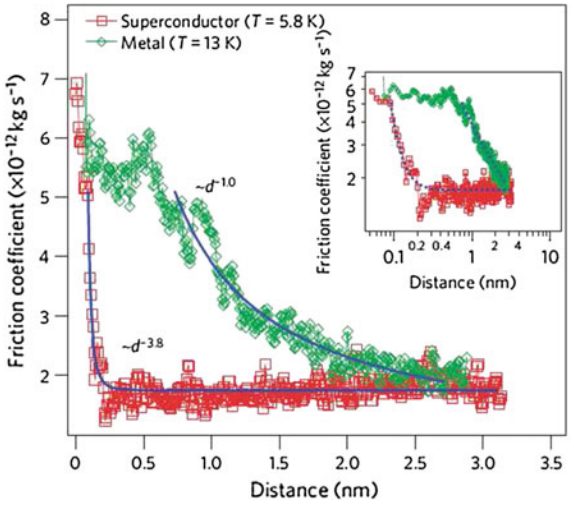

Fig. 15.3 Distance dependence of the friction coefficient in the metallic and in the superconducting state of Nb. The contact potential was compensated for both curves. The data are approximated by an inverse power law $\Gamma \sim 1/d^n$ formula, with $n = 1.0$ for metal Nb and $n = 3.8$ for superconductor. At a tip sample distance $d = 0.5$ nm, the friction coefficient is approximately three times larger in the metallic state ($\Gamma = 5.2 \times 10^{-12}$ kg s^{-1}) when compared with the superconducting state ($\Gamma = 1.8 \times 10^{-12}$ kg s^{-1}). The *inset* shows the same experimental data on a double logarithmic scale. From [166]

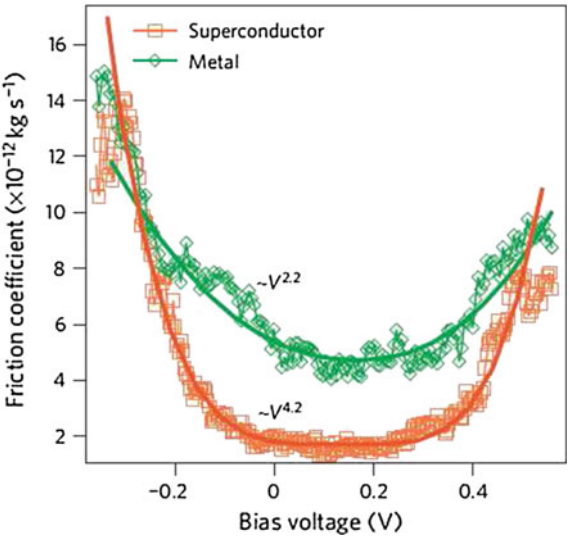

Fig. 15.4 Non-contact friction as a function of the bias voltage V in the metallic and superconducting state of Nb. The pendulum oscillates at a distance $d = 0.5$ nm from the Nb surface. Note that friction has a quadratic dependence for metal Nb, whereas it varies as the fourth power of V below the critical temperature T_c. From [166]

longitudinal acoustic surface waves. As the energy required to break up a Cooper pair into two quasiparticles ($\sim 10^{-4}$ eV) is much larger than the typical energy of acoustic phonons ($\sim 10^{-6}$ eV), the acoustic waves can interact only with the normal electrons near the Fermi surface. When the transition temperature T_c is approached from below, the acoustic wave attenuation rises rapidly, reflecting the increasing normal electron population that causes the electron-induced friction. For a BCS superconductor, the electronic friction caused by phonon electron interaction is expected to vary with the temperature T according to the relation [421]

$$\frac{\Gamma(T)}{\Gamma(T_c)} = \frac{2}{\exp\left[\Delta(T)/k_B T\right] + 1} \tag{15.13}$$

where the energy bandgap Δ depends on the temperature T as [423]

$$\Delta(T) = C \frac{k_B T_c}{\sqrt{1 - T/T_c}} \tag{15.14}$$

The proportionality coefficient C in (15.13) is the same for all BCS superconductors and is equal to 3.52. This quantity determines the ratio between the energy gap at $T = 0$ and the thermal energy at $T = T_c$. The temperature dependence given by previous equations was first verified in pioneering measurements of longitudinal acoustic wave attenuation [424], which were among the first experimental verifications of the BCS theory. The data in Fig. 15.2 are also in agreement with (15.13) and (15.14), with the fit parameter $C = 3.8 \pm 0.7$. This gives a first indication that electronic friction should play a major role, not only in the normal state but also in a

range of a few degrees below the critical point T_c. Further support for this hypothesis comes from the distance dependence of the friction coefficient in Fig. 15.3.

In their measurements on gold, Stipe et al. [21] also fitted the data using the power law $\Gamma \sim 1/d^n$, with $n = 1.3 \pm 0.2$. This value is consistent with the exponent $d = 1.5$ expected for the friction caused (on a cylindrical tip) by a 2D electron system in the metal [170, 171, 422] (see Sect. 14.1). For a spherical tip, the exponent predicted by the theory is $n = 1$, which is in very good agreement with measurements in [166] at $T = 13$ K.

The situation changes when the sample enters the superconducting regime. The steeper distance decay observed at $T = 5.8$ K shows that the electronic friction is not any more the dominant dissipation channel at this temperature. A major contribution to friction must therefore come from the excitations of phonons in the Nb surface. Again we predicted [170, 171, 422] (see also Sect. 15.1) that, when a spherical tip oscillates laterally above an elastic surface (at a fixed frequency), the phonon friction coefficient is proportional to $F^2(d)$, where $F(d)$ is the static force resulting from the interaction between the tip and the surface. According to the Lifshitz theory [42], the elastic stress caused by the van der Waals interaction leads to a static force $F(d) \sim 1/d^2$, so that the phonon friction coefficient Γ_{ph} is expected to vary as d^{-4}. The exponent $n = 3.8 \pm 0.3$ describing the dependence of friction on the inverse of d in measurements in [166] in the superconducting state of Nb is in excellent agreement with this prediction. The enhanced role of phononic friction (compared with electronic friction) below T_c is confirmed by the voltage dependence of the coefficient Γ that is shown in Fig. 15.4. As $F(d) \sim V^2$, phononic friction has to vary as the fourth power of the voltage V. Conversely, the friction coefficient Γ_{el} due to ohmic losses of the electromagnetic field energy inside the sample follows a quadratic law (see Sect. 14.1). This is exactly what was observed in measurements [166] in the superconducting and in the metallic state.

15.3 Non-contact Friction Due to the Internal Friction of the Substrate

The friction coefficient due to the internal friction is determined by (15.4). However, in contrast to the phononic friction, large values of $q \gg \omega/c_t$ play the most important role for the internal friction. For $q \gg \omega/c_s$ the tensor component M_{zz} is given by [213]

$$M_{zz} = \frac{2(1-\nu^2)}{Eq}, \tag{15.15}$$

where $E(\omega)$ is the complex elastic modulus and ν is the Poisson ratio.

15.3.1 van der Waals Interaction

For $R \gg d$, only the σ_{zz} component of the stress tensor due to the van der Waals interaction is important. In this case, for vibrations of the cylindrical tip parallel to the sample surface, we get

$$\sigma_z(\mathbf{q}) = \int d^2x e^{i\mathbf{qx}} \frac{\partial}{\partial x} \sigma_{zz}(\mathbf{x}) =$$

$$= -\frac{iq_x \hbar \omega_p R^{1/2}}{2^7 d^{5/2}} \frac{\sin(q_y w/2)}{q_y} (3 + \xi^2 + 3\xi) e^{-\xi}, \tag{15.16}$$

where σ_{zz} is given by (S.3) from Appendix S1 and $\xi = \sqrt{2dR} q_x$. Using (15.16) and (15.15) in (15.4), for cylindrical tip we get

$$\Gamma_{\parallel}^{c} = \frac{75\pi}{2^{16}} \frac{w\hbar^2\omega_p^2}{d^6} \frac{\mathrm{Im}\left(E/(1-\nu^2)\right)}{\omega |E/(1-\nu^2)|^2}. \tag{15.17}$$

For a spherical tip, similar calculations give

$$\Gamma_{\parallel}^{s} = \frac{0.25}{2^9\sqrt{2\pi}} \frac{R^{1/2}\hbar^2\omega_p^2}{d^{11/2}} \frac{\mathrm{Im}\left(E/(1-\nu^2)\right)}{\omega |E/(1-\nu^2)|^2}. \tag{15.18}$$

In general, $\mathrm{Im}\, E(\omega)$ has many resonance peaks, corresponding to different thermally activated relaxation processes. One important source of internal friction at high frequencies is related to thermal currents: elastic compression of a material is commonly associated with heating effects. If the compression takes place sufficiently rapidly, there is no opportunity for heat to be conducted away, while, for very slow compression, temperature gradients are eliminated by thermal conduction. In both of these cases, the process of compression will be reversible. In the former case it will be adiabatic and in the latter case isothermal. In both of these limiting cases, the contribution from thermal current to the internal friction will be negligible. However, in the intermediate frequency regime, we expect dissipation of mechanical energy into heat. The characteristic frequency for the maximum dissipation will be of the order of $\omega_t = 1/\tau$ where, from dimensional arguments, we expect the relaxation time $\tau \sim l^2/D$, where l is the linear size of the compression region and the thermal diffusibility $D = \kappa/\rho C_p$ (where C_p is the specific heat and κ the heat conductivity). For $l \sim 10^3$ Å this gives for gold $\omega_t \approx 10^{11}$ s^{-1}, which is much higher than the resonance frequency of the cantilever of the atomic force microscope. Another very important contribution to the internal friction is point-defect flipping. This involves thermally activated transitions of point defects or loose sites in crystalline and amorphous network. A special case is the vibrational motion of adsorbates at the surface of the substrate and/or on the tip, as was treated separately in Sect. 14.1.

Another contribution to the internal friction comes from grain-boundary slip [352]. For a copper cylindrical tip and a copper substrate using $d = 10\,\text{nm}$, $w = 7\,\mu\text{m}$, $R = 1\,\mu\text{m}$, $\omega = 10^4\ \text{s}^{-1}$, and, as is typical for metals [353], $\text{Im}\,E(\omega)/|E(\omega)| \approx 10^{-5}$ and $E \approx 10^{11}\,\text{N/m}^2$, gives $\Gamma_{\parallel}^{c} \approx 10^{-16}\,\text{kgs}^{-1}$. Thus, at this separation, the internal friction gives a much smaller contribution to the friction coefficient than the electrostatic friction due to bias voltage or spatial variation of the surface potential. However, internal friction can give the dominant contribution for small separations $d \leq 1\,\text{nm}$. For a spherical tip with $R = 1\,\mu\text{m}$, the friction coefficient is two orders of magnitude smaller. Finally we note, as a curiosity, that the internal friction of solids gives a very important contribution to the rolling resistance of the most solids [425], and is the main contribution to rubber friction on rough substrates; for example, road surface [426], where, in the transition region between the rubbery and glassy region of the rubber visco elastic spectra, $\text{Im}\,E(\omega)/|E(\omega)| \approx 1$.

Appendix A
Spectral Function of Fluctuations of the Electric Fields

Using (3.33), (3.34) and (3.62), we get

$$\left\langle E_i(\mathbf{r})E_j^*(\mathbf{r}')\right\rangle_\omega = \frac{\hbar}{8\pi^2}\coth\left(\frac{\hbar\omega}{2k_BT}\right)\int d\mathbf{r}''\int d\mathbf{r}'''\mathrm{Im}\varepsilon_{kl}(\mathbf{r}'',\mathbf{r}''')D_{ik}(\mathbf{r},\mathbf{r}'')D_{jl}^*(\mathbf{r}',\mathbf{r}''')$$

$$= \frac{\hbar}{16\pi^2 i}\coth\left(\frac{\hbar\omega}{2k_BT}\right)\int d\mathbf{r}''\int d\mathbf{r}'''\left[\varepsilon_{kl}(\mathbf{r}'',\mathbf{r}''')D_{ik}(\mathbf{r},\mathbf{r}'')\right]D_{jl}^*(\mathbf{r}',\mathbf{r}''') - D_{ik}(\mathbf{r},\mathbf{r}'')\left[\varepsilon_{kl}^*(\mathbf{r}'',\mathbf{r}''')D_{jl}^*(\mathbf{r}',\mathbf{r}''')\right]$$

$$= \frac{\hbar c^2}{16\pi^2 i\omega^2}\coth\left(\frac{\hbar\omega}{2k_BT}\right)\int dS_{1l}''\times$$

$$\times\Big\{D_{ik}(\mathbf{r},\mathbf{r}'')\left(\nabla_l''D_{jk}^*(\mathbf{r}',\mathbf{r}'') - \nabla_k''D_{jl}^*(\mathbf{r}',\mathbf{r}'')\right) -$$

$$- D_{jk}^*(\mathbf{r}',\mathbf{r}'')(\nabla_l''D_{ik}(\mathbf{r},\mathbf{r}'') - \nabla_k''D_{il}(\mathbf{r},\mathbf{r}''))\Big\}, \tag{A.1}$$

where we have transformed an integral over the volume of the body to an integral over the surface of the body. Assume that the two points $\mathbf{r}$ and $\mathbf{r}'$ lie outside the bodies. Using that outside the body for $\mathbf{r}\neq\mathbf{r}'\neq\mathbf{r}''$

$$D_{ik}(\mathbf{r},\mathbf{r}'')\nabla_k''D_{jl}^*(\mathbf{r}',\mathbf{r}'') = \nabla_k''\Big(D_{ik}(\mathbf{r},\mathbf{r}'')D_{jl}^*(\mathbf{r}',\mathbf{r}'')\Big), \tag{A.2}$$

$$D_{Jk}^*(\mathbf{r}',\mathbf{r}'')\nabla_k''D_{il}(\mathbf{r},\mathbf{r}'') = \nabla_k''\Big(D_{jk}^*(\mathbf{r}',\mathbf{r}'')D_{il}(\mathbf{r},\mathbf{r}'')\Big), \tag{A.3}$$

and performing the surface integral in (A.1) gives:

$$\left\langle E_i(\mathbf{r})E_j^*(\mathbf{r}')\right\rangle_\omega = \frac{\hbar c^2}{16\pi^2 i\omega^2}\coth\left(\frac{\hbar\omega}{2k_BT}\right)\times$$

$$\times\int d\mathbf{S}_1''\cdot\Big\{D_{ik}(\mathbf{r},\mathbf{r}'')\nabla''D_{jk}^*(\mathbf{r}',\mathbf{r}'') - D_{jk}^*(\mathbf{r}',\mathbf{r}'')\nabla''D_{ik}(\mathbf{r},\mathbf{r}'')\Big\}. \tag{A.4}$$

A.I. Volokitin and B.N.J. Persson, *Electromagnetic Fluctuations at the Nanoscale*,
NanoScience and Technology, DOI 10.1007/978-3-662-53474-8

Appendix B
Fluctuating Electromagnetic Field in the Vacuum Gap Between Two Plane Surfaces Moving Relative to Each Other

We consider two semi-infinite solids with flat parallel surfaces separated by a distance d and moving with velocity V relative to each other, see Fig. 5.1. We introduce the two the coordinate systems K and K' with coordinate axes xyz and $x'y'z'$. In the K system, body **1** is at rest, while body **2** is moving with the velocity V along the x-axis (the xy and $x'y'$ planes are in the surface of body **1**, x and x'-axes have the same direction, and the z and z'-axes point toward body **2**). In the K' system body, **2** is at rest while body **1** is moving with velocity $-V$ along the x-axis. Since the system is translational invariant in the $\mathbf{x} = (x, y)$ plane, the electromagnetic field can be represented by the Fourier integrals

$$\mathbf{E}(\mathbf{x}, z, t) = \int_{-\infty}^{\infty} d\omega \int \frac{d^2q}{(2\pi)^2} e^{i\mathbf{q}\cdot\mathbf{x} - i\omega t} \mathbf{E}(\mathbf{q}, \omega, z), \tag{B.1}$$

$$\mathbf{B}(\mathbf{x}, z, t) = \int_{-\infty}^{\infty} d\omega \int \frac{d^2q}{(2\pi)^2} e^{i\mathbf{q}\cdot\mathbf{x} - i\omega t} \mathbf{B}(\mathbf{q}, \omega, z), \tag{B.2}$$

where $\mathbf{E}$ and $\mathbf{B}$ are the electric and magnetic induction field, respectively, and $\mathbf{q}$ is the 2D wave vector in xy-plane. After Fourier transformation, it is convenient to decompose the electromagnetic field into s- and p-polarized components. For the p- and s-polarized electromagnetic waves, the electric field $\mathbf{E}(\mathbf{q}, \omega, z)$ is in the plane of incidence, and perpendicular to that plane, respectively. In the vacuum gap between the bodies, the electric field, $\mathbf{E}(\mathbf{q}, \omega, z)$, and the magnetic induction field, $\mathbf{B}(\mathbf{q}, \omega, z)$, can be written in the form

$$\mathbf{E}(\mathbf{q}, \omega, z) = \left(v_s \hat{n_s} + v_p \hat{n_p}^+\right) e^{ik_z z} + \left(w_s \hat{n_s} + w_p \hat{n_p}^-\right) e^{-ik_z z}, \tag{B.3}$$

$$\begin{aligned}\mathbf{B}(\mathbf{q}, \omega, z) = \frac{c}{\omega} \Big[&\left([\mathbf{k}^+ \times \hat{n}_s] v_s + [\mathbf{k}^+ \times \hat{n}_p^+] v_p\right) e^{ik_z z} \\ &+ \left([\mathbf{k}^- \times \hat{n}_s] w_s + [\mathbf{k}^- \times \hat{n}_p^-] w_p\right) e^{-ik_z z} \Big],\end{aligned} \tag{B.4}$$

A.I. Volokitin and B.N.J. Persson, *Electromagnetic Fluctuations at the Nanoscale*, NanoScience and Technology, DOI 10.1007/978-3-662-53474-8

$\mathbf{k}^{\pm} = \mathbf{q} \pm \hat{z}k_z$, $k_z = ((\omega/c)^2 - q^2)^{1/2}$, $\hat{n}_s = [\hat{z} \times \hat{q}] = (-q_y, q_x, 0)/q$, $\hat{n}_p^{\pm} =$, $= [\hat{k}^{\pm} \times \hat{n}_s] = (\mp q_x k_z, \mp q_y k_z, q^2)/(kq)$, $k = \omega/c$. At the surfaces of the bodies, the amplitude of the outgoing electromagnetic wave must be equal to the amplitude of the reflected wave plus the amplitude of the radiated wave. Thus, the boundary conditions for the electromagnetic field at $z = 0$ in the K-reference frame can be written in the form

$$v_{p(s)} = R_{1p(s)}(\omega, q) w_{p(s)} + E^f_{1p(s)}(\omega, q), \tag{B.5}$$

where $R_{1p(s)}(\omega)$ is the reflection amplitude for surface **1** for the $p(s)$-polarized electromagnetic field, and where $E^f_{1p(s)}(\omega)$ is the amplitude of the fluctuating electric field radiated by body **1** for a $p(s)$-polarized wave. In the $K^{'}$-reference frame the electric field can be written in the form

$$\mathbf{E}'(\mathbf{q}', \omega', z) = \left(v'_s \hat{n}'_s + v'_p \hat{n}'^{+}_p\right) e^{ik_z z} + \left(w'_s \hat{n}'_s + w'_p \hat{n}'^{-}_p\right) e^{-ik_z z}, \tag{B.6}$$

where $\mathbf{q}' = (q'_x, q_y, 0)$, $q'_x = (q_x - \beta k)\gamma$, $\omega' = (\omega - V q_x)\gamma$, $\gamma = 1/\sqrt{1-\beta^2}$, $\beta = V/c$, $\hat{n}'_s = (-q_y, q'_x, 0)/q'$, $\hat{n}'^{\pm}_p = (\mp q'_x k_z, \mp q_y k_z, q'^2)/(k' q')$,

$$q' = \gamma \sqrt{q^2 - 2\beta k q_x + \beta^2 (k^2 - q_y^2)}.$$

The boundary conditions at $z = d$ in the $K^{'}$-reference frame can be written in a form similar to (B.5):

$$w'_{p(s)} = e^{2ik_z d} R_{2p(s)}(\omega', q') v'_{p(s)} + e^{ik_z d} E'^f_{2p(s)}(\omega', q'), \tag{B.7}$$

where $R_{2p(s)}(\omega)$ is the reflection amplitude for surface **2** for the $p(s)$-polarized electromagnetic field, and where $E^f_{2p(s)}(\omega)$ is the amplitude of the fluctuating electric field radiated by body **2** for a $p(s)$-polarized wave. A Lorentz transformation for the electric field gives:

$$E'_x = E_x, \; E'_y = (E_y - \beta B_z)\gamma, \; E'_z = (E_z + \beta B_y)\gamma. \tag{B.8}$$

Using (B.3), (B.4), (B.6) and (B.8) we get

$$v'_p = \frac{k'\gamma}{kqq'} \left[-\beta k_z q_y v_s + (q^2 - \beta k q_x) v_p\right], \tag{B.9}$$

$$w'_p = \frac{k'\gamma}{kqq'} \left[\beta k_z q_y w_s + (q^2 - \beta k q_x) w_p\right], \tag{B.10}$$

$$v'_s = \frac{k'\gamma}{kqq'} \left[\beta k_z q_y v_p + (q^2 - \beta k q_x) v_s\right], \tag{B.11}$$

$$w_s' = \frac{k'\gamma}{kqq'}\left[-\beta k_z q_y w_p + (q^2 - \beta k q_x) w_s\right]. \tag{B.12}$$

Substituting (B.9)–(B.12) in (B.7) and using (B.5), we get

$$\begin{aligned}&(q^2 - \beta k q_x) D_{pp} w_p + \beta k_z q_y D_{sp} w_s \\ &= e^{2ik_z d} R_{2p}' \left[(q^2 - \beta k q_x) E_{1p}^f - \beta k_z q_y E_{1s}^f\right] + \frac{kqq'}{k'\gamma} e^{ik_z d} E_{2p}'^f,\end{aligned} \tag{B.13}$$

$$\begin{aligned}&(q^2 - \beta k q_x) D_{ss} w_s - \beta k_z q_y D_{ps} w_p \\ &= e^{2ik_z d} R_{2s}' \left[(q^2 - \beta k q_x) E_{1s}^f + \beta k_z q_y E_{1p}^f\right] + \frac{kqq'}{k'\gamma} e^{ik_z d} E_{2s}'^f,\end{aligned} \tag{B.14}$$

where

$$D_{pp} = 1 - e^{2ik_z d} R_{1p} R_{2p}',\ D_{ss} = 1 - e^{2ik_z d} R_{1s} R_{2s}',$$

$$D_{sp} = 1 + e^{2ik_z d} R_{1s} R_{2p}',\ D_{ps} = 1 + e^{2ik_z d} R_{1p} R_{2s}',$$

$R_{2p(s)}' = R_{2p(s)}(\omega', q')$. From (B.13), (B.14) and (B.5) we get

$$\begin{aligned}w_p = \Big\{ &\left[(q^2 - \beta k q_x)^2 R_{2p}' D_{ss} - \beta^2 k_z^2 q_y^2 R_{2s}' D_{sp}\right] E_{1p}^f e^{2ik_z d} \\ &- \beta k_z q_y (q^2 - \beta k q_x)(R_{2p}' + R_{2s}') E_{1s}^f e^{2ik_z d} \\ &+ \frac{kqq'}{k'\gamma}\left[(q^2 - \beta k q_x) D_{ss} E_{2p}'^f - \beta k_z q_y D_{sp} E_{2s}'^f\right] e^{ik_z d}\Big\} \Delta^{-1},\end{aligned} \tag{B.15}$$

$$\begin{aligned}v_p = \Big\{ &\left[(q^2 - \beta k q_x)^2 D_{ss} + \beta^2 k_z^2 q_y^2 D_{sp}\right] E_{1p}^f \\ &- \beta k_z q_y (q^2 - \beta k q_x) R_{1p} (R_{2p}' + R_{2s}') e^{2ik_z d} E_{1s}^f \\ &+ \frac{kqq'}{k'\gamma} R_{1p}\left[(q^2 - \beta k q_x) D_{ss} E_{2p}'^f - \beta k_z q_y D_{sp} E_{2s}'^f\right] e^{ik_z d}\Big\} \Delta^{-1},\end{aligned} \tag{B.16}$$

$$\begin{aligned}w_s = \Big\{ &\left[(q^2 - \beta k q_x)^2 R_{2s}' D_{pp} - \beta^2 k_z^2 q_y^2 R_{2p}' D_{ps}\right] E_{1s}^f e^{2ik_z d} \\ &+ \beta k_z q_y (q^2 - \beta k q_x)(R_{2p}' + R_{2s}') E_{1p}^f e^{2ik_z d} \\ &+ \frac{kqq'}{k'\gamma}\left[(q^2 - \beta k q_x) D_{pp} E_{2s}'^f + \beta k_z q_y D_{ps} E_{2p}'^f\right] e^{ik_z d}\Big\} \Delta^{-1},\end{aligned} \tag{B.17}$$

$$
\begin{aligned}
v_s = \Big\{ & \left[(q^2 - \beta k q_x)^2 D_{pp} + \beta^2 k_z^2 q_y^2 D_{ps} \right] E_{1s}^f \\
& + \beta k_z q_y (q^2 - \beta k q_x) R_{1p} (R'_{2p} + R'_{2s}) e^{2ik_z d} E_{1p}^f \\
& + \frac{kqq'}{k'\gamma} R_{1s} \left[(q^2 - \beta k q_x) D_{pp} E_{2s}^{\prime f} + \beta k_z q_y D_{ps} E_{2p}^{\prime f} \right] e^{ik_z d} \Big\} \Delta^{-1},
\end{aligned}
\tag{B.18}
$$

$$
\Delta = (q^2 - \beta k q_x)^2 D_{ss} D_{pp} + \beta^2 k_z^2 q_y^2 D_{ps} D_{sp}.
$$

The fundamental characteristic of the fluctuating electromagnetic field is the correlation function, determining the average of the product of the amplitudes $E_{p(s)}^f(\mathbf{q}, \omega)$. According to the general theory of the fluctuating electromagnetic field (see Sect. 3.2):

$$
\begin{aligned}
\left\langle |E_{p(s)}^f(\mathbf{q}, \omega)|^2 \right\rangle = \frac{\hbar\omega^2}{2c^2|k_z|^2} \left(n(\omega) + \frac{1}{2} \right) \Big[& (k_z + k_z^*)(1 - |R_{p(s)}|^2) \\
& + (k_z - k_z^*)(R_{p(s)}^* - R_{p(s)}) \Big],
\end{aligned}
\tag{B.19}
$$

where $\langle ... \rangle$ denotes the statistical average over the random field. We note that k_z is real for $q < \omega/c$ (propagating waves), and purely imaginary for $q > \omega/c$ (evanescent waves). The Bose-Einstein factor

$$
n(\omega) = \frac{1}{e^{\hbar\omega/k_B T} - 1}.
$$

Thus, for $q < \omega/c$ and $q > \omega/c$ the correlation functions are determined by the first and the second terms in (B.19), respectively.

Appendix C
The Green's Function of the Electromagnetic Field in the Vacuum Gap Between Two Plane Surfaces

Suppose that the half-space $z < 0$ is occupied by a solid at temperature T_1 with the reflection matrix $R_1(\mathbf{q}, \omega)$. Similarly, the half-space $z > d$ is occupied with a solid at temperature T_2 with the reflection matrix $R_2(\mathbf{q}, \omega)$. The 2×2 reflection matrix R_i determines the reflection amplitudes for the waves with different polarization $\lambda = (s, p)$. This matrix is diagonal for isotropic materials. However, in general cases of anisotropic materials, this matrix is non diagional

$$R_i = \begin{pmatrix} R^i_{ss} & R^i_{sp} \\ R^i_{ps} & R^i_{ss} \end{pmatrix}.$$

The region $0 < z < d$ is assumed to be vacuum. Here $\mathbf{q}$ is the surfaces component of wave vector $\mathbf{k} = (\mathbf{q}, k_z)$ and

$$k_z = \sqrt{\left(\frac{\omega}{c}\right)^2 - q^2}. \tag{C.1}$$

Since the system is uniform in the $\mathbf{x} = (x, y)$ plane, the Green's function $D_{ij}(\mathbf{r}, \mathbf{r}')$ can be represented by the Fourier integral

$$D_{ij}(\mathbf{r}, \mathbf{r}') = \int \frac{\mathrm{d}^2 q}{(2\pi)^2} e^{\mathrm{i}\mathbf{q}(\mathbf{x}-\mathbf{x}')} D_{ij}(z, z', \mathbf{q}, \omega). \tag{C.2}$$

In the xy-plane it is convenient to choose the coordinate axes along the vectors $\hat{q} = \mathbf{q}/q$ and $\hat{n} = \hat{z} \times \hat{q}$. In this coordinate system (3.33), (3.34) for the Green's functions become

$$\left(k_z^2 + \frac{\partial^2}{\partial z^2}\right) D_{nn}(z, z') = -\frac{4\pi\omega^2}{c^2}\delta(z - z'), \tag{C.3}$$

$$\left(\frac{\omega^2}{c^2} + \frac{\partial^2}{\partial z^2}\right) D_{qq}(z, z') - \mathrm{i}q \frac{\partial}{\partial z} D_{zq}(z, z') = -\frac{4\pi\omega^2}{c^2}\delta(z - z'), \tag{C.4}$$

A.I. Volokitin and B.N.J. Persson, *Electromagnetic Fluctuations at the Nanoscale*, NanoScience and Technology, DOI 10.1007/978-3-662-53474-8

$$k_z^2 D_{zq}(z,z') - \mathrm{i}q\frac{\partial}{\partial z} D_{qq}(z,z') = 0, \tag{C.5}$$

$$k_z^2 D_{zz}(z,z') - \mathrm{i}q\frac{\partial}{\partial z} D_{qz}(z,z') = -\frac{4\pi\omega^2}{c^2}\delta(z-z'), \tag{C.6}$$

$$k_z^2 D_{qz}(z,z') + \mathrm{i}q\frac{\partial}{\partial z'} D_{qq}(z,z') = 0. \tag{C.7}$$

The components D_{qn}, D_{zn} of the Green's function vanish, since the equations for them turn out to be homogeneous. Solving the system of (C.3)–(C.7) amounts to solving two equations: (C.3) for D_{nn} and the equation for D_{qq} which follows from (C.4), (C.5)

$$\left(k_z^2 + \frac{\partial^2}{\partial z^2}\right) D_{qq}(z,z') = -4\pi k_z^2 \delta(z-z'), \tag{C.8}$$

after which D_{qz}, D_{zq} and D_{zz} for $z \neq z'$ are obtained as

$$D_{qz} = -\frac{\mathrm{i}q}{k_z^2}\frac{\partial}{\partial z'} D_{qq};\ D_{zq} = \frac{\mathrm{i}q}{k_z^2}\frac{\partial}{\partial z} D_{qq}; \tag{C.9}$$

$$D_{zz} = \frac{q^2}{k_z^4}\frac{\partial^2}{\partial z \partial z'} D_{qq}. \tag{C.10}$$

In the vacuum gap, $0 < z < d$ the Green's matrix can be written in the form

$$\hat{\mathbf{D}}(z,z') = \hat{\mathbf{D}}_0(z,z') + \mathbf{v}_\lambda \hat{n}_\lambda^+ e^{ik_z z} + \mathbf{w}_\lambda \hat{n}_\lambda^- e^{-ik_z z} \tag{C.11}$$

where the Green's function of the electromagnetic field for a free space is given by

$$\hat{\mathbf{D}}_0(z,z') = e^{ik_z|z-z'|}\begin{cases} \hat{\mathbf{D}}_0^+(z,z'), \text{ for } z > z' \\ \hat{\mathbf{D}}_0^-(z,z'), \text{ for } z < z' \end{cases}, \tag{C.12}$$

where

$$\mathbf{D}_0^\pm(z,z') = \frac{2\pi i k^2}{k_z}\hat{n}_\lambda^\pm \hat{n}_\lambda^\pm \tag{C.13}$$

where $k_z = ((\omega/c)^2) - q^2)^{1/2}$, $\lambda = (s, p)$, $\hat{n}_s^\pm = [\hat{z} \times \hat{q}] = (-q_y, q_x, 0)/q$, $\hat{n}_p^\pm = [\hat{k}^\pm \times \hat{n}_s^\pm] = (\mp \mathbf{q}k_z, q^2/(kq)$, $k = \omega/c$, $\hat{k}^\pm = (\mathbf{q} \pm \hat{z}k_z)/k$, $\mathbf{q} = (q_x, q_y, 0)$. At the boundaries $z = 0$ and $z = d$, the amplitude of the scattered wave is equal to amplitude of incident wave times to the corresponding reflection amplitude. The boundary conditions for the Green's matrix give

$$\mathbf{v} = R_1\left(\frac{2\pi i k^2}{k_z} e^{ik_z z'}\hat{\mathbf{n}}^- + \mathbf{w}\right) \qquad z = 0,$$

$$\mathbf{w} = R_2 e^{2ik_z d}\left(\frac{2\pi i k^2}{k_z} e^{-ik_z z'}\hat{\mathbf{n}}^+ + \mathbf{v}\right) \qquad z = d, \tag{C.14}$$

where $\mathbf{v} = (\mathbf{v}_s, \mathbf{v}_p)$, $\mathbf{w} = (\mathbf{w}_s, \mathbf{w}_p)$, $\hat{\mathbf{n}}^{\pm} = (\hat{n}_s^{\pm}, \hat{n}_p^{\pm})$. The substitution of the solution of the system of the (C.14) in formula (C.11) gives the Green's matrix. The Green's matrix for $z > z'$ can be written in the form [195, 196]

$$\hat{\mathbf{D}} = \frac{2\pi i\omega^2}{k_z c^2}\left[\hat{\mathbf{D}}_{12}\left(\hat{\mathbf{I}}e^{\mathrm{i}k_z(z-z')} + \hat{\mathbf{R}}_1 e^{\mathrm{i}k_z(z+z')}\right) + \hat{\mathbf{D}}_{21}\left(\hat{\mathbf{R}}_2\hat{\mathbf{R}}_1 e^{2\mathrm{i}k_z d}e^{\mathrm{i}k_z(z'-z)} + \hat{\mathbf{R}}_2 e^{2\mathrm{i}k_z d}e^{-\mathrm{i}k_z(z+z')}\right)\right], \tag{C.15}$$

where

$$\hat{\mathbf{R}}_1 = \hat{\mathbf{n}}^+ R_1 \hat{\mathbf{n}}^-,\ \hat{\mathbf{R}}_2 = \hat{\mathbf{n}}^- R_2 \hat{\mathbf{n}}^+,\ \hat{\mathbf{I}} = \hat{\mathbf{n}}^+ \mathrm{I}\hat{\mathbf{n}}^+,\ \hat{\mathbf{D}}_{12} = \hat{\mathbf{n}}^+ D_{12}\hat{\mathbf{n}}^+,\ \hat{\mathbf{D}}_{21} = \hat{\mathbf{n}}^- D_{21}\hat{\mathbf{n}}^-,\ D_{ij} = [\mathrm{I} - e^{2ik_z d}R_i R_j]^{-1},$$

where I is the 2×2 unit matrix. For isotropic materials, the Green's matrix takes the form

$$\hat{\mathbf{D}}^{isotropic} = \frac{2\pi i\omega^2}{k_z c^2}\sum_{\lambda=(s,p)}\Big[\hat{\mathbf{n}}_\lambda^+\hat{\mathbf{n}}_\lambda^+ e^{\mathrm{i}k_z(z-z')} + \hat{\mathbf{n}}_\lambda^+\hat{\mathbf{n}}_\lambda^- R_{1\lambda}e^{\mathrm{i}k_z(z+z')} + \hat{\mathbf{n}}_\lambda^-\hat{\mathbf{n}}_\lambda^- R_{1\lambda}R_{2\lambda}e^{2\mathrm{i}k_z d}e^{\mathrm{i}k_z(z'-z)} + \hat{\mathbf{n}}_\lambda^-\hat{\mathbf{n}}_\lambda^+ R_{2\lambda}e^{2\mathrm{i}k_z d}e^{-\mathrm{i}k_z(z+z')}\Big]\frac{1}{1 - e^{2ik_z d}R_{1\lambda}R_{2\lambda}}, \tag{C.16}$$

In our approach, the calculation of the reflection amplitudes for s- and p-polarized waves constitutes two separate problems, which can be solved taking into account non-local effects. For the local optic case, the reflection amplitudes are determined by the well-known Fresnel formulas

$$R_{ip} = \frac{\varepsilon_i k_z + s_i}{\varepsilon_i k_z + s_i}, \qquad R_{is} = \frac{\mu_i k_z - s_i}{k_z + s_i}, \tag{C.17}$$

where ε_i and μ_i are the complex dielectric and magnetic permeability for body i, respectively, and

$$s_i = \sqrt{\frac{\omega^2}{c^2}\varepsilon_i\mu_i - q^2}. \tag{C.18}$$

Appendix D
Reflection Amplitudes for Electromagnetic Waves for Medium with Spatial Dispersion

At $d < l, v_F/\omega$, where l is the electron mean free path, and where v_F is the Fermi velocity, the system will be characterized by non-local dielectric function $\epsilon(\mathbf{q}, \omega)$. Volume non-local optic effects can be described by an approach, proposed some years ago for the investigations of the optical properties of a semi-infinite electron gas [198].

According to [198], the reflection amplitude for p-polarized electromagnetic fields, incident on the flat surface, is determined by [198]

$$R_p = \frac{p - Z_p}{q + Z_p}, \tag{D.1}$$

where the surface impedance Z_p is given by

$$Z_p = \frac{2i}{\pi} \int_0^\infty \frac{\mathrm{d}q_z}{Q^2} \left(\frac{q^2}{\epsilon_l(\omega, Q)} + \frac{\left(\frac{\omega}{c}\right)^2 q_z^2}{\left(\frac{\omega}{c}\right)^2 \epsilon_t(\omega, Q) - Q^2} \right), \tag{D.2}$$

where ϵ_l is the finite life-time generalization of the longitudinal Lindhard dielectric function, which according to [354] can be written as:

$$\epsilon_l(\omega, Q) = 1 + \frac{(1 + \mathrm{i}/\omega\tau)(\epsilon_l^0(\omega + \mathrm{i}/\tau, Q) - 1)}{1 + (\mathrm{i}/\omega\tau)(\epsilon_l^0(\omega + \mathrm{i}/\tau, Q) - 1)/(\epsilon_l^0(0, Q) - 1)}, \tag{D.3}$$

$$\epsilon_l^0(\omega, Q) = 1 + \frac{3\omega_p^2}{Q^2 v_F^2} f_l, \tag{D.4}$$

$$f_l = \frac{1}{2} + \frac{1}{8z} \left([1 - (z - u)^2] \ln \frac{z - u + 1}{z - u - 1} + [1 - (z + u)^2] \ln \frac{z + u + 1}{z + u - 1} \right), \tag{D.5}$$

A.I. Volokitin and B.N.J. Persson, *Electromagnetic Fluctuations at the Nanoscale*, NanoScience and Technology, DOI 10.1007/978-3-662-53474-8

where $Q^2 = q^2 + q_z^2$, $z = Q/2k_F$, $u = \omega/(Qv_F)$, ω_p is the plasma frequency, τ is the Drude relaxation time, and where v_F and k_F are the Fermi velocity and wave vector, respectively. For s-polarization, the reflection factor is determined by

$$R_s = \frac{1 - Z_s p}{1 + Z_s p}, \tag{D.6}$$

where

$$Z_s = \frac{2i}{\pi} \int_0^\infty \frac{\mathrm{d}q_z}{\left(\frac{\omega}{c}\right)^2 \epsilon_t(\omega, Q) - Q^2}, \tag{D.7}$$

$$\epsilon_t(\omega, Q) = 1 - \frac{\omega_p^2}{\omega(\omega + \mathrm{i}k_z)} f_t, \tag{D.8}$$

$$\begin{aligned} f_t = \frac{3}{8}(z^2 + 3u'^2 + 1) - \frac{3}{32z}\Bigg(& [1 - (z - u')^2]^2 \ln \frac{z - u' + 1}{z - u' - 1} \\ & + [1 - (z + u')^2]^2 \ln \frac{z + u' + 1}{z + u' - 1} \Bigg), \end{aligned} \tag{D.9}$$

$u' = (\omega + \mathrm{i}\tau^{-1})/(Qv_F)$. For the non-degenerate electron gas, the longitudinal and transfers dielectric functions are determined by classical equations [43]:

$$\epsilon_l^0(\omega, Q) = 1 + \left(\frac{\omega_p}{Qv_T}\right)^2 \left[1 + F\left(\frac{\omega}{\sqrt{2}Qv_T}\right)\right], \tag{D.10}$$

$$\epsilon_t(\omega, Q) = 1 + \frac{\omega_p^2}{\omega(\omega + ik_z)} F\left(\frac{\omega + ik_z}{\sqrt{2}Qv_T}\right), \tag{D.11}$$

where the function $F(x)$ is defined by the integral

$$F(x) = \frac{x}{\sqrt{\pi}} \int_{-\infty}^{+\infty} dz \frac{e^{-z^2}}{z - x - i0} \tag{D.12}$$

and $v_T = \sqrt{k_B T/m}$, where m is the electron mass.

Appendix E
Fresnel's Reflection Amplitude for Surfaces with a Layer of Adsorbed Molecules

Let us consider a semi-infinite medium with a flat surface, which coincides with the xy-plane, with the z-axis pointing into medium. The surface of the medium is assumed to be covered with an adsorbed layer, situated at $z = -a$. The plane of incidence of the electromagnetic waves coincides with the xz-plane, and the x-axis is directed along wave vector $\mathbf{q}$. The macroscopic electric field can be written in the form

$$\mathbf{E} = e^{iqx} \times \begin{cases} \mathbf{I}e^{ik_z pz} + \mathbf{R}e^{-ik_z pz}; & z < -a, \\ \mathbf{A}e^{ik_z pz} + \mathbf{B}e^{-ik_z pz}; & -a < z < 0, \\ \mathbf{T}e^{isz}; & z > 0, \end{cases} \tag{E.1}$$

where $k_z = ((\omega/c)^2 - q^2)^{1/2}$, $s = ((\omega/c)^2\varepsilon(\omega) - q^2)^{1/2}$, and $\varepsilon(\omega)$ is dielectric function for the medium. Boundary condition for the normal component of displacement field $\mathbf{D}_\perp$ at $z = -a$ can be obtained, integrating the equation $\nabla \cdot \mathbf{D} = 0$ [199]. As a result we get

$$D_\perp(z = -a + 0) - D_\perp(z = -a - 0) = -\int_{-a-0}^{-a+0} dz \nabla \cdot \mathbf{D}_\parallel, \tag{E.2}$$

where $\mathbf{D}_\parallel$ is the projection of $\mathbf{D}$ on xy-plane. Since $\mathbf{D} = \mathbf{E} + 4\pi\mathbf{P}$, and taking into account that $\mathbf{E}_\parallel$, in contrast to $\mathbf{P}_\parallel$, has no singularities in adsorbed layer, on the right side of (E.2), we can replace $\mathbf{D}_\parallel$ by $4\pi\mathbf{P}_\parallel$. Thus

$$D_\perp(z = -a + 0) - D_\perp(z = -a - 0) = -4\pi \nabla \cdot \mathbf{p}_\parallel, \tag{E.3}$$

where $\mathbf{p}_\parallel$ denotes the component of the polarization vector parallel to the surface, which can be related to electric field: $\mathbf{p}_\parallel = n_a \alpha_\parallel \mathbf{E}_\parallel$, where n_a is the surface density of adsorbed molecules, and $\alpha_\parallel$ is molecule polarizability parallel to the surface.

The boundary condition for $\mathbf{E}_\parallel$ can be derived from Faraday's law [45]

$$\oint \mathbf{E} \cdot d\mathbf{r} = \frac{i\omega}{c} \int \mathbf{B} \cdot d\mathbf{S}. \tag{E.4}$$

A.I. Volokitin and B.N.J. Persson, *Electromagnetic Fluctuations at the Nanoscale*, NanoScience and Technology, DOI 10.1007/978-3-662-53474-8

One typically takes the two integrals around the perimeter and through the interior, respectively, of a rectangle, whose long sides are parallel to and on different sides of the adsorbed layer, and whose short sides are perpendicular to and cross the adsorbed layer, and takes the limit as the short sides become macroscopically infinitesimal. Since $\mathbf{B}_\parallel$ is continuous and has no singularities, in evaluating the right-hand side of (E.4); then as the rectangle shrink to an infinitesimal macroscopic height, the right-hand side of (E.4) makes no contribution.

The macroscopic distribution singularity that may cause $\mathbf{E}_\perp$ to be discontinuous is a δ function in the charge density representing the adsorbate charge. There may also be a δ' function in the charge density representing the normal adsorbate dipole moment, which makes $\mathbf{E}_\parallel$. The integral of $\mathbf{E}$ across a short leg of the rectangle is precisely equal to 4π times the normal component of dipole moment

$$\int_{-a-0}^{-a+0} \big(E_z(\mathbf{x},z) - E_z(\mathbf{x}+\Delta\mathbf{x},z)\big)dz = 4\pi\left(p_z(\mathbf{x}+\Delta\mathbf{x}) - p_z(\mathbf{x})\right) \approx 4\pi\nabla_\parallel p_z(\mathbf{x})\cdot\Delta\mathbf{x}. \tag{E.5}$$

As a result, we get boundary condition for parallel component of electric field

$$\mathbf{E}_\parallel(-a+0) - \mathbf{E}_\parallel(-a-0) = -4\pi\nabla_\parallel p_z(\mathbf{x}). \tag{E.6}$$

In linear response approximation, the normal component of dipole moment can be written in the form

$$\mathbf{p}_\perp = n_a\alpha_\perp\mathbf{E}_\perp, \tag{E.7}$$

where $\alpha_\perp$ is the (complex frequency dependent) adsorbate polarizability perpendicular to the adsorbate layer. In (E.7), $\mathbf{E}_\perp$ can be taken at $z = -a-0$, since the account of dependence $\mathbf{E}_\perp$ on z in adsorbate layer will give rise to corrections of a higher order in q.

For the p-polarized electromagnetic field $\mathbf{I}$, $\mathbf{R}$, $\mathbf{A}$ and $\mathbf{B}$ are in the xz-plane. The components of each are related because each is the amplitude of a transverse wave: $I_x = -(k_z/q)I_z$, $R_x = (k_z/q)R_z$, $A_x = -(k_z/q)A_z$, $B_x = (k_z/q)B_z$. In this case, taking into account (E.2), (E.6), the boundary condition for evanescent waves ($q \gg \omega/c$) at $z = -a$ can be written in the form

$$A_z e^{qa} + B_z^{-qa} - R_z e^{-qa} - I_z e^{qa} = 4\pi q n_a\alpha_\parallel\left(R_z e^{-qa} - I_z e^{qa}\right), \tag{E.8}$$

$$B_z e^{-qa} - A_z e^{qa} - R_z e^{-qa} + I_z e^{qa} = -4\pi n_a\alpha_\perp\left(R_z e^{-qa} + I_z e^{qa}\right). \tag{E.9}$$

At $z = 0$ and for $q \gg \omega|\varepsilon(\omega)|^{1/2}/c$ the reflection amplitude is determined by

$$B_z = \frac{\varepsilon - 1}{\varepsilon + 1}A_z. \tag{E.10}$$

From (E.8)–(E.10) at $qa \ll 1$ we get (6.47) for reflection amplitude R_z.

Appendix F
Comparison with the Results of Philbin and Leonhardt

Philbin and Leohardt (PL) ([122, 123]) calculated the Casimir forces between moving plates and found that there is no quantum friction at all. In [122], PL used the Lifshitz theory and considered only the case of zero temperature. There are two variants of Lifshitz theory. In the first variant, the Maxwell stress tensor is calculated using the electromagnetic field, which was calculated using Rytov's theory. In the second variant, the Maxwell stress tensor is calculated using the Green's functions of the electromagnetic field, which were calculated from Maxwell's equations. Both of these variants give the same results for forces. In [122], PL used the second variant of the Lifshitz theory. The general case of finite and different temperatures was considered by PL in [123]. The theory from [123] contains, as a limiting case, the theory from [122]. In particular, in both of these theories, the authors came to conclusion that there is no lateral force on the plates in relative motion. In [123], PL used the same approach as Volokitin et al. [128] (henceforth referred to as VP; see also Sect. 7.3), but came to the opposite conclusion that there is no 'quantum' friction. Between these two studies, there is a difference only in the technical details. VP calculated the total electromagnetic field in the rest reference frame of surface **1**. The total electromagnetic field contains the contributions from quantum and thermal fluctuations in both bodies. This electromagnetic field was used in the calculations of the stress tensor and the Poynting's vector in the rest reference frame of surface **1**. LP divided the total stress tensor into two contributions from surfaces **1** and **2**. The contribution from surface **2** was first calculated in the rest reference frame of surface **2**. The contribution from the surface **2** again was divided into two components—one from quantum and the other from thermal fluctuations. The separation of the quantum-vacuum from the thermal effect is achieved by the identity

$$\coth\left(\frac{\hbar\omega}{2k_BT}\right) = \mathrm{sgn}(\omega) + 2\mathrm{sgn}(\omega)\left[\exp\left(\frac{\hbar|\omega|}{k_BT_2}\right) - 1\right]^{-1} \tag{F.1}$$

where the first term gives the quantum part and the second term, containing the Plank spectrum, gives the thermal radiation part. The Lorentz transformation for the stress

A.I. Volokitin and B.N.J. Persson, *Electromagnetic Fluctuations at the Nanoscale*, NanoScience and Technology, DOI 10.1007/978-3-662-53474-8

tensor was used to obtain the contribution from thermal fluctuations in body **2** in the rest reference frame of surface **1**. The integrand of this contribution contains the factor

$$2\mathrm{sgn}(\omega')\left[\exp\left(\frac{\hbar|\omega'|}{k_B T_2}\right)-1\right]^{-1} \tag{F.2}$$

As a result, for the total contribution from thermal fluctuations in both bodies, PL obtained exactly the same results as obtained by VP. However, for the contribution from quantum fluctuations, PL proposed that the Lorentz transformation is not valid, and arrived at the conclusion that the zero-point radiation from plate **2** can be obtained by the replacement of a factor in the integrand in the expression for contribution from thermal fluctuations:

$$2\mathrm{sgn}(\omega')\left[\exp\left(\frac{\hbar|\omega'|}{k_B T_2}\right)-1\right]^{-1} \to \mathrm{sgn}(\omega)+2\mathrm{sgn}(\omega')\left[\exp\left(\frac{\hbar|\omega'|}{k_B T_2}\right)-1\right]^{-1} \tag{F.3}$$

The contribution from plate **1** is given by a similar expression as from plate **2**. As a result, for friction force PL obtained expression similar to (7.28) but with the replacement

$$\big(n_2(\omega')-n_1(\omega)\big) \to \big(\mathrm{sgn}(\omega')n_2(|\omega'|)-n_1(\omega)\big). \tag{F.4}$$

For finite temperatures, PL obtained the same contribution to friction from thermal fluctuations as VP. However, it is clear from (F.4) that at $T = 0$ K the factor on the right side of (F.4) is equal to zero, which led PL to the conclusion that there is no lateral force at zero temperature. PL claimed that the vanishing of the lateral force at zero temperature can be viewed as a consequence of the Lorentz invariance of the quantum zero-point radiation–it has the same 'spectrum' in every inertial reference frame. However, instead of proving this PL just postulated the existence of such an invariance. If the Lorentz transformation is used also to calculate the contribution to stress tensor from quantum fluctuations in plate **2**, in the rest reference frame of plate **1**, then instead of the factor given by the right side of (F.3), in the integrand will occur the factor

$$\mathrm{sgn}(\omega')+2\mathrm{sgn}(\omega')\left[\exp\left(\frac{\hbar|\omega'|}{k_B T_2}\right)-1\right]^{-1}=1+2n_2(\omega'), \tag{F.5}$$

which will result in the friction force given by (7.28). For the propagating waves, $\mathrm{sgn}(\omega') = \mathrm{sgn}(\omega)$ (for $\omega > 0$) and from (7.28) it follows that the contribution to friction from propagating waves is equal to zero at zero temperature, which agrees with the principle of relativity. However, the contribution from evanescent waves is not equal to zero even at zero temperature because in this case $\mathrm{sgn}(\omega') < 0$ for $\omega < q_x V$. PL claim that perhaps the Lorentz transformation for the stress tensor is not valid for the contribution to stress tensor from quantum fluctuations. However, VP, instead of using the Lorentz transformation for the stress tensor, apply this transformation for the calculation of the electromagnetic field. This electromagnetic field is used to cal-

culate the stress tensor in the rest reference frame of plate **1**. The result was the same. Thus, contrary to the opinion of PL, we argue that the Lorentz invariance exists only for quantum fluctuations corresponding to propagating waves. This means that the spectral characteristics of the electromagnetic field in absolute vacuum (without of any bodies) are the same in all inertial reference frames; otherwise it will contradict the principle of relativity. This result follows from the Lorentz transformation for the electromagnetic field corresponding to the propagating electromagnetic waves. For evanescent waves, there is no Lorentz invariance of the spectral properties of the electromagnetic field. This result, which also follows from the Lorentz transformation, does not contradict the principle of relativity because there are no evanescent waves in absolute vacuum.

At zero temperature, the integration in (7.28) includes only the interval $0 < \omega < q_x V$. This integration takes into account the contribution to the friction from excitations in this frequency range, which exists even at zero temperature. PL did not include these excitations, and as a result they got zero friction. Excitations that exist even at zero temperature contribute not only to the lateral force, but also to the normal force (see (5.30)). Thus the conservative Casimir-Lifshitz force also contains some additional terms that were overlooked by PL.

Pendry [12, 124] has also showed that the friction is finite even at zero temperature, in qualitative agreement with most previous approaches to the problem, but in contradiction to the conclusion of PL. However, Pendry considered a very simple non-retarded and non-relativistic model. In contrast to Pendry, in the framework of the same model, we showed that the calculation of PL is in error. We have shown that this error is due to the assumption that the zero-point radiation, corresponding to the evanescent electromagnetic waves, obey Lorentz invariance. In addition, we also show that normal component of Casimir-Lifshitz force calculated by PL is also incorrect.

Since theory from [122] is a limiting case of theory from [123], our discussion is applicable for both of these papers.

Appendix G
Derivation of (7.57) and (7.58)

After substituting (7.40) and (7.42) into formula (7.55), we get to linear order in vibrational coordinate u_0 and the frequency ω_0:

$$\sigma_{zz} = \frac{1}{4\pi}\int_0^\infty d\omega \int \frac{d^2q}{(2\pi)^2}\Bigg(\frac{k_z}{q^2}\Big[\big(k_z + k_z^*\big)\big(\langle\,|w_{0z}|^2\,\rangle + \langle\,|v_{0z}|^2\,\rangle\big)$$
$$+\big(k_z - k_z^*\big)\big(\langle w_{0z}v_{0z}^*\rangle + c.c\big)\Big] + \Big(\frac{c}{\omega}\Big)^2 p\Big[\big(k_z + k_z^*\big)\big(\langle\,|w_{0n}|^2\,\rangle + \langle\,|v_{0n}|^2\,\rangle\big)$$
$$+\big(k_z - k_z^*\big)\big(\langle w_{0y}v_{0n}^*\rangle + c.c\big)\Big] + \Bigg(\frac{k_z^+}{q^2}\Big[\big(k_z + k_z^*\big)\big(\langle w_{1z}w_{0z}^*\rangle + \langle v_{1z}v_{0z}^*\rangle + c.c.\big)$$
$$+\big(k_z - k_z^*\big)\big(\langle w_{1z}v_{0z}^*\rangle + \langle v_{1z}w_{0z}^*\rangle + c.c.\big)\Big] + \frac{c^2}{\omega(\omega \quad + \omega_0)}k_z^+\Big[\big(k_z + k_z^*\big)\big(\langle w_{1n}w_{0n}^*\rangle$$
$$+\langle v_{1n}v_{0n}^*\rangle + c.c.\big) + \big(k_z - k_z^*\big)\big(\langle w_{1n}v_{0n}^*\rangle + \langle v_{1n}w_{0n}^*\rangle + c.c.\big)\Big]\Bigg)e^{-i\omega_0 t}\Bigg). \tag{G.1}$$

$$\gamma_\perp = \frac{1}{4\pi u_0 i}\int_0^\infty d\omega_0 \int \frac{d^2q}{(2\pi)^2}\Bigg(\frac{\partial}{\partial\omega_0}\Bigg(\frac{k_z^+}{q^2}\Big[\big(k_z + k_z^*\big)\big(\langle w_{1z}w_{0z}^*\rangle + \langle v_{1z}v_{0z}^*\rangle - c.c.\big)$$
$$+\big(k_z - k_z^*\big)\big(\langle v_{1z}w_{0z}^*\rangle + \langle w_{1z}v_{0z}^*\rangle - c.c.\big)\Big] + \frac{c^2}{\omega(\omega + \omega_0)}k_z^+\Big[\big(k_z + k_z^*\big)\big(\langle w_{1n}w_{0n}^*\rangle$$
$$+\langle v_{1n}v_{0n}^*\rangle - c.c.\big) + \big(k_z - k_z^*\big)\big(\langle v_{1n}v_{0y}^*\rangle + \langle v_{1n}w_{0n}^*\rangle - c.c.\big)\Big]\Bigg)\Bigg)_{\omega_0=0} \tag{G.2}$$

Using (4.3) and (4.18), and (7.49)–(7.53), we get

$$\frac{1}{q^2}\frac{\partial}{\partial\omega_0}\big(k_z^+\big(k_z + k_z^*\big)\big(\langle w_{1z}w_{0z}^*\rangle + \langle v_{1z}v_{0z}^*\rangle\big) - c.c.\big)_{\omega_0=0} = 2iu_0\left(n(\omega) + \frac{1}{2}\right)$$
$$\times\,\frac{\partial}{\partial\omega}k_z^2\Bigg[\frac{\big(1 - |R_{1p}R_{2p}|^2\big)^2 + |\big(1 - |R_{1p}|^2\big)R_{2p}e^{ik_zd} + \big(1 - |R_{2p}|^2\big)R_{1p}^*e^{-ik_zd}|^2}{|\Delta_p|^4}\Bigg], \tag{G.3}$$

A.I. Volokitin and B.N.J. Persson, *Electromagnetic Fluctuations at the Nanoscale*,
NanoScience and Technology, DOI 10.1007/978-3-662-53474-8

$$\frac{1}{q^2}\frac{\partial}{\partial\omega_0}\left(k_z^+\left(k_z-k_z^*\right)\left(\langle w_{1z}v_{0z}^*\rangle+\langle v_{1z}w_{0z}^*\rangle\right)-c.c.\right)_{\omega_0=0}=8iu_0\left(n(\omega)+\frac{1}{2}\right)$$
$$\times\frac{\partial}{\partial\omega}\frac{k_z^2}{|\Delta_p|^4}\Big[\left(\mathrm{Im}R_{1p}+e^{-2|k_z|d}|R_{1p}|^2\mathrm{Im}R_{2p}\right)\left(\mathrm{Im}R_{2p}+e^{-2|k_z|d}|R_{1p}|^2\mathrm{Im}R_{2p}\right)$$
$$+e^{-2|k_z|d}\mathrm{Im}\left(R_{1p}R_{2p}\right)^2\Big]e^{-2|k_z|d}. \tag{G.4}$$

Other similar expressions for the s-wave contribution can be obtained from (G.3) and (G.4) by replacement of the reflection amplitude R_p for p-polarized waves by the reflection amplitude R_s for s-polarized waves. After substituting (G.3) and (G.4), and similar expression for s-polarized waves, in (G.2) we get (7.57)–(7.58) for the friction coefficient for normal relative motion.

Appendix H
Derivation of the Friction Force on a Particle from the Energy Conservation Law

The relation between the current densities in the laboratory reference frame, and in the reference frame where the particle is at rest and the metal is moving with velocity $-\mathbf{V}$, in the non-relativistic limit, is given by: $\mathbf{j}^{sp(ind)} = \mathbf{j}^{sp(ind)'} + \rho^{sp(ind)}\mathbf{V}$, where $\mathbf{j}^{sp(ind)'}$ and $\rho^{sp(ind)}$ are the spontaneous (induced) current and charge density in the particle in the moving reference frame, and $\mathbf{j}^{sp(ind)}$ and $\rho^{sp(ind)}$ are the same quantities in laboratory reference frame (we take into account that, in the non-relativistic theory, the charge density is the same for both reference frame). Using this relation we get the relation between the rate of the work of the electric field in the volume of the particle in the laboratory and moving reference frame:

$$\begin{aligned} -\frac{\mathrm{d}W}{\mathrm{d}t} &= \int \left\langle \mathbf{j}^{sp}\mathbf{E}^{ind} \right\rangle \mathrm{d}^3 r + \int \left\langle \mathbf{j}^{ind}\mathbf{E}^{sp} \right\rangle \mathrm{d}^3 r \\ &= \int \left\langle \mathbf{j}^{sp'}\mathbf{E}^{ind} \right\rangle \mathrm{d}^3 r + \int \left\langle \mathbf{j}^{ind'}\mathbf{E}^{sp} \right\rangle \mathrm{d}^3 r \\ &\quad + \mathbf{V}\cdot \left(\int \left\langle \rho^{sp}\mathbf{E}^{ind} \right\rangle \right) \mathrm{d}^3 r + \left(\int \left\langle \rho^{ind}\mathbf{E}^{sp} \right\rangle \right) \mathrm{d}^3 r \\ &= -\frac{\mathrm{d}W_0}{\mathrm{d}t} + \mathbf{V}\cdot\mathbf{F}, \end{aligned} \tag{H.1}$$

where $\mathbf{E}^{sp}$ is the fluctuating electric field outside the metal in absence of the particle. $\mathbf{E}^{ind}$ is the electric field from the metal induced by the spontaneous current density $\mathbf{j}^{sp}$, $-\mathrm{d}W_0/\mathrm{d}t$ is the rate of the work in the moving reference frame, which is equal to the rate of the heat production in the volume of the particle, and $\mathbf{F}$ is the total force that acts on the particle, which, in the present case, is equal to the friction force. We note that the electric field in the non-relativistic limit is the same in both reference frames. For a moving point dipole, the spontaneous current density $\mathbf{j}^{\mathrm{sp}}(\mathbf{r}, t)$ is given by

$$\mathbf{j}^{\mathrm{sp}}(\mathbf{r}, t) = -\mathrm{i}\delta(z - z_0)\mathbf{p}^f \int \frac{\mathrm{d}^2 q}{(2\pi)^2} \left(\omega + q_x V\right) e^{\mathrm{i}\mathbf{q}\cdot\mathbf{r} - \mathrm{i}(\omega + q_x V)t}, \tag{H.2}$$

A.I. Volokitin and B.N.J. Persson, *Electromagnetic Fluctuations at the Nanoscale*,
NanoScience and Technology, DOI 10.1007/978-3-662-53474-8

and without screening effects, the induced electric field is given by

$$E_l^{\text{ind}}(\mathbf{r},t)=\int\frac{\mathrm{d}^2q}{(2\pi)^2}D_{lj}(\mathbf{q},\omega+q_xV,z,z_0)p_j^f e^{\mathrm{i}\mathbf{q}\cdot\mathbf{r}-\mathrm{i}(\omega+q_xV)t}. \tag{H.3}$$

Using (H.2) and (H.3), we get

$$\int\left\langle\mathbf{j}^{sp}\mathbf{E}^{ind*}\right\rangle\mathrm{d}^3r=-8\int_0^\infty\mathrm{d}\omega\int\mathrm{d}^2qqe^{-2qz_0}A(\omega,T)\times(\omega+q_xV)\mathrm{Im}R_p(\omega+q_xV)\mathrm{Im}\alpha(\omega), \tag{H.4}$$

where we have used spectral function of fluctuations of dipole moment given by (8.28), and take into account that, in the nonrelativistic limit (see Appendix C):

$$\sum_{l=x,y,z}D_{ll}(\mathbf{q},\omega,z,z_0)=2D_{qq}(\mathbf{q},\omega,z,z_0)=4\pi qe^{-q(z+z_0)}R_p(\omega). \tag{H.5}$$

After the Fourier decomposition of the fluctuating electric field from the metal

$$\mathbf{E}^s(\mathbf{r},t)=\int\frac{\mathrm{d}^2q}{(2\pi)^2}\mathbf{E}^s(\mathbf{q},\omega,z)e^{\mathrm{i}(\mathbf{q}\cdot\mathbf{r}-\omega t)}, \tag{H.6}$$

the induced current density in the particle is given by

$$\mathbf{j}^{\text{ind}}(\mathbf{r},t)=-\mathrm{i}\delta(z-z_0)\int\frac{\mathrm{d}^2q}{(2\pi)^2}\int\frac{\mathrm{d}^2q'}{(2\pi)^2}\left[\omega-V(q_x-q_x')\right]\times\alpha(\omega-q_xV)\mathbf{E}^s(\mathbf{q},\omega,z_0)e^{\mathrm{i}\mathbf{q}'\cdot\mathbf{r}-\mathrm{i}[\omega-V(q_x-q_x')t]}. \tag{H.7}$$

From (H.6) and (H.7), we get

$$\int\left\langle\mathbf{j}^{ind}\mathbf{E}^{s*}\right\rangle\mathrm{d}^3r=\frac{8}{\pi}\int_0^\infty\mathrm{d}\omega\int\mathrm{d}^2qqe^{-2qz_0}\left(\frac{1}{2}+n(\omega)\right)\omega\mathrm{Im}R_p(\omega)\mathrm{Im}\alpha(\omega-q_xV). \tag{H.8}$$

For the total rate of work performed by the electric field in the volume of the moving particle, we get

$$-\frac{\mathrm{d}W}{\mathrm{d}t}=\frac{8}{\pi}\int_0^\infty\mathrm{d}\omega\int\mathrm{d}^2qqe^{-2qz_0}\left(\frac{1}{2}+n(\omega)\right)\Big[\omega\mathrm{Im}R(\omega)\mathrm{Im}\alpha(\omega-q_xV)-(\omega+q_xV)\mathrm{Im}R_p(\omega+q_xV)\mathrm{Im}\alpha(\omega)\Big]. \tag{H.9}$$

The rate of work performed by the electric field in the volume of the particle in the reference frame where the particle is at rest and the metal is moving with velocity $-V$ can be found in a similar way to the laboratory system, and is given by

$$-\frac{\mathrm{d}W_0}{\mathrm{d}t}=\frac{8}{\pi}\int_0^\infty \mathrm{d}\omega\int \mathrm{d}^2q q e^{-2qz_0}\left(\frac{1}{2}+n(\omega)\right)$$

$$\times\left[(\omega-q_xV)\,\mathrm{Im}R_p(\omega)\mathrm{Im}\alpha(\omega-q_xV)-\omega\mathrm{Im}R(\omega+q_xV)\mathrm{Im}\alpha(\omega)\right]. \quad \text{(H.10)}$$

From (H.1), (H.9) and (H.10), we get friction force

$$\begin{aligned}F&=\frac{8}{\pi}\int_0^\infty \mathrm{d}\omega\int \mathrm{d}^2q q q_x e^{-2qz_0}\\&\quad\times\left(\frac{1}{2}+n(\omega)\right)\left[\mathrm{Im}R_p(\omega)\mathrm{Im}\alpha(\omega-q_xV)-\mathrm{Im}R_p(\omega+q_xV)\mathrm{Im}\alpha(\omega)\right]\\&=\frac{2\hbar}{\pi^2}\int_{-\infty}^\infty \mathrm{d}q_y\int_0^\infty \mathrm{d}q_x q_x q e^{-2qz_0}\left\{\int_0^\infty \mathrm{d}\omega\,[n(\omega+q_xV)-n(\omega)]\right.\\&\quad\times\left[\mathrm{Im}R_p(\omega)\mathrm{Im}\alpha(\omega+q_xV)+\mathrm{Im}R_p(\omega+q_xV)\mathrm{Im}\alpha(\omega)\right]\\&\quad+\int_0^{q_xV}\mathrm{d}\omega\left(\frac{1}{2}+n(\omega)\right)\\&\quad\left.\times\left[\mathrm{Im}R_p(\omega)\mathrm{Im}\alpha(\omega-q_xV)+\mathrm{Im}R_p(\omega-q_xV)\mathrm{Im}\alpha(\omega)\right].\right\}\end{aligned} \quad \text{(H.11)}$$

This formula is in complete agreement with the results in [13, 115, 121, 145] (see also Sect. 8.1). To linear order in the sliding velocity V from (H.11), we get

$$F=\frac{2\hbar V}{\pi}\int_0^\infty \mathrm{d}\omega\frac{\partial n(\omega)}{\partial\omega}\int_0^\infty \mathrm{d}q q^4 e^{-2qd}\mathrm{Im}R_p(q,\omega)\mathrm{Im}\alpha(\omega). \quad \text{(H.12)}$$

Appendix I
Derivation of (8.47) and (8.48)

The forces on a particle from the electric and magnetic induction fields in (8.39), to linear order in the vibrational coordinate $\mathbf{u}(t)$, can be written in the form:

$$\int_{-\infty}^{\infty} \mathrm{d}\omega \int \mathrm{d}^3 r \left\langle \rho \mathbf{E}^* \right\rangle = \int_{-\infty}^{\infty} \mathrm{d}\omega \int \mathrm{d}^3 r \left\langle p_l(\mathbf{r}, t) \frac{\partial}{\partial x_l} \mathbf{E}^*(\mathbf{r}, t) \right\rangle$$

$$= \int_{-\infty}^{\infty} \mathrm{d}\omega \frac{\partial}{\partial x_l} \Bigg(\left\langle p_{0l} \left(1 + \mathbf{u}_0 \cdot \frac{\partial}{\partial \mathbf{r}} \right) \left(\mathbf{E}^*_{d0}(\mathbf{r}, \omega) + \mathbf{E}^{s*}(\mathbf{r}, \omega) \right) \right\rangle$$

$$+ \left[\left\langle p_{0l} \mathbf{E}^*_1(\mathbf{r}, \omega - \omega_0) \right\rangle + \left\langle p_{1l} \left(\mathbf{E}^*_{d0}(\mathbf{r}, \omega) + \mathbf{E}^{s*}(\mathbf{r}, \omega) \right) \right\rangle \right] e^{-\mathrm{i}\omega_0 t} \Bigg)_{\mathbf{r}=\mathbf{r}_0}, \tag{I.1}$$

$$\frac{1}{c} \int_{-\infty}^{\infty} \mathrm{d}\omega \int \mathrm{d}^3 r \left\langle \mathbf{j} \times \mathbf{B}^* \right\rangle = \int_{-\infty}^{\infty} \mathrm{d}\omega \Bigg\{ \left\langle \mathbf{p}_0 \times \nabla \times \left(\mathbf{E}^*_{d0}(\mathbf{r}) + \mathbf{E}^{s*}(\mathbf{r}) \right) \right\rangle$$

$$+ \Bigg[\frac{\omega}{\omega - \omega_0} \Big(\nabla \left\langle \mathbf{p}_0 \cdot \mathbf{E}^*_1(\mathbf{r}, \omega - \omega_0) \right\rangle - \frac{\partial}{\partial x_l} \left\langle p_{0l} \mathbf{E}^*_1(\mathbf{r}, \omega - \omega_0) \right\rangle \Big)$$

$$+ \frac{\omega + \omega_0}{\omega} \Bigg(\nabla \left\langle \left(\mathbf{p}_1 + \mathbf{p}_0 \, \mathbf{u}_0 \cdot \frac{\partial}{\partial \mathbf{r}} \right) \cdot \left(\mathbf{E}^*_{d0}(\mathbf{r}) + \mathbf{E}^{s*}(\mathbf{r}) \right) \right\rangle$$

$$- \frac{\partial}{\partial x_l} \left\langle \left(p_{1l} + p_{0l} \mathbf{u}_0 \cdot \frac{\partial}{\partial \mathbf{r}} \right) \left(\mathbf{E}^*_{d0}(\mathbf{r}) + \mathbf{E}^{s*}(\mathbf{r}) \right) \right\rangle \Bigg) \Bigg] e^{-\mathrm{i}\omega_0 t} \Bigg\}_{\mathbf{r}=\mathbf{r}_0}. \tag{I.2}$$

A.I. Volokitin and B.N.J. Persson, *Electromagnetic Fluctuations at the Nanoscale*,
NanoScience and Technology, DOI 10.1007/978-3-662-53474-8

From (I.1) and (I.2), it follows that the friction force is determined by the formula

$$\mathbf{F}_{fric} = \frac{1}{2}\omega_0 \int_{-\infty}^{\infty} \mathrm{d}\omega \Bigg[\nabla \frac{\partial}{\partial \omega_0} \Bigg(\frac{\omega}{\omega - \omega_0} \left\langle \mathbf{p}_0 \cdot \mathbf{E}_1^*(\mathbf{r}, \omega - \omega_0) \right\rangle + \frac{\omega + \omega_0}{\omega} \left\langle \mathbf{p}_1 \cdot \left(\mathbf{E}_{d0}^*(\mathbf{r}) + \mathbf{E}^{s*}(\mathbf{r}) \right) \right\rangle \Bigg)_{\omega_0 = 0} - c.c. \Bigg]_{\mathbf{r}=\mathbf{r}_0}. \tag{I.3}$$

Next, to simplify (I.3), note that

$$\begin{aligned} &\left(\frac{\partial}{\partial \omega_0} \frac{E_{1l}^*(\mathbf{r}, \omega - \omega_0)}{\omega - \omega_0} \right)_{\omega_0 = 0} \\ &= -\mathbf{u}_0 \cdot \frac{\partial}{\partial \mathbf{r}'} \Bigg[\frac{\partial}{\partial \omega} \left(\frac{\alpha^*(\omega) D_{lk}^*(\mathbf{r}, \mathbf{r}_0, \omega)}{\omega \left(1 - \alpha^*(\omega) D_{kk}^*(\mathbf{r}_0, \mathbf{r}_0, \omega) \right)} \right) \\ &\times \left(E_k^{s*}(\mathbf{r}', \omega) + D_{kk}^*(\mathbf{r}', \mathbf{r}', \omega) p_{0k} \right) + \frac{\alpha^*(\omega) D_{lk}^*(\mathbf{r}, \mathbf{r}_0, \omega)}{\omega \left(1 - \alpha^*(\omega) D_{kk}^*(\mathbf{r}_0, \mathbf{r}_0, \omega) \right)} \\ &\times \frac{\partial}{\partial \omega} \left(D_{ks}^*(\mathbf{r}_0, \mathbf{r}', \omega) \right) p_{0s}^* + \frac{\partial}{\partial \omega} \left(\frac{D_{lk}^*(\mathbf{r}, \mathbf{r}', \omega)}{\omega} \right) p_{0k}^* \Bigg]_{\mathbf{r}'=\mathbf{r}_0}, \end{aligned} \tag{I.4}$$

$$\left(\frac{\partial}{\partial \omega_0} (\omega + \omega_0) p_{1l} \right)_{\omega_0 = 0} = \left(\frac{\partial}{\partial \omega_0} (\omega + \omega_0) \alpha(\omega + \omega_0) E_{1l} \right)_{\omega_0 = 0}$$

$$\begin{aligned} &= \mathbf{u}_0 \cdot \frac{\partial}{\partial \mathbf{r}'} \Bigg[\frac{\partial}{\partial \omega} \left(\frac{\omega \alpha(\omega)}{1 - \alpha(\omega) D_{ll}(\mathbf{r}_0, \mathbf{r}_0, \omega)} \right) \left(E_l^s(\mathbf{r}', \omega) + D_{ll}(\mathbf{r}', \mathbf{r}', \omega) p_{0l} \right) \\ &+ \frac{\omega \alpha(\omega)}{1 - \alpha(\omega) D_{ll}(\mathbf{r}_0, \mathbf{r}_0, \omega)} \frac{\partial}{\partial \omega} \left(D_{lk}(\mathbf{r}_0, \mathbf{r}', \omega) \right) p_{0k} \Bigg]_{\mathbf{r}'=\mathbf{r}_0}, \end{aligned} \tag{I.5}$$

and the following expression for the spectral function of fluctuations

$$\langle p_{0l} p_{0k} \rangle = \frac{\hbar}{\pi} \left(\frac{1}{2} + n(\omega) \right) \delta_{lk} \mathrm{Im} \frac{\alpha(\omega)}{1 - \alpha(\omega) D_{ll}(\mathbf{r}_0, \mathbf{r}_0, \omega)}, \tag{I.6}$$

$$\left\langle p_{0l} E_k^{s*}(\mathbf{r}', \omega) \right\rangle = \frac{\hbar}{\pi} \left(\frac{1}{2} + n(\omega) \right) \frac{\alpha(\omega)}{1 - \alpha(\omega) D_{ll}(\mathbf{r}_0, \mathbf{r}_0, \omega)} \mathrm{Im} D_{lk}(\mathbf{r}_0, \mathbf{r}', \omega), \tag{I.7}$$

$$\begin{aligned}
&\left\langle \left(E_l^s(\mathbf{r}',\omega)+D_{ll}(\mathbf{r}',\mathbf{r}',\omega)p_{0l}\right)\left(E_l^{s*}(\mathbf{r},\omega)+D_{lk}^*(\mathbf{r},\mathbf{r}_0,\omega)p_{0k}^*\right)\right\rangle \\
&=\frac{\hbar}{\pi}\left(\frac{1}{2}+n(\omega)\right)\Bigg[\mathrm{Im}D_{ll}(\mathbf{r},\mathbf{r}',\omega)+\frac{\alpha^*(\omega)}{1-\alpha^*(\omega)D_{kk}^*(\mathbf{r}_0,\mathbf{r}_0,\omega)}D_{lk}^*(\mathbf{r},\mathbf{r}_0,\omega) \\
&\quad\times\mathrm{Im}D_{lk}(\mathbf{r}',\mathbf{r}_0,\omega)+D_{ll}(\mathbf{r}',\mathbf{r}',\omega)\mathrm{Im}\left(\frac{\alpha(\omega)D_{ll}(\mathbf{r},\mathbf{r}_0,\omega)}{1-\alpha(\omega)D_{ll}(\mathbf{r}_0,\mathbf{r}_0,\omega)}\right)\Bigg]. \qquad \text{(I.8)}
\end{aligned}$$

Using (I.4) and (I.5) for the vibration along the x-axis, (I.3) is reduced to

$$\begin{aligned}
\left(\mathbf{F}_{fric}\right)_x =&u_0\omega_0\int_{-\infty}^{\infty}\mathrm{d}\omega\frac{\hbar}{\pi}\left(\frac{1}{2}+n(\omega)\right) \\
&\times\frac{\partial}{\partial\omega}\Bigg[\sum_{l=x,y,z}\left(\frac{\partial^2}{\partial x\partial x'}\mathrm{Im}D_{ll}(\mathbf{r},\mathbf{r}')\mathrm{Im}\frac{\alpha(\omega)}{1-\alpha(\omega)D_{ll}(\mathbf{r}_0,\mathbf{r}_0,\omega)}\right) \\
&-2\,|\alpha(\omega)\,|^2\,\mathrm{Re}\left(\frac{1}{(1-\alpha(\omega)^*D_{zz}(\mathbf{r}_0,\mathbf{r}_0,\omega)^*)\,(1-\alpha(\omega)^*D_{xx}(\mathbf{r}_0,\mathbf{r}_0,\omega))}\right) \\
&\times\left(\frac{\partial}{\partial x}\mathrm{Im}D_{xz}(\mathbf{r},\mathbf{r}_0)\right)^2\Bigg]_{\substack{\mathbf{r}=\mathbf{r}_0\\ \mathbf{r}'=\mathbf{r}_0}}, \qquad \text{(I.9)}
\end{aligned}$$

where we have used that for the vibrations parallel to the surface

$$\frac{\partial}{\partial x}D_{ll}(\mathbf{r},\mathbf{r})=0, \qquad \text{(I.10)}$$

$$\begin{aligned}
\frac{\partial}{\partial x}D_{lk}(\mathbf{r},\mathbf{r}_0)\Big|_{\mathbf{r}=\mathbf{r}_0} &= -\frac{\partial}{\partial x}D_{lk}(\mathbf{r}_0,\mathbf{r})\Big|_{\mathbf{r}=\mathbf{r}_0} \\
&= \frac{\partial}{\partial x}D_{xz}(\mathbf{r},\mathbf{r}_0)\Big|_{\mathbf{r}=\mathbf{r}_0}(\delta_{xl}\delta_{zk}-\delta_{xk}\delta_{zl})\,. \qquad \text{(I.11)}
\end{aligned}$$

For vibrations normal to the surface, only the diagonal elements of the Green's function are non-vanishing and, for this case, (I.3) reduces to

$$\begin{aligned}
\left(\mathbf{F}_{fric}\right)_z = u_0\omega_0\int_{-\infty}^{\infty}\mathrm{d}\omega\frac{\hbar}{\pi}\left(\frac{1}{2}+n(\omega)\right)\frac{\partial}{\partial\omega}\sum_{l=x,y,z}\Bigg\{&\frac{\partial^2}{\partial z\partial z'}\Bigg[\mathrm{Im}D_{ll}(\mathbf{r},\mathbf{r}',\omega) \\
&+\mathrm{Im}\left(\frac{\alpha(\omega)D_{ll}(\mathbf{r},\mathbf{r}_0,\omega)D_{ll}(\mathbf{r}',\mathbf{r}_0,\omega)}{1-\alpha(\omega)D_{ll}(\mathbf{r}_0,\mathbf{r}_0,\omega)}\right)\Bigg]\mathrm{Im}\frac{\alpha(\omega)}{1-\alpha(\omega)D_{ll}(\mathbf{r}_0,\mathbf{r}_0,\omega)} \\
&+\left(\frac{\partial}{\partial z}\mathrm{Im}\left(\frac{\alpha(\omega)D_{ll}(\mathbf{r},\mathbf{r}_0,\omega)}{1-\alpha(\omega)D_{ll}(\mathbf{r}_0,\mathbf{r}_0,\omega)}\right)\right)^2\Bigg\}_{\substack{\mathbf{r}=\mathbf{r}_0\\ \mathbf{r}'=\mathbf{r}_0}}. \qquad \text{(I.12)}
\end{aligned}$$

Appendix J
Calculation of the Casimir Friction Between Plane Surfaces Using Quantum Field Theory

J.1 Parallel Relative Motion

Assume that the xy-plane coincides with one of the surfaces. For parallel relative motion, the friction coefficient $\Gamma_\parallel = \Gamma_{xx} = \Gamma_{yy}$. Using quantum field theory [183], the expression for the friction coefficient (7.7) for parallel relative motion can be written in the form

$$\Gamma_\parallel = \lim_{\omega_0 \to 0} \mathrm{Im} \frac{G^R_{xx}(\omega_0 + i\delta)}{\omega_0}, \tag{J.1}$$

where G^R_{xx} is the retarded Green's function given by

$$G^R_{xx}(\omega) = \frac{i}{\hbar} \int_0^\infty dt e^{i\omega t} \left\langle \hat{F}_x(t)\hat{F}_x(0) - \hat{F}_x(0)\hat{F}_x(t) \right\rangle, \tag{J.2}$$

where

$$\hat{F}_x = \int dS_z \hat{\sigma}_{xz}, \tag{J.3}$$

where the surface integral is taken over the surface of the body at $z = 0$,

$$\hat{\sigma}_{xz} = \left(E_x E_z + E_z E_x + B_x B_z + B_z B_x\right)/8\pi. \tag{J.4}$$

The function G^R_{xx} can be obtained by analytic continuation in the upper half of ω-plane of the temperature Green's function $G_{xx}(\omega)$, determined on the discrete set of point $i\omega_n = i2\pi n/\beta$ by the formula

$$G_{xx}(i\omega_n) = -\frac{1}{\hbar} \int_0^\beta d\tau e^{i\omega_n \tau} \left\langle T_\tau \hat{F}_x(\tau)\hat{F}_x(0) \right\rangle, \tag{J.5}$$

where n is an integer and $\beta = \hbar/k_B T$, and where T_τ is the time-ordering operator. The function $G_{xx}(i\omega_n)$ can be calculated using standard techniques of quantum

A.I. Volokitin and B.N.J. Persson, *Electromagnetic Fluctuations at the Nanoscale*,
NanoScience and Technology, DOI 10.1007/978-3-662-53474-8

field theory [183, 233], and can be represented through the Green's functions of the electromagnetic field

$$D_{ij}^{EE}(\mathbf{r},\mathbf{r}',i\omega_n)=D_{ij}(\mathbf{r},\mathbf{r}',i\omega_n)=-\frac{1}{\hbar}\int_0^\beta d\tau e^{i\omega_n\tau}\left\langle T_\tau\hat{E}_i(\tau)\hat{E}_j(0)\right\rangle, \tag{J.6}$$

where the retarded Green's functions $D_{ij}(\mathbf{r},\mathbf{r}',\omega)$ obey the equations [183]:

$$\left(\nabla_i\nabla_k-\delta_{ik}\nabla^2\right)D_{kj}(\mathbf{r},\mathbf{r}',\omega)-\left(\frac{\omega}{c}\right)^2\int d^3x''\varepsilon_{ik}(\mathbf{r},\mathbf{r}'',\omega)D_{kj}(\mathbf{r}'',\mathbf{r}',\omega)$$
$$=\left(\frac{4\pi\omega^2}{c^2}\right)\delta_{ij}\delta(\mathbf{r}-\mathbf{r}'), \tag{J.7}$$

$$\left(\nabla'_j\nabla'_k-\delta_{jk}\nabla'^2\right)D_{ik}(\mathbf{r},\mathbf{r}',\omega)-\left(\frac{\omega}{c}\right)^2\int d^3x''\varepsilon_{kj}(\mathbf{r}'',\mathbf{r}',\omega)D_{ik}(\mathbf{r},\mathbf{r}'',\omega)$$
$$=\left(\frac{4\pi\omega^2}{c^2}\right)\delta_{ij}\delta(\mathbf{r}-\mathbf{r}'). \tag{J.8}$$

For the plane surface, it is convenient to decompose the electromagnetic field into s- and p-polarized plane waves. Introducing $\hat{q}=\mathbf{q}/q$ and $\hat{n}=[\hat{z}\times\hat{q}]$, where $\mathbf{q}$ is the surface component of the wave vector, the Green's tensor is given by

$$\overleftrightarrow{\mathbf{D}}^{EE}(\mathbf{r},\mathbf{r}')=\int\frac{d^2q}{(2\pi)^2}\Big(\hat{n}D_{nn}^{EE}(z,z',\mathbf{q})\hat{n}+\hat{q}D_{qq}^{EE}(z,z',\mathbf{q})\hat{q}+\hat{z}D_{zz}^{EE}(z,z',\mathbf{q})\hat{z}$$
$$+\hat{z}D_{zq}^{EE}(z,z',\mathbf{q})\hat{q}+\hat{q}D_{qz}^{EE}(z,z',\mathbf{q})\hat{z}\Big)e^{i\mathbf{q}\cdot(\mathbf{x}-\mathbf{x}')}. \tag{J.9}$$

where we have taken into account that $D_{nz}^{EE}=D_{nq}^{EE}=0$ (see Appendix A and C). For two plane parallel surfaces, the solution of (3.33) and (3.34) is derived in Appendix C. Using the methods of the quantum field theory [183, 233] for the Green's function G_{xx} we get

$$G_{xx}(i\omega_n)=\frac{\hbar A}{16\pi^2\beta}\int\frac{d^2\mathbf{q}}{(2\pi)^2}\sum_{\omega_m}\frac{q_x^2}{q^2}\Big[D_{qq}^{EE}(\mathbf{q},i\omega_m,z,z')D_{zz}^{EE}(-\mathbf{q},i\omega_n-i\omega_m,z,z')$$
$$+D_{qz}^{EE}(\mathbf{q},i\omega_m,z,z')D_{zq}^{EE}(-\mathbf{q},i\omega_n-i\omega_m,z,z')$$
$$+D_{qq}^{BB}(\mathbf{q},i\omega_m,z,z')D_{zz}^{BB}(-\mathbf{q},i\omega_n-i\omega_m,z,z')$$
$$+D_{qz}^{BB}(\mathbf{q},i\omega_m,z,z')D_{zq}^{BB}(-\mathbf{q},i\omega_n-i\omega_m,z,z')\Big]_{z=z'=0}, \tag{J.10}$$

where A is the surface area, and $D_{ij}^{BB}(\mathbf{q},i\omega_m,z,z')$ is given by [183]

$$D_{ij}^{BB}(\mathbf{r},\mathbf{r}',i\omega_n) = -\left(\frac{c}{\omega_n}\right)^2 e_{ilk}e_{jst}\nabla_l\nabla_s' D_{kt}^{EE}(\mathbf{r},\mathbf{r}',i\omega_n), \tag{J.11}$$

where e_{ijl} is the completely asymmetric unit tensor. In (J.10), we omitted terms involving products of Green's functions associated with the p- and s-polarized electromagnetic field because, after the frequency summations, they cancel out each other.

All sums on ω_m in (J.10) can be calculated as a result of similar calculations. Thus, as an illustration, we consider only the sum:

$$\frac{1}{\beta}\sum_{\omega_m} D_{qz}^{EE}(\mathbf{q},i\omega_m)D_{zq}^{EE}(-\mathbf{q},i\omega_n - i\omega_m). \tag{J.12}$$

According to the Lehmann representation [183, 233], the Green's function can be written in the form

$$D_{\alpha\beta}^{EE}(\omega_n,\mathbf{r},\mathbf{r}') = \frac{1}{\pi}\int_{-\infty}^{\infty} dx \frac{\rho_{\alpha\beta}^{EE}(x,\mathbf{r},\mathbf{r}')}{x - i\omega_n}, \tag{J.13}$$

where

$$\rho_{\alpha\beta}^{EE}(\omega,\mathbf{r},\mathbf{r}') = \sum_{n,m}\exp(F - E_n)(E_\alpha(\mathbf{r}))_{nm}(E_\alpha(\mathbf{r}'))_{mn}(1 - e^{-\beta\omega_{mn}})\delta(\omega - \omega_{mn}).$$

Using (J.13) and standard rules for the evaluation of the sum such as (J.12) [233] we get

$$\begin{aligned}
&\frac{1}{\beta}\sum_{\omega_m} D_{qz}^{EE}(\mathbf{q},\omega_m)D_{zq}^{EE}(-\mathbf{q},i\omega_n - i\omega_m)\\
&= \int_{-\infty}^{\infty} d\omega\Big[\left(\rho_{qz}^{EE}(\mathbf{q},\omega)D_{zq}^{EE}(-\mathbf{q},i\omega_n - \omega)\right)n(\omega)\\
&+ \left(D_{qz}^{EE}(\mathbf{q},i\omega_n - \omega)\rho_{zq}^{EE}(-\mathbf{q},\omega)\right)(n(\omega)+1)\Big],
\end{aligned} \tag{J.14}$$

where $n(\omega) = [\exp(\hbar\omega/k_BT) - 1]^{-1}$. Using (C.9) and (C.10) in (J.14), we get

$$\begin{aligned}
&\frac{\hbar}{\beta}\sum_{\omega_m} D_{qz}^{EE}(\mathbf{q},i\omega_m)D_{zq}^{EE}(-\mathbf{q},i\omega_n - i\omega_m)\\
&= -q^2\frac{\hbar}{\pi}\int_{-\infty}^{\infty} d\omega\Bigg[\left(\frac{\partial}{\partial z'}\frac{\rho_{qq}^{EE}(\omega,z,z')}{k_z^2(\omega)}\frac{\partial}{\partial z}\frac{D_{qq}(i\omega_n - \omega,z,z')}{k_z^2(i\omega_n - \omega)}\right)n(\omega)\\
&+ \left(\frac{\partial}{\partial z'}\frac{D_{qq}^{EE}(i\omega_n - \omega,z,z')}{k_z^2(i\omega_n - \omega)}\frac{\partial}{\partial z}\frac{\rho_{qq}^{EE}(\omega,z,z')}{k_z^2(\omega)}\right)(n(\omega)+1)\Bigg],
\end{aligned} \tag{J.15}$$

where $k_z^2(\omega) = (\omega/c)^2 - q^2$. Replacing $i\omega_n \to \omega_0 + i\delta$ and taking the imaginary part of (J.15) in the limit $\omega_0 \to 0$ we get the following contribution to the friction from (J.15)

$$\lim_{\omega_0\to 0}\frac{1}{\omega_0}\mathrm{Im}\lim_{i\omega_n\to\omega_0+i\delta}\frac{\hbar}{\beta}\sum_{\omega_m} D_{qz}^{EE}(\mathbf{q}, i\omega_m)D_{zq}^{EE}(-\mathbf{q}, i\omega_n - i\omega_m)$$
$$= -\frac{2\hbar q^2}{\pi k_z^4}\int_0^\infty d\omega\left(-\frac{\partial n}{\partial\omega}\right)\left(\frac{\partial}{\partial z}\,\mathrm{Im}D_{qq}(\omega)\right)\left(\frac{\partial}{\partial z'}\,\mathrm{Im}D_{qq}(\omega)\right). \tag{J.16}$$

Calculating in a similar way the other sums on frequencies in (J.10), we get

$$\gamma_{xx} = \frac{\hbar}{8\pi^3}\int_0^\infty d\omega\left(-\frac{\partial n}{\partial\omega}\right)\int\frac{d^2\mathbf{q}}{(2\pi)^2}\frac{q_x^2}{q^2}\left\{\left[\mathrm{Im}D_{qq}\mathrm{Im}D_{zz}\right.\right.$$
$$\left.-\frac{q^2}{k_z^4}\left(\frac{\partial}{\partial z}\mathrm{Im}D_{qq}\right)\left(\frac{\partial}{\partial z'}\mathrm{Im}D_{qq}\right)\right] + \left(\frac{c}{\omega}\right)^4 q^2\left[\mathrm{Im}D_{nn}\frac{\partial^2}{\partial z\partial z'}\mathrm{Im}D_{nn}\right.$$
$$\left.\left.\left.-\left(\frac{\partial}{\partial z}\mathrm{Im}D_{nn}\right)\left(\frac{\partial}{\partial z'}\mathrm{Im}D_{nn}\right)\right]\right\}_{z=z'=0}. \tag{J.17}$$

Using (C.9), (C.10), (C.16) for the Green's functions in (J.17), the contribution to the friction from the propagating ($q < \omega/c$) waves becomes:

$$\gamma_\parallel^{rad} = \frac{\hbar}{8\pi^3}\int_0^\infty d\omega\left(-\frac{\partial n}{\partial\omega}\right)\int_{q<\frac{\omega}{c}} d^2\mathbf{q}q_x^2$$

$$\times\left[\mathrm{Re}\left(\frac{1+R_{1p}R_{2p}e^{2ik_zd}-R_{1p}-R_{2p}e^{2ik_zd}}{1-e^{2ik_zd}R_{1p}R_{2p}}\right)\mathrm{Re}\left(\frac{1+R_{1p}R_{2p}e^{2ik_zd}+R_{1p}+R_{2p}e^{2ik_zd}}{1-e^{2ik_zd}R_{1p}R_{2p}}\right)\right.$$

$$\left.-\left(\mathrm{Im}\frac{R_{1p}-R_{2p}e^{2ik_zd}}{1-e^{2ik_zd}R_{1p}R_{2p}}\right)^2+[p\to s]\right]$$

$$= \frac{\hbar}{8\pi^2}\int_0^\infty d\omega\left(-\frac{\partial n}{\partial\omega}\right)\int_0^{\frac{\omega}{c}} dqq^3\frac{(1-|R_{1p}|^2)(1-|R_{2p}|^2)}{|1-e^{2ik_zd}R_{1p}R_{2p}|^2}+[p\to s]. \tag{J.18}$$

Similarly, the contribution to the friction from the evanescent electromagnetic waves ($q > \omega/c$):

$$\gamma_\parallel^{evan} = \frac{\hbar}{8\pi^3}\int_0^\infty d\omega\left(-\frac{\partial n}{\partial\omega}\right)\int_{q>\frac{\omega}{c}} d^2\mathbf{q}q_x^2$$

$$\times\left[-\mathrm{Im}\left(\frac{2R_{1p}R_{2p}e^{-2|k_z|d}-R_{1p}-R_{2p}e^{-2|k_z|d}}{1-e^{-2|k_z|d}R_{1p}R_{2p}}\right)\right.$$

$$\times \mathrm{Im}\left(\frac{2R_{1p}R_{2p}e^{-2|k_z|d}+R_{1p}+R_{2p}e^{-2|k_z|d}}{1-e^{-2|k_z|d}R_{1p}R_{2p}}\right)$$
$$-\left(\mathrm{Im}\frac{R_{1p}-R_{2p}e^{-2|k_z|d}}{1-e^{-2|k_z|d}R_{1p}R_{2p}}\right)^2+[p\to s]\Bigg]$$
$$=\frac{\hbar}{2\pi^2}\int_0^\infty d\omega\left(-\frac{\partial n}{\partial\omega}\right)\int_{\frac{\omega}{c}}^\infty dqq^3e^{-2|k_z|d}\frac{\mathrm{Im}R_{1p}\mathrm{Im}R_{2p}}{|1-e^{-2|k_z|d}R_{1p}R_{2p}|^2} \tag{J.19}$$
$$+[p\to s].$$

Equations (J.18) and (J.20) were first derived in [100] using the dynamical modification of the Lifshitz theory.

J.2 Normal Relative Motion

For two plane surfaces in normal relative motion, the force operator is given by

$$\hat{F}_z=\int dS_z\hat{\sigma}_{zz}, \tag{J.20}$$

$$\hat{\sigma}_{zz}=\left(E_zE_z-E_xE_x-E_yE_y+B_zB_z-B_xB_x-B_yB_y\right)/8\pi. \tag{J.21}$$

The friction coefficient for normal relative motion can be obtained from the analytical continuation in the upper part of ω-plane of the Green's function $G_{zz}(i\omega_n)$, which is determined by

$$G_{zz}(i\omega_n)=\frac{\hbar A}{32\pi^2\beta}\int\frac{d^2\mathbf{q}}{(2\pi)^2}\sum_{\omega_m}\frac{q_x^2}{q^2}\Big[D_{zz}^{EE}D_{zz}^{EE}+D_{qq}^{EE}D_{qq}^{EE}+D_{nn}^{EE}D_{nn}^{EE}$$
$$-D_{zq}^{EE}D_{zq}^{EE}-D_{qz}^{EE}D_{qz}^{EE}-D_{zn}^{EB}D_{zn}^{EB}-D_{nz}^{EB}D_{nz}^{EB}$$
$$+D_{qn}^{EB}D_{qn}^{EB}+D_{nq}^{EB}D_{nq}^{EB}+[E\leftrightarrow B]\Big], \tag{J.22}$$

where the arguments of the Green functions in (J.22) are the same as in (J.10), $[E\leftrightarrow B]$ denotes the terms which can be obtained from the first terms by permutation of the upper case indexes E and B, and

$$D_{ij}^{EB}(\mathbf{r},\mathbf{r}',\omega_n)=\frac{c}{\omega_n}e_{jkl}\nabla_k'D_{il}^{EE}(\mathbf{r},\mathbf{r}',\omega_n), \tag{J.23}$$

$$D_{ij}^{BE}(\mathbf{r},\mathbf{r}',\omega_n)=-\frac{c}{\omega_n}e_{ikl}\nabla_kD_{lj}^{EE}(\mathbf{r},\mathbf{r}',\omega_n). \tag{J.24}$$

Performing similar calculations as for the parallel relative motion we get

$$\gamma_\perp = \frac{\hbar}{16\pi^3}\int_0^\infty d\omega\left(-\frac{\partial n}{\partial\omega}\right)\int\frac{d^2\mathbf{q}}{(2\pi)^2}$$
$$\times\left\{\left[\left(\mathrm{Im}D_{qq}\right)^2+\frac{k_z^4}{q^4}\left(\mathrm{Im}D_{zz}\right)^2+\frac{2}{k_z^2}\left(\frac{\partial}{\partial z}\mathrm{Im}D_{zz}\right)^2\right]\right.$$
$$+\left(\frac{c}{\omega}\right)^4\left[k_z^4\left(\mathrm{Im}D_{nn}\right)^2+\left(\frac{\partial^2}{\partial z\partial z'}\mathrm{Im}D_{nn}\right)^2\right.$$
$$\left.\left.+2k_z^2\left(\frac{\partial}{\partial z'}\mathrm{Im}D_{nn}(z,z')\right)^2\right]\right\}_{z=z'=0}. \tag{J.25}$$

Substitution of the expressions for the Green's functions from (C.9), (C.10), (C.16) in (J.25) gives the contribution to the friction from the propagating waves:

$$\gamma_\perp^{rad} = \frac{\hbar}{16\pi^3}\int_0^\infty d\omega\left(-\frac{\partial n}{\partial\omega}\right)\int_{q<\frac{\omega}{c}} d^2\mathbf{q}k_z^2$$
$$\times\left[\left(\mathrm{Re}\frac{1+R_{1p}R_{2p}e^{2ik_zd}-R_{1p}-R_{2p}e^{2ik_zd}}{1-e^{2ik_zd}R_{1p}R_{2p}}\right)^2+\left(\mathrm{Re}\frac{1+R_{1p}R_{2p}e^{2ik_zd}+R_{1p}+R_{2p}e^{2ik_zd}}{1-e^{2ik_zd}R_{1p}R_{2p}}\right)^2\right.$$
$$\left.+2\left(\mathrm{Im}\frac{R_{1p}-R_{2p}e^{2ik_zd}}{1-e^{2ik_zd}R_{1p}R_{2p}}\right)^2+[p\to s]\right]=\frac{\hbar}{4\pi^2}\int_0^\infty d\omega\left(-\frac{\partial n}{\partial\omega}\right)\int_0^{\frac{\omega}{c}} dqqk_z^2$$
$$\times\frac{(1-|R_{1p}|^2|R_{2p}|^2)^2+|(1-|R_{1p}|^2)R_{2p}e^{ik_zd}+(1-|R_{2p}|^2)R_{1p}^*e^{-ik_zd}|^2}{|1-e^{2ik_zd}R_{1p}R_{2p}|^4}+[p\to s]. \tag{J.26}$$

In similar way one can obtain the contribution to the friction from the evanescent electromagnetic waves:

$$\gamma_\perp^{evan} = \frac{\hbar}{4\pi^3}\int_0^\infty d\omega\left(-\frac{\partial n}{\partial\omega}\right)\int_{q>\frac{\omega}{c}} d^2\mathbf{q}|k_z|^2$$
$$\times\left[\left(\mathrm{Im}\frac{2R_{1p}R_{2p}e^{-2|k_z|d}-R_{1p}-R_{2p}e^{-2|k_z|d}}{1-e^{-2|k_z|d}R_{1p}R_{2p}}\right)^2\right.$$
$$\left.+\left(\mathrm{Im}\frac{2R_{1p}R_{2p}e^{-2|k_z|d}+R_{1p}+R_{2p}e^{-2|k_z|d}}{1-e^{-2|k_z|d}R_{1p}R_{2p}}\right)^2\right. \tag{J.27}$$

$$-2\left(\mathrm{Im}\frac{R_{1p}-R_{2p}e^{-2|k_z|d}}{1-e^{-2|k_z|d}R_{1p}R_{2p}}\right)^2+[p\to s]\Big]=\frac{\hbar}{\pi^2}\int_0^\infty d\omega\left(-\frac{\partial n}{\partial\omega}\right)\int_{\frac{\omega}{c}}^\infty dqq|k_z|^2e^{-2|k_z|d}$$
$$\times\Big[\Big(\mathrm{Im}R_{1p}+e^{-2|k_z|d|}|R_{1p}|^2\mathrm{Im}R_{2p}\Big)\Big(\mathrm{Im}R_{2p}+e^{-2|k_z|d|}|R_{2p}|^2\mathrm{Im}R_{1p}\Big)$$
$$+e^{-2|k_z|d}\Big(\mathrm{Im}(R_{1p}R_{2p})\Big)^2\Big]\frac{1}{|1-e^{-2|k_z|d}R_{1p}R_{2p}|^4}+[p\to s]. \quad \text{(J.28)}$$

Equations (J.26) and (J.28) were first presented without derivation in [99]. In [100], (J.26) and (J.28) were derived using the dynamical modification of the semiclassical Lifshitz theory [42] of the van der Waals interaction, and the Rytov theory [5–7] of the fluctuating electromagnetic field.

Appendix K
Calculation of the Casimir Friction Between a Small Particle and Plane Surface Using Quantum Field Theory

K.1 Parallel Relative Motion

For parallel relative motion, the friction coefficient $\Gamma_{\parallel} = \Gamma_{xx} = \Gamma_{yy}$. The Lorentz force acting on a small particle located at point $\mathbf{r}_0$ can be written in the form

$$\hat{F}_x = \left[p_k \frac{\partial}{\partial x_k} E_x(\mathbf{r}) + \frac{1}{c} \left(j_y B_z - j_z B_y \right) \right]_{\mathbf{r}=\mathbf{r}_0}, \tag{K.1}$$

where $\mathbf{p}$ and $\mathbf{j}$ are the dipole moment and current operators of the particle, respectively. $\mathbf{E}$ and $\mathbf{B}$ are the external electric and magnetic induction field operators, respectively. The interaction of the electromagnetic field with the particle is described by the Hamiltonian

$$H_{int} = -\frac{1}{c} \mathbf{A}(\mathbf{r}_0) \cdot \mathbf{j}, \tag{K.2}$$

where $\mathbf{A}(\mathbf{r})$ is the vector potential operator. Taking into account that

$$\mathbf{j} = \frac{\partial}{\partial t} \mathbf{p}, \tag{K.3}$$

$$\nabla \times \mathbf{E} = \frac{1}{c} \frac{\partial}{\partial t} \mathbf{B}, \tag{K.4}$$

one can prove that the friction coefficient is determined by (J.1) where

$$G^R_{xx}(\omega) = \frac{i}{\hbar} \int_0^{\infty} dt e^{i\omega t} \times \left\langle p_k(t) \frac{\partial}{\partial x} E_k(\mathbf{r}, t) p_l(0) \frac{\partial}{\partial x'} E_l(\mathbf{r}', 0) - p_l(0) \frac{\partial}{\partial x'} E_l(\mathbf{r}', 0) p_k(t) \frac{\partial}{\partial x} E_k(\mathbf{r}, t) \right\rangle_{\mathbf{r}=\mathbf{r}'=\mathbf{r}_0}, \tag{K.5}$$

A.I. Volokitin and B.N.J. Persson, *Electromagnetic Fluctuations at the Nanoscale*, NanoScience and Technology, DOI 10.1007/978-3-662-53474-8

where summation over repeated indexes is assumed. Performing similar calculations as in Appendix J and using the relation

$$\mathbf{E}(\mathbf{r},t) = -\frac{1}{c}\frac{\partial}{\partial t}\mathbf{A}(\mathbf{r},t), \tag{K.6}$$

we get

$$\Gamma_{\parallel} = \frac{2\hbar}{\pi}\int_0^{\infty} d\omega \left(-\frac{\partial n}{\partial \omega}\right)\left\{\sum_{k=x,y,z} \mathrm{Im}\alpha_{kk}\frac{\partial^2}{\partial x \partial x'}\mathrm{Im}D_{kk}(\mathbf{r},\mathbf{r}',\omega)\right.$$
$$\left. - 2\mathrm{Re}\left(\alpha_{xx}(\omega)\alpha_{zz}^{*}(\omega)\right)\left(\frac{\partial}{\partial x}\mathrm{Im}D_{xz}(\mathbf{r},\mathbf{r}_0,\omega)\right)^2\right\}_{\mathbf{r}=\mathbf{r}'=\mathbf{r}_0}, \tag{K.7}$$

where $D_{ij}(\mathbf{r},\mathbf{r}')$ is the Green's functions of the electromagnetic field for one plane surface. These Green's functions can be obtained from the Green's functions for the two-plane surface geometry (see Appendix C) by putting $R_{2p(s)} = 0$. The polarizability of the particle

$$\alpha_{kk}(\omega) = \frac{i}{\hbar}\int_0^{\infty} dt e^{i\omega t}\left\langle p_k(t)p_k(0) - p_k(0)p_k(t)\right\rangle \tag{K.8}$$

can be written as

$$\alpha_{ii}(\omega) = \frac{\alpha_{ii}^0(\omega)}{1-\alpha_{ii}^0(\omega)D_{ii}(\mathbf{r}_0,\mathbf{r}_0)}, \tag{K.9}$$

where $\alpha_{ii}^0(\omega)$ is the free-particle polarizability. In deriving (K.7) we have also used the identity

$$\mathrm{Im}\alpha_{xx}(\omega)\mathrm{Im}\left[\alpha_{zz}(\omega)\frac{\partial}{\partial x}D_{xz}(\mathbf{r},\mathbf{r}_0,\omega)\frac{\partial}{\partial x}D_{xz}(\mathbf{r},\mathbf{r}_0,\omega)\right]$$
$$+\mathrm{Im}\alpha_{zz}(\omega)\mathrm{Im}\left[\alpha_{xx}(\omega)\frac{\partial}{\partial x}D_{xz}(\mathbf{r},\mathbf{r}_0,\omega)\frac{\partial}{\partial x}D_{xz}(\mathbf{r},\mathbf{r}_0,\omega)\right]$$
$$-2\mathrm{Im}\left[\alpha_{xx}(\omega)\frac{\partial}{\partial x}D_{xz}(\mathbf{r},\mathbf{r}_0,\omega)\right]\mathrm{Im}\left[\alpha_{zz}(\omega)\frac{\partial}{\partial x}D_{xz}(\mathbf{r},\mathbf{r}_0,\omega)\right]$$
$$= 2\mathrm{Re}\left(\alpha_{xx}(\omega)\alpha_{zz}^{*}(\omega)\right)\left(\frac{\partial}{\partial x}\mathrm{Im}D_{xz}(\mathbf{r},\mathbf{r}_0,\omega)\right)^2. \tag{K.10}$$

K.2 Normal Relative Motion

The friction coefficient for a particle moving normal to the sample surface can be obtained in a similar as for parallel relative motion. In this case the Green's function G^R_{xx} must be replaced by G^R_{zz} where

$$G^R_{zz}(\omega) = \frac{i}{\hbar}\int_0^\infty dt e^{i\omega t} \times \left\langle p_k(t)\frac{\partial}{\partial z}E_k(\mathbf{r},t)p_l(0)\frac{\partial}{\partial z'}E_l(\mathbf{r}',0) - p_l(0)\frac{\partial}{\partial z'}E_l(\mathbf{r}',0)p_k(t)\frac{\partial}{\partial z}E_k(\mathbf{r},t)\right\rangle_{\mathbf{r}=\mathbf{r}'=\mathbf{r}_0}. \tag{K.11}$$

Performing similar calculations as in Appendix K.1, we get

$$\Gamma_\perp = \frac{2\hbar}{\pi}\int_0^\infty d\omega\left(-\frac{\partial n}{\partial\omega}\right)\sum_{k=x,y,z}\left\{\mathrm{Im}\alpha_{kk}(\omega)\frac{\partial^2}{\partial z\partial z'}\Big[\mathrm{Im}D_{kk}(\mathbf{r},\mathbf{r}',\omega) + \mathrm{Im}\left(\alpha_{kk}D_{kk}(\mathbf{r},\mathbf{r}_0,\omega)D_{kk}(\mathbf{r}',\mathbf{r}_0,\omega)\right)\Big] + \Big[\frac{\partial}{\partial z}\mathrm{Im}\left(\alpha_{kk}(\omega)D_{kk}(\mathbf{r},\mathbf{r}_0,\omega)\right)\Big]^2\right\}_{\mathbf{r}=\mathbf{r}'=\mathbf{r}_0}. \tag{K.12}$$

For a spherical particle with radius R, (K.12) is only valid if $R \ll d$. In the non-resonant case $\alpha^0_{kk} \sim R^3$ and $D_{kk} \sim d^{-3}$. Thus in this case $\alpha D \sim (R/d)^3 \ll 1$ and we can neglect screening effects. For a spherical particle $\alpha_{kk} = \alpha$, and using the formula (which is valid in the non-retarded limit, formally obtained as $c \to \infty$, see [139] and also Appendix C)

$$\sum_{k=x,y,z} D_{kk}(\mathbf{r},\mathbf{r}',\omega) = 4\pi\int\frac{d^2qq}{(2\pi)^2}\left[e^{-q|z-z'|} + R_p(q,\omega)e^{-q(z+z')}\right]e^{i\mathbf{q}(\mathbf{x}-\mathbf{x}')}, \tag{K.13}$$

from (K.7) and (K.12) we get

$$\Gamma_\parallel = 2\frac{\hbar}{\pi}\int_0^\infty \mathrm{d}\omega\left(-\frac{\partial n(\omega)}{\partial\omega}\right)\int_0^\infty \mathrm{d}qq^4e^{-2qd}\mathrm{Im}R_p(q,\omega)\mathrm{Im}\alpha(\omega) \tag{K.14}$$

Equations (K.7) and (K.12) were obtained in [139] using the dynamical modification of the semi-classical Rytov theory [5–7] of the fluctuating electromagnetic field, and (K.14) was derived in [145] using the fluctuation-dissipation theorem.

Appendix L
Derivation of (8.77)

Assume that $\{\phi_n\}$ forms an incomplete set of basis function and that we want to approximate a function f that is as accurate as possible by a sum $f \approx \sum_n a_n \phi_n$. The standard way of doing this is to form $I = \int d^3x (f - \sum_n a_n \phi_n)^2$ and minimize I with respect to the expansion coefficients a_n. In the present case this gives (8.77). If we define the error $\epsilon = I / \int d^3x f^2$ then, in the present case, we obtain $\epsilon = 0.07$ and $\epsilon = 0.18$ for the case $\mathbf{e} = \hat{x}$ and $\hat{z}$, respectively.

A.I. Volokitin and B.N.J. Persson, *Electromagnetic Fluctuations at the Nanoscale*,
NanoScience and Technology, DOI 10.1007/978-3-662-53474-8

Appendix M
Reflection Amplitudes for a 2D Quantum Well

The reflection amplitudes for a 2D-electron system are determined by [144]

$$R_{s(p)} = \frac{\epsilon_{s(p)} - 1}{\epsilon_{s(p)} + 1}, \qquad \epsilon_s = \frac{4\pi\omega\sigma_t}{k_z c^2} + 1, \qquad \epsilon_p = \frac{4\pi k_z \sigma_l}{\omega\varepsilon} + 1, \tag{M.1}$$

where σ_l and σ_t are the transverse and longitudinal conductivities of the layer. The longitudinal conductivity can be written in the form

$$\sigma_l(\omega, q) = \frac{-\mathrm{i}\omega}{q^2}\chi_l(\omega, q), \tag{M.2}$$

where χ_l is the finite lifetime generalization of the longitudinal 2D-Lindhard response function, which can be written as [354]:

$$\chi_l(\omega, Q) = \frac{(1 + i/\omega\tau)\chi_l^0(\omega + i/\tau, Q)}{1 + (i/\omega\tau)\chi_l^0(\omega + i/\tau, Q)/\chi_l^0(0, Q)}, \tag{M.3}$$

where, for a degenerate electron gas,

$$\chi_l^0(\omega, q) = \frac{n_s e^2}{z m^* v_F^2}\left\{2z + \sqrt{(u - z)^2 - 1} - \sqrt{(u + z)^2 - 1}\right\}, \tag{M.4}$$

where τ is the relaxation time, $z = q/2k_F$, $u = \omega/(q v_F)$, and k_F and v_F are the Fermi wave vector and Fermi velocity, respectively, and n_s is the 2D electron density in the layer. The transverse conductivity of the layer is determined by

$$\sigma_t(\omega, q) = -\frac{i n_s e^2}{3(\omega + i\tau^{-1})m^* z}\left\{\left[(u' + z)^2 - 1\right]^{3/2} - \left[(u' - z)^2 - 1\right]^{3/2} - 2z\left[3u'^2 + z^2\right]\right\}, \tag{M.5}$$

A.I. Volokitin and B.N.J. Persson, *Electromagnetic Fluctuations at the Nanoscale*,
NanoScience and Technology, DOI 10.1007/978-3-662-53474-8

where $u' = \omega + i\tau^{-1}$. For a non-degenerate electron gas the longitudinal conductivity is determined by (M.2) with

$$\chi_l^0(\omega, q) = \frac{n_s e^2}{k_B T}\left[1 + F\left(\frac{\omega}{\sqrt{2}q v_T}\right)\right], \tag{M.6}$$

and transverse conductivity is given by

$$\sigma_t(\omega, q) = -\frac{\mathrm{i}n_s e^2}{m^*(\omega + \mathrm{i}k_z)} F\left(\frac{\omega}{\sqrt{2}q v_T}\right), \tag{M.7}$$

where $v_T = \sqrt{k_B T/m^*}$ and m^* is the effective electron mass, and where the function $F(x)$ is defined by the integral

$$F(x) = \frac{x}{\sqrt{\pi}} \int_{-\infty}^{+\infty} dz \frac{e^{-z^2}}{z - x - i0}. \tag{M.8}$$

Appendix N
Quantum VC Radiation in the Plate-Plate Configuration

N.1 Close to the Threshold Velocity

Close to the threshold ($(v - v_c)/v_0 \ll 1$), the range in ω becomes narrow. For small $\omega - q_x v$:

$$k_{zn}^2 = n^2\left(\frac{\omega}{c}\right)^2 - q^2 = \left[\frac{(\omega - q_x v_0)(\omega + q_x v_0)}{v_0^2} - q_y^2\right] \approx \left(\frac{\omega - q_x v_0}{v_0}\right) 2q_x - q_y^2, \tag{N.1}$$

$$\begin{aligned} k_{nz}'^2 &= \left(\frac{\omega'}{v_0}\right)^2 - q'^2 \\ &= -\gamma^2 \frac{[q_x(v - v_0) - \omega(1 - vv_0/c^2)][q_x(v + v_0) - \omega(1 + vv_0/c^2]}{v_0^2} - q_y^2 \\ &= \frac{1}{v_0}\left[\frac{(n^2+1)^2}{n^2(n^2-1)}(v - v_c)q_x - (\omega - q_x v_0)\right] 2q_x - q_y^2. \end{aligned} \tag{N.2}$$

From (N.1) and (N.2) follow the ranges in ω and q_y: $\omega_- < \omega < \omega_+$ where

$$\omega_- = q_x v_0 + \frac{v_0 q_y^2}{2q_x}, \quad \omega_+ = q_x v_0 + \frac{(n^2+1)^2}{n^2(n^2-1)}(v - v_c)q_x - \frac{v_0 q_y^2}{2q_x},$$

and $0 \le q_y \le q_{max}$, where

$$q_{max}^2 = \frac{(n^2+1)^2}{n^2(n^2-1)}\frac{v - v_c}{v_0} q_x^2 \ll q_x^2.$$

After changing the variables $q_y \to q_x y_{max} y$,

A.I. Volokitin and B.N.J. Persson, *Electromagnetic Fluctuations at the Nanoscale*, NanoScience and Technology, DOI 10.1007/978-3-662-53474-8

$$\omega \to q_x v_0 \left(1 + \frac{y_{max}^2}{2} + z y_{max}^2 \frac{1-y^2}{2}\right),$$

where

$$y_{max}^2 = \frac{(n^2+1)^2}{n^2(n^2-1)} \frac{v - v_c}{v_0},$$

the imaginary parts for the reflection amplitudes can be written in the form

$$\mathrm{Im} R_s = \frac{2k_z k_{zn}}{k_z^2 + k_{zn}^2} \approx \frac{2k_{zn}}{k_z} \approx \frac{2n}{q_x\sqrt{n^2-1}} \sqrt{\left(\frac{\omega - q_x v_0}{v_0}\right) 2q_x - q_y^2} = \frac{2n y_{max}}{\sqrt{n^2-1}} \sqrt{1-y^2}\sqrt{1+z} \sim \sqrt{\frac{v-v_c}{v_0}}, \tag{N.3}$$

$$\mathrm{Im} R_s' = \frac{2k_z k_{zn}'}{k_z^2 + k_{zn}'^2} \approx \frac{2k_{zn}'}{k_z} \approx \frac{2n}{q_x\sqrt{n^2-1}} \sqrt{\frac{1}{v_0}\left[\frac{(n^2+1)^2}{n^2-1}(v-v_c)q_x - (\omega - q_x v_0)\right] 2q_x - q_y^2}$$

$$= \frac{2n y_{max}}{\sqrt{n^2-1}} \sqrt{1-y^2}\sqrt{1-z} \sim \sqrt{\frac{v-v_c}{v_0}}, \tag{N.4}$$

$\mathrm{Im} R_p \approx \mathrm{Im} R_s/n^2$, $\mathrm{Im} R_p' \approx \mathrm{Im} R_s'/n^2$. Because the integrand in (11.20) is proportional to the product of the imaginary parts of the reflection amplitudes, which are of the order $(v - v_c)/v_0$ to lowest order in $(v - v_c)/v_0$, all other terms in the integrand should be taken at $v = v_c$. In this approximation, the mixing of the waves with the different polarization can be neglected because they are of order $q_y^2 \sim (v - v_c)/v_0$ and the reflection amplitudes $R_s = R_p = 1$, and the integral for the contribution to the friction force from s-polarized waves is reduced to

$$F_{1x}^s \approx \frac{\hbar v_0}{\pi^3} \int_0^\infty dq_x q_x^3 \frac{e^{-2q_x d\sqrt{n^2-1}/n}}{(1 - e^{-2q_x d\sqrt{n^2-1}/n})^2} \left(\frac{2n}{\sqrt{n^2-1}}\right)^2 y_{max}^5 \int_0^1 dy (1-y^2)^2 \int_{-1}^1 dz \sqrt{1-z^2} \tag{N.5}$$

which produces (11.28).

N.2 Close to the Light Velocity: $v \to c$

Introducing new variables $\omega = q_x v \xi$ and $q_y = q_x y$ the integration in (11.27) over q_x can be performed analytically giving

$$\begin{pmatrix} F_x \\ P_1 \end{pmatrix} = -\frac{3\hbar v}{8\pi^3 d^4} \int_{\xi_{min}}^{\xi_{max}} d\xi \int_0^{y_{max}} dy \begin{pmatrix} 1 \\ v\xi \end{pmatrix} \frac{1}{\kappa_z^4} \left[\left(\mathrm{Im} R_{1p} \mathrm{Im} R_{2p}' + \mathrm{Im} R_{1s} \mathrm{Im} R_{2s}'\right) \left(1 + \gamma^2\beta^2 \frac{\kappa_z^2 y^2}{w^2 w'^2}\right) \right.$$
$$\left. + \gamma^2\beta^2 \frac{\kappa_z^2 y^2}{w^2 w'^2} \left(\mathrm{Im} R_{1p} \mathrm{Im} R_{2s}' + \mathrm{Im} R_{1s} \mathrm{Im} R_{2p}'\right) \right] \tag{N.6}$$

where: $\kappa_z^2 = 1 - \beta^2\xi^2 + y^2$, $w^2 = 1 + y^2$, $w'^2 = \gamma^2(1 - \beta^2\xi)^2 + y^2$,

$$\xi_{min} = \frac{1}{n\beta},\ \xi_{max} = 1 - \frac{1}{\gamma^2\beta(n-\beta)} = \frac{n\beta - 1}{\beta(n-\beta)}.$$

In new variables $k_z = q_x\kappa_z$,

$$k_{nz}^2 = (n^2-1)\left(\frac{\omega}{c}\right)^2 - k_z^2 = q_x^2(y_1^2 - y^2),$$

$$k_{nz}'^2 = (n^2-1)\left(\frac{\omega'}{c}\right)^2 - k_z^2 = q_x^2(y_0^2 - y^2),$$

where $y_1 = n^2\beta^2\xi^2 - 1$,

$$y_0^2 = \gamma^2[n^2\beta^2(1-\xi)^2 - (1-\beta^2\xi)^2]$$

$$\mathrm{Im}R_s = \frac{2k_zk_{nz}}{k_z^2 + k_{nz}^2} = \frac{2\sqrt{1-\beta^2\xi^2+y^2}\sqrt{y_1^2-y^2}}{(n^2-1)\beta^2\xi^2},$$

$$\mathrm{Im}R_s' = \frac{2k_zk_{nz}'}{k_z^2 + k_{nz}'^2} = \frac{2\sqrt{1-\beta^2\xi^2+y^2}\sqrt{y_0^2-y^2}}{(n^2-1)\gamma^2\beta^2(1-\xi)^2},$$

$$\mathrm{Im}R_p = \frac{2n^2k_zk_{nz}}{n^4k_z^2 + k_{nz}^2} = \frac{2n^2\sqrt{1-\beta^2\xi^2+y^2}\sqrt{n^2\beta^2\xi^2-1-y^2}}{(n^2-1)\beta^2\xi^2 + (n^4-1)(1-\beta^2\xi^2+y^2)},$$

$$\mathrm{Im}R_p' = \frac{2n^2k_zk_{nz}}{n^4k_z^2 + k_{nz}^2} = \frac{2n^2\sqrt{1-\beta^2\xi^2+y^2}\sqrt{y_0^2-y^2}}{y_0^2 + (n^4-1)(1-\beta^2\xi^2+y^2) + 1 - \beta^2\xi^2},$$

$$y_{max} = \begin{cases} y_0 \text{ for } \xi_c < \xi < \xi_{max} \\ y_1 \text{ for } \xi_{min} < \xi < \xi_c \end{cases},$$

where $\xi_c = \gamma/(1+\gamma) \approx 1 - 1/\gamma$. For $\gamma \gg 1$, the main contribution to the integral over ξ in (N.6) comes from the region $\xi_c < \xi < \xi_{max}$. The s-wave contribution is given by

$$\begin{pmatrix} F_{xs} \\ P_{1s} \end{pmatrix} \approx \frac{3\hbar w}{8\pi^3 d^4}\int_{\xi_c}^{\xi_{max}} d\xi \int_0^1 dy \begin{pmatrix} 1 \\ v \end{pmatrix} \frac{4y_0^2\sqrt{1-y^2}}{(n^2-1)^{3/2}\gamma^2(1-\xi)^2}$$

$$\times\left\{\frac{1}{1-\beta^2\xi^2+y_0^2y^2} + \gamma^2\frac{y_0^2y^2}{(1+y_0^2y^2)[\gamma^2(1-\beta^2\xi)^2 + y_0^2y^2]}\right\}$$

$$\approx \frac{3\hbar v}{4\pi^2 d^4}\begin{pmatrix}1\\ v\end{pmatrix}\left\{\left[\frac{\sqrt{2}}{n^2-1}\ln(n+\sqrt{n^2-1})-\frac{1}{\sqrt{n^2-1}(n+1)}-\frac{2}{(n^2-1)\sqrt{\gamma}}+\frac{1}{(n^2-1)^{3/2}\gamma}\right]\right.$$

$$\left.+\left[\frac{\sqrt{n-1}}{2(n+1)^{3/2}}\gamma-\frac{1}{\sqrt{n^2-1}(n+1)}\ln(n-1)\gamma-\frac{1}{2(n^2-1)^{3/2}\gamma}\right]\right\}. \quad \text{(N.7)}$$

The other contributions can be estimated in a similar way.

Appendix O
Quantum VC Radiation in the Particle–Plate Configuration

O.1 Particle with No Losses

O.1.1 Close to the Threshold Velocity

The resonant contribution to the friction force comes from ω in the range

$$\omega_0 < \omega < \frac{v - v_0}{1 - vv_0/c^2} q_x.$$

Near resonance, the particle polarazibility can be approximated by the formula

$$\mathrm{Im}\alpha = R^3\omega_0^2 \frac{\omega\gamma}{(\omega^2 - \omega_0^2)^2 + \omega^2\gamma^2} \approx R^3\omega_0 \frac{\pi}{2}[\delta(\omega - \omega_0) - \delta(\omega + \omega_0)] \qquad \text{(O.1)}$$

Close to the threshold velocity ($(v - v_0)/v_0 \ll 1$) and at the resonance

$$k_{nz}'^2 = -\frac{1}{v_0}\left[\frac{n^2}{(n^2 - 1)}(v - v_0)q_x - \omega_0\right] 2q_x - q_y^2. \qquad \text{(O.2)}$$

Introducing new variables $q_x = q_0 x$, $q_y = q_0 y_{max} y$ where $q_0 = \omega_0(n^2 - 1)/((v - v_0)n^2)$,

$$y_{max}^2 = 2\frac{n^2}{n^2 - 1} x(x - 1)\frac{v - v_0}{v_0} \ll x^2$$

the imaginary part of the reflection amplitudes can be written in the form

$$\mathrm{Im}R_w' \approx \frac{2}{x} y_{max}\sqrt{1 - y^2}$$

A.I. Volokitin and B.N.J. Persson, *Electromagnetic Fluctuations at the Nanoscale*, NanoScience and Technology, DOI 10.1007/978-3-662-53474-8

The p-wave resonant contribution to the friction force in the K' frame is given by

$$f'_x \approx -\frac{2^4\hbar q_0^4}{\pi^2(n^2-1)}\left(\frac{\pi}{2}R^3\omega_0\right)\frac{v-v_0}{v_0}\int_1^\infty dx x^2(x-1)e^{-2q_0dx}\int_0^1 dy\sqrt{1-y^2}$$

$$= -\frac{\hbar R^3\omega_0}{4d^4(n^2-1)}\frac{v-v_0}{v_0}[3+4q_0d+2(q_0d)^2]e^{-2q_0d} \tag{O.3}$$

$$w' \approx \frac{2^4\hbar\omega_0 q_0^3}{\pi^2(n^2-1)}\left(\frac{\pi}{2}R^3\omega_0\right)\frac{v-v_0}{v_0}\int_1^\infty dx x(x-1)\int_0^1 dy\sqrt{1-y^2}$$

$$= \frac{\hbar R^3\omega_0^2}{2d^3(n^2-1)}\frac{v-v_0}{v_0}(1+q_0d)e^{-2q_0d}]. \tag{O.4}$$

O.1.2 Limiting Case $v \to c$

In the ultra relativistic limit ($\gamma \gg 1$)

$$\mathrm{Im}\alpha(\omega') = -\frac{\pi}{2}\omega_0 R^3\delta(\omega'+\omega_0) = -\frac{\pi}{2\gamma}\frac{\omega_0 R^3}{v}\delta\left(q_x - \frac{\omega}{v} - \frac{\omega_0}{\gamma v}\right) \tag{O.5}$$

After the integration in (11.31) over q_x

$$k_z^2 = \left(\frac{\omega}{\gamma v}\right)^2 + \frac{2\omega\omega_0}{\gamma v} + \left(\frac{\omega_0}{\gamma v}\right)^2 + q_y^2 \tag{O.6}$$

$$k_{nz}^2 = \left[\frac{\omega}{v}(n\beta-1) - \frac{\omega_0}{\gamma v}\right]\left[\frac{\omega}{v}(n\beta+1) + \frac{\omega_0}{\gamma v}\right] - q_y^2 \tag{O.7}$$

For $\omega < C\gamma v/d$ where $C \ll 1$: $k_z \approx q_y$,

$$k_{nz}^2 \approx (n^2-1)\left(\frac{\omega}{v}\right)^2 - q_y^2 \tag{O.8}$$

Introducing the new variable

$$q_y = \frac{\omega}{v}y\sqrt{n^2-1}$$

where $0 \le y \le 1$, the imaginary part of the reflection amplitudes can be written in the form

$$\mathrm{Im}R_s = \frac{2k_z k_{nz}}{k_z^2+k_{nz}^2} = 2y\sqrt{1-y^2}, \tag{O.9}$$

$$\mathrm{Im}R_p = \frac{2n^2k_zk_{nz}}{n^4k_z^2+k_{nz}^2} = \frac{2n^2y\sqrt{1-y^2}}{1+(n^4-1)y^2}, \tag{O.10}$$

and

$$\phi_p \approx \phi_s \approx 2\gamma^2\left(\frac{\omega}{v}\right)^2\frac{(n^2-1)^2y^4}{1+(n^2-1)y^2}. \tag{O.11}$$

The contributions from the s- and p-polarized waves in the K frame are given by

$$f_{sx} = -\frac{4\hbar}{\pi}\omega_0R^3\int_0^1 dy\frac{(n^2-1)^2y^4\sqrt{1-y^2}}{1+(n^2-1)y^2}\int_0^\infty d\left(\frac{\omega}{v}\right)\left(\frac{\omega}{v}+\frac{\omega_0}{\gamma v}\right)\left(\frac{\omega}{v}\right)^2 e^{-2(\omega/v)yd\sqrt{n^2-1}}$$

$$= -\frac{3\hbar\omega_0R^3}{2d^4(n+1)}\left[1+\left(\frac{\omega_0d}{c\gamma}\right)C\right] \tag{O.12}$$

where

$$C = \frac{2}{3\pi}\sqrt{\frac{n+1}{n-1}}\left[\frac{n}{\sqrt{n^2-1}}\tanh^{-1}\frac{\sqrt{n^2-1}}{n}-1\right],$$

$$w_s = -\frac{4\hbar v}{\pi}\omega_0R^3\int_0^1 dy\frac{(n^2-1)^2y^4\sqrt{1-y^2}}{1+(n^2-1)y^2}\int_0^\infty d\left(\frac{\omega}{v}\right)\left(\frac{\omega}{v}\right)^3 e^{-2(\omega/v)yd\sqrt{n^2-1}}$$

$$= -\frac{3\hbar v\omega_0R^3}{2d^4(n+1)}, \tag{O.13}$$

$$f_{px} = -\frac{4\hbar}{\pi}\omega_0R^3\int_0^1 dy\frac{n^2(n^2-1)^2y^4\sqrt{1-y^2}}{[1+(n^2-1)y^2][1+(n^4-1)y^2]}\int_0^\infty d\left(\frac{\omega}{v}\right)\left(\frac{\omega}{v}+\frac{\omega_0}{\gamma v}\right)\left(\frac{\omega}{v}\right)^2 e^{-2(\omega/v)yd\sqrt{n^2-1}}$$

$$= -\frac{3\hbar\omega_0R^3}{2d^4}\frac{n}{n+1}\left[1+\left(\frac{\omega_0d}{c\gamma}\right)C'\right], \tag{O.14}$$

where

$$C' = \frac{2}{3\pi}n\sqrt{\frac{n+1}{n-1}}\left[\frac{n^2}{\sqrt{n^4-1}}\tanh^{-1}\frac{\sqrt{n^4-1}}{n^2}-\frac{n}{\sqrt{n^2-1}}\tanh^{-1}\frac{\sqrt{n^2-1}}{n}\right],$$

$$w_p = -\frac{4\hbar}{\pi}\omega_0R^3\int_0^1 dy\frac{n^2(n^2-1)^2y^4\sqrt{1-y^2}}{[1+(n^2-1)y^2][1+(n^4-1)y^2]}\int_0^\infty d\left(\frac{\omega}{v}\right)\left(\frac{\omega}{v}\right)^3 e^{-2(\omega/v)yd\sqrt{n^2-1}}$$

$$= -\frac{3\hbar v\omega_0R^3}{2d^4}\frac{n}{n+1}. \tag{O.15}$$

In deriving (O.12)–(O.15), the following integrals were used

$$\int_0^1 dy\frac{\sqrt{1-y^2}}{1+(n^2-1)y^2} = \frac{\pi}{n+1},$$

$$\int_0^1 dy\frac{y\sqrt{1-y^2}}{1+(n^2-1)y^2} = \frac{1}{n^2-1}\left[\frac{n}{\sqrt{n^2-1}}\tanh^{-1}\frac{\sqrt{n^2-1}}{n}-1\right],$$

$$\int_0^1 dy \frac{\sqrt{1-y^2}}{]1+(n^2-1)y^2][1+(n^4-1)y^2]} = \frac{\pi}{n(n+1)},$$

$$\int_0^1 dy \frac{\sqrt{1-y^2}}{]1+(n^2-1)y^2][1+(n^4-1)y^2]} = \frac{1}{n^2(n^2-1)}\left[\frac{n^2}{\sqrt{n^4-1}}\tanh^{-1}\frac{\sqrt{n^4-1}}{n^2} - \frac{n}{\sqrt{n^2-1}}\tanh^{-1}\frac{\sqrt{n^2-1}}{n}\right].$$

In the K', frame the friction force and the heat absorbed by a particle can be obtained from the corresponding quantities in the K frame using the Lorenz transformations (8.24). For example, for the contributions from the s-polarized waves

$$f_s' = \gamma^2(f_s - \beta w_s) \approx -\frac{3\hbar\omega_0 R^3}{2d^4(n+1)}\left[1 + C\gamma\frac{\omega_0 d}{c}\right], \tag{O.16}$$

and

$$w_s' = \gamma^2(w_s - v f_s) \approx \frac{3\hbar v\omega_0 R^3}{2d^4(n+1)} C\gamma\frac{\omega_0 d}{c}. \tag{O.17}$$

Thus, contrary to the K frame where the friction force and the power of photon emission are finite, in the K' frame the friction force and the radiation power both diverge as $(1-\beta)^{-1/2}$. These results can be confirmed by the direct calculations in the K' where

$$\mathrm{Im}\alpha(\omega) = -\frac{\pi}{2}\omega_0 R^3\delta(\omega-\omega_0) \tag{O.18}$$

After the integration in (11.32) over ω

$$k_z^2 = q_x^2 + q_y^2 - \left(\frac{\omega_0}{c}\right)^2 \tag{O.19}$$

$$k_{nz}'^2 = \gamma^2\left[n^2\beta^2\left(q_x - \frac{\omega_0}{v}\right)^2 - \left(q_x - \frac{\omega_0}{c}\right)^2\right] - q_y^2$$

$$\approx \gamma^2(n^2-1)\left(q_x - \frac{\omega_0}{v}\right)^2 - q_y^2 \tag{O.20}$$

Introducing the new variable

$$q_y = \gamma\sqrt{n^2-1}\left(q_x - \frac{\omega_0}{v}\right) y$$

where $0 \le y \le 1$ and $q_x \ge \omega_0/v$, the same (O.9) and (O.10) are obtained for $\mathrm{Im}R_{p(s)}$ and

$$\phi_p \approx \phi_s \approx 2\gamma^4\left(q_x - \frac{\omega_0}{v}\right)^2 \frac{(n^2-1)^2 y^4}{1+(n^2-1)y^2}. \tag{O.21}$$

The contributions from the s- and p-polarized waves in the K' frame are given by

$$f'_{sx} = -\frac{4\hbar}{\pi}\omega_0 R^3\gamma^4\int_0^1 dy\frac{(n^2-1)^2y^4\sqrt{1-y^2}}{1+(n^2-1)y^2}\int_0^\infty dq_x q_x\left(q_x-\frac{\omega_0}{v}\right)^2 e^{-2(q_x-\omega_0/v)yd\gamma\sqrt{n^2-1}}$$
$$= -\frac{3\hbar\omega_0 R^3}{2d^4(n+1)}\left[1+C\gamma\frac{\omega_0 d}{c}\right], \tag{O.22}$$

$$w'_s = \frac{4\hbar}{\pi}\omega_0^2 R^3\gamma^4\int_0^1 dy\frac{(n^2-1)^2y^4\sqrt{1-y^2}}{1+(n^2-1)y^2}\int_0^\infty dq_x\left(q_x-\frac{\omega_0}{v}\right)^2 e^{-2(q_x-\omega_0/v)yd\gamma\sqrt{n^2-1}}$$
$$= \frac{3\hbar v\omega_0 R^3}{2d^4(n+1)}C\gamma\frac{\omega_0 d}{c}. \tag{O.23}$$

O.2 The Off-Resonant Contribution for a Particle with Losses Close to the Threshold Velocity

The off-resonant contribution to the friction force comes from ω in the range

$$0 < \omega < \frac{v-v_0}{1-vv_0/c^2}q_x \ll \omega_0.$$

In this frequency range, the low-frequency approximation for the particle polarizability can be used

$$\mathrm{Im}\alpha = R^3\omega_0^2\frac{\omega\gamma}{(\omega^2-\omega_0^2)^2+\omega^2\gamma^2} \approx R^3\frac{\omega\gamma}{\omega_0^2}$$

Close to the threshold velocity ($(v-v_0)/v_0 \ll 1$), ω is small and to lowest order in $(v-v_0)/v_0 \ll 1$

$$k'^2_{nz} = \left(\frac{\omega'}{v_0}\right)^2 - q'^2$$
$$= \gamma^2\frac{[q_x(v-v_0)-\omega(1-vv_0/c^2)][q_x(v+v_0)-\omega(1+vv_0/c^2]}{v_0^2} - q_y^2$$
$$= \frac{1}{v_0}\left[\frac{n^2}{(n^2-1)}(v-v_0)q_x-\omega\right]2q_x - q_y^2. \tag{O.24}$$

The integration over q_y is restricted by the range $0 < q_y < q_x y_{max}$, where

$$y_{max}^2 = 2\frac{n^2}{n^2-1}\frac{v-v_0}{v_0} \ll 1.$$

Introducing new variables $q_y = q_x y_{max} y$,

$$\omega = q_x v_0 y_{max}^2 \frac{1-y^2}{2} z$$

the imaginary part of the reflection amplitudes can be written in the form

$$\mathrm{Im}\, R_s' = \frac{2k_z k_{zn}'}{k_z^2 + k_{zn}'^2} \approx \frac{2k_{zn}'}{k_z} \approx \frac{2}{q_x}\sqrt{\frac{1}{v_0}\left[\frac{n^2}{(n^2-1)}(v-v_0)q_x - \omega\right] 2q_x - q_y^2}$$

$$= 2y_{max}\sqrt{1-y^2}\sqrt{1-z} \sim \sqrt{\frac{v-v_0}{v_0}}, \tag{O.25}$$

and $\mathrm{Im}\, R_s' = \mathrm{Im}\, R_s'/n^2$,

$$\phi_s' \approx 2q_x^2, \;\; \phi_s' \sim q_x^2 y_{max}^2 \ll q_x^2.$$

To lowest order in $(v-v_0)/v_0$ the friction force is determined only by the contribution from the p-polarized waves, which is given by

$$f_x' \approx \frac{2\hbar y_{max}^6 v_0^2 R^3}{n^2\pi^2}\int_0^\infty dq_x q_x^5 e^{-2q_x d}\int_0^1 dy(1-y^2)^{5/2}\int_0^1 dz z\sqrt{1-z}$$

$$= -\frac{5}{4\pi}\frac{\hbar R^3 v_0^2}{d^6\omega_0^2\tau}\frac{n^4}{(n^2-1)^3}\left(\frac{v-v_0}{v_0}\right)^3, \tag{O.26}$$

and the heat absorbed by the particle in the K' frame is given by

$$w' \approx \frac{\hbar y_{max}^8 v_0^3 R^3}{n^2\pi^2}\int_0^\infty dq_x q_x^5 e^{-2q_x d}\int_0^1 dy(1-y^2)^{7/2}\int_0^1 dz z\sqrt{1-z}$$

$$= \frac{35}{64\pi}\frac{\hbar R^3 v_0^3}{d^6\omega_0^2\tau}\frac{n^6}{(n^2-1)^4}\left(\frac{v-v_0}{v_0}\right)^4. \tag{O.27}$$

Appendix P
Phononic Heat Transfer at Planar Interfaces

P.1 Derivation of (12.7)

Here, we prove (12.7). We get

$$\langle |u_{0\mathrm{f}}(\mathbf{q},\omega)|^2\rangle = \frac{1}{(2\pi)^6}\int d^2x dt d^2x' dt'$$

$$\times \langle u_{0\mathrm{f}}(\mathbf{x},t)u_{0\mathrm{f}}(\mathbf{x}',t')\rangle e^{i[\mathbf{q}\cdot(\mathbf{x}-\mathbf{x}')-\omega(t-t')]}$$

$$= \frac{1}{(2\pi)^6}\int d^2x dt d^2x' dt'$$

$$\times \langle u_{0\mathrm{f}}(\mathbf{x}-\mathbf{x}',t-t')u_{0\mathrm{f}}(\mathbf{0},0)\rangle e^{i[\mathbf{q}\cdot(\mathbf{x}-\mathbf{x}')-\omega(t-t')]}$$

$$= \frac{1}{(2\pi)^6}\int d^2x dt d^2x' dt' \langle u_{0\mathrm{f}}(\mathbf{x},t)u_{0\mathrm{f}}(\mathbf{0},0)\rangle e^{i[\mathbf{q}\cdot\mathbf{x}-i\omega t]}$$

$$= \frac{A_0 t_0}{(2\pi)^3} C_{uu}(\mathbf{q},\omega)$$

P.2 Derivation of (12.8)

Here we present an alternative derivation of (12.8). Assume that the two solids interact weakly. In this case the energy transfer from solid **0** to solid **1** is given by (12.6) with $K \to 0$:

$$\Delta E = (2\pi)^3 \int d^2q d\omega\, \omega K^2 \mathrm{Im} M_1(\mathbf{q},\omega)\langle |u_{0\mathrm{f}}(\mathbf{q},\omega)|^2\rangle. \tag{P.1}$$

A.I. Volokitin and B.N.J. Persson, *Electromagnetic Fluctuations at the Nanoscale*,
NanoScience and Technology, DOI 10.1007/978-3-662-53474-8

At thermal equilibrium this must equal the energy transfer from solid **1** to solid **0** given by

$$\Delta E = (2\pi)^3 \int d^2q d\omega \, \omega K^2 \mathrm{Im} M_0(\mathbf{q}, \omega) \langle |u_{1\mathrm{f}}(\mathbf{q}, \omega)|^2 \rangle \tag{P.2}$$

From (P.1) and (P.2) we get

$$\mathrm{Im} M_1(\mathbf{q}, \omega) \langle |u_{0\mathrm{f}}(\mathbf{q}, \omega)|^2 \rangle = \mathrm{Im} M_0(\mathbf{q}, \omega) \langle |u_{1\mathrm{f}}(\mathbf{q}, \omega)|^2 \rangle \tag{P.3}$$

We now assume that solid **1** is a layer of non-interacting harmonic oscillators. Thus if ρ_1 is the mass per unit area we have

$$\rho_1 \ddot{u}_1 + \omega_1^2 u_1 = \sigma$$

or

$$u_1(\mathbf{q}, \omega) = \frac{\sigma(\mathbf{q}, \omega)}{\rho_1(\omega_1^2 - \omega^2) - i0^+}$$

Thus

$$M_1(\mathbf{q}, \omega) = \frac{1}{\rho_1(\omega_1^2 - \omega^2) - i0^+}$$

and for $\omega > 0$

$$\mathrm{Im} M_1(\mathbf{q}, \omega) = \frac{\pi}{2\rho_1\omega_1} \delta(\omega - \omega_1) \tag{P.4}$$

We write u_1 in the standard form:

$$u_1 = \frac{1}{(2\pi)^2} \int d^2q \left(\frac{\hbar}{2\rho_1\omega_1} \right)^{1/2} \left(b_{\mathbf{q}} e^{i(\mathbf{q}\cdot\mathbf{x} - \omega_1 t)} + b_{\mathbf{q}}^+ e^{-i(\mathbf{q}\cdot\mathbf{x} - \omega_1 t)} \right),$$

so that for $\omega > 0$:

$$u_1(\mathbf{q}, \omega) = \frac{1}{(2\pi)^2} \left(\frac{\hbar}{2\rho_1\omega_1} \right)^{1/2} b_{\mathbf{q}} \delta(\omega - \omega_1)$$

Thus we get

$$\langle |u_1(\mathbf{q}, \omega)|^2 \rangle = \frac{t_0}{(2\pi)^5} \frac{\hbar}{2\rho_1\omega_1} \frac{1}{2} \langle b_{\mathbf{q}} b_{\mathbf{q}}^+ + b_{\mathbf{q}}^+ b_{\mathbf{q}} \rangle \delta(\omega - \omega_1)$$

where we have used that

$$[\delta(\omega - \omega_1)]^2 = \delta(\omega - \omega_1) \frac{1}{2\pi} \int dt = \delta(\omega - \omega_1) \frac{t_0}{2\pi}$$

Using

$$\langle b_{\mathbf{q}} b_{\mathbf{q}}^{+} + b_{\mathbf{q}}^{+} b_{\mathbf{q}} \rangle = [2n(\omega_1) + 1](2\pi)^2 \delta(\mathbf{q} - \mathbf{q}) = [2n(\omega_1) + 1] A_0$$

we get

$$\langle |u_{1\mathrm{f}}(\mathbf{q}, \omega)|^2 \rangle = \frac{A_0 t_0}{(2\pi)^5} \frac{\hbar}{2\rho_1 \omega_1} \left(n(\omega) + \frac{1}{2} \right) \delta(\omega - \omega_1) \tag{P.5}$$

Combining (P.3)–(P.5) gives

$$\langle |u_{0\mathrm{f}}(\mathbf{q}, \omega)|^2 \rangle = \frac{2A_0 t_0 \hbar}{(2\pi)^6} \left(n(\omega) + \frac{1}{2} \right) \mathrm{Im} M_0(\mathbf{q}, \omega). \tag{P.6}$$

P.3 Alternative Derivation of (12.8)

Equation (12.8) is a standard result but the derivation is repeated here for the readers convenience. Let us write the Hamiltonian as

$$H = H_0 + \int d^2x \; u(\mathbf{x}, t) \sigma(\mathbf{x}, t)$$

where $\sigma(\mathbf{x}, t)$ is an external stress acting on the surface $z = 0$ of the solid. We first derive a formal expression for $M(\mathbf{q}, \omega)$ defined by the linear response formula

$$\langle u(\mathbf{q}, \omega) \rangle = M(\mathbf{q}, \omega) \sigma(\mathbf{q}, \omega)$$

We write $\langle u \rangle = \mathrm{Tr}(\rho u)$ where the density operator satisfies

$$i\hbar \frac{\partial \rho}{\partial t} = [H, \rho]$$

We write $\rho = \rho_0 + \rho_1$ and get

$$\rho_1 = \frac{1}{i\hbar} \int_{-\infty}^{t} dt' e^{-iH_0(t-t')/\hbar} [V(t'), \rho_0] e^{iH_0(t-t')/\hbar}$$

Thus, using $\langle u \rangle = \mathrm{Tr}(\rho_1 u)$ we get

$$\langle u \rangle = \frac{1}{i\hbar} \int d^2x' dt' \; \theta(t - t') \langle [u(\mathbf{x}, t), u(\mathbf{x}', t')] \rangle \sigma(\mathbf{x}', t')$$

$$= \frac{1}{i\hbar} \int d^2x' dt' \theta(t - t') \langle [u(\mathbf{x} - \mathbf{x}', t - t'), u(\mathbf{0}, 0)] \rangle \sigma(\mathbf{x}', t')$$

Thus

$$M(\mathbf{q},\omega)=\frac{1}{i\hbar}\int d^2x dt\ \theta(t)\langle[u(\mathbf{x},t),u(\mathbf{0},0)]\rangle e^{-i(\mathbf{q}\cdot\mathbf{x}-\omega t)} \tag{P.7}$$

where

$$u(\mathbf{x},t)=e^{-iH_0t/\hbar}u(\mathbf{x},0)e^{iH_0t/\hbar}.$$

Let $|n\rangle$ be an eigenstate of H_0 corresponding to the energy E_n. Using (P.7), we get

$$\begin{aligned}M(\mathbf{q},\omega)&=\frac{1}{i\hbar}\int d^2x dt\ \theta(t)\sum_{nm}Z^{-1}e^{-\beta E_n}e^{-i(\mathbf{q}\cdot\mathbf{x}-\omega t)}\\&\times\left(\langle n|u(\mathbf{x},0)|m\rangle\langle m|u(\mathbf{0},0)|n\rangle e^{-i(E_n-E_m)t/\hbar}\right.\\&\left.-\langle n|u(\mathbf{0},0)|m\rangle\langle m|u(\mathbf{x},0)|n\rangle e^{i(E_n-E_m)t/\hbar}\right)\\&=\frac{1}{i\hbar}\int d^2x\sum_{nm}Z^{-1}e^{-\beta E_n}e^{-i\mathbf{q}\cdot\mathbf{x}}\\&\times\left(\frac{\langle n|u(\mathbf{x},0)|m\rangle\langle m|u(\mathbf{0},0)|n\rangle}{i(E_n-E_m)/\hbar-i\omega+0^+}\right.\\&\left.+\frac{\langle n|u(\mathbf{0},0)|m\rangle\langle m|u(\mathbf{x},0)|n\rangle}{i(E_n-E_m)/\hbar+i\omega-0^+}\right)\end{aligned} \tag{P.8}$$

where $\beta=1/k_BT$ and $Z=\sum_n\exp(-\beta E_n)$. From (P.8), we get

$$\begin{aligned}\mathrm{Im}M(\mathbf{q},\omega)&=\frac{\pi}{\hbar}\int d^2x\sum_{nm}Z^{-1}e^{-\beta E_n}e^{-i\mathbf{q}\cdot\mathbf{x}}\\&\times\left(\langle n|u(\mathbf{x},0)|m\rangle\langle m|u(\mathbf{0},0)|n\rangle(-\delta[\omega-(E_n-E_m)/\hbar])\right.\\&\left.+\langle n|u(\mathbf{0},0)|m\rangle\langle m|u(\mathbf{x},0)|n\rangle\delta[\omega+(E_n-E_m)/\hbar]\right)\end{aligned} \tag{P.9}$$

Changing the summation index from $(n,m)\to(m,n)$, the (m,n)-dependent part of the second term in (P.9) can be rewritten as

$$\begin{aligned}&\sum_{nm}e^{-\beta E_m}\langle m|u(\mathbf{0},0)|n\rangle\langle n|u(\mathbf{x},0)|m\rangle\\&\qquad\times\delta[\omega-(E_n-E_m)/\hbar]\\&=\sum_{nm}e^{-\beta E_n}e^{-\beta(E_m-E_n)}\langle n|u(\mathbf{x},0)|m\rangle\langle m|u(\mathbf{0},0)|n\rangle\end{aligned}$$

$$\times\delta[\omega-(E_n-E_m)/\hbar]$$

$$=e^{\beta\omega}\sum_{nm}e^{-\beta E_n}\langle n|u(\mathbf{x},0)|m\rangle\langle m|u(\mathbf{0},0)|n\rangle$$

$$\times\delta[\omega-(E_n-E_m)/\hbar]$$

Replacing the second term in (P.9) with this expression gives

$$\mathrm{Im}M(\mathbf{q},\omega)=\frac{1}{2\hbar}\left(e^{\beta\hbar\omega}-1\right)$$

$$\times\int d^2x dt\; e^{-i(\mathbf{q}\cdot\mathbf{x}-i\omega t)}\langle u(\mathbf{x},t)u(\mathbf{0},0)\rangle$$

$$=\frac{1}{2\hbar}\left(e^{\beta\hbar\omega}-1\right)(2\pi)^3C_{uu}(\mathbf{q},\omega)$$

From the last equation follows the fluctuation–dissipation theorem:

$$C_{uu}(\mathbf{q},\omega)=\frac{1}{(2\pi)^3}\frac{2\hbar}{e^{\beta\hbar\omega}-1}\mathrm{Im}M(\mathbf{q},\omega).$$

P.4 Phonon Heat Transfer at Disordered Interfaces

We assume high temperatures and interfacial disorder. In this case, the elastic waves generated by the stochastic pulsating forces between the atoms at the interface give rise to (nearly) incoherent emission of sound waves (or phonons). Thus, we can obtain the total energy transfer by just adding up the contributions from the elastic waves emitted from each interfacial atom. Assume for simplicity that the interfacial atoms of solid **0** for a simple square lattice with lattice constant a_0. Consider the atom at $\mathbf{x}=\mathbf{0}$ and let $u_0(t)$ denote the vertical displacement of the atom. The force

$$F(t)=k[u_0(t)-u_1(t)],$$

or

$$F(\omega)=k[u_0(\omega)-u_1(\omega)], \tag{P.10}$$

is acting on solid **1** at $\mathbf{x}=\mathbf{0}$. We can write $k=Ka_0^2$ where K is the force constant per unit area. The force $F(t)$ gives a stress

$$\sigma(\mathbf{x},t)=F(t)\delta(\mathbf{x})$$

acting on solid **1**. We can also write

$$\sigma(\mathbf{q},\omega) = (2\pi)^{-2} F(\omega)$$

Note that

$$\begin{aligned} u_1(\omega) = u_1(\mathbf{x}=\mathbf{0},\omega) &= \int d^2q\ u_1(\mathbf{q},\omega) \\ &= \int d^2q\ M_1(\mathbf{q},\omega)\sigma(\mathbf{q},\omega) \\ &= \frac{1}{(2\pi)^2}\int d^2q\ M_1(\mathbf{q},\omega)F(\omega) = \bar{M}_1(\omega)F(\omega), \end{aligned} \tag{P.11}$$

where

$$\bar{M}_1(\omega) = \frac{1}{(2\pi)^2}\int d^2q\ M_1(\mathbf{q},\omega)$$

In a similar way, we get

$$u_0(\omega) = u_{0\mathrm{f}}(\omega) - \bar{M}_0(\omega)F(\omega). \tag{P.12}$$

Combining (P.10)–(P.12) gives

$$u_1(\omega) = \frac{k\bar{M}_1(\omega)}{1+k[\bar{M}_0(\omega)+\bar{M}_1(\omega)]}u_{0\mathrm{f}}(\omega), \tag{P.13}$$

$$u_0(\omega) = \frac{1+k\bar{M}_1(\omega)}{1+k[\bar{M}_0(\omega)+\bar{M}_1(\omega)]}u_{0\mathrm{f}}(\omega). \tag{P.14}$$

The energy transferred to solid **1** from solid **0** during the time period t_0 can be written as

$$\Delta E = N\int dt\ \dot{u}_1(t)F(t),$$

where $N = A_0/a_0^2$ is the number of interfacial atoms of solid **0**. One can also write

$$\Delta E = 2\pi N\int d\omega\ (-i\omega)u_1(\omega)F(-\omega)$$

Using (P.10) and (P.13) and (P.14), we obtain

$$\Delta E = 2\pi N\int d\omega \frac{\omega k^2 \mathrm{Im}\bar{M}_1(\omega)}{|1+k[\bar{M}_0(\omega)+\bar{M}_1(\omega)]|^2}\langle|u_{0\mathrm{f}}(\omega)|^2\rangle, \tag{P.15}$$

where we have performed an ensemble (or thermal) average denoted by $\langle..\rangle$. Next, note that

$$\langle|u_{0\mathrm{f}}(\omega)|^2\rangle = \frac{1}{(2\pi)^2}\int dtdt'\ \langle u_{0\mathrm{f}}(t)u_{0\mathrm{f}}(t')\rangle e^{-i\omega(t-t')}$$

$$= \frac{1}{(2\pi)^2}\int dtdt'\langle u_{0\mathrm{f}}(t-t')u_{0\mathrm{f}}(0)\rangle e^{-i\omega(t-t')}$$

$$= \frac{1}{(2\pi)^2}\int dtdt'\langle u_{0\mathrm{f}}(t)u_{0\mathrm{f}}(0)\rangle e^{i\omega t} = \frac{2t_0}{2\pi}\bar{C}_{uu}(\omega), \tag{P.16}$$

where

$$\bar{C}_{uu}(\omega) = \frac{1}{2\pi}\int dt\ \langle u_{0\mathrm{f}}(t)u_{0\mathrm{f}}(0)\rangle e^{-i\omega t},$$

is the displacement correlation function. Note that

$$\bar{C}_{uu}(\omega) = \int d^2q\ C_{uu}(\mathbf{q},\omega)$$

Thus, using (12.8), we get

$$\bar{C}_{uu}(\omega) = \frac{2}{(2\pi)^3}\frac{\Pi(\omega)}{\omega}\mathrm{Im}\int d^2q\ M_0(\mathbf{q},\omega) = \frac{2}{2\pi}\frac{\Pi(\omega)}{\omega}\mathrm{Im}\bar{M}_0(\omega) \tag{P.17}$$

Substituting (P.16) in (P.15) and using (P.17) gives the heat current $J_{0\to1} = \Delta E/A_0t_0$ from solid **0** to solid **1**:

$$J_{0\to1} = \frac{4A^*}{(2\pi)^3}\int_0^\infty d\omega\ \Pi(\omega)\frac{K\mathrm{Im}M_0(\omega)K\mathrm{Im}M_1(\omega)}{|1+K[M_0(\omega)+M_1(\omega)]|^2},$$

where $A^* = (2\pi)^2/a_0^2$ is the area of the Brillouin zone and where we have defined

$$M(\omega) = a_0^2\bar{M}(\omega) = \frac{1}{A^*}\int_{q<q_\mathrm{c}} d^2q\ M(\mathbf{q},\omega)$$

where the q-integral is over $|\mathbf{q}| < q_\mathrm{c}$ with $\pi q_\mathrm{c}^2 = A^*$. A similar equation with T_0 replaced by T_1 gives the energy transfer from solid **1** to solid **0**, and the net energy flow $J = J_{0\to1} - J_{1\to0}$. The heat transfer coefficient $\alpha = (J_{0\to1} - J_{1\to0})/(T_0 - T_1)$ gives in the limit $(T_0 - T_1) \to 0$:

$$\alpha = \frac{4A^*}{(2\pi)^3}\int_0^\infty d\omega\ \frac{\partial\Pi(\omega)}{\partial T}\frac{K\mathrm{Im}M_0(\omega)K\mathrm{Im}M_1(\omega)}{|1+K[M_0(\omega)+M_1(\omega)]|^2}.$$

The derivation above is only valid for high temperatures where $k_\mathrm{B}T > \hbar\omega_0$, where $\hbar\omega_0$ is the highest phonon energy of solid **0**. However, we can apply the theory

(approximately) to all temperatures if we take the cut-off wavevector q_c to be the smallest of q_1 and q_2, where $\pi q_1^2 = (2\pi)^2/a_0^2$ (where a_0 is the lattice constant) and where $q_2 = k_B T/\hbar c_0$ (where c_0 is the smallest sound velocity of solid **0**) is the thermal wavevector.

P.5 Derivation of (12.20) from (12.21)

Here we show that (12.21) reduces to (12.20) for high temperatures and when solid **0** is described by an Einstein model. At high temperatures and weak interfacial coupling, (12.21) becomes

$$\alpha = \frac{4k_B A^*}{(2\pi)^3}\int_0^\infty d\omega\ K^2 \mathrm{Im}M_0(\omega)\mathrm{Im}M_1(\omega) \tag{P.18}$$

We assume for solid **0** that

$$M_0(\omega) = \frac{1}{\rho_0(\omega_0^2 - \omega^2) - i0^+}$$

where $\rho_0 = m_0/a_0^2$ is the mass per unit area. Thus

$$\mathrm{Im}M_0(\omega) = \frac{\pi}{2\rho_0\omega_0}\delta(\omega_0 - \omega)$$

Substituting this in (P.18) gives

$$\begin{aligned}\alpha &= \frac{4k_B K^2 A^*}{(2\pi)^3}\frac{\pi}{2\rho_0\omega_0}\mathrm{Im}M_1(\omega_0)\\ &= \frac{k_B K^2}{(2\pi)^2}\frac{1}{\rho_0\omega_0}\int d^2q\ \mathrm{Im}M_1(\mathbf{q},\omega_0)\end{aligned}$$

Substituting (12.10) into this equation and denoting $q = (\omega_0/c_T)x^{1/2}$ gives

$$\alpha = \frac{k_B K^2}{\rho_0\rho_1 c_T^3}\frac{1}{8\pi}\mathrm{Re}\int_0^\infty dx\frac{2(\gamma - x)^{1/2}}{(1-2x)^2 + 4(1-x)^{1/2}(\gamma - x)^{1/2}} \tag{P.19}$$

where $\gamma = (c_T/c_L)^2$, which agrees with (12.20).

P.6 Derivation of (12.26)

Let $1/\alpha_c$ be the interfacial contact resistance associated with the jump in the temperature (on an atomistic scale) in the contact area between two solids, and let $1/\alpha_{spred}$ be the spreading resistance associated with the interaction between the heat filaments emerging from all the contact regions. Since these two resistances act in series one, expect the total contact resistance to be the sum of the two contributions, i.e.,

$$\frac{1}{\alpha} \approx \frac{1}{\alpha_{spred}} + \frac{1}{\alpha_c}$$

We can prove this equation and (12.25) using the formalism developed in [296]. We assume that all the heat energy flows via the area of real contact. In this case, the interfacial heat current $J_z(\mathbf{x})$ vanishes in the non-contact area. In the area of real contact, the temperature $T(\mathbf{x}, z)$ changes abruptly (on an atomistic scale) when z increases from $z = -0^+$ (in solid $\mathbf{0}$) to $z = 0^+$ (in solid $\mathbf{1}$), and the jump determines the heat current: $J_z(\mathbf{x}) = \alpha_b[T(\mathbf{x}, -0) - T(\mathbf{x}, +0)]$. If we denote $\psi(\mathbf{x}) = T(\mathbf{x}, -0) - T(\mathbf{x}, +0)$, the equation

$$J_z(\mathbf{x})[J_z(\mathbf{x}) - \alpha_b \psi(\mathbf{x})] = 0$$

will be valid everywhere at the interface. From this equation, we get

$$\int d^2q' J_z(\mathbf{q} - \mathbf{q}')[J_z(\mathbf{q}') - \alpha_b \psi(\mathbf{q}')] = 0$$

Following the derivation in Sect. 2.2.1 in [296], we get the equation

$$\frac{1}{\alpha} = \frac{(2\pi)^2}{\kappa} \frac{1}{A_0 J_0^2} \int d^2q \, \frac{1}{q} \langle |\Delta J_z(\mathbf{q})|^2 \rangle + \frac{1}{\alpha_b} \frac{1}{A_0 J_0^2} \int d^2x \, J_z^2(\mathbf{x}) = \frac{1}{\alpha_{spred}} + \frac{1}{\alpha_c} \tag{P.20}$$

Here J_0 is the average or nominal heat current, $\Delta J_z(\mathbf{x}) = J_z(\mathbf{x}) - J_0$, and κ an effective heat conductivity ($\kappa^{-1} = \kappa_0^{-1} + \kappa_1^{-1}$). The first term in (P.20) is the spreading resistance studied in [296] while the second term is the contribution from the temperature jump on the atomistic scale across the area of real contact.

Appendix Q
Heat Transfer: Role of Surface Roughness

Q.1 Derivation of the Relation Between the Heat Transfer Coefficient and the Contact Stiffness

Consider two elastic blocks with nominally flat surfaces squeezed together with the nominal pressure p_0. In [213], it was shown that the normal displacement u_{0z} of the surface of solid 0 is related to the normal stress σ_z via

$$u_{0z}(\mathbf{q}) = \frac{2}{E_0^* q}\sigma_z(\mathbf{q}), \tag{Q.1}$$

where $E_0^* = E_0/(1-\nu_0^2)$. In a similar way

$$u_{1z}(\mathbf{q}) = -\frac{2}{E_1^* q}\sigma_z(\mathbf{q}). \tag{Q.2}$$

Let $u_z = u_{0z} - u_{1z}$ be the difference between the (interfacial) surface displacement fields. Using (Q.1) and (Q.2) gives

$$u_z(\mathbf{q}) = \frac{2}{E^* q}\sigma_z(\mathbf{q}) \tag{Q.3}$$

where

$$\frac{1}{E^*} = \frac{1}{E_0^*} + \frac{1}{E_1^*}$$

The normal (interfacial) stress $\sigma_z(\mathbf{x})$ and the difference in the surface displacement $u_z(\mathbf{x}) = u_{0z}(\mathbf{x}) - u_{1z}(\mathbf{x})$ at the interface depend on the squeezing pressure p_0 applied to the upper surface of the block. Alternatively, since the average separation $\bar{u}$ between the surfaces at the interface decreases monotonically with increasing p we can

A.I. Volokitin and B.N.J. Persson, *Electromagnetic Fluctuations at the Nanoscale*,
NanoScience and Technology, DOI 10.1007/978-3-662-53474-8

consider u_z and σ_z to depend parametrically on $\bar{u}$. The derivatives of these quantities with respect to $\bar{u}$ are denoted by σ_z' and u_z'. Using (Q.3) we get

$$u_z'(\mathbf{q}) = \frac{2}{E^* q}\sigma_z'(\mathbf{q}). \tag{Q.4}$$

with the boundary conditions that $\sigma_z'(\mathbf{x})$ vanishes in the non-contact region, while $u_z'(\mathbf{x})$ vanishes in the contact regions (since $h(\mathbf{x})$ is a fix function, *independent of* u). In addition, the condition

$$\frac{1}{A_0}\int d^2x\ \sigma_z(\mathbf{x}) = p_0,$$

takes the form

$$\frac{1}{A_0}\int d^2x\ \sigma_z'(\mathbf{x}) = p_0'.$$

If we denote $\psi_z = \sigma_z'/p'$, we can write

$$\frac{1}{A_0}\int d^2x\ \psi_z(\mathbf{x}) = 1,$$

and (Q.4) takes the form

$$\phi_z(\mathbf{q}) = q^{-1}\psi_z(\mathbf{q}), \tag{Q.5}$$

where

$$\phi_z = \frac{E^*}{2p_0'}u_z'. \tag{Q.6}$$

Consider now the relation between $J_z(\mathbf{x})$ and $\Delta T(\mathbf{x})$. The relevant boundary condition are that $J_z(\mathbf{x})$ vanish in the non-contact region while $\Delta T(\mathbf{x})$ vanish in the contact regions. In addition, we must have

$$\frac{1}{A_0}\int d^2x\ J_z(\mathbf{x}) = J_0,$$

If we denote $\psi = J_z/J_0$ we can write

$$\frac{1}{A_0}\int d^2x\ \psi(\mathbf{x}) = 1,$$

and (13.15) takes the form

$$\phi(\mathbf{q}) = q^{-1}\psi(\mathbf{q}), \tag{Q.7}$$

where

$$\phi = -(\kappa/J_0)\Delta T \tag{Q.8}$$

Note that the systems of equations for (ϕ_z, ψ_z) and (ϕ, ψ) are identical and therefore $\phi_z = \phi$ and $\psi_z = \psi$. Using that $\phi_z = \phi$ from (Q.6) and (Q.8), we get

$$\Delta T = -\frac{J_0 E^*}{\kappa 2 p_0'} u_z' \tag{Q.9}$$

Next note that

$$\int d^2x \; u_z'(\mathbf{x}) = \frac{d}{du} \int d^2x \; u_z(\mathbf{x}) = \frac{d}{du} A_0 u = A_0,$$

while

$$\int d^2x \; \Delta T(\mathbf{x}) = A_0 J_0/\alpha,$$

Thus, integrating (Q.9) over $\mathbf{x}$ gives

$$\alpha = -\frac{2\kappa}{E^*} p_0'.$$

Q.2 Convective Heat Transfer

Here we briefly summarize some results related to forced convective heat transfer [414]. When a fluid (e.g., air) flows around a solid object, the tangential (and the normal) component of the fluid velocity usually vanishes on the surface of the solid. This results in the formation of a thin boundary layer (thickness δ) at the surface of the solid where the fluid velocity rapidly increases from zero to some value that is of order the main stream velocity outside of the solid. If the temperature T_1 at the solid surface is different from the fluid temperature T_{fluid}, the fluid temperature in the boundary layer will also change rapidly from T_1 to T_{fluid}. Depending on the fluid flow velocity, the fluid viscosity and the dimension of the solid object the flow will be laminar or turbulent, and the heat transfer process is fundamentally different in these two limiting cases. In a typical case (for air), the thickness $\delta \approx 1$ mm and the heat transfer coefficient $\alpha \approx \kappa/\delta \approx 10 \, \text{W/m}^2\text{K}$.

Let us consider heat transfer from a rotating disk as a model for the heat transfer from a tire [415]. In this case, it has been shown [416] that fully turbulent flow occur if the Reynolds number $\text{Re} > 2.5 \times 10^5$ where

$$\text{Re} = \frac{\omega R^2}{\nu} = \frac{v_R R}{\nu}$$

where R is the radius of the disk (or rather the distance from the center of the disk to some surface patch on the disk), ω the angular velocity and ν the kinematic viscosity of air. In typical tire applications $\text{Re} > 2.5 \times 10^5$ so turbulent flow will prevail in most

tire applications. In this case, the heat transfer coefficient is given approximately by [416]:

$$\alpha_{\text{air}} \approx 0.019 \frac{\kappa_{\text{air}}}{R} \left(\frac{v_{\text{R}} R}{\nu} \right)^{0.8} .$$

As an example, at $T = 300$ K for air $\nu = 15.7 \times 10^{-6}$ m^2/s and $\kappa_{\text{air}} = 0.025$ W/mK and assuming $R = 0.3$ m and $v_{\text{R}} = 30$ m/s we get $\alpha_{\text{air}} \approx 63$ W/m^{2}K.

Q.3 Thermal and Electric Conductivities

Heat conduction results from the collisions between atoms, as in fluids; or by free electron diffusion, as predominant in metals; or phonon diffusion as predominant in insulators. In liquids and gases, the molecules are usually further apart than in solids, giving a lower chance of molecules colliding and passing on thermal energy. Metals are usually the best conductors of thermal energy. This is due to the free-moving electrons, which are able to transfer thermal energy rapidly through the metal. However, the difference in the thermal conductivity of metals and non-metals are usually not more than a factor ~100. Typical values for the heat conductivity are $\kappa \approx 100$ W/mK for metals, ≈1 W/mK for insulators (e.g., metal oxides or polymers), ≈0.1 W/mK for fluids (but for water $\kappa \approx 0.6$ W/mK) and ≈0.02 W/mK for gases at normal atmospheric pressure and room temperature.

In contrast to thermal heat transfer, electric conduction always involves the motion of charged particles (electrons or ions). For this reason, the electric contact resistance is much more sensitive to oxide or contamination layers at the contacting interface then for the heat transfer. For the electric conduction, the variation of the conductivity between good conductors (most metals), with the typical electric conductivity $\kappa' \approx 10^7$ $(\Omega\text{m})^{-1}$, and bad conductors, such as silicon dioxide glass or (natural) rubber where $\kappa' \approx 10^{-14}$ $(\Omega\text{m})^{-1}$, is huge. This makes the electrical contact resistance of metals sensitive to (nanometer) thin oxide or contamination layers. However, as highlighted in the Introduction, if there is a large number of small breaks in the film, the resistance may be almost as low as with no film.

Appendix R
Friction Coefficient for Point Charges Moving Relative to a Plane Surface: Non-relativistic Theory

Consider a semi-infinite metal with a flat surface that coincides with the xy coordinate plane, and with the z-axes pointed along the upward normal. The electric field above the flat surface can be represented by the Fourier integral

$$\mathbf{E}(\mathbf{r}) = \int \frac{d^2q}{(2\pi)^2} e^{i\mathbf{q}\cdot\mathbf{r}-i\omega t}\mathbf{E}(\mathbf{q}, z) \tag{R.1}$$

with similar expression for the magnetic induction field $\mathbf{B}(\mathbf{r})$. For $q \gg \omega/c$ and $z > 0$, the electric and magnetic induction field can be written in the form

$$\mathbf{E}(\mathbf{q}, z) = v_{0q}[\hat{\mathbf{z}}(e^{qz} + R_p e^{-qz}) + \hat{\mathbf{q}}i(e^{qz} - R_p e^{-qz})], \tag{R.2}$$

$$\mathbf{B}(\mathbf{q}, z) = -\frac{\omega}{cq}\hat{\mathbf{n}}E_z(\mathbf{q}, z), \tag{R.3}$$

where $\hat{n} = \hat{z} \times \hat{q}$, and where R_p is the reflection amplitude for the p-polarized electromagnetic field. The energy dissipation induced by the electromagnetic field in the bulk of the metal is determined by integrating the Poynting vector over the surface of the metal, and is given by

$$\dot{Q} = -\frac{c}{4\pi}\int \frac{d^2q}{(2\pi)^2}(E_{\mathbf{q}}B^*_{\mathbf{n}} + c.c.) = \frac{\omega}{\pi}\int \frac{d^2q}{(2\pi)^2 q}\mathrm{Im}R(\omega)\left|v_{0q}\right|^2. \tag{R.4}$$

Consider now a point charges e_i located at $(\mathbf{r}_i, d + z_i)$, and performing small amplitude vibrations with the vibrational coordinate $\mathbf{u}(t) = \hat{\mathbf{z}}u_0 e^{-i\omega t}$. In this case

$$v_{0q} = -2\pi i u_0 \sum_i e_i e^{i\mathbf{q}\cdot\mathbf{r}_i - q(d+z_i)} q_x. \tag{R.5}$$

A.I. Volokitin and B.N.J. Persson, *Electromagnetic Fluctuations at the Nanoscale*,
NanoScience and Technology, DOI 10.1007/978-3-662-53474-8

Taking into account that the energy dissipation per unit time must be equal to $2\omega^2\Gamma\,|u_0|^2$, using (R.4) and (R.5) gives the friction coefficient:

$$\Gamma_{\parallel} = \lim_{\omega\to 0}\int_0^{\infty}\frac{\mathrm{d}^2 q}{\pi q}q_x^2\,e^{-2qd}\,\frac{\mathrm{Im}R_p(\omega,q)}{\omega}\left|\sum_i e_i e^{i\mathbf{q}\cdot\mathbf{r}_i - qz_i}\right|^2. \tag{R.6}$$

For a uniformly charged wire with the length w passing through point $z = d$ along the y-axis, from (R.6), we get

$$\begin{aligned}\Gamma_{\parallel} &= \lim_{\omega\to 0} Q^2\int_{-\infty}^{\infty}dq_x\int_{-\infty}^{\infty}dq_y\,\frac{q_x^2}{2\pi q}e^{-2qd}\,\frac{\mathrm{Im}R(q,\omega)}{\omega}\left|\int_{-w/2}^{w/2}dy e^{iq_y y}\right| \\ &= \lim_{\omega\to 0} Q^2 w\int_{-\infty}^{\infty}dq_x\int_{-\infty}^{\infty}dq_y\,\frac{q_x^2}{q}e^{-2qd}\,\frac{\mathrm{Im}R(q,\omega)}{\omega}\delta(q_y) \\ &= \lim_{\omega\to 0} 2Q^2 w\int_0^{\infty}dq_x q_x e^{-2qd}\,\frac{\mathrm{Im}R(q,\omega)}{\omega}.\end{aligned} \tag{R.7}$$

Appendix S
Attracting Force Between a Tip and a Flat Surface of a Body

S.1 van der Waals Interaction

Accordingly to the Lifshitz theory [43, 44], the stress $\sigma_{zz}(d)$ acting on the surfaces of two identical semi-infinite bodies due to van der Waals interaction, at small separation $d \ll c/\omega_p$ (where ω_p is the plasma frequency) and for $d \ll \lambda_T$, is given by:

$$\sigma_{zz}(d) = \frac{\hbar}{8\pi^2 d^3} \int_0^\infty d\xi \frac{[\varepsilon(i\xi) - 1]^2}{[\varepsilon(i\xi) + 1]^2}. \tag{S.1}$$

In the Drude model, the explicit form of ε is

$$\varepsilon(i\xi) = 1 + \frac{\omega_p^2}{\xi(\xi + \eta)}. \tag{S.2}$$

For many metals, the damping constant $\eta \ll \omega_p$ and be neglected in integral (S.1). It follows from (S.1) and (S.2) that

$$\sigma_{zz} = \frac{\hbar\omega_p}{32\sqrt{2}\pi d^3}. \tag{S.3}$$

For a spherical tip of radius R, using the same approximation as in (6.95), we get

$$F_z(d) = \frac{R\hbar\omega_p}{32\sqrt{2}d^2}. \tag{S.4}$$

Similarly, in the case of a cylindrical tip, we have

$$F_z^c(d) = \frac{3wR^{1/2}\hbar\omega_p}{2^8 d^{5/2}}. \tag{S.5}$$

A.I. Volokitin and B.N.J. Persson, *Electromagnetic Fluctuations at the Nanoscale*, NanoScience and Technology, DOI 10.1007/978-3-662-53474-8

S.2 Electrostatic Interaction due to a Bias Voltage

In the presence of the bias voltage V, the attractive force per unit area between two plane surfaces given by

$$\sigma_{zz}(V) = \frac{V^2}{8\pi d^2}. \tag{S.6}$$

Using this formula and the 'proximity' approximation, as in (6.95), we get attraction force between tip and sample at $d \ll R$

$$F^c(d) = \frac{wV^2R^{1/2}}{2^{7/2}d^{3/2}} \tag{S.7}$$

for a cylindrical tip, and

$$F^s(d) = \frac{RV^2}{4d} \tag{S.8}$$

for a spherical tip.

Let us consider now an ellipsoidal tip surface with two different principle curvatures. In the vicinity of a sample, the equation describing this surface involves a quadratic dependence on x and y:

$$z(x, y) = d + \frac{x^2}{2R_x} + \frac{y^2}{2R_y}, \tag{S.9}$$

where R_x and R_y are the radii of curvature in the two directions. In the 'proximity' approximation, after changing integration variables $x = (R_x/R_y)^{1/4}x'$ and $y = (R_y/R_x)^{1/4}y'$ we get (S.8) as for spherical tip with $R = (R_xR_y)^{1/2}$.

Appendix T
Friction Coefficient due to Excitation of the Acoustic Waves

According to [213] the tensor $\overleftrightarrow{\mathbf{M}}$ in (15.3) is given by

$$\overleftrightarrow{\mathbf{M}} = \frac{i}{\rho c_t}\left(\frac{1}{S(q,\omega}\Big[Q(q,\omega)(\hat{z}\mathbf{q} - \mathbf{q}\hat{z}) + \left(\frac{\omega}{c_t}\right)^2 (p_l \hat{z}\hat{z} + p_t \hat{q}\hat{q})\Big] + \mathbf{nn}\frac{1}{p_t}\right), \tag{T.1}$$

where $\hat{q} = \mathbf{q}/q$, $\mathbf{n} = \hat{z} \times \hat{q}$ and

$$S = \left(\frac{\omega^2}{c_t^2} - 2q^2\right)^2 + 4q^2 p_t p_l, \tag{T.2}$$

$$Q = 2q^2 - \frac{\omega^2}{c_t^2} + 2p_t p_l, \tag{T.3}$$

$$p_t = \sqrt{\frac{\omega^2}{c_t^2} - q^2}, \quad p_l = \sqrt{\frac{\omega^2}{c_l^2} - q^2}, \tag{T.4}$$

where ρ, c_t, and c_l are the mass density and the transverse and longitudinal sound velocities of the solid, respectively. Note that c_t and c_l are, in general, complex frequency-dependent quantities given by

$$c_t^2 = \frac{E}{2\rho(1+\nu)}, \tag{T.5}$$

$$c_l^2 = \frac{E(1-\nu)}{\rho(1+\nu)(1-2\nu)}, \tag{T.6}$$

where $E(\omega)$ is the complex elastic modulus and ν is the Poisson ration.

The acoustic waves have wave number $q < \omega/c_t$. In typical cases the frequency of the vibrations of AFM tip $\omega \sim 10^3 - 10^6$ s^{-1} and $qR_{int} < \omega R_{int}/c_t \ll 1$, where

A.I. Volokitin and B.N.J. Persson, *Electromagnetic Fluctuations at the Nanoscale*, NanoScience and Technology, DOI 10.1007/978-3-662-53474-8

$R_{int} \sim \sqrt{dR}$ is the effective radius of the interaction of the tip with the sample surface. In this case, for vibrations of the tip normal to the surface, the Fourier transform of the surface stress is

$$\sigma_{\perp i}(q) = \int d^2x e^{i\mathbf{qx}} \frac{\partial}{\partial d} \sigma^0_{iz}(\mathbf{x}, d)$$

$$\approx \delta_{iz} \int d^2x \frac{\partial}{\partial d} \sigma^0_{zz}(\mathbf{x}, d) = \frac{\partial}{\partial d} F_z(d), \tag{T.7}$$

where σ^0_{iz} is the static stress acting on the surface of the sample. Using (T.7) and (T.1) in (15.4) we get

$$\Gamma_\perp = \frac{\xi_\perp}{4\pi} \frac{K^2}{\rho c_t^3}, \tag{T.8}$$

where $\xi_\perp = \xi_{\perp l} + \xi_{\perp t} + \xi_{\perp s}$, $K = \partial F_z/\partial d$ and where the contributions from the longitudinal $\xi_{\perp l}$, the transverse $\xi_{\perp t}$, and surface (Rayleigh) $\xi_{\perp s}$ acoustic waves are given by

$$\xi_{\perp l} = \int_0^{(c_t/c_l)^2} dx \frac{\sqrt{(c_t/c_l)^2 - x}}{(1-2x)^2 + 4x\sqrt{(1-x)}\sqrt{(c_t/c_l)^2 - x}}, \tag{T.9}$$

$$\xi_{\perp t} = \int_{(c_t/c_l)^2}^1 dx \frac{4x[x - (c_t/c_l)^2]\sqrt{1-x}}{(1-2x)^4 + 16x^2[x - (c_t/c_l)^2](1-x)}, \tag{T.10}$$

$$\xi_{\perp s} = \pi\sqrt{x_c - (c_t/c_l)^2}/f'(x_c), \tag{T.11}$$

where

$$f(x) = 4x\sqrt{x-1}\sqrt{x - (c_t/c_l)^2} - (2x-1)^2 \tag{T.12}$$

and where x_c is the solution of the equation $f(x) = 0$. In (T.9)–(T.11), the sound velocities c_t and c_l are assumed real, taken at $\omega = 0$. For vibrations of the tip parallel to the surface, the main contribution to the energy dissipation is due to the excitation of acoustic waves, which are excited by the component, of the surface stress acting normal to the surface. For this component we get

$$\sigma_{\parallel z}(q) = \int d^2x e^{i\mathbf{q}\cdot\mathbf{x}} \frac{\partial}{\partial x} \sigma^0_{zz}(\mathbf{x}) \approx iq_x F_z(d). \tag{T.13}$$

Using (T.13) and (T.1) in (15.4), we get

$$\Gamma_\parallel = \frac{\xi_\parallel}{8\pi} \frac{\omega^2}{\rho c_t^5} F_z^2(d), \tag{T.14}$$

$\xi_\parallel = \xi_{\parallel l} + \xi_{\parallel t} + \xi_{\parallel s}$,

$$\xi_{\|l} = \int_0^{(c_t/c_l)^2} dx x \frac{\sqrt{(c_t/c_l)^2 - x}}{(1-2x)^2 + 4x\sqrt{(1-x)}\sqrt{(c_t/c_l)^2 - x}}, \tag{T.15}$$

$$\xi_{\|t} = \int_{(c_t/c_l)^2}^1 dx x \frac{4x[x - (c_t/c_l)^2]\sqrt{1-x}}{(1-2x)^4 + 16x^2[x - (c_t/c_l)^2](1-x)}, \tag{T.16}$$

$$\xi_{\|s} = \pi x_c \sqrt{x_c - (c_t/c_l)^2}/f'(x_c). \tag{T.17}$$

For most metals $c_t/c_l \approx 1/2$ and for this case $\xi_\perp = 1.62$ and $\xi_\| = 1.50$.

References

1. A. Einstein, Ann. Phys. **17**, 549 (1905)
2. A. Einstein, Ann. Phys. **19**, 371 (1906)
3. M. von Smoluchowski, Ann. Phys. **21**, 756 (1906)
4. P. Langevin, C.R. Acad, Sci. Paris **146**, 530 (1908)
5. S.M. Rytov, *Theory of Electrical Fluctuation and Thermal Radiation* (Academy of Science of USSR Publishing, Moscow, 1953)
6. M.L. Levin, S.M. Rytov, *Theory of Equilibrium Thermal Fluctuations in Electrodynamics* (Science Publishing, Moscow, 1967)
7. S.M. Rytov, Y.A. Kravtsov, V.I. Tatarskii, *Principles of Statistical Radiophyics*, vol. 3 (Springer, New York, 1989)
8. H.R. Callen, T.A. Welton, Phys. Rev. **83**, 334 (1951)
9. K. Joulain, J.P. Mulet, F. Marquier, R. Carminati, J.J. Greffet, Surf. Sci. Rep. **57**, 59 (2005)
10. A.I. Volokitin, B.N.J. Persson, Usp. Fiz. Nauk 177, 921 (2007). Phys. Usp. **50**, 879 (2007)
11. A.I. Volokitin, B.N.J. Persson, Rev. Mod. Phys. **79**, 1291 (2007)
12. J.B. Pendry, J. Phys. Condens. Matter **11**, 6621 (1999)
13. A.I. Volokitin, B.N.J. Persson, Phys. Rev. B **63**, 205404 (2001); Phys. Low-Dim. Struct. **5/6**, 151 (2001)
14. A.I. Volokitin, B.N.J. Persson, Phys. Rev. B **69**, 045417 (2004)
15. A.I. Volokitin, B.N.J. Persson, JETP Lett. **78**, 457 (2003)
16. J.P. Mulet, K. Joulin, R. Carminati, J.J. Greffet, Appl. Phys. Lett. **78**, 2931 (2001)
17. A. Majumdar, Ann. Rev. Mater. Sci. **29**, 505 (1999)
18. A. Kittel, W. Müller-Hirch, J. Parisi, S.-A. Biehs, D. Reddig, M. Holthaus, Phys. Rev. Lett. **95**, 224301 (2005)
19. I. Dorofeyev, H. Fuchs, G. Wenning, B. Gotsmann, Phys. Rev. Lett. **83**, 2402 (1999)
20. B. Gotsmann, H. Fuchs, Phys. Rev. Lett. **86**, 2597 (2001)
21. B.C. Stipe, H.J. Mamin, T.D. Stowe, T.W. Kenny, D. Rugar, Phys. Rev. Lett. **87**, 096801 (2001)
22. H.J. Mamin, D. Rugar, Appl. Phys. Lett. **79**, 3358 (2001)
23. P.M. Hoffmann, S. Jeffery, J.B. Pethica, H.Ö. Özer, A. Oral, Phys. Rev. Lett. **87**, 265502 (2001)
24. S. Kuehn, R.F. Loring, J.A. Marohn, Phys. Rev. Lett. **96**, 156103 (2006)
25. S. Rast, U. Gysin, E. Meyer, D.W. Lee, in *Fundamentals of Friction and Wear on the Nanoscale*, ed. by E. Gnecco, E. Meyer (Springer, Berlin, 2007), pp. 437–451

A.I. Volokitin and B.N.J. Persson, *Electromagnetic Fluctuations at the Nanoscale*,
NanoScience and Technology, DOI 10.1007/978-3-662-53474-8

26. M. Kiesel, M. Langer, U. Gysin, S. Rast, E. Meyer, D.W. Lee, in *Fundamentals of Friction and Wear on the Nanoscale*, 2nd edn., ed. by E. Gnecco, E. Meyer (Springer, Berlin, 2015), pp. 609–626
27. E. Gnecco, E. Meyer, *Elements of Friction Theory and Nanotribology*, ed. by E. Gnecco, E. Meyer (Cambridge University Press, 2015)
28. J.J. Greffet, R. Carminati, K. Joulain, J.P. Mulet, S. Mainguy, Y. Chen, Nature **416**, 61 (2002)
29. R. Carminati, J.-J. Greffet, Phys. Rev. Lett. **82**, 1660 (1999)
30. A.V. Shcheglov, K. Joulain, R. Carminati, J.J. Greffet, Phys. Rev. Lett. **85**, 1548 (2000)
31. C. Henkel, K. Joulain, R. Carminati, J.J. Greffet, Opt. Commun. **186**, 57 (2000)
32. P. Hesketh, J.N. Zemel, B. Gebhart, Nature **324**, 549 (1986)
33. P. Hesketh, J.N. Zemel, B. Gebhart, Phys. Rev. B **37**, 10795 (1988)
34. P. Hesketh, J.N. Zemel, B. Gebhart, Phys. Rev. B **37**, 10803 (1988)
35. M. Kreiter, J. Auster, R. Sambles, S. Herminghaus, S. Mittler-Neher, W. Knoll, Opt. Commun. **168**, 117 (1999)
36. F. Marquier, K. Joulain, J. Mulet, R. Carminati, Y. Chen, Phys. Rev. B **69**, 155412 (2004)
37. F. Marquier, K. Joulain, J.P. Mulet, R. Carminati, J.J. Greffet, Opt. Commun. **237**, 379 (2004)
38. M.U. Pralle et al., Appl. Phys. Lett. **81**, 4685 (2002)
39. H. Casimir, Proc. Konikl. Ned. Akad. Wetenschap **51**, 793 (1948)
40. F. London, Z. Phys. **63**, 245 (1930)
41. H. Casimir, D. Polder, Phys. Rev. **73**, 360 (1948)
42. E.M. Lifshitz, Zh. Eksp. Teor. Fiz. **29**, 94 (1955); Sov. Phys. -JETP **2**, 73 (1956)
43. I.E. Dzyaloshinskii, E.M. Lifshitz, L.P. Pitaevskii, Adv. Phys. **10**, 165 (1961)
44. S.K. Lamoreaux, Phys. Today **60**, 40 (2007)
45. P.W. Milonni, *The Quantum Vacuum: An Introduction to Quantum Electrodynamics* (Academic Press, San Diego, 1994)
46. G. Plunien, B. Muller, W. Greiner, Phys. Rep. **134**, 87 (1986)
47. M. Bordag, U. Mohideen, V. Mostepanenko, Phys. Rep. **53**, 1 (2001)
48. S.K. Lamoreaux, Am. J. Phys. **67**, 850 (1999)
49. S.K. Lamoreaux, Phys. Rev. Lett. **78**, 5 (1997)
50. U. Mohideen, A. Roy, Phys. Rev. Lett. **81**, 4549 (1998)
51. B.W. Harris, F. Chen, U. Mohideen, Phys. Rev. A **62**, 052109 (2000)
52. T. Ederth, Phys. Rev. A **62**, 062104 (2000)
53. G. Bressi, G. Carugno, G. Ruos, Phys. Rev. Lett. **88**, 041804 (2002)
54. R. Decca, D. Loperz, E. Fischbach, D. Krause, Phys. Rev. Lett. **91**, 050402 (2003)
55. H. Chan, V. Akssyuk, R. Kleinman, D. Bishop, F. Capasso, Phys. Rev. Lett. **87**, 211801 (2001)
56. H. Chan, V. Akssyuk, R. Kleinman, D. Bishop, F. Capasso, Science **291**, 1941 (2001)
57. A.O. Sushkov, W.J. Kim, D.A.R. Dalvit, S.K. Lamoreaux, Nature Phys. **7**, 230 (2011)
58. F.M. Serry, D. Walliser, G.J. Maclay, J. Appl. Phys. **84**, 2501 (1998)
59. E. Buks, M.L. Roukes, Phys. Rev. B **63**, 033403 (2001)
60. G.L. Klimchitskaya, U. Mohideen, V.M. Mostepanenko, Rev. Mod. Phys. **81**, 1827–1885 (2009)
61. J.N. Munday, F. Capasso, V.A. Parsegian, Nature (London) **457**, 170 (2007)
62. A.O. Sushkov, W.J. Kim, D.A.R. Dalvit, S.K. Lamoreaux, Phys. Rev. Lett. **107**, 171101 (2011)
63. Y. Bao, R. Guérout, J. Lussange, A. Lambrecht, R.A. Cirelli, F. Klemens, W.M. Mansfield, C.S. Pai, H.B. Chan, Phys. Rev. Lett. **105**, 250402 (2010)
64. A.W. Rodriguez, W.J. Kim, F. Capasso, S.G. Johnson, Nature Photon. **5**, 211 (2011)
65. R. Zhao, J. Zhou, T. Koschny, E.N. Economou, C.M. Soukoulis, Phys. Rev. Lett. **103**, 103602 (2009)
66. A. Lambrecht, S. Reynand, Eur. Phys. J. D **8**, 309 (2000)
67. C. Genet, A. Lambrecht, S. Reynand, Phys. Rev. A **62**, 012110 (2000)
68. G. Klimchitskaya, V. Mostepanenko, Phys. Rev. A **63**, 062108 (2001)
69. M. Antezza, L.P. Pitaevskii, S. Stringari, V.B. Svetovoy, Phys. Rev. A **77**, 022901 (2008)
70. M. Antezza, L.P. Pitaevskii, S. Stringari, V.B. Svetovoy, Phys. Rev. Lett. **97**, 223203 (2006)
71. M. Antezza, L.P. Pitaevskii, S. Stringari, Phys. Rev. Lett. **95**, 113202 (2005)

72. N.G Van Kampen, B.R.A. Nijboer, K. Schram, Phys. Lett. **26A**, 307 (1968)
73. B.W. Ninham, V.A. Parsegian, J.H. Weiss, J. Stat. Phys. **2**, 323 (1970)
74. E. Gerlach, Phys. Rev. B **4**, 393 (1971)
75. K. Schram, Phys. Lett. **43A**, 282 (1973)
76. Y.S. Barash, V.L. Ginzburg, Usp. Fiz. Nauk 116, 5 (1975). Sov. Phys. Usp. **18**, 365 (1975)
77. V.M. Mostepanenko, N.N. Trunov, *The Casimir Effect and its Applications* (Clarendon, Oxford, 1997)
78. C. Genet, A. Lambrecht, S. Reynaud, Phys. Rev. A **67**, 043811 (2003)
79. M.S. Tomaš, Phys. Rev. A **66**, 052103 (2002)
80. C. Raabe, D.-G. Welsch, Phys. Rev. A **73**, 063822 (2006)
81. R.L Jaffe, Phys. Rev. D **72**, 021301 (92005)
82. T. Emig, R.L. Jaffe, M. Kardar, A. Scardicchio, Phys. Rev. Lett. **96**, 080403 (2006)
83. O. Kenneth, I. Klich, Phys. Rev. Lett. **97**, 160401 (2006)
84. O. Kenneth, I. Klich, Phys. Rev. B **78**, 014103 (2008)
85. A. Bulgac, P. Magierski, A. Wirzba, Phys. Rev. D **73**, 025007 (2006)
86. A. Lambrecht, P.A. Maia, N.S. Reynaud, New J. Phys. **8**, 243 (2006)
87. K.A. Milton, *The Casimir Effect: Physical Manifestations of Zero-Point Energy* (World Scientific, Singapore, 2001)
88. M. Bordag, G.I. Klimchitskaya, U. Mohideen, V.M. Mostepanenko, *Advances in the Casimir Effect* (Oxford University Press, Oxford, 2009)
89. D.A.R. Dalvit, P. Milonni, D. Roberts, F. da Rosa (eds.), *Casimir Physics* (Springer, Berlin, 2011)
90. W.M.R. Simpson, U. Leonhardt, *Forcen of the Quantum Vacuum: An Introduction to Casimir Physics* (World Scientific, Singapore, 2015)
91. J.R. Barnes, R.J. Stephenson, M.E. Welland, C. Gerber, J.K. Gimzewski, Nature **372**, 79 (1994)
92. B.N.J. Persson, T. Kato, H. Ueba, A.I. Volokitin, Phys. Rev. B **75**, 193404 (2007)
93. D. Polder, M. Van Hove, Phys. Rev. B **4**, 3303 (1971)
94. M.L. Levin, V.G. Polevoy, S.M. Rytov, Zh Exsp, Teor. Fiz. 79, 2087 (1980). Sov. Phys. JETP **52**, 1054 (1980)
95. J.J. Loomis, H.J. Maris, Phys. Rev. B **50**, 18517 (1994)
96. J.B. Pendry, J. Phys. A Math. Gen. **16**, 2161 (1983)
97. C. Henkel, K. Joulain, Appl. Phys. B Laser Opt. **84**, 61 (2006)
98. A. Krishnan, T. Thio, T.J. Kim, H.J. Lezec, T.W. Ebbesen, P.A. Wolf, J. Pendry, L. Martin-Moreno, F.J. Garcia-Vidal, Opt. Commun. **200**, 1 (2001)
99. A.I. Volokitin, B.N.J. Persson, Phys. Rev. Lett. **91**, 106101 (2003)
100. A.I. Volokitin, B.N.J. Persson, Phys. Rev. B **68**, 155420 (2003)
101. G. Domingues, S. Volz, K. Joulain, J.J. Greffet, Phys. Rev. Lett. **94**, 085901 (2005)
102. T.H. Forster, Ann. Phys. (Leipzig) **6**, 55 (1948)
103. C.M. Hargreaves, Phys. Lett. **30A**, 491 (1969)
104. J.-B. Xu, K. Läuger, R. Möller, K. Dransfeld, I.H. Wilson, J. Appl. Phys. **76**, 7209 (1994)
105. W. Müller-Hirch, A. Kraft, M. Hirsch, J. Parisi, A. Kittel, J. Vac. Sci. Technol. A **17**, 1205 (1999)
106. U.F. Wischnath, J. Welker, M. Munzel, A. Kittel, Rev. Sci. Instrum. **79**, 073708 (2008)
107. E.M. Lifshitz, L.P. Pitaevskii, *Statistical Physics: Theory of the Condensed State* (Pergamon Press, Oxford, 1980)
108. A. Narayanaswamy, G. Chen, Phys. Rev. B **78**, 115303 (2008)
109. S. Shen, A. Narayanaswamy, G. Chen, Nano Lett. **9**, 2909 (2009)
110. E. Rousseau, A. Siria, G. Jourdan, S. Volz, F. Comin, J. Chevrier, J.J. Greffet, Nature Photon. **3**, 514 (2009)
111. K. Kim, B. Song, V. Fernndez-Hurtado, W. Lee, W. Jeong, L. Cui, D. Thompson, J. Feist, M.T.H. Reid, F.J. Garca-Vidal, J.C. Cuevas, E. Meyhofer, P. Reddy, Nature **528**, 387 (2015)
112. T.J. Gramila, J.P. Eisenstein, A.H. MacDonald, L.N. Pfeiffer, K.W. West, Phys. Rev. Lett. 66, 1216 (1991). Surf. Sci. **263**, 446 (1992)

113. T.J. Gramila, J.P. Eisenstein, A.H. MacDonald, L.N. Pfeiffer, K.W. West, Phys. Rev. B 47, 12957 (1993). Physica B **197**, 442 (1994)
114. U. Sivan, P.M. Solomon, H. Shtrikman, Phys. Rev. Lett. **68**, 1196 (1992)
115. J.B. Pendry, J. Phys. Condens. Matter **9**, 10301 (1997)
116. J.B. Pendry, J. Mod. Opt. **45**, 2389 (1998)
117. B.N.J. Persson, Z. Zhang, Phys. Rev. B **57**, 7327 (1998)
118. G. Barton, New J. Phys. **12**, 113045 (2010)
119. J.S. Høye, I. Brevik, Entropy **15**, 3045 (2013)
120. J.S. Høye, I. Brevik, Eur. Phys. J. D **68**, 61 (2014)
121. A.I. Volokitin, B.N.J. Persson, J. Phys. Condens. Matter **11**, 345 (1999); Phys. Low-Dim.Struct. **7/8**, 17 (1998)
122. T.G. Philbin, U. Leonhardt, New J. Phys. **11**, 033035 (2009)
123. T.G. Philbin, U. Leonhardt, arXiv:0904.2148v3 [quant-ph] (2009)
124. J.B. Pendry, New J. Phys. **12**, 033028 (2010)
125. U. Leonhardt, New J. Phys. **12**, 068001 (2010)
126. A.I. Volokitin, B.N.J. Persson, New J. Phys. **13**, 068001 (2011)
127. T.G. Philbin, U. Leonhardt, New J. Phys. **13**, 68002 (2011)
128. A.I. Volokitin, B.N.J. Persson, Phys. Rev. B **78**, 155437 (2008); *ibid*, **81**, 239901 (2010)
129. A.I. Volokitin, B.N.J. Persson, Phys. Rev. B **74**, 205413 (2006)
130. D. Rugar, R. Budakian, H.J. Mamin, B.W. Chui, Nature **430**, 329 (2004)
131. J.A. Sidles, J.L. Carbini, K.J. Bruland, D. Rugar, O. Zuger, S. Hoen, C.S. Yannoni, Rev. Mod. Phys. **67**, 249 (1995)
132. G.P. Berman, G.D. Doolen, P.C. Hammel, V.I. Tsifrinovich, Phys. Rev. B **61**, 14694 (2000)
133. N. Arkani-Hamed, S. Dimopoulos, G. Dvali, Phys. Lett. B 429, 263 (1998). Sci. Am. **283**, 62 (2000)
134. B. Gotsmann, Nature Mat. **10** (2011)
135. E.V. Teodorovitch, Proc. Roy. Soc. A **362**, 71 (1978)
136. J. Mahanty, J. Phys. B: At. Mol. Phys. **13**, 4391 (1980)
137. G.V. Dedkov, A.A. Kyasov, Phys. Lett. A **259**, 38 (1999)
138. A.A. Kyasov, G.V. Dedkov, Surf. Sci. **463**, 11 (2000)
139. A.I. Volokitin, B.N.J. Persson, Phys. Rev. B **65**, 115419 (2002)
140. W.L. Schaich, J. Harris, J. Phys. F **11**, 65 (1981)
141. L.S. Levitov, Europhys. Lett. **8**, 499 (1989)
142. V.G. Polevoi, Zh Eksp, Teor. Fiz. 98, 1990 (1990). Sov. Phys. JETP **71**, 1119 (1990)
143. V.E. Mkrtchian, Phys. Lett. **207**, 299 (1995)
144. A.I. Volokitin, B.N.J. Persson, J. Phys. Condens. Matter **13**, 859 (2001)
145. M.S. Tomassone, A. Widom, Phys. Rev. B **56**, 4938 (1997)
146. M.G. Silveirinha, Phys. Rev. X **4**, 031013 (2014)
147. M.G. Silveirinha, New J. Phys. **16**, 063011 (2014)
148. M.G. Silveirinha, Phys. Rev. A **88**, 043846 (2013)
149. A.I. Volokitin, B.N.J. Persson, Phys. Rev. Lett. **106**, 094502 (2011)
150. A.I. Volokitin, B.N.J. Persson, New J. Phys. **16**, 118001 (2014)
151. G.V. Dedkov, A.A. Kyasov, Phys. Lett. A **339**, 212 (2005)
152. G.V. Dedkov, A.A. Kyasov, J. Phys. Condens. Matter **20**, 354006 (2008)
153. M.F. Maghrebi, R. Colestanian, M. Kardar, Phys. Rev. D **87**, 025016 (2013)
154. F. Intravaia, R.O. Behunin, D.A.R. Dalvit, Phys. Rev. A **89**, 050101(R) (2014)
155. G. Pieplow, C. Henkel, New J. Phys. **15**, 023027 (2013)
156. G. Pieplow, C. Henkel, J. Phys. Condens. Matter **27**, 214001 (2015)
157. V. Mkrtchian, V.A. Parsegian, R. Podgornik, W.M. Saslow, Phys. Rev. Lett. **91**, 220801 (2003)
158. G.V. Dedkov, A.A. Kyasov, Nucl. Instrum. Methods Phys. Res., Sect. B **268**, 599 (2010)
159. G. Lach, M. DeKieviet, U.D. Jentschura, Phys. Rev. Lett. **108**, 043005 (2012)
160. U.D. Jentschura, G. ach, M. De Kieviet, K. Pachucki, Phys. Rev. Lett. **114**, 043001. Published 27 January 2015
161. A.I. Volokitin, Phys. Rev. A **91**, 032505 (2015)

162. S. Kim, I. Jo, J. Nah, Z. Yao, S.K. Banerjee, E. Tutuc, Phys. Rev. B **83**, 161401 (2011)
163. R.V. Gorbachev, A.K. Geim, M.I. Katsnelson, K.S. Novoselov, T. Tudorovskyiy, T.V. Grigorieva, A.H. MacDonald, K. Watanabe, T. Taniguchi, L.P. Ponamarenko, Nature Phys. **8**, 896 (2012)
164. M. Freitag, M. Steiner, Y. Martin, V. Perebeinos, Z. Chen, J.C. Tsang, P. Avouris, Nano Lett. **9**, 1883 (2009)
165. A.I. Volokitin, B.N.J. Persson, EPL **103**, 24002 (2013)
166. M. Kisiel, E. Gnecco, U. Gysin, L. Marot, S. Rast, E. Meyer, Nat. Mater. **10**, 119122 (2011)
167. B.N.J. Persson, A.I. Volokitin, Phys. Rev. Lett. **84**, 3504 (2000)
168. J.R. Zurita-Sánchez, J.J. Greffet, L. Novotny, Phys. Rev. A **69**, 022902 (2004)
169. A.A. Chumak, P.W. Milonni, G.P. Berman, Phys. Rev. B **70**, 085407 (2004)
170. A.I. Volokitin, B.N.J. Persson, Phys. Rev. Lett. **94**, 86104 (2005)
171. A.I. Volokitin, B.N.J. Persson, H. Ueba, Phys. Rev. B **73**, 165423 (2006)
172. S. Kuehn, J.A. Marohn, R.F. Loring, J. Phys. Chem. B **110**, 14525 (2006)
173. C. Kittel, *Introduction to Solid State Physics*, 7th edn. (Wiley, New York, 1996)
174. A.S. Davydov, *Theory of Solid State* (Nauka, Moscow, 1976)
175. J. Ziman, *Electrons and Phonons* (Oxford University Press, Oxford, 1960)
176. H. Raether, *Surface Plasmon* (Springer, Berlin, 1988)
177. V. Agranovich, D. Mills, *Surface Polaritons* (North-Holland, Amsterdam, 1982)
178. E. Economou, K. Ngai, Adv. Chem. Phys. **27**, 265 (1974)
179. E.A. Vinogradov, G.N. Zhizhin, V.I. Yudson, in *Surface Polaritons*, ed. by V.M. Agranovich, D.L. Mills (North-Holland, Amsterdam, 1982), p. 145
180. E.D. Palik, *Handbook of Optical Constants of Solids* (Academic, San Diego, CA, 1985)
181. L. Mandel, E. Wolf, *Optical Coherence and Quantum Optics* (Cambridge University Press, Cambridge, 1995)
182. J. Goodman, *Statistical Optics* (Wiley, New York, 1985)
183. A.A. Abrikosov, L.P. Gor'kov, I.Y. Dzyaloshinskii, *Quantum Field Theoretical Methods in Statistical Physics* (Pergamon, Oxford., 1962)
184. L.D. Landau, E.M. Lifshitz, *Statistical Physics* (Pergamon, Oxford, 1970)
185. G.S. Agarwal, Phys. Rev. A **11**, 230 (1975)
186. H. Ibach, D.L. Mills, *Electron Energy Loss Spectroscopy and Surface Vibrations* (Academic Press, New York., 1982)
187. S. Andersson, B.N.J. Persson, Phys. Rev. Lett. **45**, 1421 (1980)
188. S. Andersson, B.N.J. Persson, Phys. Rev. Lett. **50**, 2028 (1983)
189. S. Andersson, B.N.J. Persson, M. Persson, N.D. Lang, Phys. Rev. Lett. **52**, 273 (1984)
190. B.N.J. Persson, N.D. Lang, Phys. Rev. B. **26**, 5409 (1982)
191. L.D. Landau, E.M. Lifshitz, *Electrodynamics of Continuous Media* (Pergamon, Oxford, New York, 1984)
192. J. Tersoff, D. Hamann, Phys. Rev. B **31**, 805 (1985)
193. A. Babuty, K. Joulain, P.-O. Chapuis, J.-J. Greffet, Y. De Wilde, Phys. Rev. Lett. **110**, 146103 (2013)
194. J. Schwinger, L. DeRaad, K. Milton, Ann. Phys. **115**, 1 (1978)
195. S.A. Biehs, P. Ben-Abdallah, F.S.S. Rosa, K. Joulain, J.J. Greffet, Opt. Express **19**, A1088 (2011)
196. S.-A. Biehs, P. Ben-Abdallah, F.S. Rosa, in *Infrared Radiation*, ed. by V. Morozhenko (InTech, Rijeka, Croatia, 2012), ch. 1
197. E.M. Lifshitz, L.P. Pitaevskii, *Physical Kinetics* (Pergamon, Oxford, 1981)
198. K.L. Kliewer, R. Fuchs, Phys. Rev. 172, 607 (1968); R. Fuchs, K.L. Kliewer. Phys. Rev. **186**, 905 (1969)
199. D.C. Langreth, Phys. Rev. B **39**, 10020 (1989)
200. P. Senet, J.P. Toennis, G. Witte, Chem. Phys. Lett. **299**, 389 (1999)
201. B.N.J. Persson, M. Persson, Solid State Commun. **36**, 175 (1980)
202. M.H. Gordon, J.C. Tully, Phys. Rev. B **46**, 1853 (1992)
203. B.N.J. Persson, Phys. Rev. B **44**, 3277 (1991)

204. H.C. Chang, G.E. Ewing, in *Vibrations at surfaces 1990*, ed. by Y.T. Chabal, F.M. Hoffmann, G.P. Williams (Elsevier 1990), p. 39
205. A.I. Volokitin, B.N.J. Persson, in *Inelastic Energy Transfer in Interactions with Surfaces and Adsorbates*, ed. by B. Gumhalter, A.C. Levi, F. Flores (World Scientific, Singapore 1993), pp. 217–248
206. O.M. Braun, A.I. Volokitin, V.P. Zhdanov, Sov. Phys. Usp. **32**, 605 (1989)
207. T. Komeda, Y. Kim, M. Karai, B.N.J. Persson, H. Ueba, Science **295**, 2055 (2002)
208. J.I. Pascual, N. Lorente, Z. Song, H. Conrad, H.-P. Rust, Nature **432**, 525 (2003)
209. H.C. Chang, H.H. Richardson, G.E. Ewing, J. Chem. Phys. **89**, 7561 (1988)
210. J.D. Beckerle, M.P. Casassa, E.J. Heilweil, R.R. Cavanagh, J.C. Stephenson, in *Vibrations at Surfaces*, ed. by Y.T. Chabal, F.M. Hoffmann, G.P. Williams (Elsevier, 1990), p. 17
211. J.R. Hahn, W. Ho, Phys. Rev. Lett. **87**, 166102 (2001)
212. M. Brownnutt, M. Kumph, P. Rabl, R. Blatt, Rev. Mod. Phys. **87**, 1419 (2015)
213. B.N.J. Persson, J. Chem. Phys. **115**, 3840 (2001)
214. P. Ben-Abdallah, S.-A. Biehs, K. Joulain, Phys. Rev. Lett. **107**, 114301 (2011)
215. B. Derjaguin, Kolloid-Z. **69**, 155 (1934)
216. J. Blocki, J. Randrup, W.J. Swiatecki, C.F. Tsang, Ann. Phys. (N.Y) **105**, 427 (1977)
217. U. Hartmann, Phys. Rev. B **42**, 1541 (1990); **43**, 2404 (1991)
218. P. Johansson, P. Apell, Phys. Rev. B **56**, 4159 (1997)
219. R. Messina, M. Antezza, Phys. Rev. A **84**, 042102 (2011)
220. M. Kruger, G. Bimonte, T. Emig, M. Kardar, Phys. Rev. B **86**, 115423 (2012)
221. G. Bimonte, Phys. Rev. A **80**, 042102 (2009)
222. S.J. Rahi, T. Emig, N. Graham, R.L. Jaffe, M. Kardar, Phys. Rev. D **80**, 085021 (2009)
223. M. Kruger, T. Emig, M. Kardar, Phys. Rev. Lett. **106**, 210404 (2011)
224. R. Messina, M. Antezza, EPL **95**, 61002 (2011)
225. A.P. McCauley, M.T.H. Reid, M. Kruger, S.G. Johnson, Phys. Rev. B **85**, 165104 (2012)
226. R. Guerout, J. Lussange, F.S.S. Rosa, J.P. Hugonin, D.A.R. Dalvit, J.J. Greffet, A. Lambrecht, S. Reynaud, Phys. Rev. B **85**, 180301(R) (2012)
227. J. Lussange, R. Guerout, F.S.S. Rosa, J.J. Greffet, A. Lambrecht, S. Reynaud, Phys. Rev. B **86**, 085432 (2012)
228. C. Otey, S.H. Fan, Phys. Rev. B **84**, 245431 (2011)
229. H. Schmid, H. Biebuyck, B. Michel, O.J.F. Martin, Appl. Phys. Lett. **72**, 2379 (1998)
230. W.L. Schaich, J. Chem. Phys. **60**, 1087 (1874); Solid. State Commun. **15**, 357 (1974)
231. E.G. d'Agliano, P. Kumar, W. Schaich, H. Suhl, Phys. Rev. B **11**, 2122 (1975)
232. A. Nourtier, J. Phys. **38**, 479 (1977)
233. G. Mahan, *Many-particle Physics*, 2nd edn. (Plenum Press, New York, 1990)
234. B.N.J. Persson, A. Baratoff, Phys. Rev. B **38**, 9616 (1998)
235. P. Debye, *Polar Molecules* (Chemical Catalog Co., New York, 1929). Chapter V
236. B.E. Sernelius, *Surface Modes in Physics* (WILEY-VCH Verlag Berlin, 2001). Chap. 2
237. B.J. Hinch, A. Lock, H.H. Madden, J.P. Toennies, G. Witte, Phys. Rev. B **42**, 1547 (1990)
238. J. Krim, D.H. Solina, R. Chiarello, Phys. Rev. Lett. **66**, 181 (1991)
239. H. Grabborn, A. Otto, D. Schumacher, B.N.J. Persson, Surf. Sci. **264**, 327 (1992)
240. B.N.J. Persson, D. Schumacher, A. Otto, Chem. Phys. Lett. **178**, 204 (1991)
241. J.B. Sokoloff, Phys. Rev. B **52**, 5318 (1995)
242. B.N.J. Persson, Phys. Rev. B **44**, 3277 (1991)
243. B.N.J. Persson, A.I. Volokitin, J. Chem. Phys. **103**, 8679 (1995)
244. B.N.J. Persson, E. Zaremba, Phys. Rev. B **31**, 1863 (1985)
245. B.N.J. Persson, S. Andersson, Phys. Rev. B **29**, 4382 (1984)
246. A. Liebsch, Phys. Rev. Lett. **54**, 67 (1985)
247. C. Holzapfel, F. Stubenrauch, D. Schumacher, A. Otto, Thin Solid Films **188**, 7 (1990)
248. K. Wandelt, W. Jacob, N. Memmel, V. Dose, Phys. Rev. Lett. **57**, 1643 (1986)
249. M. Fuhrmann, C. Wöll, Surf. Sci. **368**, 20 (1996)
250. B.N.J. Persson, R. Ryberg, Phys. Rev. B **32**, 3586 (1985)

251. P.J.E. Peebles, *Principles of Physical Cosmology* (Princeton University Press, Princeton, NY, 1993)
252. J.M. Kovac, E.M. Leitch, C. Pryke, J.E. Carlstom, N.W. Halverson, W.L. Holzapfel, Nature (London) **420**, 772 (2002)
253. L.D. Landau, E.M. Lifshitz, *The Classical Theory of Field* (Pergamon, Oxford, 1975)
254. A. Einstein, L. Hopf, Ann. Phys. (Leipzig) **33**, 1105 (1910)
255. M.B. Pogrebinskii, Fiz. Tekh. Poluprovodn. **11**, 637 (1977); Sov. Phys. Semicond. **11**, 372 (1977)
256. P.J. Price, Physica B+C **117**, 750 (1983)
257. L. Zheng, A.H. MacDonald, Phys. Rev. B **48**, 8203 (1993)
258. H.C. Tso, P. Vasilopoulos, Phys. Rev. B **45**, 1333 (1992)
259. A.-P. Jauho, H. Smith, Phys. Rev. B **47**, 4420 (1993)
260. K. Flensberg, B.Y.-K. Hu, A.-P. Jauho, J. Kinaret, Phys. Rev. B **52**, 14761 (1995)
261. A. Kamenev, Y. Oreg, Phys. Rev. B **52**, 7516 (1995)
262. S. Ghost, A.K. Sood, N. Kumar, Science **299**, 1042 (2003)
263. S. Ghost, A.K. Sood, S. Ramaswamy, N. Kumar, Phys. Rev. B **70**, 205423 (2004)
264. A.E. Cohen, Science **300**, 1235 (2003)
265. S. Ghosh, A.K. Sood, N. Kumar, Science **300**, 1235 (2003)
266. P. Král, M. Shapiro, Phys. Rev. Lett. **86**, 131 (2001)
267. M. Das, S. Ramaswamy, A.K. Sood, G. Ananthakrishna, Phys. Rev. E **73**, 061409 (2006)
268. B.N.J. Persson, U. Tartaglino, E. Tosatti, H. Ueba, Phys. Rev. B **69**, 235410 (2004)
269. A.I. Volokitin, B.N.J. Persson, Phys. Rev. B **77**, 033413 (2008)
270. K.S. Novoselov, A.K. Geim, S.V. Morozov, D. Jiang, Y. Zhang, S.V. Dubonos, I.V. Grigorieva, A.A. Firsov, Science **306**, 666 (2004)
271. K.S. Novoselov, A.K. Geim, S.V. Morozov, M.I. Katsnelson, I.V. Grigorieva, S.V. Dubonos, A.A. Firsov, Nature (London) **438**, 197 (2005)
272. A.K. Geim, K.S. Novoselov, Nat. Mater. **6**, 183 (2007)
273. A.K. Geim, Science **324**, 1530 (2009)
274. M. Bordag, B. Geyer, G.L. Klimchitskaya, V.M. Mostepanenko, Phys. Rev. B **74**, 205431 (2006)
275. M. Bordag, I.V. Fialkovsky, D.M. Gitman, D.V. Vassilevich, Phys. Rev. B **80**, 245406 (2009)
276. D. Drosdoff, L.M. Woods, Phys. Rev. A **84**, 062501 (2011)
277. D. Drosdoff, L.M. Woods, Phys. Rev. B **82**, 155459 (2010)
278. I.V. Fialkovsky, V.N. Marachvsky, D.V. Vassilevich, Phys. Rev. B **84**, 035446 (2011)
279. B.E. Sernelius, EPL **95**, 57003 (2011)
280. V. Svetovoy, Z. Moktadir, M. Elwenspoek, H. Mizuta, EPL **96**, 14006 (2011)
281. J. Sarabadani, A. Naji, R. Asgari, R. Podgornik, Phys. Rev. B **84**, 155407 (2011)
282. G. Gómez-Santos, Phys. Rev. B **95**, 245424 (2009)
283. B. Shapiro, Phys. Rev. B **82**, 075205 (2010)
284. P.A. Cherenkov, Dokl. Akad. Nauk. SSSR **2**, 451 (1934); Comptes. Rendus Acad. Science USSSR **2**, 451 (1934)
285. S.I. Vavilov, Dokl. Akad. Nauk. SSSR **2**, 457 (1934); Comptes. Rendus Acad. Science USSSR **2**, 457 (1934)
286. P.A. Cherenkov, Phys. Rev. **52**, 378 (1937)
287. I.E. Tamm, I.M. Frank, Dokl. Akad. Nauk. SSSR **14**, 107 (1937); Comptes. Rendus Acad. Science USSSR **14**, 107 (1937)
288. I.E. Tamm, Usp. Phys. Nauk 68, 387 (1959). Science **131**, 206 (1960)
289. V.L. Ginzburg, Phys. -Usp. **39**, 973 (1996)
290. I.M. Frank, J. Phys. USSR **7**, 49 (1943)
291. V.L. Ginzburg, J. Phys. USSR **9**, 353 (1945)
292. B.M. Bolotovskii, Sov. Phys.-Usp. **4**, 781 (1962)
293. V.P. Frolov, V.L. Ginzburg, Phys. Lett. A **116**, 423 (1986)
294. Y.B. Zel′dovich, JETP Lett. **14**, 180 (1971)

295. S. Jahani, Z. Jacob, Nat. Nanotech. 11, 23 (2016); PSSR B.N.J. Persson. Surf. Sci. Rep. **61**, 201 (2006)
296. B.N.J. Persson, B. Lorenz, A.I. Volokitin, Eur. Phys. J. E **31**, 3 (2010)
297. E.T. Swartz, R.O. Pohl, Rev. Mod. Phys. **61**, 605 (1989)
298. B.V. Budaev, D.B. Bogy, J. Phys. A: Math. Theor. **43**, 425201 (2010)
299. R. Prasher, Appl. Phys. Lett. **94**, 041905 (2009)
300. S. Doniach, E.H. Sondheimer, *Green's Functions for Solid State Physics* (Benjamin, New York, 1974)
301. B.N.J. Persson, J. Chem. Phys. **115**, 3840 (2001)
302. B.N.J. Persson, R. Ryberg, Phys. Rev. B **32**, 3586 (1985)
303. A. Fasolino, J.H. Los, M.I. Katsnelson, Nature **6**, 858 (2007)
304. In [302] we have calculated $\xi' = \xi_\perp/8\pi$ within the elastic continuum model. It only depends on the ratio $\lambda = c_\mathrm{T}/c_\mathrm{L}$. For $\lambda = 0.5$ the contribution to $\xi_\perp$ from emission of surface phonons is 2.10 and the contribution from bulk longitudinal and transverse phonons is 1.19, giving $\xi' = (2.10 + 1.19)/8\pi \approx 0.13$
305. P.L. Kapitza, J. Phys. (USSR) **4**, 181 (1941)
306. G.L. Pollack, Rev. Modern Phys. **41**, 48 (1969)
307. J.I. Gittleman, S. Bozowski, Phys. Rev. **128**, 646 (1962)
308. L.J. Challis, K. Dransfeld, J. Wilks, Proc. Roy. Soc. (London) **A260**, 31 (1961)
309. In the calculation we have used: Sound velocity and mass density of ^{4}He: $c_{L0} = 238$ m/s and $\rho_0 = 150$ kg/m^3. Sound velocity and mass density of a-SiO_2: $c_{T1} = 3743$ m/s, $c_{L1} = 5953$ m/s, and $\rho_1 = 2200$ kg/m^3
310. A.K. Geim, K.S. Novoselov, Nat. Mater. **6**, 183 (2007)
311. M. Boninsegni, J. Low Temp Phys. **159**, 441 (2010)
312. Z.-Y. Ong, E. Pop, Phys. Rev. B **81**, 155408 (2010)
313. M. Fuhrmann, C. Wöll, New J. Phys. **1**, 1 (1998)
314. H. Maune, H.-Y. Chiu, M. Bockrath, Appl. Phys. Lett. **89**, 013109 (2006)
315. Z. Chen, W. Jang, W. Bao, C.N. Lau, C. Dames, Appl. Phys. Lett. **95**, 161910 (2009)
316. W. Steurer, A. Apfolter, M. Koch, W.E. Ernst, B. Holst, E. Sondergard, S.C. Parker, Phys. Rev. B **78**, 035402 (2008)
317. N.D. Lang, W. Kohn, Phys. Rev. B **3**, 1215 (1971)
318. C.C. Speake, C. Trenkel, Phys. Rev. Lett. **90**, 160403 (2003)
319. Z.H. Liu, N.M.D. Brown, A. McKinley, J. Phys.: Condens. Matter **9**, 59 (1997)
320. F. Rossi, G.I. Opat, J. Phys. D **25**, 1349 (1992)
321. C.R. Lide (ed.), *CRC Handbook of Chemistry and Physics*, 82nd edn. (CRC Press, BOCA Raton, FL, 2001)
322. C.I. Sukenik et al., Phys. Rev. Lett. **70**, 560 (1993)
323. S. Hudlet, M.S. Jean, C. Guthmann, J. Berger, Eur. Phys. J. B **2**, 5 (1998)
324. T.D. Stowe, W. Kenn, D.J. Thomson, D. Rugar, Appl. Phys. Lett. **75**, 2785 (1999)
325. K.-T. Wan, J. Am. Ceram. Soc. **75**, 667 (1992)
326. C.G. Camara, J.V. Escobar, J.R. Hird, S.J. Putterman, Nature **455**, 1089 (2008)
327. C.G. Camara, J.V. Escobar, J.R. Hird, S.J. Putterman, J. Appl. Phys. B **99**, 613 (2010)
328. A.R. Akande, J. Lowell, J. Phys. D: Appl. Phys. **20**, 565 (1987)
329. J. Lowell, W.S. Truscott, J. Phys. D: Appl. Phys. **19**, 1281 (1986)
330. S. Wang, L. Lin, Y. Xie, Q. Jing, S. Niu, Z.L. Wang, Nanoletters (2013)
331. D.J. Lacks, R.M. Sankaran, J. Phys. D: Appl. Phys. **44**, 453001 (2011)
332. B.N.J. Persson, J. Phys.: Condens. Matter **20**, 312001 (2008)
333. C. Campana, M.H. Müser, M.O. Robbins, J. Phys.: Condens. Matter **20**, 354013 (2008)
334. B.N.J. Persson, A. Kovalev, M. Wasem, E. Gnecco, S.N. Gorb, EPL **92**, 46001 (2010)
335. P. Lazic, B.N.J. Persson, EPL **91**, 46003 (2010)
336. S. Soh, S.W., Kwok, H. Liu, G.W. Whitesides. J. Am. Chem. Soc. **134**, 20151 (2012)
337. B.V. Derjaguin, V. Smilga, J. Appl. Phys. **38**, 4609 (1967)
338. B.V. Derjaguin, Prog. Surf. Sci. **45**, 223 (1994)
339. A.D. Roberts, J. Phys. D: Appl. Phys. **10**, 1801 (1977)

340. M.M. Apodaca, P.J. Wesson, K.J.M. Bishop, M.A. Ratner, B.A. Grzybowski, Angew. Chem. Int. Ed. **49**, 946 (2010)
341. H.T. Baytekin, A.Z. Patashinski, M. Branicki, B. Baytekin, S. Soh, B.A. Grzybowski, Science **333**, 308 (2011)
342. B. Baytekin, H.T. Baytekin, B.A. Grzybowski, J. Am. Chem. Soc. **134**, 7223 (2012)
343. K. Brörmann, K. Burger, A. Jagota, R. Bennewitz, J. Adhes. **88**, 598 (2012)
344. J.E. Lennard-Jones, B.M. Dent, Trans. Faraday Soc. **24**, 92 (1928)
345. A. Naji, D.S. Dean, J. Sarabadani, R.R. Horgan, R. Podgornik, Phys. Rev. Lett. **104**, 060601 (2010)
346. B. Lorenz, B.A. Krick, N. Mulakaluri, M. Smolyakova, S. Dieluweit, W.G. Sawyer, B.N.J. Persson, J. Phys.: Condens. Matter **25**, 225004 (2013)
347. Sylgard- 184, Materials Safety Data Sheet, Dow Corning Corporation, Midland, MI
348. K.H. Kim, M.K. Chaudhury, J. Adhes. **85**, 792 (2009)
349. B.N.J. Persson, Phys. Rev. Lett. **81**, 3439 (1998)
350. M.K. Chaudhury, J. Phys. Chem. B **103**, 6562 (1999)
351. L.D. Landau, E.M. Lifshitz, *Theory of Elasticity* (Pergamon, Oxford, 1970)
352. F.A. McClintock, A.S. Argon, *Mechanical Behavior of Material* (Reading, Massachusetts, Agdison-Wesley, 1966)
353. B.N.J. Persson, *Sliding Friction: Physical Principle and Applications*, 2nd edn. (Springer, Heidelberg, 2000)
354. N.D. Mermin, Phys. Rev. B **1**, 2362 (1970)
355. B. Wunscvh, T. Stauber, F. Sols, F. Guinea, New J. Phys. **8**, 318 (2006)
356. E.H. Hwang, S. Das, Sarma. Phys. Rev. B **75**, 205418 (2007)
357. J.H. Chen, C. Jang, S. Xiao, M. Ishigami, M.S. Fuhrer, Nat. Nanotechnol. **3**, 206 (2008)
358. D.Z.A. Chen, R. Hamam, M. Soljacic, J.D. Joannopoulos, G. Chen, Appl. Phys. Lett. **90**, 181921 (2007)
359. K. Saitoh, K. Hayashi, Y. Shibayama, K. Shirahama, Phys. Rev. Lett. **105**, 236103 (2010)
360. S.V. Rotkin, V. Perebeinos, A.G. Petrov, P. Avouris, Nano Letters **9**, 1850 (2009)
361. V. Perebeinos, P. Avouris, Phys. Rev. B **81**, 195442 (2010)
362. W.K. Tse, B.-K. Hu, S. DasSarma, Phys. Rev. B **76**, 081401 (2007)
363. M.I. Katsnelson, Phys. Rev. B **84**, 041407(R) (2011)
364. N.M.R. Peres, J.M.R. Lopes des Santos, A.H. Castro Neto. Europhys. Lett **95**, 18001 (2011)
365. E.H. Hwang, R. Sensarma, S. DasSarma, Phys. Rev. B **84**, 245441 (2011)
366. B.N. Narozhny, M. Titov, I.V. Gornyi, P.M. Ostrovsky, Phys. Rev. B **85**, 195421 (2012)
367. M. Carrega, T. Tudorovskiy, A. Principi, M.I. Katsnelson, M. Polini, New J. Phys. **14**, 063033 (2012)
368. B. Amorin, N.M.R. Peres, J. Phys.: Condens. Matter. **24**, 335602 (2012)
369. A.I. Volokitin, B.N.J. Persson, Phys. Rev. B **83**, 241407(R) (2011)
370. B.N.J. Persson, H. Ueba, Eur. Phys. Lett. **91**, 56001 (2010)
371. B.N.J. Persson, H. Ueba, J. Phys.: Condens. Matter **22**, 462201 (2010)
372. J.C. Meyer, A.K. Geim, M.I. Katsnelson, K.S. Novoselov, T.J. Booth, S. Roth, Nature (London) **446**, 60 (2007)
373. B.N.J. Persson, J. Phys.: Condens. Matter **18**, 7789 (2006)
374. B.N.J. Persson, J. Chem. Phys. **143**, 224701 (2015)
375. For a review of thermal joint resistance models for rough surfaces, see, e.g., M. Bahrami, J.R. Culham, M.M. Yanavovich, G.E. Schneider, Appl. Mech. Rev. **59**, 1 (2006)
376. J.A. Greenwood, J.B.P. Williamson, Proc. Roy. Soc. London A **295**, 300 (1966)
377. A.W. Bush, R.D. Gibson, T.R. Thomas, Wear **35**, 87 (1975)
378. C. Campana, M.H. Müser, M.O. Robbins, J. Phys.: Condens. Matter **20**, 354013 (2008)
379. G. Carbone, F. Bottiglione, J. Mech. Phys. Solids **56**, 2555 (2008). See also Appendix A in B.N.J. Persson et al., J. Phys.: Condens. Matter **20**, 395006 (2008)
380. B.N.J. Persson, J. Phys.: Condens. Matter **20**, 312001 (2008)
381. B.N.J. Persson, F. Bucher, B. Chiaia, Phys. Rev. B **65**, 184106 (2002)
382. B.N.J. Persson, J. Chem. Phys. **115**, 3840 (2001); B.N.J. Persson, Eur. Phys. J. E**8**, 385 (2002)

383. B.N.J. Persson, Phys. Rev. Lett. **99**, 125502 (2007)
384. C. Yang, B.N.J. Persson, J. Phys.: Condens. Matter **20**, 215214 (2008)
385. B.N.J. Persson, Surf. Sci. Rep. **61**, 201 (2006)
386. B.N.J. Persson, C. Yang, J. Phys.: Condens. Matter **20**, 315011 (2008)
387. M. Borri-Brunetto, B. Chiaia, M. Ciavarella, Comput. Methods Appl. Mech. Eng. **190**, 6053 (2001)
388. L. Pei, S. Hyun, J.F. Molinari, M.O. Robbins, J. Mech. Phys. Solids **53**, 2385 (2005)
389. See, e.g., B.N.J. Persson, O. Albohr, U. Tartaglino, A.I. Volokitin, E. Tosatti, J. Phys. Condens. Matter **17**, R1 (2005)
390. B.N.J. Persson, *Sliding Friction: Physical Principles and Applications*, 2nd edn. (Springer, Heidelberg, 2000)
391. C. Yang, U. Tartaglino, B.N.J. Persson, Eur. Phys. J. E **19**, 47 (2006)
392. S. Hyun, L. Pei, J.F. Molinarie, M.O. Robbins, Phys. Rev. E **70**, 026117 (2004)
393. Y.F. Mo, K.T. Turner, I. Szlufarska, Nature **457**, 1116 (2009)
394. J.A. Greenwood, Brit. J. Appl. Phys. **17**, 1621 (1966)
395. J.R. Barber, Proc. R. Soc. London A **459**, 53 (2003)
396. J.F. Archard, Wear **2**, 438 (1959)
397. B.N.J. Persson, Tribology Lett. **54**, 99 (2014)
398. D. Pires, B. Gotsmann, F. Porro, D. Wiesmann, U. Duerig, A. Knoll, Langmuir **25**, 5141 (2009)
399. D. Segal, A. Nitzan, Chem. Phys. 268, 315 (2001). Chem. Phys. **281**, 235 (2002)
400. Y. Selzer, M.A. Cabassi, T.S. Mayer, D.L. Allara, Nanotechnology **15**, S483 (2004)
401. V. Popov, *Kontaktmechanik und Reibung* (Springer, Heidelberg, 2009)
402. M. Bahrami, J.R. Culham, M.M. Yanavovich, *Proceedings of IMECE 2003* (Washington, USA, 2003)
403. M. Bahrami, M.M. Yanavovich, J.R. Culham, J. Thermophys. Heat Transf. **18**, 326 (2004)
404. B.N.J. Persson, J. Phys.: Condens. Matter **20**, 315007 (2008)
405. K.L. Johnson, *Contact Mechanics* (Cambridge University Press, Cambridge, 1985)
406. L. Shi, A. Majumdar, J. Heat Transf. **124**, 329 (2002)
407. C. Yang, B.N.J. Persson, J. Israelachvili, K. Rosenberg, Eur. Phys. Lett. **84**, 46004 (2008)
408. In [385] we used $A_{\rm pl}/A_{\rm pl}^0$ instead of $(A_{\rm pl}/A_{\rm pl}^0)^6$ in the expression for $\bar{C}$, but we have found that the latter (more rapid) cut-off, gives better results: The contact area as a function of magnification, for elastic contact with the latter $\bar{C}$, gives virtually the same result as the calculated (total) contact area using the elastoplastic contact mechanics theory and the original surface roughness power spectrum
409. B.S. Oh, Y.N. Kim, N.J. Kim, H.Y. Moon, H.W. Park, Tire. Sci. Technol. **23**, 11 (1995)
410. H. Yüncü, Heat Mass Transf. **43**, 1 (2006)
411. M.M. Yavanovich, AIAA-86-1164, *Presented at 16th thermo Physics Conference* (Polo Alto, CA, USA, 1981)
412. As an example, using AFM we have measured the height profile of a polished steel surface over a $10\mu{\rm m} \times 10\mu{\rm m}$ surface area with the resolution $a = 20$ nm. From the numerical data we calculated the root-mean-square (rms) roughness $h_{\rm rms} \approx 0.1$ μm and the rms slope $s \approx 0.6$. Increasing the lateral resolution would increase the slope further since the slope is mainly determined by the short wavelength roughness
413. It may be argued that, due to plastic deformation, the slope in (71) should be calculated including only the roughness with wavelength above some cut-off length. However, no discussion of this point was presented in [411]
414. L.D. Landau, E.M. Lifshitz, *Fluid Mechanics* (Pergamon Press, Oxford, 1959)
415. J. Mc Allen, A.M. Cuitino, V. Sernas, *Finite Elements in Analysis and Design*. **23**, 265 (1996)
416. C.O. Popiel, L. Boguslawski, Int. J. Heat Mass Transf. **18**, 170 (1975)
417. R.J. Cannara, M.J. Brukman, K. Cimatu, A.V. Sumant, S. Baldelli, R.W. Carpick, Science **318**, 780 (2007)
418. J.Y. Park, D.F. Ogletree, P.A. Thiel, M. Salmeron, Science **313**, 186 (2006)
419. A. Dayo, W. Alnasrallah, J. Krim, Phys. Rev. Lett. **80**, 1690 (1998)

420. B.N.J. Persson, Solid State Commun. **115**, 145 (2000)
421. J.R. Schrieffer, *Theory of Superconductivity* (Benjamin, 1966)
422. A.I. Volokitin, B.N.J. Persson, H. Ueba, J. Exp. Theor. Phys. **104**, 96 (2007)
423. J. Bardeen, L.N. Cooper, J.R. Schrieffer, Phys. Rev. **108**, 1175 (1957)
424. R.W. Morse, H.V. Bohm, Phys. Rev. **108**, 1094 (1957)
425. B.N.J. Persson, Surf. Sci. **401**, 445; **401**, 445 (1998)
426. B. Lorez, Y.R. Oh, S.K. Nam, S.H. Keon, B.N.J. Persson, J. Chem. Phys. **142**, 194701 (2015)

Index

A.I. Volokitin and B.N.J. Persson, *Electromagnetic Fluctuations at the Nanoscale*, NanoScience and Technology, DOI 10.1007/978-3-662-53474-8